NASA Contractor Report 3596

Free-Jet Investigation of Mechanically Suppressed, High-Radius-Ratio Coannular Plug Model Nozzles

B. A. Janardan, R. K. Majjigi,
J. F. Brausch, and P. R. Knott

CONTRACT NAS3-21608
MAY 1985

Date for general release May 1987

NASA

NASA Contractor Report 3596

Free-Jet Investigation of Mechanically Suppressed, High-Radius-Ratio Coannular Plug Model Nozzles

B. A. Janardan, R. K. Majjigi,
J. F. Brausch, and P. R. Knott
General Electric Company
Cincinnati, Ohio

Prepared for
Lewis Research Center
under Contract NAS3-21608

National Aeronautics
and Space Administration

Scientific and Technical Information Branch

1985

TABLE OF CONTENTS

TABLE OF CONTENTS (Concluded)

1.0 INTRODUCTION

The General Electric Company has been involved in exploratory acoustic and aerodynamic performance measurements on scale-model unsuppressed and mechanically suppressed coannular plug nozzles with inverted velocity and temperature profiles. These studies, under the sponsorship of NASA-Lewis Research Center, are directed toward the development of jet noise technology that is applicable for advanced high speed aircrafts. This report summarizes the results of one such investigation specifically directed to obtain flight simulated acoustic data on mechanically suppressed coannular plug nozzles and convergent-divergent terminated unsuppressed coannular plug nozzles. A companion Comprehensive Data Report (Reference 1) contains the detailed test data.

Nine coannular configurations along with a reference conical nozzle were evaluated in General Electric's Anechoic Free-Jet Facility. A total of 212 acoustic test points and velocity measurements on a selected number of plumes using the laser velocimeter were conducted over a wide range of exhaust nozzle conditions under both static and simulated flight conditions. The tested suppressed nozzles included configurations with 20- and 40-shallow-chute mechanical suppressors in the outer stream. The tested unsuppressed configurations included annular and coannular plug nozzles with convergent and convergent-divergent (C-D) terminations in order to evaluate the C-D effectiveness in the reduction of shock-cell noise. Details of test configurations and scope of acoustic and laser velocimeter tests are presented in Section 2.0.

The measured acoustic and diagnostic data are discussed in Section 3.0. The discussion includes verification of the procedures adopted to scale model-scale static acoustic data of convergent unsuppressed coannular nozzles to engine size configurations. The model nozzle data of this program are compared with data obtained during GE/NASA YJ101/VCE test-bed engine program. The acoustic data of the suppressor configurations are compared with those of baseline, conical and similitude coannular plug nozzles in order to establish the suppression levels obtainable with the tested configurations. At mixed jet velocity of 700 m/sec (~2300 fps), the similitude 20-shallow-chute suppressor configuration yielded peak aft quadrant suppression of 11.5 and 9 PNdB and forward quadrant suppression of 7 and 6 PNdB relative to a baseline conical nozzle during static and simulated flight (122 m/sec or 400 fps), respectively. No significant acoustic benefit is indicated in both the front and the aft quadrants with a C-D inner termination on the similitude 20-shallow-chute suppressor nozzle instead of the convergent inner termination. In addition, the static pressures measured in the base region of the chutes of the suppressor nozzles indicated that the gas total temperature has little influence on suppressor base drag. The C-D termination on unsuppressed annular and coannular plug nozzles is shown to reduce front quadrant noise under both static and simulated flight conditions. However, for a given V_J^{mix}, the coannular plug nozzle with both streams C-D terminated resulted in higher noise level in the aft quadrant compared to the convergent coannular plug nozzle. However, based on available data, this increase in the aft angle PNL data is attributed to the lower radius ratio of the model C-D nozzle relative to the convergent nozzle.

Details of the engineering spectral prediction method formulated for suppressed coannular plug nozzles are provided in Section 4.0. Appropriate length and velocity scales have been identified, and a new convection amplification model has been developed.

2.0 DESCRIPTIONS OF TEST FACILITY AND SCALE-MODEL NOZZLES

All of the acoustic and laser velocimeter tests of this program were conducted in the General Electric Anechoic Free-Jet Facility located in Evendale, Ohio. Brief descriptions of the facility, data acquisition and reduction procedures, and scale-model test nozzles are presented in this section. Detailed descriptions of the facility and acoustic data acquisition, reduction, and flight transformation procedures are provided in the Comprehensive Data Report (Ref. 1) of this program and in References 2 through 5.

Tabulations that summarize the aerodynamic flow conditions of the acoustic, laser velocimeter (LV) and base pressure tests conducted with the scale-model configurations of this investigation are presented in Appendices I through III, respectively.

2.1 ANECHOIC FREE-JET FACILITY

The test facility, schematically shown in Figure 2-1, is a cylindrical chamber having a diameter of 13.1 meters (42 feet) and a height of 21.95 meters (72 feet). The inner surfaces of the chamber are lined with anechoic wedges made of fiberglass to yield a low frequency cutoff below 220 Hz and an absorption coefficient of 0.99 above 220 Hz.

A tertiary duct surrounds the model nozzles with the necessary airflow to simulate a forward flight up to a Mach number of 0.36. The tertiary air passes through a silencer plenum chamber before it is discharged through the 1.22 meter (4 feet) free-jet exhaust. An overhead view of the tertiary exhaust surrounding a test conical nozzle is presented in Figure 2-2.

2.2 ACOUSTIC DATA ACQUISITION AND REDUCTION SYSTEMS

A schematic of the microphone data acquisition system used to obtain the acoustic data during tests in the anechoic chamber is shown on Figure 2-3. This system is optimized for obtaining the acoustic data up through the 80 kHz 1/3-octave center frequency. The microphones used to obtain the data are the B&K 4135, 0.64-centimeter (0.25 inch) condenser microphones for far-field measurements. All the tests are conducted with microphone grid caps removed to obtain the best frequency response. The cathode followers are the transistorized B&K 2619 for optimum frequency response and lower inherent system noise characteristics. All systems utilize the B&K 2801 power supply operated in the direct mode.

The output of the power supply is connected to a line driver adding 10 dB of amplification to the signal as well as adding "preemphasis" to the high frequency portion of the spectrum. The net effect of this amplifier is a 10 dB gain at all frequencies, plus an additional 3 dB at 40 kHz and 6 dB at 80kHz due to "preemphasis." This procedure improves low amplitude, high frequency data. In order to remove low frequency noise, high-pass filters with attenuations of approximately 26 dB at 12.5 Hz and decreasing to 0 dB at 200 Hz are installed in the system.

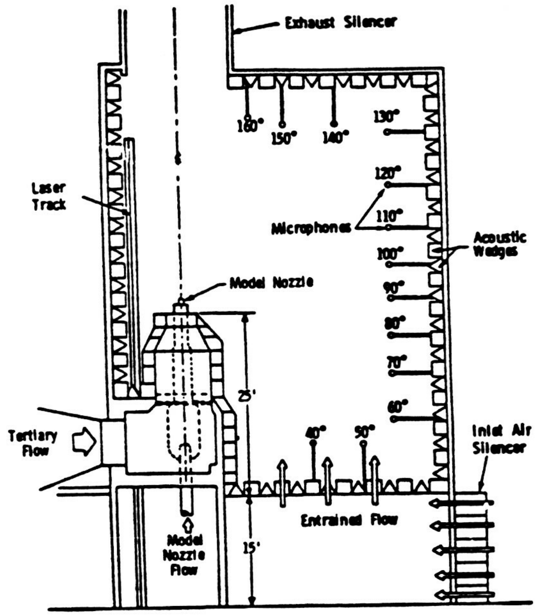

Angle (Degrees)	Radial Distance m	Radial Distance ft
40	7.92	26.0
50	9.48	31.1
60	9.50	31.18
70	8.76	28.73
80	8.36	27.42
90	8.23	27.00
100	8.36	27.42
110	8.76	28.73
120	9.5	31.18
130	10.74	35.25
140	9.17	30.17
150	8.23	27.0
160	7.92	26.0

Microphone Arrangement

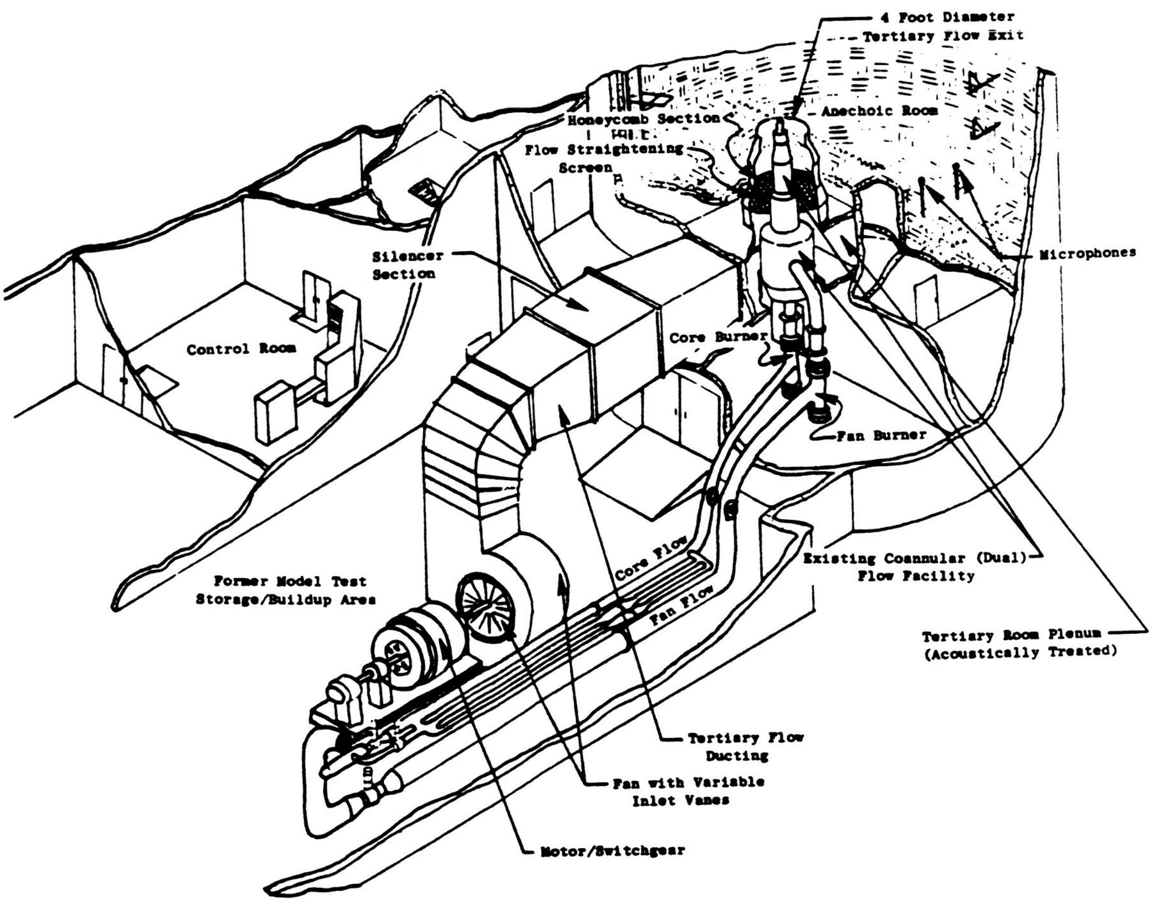

Figure 2-1. Anechoic Free-Jet/Jet Noise Facility Schematic.

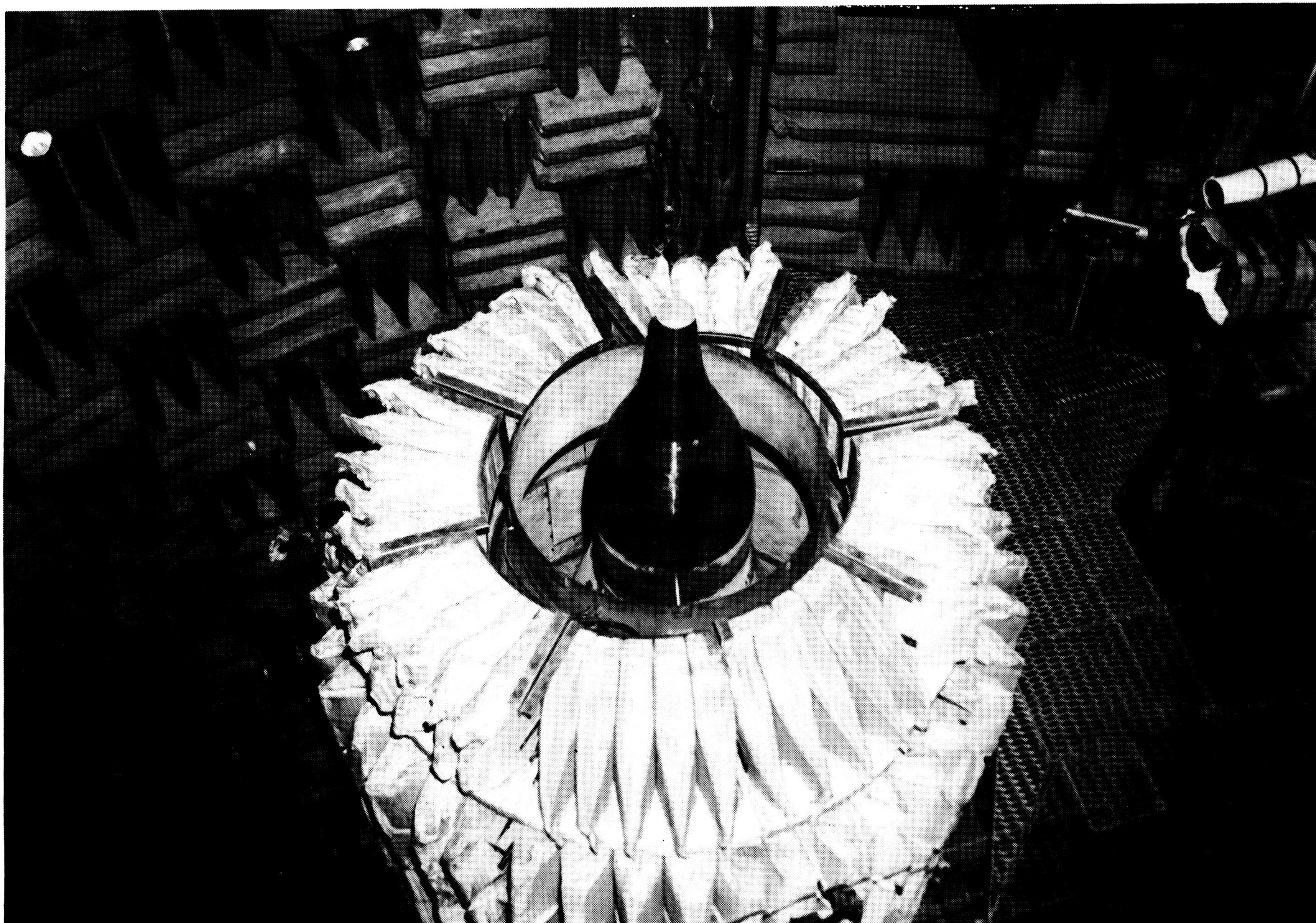

Figure 2-2. Overview of Tertiary Exhaust Surrounding a Test Conical Nozzle.

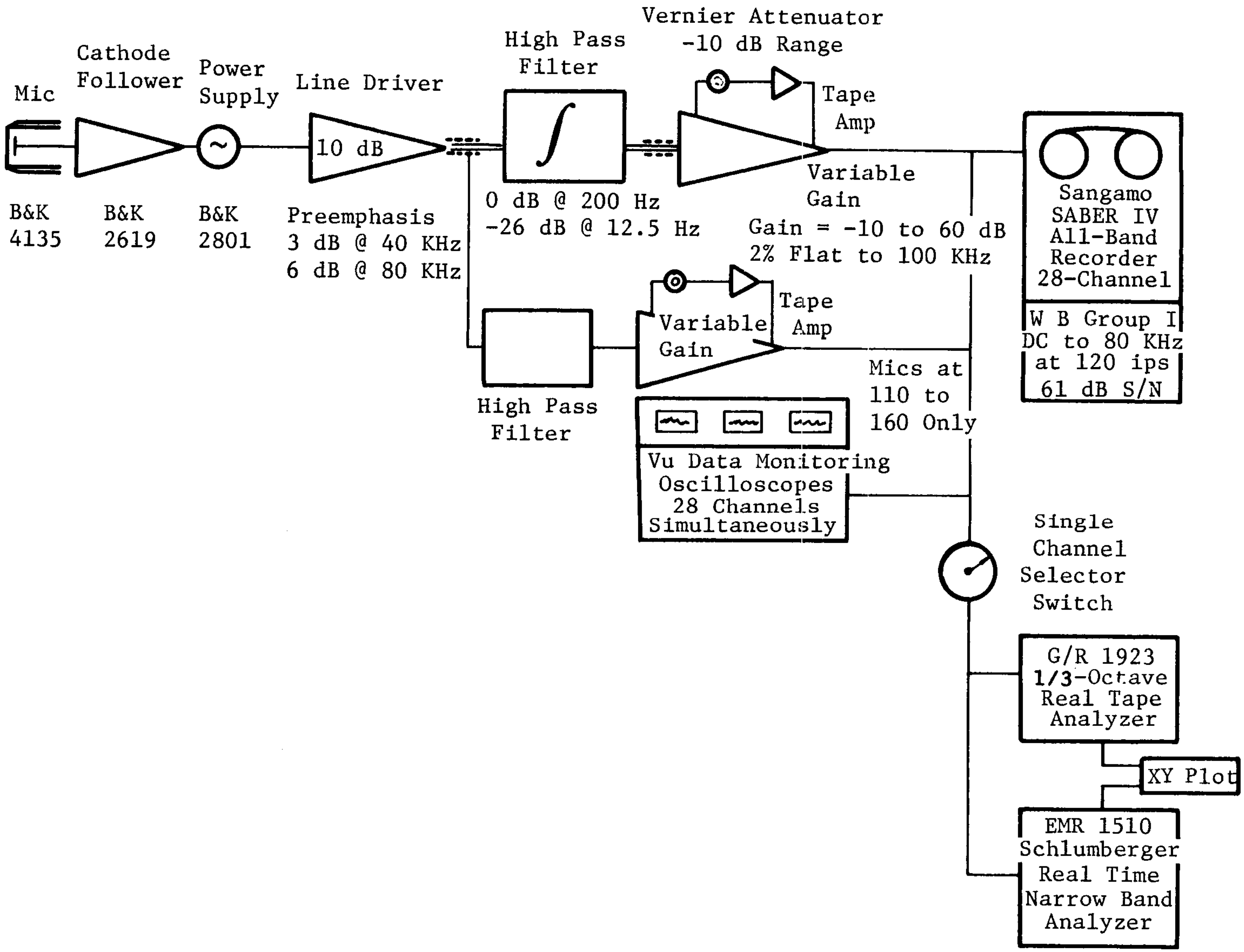

Figure 2-3. Acoustic Data Acquisition System.

The tape recorder amplifiers have a variable gain from -10 dB to +60 dB in 10 dB steps and a gain trim capability for normalizing incoming signals. The prime system used for recording acoustic data is a Sangamo/Sabre IV, 28-track FM recorder. The system is set up for Wideband Group I (intermediate band double extended) at 120 ips tape speed. Operating at this tape speed provides a better dynamic range that is necessary for obtaining the high frequency/low amplitude portion of the acoustic signal. The tape recorder is set up for ±40% carrier deviation with a recording level of 8 volts peak-to-peak. During recording, the signal is displayed on a calibrated master oscilloscope, and the signal gain is adjusted to maximum without exceeding the 8 volt peak-to-peak level.

High-pass filters are incorporated in the acoustic data acquisition systems to enhance the high frequency data of microphones from 110° through 160°. The microphone signal below the 20 kHz 1/3-octave band is filtered out, and the gain is increased to boost the signal to noise ratio. Both the filtered and unfiltered signals are recorded on tape. For data below 20 kHz, the unfiltered signal is used to calculate the sound pressure levels; while for high frequencies, the filtered signal is employed. The entire jet noise spectra at a given angle is obtained by computationally merging these two spectra.

Standard data reduction is conducted in the General Electric AEG Instrumentation and Data Room (IDR). As shown in Figure 2-4, the data tapes are played back on a CBC3700B tape deck with electronics capable of reproducing single characteristics within the specifications indicated for Wideband Group I. An automatic shuttling control is incorporated in the system. In normal operation, a tone is inserted on the recorder in the time slot designed for data analysis. Tape control automatically shuttles the tape initiating an integration start signal to the analyzer at the tone as the tape moves in its forward motion. This motion continues until an "integration complete" signal is received from the analyzer at which time the tape direction is reversed and at the tone, the tape restarts in the forward direction advancing to the next channel to be analyzed until all the channels have been processed. In addition, a time code generator is utilized to signal tape position as directed by the computer program control.

All 1/3-octave analyses are performed on a General Radio 1921 analyzer. Normal integration time is set for 32 seconds to ensure good interaction for the low frequency content. The analyzer has 1/3-octave filter sets from 12.5 Hz to 100 kHz and has a rated accuracy of ±1/4 dB in each band. Each data channel is passed through an interface to the GEPAC 30 computer where the data are corrected for the frequency response of the microphone and the data acquisition system, corrected to standard day (15° C, 70% RH atmospheric attenuation conditions) as recommended by Shield and Bass (Ref. 6), and processed to calculate the perceived noise level and OASPL from the spectra. For calculation of the acoustic power, scaling to other nozzle sizes, or extrapolation to different far-field distances, the data are sent to the Honeywell 6000 computer for processing. This is accomplished by transmitting the SPL via direct time-share link to the 6000 computer through a 1200 Band Modem. In the 6000 computer, the data are processed through the Flight Transformed Full Scale Data Reduction (FTFSDR) Program as per the flow chart shown in Figure 2-5. The data printout is accomplished on a high speed "remote" terminal. In addition, the FTFSDR Program writes a magnetic tape for CALCOMP plotting of the data. Detailed descriptions of the acoustic data reduction and processing systems are given in the Comprehensive Data Report (Ref. 1) of this program.

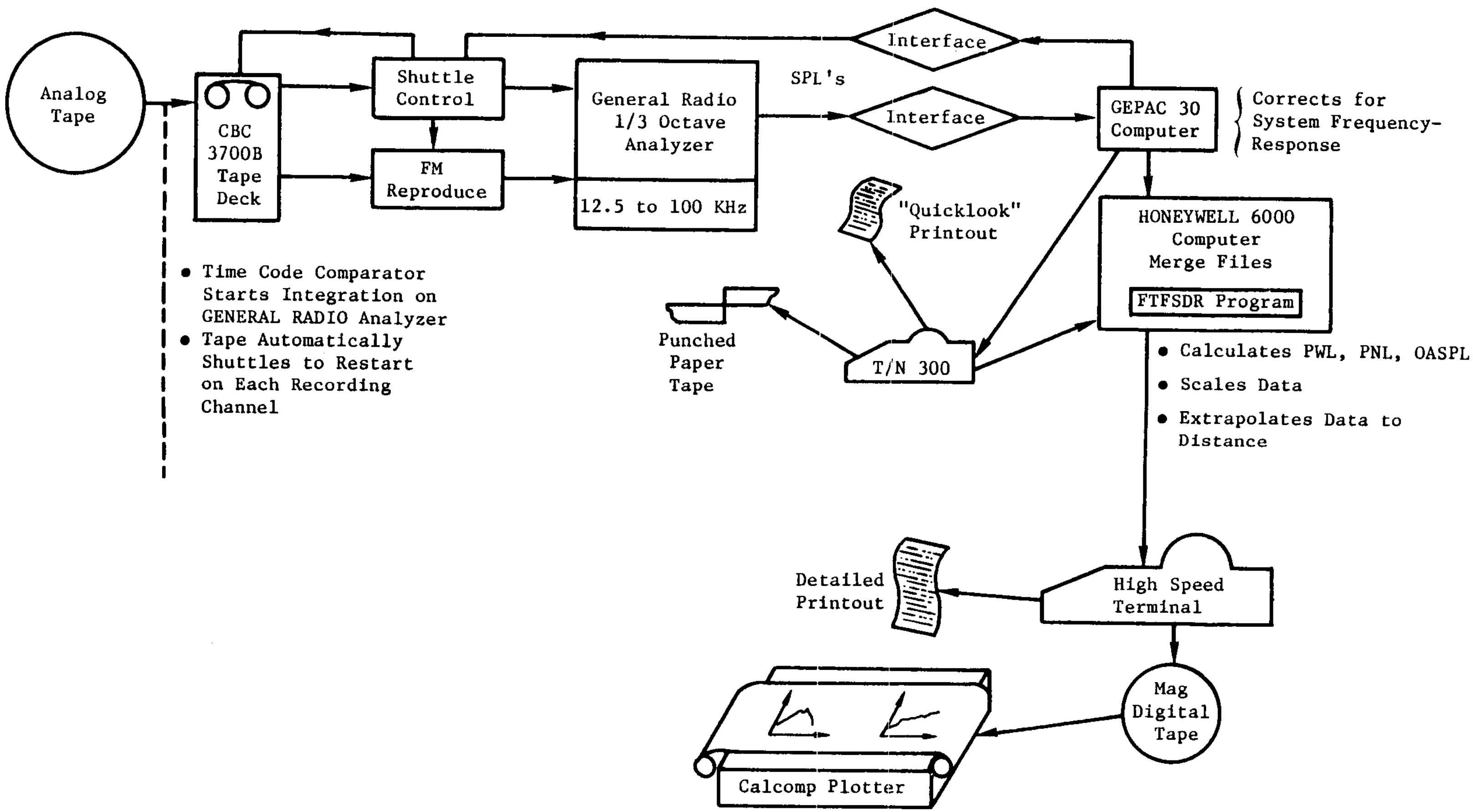

Figure 2-4. Acoustic Data Reduction System.

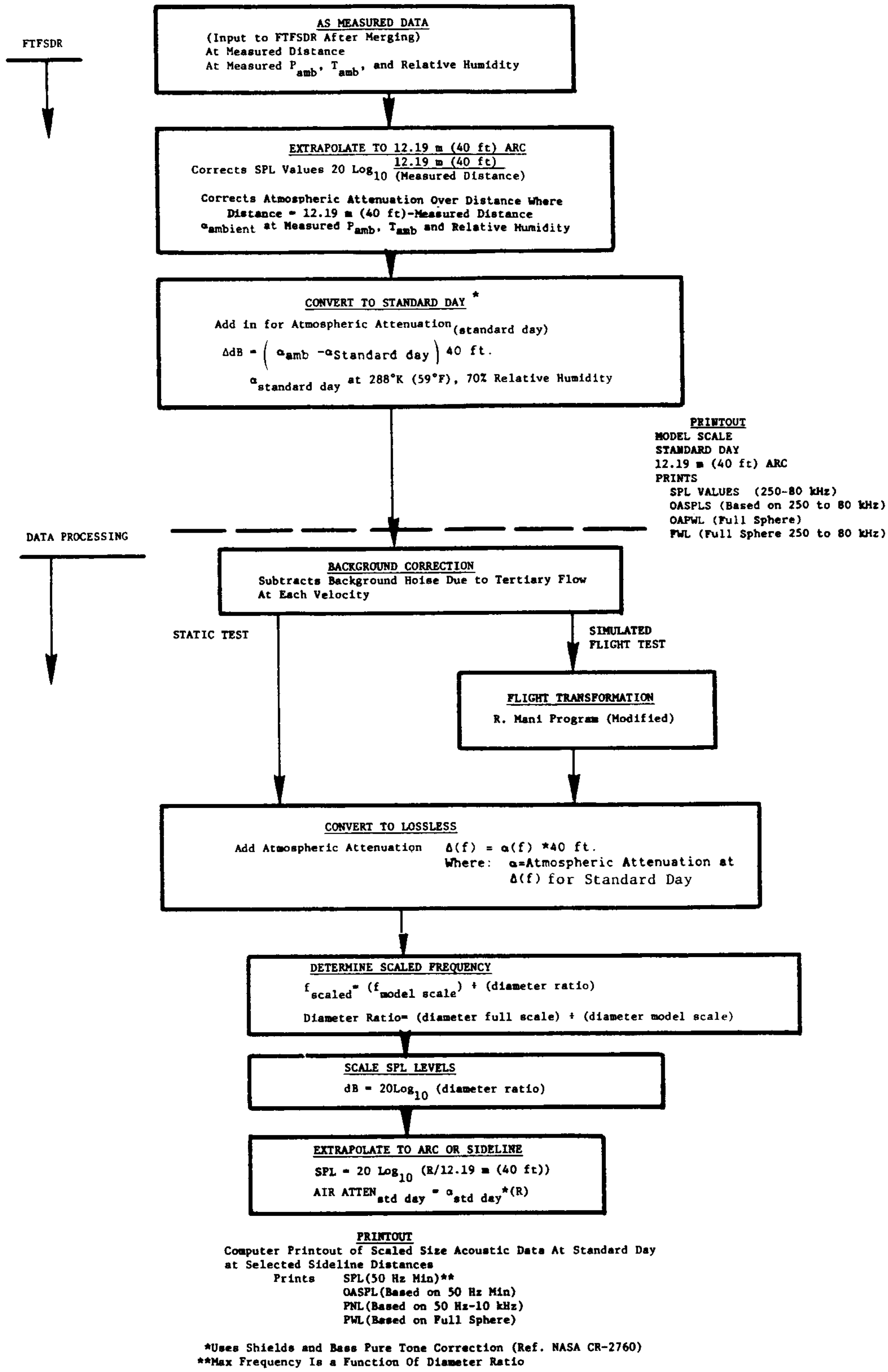

Figure 2-5. Acoustic Data Processing and Scaling Flow Chart.

2.3 GENERAL ELECTRIC LASER VELOCIMETER

The laser velocimeter used is a system developed under a USAF/DOT-sponsored program and reported in detail in References 4 and 5. The basic optical system is a differential Doppler, backscatter, single-package arrangement that has the proven feature of ruggedness for the severe environments encountered in high velocity, high temperature jets. Figure 2-6 shows a photograph of the LV system in the General Electric Anechoic Test Facility and a schematic arrangement of the laser package. The laser beams are projected from below the lens, forming an angle that keeps the major axis of the control volume ellipsoid to a minimum. The dimensions of the control volume are 0.635 centimeter (0.25 inch) for the major axis and 0.508 centimeter (0.20 inch) for the minor axis. The range of the LV control volume from the laser hardware is 2.16 meters (85 inches). The three steering mirrors and the beam splitter are mounted on adjustable supports that are made from the same aluminum alloy to eliminate any temperature-oriented alignment problems.

The remotely actuated platform has vertical, horizontal, and axial travel capabilities of 0.813 meter (32 inches), 0.813 meter (32 inches), and 5.79 meters (228 inches), respectively. The resolution is ±0.1588 centimeter (0.0625 inch) for each axis except for the last 5.28 meters (208 inches) of axial travel which has a resolution of ±0.3175 centimeters (0.125 inch).

Seeding is by injection of aluminum oxide (Al_2O_3) powder having a nominal 1-micron diameter into the air supply to the burners and into a region exterior of the test nozzle so as to seed the tertiary air. The powder-feed equipment used is described in Reference 5. However, the air supply to the fluidized bed column is heated currently to about 394 K (250° F) to prevent powder aggregation by moisture absorption.

The laser velocimeter signal processor is a direct-counter (time domain) type similar to that reported in Reference 5, but with improvements. These improvements result in a lowered rate of false validations and improved linearity and resolution. Turbulent-velocity probability distributions (histograms) are recorded by a 256-channel, NS633 pulse-height analyzer. The data acquired from the LV are transmitted to a minicomputer system (PDP 11/45) for storage on disk and perform data reduction.

The processing capabilities of the LV system are as follows:

- Velocity range - 35 to 5,000 fps
- Random error for single particle accuracy (error associated with system inaccuracies such as fringe spacing, linearity, stability, burst noise) - 0.75%
- Bias error for mean velocity - 0.5%
- False data rejection capability (possibility of accepting bad data) - 0.0002%. The system uses a 16-fringe control volume where all of the 8 center fringes are used in the data acceptance/rejection testing. On an average, 1,000 accepted data samples are taken during a histogram.

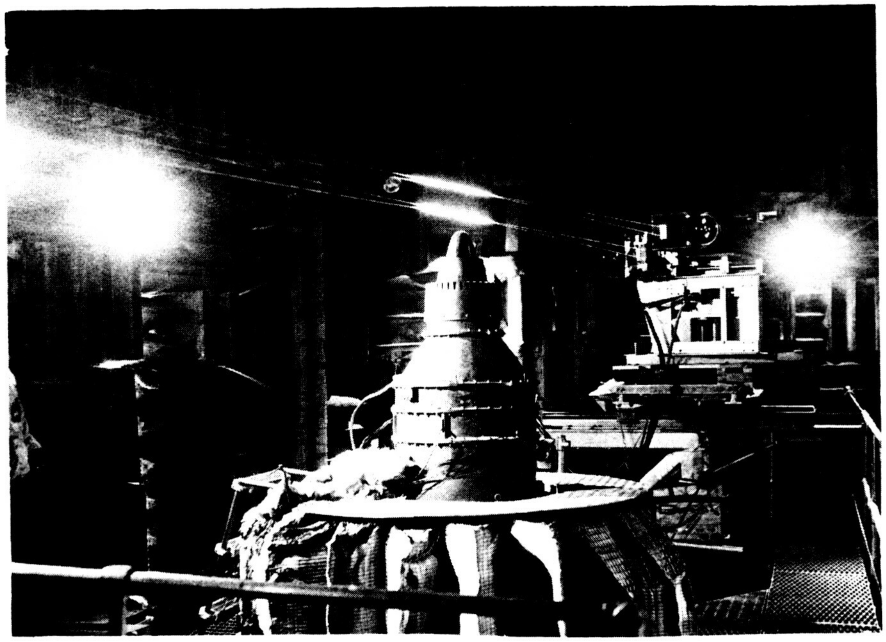

a. LV System in the GE Anechoic Acoustic Test Facility

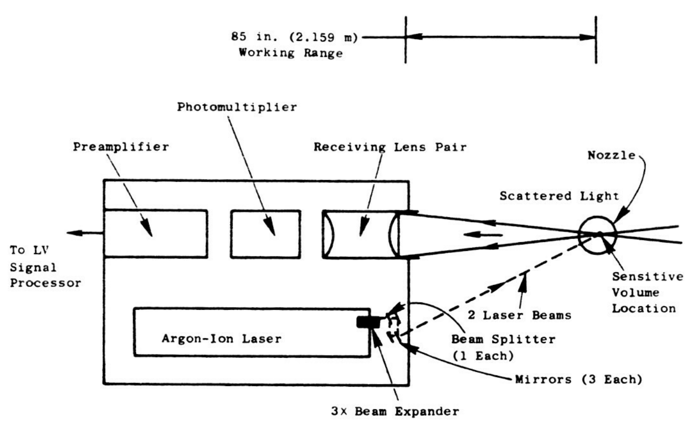

b. Schematic of LV Optics Package

Figure 2-6. General Electric Laser Velocimeter.

2.4 SCALE-MODEL TEST NOZZLES

During this program, scale-model nozzles were tested in the Anechoic Free-Jet Facility to determine their acoustic characteristics under both static and simulated flight conditions and over a wide range of operating flow variables. In this subsection, schematics of these configurations are presented and the objectives and scopes of tests conducted are indicated. Significant dimensions are summarized in Table 2-I. Detailed dimensions and drawings are provided in the Comprehensive Data Report (Ref. 1).

2.4.1 Conical Baseline Nozzle (Model 5)

This configuration, schematically presented in Figure 2-7, was tested earlier (Ref. 2) as Model 5. For the sake of continuity, it is referred to also as Model 5 herein. The objective behind the selection of the configuration is to complement the static and flight simulated baseline acoustic data obtained in Reference 2. The scope of tests includes conditions that correspond to those taken in 1978 on the YJ101 test-bed engine with a conical nozzle (Ref. 7).

2.4.2 Unsuppressed Coannular Plug Nozzle with Convergent Flowpaths (Model 8)

This configuration, which is a scale model of a coannular plug nozzle tested on the YJ101 VCE test-bed engine (Ref. 7), is schematically shown in Figure 2-8. This nozzle has convergent flowpaths on both the inner and outer streams. In order to validate the static scaling criteria of unsuppressed coannular nozzles, the scope of tests with this similitude configuration includes aerodynamic conditions that match test-bed engine test points.

2.4.3 Unsuppressed Coannular Plug Nozzle with Convergent-Divergent Flowpaths (Model 9)

One of the principal objectives of this program is the evaluation of the effectiveness of convergent-divergent (C-D) flowpath is alleviating shock-cell associated broadband noise and its impact on jet total noise. To realize this objective, the following four test configurations, designated as the Model 9 series, have been tested:

1. A convergent-divergent annular nozzle with the inner plug closed and inner flow blocked (Model 9.1). This configuration is schematically shown in Figure 2-9. The scope of tests conducted with this nozzle includes an excursion in the stream total pressure ratio, with the stream total temperature held at the design value so as to confirm the optimum operating condition and determine the reduction in the shock-cell associated noise in the front quadrant.

2. The C-D configuration of Item 1 as the outer nozzle and having a convergent inner flowpath (Model 9.2). This is shown in Figure 2-10. The test scope is similar to that of Item 1 except that the inner stream is maintained at a constant subsonic condition so as to determine the consequence of a subsonic inner stream on the effectiveness of a C-D outer nozzle.

Table 2-I. Summary of Significant Geometric Dimensions of Test Nozzle.

			Conical Baseline	Similitude Coannular Plug Nozzle with Conv. Terminations	C-D Annular Plug Nozzle	Coannular Plug Nozzle; Outer C-D and Inner Conv.	Coannular Plug Nozzle; Outer Conv. and Inner C-D	Coannular Plug Nozzle; Outer and Inner C-D	Similitude 20-Shallow Chute with Inner Conv.	Similitude 20-Shallow Chute with C-D Inner	Modified 20-Shallow Chute	Modified 40-Shallow Chute
Model Description			5	8	9.1	9.2	9.3	9.4	10.1	10.2	DOT-20	DOT-40
<u>Outer Nozzle Characteristics</u>												
Throat Height	h_t^o	cm	---	1.81	1.72	1.72	1.81	1.72	3.76	3.76	3.76	3.76
Throat Area	A_t^o	cm^2	131.5	116.4	116.4	116.4	116.4	116.4	128.2	128.2	153.3	153.3
Exit Height	h_e^o	cm	---	---	2.26	2.26	---	2.26	---	---	---	---
Exit Area	A_e^o	cm^2	131.5	116.4	133.2	133.2	116.4	133.2	128.2	128.2	153.3	153.3
Radius Ratio	R_r^o	---	---	0.846	0.864	0.864	0.846	0.864	0.764	0.764	0.716	0.716
C-D/Conv.	---	---	Conv	Conv	C-D	C-D	Conv	C-D	Conv	Conv	Conv	Conv
<u>Inner Nozzle Characteristics</u>												
Throat Height	h_t^i	cm	---	0.51	---	0.51	0.57	0.57	0.51	0.51	0.63	0.63
Throat Area	A_t^i	cm^2	---	22.6	---	22.6	24.2	24.2	25.8	25.8	30.6	30.6
Exit Height	h_e^i	cm	---	---	---	---	0.67	0.67	---	0.56	---	---
Exit Area	A_e^i	cm^2	---	22.6	---	22.6	4.39	4.39	25.8	4.2	30.6	30.6
Radius Ratio	R_r^i	---	---	0.933	---	0.933	0.908	0.908	0.941	0.932	0.922	0.922
C-D/Conv.	---	---	---	Conv	---	Conv	C-D	C-D	Conv	C-D	Conv	Conv
<u>Total Nozzle Characteristics</u>												
Total Throat Area	A_t^T	cm^2	131.5	139	116.4	139	140.3	140.3	154	154	183.9	183.9
Total Exit Area	A_e^T	cm^2	131.5	139	133.2	155.7	144.7	161.5	154	155.3	183.9	183.9
Internal Struts	---	---	No	Yes	Yes	Yes	Yes	Yes	Yes	Yes	No	No
Exit Stagger	x^o	cm	---	8.5	---	2.54	10.83	3.52	6.18	7.57	5.3	5.3
Throat Area Ratio	A_t^i/A_t^o	---	---	0.194	---	0.194	0.208	0.208	0.201	0.201	0.2	0.2

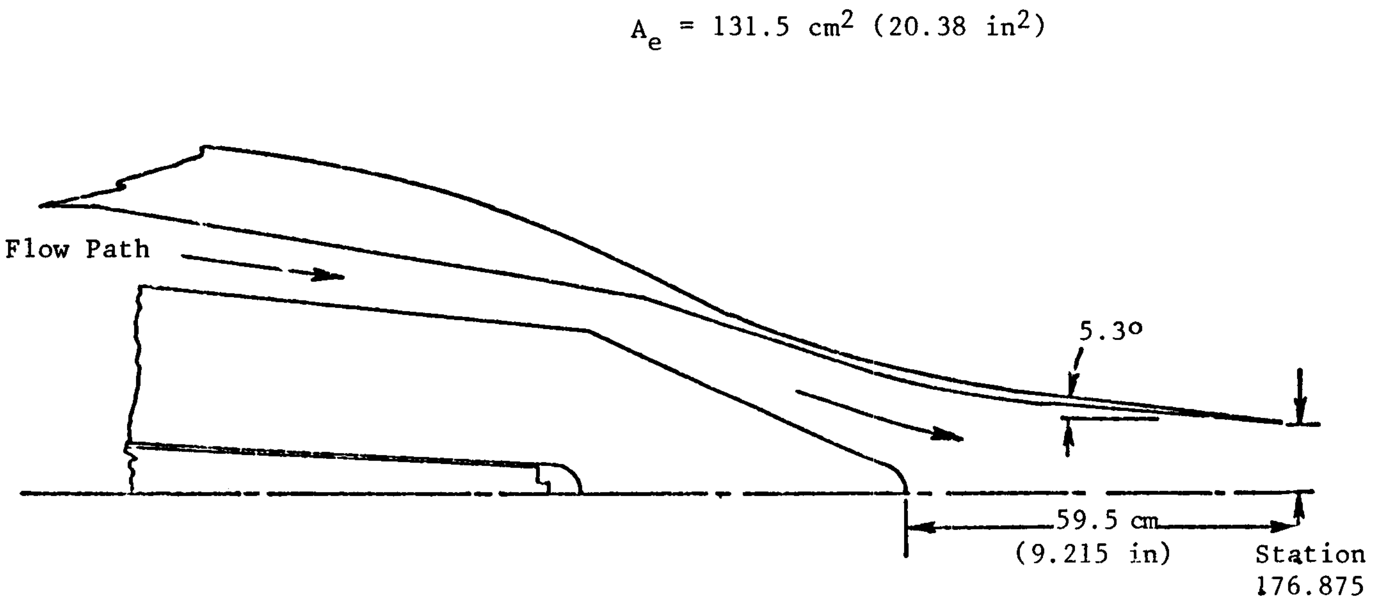

Figure 2-7. A Schematic of Conical Baseline Nozzle (Model 5).

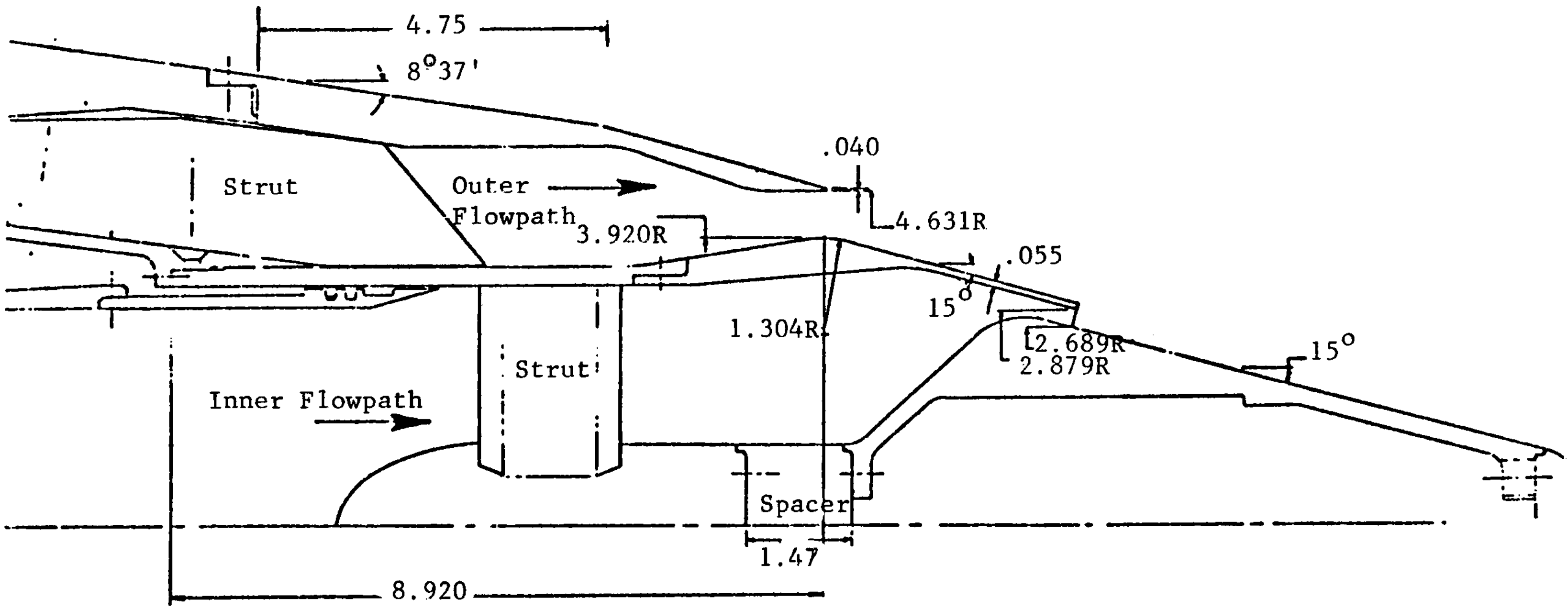

Figure 2-8. A Schematic of Similitude Unsuppressed Coannular Plug Nozzle with Convergent Flowpaths (Model 8).

1. Barrel
2. Outer Nozzle
3. Strut
4. Plug Assembly
5. Inner Transition Sleeve
6. Inner to Outer Seal
7. Inner Shroud
8. Plug Body
9. Plug Tip
10. Spacer

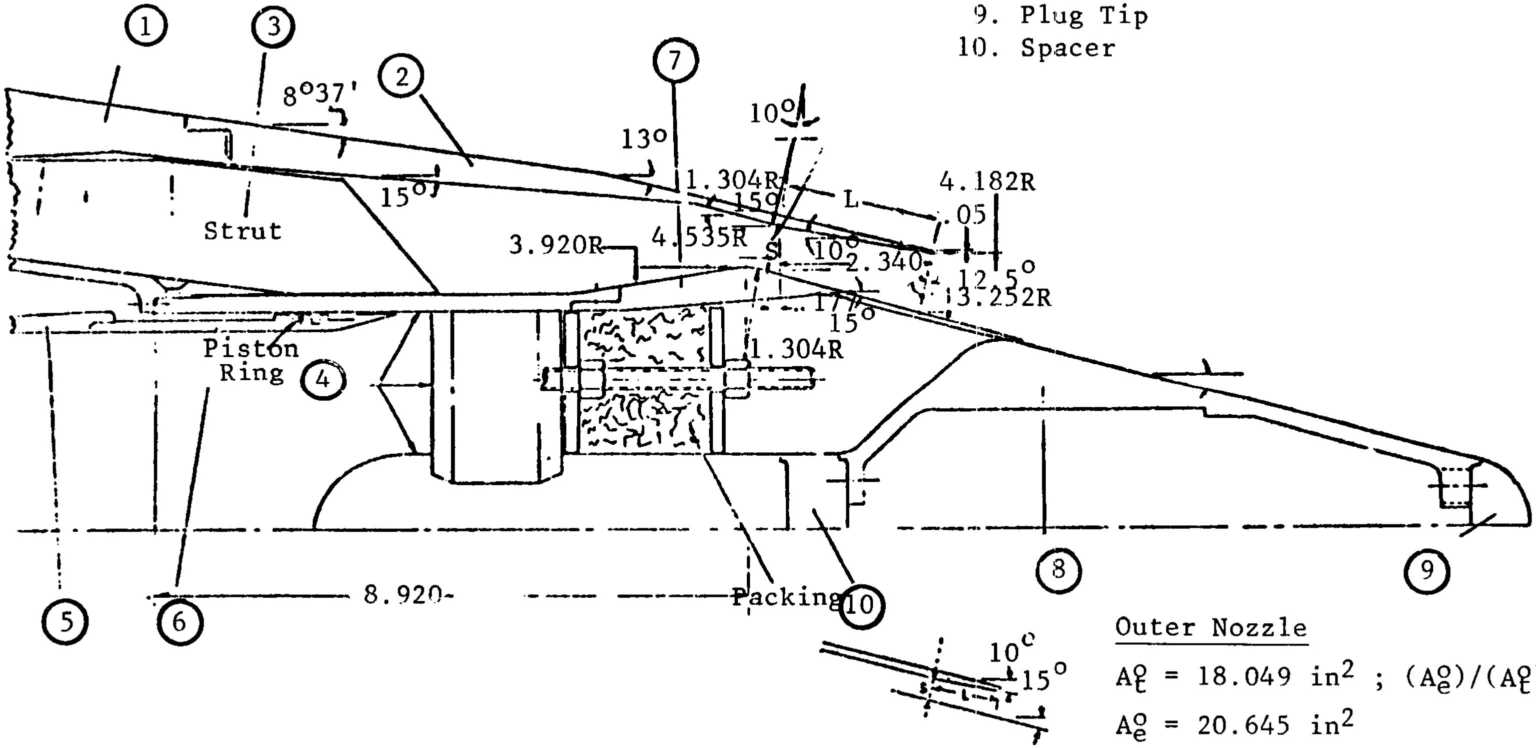

Outer Nozzle

$A_t^o = 18.049\ in^2$; $(A_e^o)/(A_t^o) = 1.144$

$A_e^o = 20.645\ in^2$

$(R_r^o)_8 = 0.789$; $(R_r^o)_t = .855$

$L/S = 3.4$

Figure 2-9. A Schematic of Convergent-Divergent Annular Nozzle with a Center Plug (Model 9.1).

1. Barrel
2. Outer Nozzle
3. Strut
4. Plug Assembly
5. Inner Transition Sleeve
6. Inner to Outer Seal
7. Inner Shroud
8. Plug Body
9. Plug Tip
10. Spacer

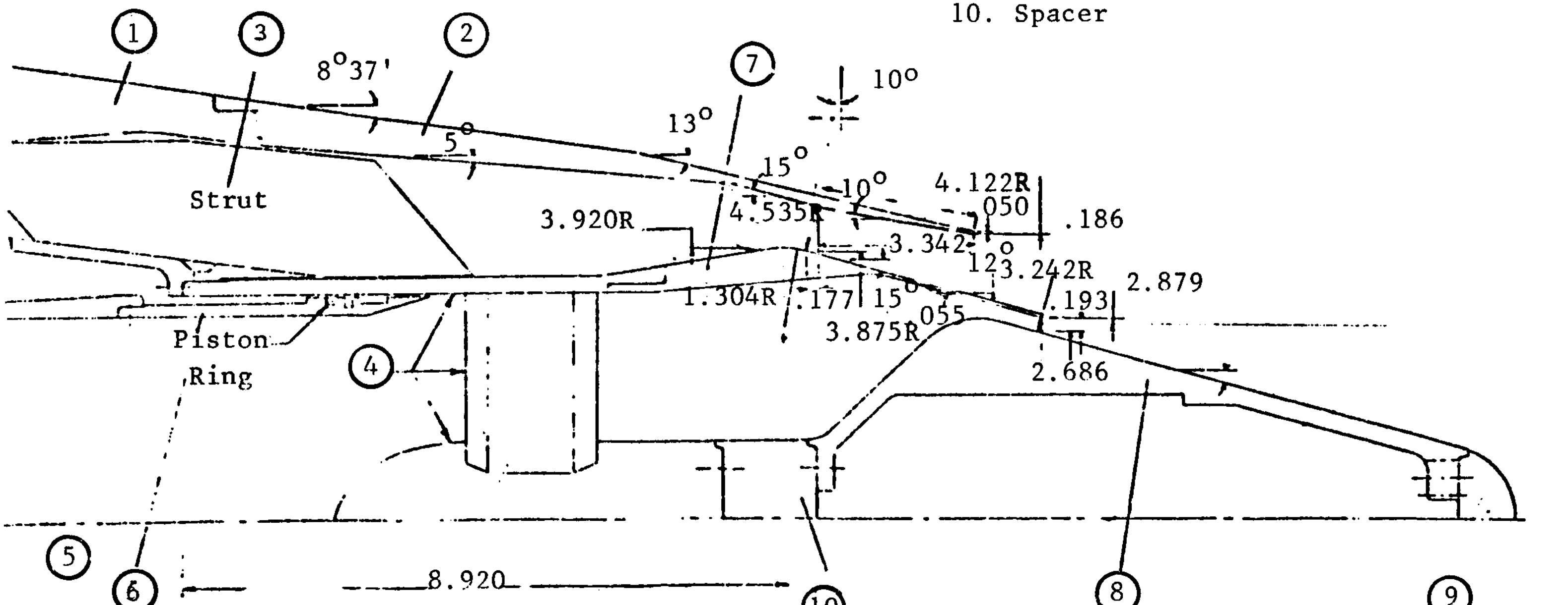

Inner Nozzle

$A_t^i = 3.496\ in^2$

Outer Nozzle

$A_t^o = 18.049\ in^2$; $(A_e^o)/(A_t^o) = 1.144$

$A_e^o = 20.645\ in^2$

$(R_r^o)_8 = 0.789$; $(R_r^o)_t = .855$

L/S = 3.4

Figure 2-10. A Schematic of Coannular Nozzle with C-D Outer Stream and Convergent Inner Stream (Model 9.2).

3. A convergent outer nozzle, identical to the outer configuration of Model 8 and having a convergent-divergent inner nozzle. This configuration (Model 9.3) is schematically shown in Figure 2-11. The extent of tests with this nozzle is mainly to confirm, with the outer stream held at a subsonic condition, the optimum design condition of the inner C-D flowpath.

4. An all C-D coannular configuration shown schematically in Figure 2-12 and made up of the outer C-D nozzle of Item 1 and the inner C-D nozzle of Item 3 (Model 9.4). The scope of testing is to determine the total C-D effectiveness of this configuration (with the two streams operating at their optimum conditions as determined under Items 1 and 3) relative to a similar coannular nozzle with convergent flowpaths.

Background information, along with design considerations adopted for the development of the C-D nozzles, is provided in Appendix IV.

2.4.4 Similitude 20-Shallow-Chute Mechanical Suppressor with a Convergent Inner Nozzle (Model 10.1)

This nozzle is a scaled model of the suppressor configuration designed for testing on the YJ101 VCE test-bed engine. This engine configuration, the details of which are presented in Reference 8, has been selected after a review of promising suppressor exhaust systems that were tested during the study of Reference 3. Other pertinent information that influenced the scaling included a GE preliminary design concept layout of a 20-shallow-chute suppressor for the AST/VCE product engine (Ref. 9) based on the GE21/J11B18 cycle requirements. Some of the overall dimensions of the product, YJ101 engine and model size suppressor nozzles, are summarized as follows:

Parameter		AST/VCE	YJ101	Model 10.1
A^o_t (cold)	cm^2	8290	985.8	128.26
	$in.^2$	1285	152.8	19.88
D^o_{eq}	cm	102.74	35.55	12.78
	in.	40.45	13.95	5.03
A^i_t (cold)	cm^2	1625.2	193.6	25.81
	$in.^2$	251.9	30.0	4.00
D^i_{eq}	cm	45.49	15.70	5.72
	in.	17.91	6.18	2.25
$A^T = A^o_t + A^i_t$	cm^2	9915.5	1179.4	154.1
	in^2	1536.9	182.8	23.88
A^i_t/A^o_t		0.196	0.196	0.201

A schematic of the model configuration and a photograph of the hardware are presented, respectively, in Figures 2-13 and 2-14. The model flowpath is designed to be compatible with the two-dimensional Mach number distribution of the YJ101 engine design. Also, the structural support pins in the chutes simulate the test-bed engine design. The static pressure taps shown in

1. Barrel
2. Outer Nozzle
3. Strut
4. Plug Assembly
5. Inner Transition Sleeve
6. Inner to Outer Seal
7. Inner Nozzle Shroud
8. Plug
9. Plug Tip
10. Spacer

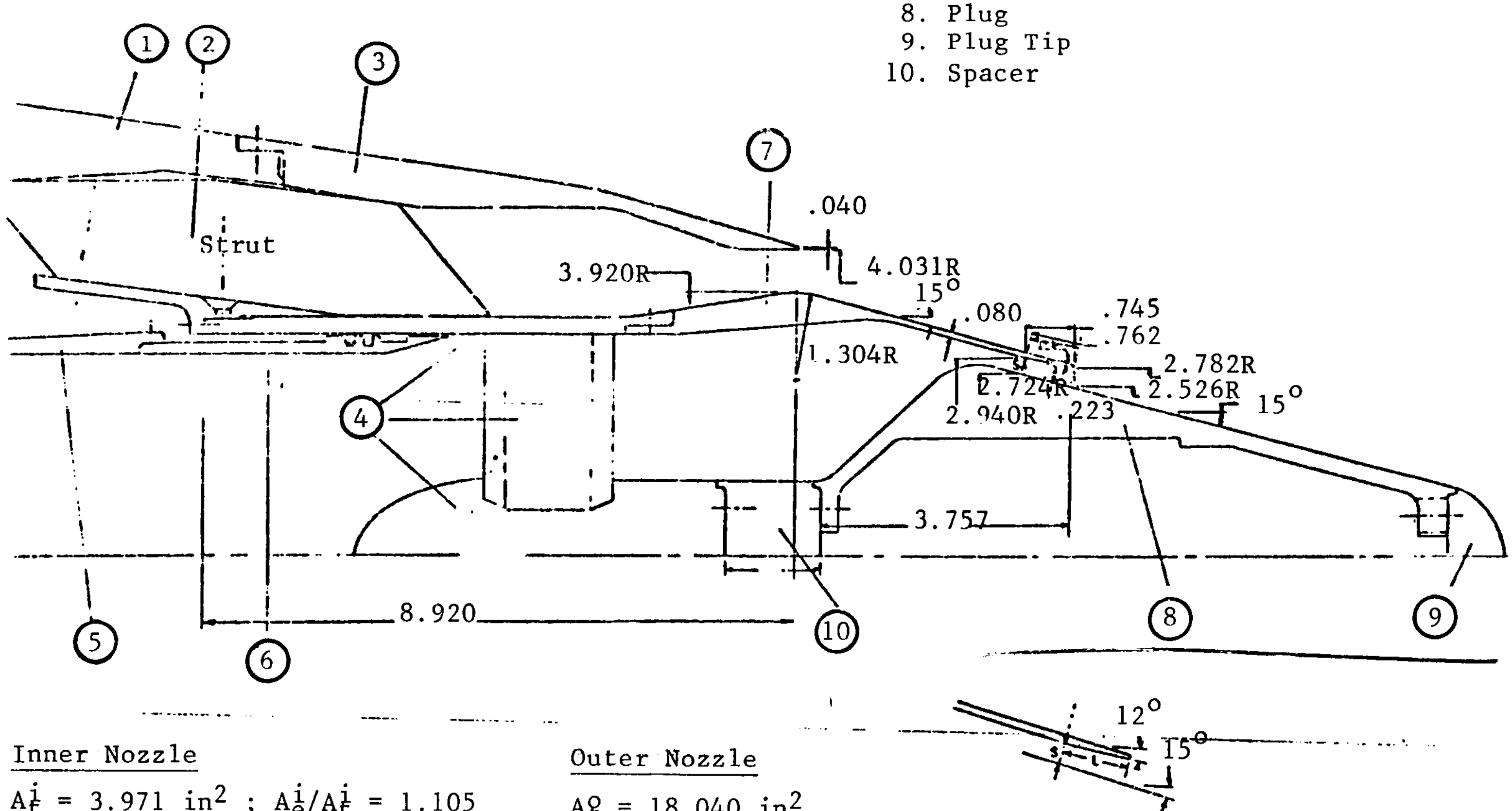

Inner Nozzle

$A_t^i = 3.971\ in^2$; $A_e^i/A_t^i = 1.105$

$A_e^i = 4.387\ in^2$

$(R_r^i)_e = .908$; $(R_r^i)_t = .927$

L/S = 3.42

Outer Nozzle

$A_t^o = 18.040\ in^2$

Figure 2-11. A Schematic of Coannular Nozzle with Convergent Outer Stream and C-D Inner Stream (Model 9.3).

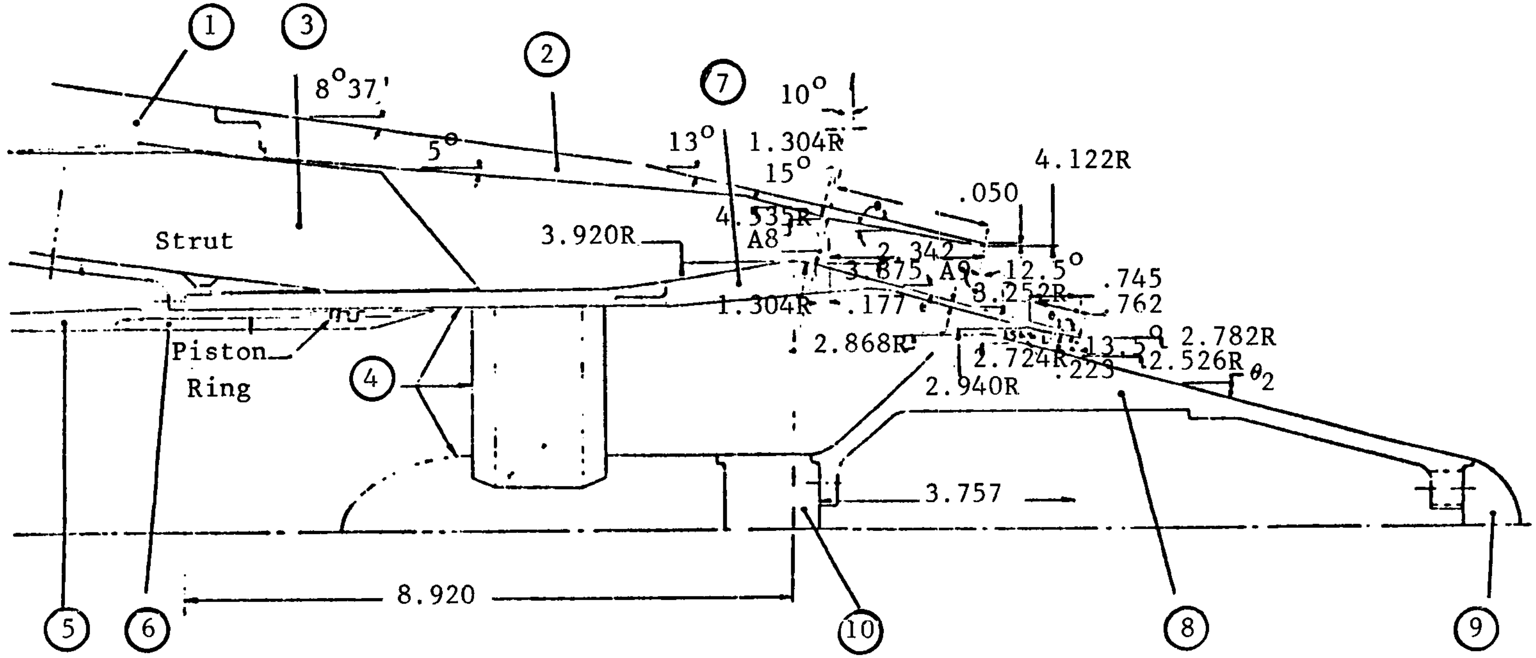

Inner Nozzle

$A_t^i = 3.971\ in^2$; $A_e^i/A_t^i = 1.105$

$A_e^i = 4.387\ in^2$

$(R_r^i)_e = .908$; $(R_r^i)_t = .927$

L/S = 3.42

Outer Nozzle

$A_t^o = 18.049\ in^2$; $(A_e^o)/(A_t^o) = 1.144$

$A_e^o = 20.645\ in^2$

$(R_r^o)_8 = 0.789$; $(R_r^o)_t = .855$

L/S = 3.4

Figure 2-12. A Schematic of a Coannular Nozzle with C-D Flowpaths on Both Inner and Outer (Model 9.4).

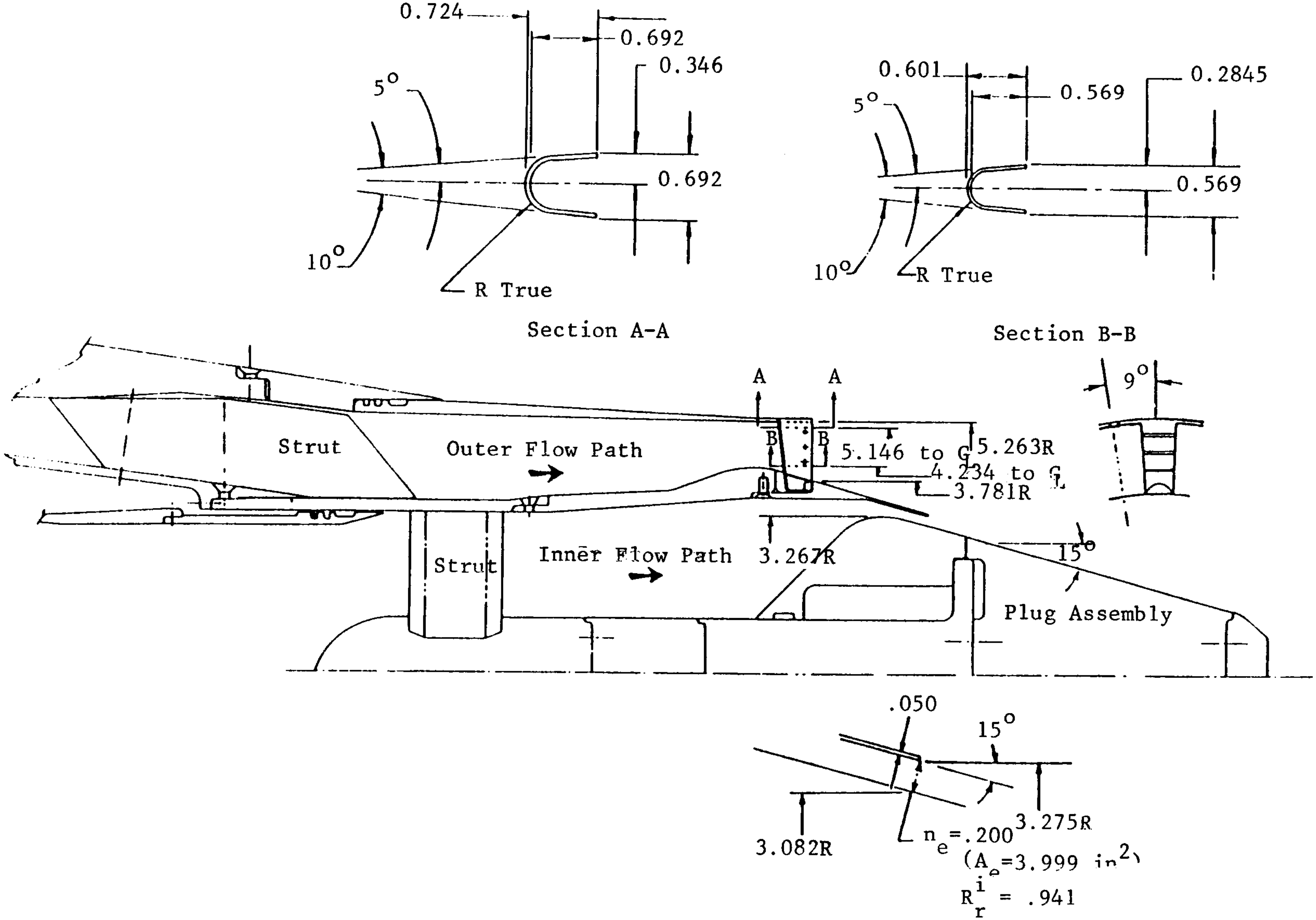

Figure 2-13. A Schematic of the Similitude 20-Shallow-Chute Mechanical Suppressor Nozzle with Convergent Inner Flowpath (Model 10.1).

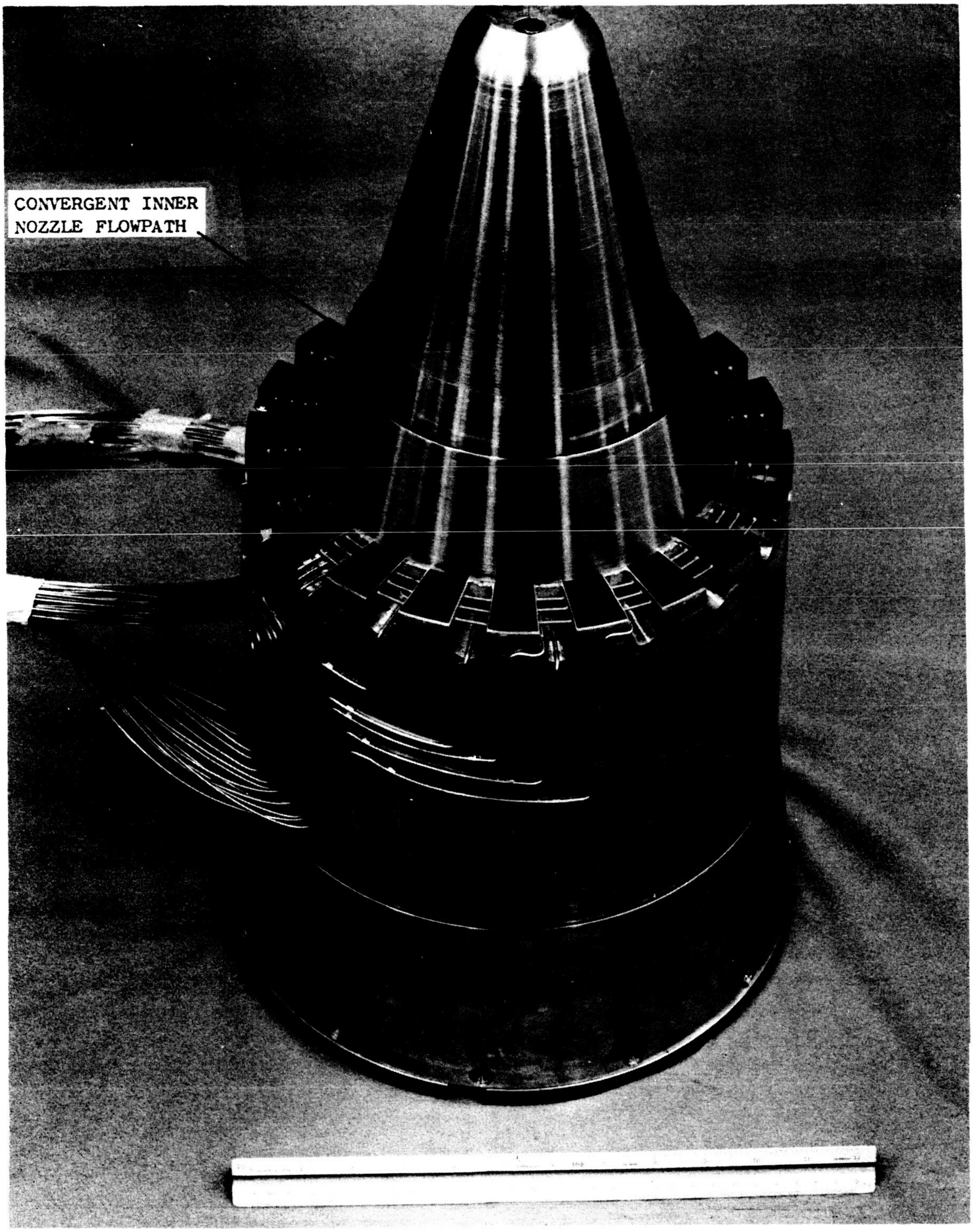

Figure 2-14. Full View of the Assembled Similitude 20-Shallow-Chute Mechanical Suppressor with a Convergent Inner Nozzle (Model 10.1).

Figure 2-14 are located at several wall locations in the chutes of the suppressor to obtain base pressure measurements. These data are to be employed to assess the influence of the suppressor stream temperature on the nozzle thrust coefficient.

The scope of tests performed with this model includes static and simulated flight acoustic tests at typical AST/VCE cycle conditions and matching YJ101 operating conditions. In addition, LV measurements were obtained at operating conditions that correspond to two of the static acoustic tests.

2.4.5 Similitude 20-Shallow-Chute Mechanical Suppressor with a Convergent-Divergent Inner Nozzle (Model 10.2)

In order to determine the benefits of a convergent-divergent inner stream on the similitude model suppressor (Model 10.1) acoustic data, the scale model suppressor was assembled and tested with a C-D inner nozzle. This configuration, designated as Model 10.2, is schematically shown in Figure 2-15.

The scope of tests conducted with this model includes static and simulated flight acoustic tests for a concept demonstration of C-D inner nozzle and static and flight LV measurements at typical AST/VCE takeoff condition that includes the design condition of the C-D inner nozzle.

2.4.6 20-Shallow-Chute Mechanical Suppressor of DOT Program Modified for a System Area Ratio, $A_r = 0.2$

During the DOT high velocity jet noise source location and reduction program (Ref. 3), 20-shallow-chute hardware having an area ratio $A_r = 0.52$ had been fabricated and acoustically tested. During the course of this program, it was decided to modify the DOT hardware to an area ratio of 0.2 by fabricating a new center plug and conduct acoustic tests with the resulting configuration. The measured data are compared with those of the similitude suppressor nozzle in order to determine the effect of geometrical differences such as flow element width to height ratio on the acoustic data. Comparison of the significant geometrical dimensions of the two suppressors are provided in Table 2-II. A schematic of the modified configuration is presented in Figure 2-16. Differences in the flow lines of the similitude and modified suppressor model nozzles could be noted by comparing Figure 2-13 with 2-16.

The scope of tests performed with the modified DOT configuration includes static and simulated flight acoustic measurements at selected AST/VCE cycle conditions.

2.4.7 40-Shallow-Chute Mechanical Suppressor of DOT Program Modified for System Area Ratio, $A_r = 0.2$

The center plug that was fabricated to modify the DOT 20-shallow-chute hardware was used also to modify the DOT 40-shallow-chute hardware to a system area ratio of 0.2. Acoustic tests with this modified 40-shallow-chute configuration, schematically shown in Figure 2-17, were conducted at cycle conditions identical to those of the modified 20-shallow-chute series of tests so as to obtain acoustic data on the effect of chute number.

Table 2-II. Geometrical Comparison Between Modified DOT and Similitude 20-Shallow-Chute Suppressor Model Configurations

	Modified DOT Suppressor	Similitude Suppressor (Model 10.1)
Number of Elements	20	20
Suppressor Stream Exit Area, in.^{2}, A_t^o	23.76	19.88
Inner Stream Exit Area, in.^{2}, A_t^i	4.75	4.00
Exit Area Ratio A_t^i/A_t^o	0.20	0.20
Equivalent Diameter Based on Total Exit Area, in., D_{eq}^T	6.025	5.514
Suppressor Element Hydraulic Diameter (Defined in Section 4.0), in., D_{hyd}^o	1.219	1.183
Suppressor Stream Radius Ratio, R_r^o	0.716	0.764
Suppressor Area Ratio, A_R	1.75	1.75
Flow Element Width at Hub, in., W_1^F	0.671	0.534
Flow Element Width at Tip, in., W_2^F	0.935	0.928
Flow Element Height, in.	1.480	1.482
Flow Element Width at Hub/Flow Element Height	0.45	0.36
Flow Element Width at Tip/Flow Element Height	0.63	0.63
Chute Width at Hub, in., W_1^c	0.504	0.569
Chute Width at Tip, in., W_2^c	0.702	0.692
Chute Depth at Hub, in., d_1^c	0.567	0.495
Chute Depth at Tip, in., d_2^c	0.765	0.690

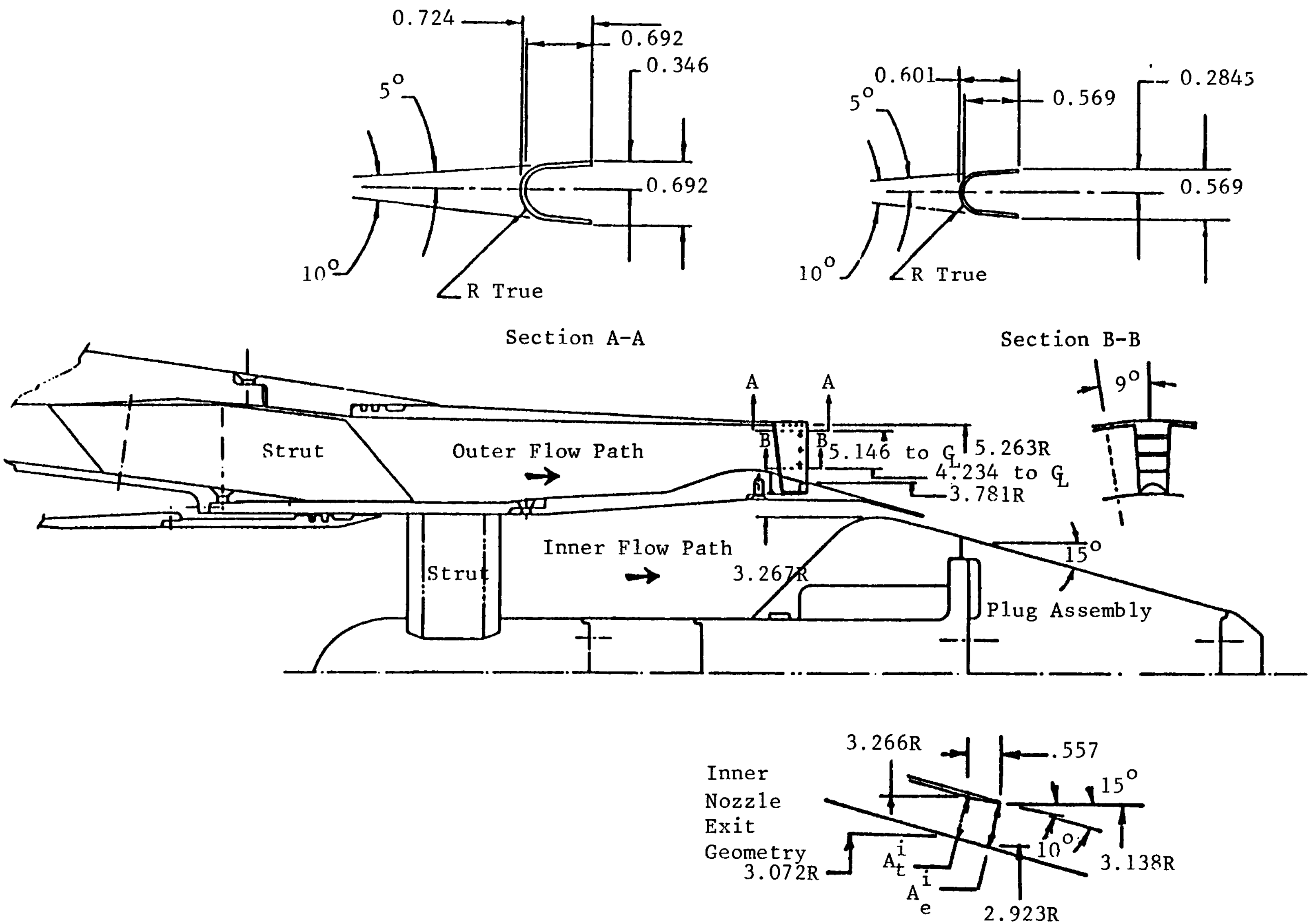

Figure 2-15. A Schematic of the Similitude 20-Shallow-Chute Mechanical Suppressor Nozzle with Convergent-Divergent Inner Flowpath (Model 10.2).

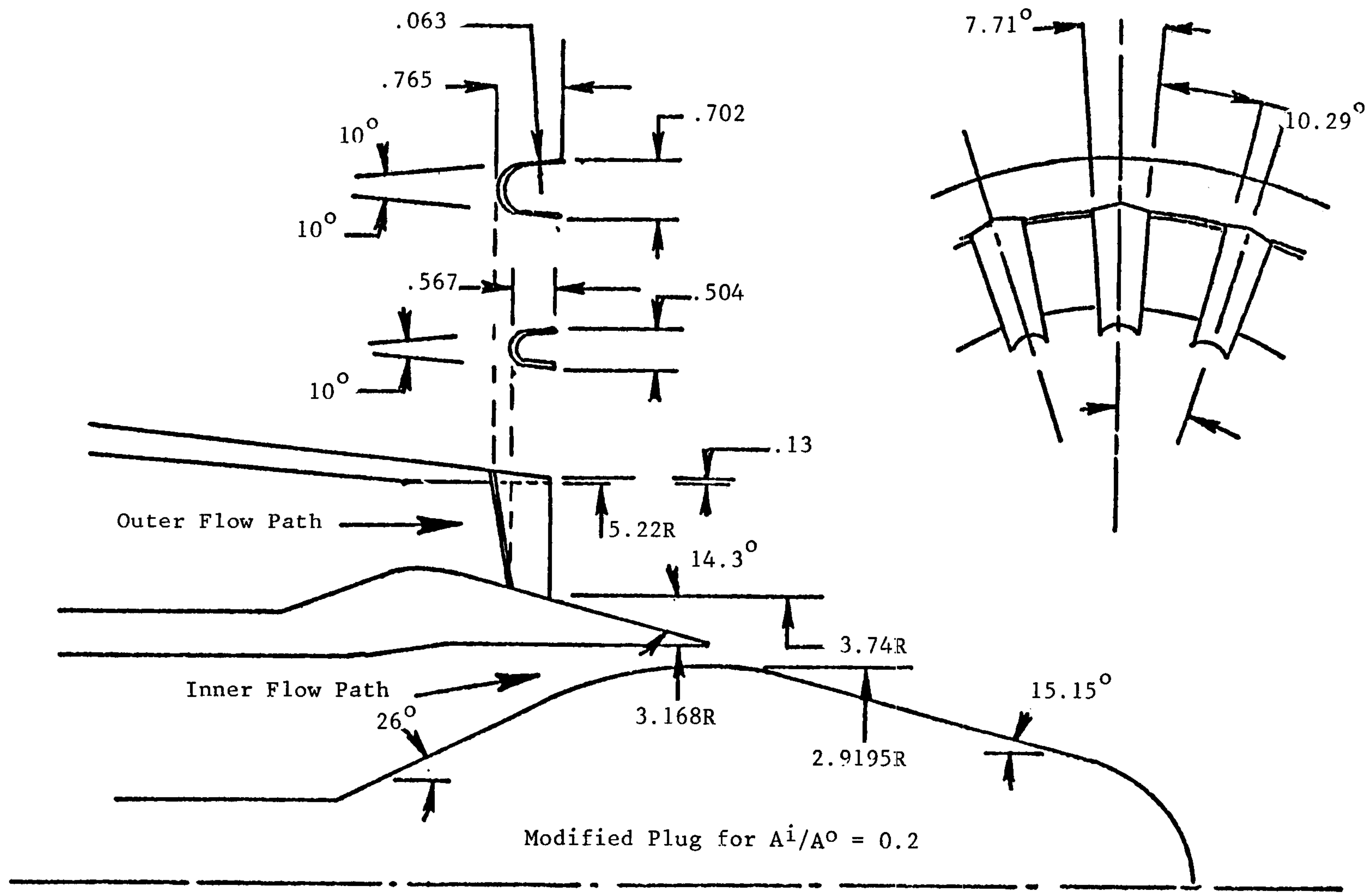

Figure 2-16. A Schematic of 20-Shallow-Chute Suppressor of DOT Program Modified for System Area Ratio of 0.2.

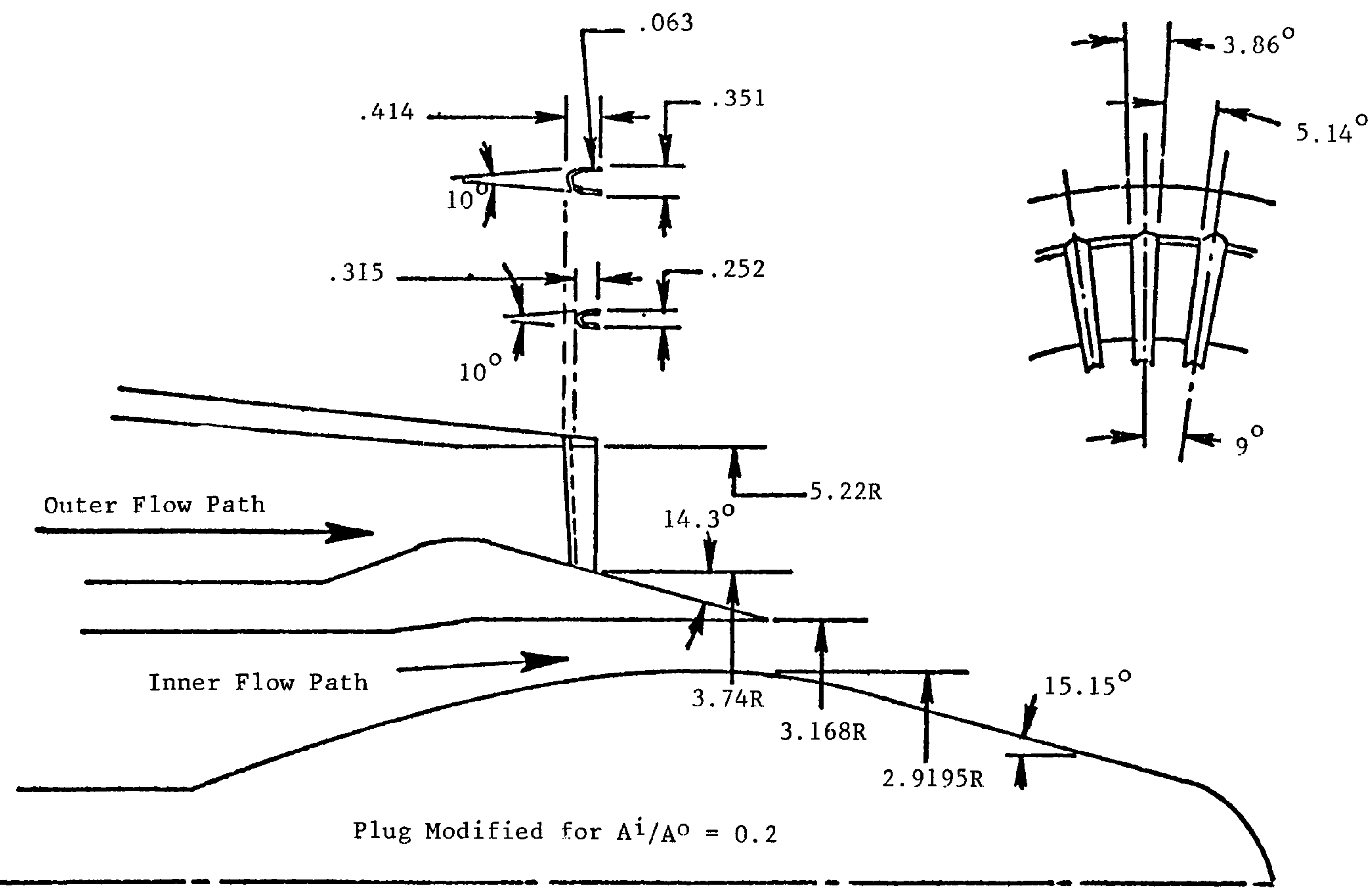

Figure 2-17. A Schematic of 40-Shallow-Chute Suppressor of DOT Program Modified for System Area Ratio of 0.2.

2.5 AERODYNAMIC AND ACOUSTIC TEST DATA

2.5.1 Acoustic Tests

A total number of 113 static and 99 simulated flight acoustic tests were performed with the 10 model configurations described in Subsection 2.4. The aerodynamic flow conditions of the outer, inner, and mixed streams that correspond to each of these acoustic tests are tabulated in Appendix I. The aerodynamic data are tabulated in both the International System of Units and the English Units. These tables also summarize the standard day (15° C, 70% relative humidity) far-field PNL data on a 731.5 meter (2,400 feet) sideline and scaled to an AST nozzle size of 9,032 square centimeter (1,400 square inches) at angles of θ_i = 50°, 60°, 70°, 90°, 120°, 130°, and 140° relative to the inlet. In addition, the ambient pressure, temperature, and relative humidity in the GE Anechoic Facility at the time of the tests are presented in these tables.

2.5.2 LV Tests

Three static and one simulated flight LV tests were performed with the similitude 20-shallow-chute suppressor having a convergent inner (Model 10.1) and C-D inner (Model 10.2) nozzles. The aerodynamic flow conditions of these test plumes are tabulated in Appendix II.

2.5.3 Base Pressure Tests

Suppressor base pressure measurements with the similitude 20-shallow-chute nozzle (Model 10.1) were obtained simultaneously along with the acoustic tests. In addition, base pressure data alone were obtained over a range of suppressor pressure ratios but under ambient temperature conditions. These data were recorded with free-jet velocities of 0, 61 m/sec (200 fps), and 122 m/sec (400 fps). A summary of the aerodynamic flow conditions of the base pressure tests is provided in Appendix III along with the locations of the fixed static pressure probes in the chutes of the suppressor nozzle.

3.0 ACOUSTIC, DIAGNOSTIC LV, AND BASE PRESSURE TEST RESULTS

The acoustic, laser velocimeter, and suppressor base pressure measurements conducted with the scale-model nozzles of this program are analyzed and presented in this section. Description of the nozzle configurations and a summary of the test conditions were covered earlier under Section 2.0.

This section is divided into three major subsections. General acoustic characteristics of tested nozzles are presented and discussed in Subsection 3.1. Analyses of the test acoustic data include verification of the static scaling procedures using conical baseline and similitude coannular nozzles, evaluation of the similitude 20-shallow-chute mechanical suppressor nozzle under static and simulated flight conditions, and determination of the effectiveness of contoured convergent-divergent flowpaths of annular and coannular plug nozzles. The results of the LV measurements on a selected number of plumes of the similitude 20-shallow-chute suppressor nozzle are analyzed in Subsection 3.2. The analyses include comparison of the suppressor plume characteristics with those of the coannular plug and conical baseline nozzles, and evaluation of the effect on simulated flight on the plume decay rate of the suppressor nozzle. Finally, the results of a preliminary estimate of the effect of base drag on the thrust coefficient of the similitude suppressor nozzle (Model 10.1) are summarized in Subsecton 3.3

3.1 DISCUSSION OF ACOUSTIC RESULTS

The acoustic characteristics of the nozzle configurations of this program are presented and discussed in this subsection. Unless otherwise stated, the presented results are measured data that are scaled to a product size of A^T = 0.903 square meters (1,400 square inches), extrapolated to a sideline of 731.5 meters (2,400 feet) and corrected to a standard day [15° C (59° F) and 70% relative humidity] atmospheric attenuation (Shields and Bass method, Ref. 6).

3.1.1 Conical Nozzle Baseline Data

In order to ascertain the repeatability of the acoustic data and to broaden the data base of a reference conical nozzle, the Model 5 conical configuration was tested during this program over a range of aerodynamic flow conditions. The measured forward quadrant PNL data at θ_i = 60° and 90° and normalized aft quadrant PNL data at θ_i = 120° and 130° are presented in Figures 3-1 and 3-2, respectively, and compared with conical nozzle data obtained over the years at the General Electric test facilities (Refs. 2, 3 and 10). An examination of the presented data indicates that the data measured over the years agree with one another and are within acceptable data scatter.

Figures 3-1 and 3-2 also demonstrates the effect of flight ($V_{ac} \simeq$ 122 m/sec or 400 fps) on the static PNL data of the conical baseline nozzle. While the effect of flight on the conical nozzle data has been discussed in detail in Reference 2, it is of interest to this program to study the effect of flight on the PNL and OASPL directivity and spectral characteristics of the conical nozzle at a typical AST takeoff condition. These data, which will be used later in this report to determine the acoustic benefits of the other test

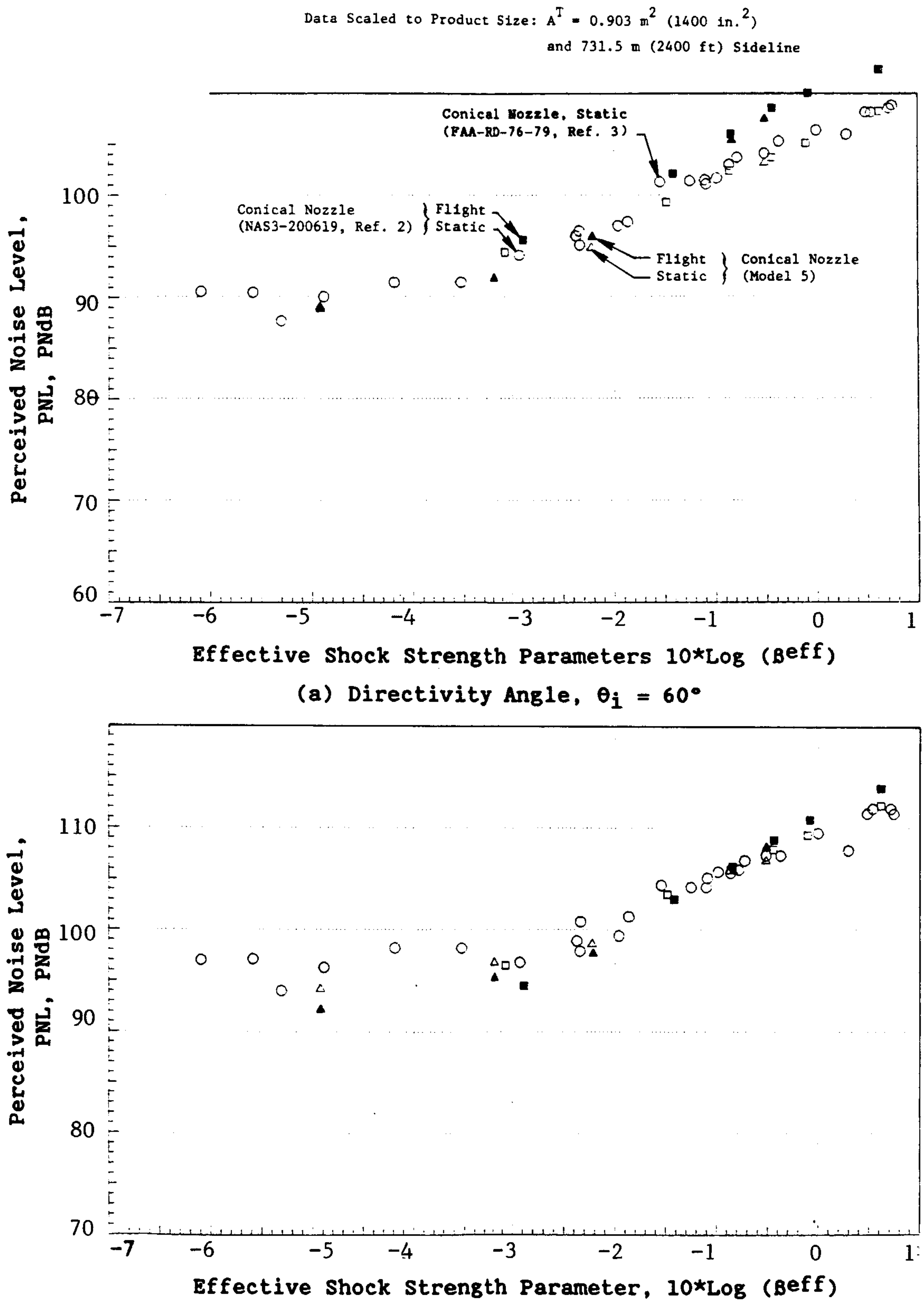

(a) Directivity Angle, θ_i = 60°

(b) Directivity Angle, θ_i = 90°

Figure 3-1. Summary of Forward Quadrant PNL Data of Conical Baseline Model Nozzle Measured Over the Years at General Electric Facilities.

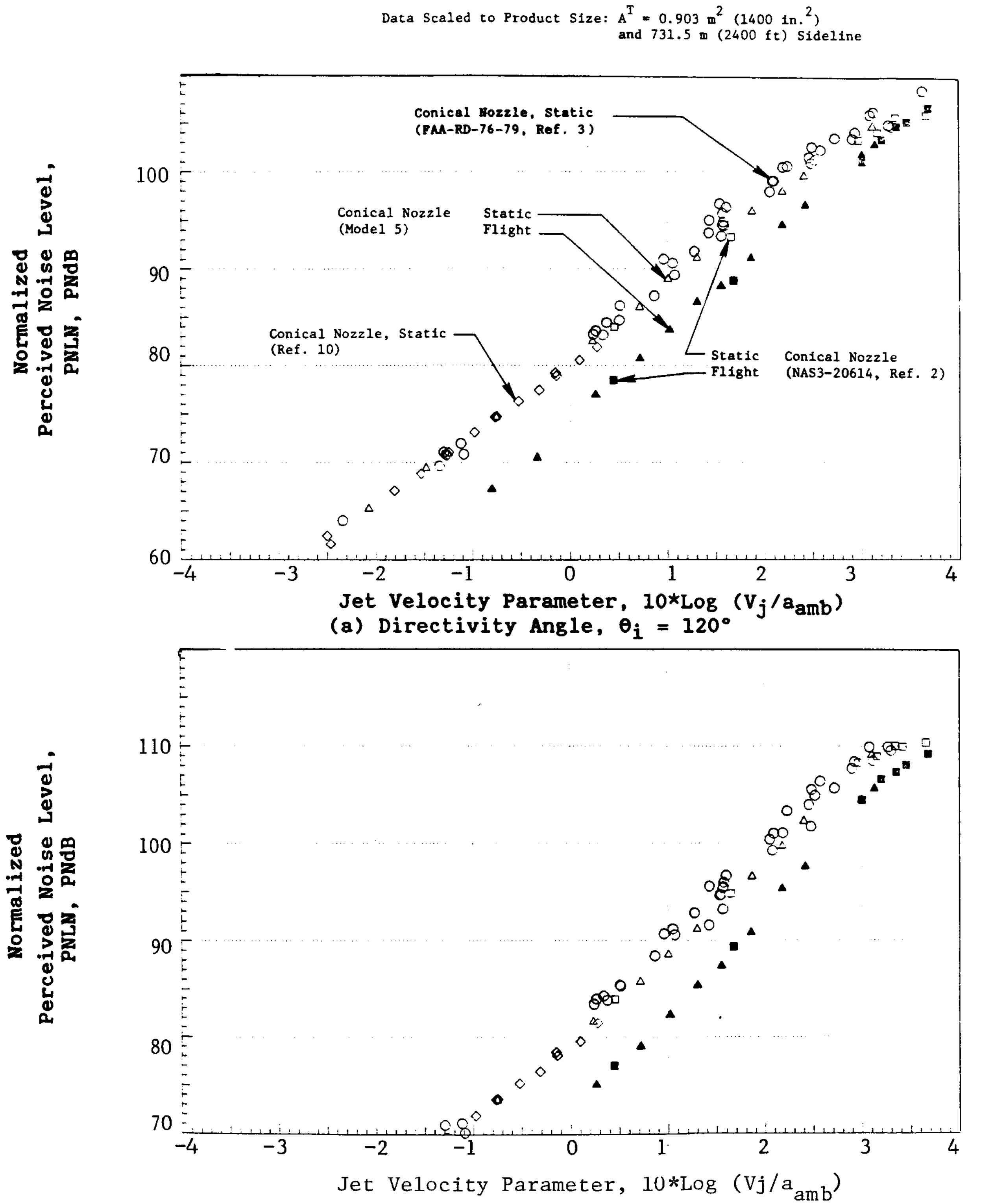

(b) Directivity Angle, θ_i = 130°

Figure 3-2. Summary of Aft Quadrant Normalized PNL Data of Conical Baseline Model Nozzle Measured Over the Years at General Electric Facilities.

configurations relative to the conical nozzle, are presented in Figures 3-3 and 3-4. The directivity data indicate the expected front quadrant shock noise amplification (for example, at $\theta_i = 60°$ the amplification in PNL is 4.3 dB) and aft quadrant jet noise suppression (for example, at $\theta_i = 130°$ the reduction in PNL is 3.5 dB) due to flight. The spectral comparison presented in Figure 3-4 indicates, as expected, a Doppler shift of the shock-associated peak frequency to higher frequencies in the front quadrant, lower values in the aft quadrant, and no change in the neighborhood of 90°.

3.1.2 Scaling of Static Acoustic Data

Current static acoustic scaling procedures for jet noise are based on an agreement of normalized far-field acoustic data of geometrically similar model and full-size nozzles. The normalization method mainly consists of sound pressure level changes proportional to the ratio of full-scale-to-model-size areas (which is assumed also equal to the ratio of the corresponding weight flow rates) and frequency shifts that maintain a constant Strouhal number (fD/V) for a given jet velocity. This later criteria results in shift of the 1/3-octave band center frequency proportional to the ratio of the diameters of the two nozzles. The resultant spectrum is extrapolated next to a constant arc or sideline distance using the inverse square law and standard day atmospheric attenuations. This scaling procedure (see Figure 2-5 for a data scaling flow chart) has been found to be valid in the case of single stream unsuppressed and suppressed nozzles of turbojets (Ref. 11). It is one of the objectives of this investigation to validate this static scaling procedure for unsuppressed and suppressed coannular configurations with inverted velocity profiles.

At the present time, single engine data are available from the 1978 YJ101 VCE tests (with a treated inlet) having an unsuppressed coannular nozzle with an inverted velocity profile and a conical baseline nozzle (Ref. 7). These results, extrapolated to a common total exhaust area of 0.9032 m^2 (1,400 $in.^2$) and sideline distance of 731.5 meters (2,400 feet) are compared in this subsection with the corresponding extrapolated data of scale-model similitude unsuppressed coannular (Model 8) and conical (Model 5) nozzles of this program. While the similitude scale-model suppressor (Model 10.1) data were measured during this investigation (and presented later in this section), their comparison with similar engine data cannot be made at this time as the planned YJ101 VCE tests with suppressor nozzles have been cancelled.

3.1.2.1 Conical Nozzle Scaling

A comparison of the extrapolated conical nozzle PNL data obtained from engine and model static tests at $\theta_i = 60°$, 90°, 130°, and 140° is presented in Figures 3-5 and 3-6 over a range of operating flow conditions. An examination of the data indicates a good correlation over the test range.

Comparisons of PNL directivity and selected spectral data of model and engine conical nozzle results at a typical AST takeoff condition of V_j = 700 m/sec (~2,300 fps) are presented in Figure 3-7. For a given 1/3-octave band, the data indicate an average deviation of less than 2 dB between the two sets of results.

Test Point	P_r	T_T	V_j	NF
△ 567	2.91	1685	2324	-6.5
▲ 568	2.92	1689	2327	-6.5

Data Scaled to Product Size: $A^T = 0.903m^2$ (1400 in.) and 731.5m (2400 ft.) Sideline

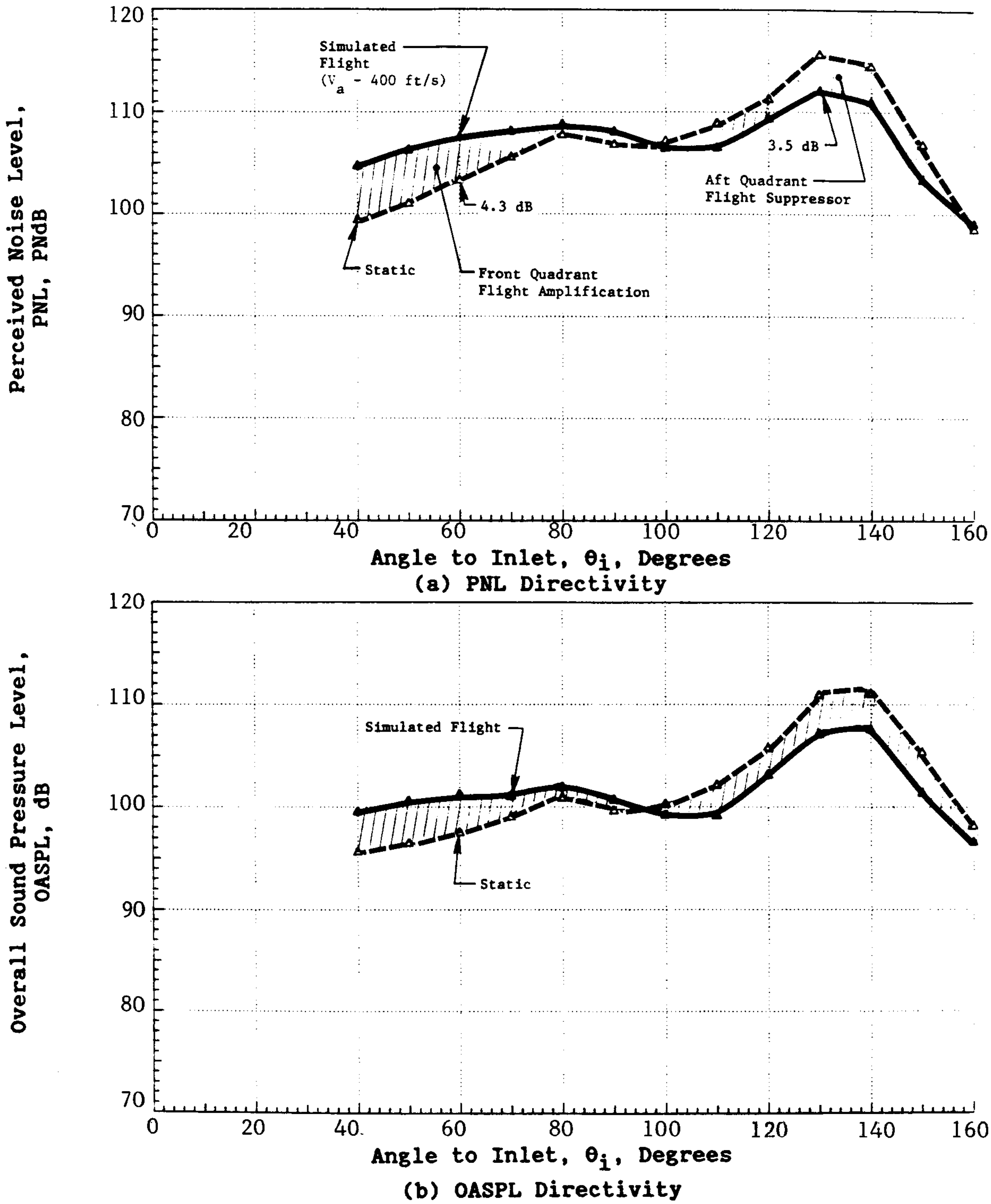

Figure 3-3. Effects of Flight on the PNL and OASPL Directivity of Conical Baseline Nozzle at Typical AST Takeoff Condition.

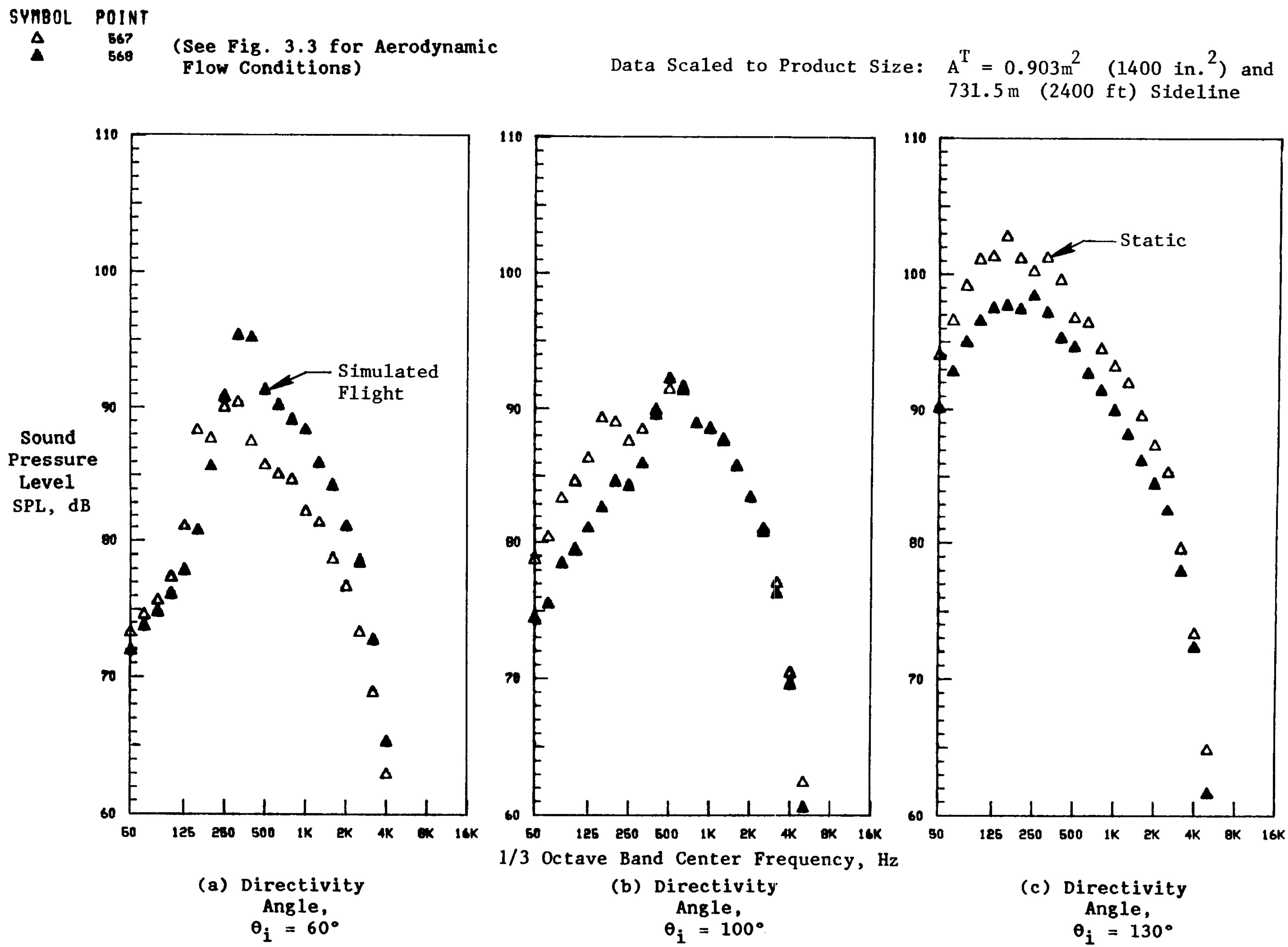

Figure 3-4. Spectral Comparison of Static with Simulated Flight Data of Conical Baseline Nozzle at Typical AST Takeoff Condition.

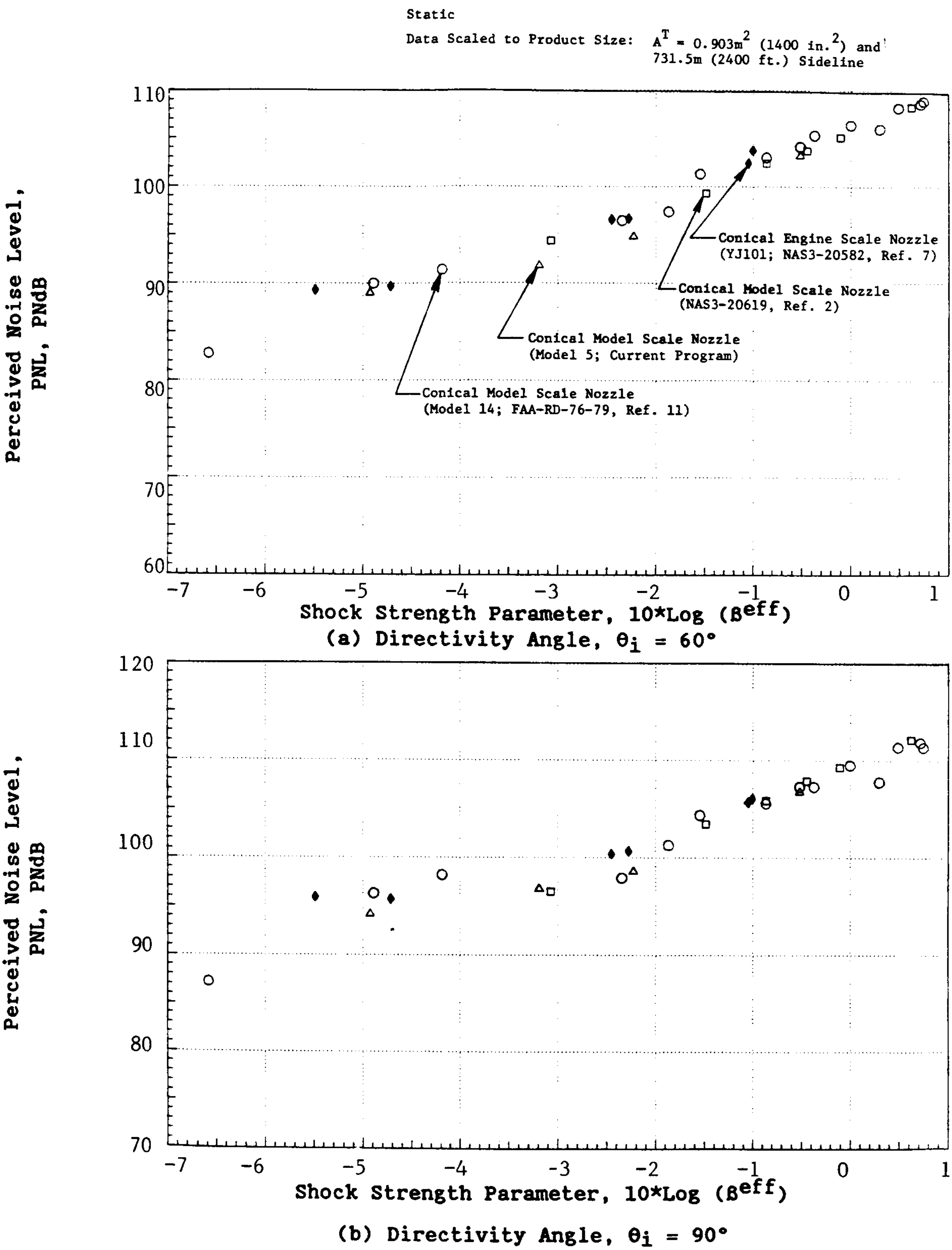

Figure 3-5. Comparison of Model and YJ101 Engine Measured Conical Baseline Nozzle PNL Data in the Forward Quadrant.

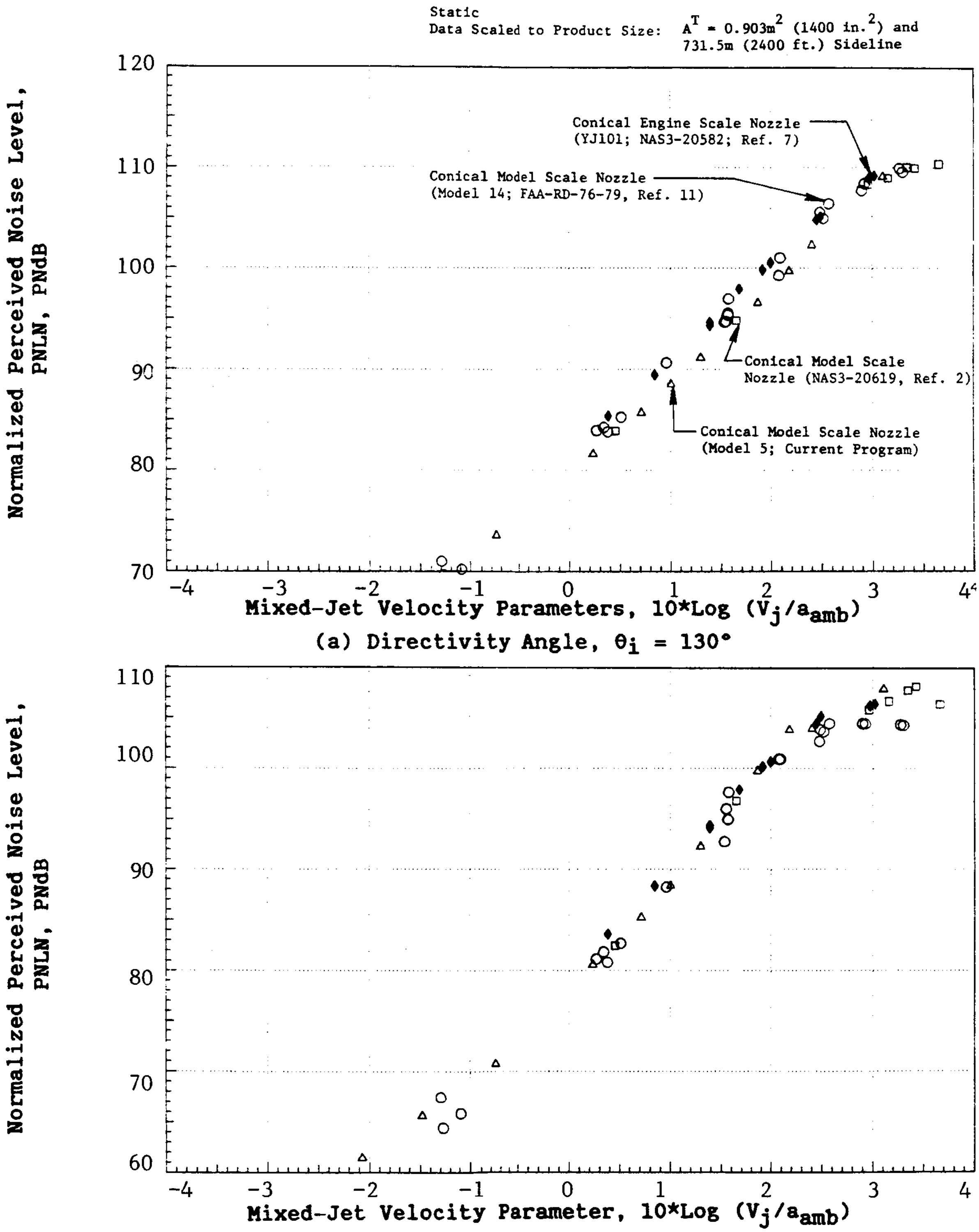

(a) Directivity Angle, θ_i = 130°

(b) Directivity Angle, θ_i = 140°

Figure 3-6. Comparison of Model and YJ101 Engine Measured Conical Baseline Nozzle Normalized PNL Data in the Aft Quadrant.

SYMBOL	Test POINT	Pr	T_T (° R)	V_j(fps)	NF	Scale	Reference
◇	601	2.75	1690	2270	-5.8	Model	NAS3-20619, Ref. 2
△	567	2.92	1685	2324	-6.5	Model	Current Program
◊	9094	2.73	1650	2236	-5.7	Engine	NAS3-20582 Ref. 7

Data Scaled to Product Size: $A^T = 0.903m^2$ (1400 in.^{2}) and 731.5m (2400 ft.) Sideline

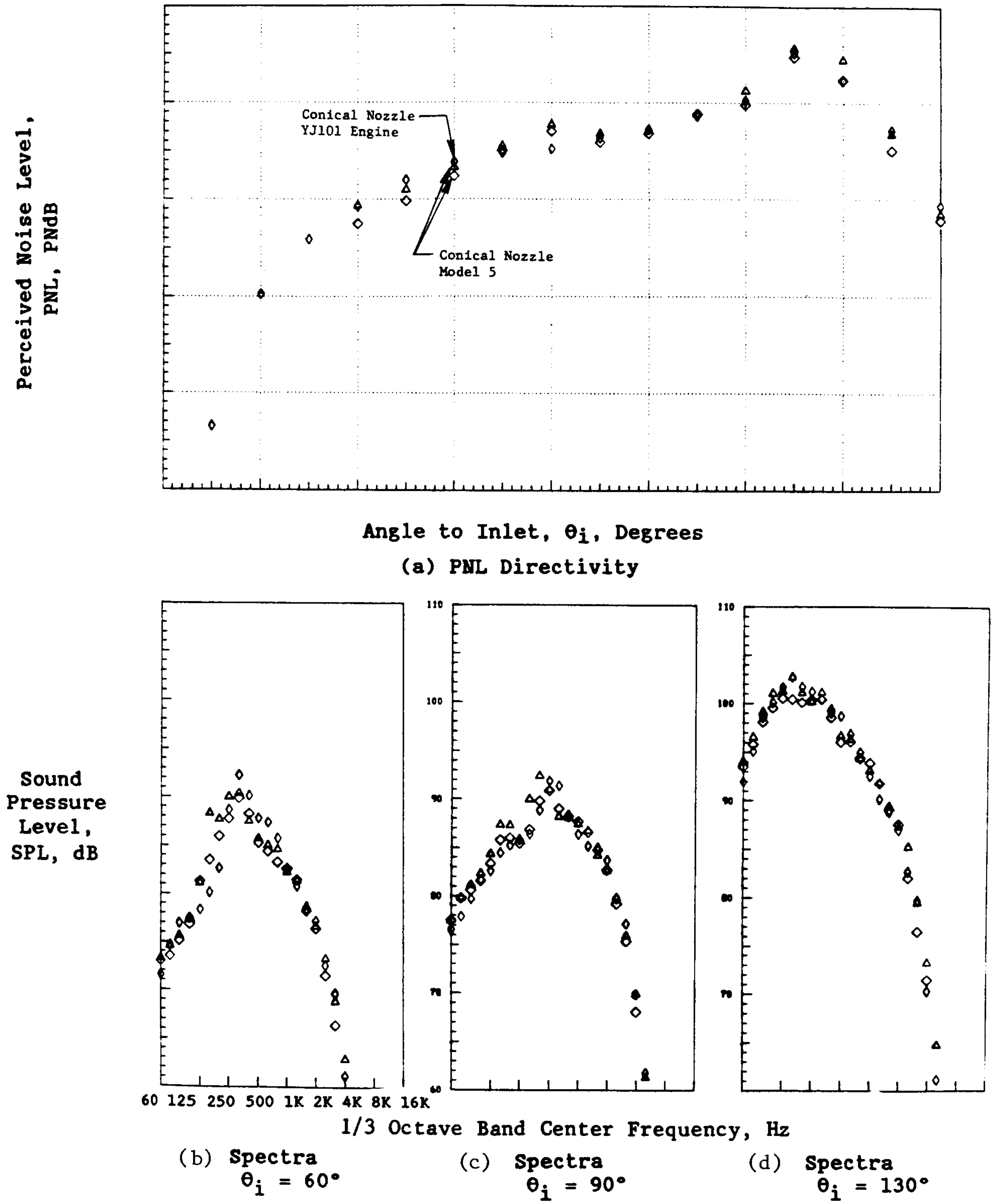

Figure 3-7. Comparison of PNL-Directivity and Selected Spectral Data of Model and Engine Conical Baseline Nozzle at AST Takeoff Condition of 700 M/Sec (2300 FPS).

3.1.2.2 Coannular Nozzle (With Inverted Velocity Profile) Scaling

The normalized PNL_{max} comparison between the YJ101 engine and the geometrically similar Model 8 coannular nozzle (A_r = 0.2, R_r^o = 0.853) over the test velocity range is provided in Figure 3-8. A good agreement between the two sets of data is noted for values of V_j^{mix} > 460 m/sec (~1,500 fps). The disagreement observed at lower velocities is due to the contamination of engine jet spectra with the turbomachinery noise.

Individual OASPL, PNL directivity and spectral comparisons between the engine and similitude model data at reasonably well-matched aerodynamic flow variables that simulate a typical AST engine takeoff condition are presented in Figures 3-9 and 3-10. Similar comparisons at typical AST engine approach conditions are provided in Figures 3-11 and 3-12. An examination of the model spectral data indicates the presence of a shock-screech tone in the model data and no such tone in the engine data. However, the good agreement noted otherwise between the model and engine spectral data at all angles confirms the adopted scaling procedure.

In summary, the results of the scale-model study confirm the conventional diametric scaling method adopted to extrapolate model size unsuppressed coannular nozzle (with inverted velocity profiles) acoustic data to typical AST nozzle characteristics over a range of velocities from takeoff to approach.

3.1.3 Flight Acoustic Data of Similitude Unsuppressed Coannular Nozzle (Model 8)

The effect of flight on the acoustic characteristics of a number of high radius-ratio (for example, R_r = 0.853 and 0.902) unsuppressed coannular plug nozzles has been discussed in Reference 2. In this subsection, the data measured during this program on the similitude unsuppressed coannular plug nozzle (Model 8, R_r = 0.853 and A_r = 0.2) are presented and discussed to verify that the coannular nozzle benefit obtained under static conditions relative to the conical baseline nozzle is retained in flight.

The static and simulated flight measured PNL data of the similitude unsuppressed coannular nozzle at θ_i = 130° and 60° are presented in Figures 3-13 and 3-14, respectively. The coannular nozzle data are compared in these figures with the static and simulated flight conical baseline nozzle data that were presented earlier in Figures 3-2 and 3-1. The comparison indicates that, in the region of mixed jet conditions that are of interest in a typical AST/VCE application (V_j^{mix} > 580 m/sec or 1,950 fps, P_r^{mix} > 2.5), the coannular nozzle benefits observed under static tests relative to a conical nozzle are retained in flight. This is made clear from the static and simulated flight PNL-directivity and spectral comparisons between the unsuppressed coannular plug nozzle (Model 8) and conical baseline nozzle data that are, respectively, presented in Figures 3-15 and 3-16. The data in these figures correspond to a typical AST/VCE takeoff mixed condition of V_j^{mix} ~700 m/sec (2,300 fps). They confirm, under flight, the static measured PNL benefits obtained with the coannular nozzle relative to a conical nozzle. For example, the PNL benefit of 6.0 and 5.5 dB established, respectively, at θ_i = 60° and 130° during static tests (Figure 3-15) is retained mostly during the simulated flight tests (Figure 3-16) as well.

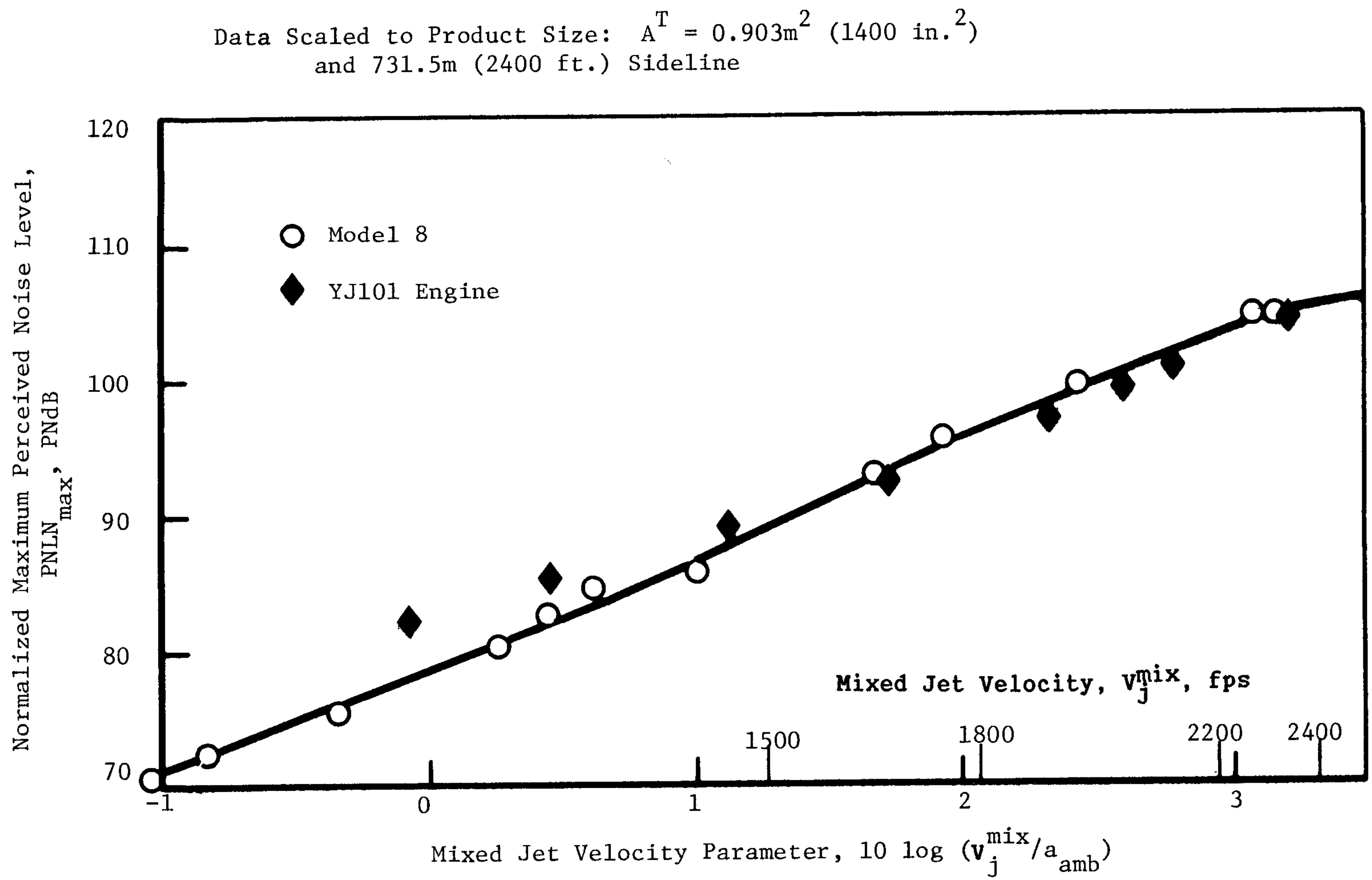

Figure 3-8. Comparison of Normalized PNL_{max} Between YJ101 and Geometrically Similar Model 8 Over the Engine Operating Line.

Symbol	Point	P_r^o	T_T^o (° F)	V_j^o (f/s)	P_r^i	T_T^i (° R)	V_j^i (f/s)	P_r^{mix}	T_T^{mix} (° R)	V_j^{mix} (f/s)	NF
○	8211	3.3	1757	2487	1.45	931	1062	3.0	1674	2344	-6.7
◇	435	2.90	1971	2527	2.78	250	1608	2.83	1717	2319	-5.9

Data Scaled to Product Size: $A^T = 0.903m^2$ (1400 in.^{2}) and 731.5m (2400 ft.) Sideline

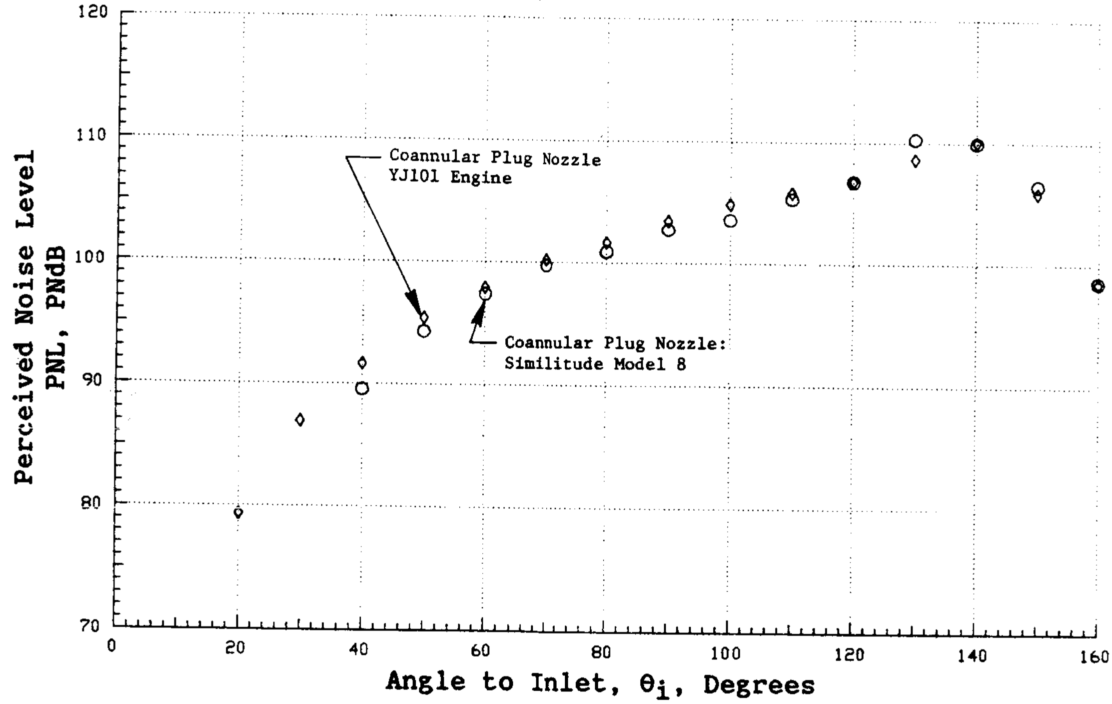

(a) PNL Directivity

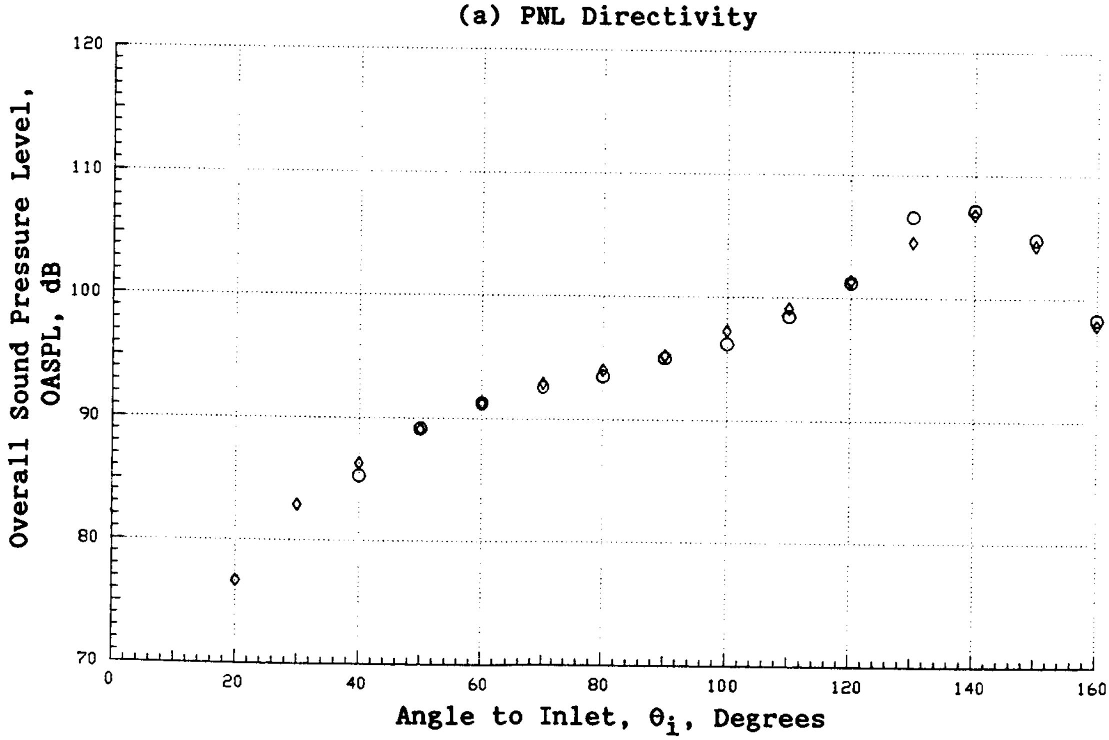

(b) OASPL Directivity

Figure 3-9. Comparison of Model and YJ101 Engine Measured Coannular Nozzle PNL- and OASPL-Directivity Data at AST Takeoff Condition of V_j^{mix} ~700 M/Sec (2300 FPS).

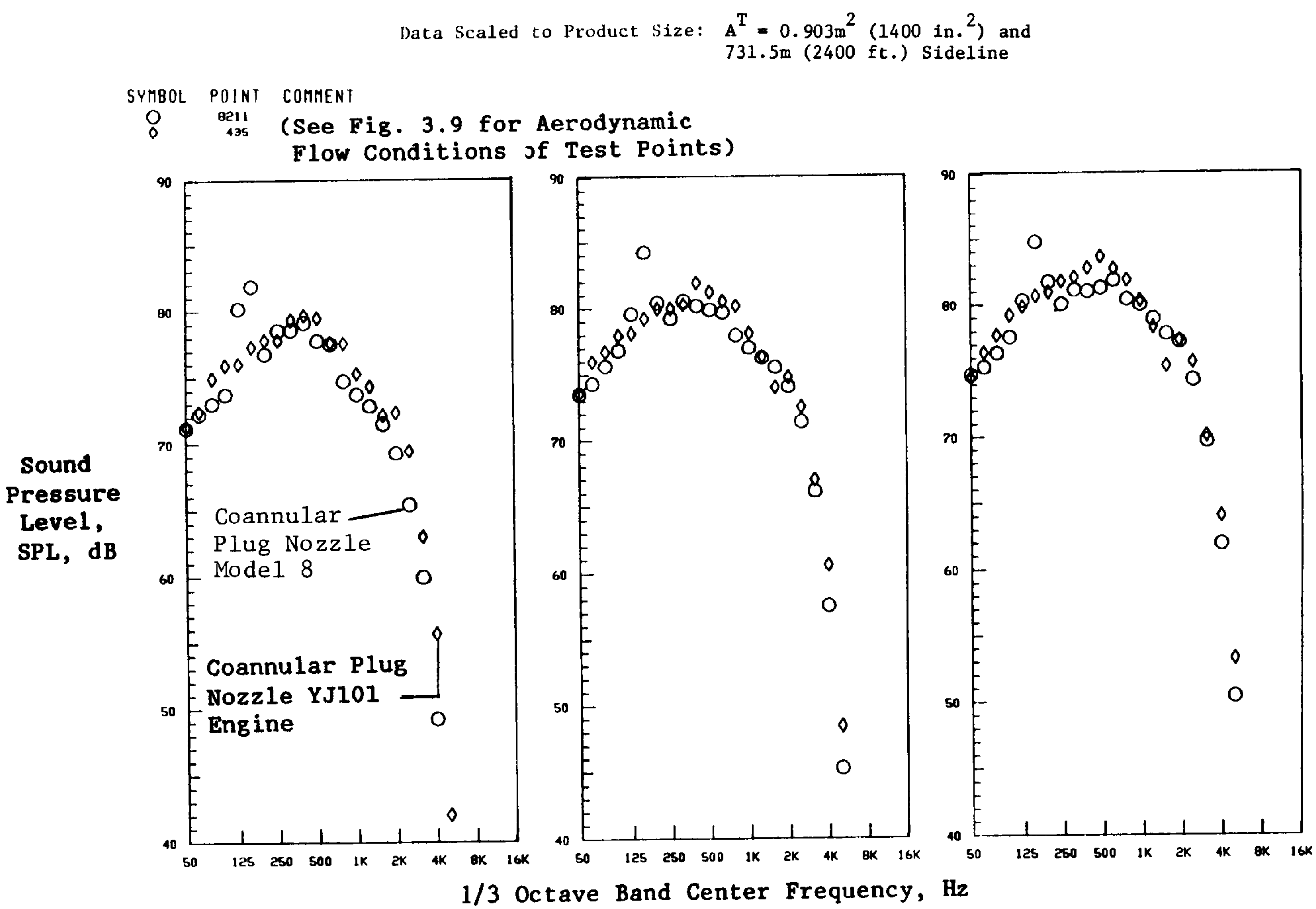

(a) Directivity Angle, $\theta_i = 50°$

(b) Directivity Angle, $\theta_i = 60°$

(c) Directivity Angle, $\theta_i = 70°$

Figure 3-10. Comparison of Model and YJ101 Engine Measured Coannular Nozzle Spectral Data at AST Takeoff Condition of V_J^{mix} ~700 M/Sec (or 2300 FPS).

Data Scaled to Product Size: $A^T = 0.903 m^2$ (1400 in.^{2}) and 731.5m (2400 ft.) Sideline

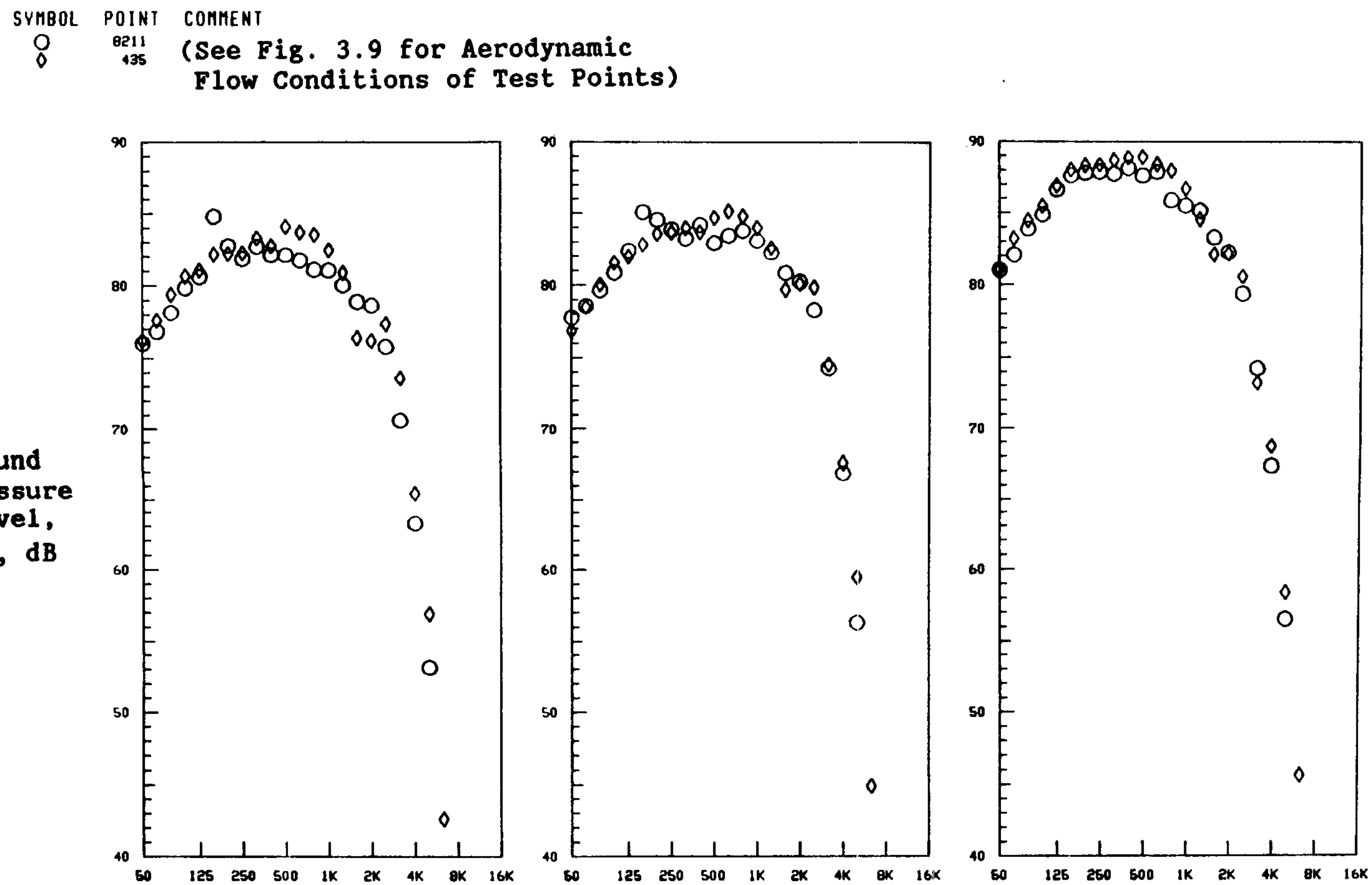

(d) Directivity Angle, $\theta_i = 80°$

(e) Directivity Angle, $\theta_i = 90°$

(f) Directivity Angle, $\theta_i = 110°$

3-10. (Continued)

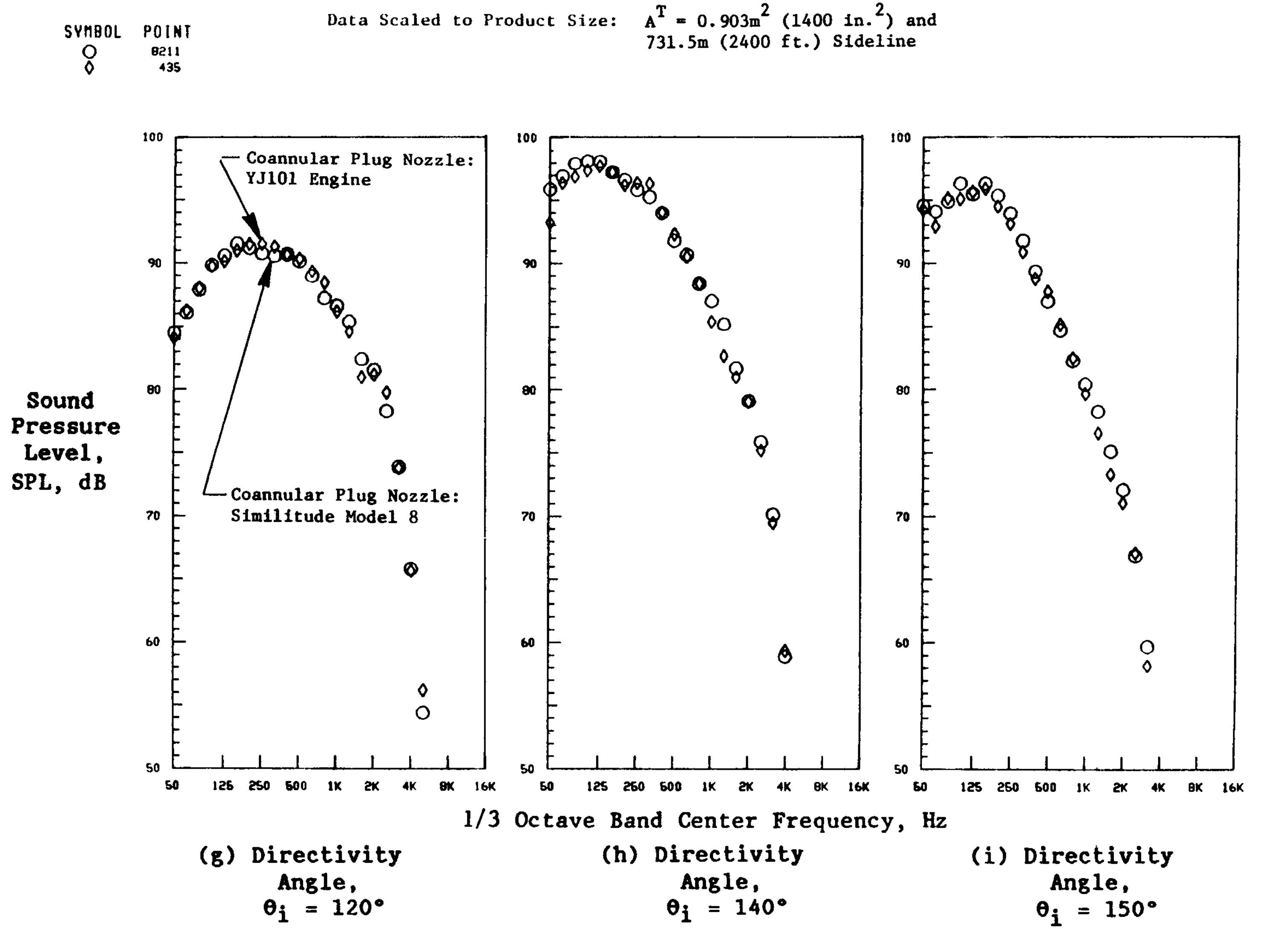

3-10. (Concluded).

Data Scaled to Product Size: $A^T = 0.903 m^2$ (1400 in.^{2}) and 731.5m (2400 ft.) Sideline

Symbol	Point	P_r^o	T_T^o (° R)	V_j^o (f/s)	P_r^i	T_T^i (° R)	V_j^i (f/s)	P_r^{mix}	T_T^{mix} (° R)	V_j^{mix} (f/s)	NF
○	8309	1.95	1543	1804	2.15	625	1213	1.94	1311	1655	-5.1
◇	432	1.92	1551	1786	1.86	731	1192	1.88	1369	1654	-4.3

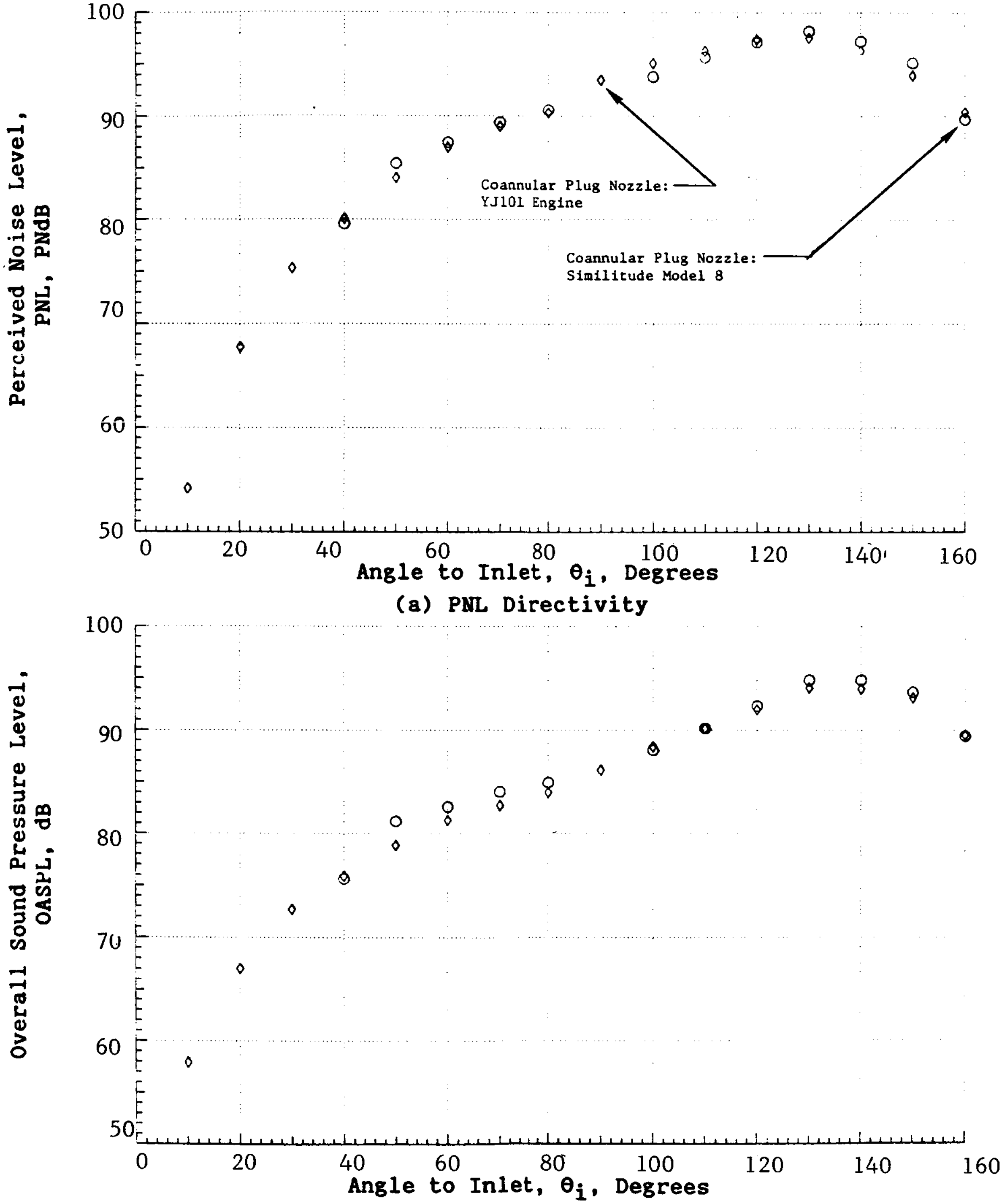

(a) PNL Directivity

(b) OASPL Directivity

Figure 3-11. Comparison of Model and YJ101 Engine Measured Coannular Plug Nozzle PNL- and OASPL-Directivity Data at AST Approach Condition of V_j^{mix} ~500 M/Sec (or 1650 FPS).

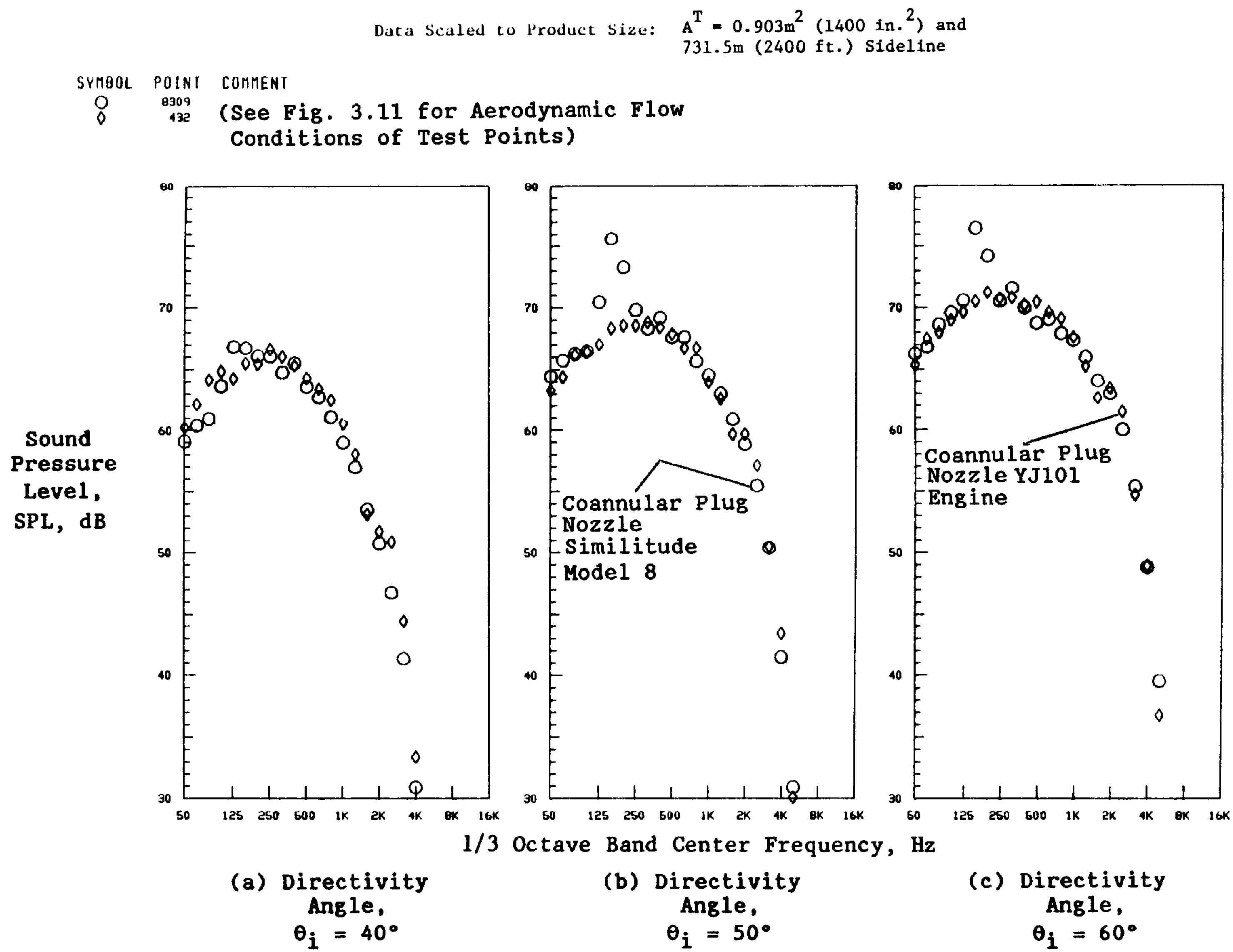

Figure 3-12. Comparison of Model and YJ101 Engine Measured Coannular Plug Nozzle Spectral Data at AST Approach Condition of V_j^{mix} ~500 M/Sec (or 1650 FPS).

Data Scaled to Product Size: $A^T = 0.903 m^2$ (1400 in.^{2}) and 731.5m (2400 ft.) Sideline

SYMBOL	POINT	COMMENT
○	8309	(See Fig. 3.11 for Aerodynamic Flow Conditions of Test Points)
◊	432	

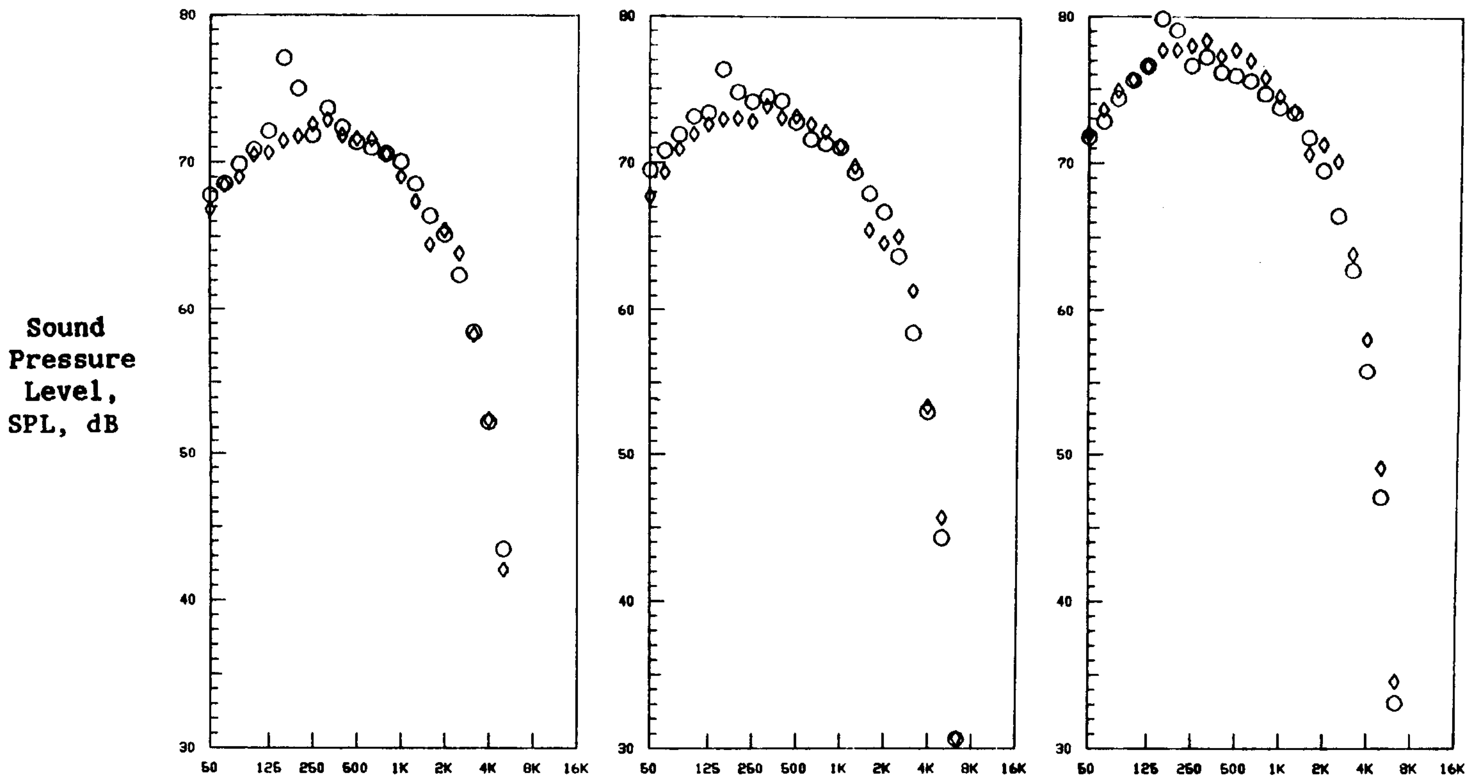

1/3 Octave Band Center Frequency, Hz

(d) Directivity Angle, $\theta_i = 70°$

(e) Directivity Angle, $\theta_i = 80°$

(f) Directivity Angle, $\theta_i = 100°$

Figure 3-12. (Continued)

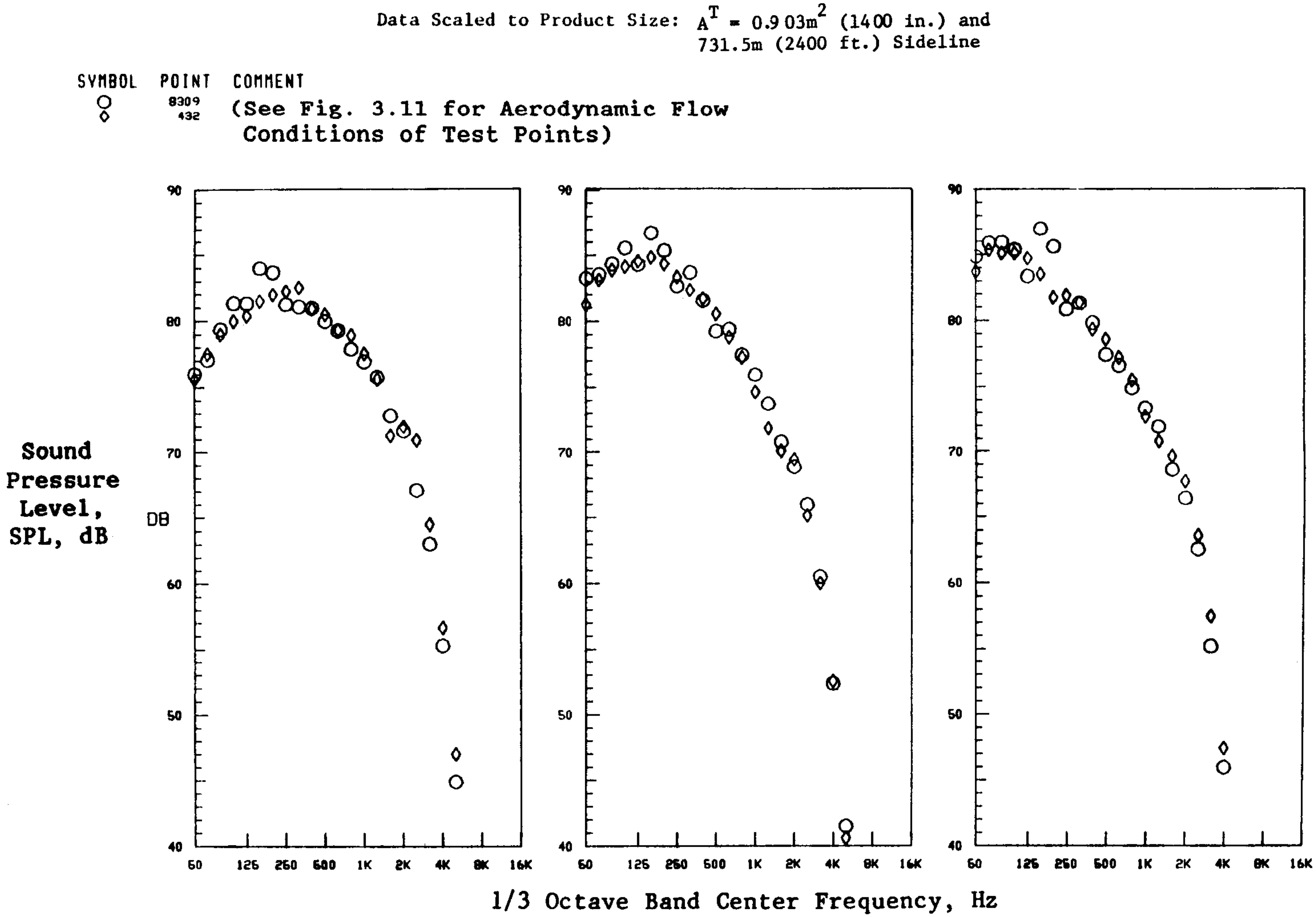

(g) Directivity Angle, $\theta_i = 120°$

(h) Directivity Angle, $\theta_i = 130°$

(i) Directivity Angle, $\theta_i = 140°$

Figure 3-12. (Concluded)

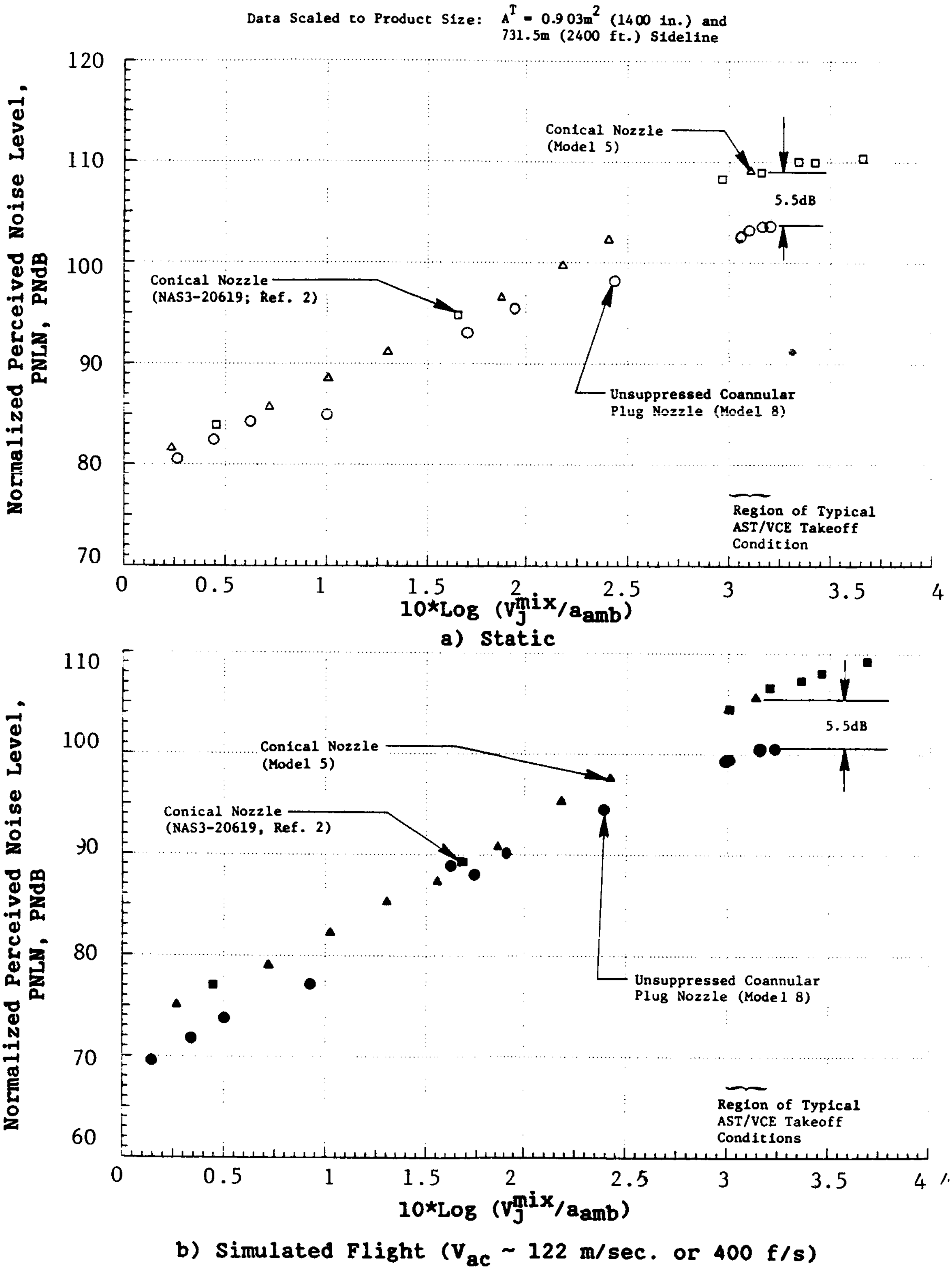

b) Simulated Flight (V_{ac} ~ 122 m/sec. or 400 f/s)

Figure 3-13. Comparison of Normalized PNL at θ_i = 130° for Similitude Coannular Nozzle (Model 8) with Those of Conical Baseline Nozzle.

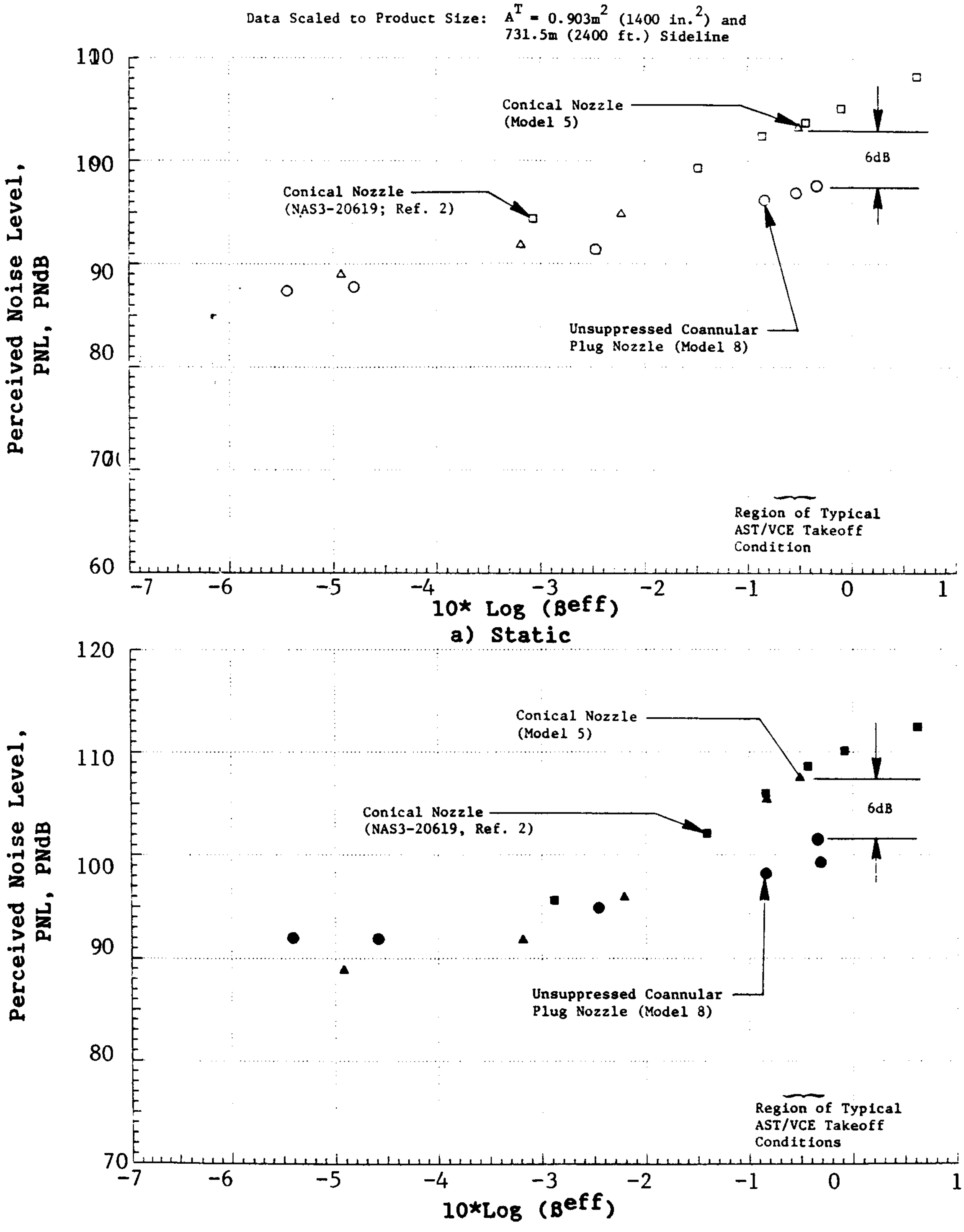

b) Simulated Flight (V_{ac} ~ 122 m/sec. or 400 f/s)

Figure 3-14. Comparison of Typical Forward Quadrant (θ_i = 60°) PNL of Similitude Coannular Nozzle with Those of Conical Baseline Nozzle.

Symbol	Model	Test Point	V_j^o (f/s)	T_T^o (°R)	P_r^o	V_j^i (f/s)	T_T^i (° R)	P_r^i	V_j^{mix} (f/s)	T_T^{mix} (° R)	P_r^{mix}	NF
△	5	567	2324	1685	2.92	-	-	-	2324	1685	2.92	-6.5
○	8	8211	2467	1757	3.30	1062	931	1.45	2344	1674	3.01	-6.7

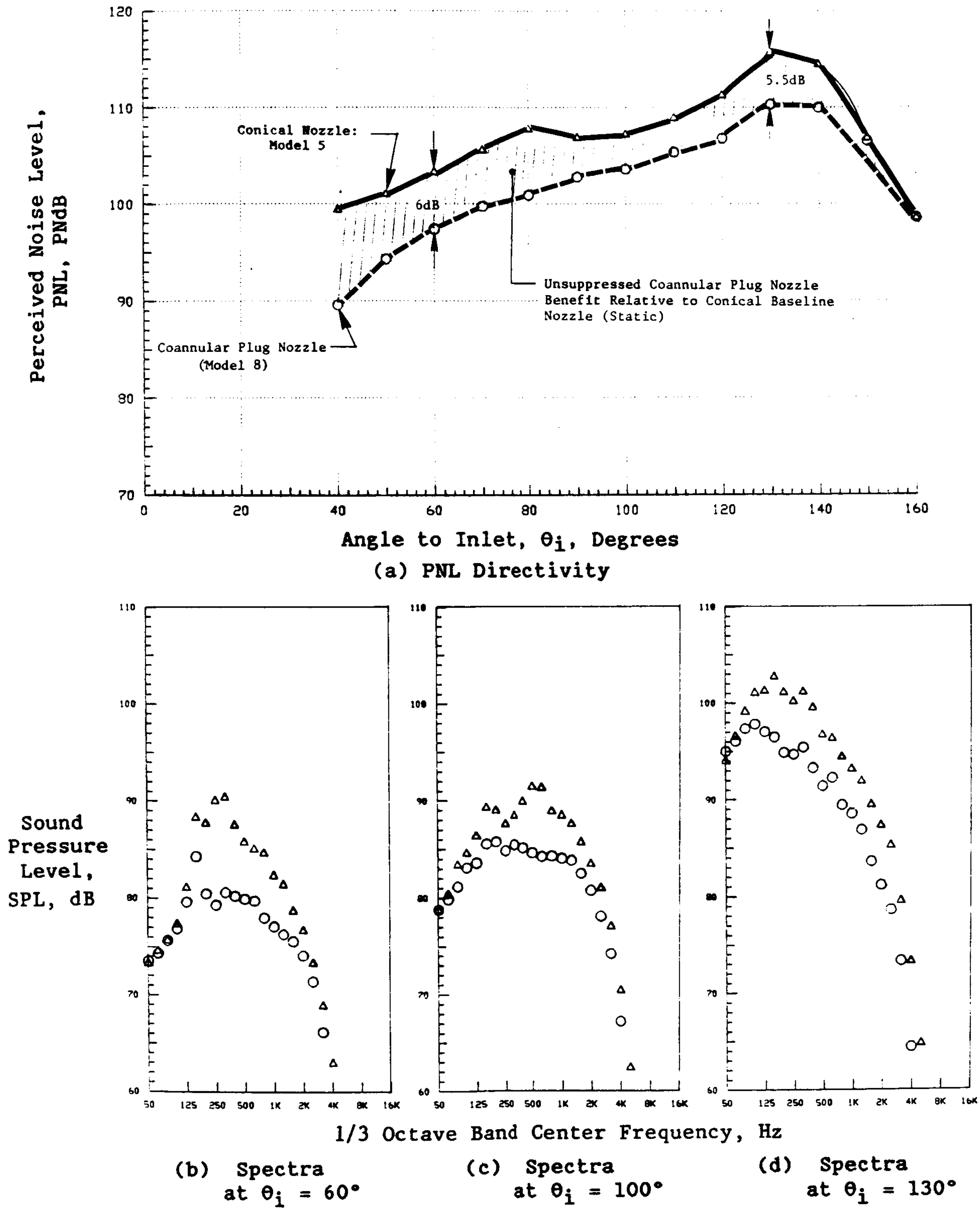

Figure 3-15. Comparison of PNL Directivity and Spectra of Unsuppressed Co-Annular Plug Nozzle (Model 8) with Those of Conical Baseline Nozzle (Model 5) at AST/VCE Takeoff Velocity (Static).

Data Scaled to Product Size: $A^T = 0.903 m^2$ (1400 in.^{2}) and 731.5m (2400 ft.) Sideline

Symbol	Model	Test Point	V_j^o (f/s)	T_T^o (° R)	P_r^o	V_j^i (f/s)	T_T^i	P_r^o	V_m^{mix}	T_T^{mix}	P_r^{mix}	NF
△	5	568	2327	1689	2.92	-	-	-	2327	1687	2.92	-6.5
○	8	8212	2502	1774	3.31	1080	957	1.45	2361	1693	3.02	-6.8

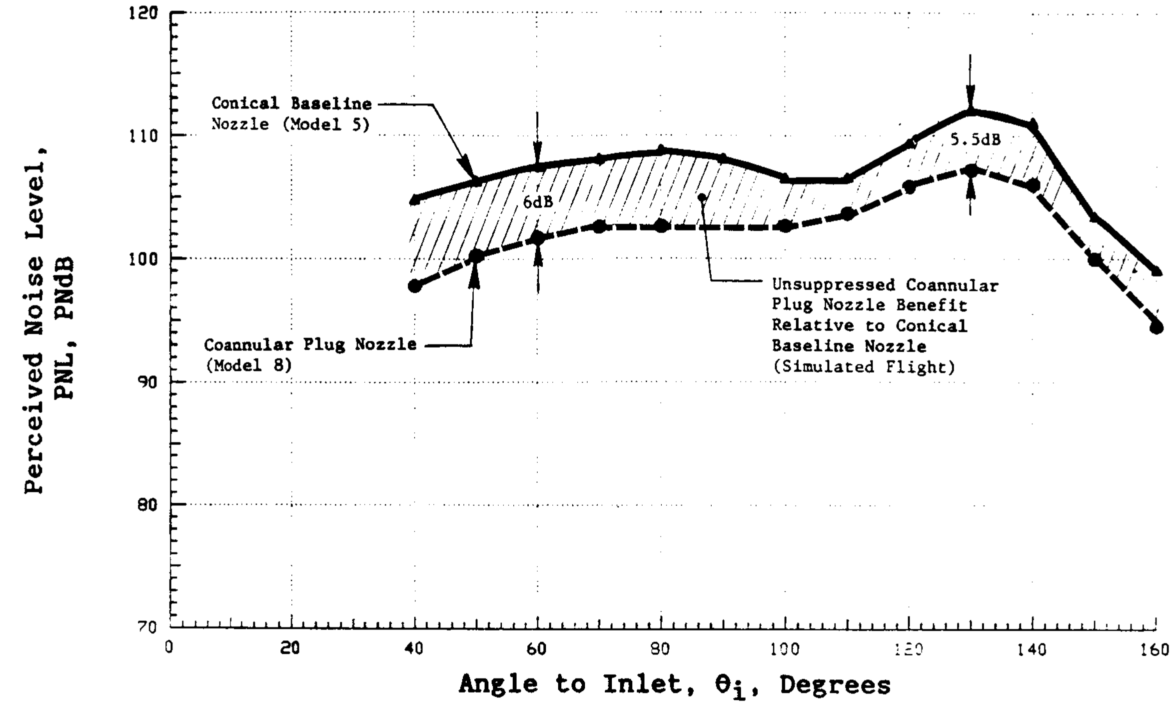

(a) PNL Directivity

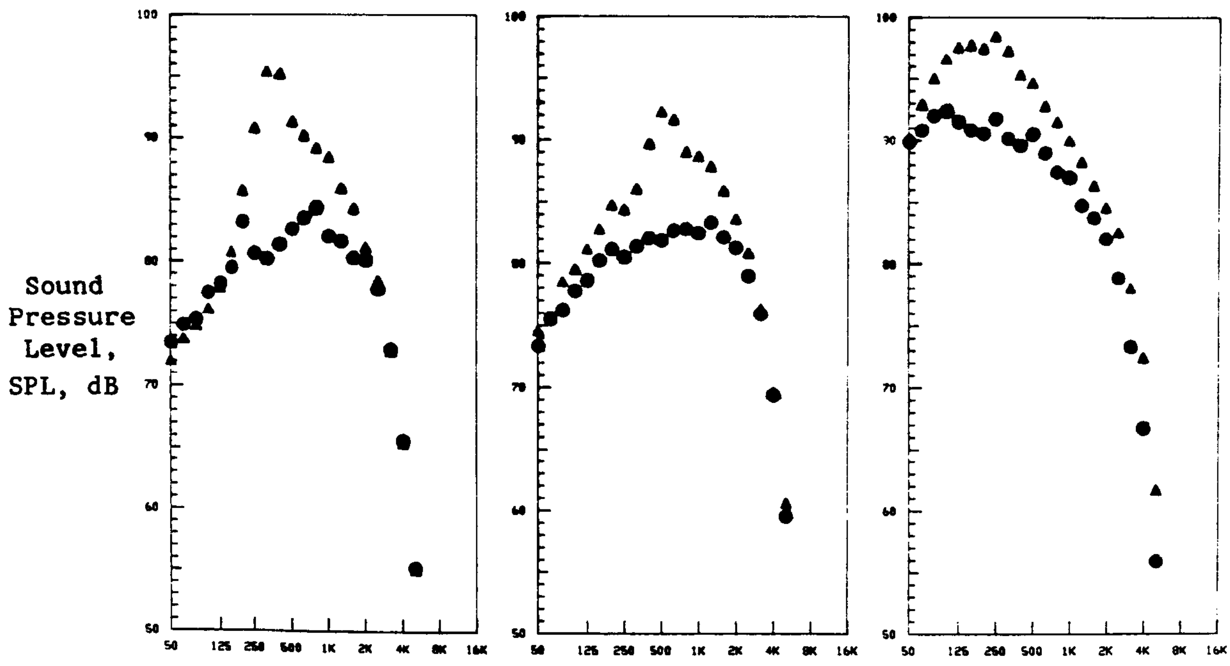

1/3 Octave Band Center Frequency, Hz

(b) Spectra at $\theta_i = 60°$

(c) Spectra at $\theta_i = 100°$

(d) Spectra at $\theta_i = 130°$

Figure 3-16. Comparison of PNL Directivity and Spectra of Similitude Unsuppressed Coannular Plug Nozzle (Model 8) with Those of Conical Baseline Nozzle (Model 5) at Typical Takeoff Condition (Flight Case).

Figure 3-17 demonstrates the effect of flight ($V_{ac} \sim 122$ m/sec or 400 fps) on the PNL directivity and typical spectral data of similitude coannular nozzle at a typical AST takeoff condition ($V_j^{mix} \sim$ 2,300 fps). The data indicate that, for example, a 4.3 and 3.1 dB flight amplification and suppression are observed at $\theta_i = 60°$ and 130°, respectively . A comparison of this figure with similar results obtained with conical baseline nozzle (Figure 3-3) indicates that, for equivalent mixed conditions, the effect of flight on the similitude coannular static results is very similar to those observed with the conical baseline nozzle.

3.1.4 Evaluation of Mechanical Suppressors

During this program, acoustic measurements have been conducted with the following four dual flow nozzles (with inverted velocity profiles) having mechanical suppressors in each of their outer streams:

1. Similitude 20-shallow-chute suppressor with a convergent inner nozzle (Model 10.1: $A_r = 0.2$, $R_r^o = 0.764$)

2. Similitude 20-shallow-chute suppressor with a convergent-divergent inner nozzle (Model 10.2: A_r at throat = 0.2, $R_r^o = 0.764$)

3. 20-shallow-chute suppressor of DOT program (Ref. 11) modified for a system area ratio $A_r = 0.2$ ($R_r^o = 0.716$)

4. 40-shallow-chute suppressor of DOT program (Ref. 11) modified for a system area ratio $A_r = 0.2$ ($R_r^o = 0.716$)

Geometrical details of these configurations were presented in Subsections 2.4.4 through 2.4.7. Comparison of the significant dimensions of the similitude 20-shallow-chute model with those of the modified DOT 20-shallow-chute suppressor is provided in Table 2-II. In this subsection, the measured acoustic data of these four suppressor configurations are presented. The data are compared with the data of conical baseline and similitude coannular plug nozzles in order to establish the suppression levels of the tested configurations.

3.1.4.1 Acoustic Characteristics of the Similitude 20-Shallow-Chute Suppressor With Convergent Inner Nozzle (Model 10.1)

The normalized PNL and OASPL at $\theta_i = 130°$ for the similitude 20-shallow-chute suppressor with a convergent terminated inner nozzle and measured during static and simulated flight tests are summarized in Figures 3-18 and 3-19, respectively. (The results for Model 10.2 with a C-D inner nozzle that are presented in these figures will be discussed in the next section.) The data are presented as a function of 10 log (V_j^{mix}/a_{amb}) and were obtained over a range of flow variables that are typical of an AST/VCE operating cycle conditions. The measured data are compared in each of these figures with the corresponding data of the conical baseline and similitude coannular nozzles (see Subsections 3.1.1 and 3.1.3). The comparison indicates that under static conditions and at a mixed jet velocity of 700 mps (or 2,300 fps, a typical AST takeoff condition) suppression to the extent of 11.5 and 12 dB (relative to a baseline conical nozzle) is obtained in the PNL and OASPL's at $\theta_i = 130°$. However, the corresponding suppressions during the simulated flight cases are observed to be 9 and 12 dB, Data Scaled to Product Size: $A^T = 0.903\ m^2$ (1400 in.^{2}) and 731.5 m (2400 ft) Sideline

Symbol	V_{ac} (f/s)	Test Point	V_j^o (f/s)	T_T^o (° R)	P_r^o	V_j^i (f/s)	T_T^i (° R)	P_r^i	V_j^{mix} (f/s)	T_T^{mix} (° F)	P_r^{mix}	NF
○	0	8211	2467	1757	3.30	1062	931	1.45	2344	1674	3.01	-6.7
●	4 00	8712	2502	1774	3.31	1080	957	1.45	2361	1693	3.02	-6.8

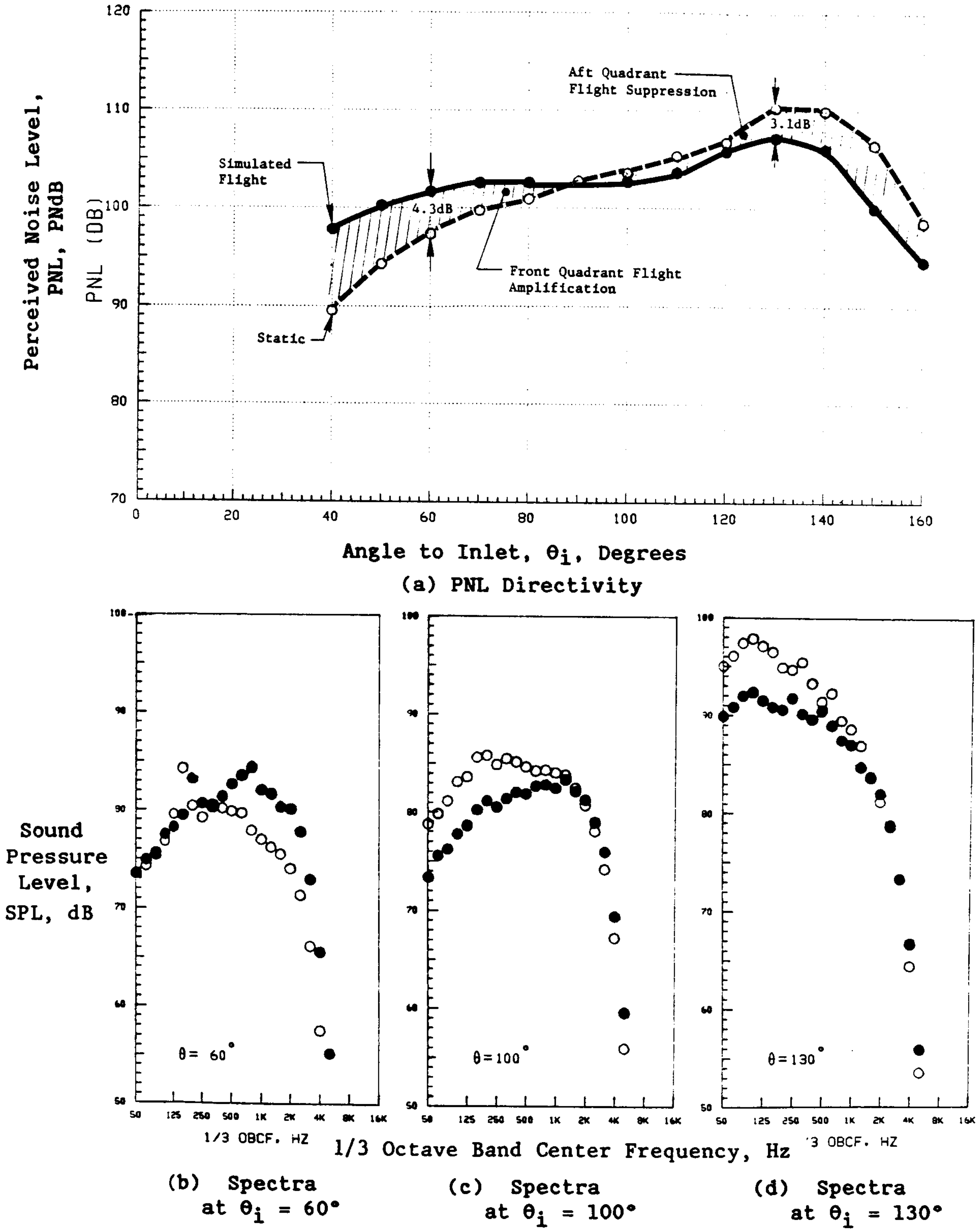

Figure 3-17. Comparison of Static with Simulated Flight Data of Similitude Coannular Nozzle at Typical AST Takeoff Condition (V_j^{mix} ~700 mps or 2300 FPS)

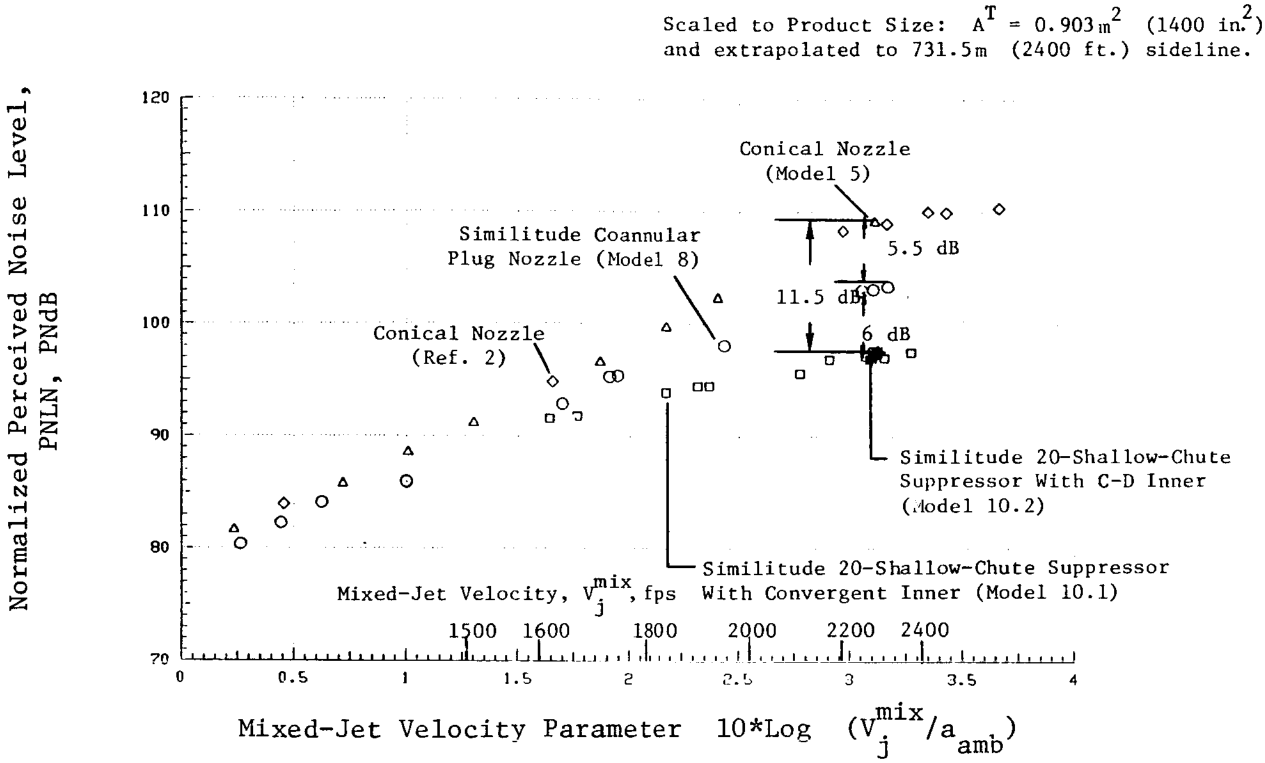

(a) Static

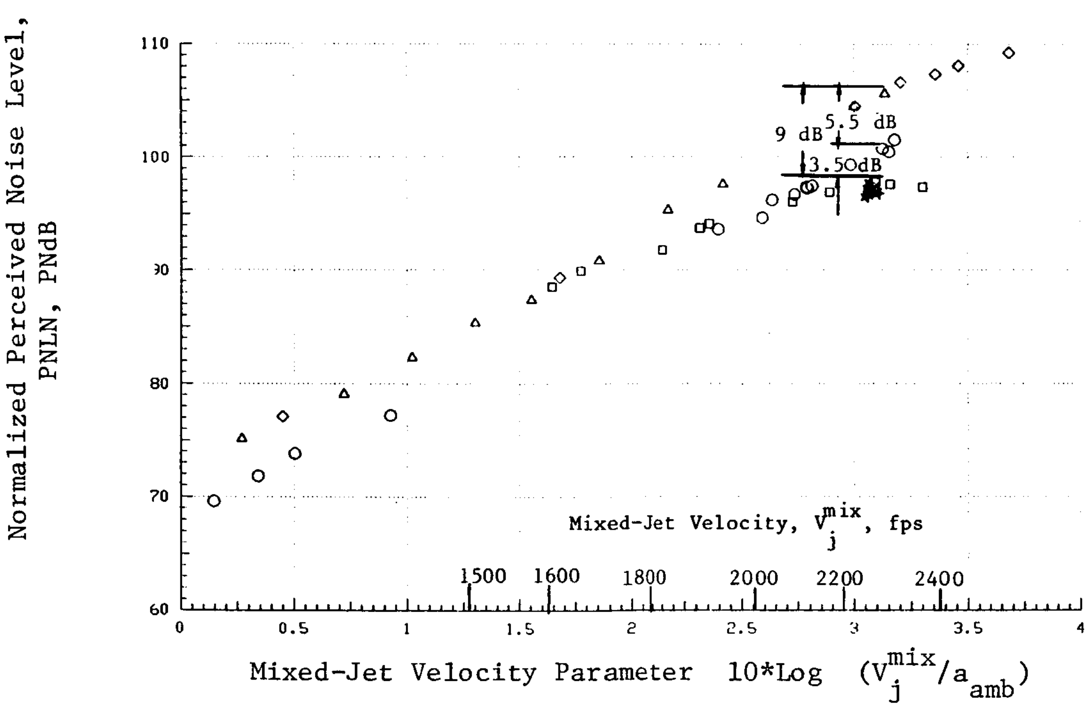

(b) Simulated Flight

Figure 3-18. Normalized PNL Data at $\theta_i = 130°$ for the Similitude 20-Shallow-Chute Suppressor with Convergent Terminated Inner (Model 10.1) and C-D Terminated Inner (Model 10.2) Nozzles.

Data Scaled to Product Size: $A^T = 0.903\ m^2$ (1400 in^2) and Extrapolated to 731.5 m (2400 ft.) Sideline

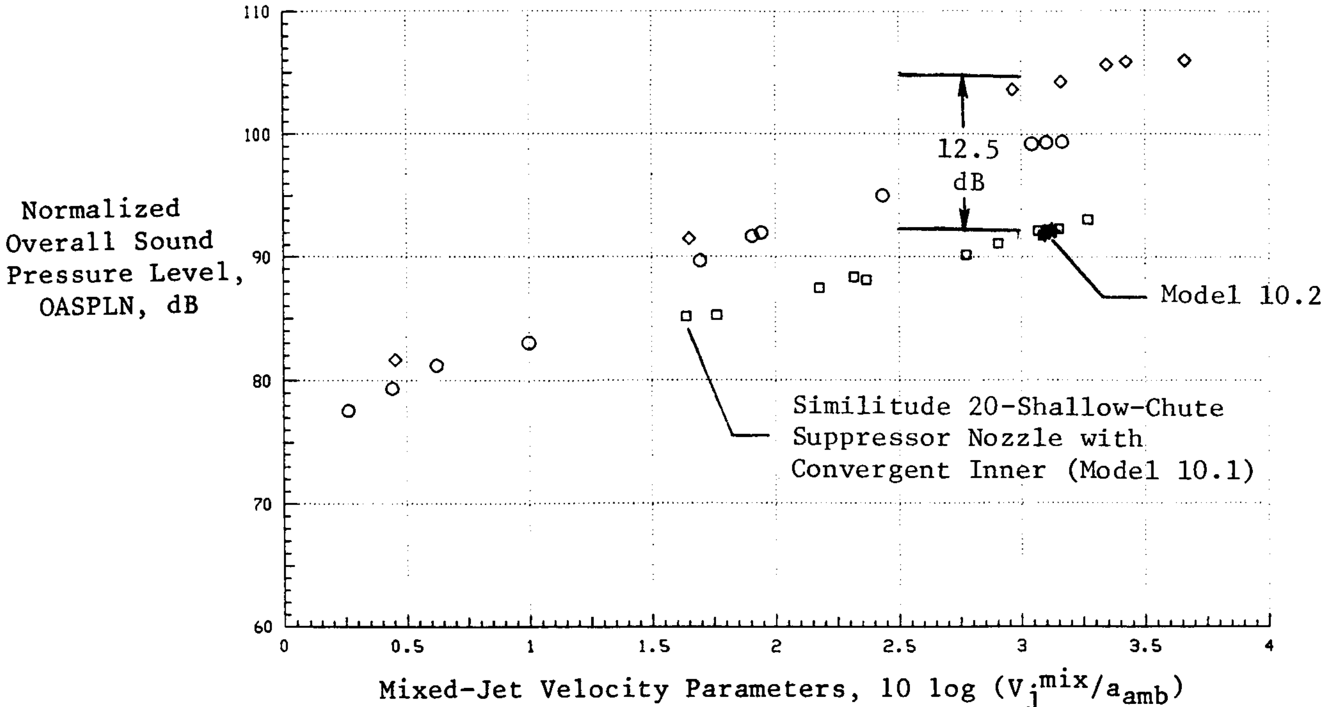

(a) Static

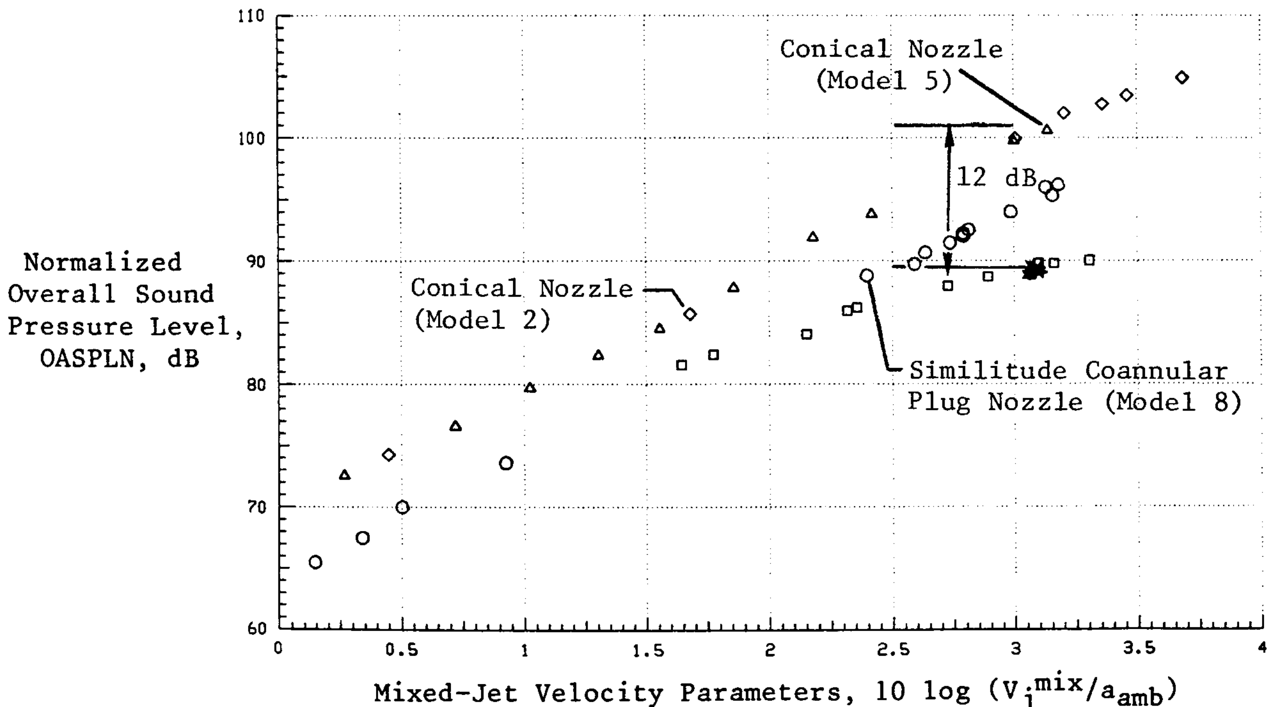

(b) Simulated Flight

Figure 3-19. Normalized OASPL Data at θ_i=130° for the Similitude 20-Shallow-Chute Suppressor with Convergent Terminated Inner (Model 10.1) and C-D Terminated Inner (Model 10.2) Nozzles.

respectively. This static-to-flight suppression loss (e.g., 3 dB in the PNL data at θ_i = 130°) and no loss in the corresponding OASPL suppression are observed at all mass-averaged velocities greater than 1,600 fps. Similar trends in the flight PNL data are observed at all aft angles. Normalized OASPL data at θ_i = 120° are presented in Figure 3-20 to confirm the observation made earlier that no static-to-flight suppression loss in the measured aft angle OASPL data existed.

Typical forward angle PNL and OASPL data are presented in Figures 3-21 and 3-22 for the static and simulated flight cases, respectively. The data are at θ_i = 60° and are presented as a function of the mixed stream parameter β^{eff}. The data also are compared with those of the conical baseline and similitude coannular nozzles. The data indicate that the similitude suppressor configuration (Model 10.1) is not effective in reducing the shock cell noise in the front quadrant under both static and flight conditions. In addition, for a given β^{eff}, the PNL and OASPL levels of the similitude suppressor nozzle are observed, respectively, to be higher and equal to those of the similitude coannular plug nozzle (Model 8) results.

A comparison of the PNL- and OASPL-directivities of the similitude suppressor nozzle with the corresponding data of a conical baseline and similitude coannular plug nozzle is provided in Figures 3-23 and 3-24. The peak noise level with the suppressor nozzle is observed to occur at θ_i = 120° while those of the conical and coannular plug nozzles are at θ_i = 130°. Relative to the coannular nozzle, considerable suppression is observed at inlet angles greater than 130°. These observations are applicable to both PNL and OASPL aft angle data and under both static and simulated flight conditions. In the front quadrant, as noted earlier, the similitude suppressor nozzle is not effective in reducing the PNL levels relative to the coannular plug nozzle.

Typical spectral data corresponding to the flow conditions of Figures 3-23 and 3-24 are provided in Figure 3-25. An examination of this figure indicates significant amount of reduction in low and high frequency SPL levels relative to a conical nozzle at all aft angles. However, the PNL increase observed earlier in the front quadrant data of the similitude suppressor relative to the coannular plug nozzle can be accounted due to the presence of high frequency noise of the suppressor elements. Also, there appears to be no significant high frequency benefit relative to the coannular plug nozzle at the aft angles. This is particularly true in the flight cases. In addition, the relative relationship between the high and low frequency SPL levels of the suppressor is observed to be different under static and simulated flight conditions. This is made clear by the spectral comparison presented in Figure 3-26 wherein the static and flight spectra of the suppressor nozzle (earlier presented in Figures 3-24 and 3-25) are replotted referenced to one another. An examination of this figure indicates that in the aft quadrant a significant flight suppression is observed in the low and midfrequency range SPL levels. However, there is no change and perhaps even a small increment in the high frequency flight SPL data relative to the static levels. This observation in the high frequency ranges is opposite to the trend earlier noted with the conical and coannular plug nozzles (Figures 3-4 and 3-17, respectively). In the latter cases, a significant reduction in both the frequency ranges has been observed with flight. These trends affect the PNL and OASPL calculations differently, hence the earlier noted differences in the PNL and OASPL suppression levels achieved

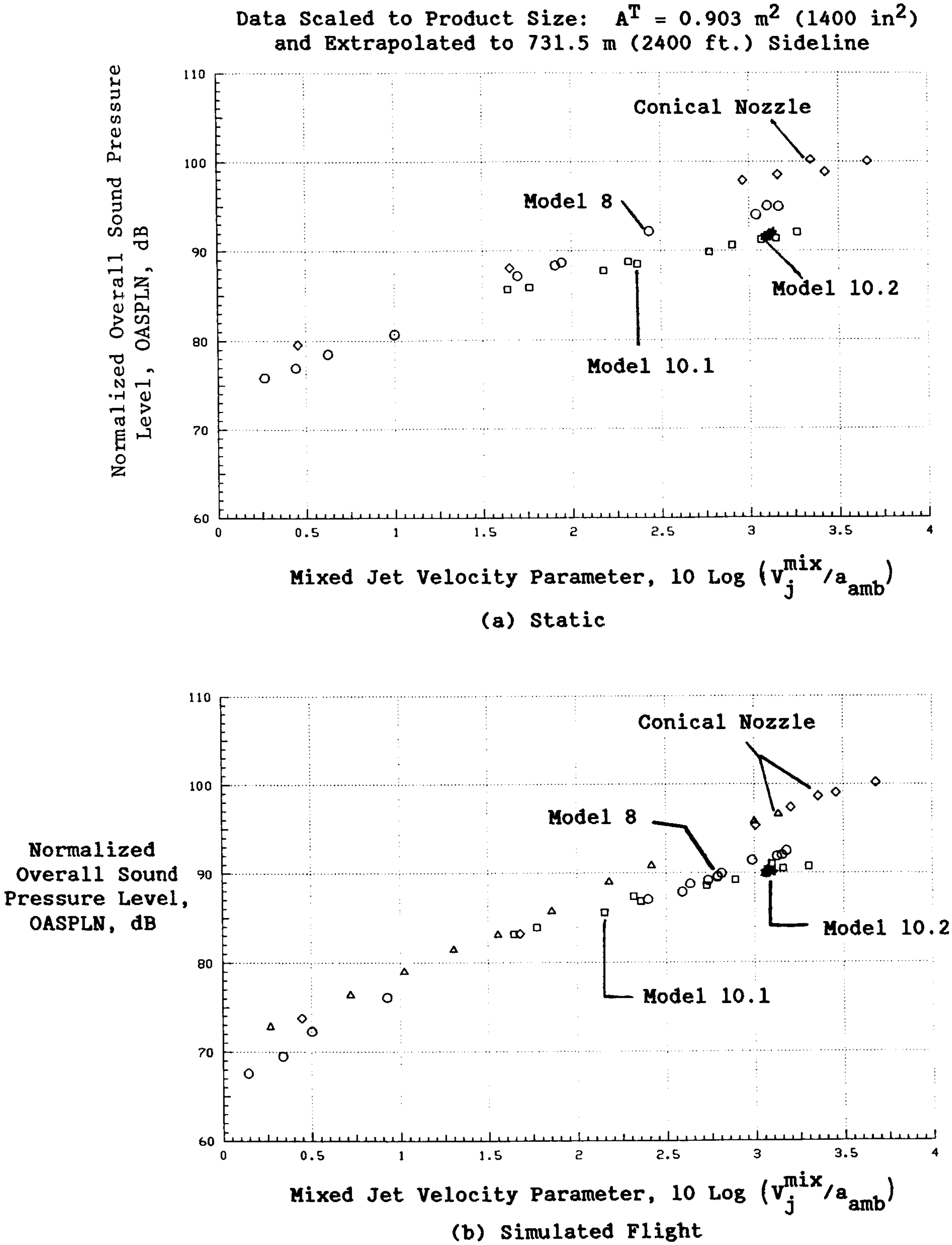

Figure 3-20. Normalized OASPL Data at θ_i = 120° for the Similitude 20-Shallow-Chute Suppressor with Convergent Terminated Inner (Model 10.1) and C-D Terminated Inner (Model 10.2) Nozzles.

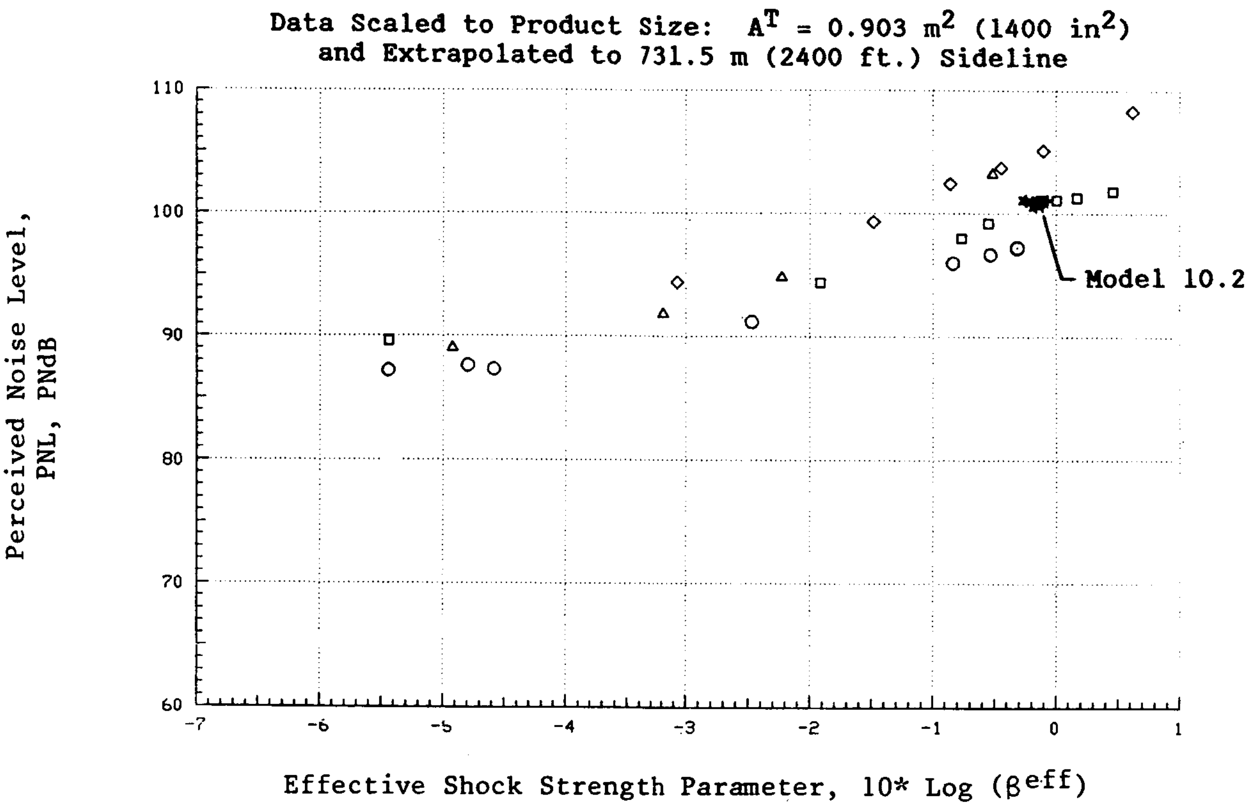

(a) Static

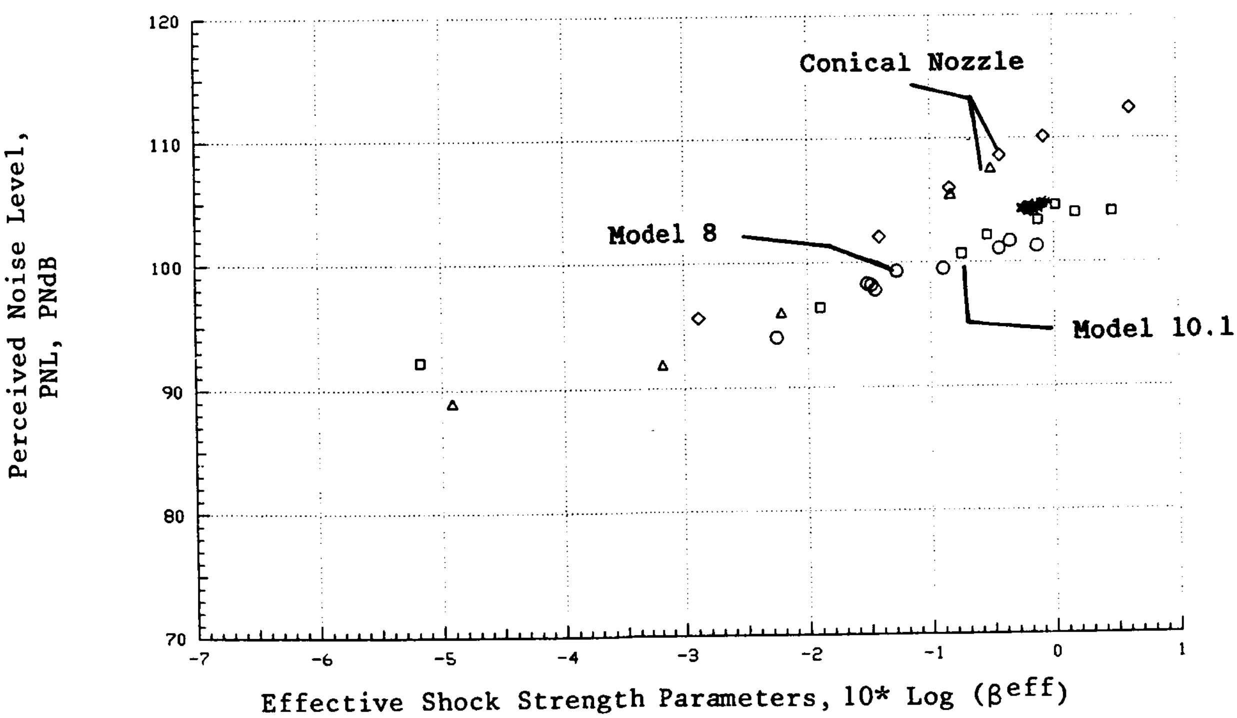

(b) Simulated Flight

Figure 3-21. PNL Data at θ_i = 60° for Similitude 20-Shallow-Chute Suppressor with Convergent Terminated Inner (Model 10.1) and Convergent-Divergent Terminated Inner (Model 10.2) Nozzles.

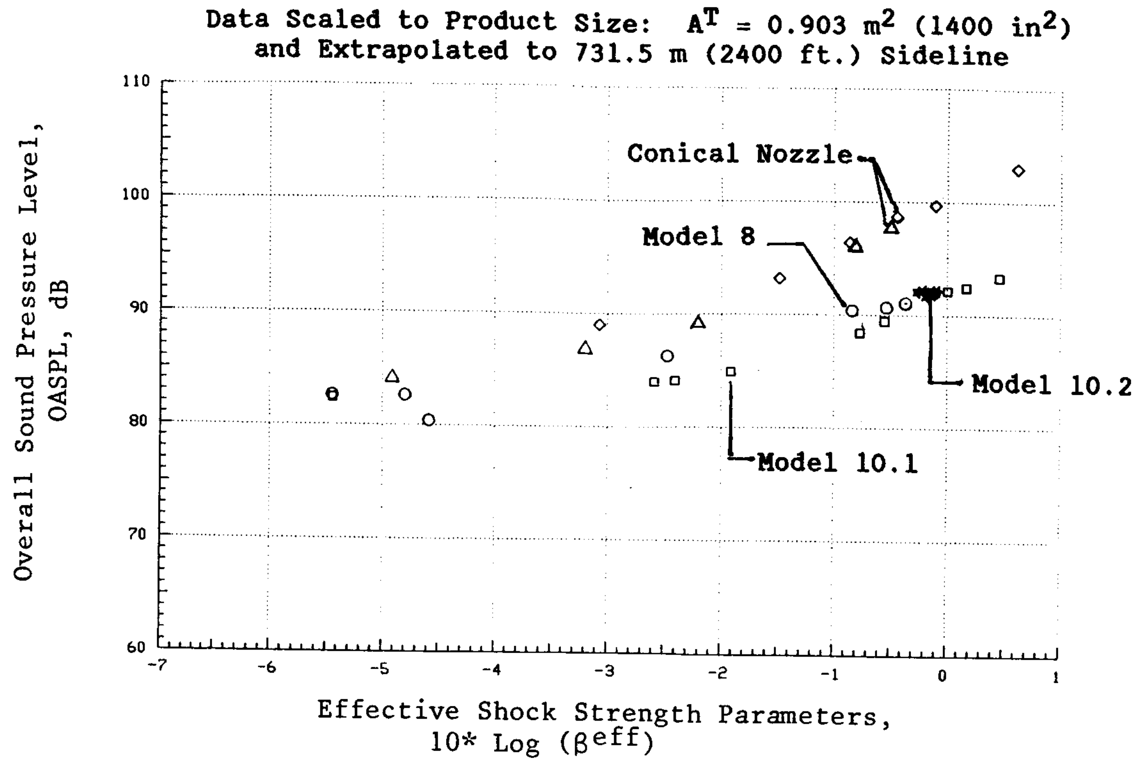

a) Static

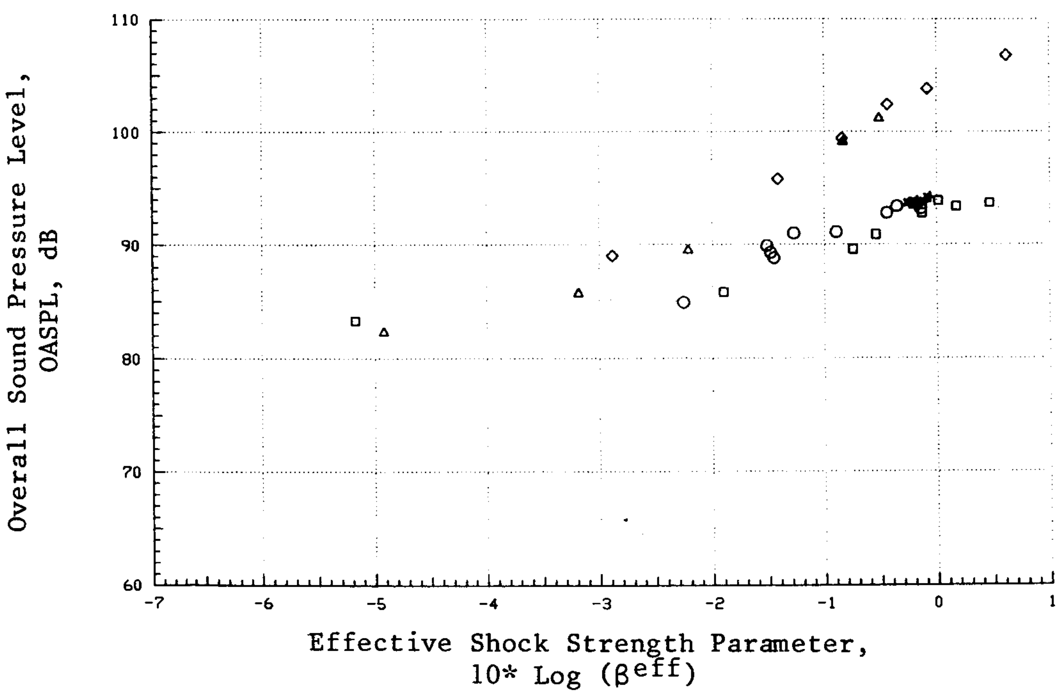

(b) Simulated Flight

Figure 3-22. OASPL Data at 60° for Similitude 20-Shallow-Chute Suppressor with Convergent Terminated Inner (Model 10.1) and Convergent-Divergent Terminated Inner (Model 10.2) Nozzles.

SYMBOL	POINT	COMMENT	P_r^o	T_T^o(°R)	V_j^o(tps)	P_r^i	T_T^i	V_j^i	P_r^{mix}	T_T^{mix}	V_j^{mix}	NP
◇		Conical	2.92	1685	2324				2.92	1685	2324	-65
□		Model 10·1	3.25	1745	2464	2.63	8.76	1594	3.11	1601	2320	
○		Model 8	3.30	1757	2467	1.45	9.31	1062	3.01	1674	2344	-67

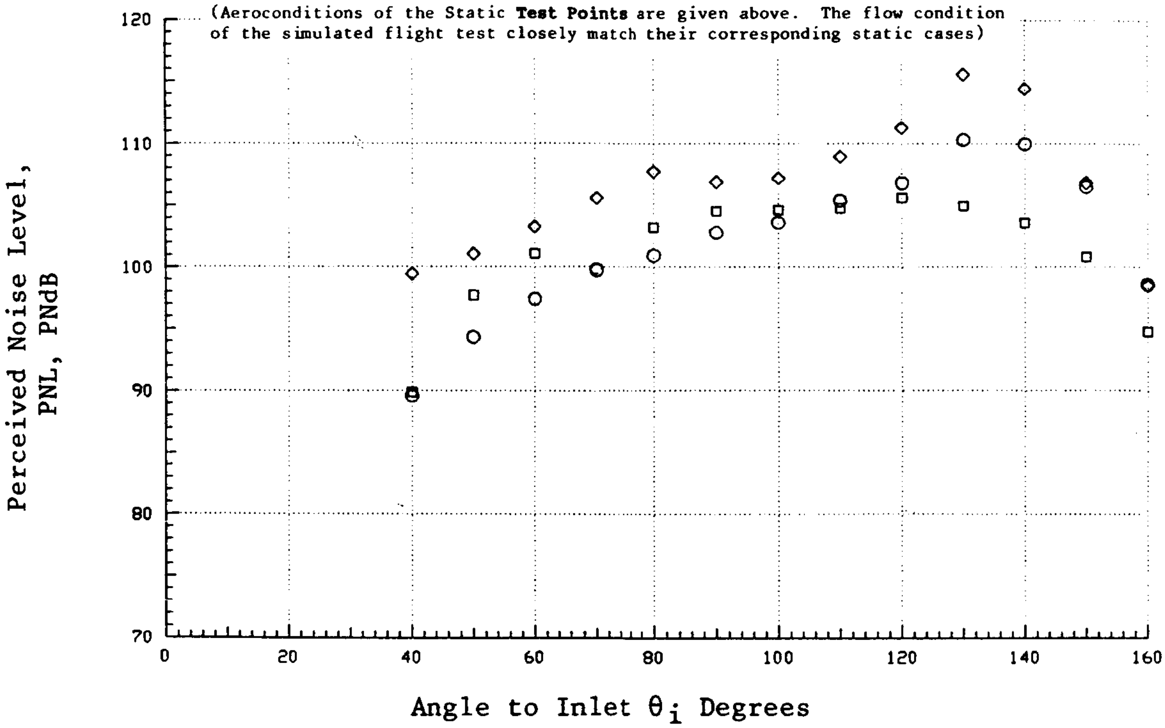

(a) Static

SYMBOL	POINT	COMMENT
◇	568	**Conical**
□	1016	**Model 10·1**
○	8212	**Model 8**

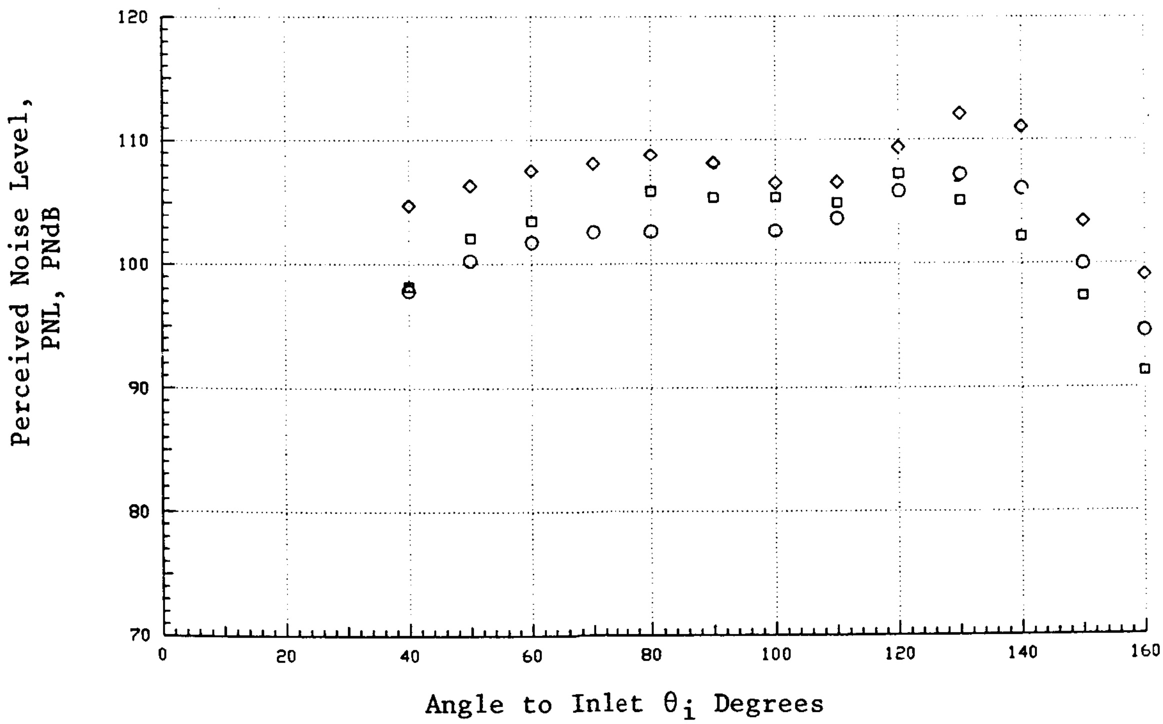

(b) Simulated Flight

Figure 3-23. Static and Simulated Flight PNL Directivities of the Similitude 20-Shallow-Chute Suppressor Nozzle (Model 10.1) at Typical AST Takeoff Condition.

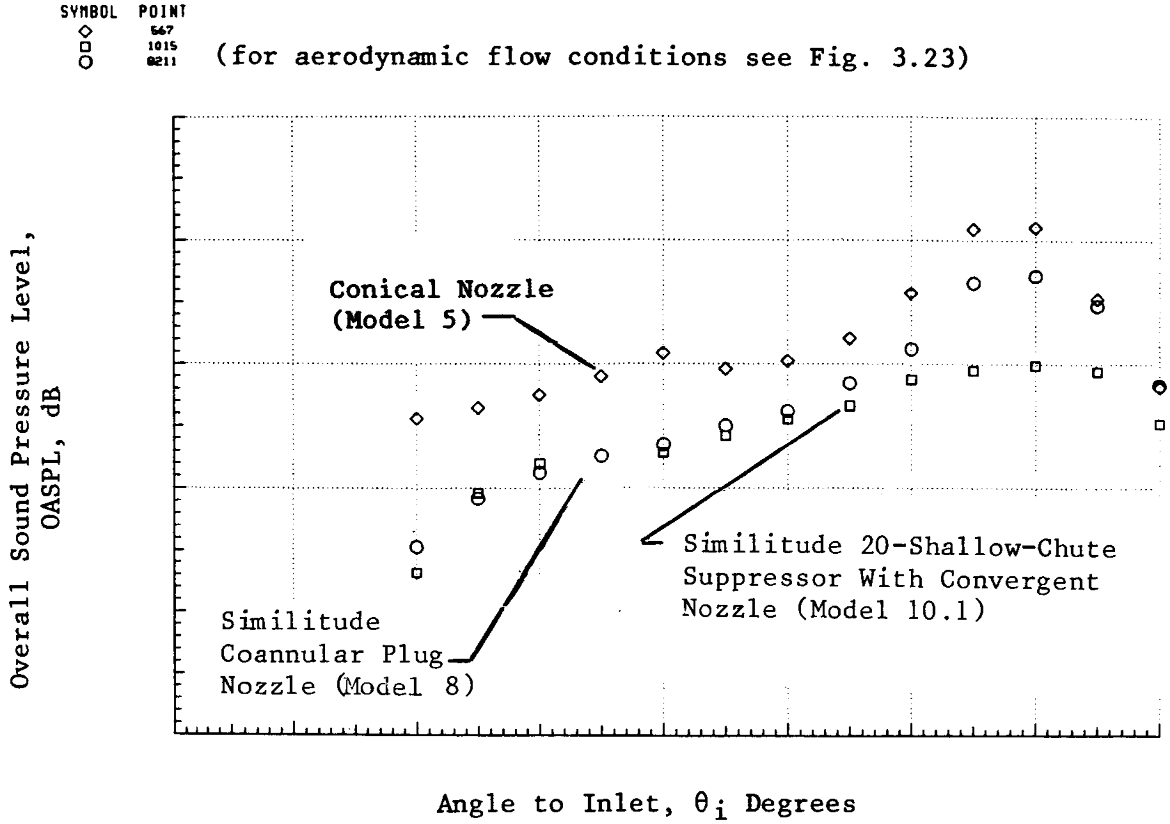

(a) Static

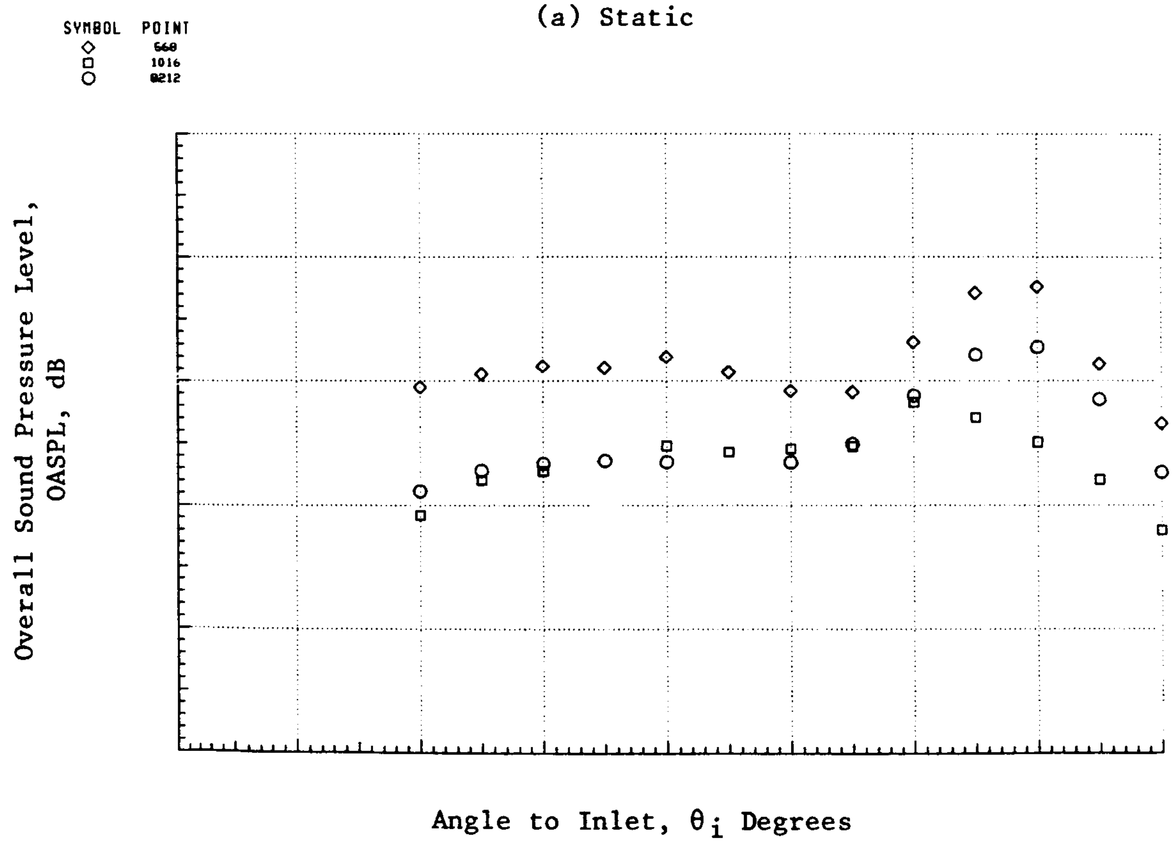

(b) Simulated Flight

Figure 3-24. Static and Simulated Flight OASPL Directivities of Similitude 20-Shallow-Chute Suppressor Nozzle (Model 10.1) at Typical AST Takeoff Condition.

(for aerodynamic Flow Conditions see Figure 3.23)

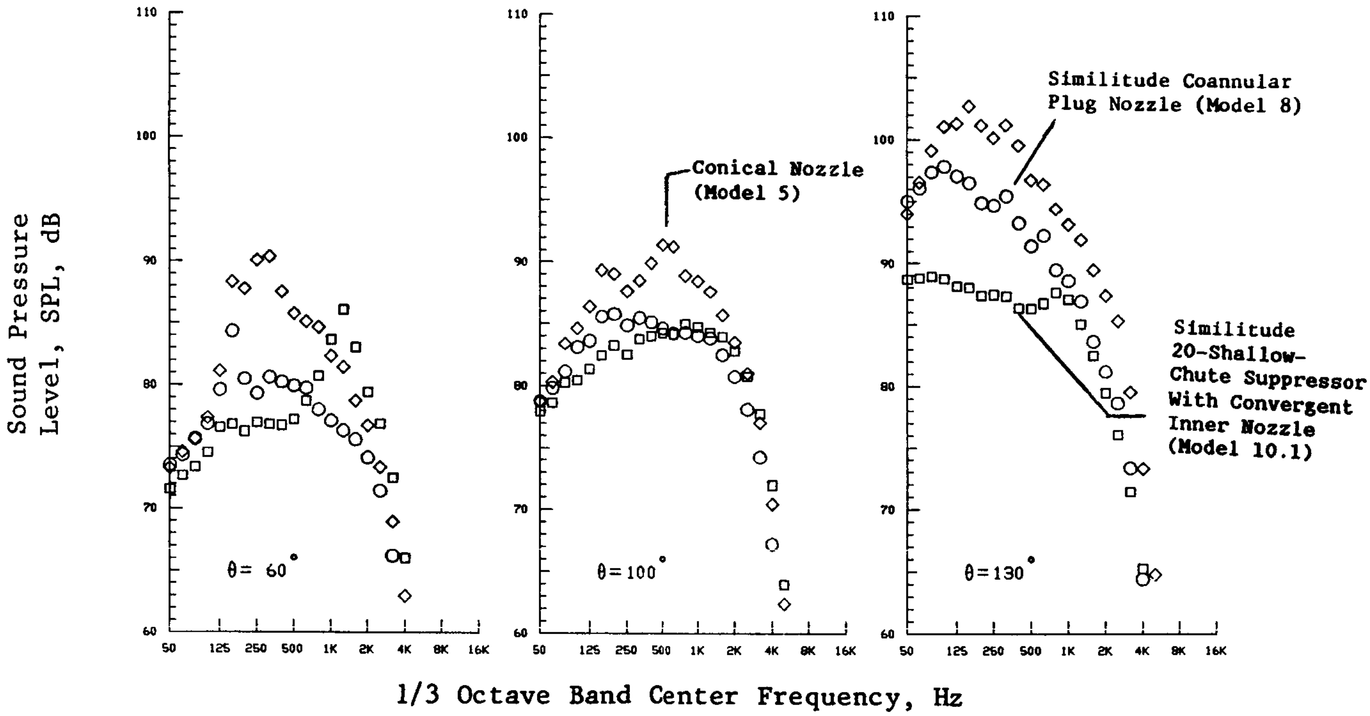

(a) Static

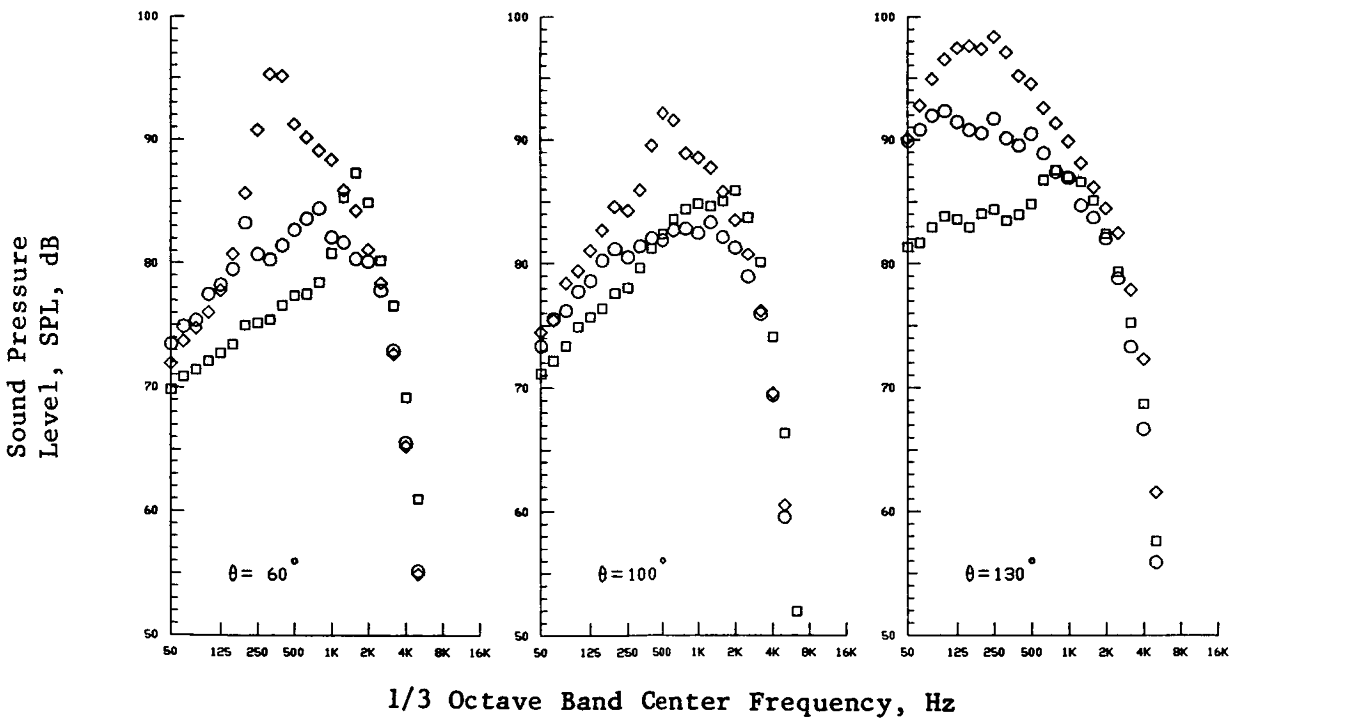

(b) Simulated Flight

Figure 3-25. Static and Simulated Flight Spectral Data of Similitude 20-Shallow-Chute Suppressor Nozzle (Model 10.1) at Typical AST Takeoff Condition.

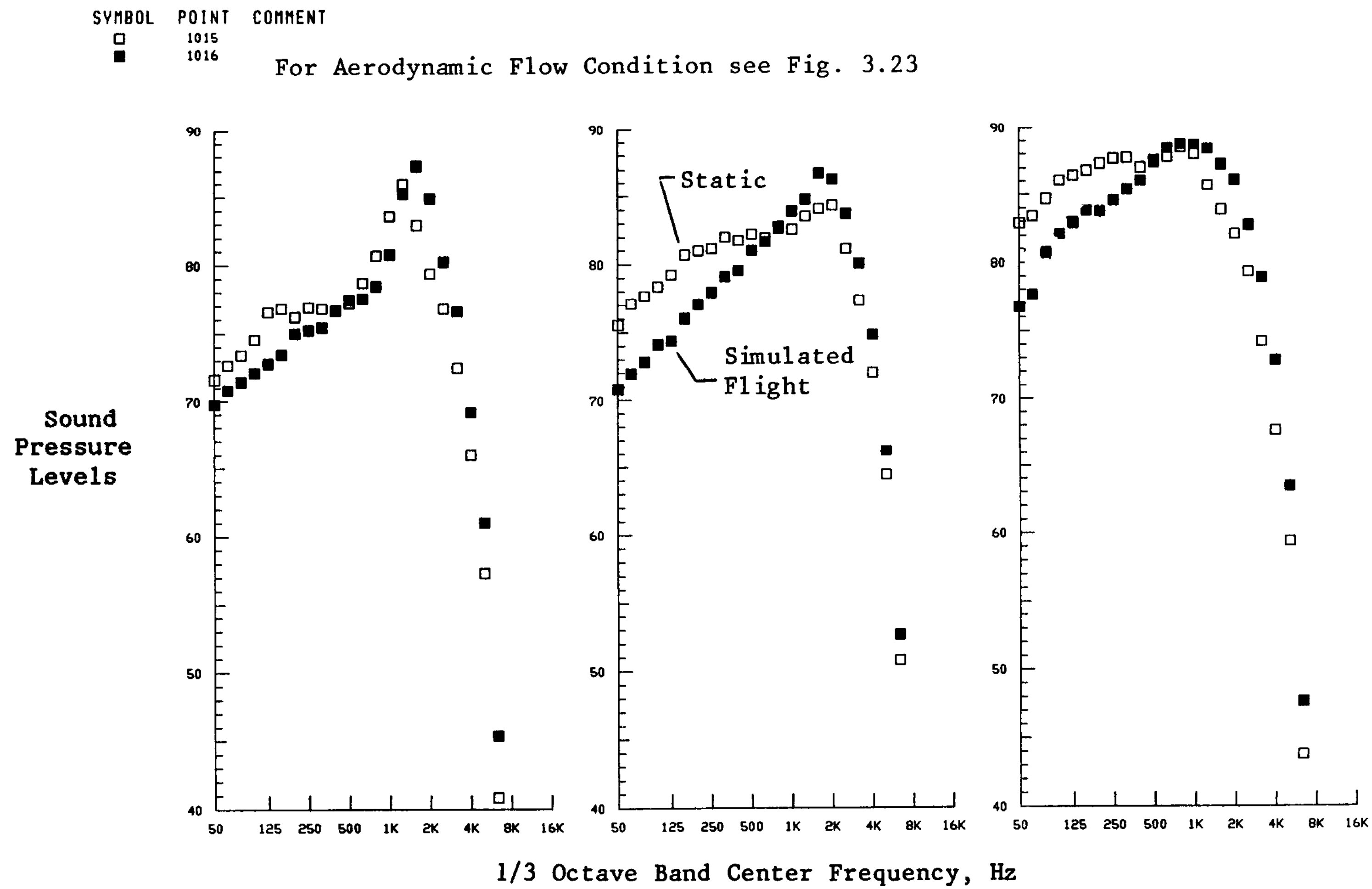

(a) Directivity Angle, $\theta_i = 60°$

(b) Directivity Angle, $\theta_i = 90°$

(c) Directivity Angle, $\theta_i = 120°$

Figure 3-26. Comparison of Static with Simulated Flight Spectra of Similitude 20-Shallow-Chute Suppressor Nozzle (Model 10.1) at Typical AST Takeoff Condition.

by the similitude suppressor in flight. This is made clear by the data in Figure 3-27. In this figure, the PNL and OASPL directivity for the test case of Figure 3-26 is compared with the corresponding flight data. An examination of this figure relative to similar sets of data of conical and coannular plug nozzle (Figures 3-3 and 3-17) demonstrate the differences between these three configurations in their forward quadrant flight amplification and aft quadrant flight suppression. A similar observation has been made in Reference 17 based on static and flight tests with a conical and 32-chute-suppressor configuration.

In summary, it is noted that comparable OASPL suppression levels in the aft quadrant are achieved by the similitude suppressor under static and simulated flight conditions. However, a static-to-flight suppression loss of 3 dB is observed in the corresponding PNL results. This is mainly due to the no change observed between the static and simulated flight SPL levels of the high frequency premerged noise of the similitude suppressor. In addition, significant suppression is achieved with this configuration, under both static and simulated flight conditions, at low and middle range frequencies. In the forward quadrant, the similitude suppressor is observed to be ineffective in reducing the shock cell noise relative to the coannular nozzle.

3.1.4.2 Effectiveness of C-D Termination on the Inner Stream of the Similitude 20-Shallow-Chute Configuration (Model 10.2)

In order to determine the acoustic benefits of incorporating a C-D termination on the inner stream of the similitude suppressor, the Model 10.2 nozzle has been tested under both static and simulated flight conditions. The inner C-D termination is designed for a complete expansion at a pressure ratio $P_r^i = 2.6$. In order to determine the effectiveness of the C-D termination on the inner nozzle, acoustic tests were conducted over an inner stream pressure ratio range of 2.2 to 2.9. The outer stream was kept constant at AST/VCE takeoff condition of $P_r^o \sim 3.25$. Typical forward and aft quadrant PNL and OASPL data of the Model 10.2 nozzle were presented earlier in Figures 3-18 through 3-22. The data have been compared in these figures with the corresponding data of the similitude suppressor having the convergent terminated inner nozzle (Model 10.1). The results indicate no significant acoustic benefits in the front quadrant due to the C-D terminated inner nozzle under both static and simulated flight conditions. In addition, there appears to be no definitive trends to indicate any benefit in the aft quadrant acoustic data. This is made further clear in Figure 3-28 where the measured PNL_{60} and normalized PNL_{130} data of Model 10.2 nozzle is replotted as a function of P_r^i. The acoustic data of Model 10.1, obtained with the convergent terminated inner configuration at $P_r^i = 2.6$ (which is the design condition of the C-D termination of Model 10.2) also is indicated on this figure.

The static and simulated flight PNL- and OASPL-directivities, and typical spectra of the similitude suppressor nozzle with its C-D inner stream operating at its design flow condition are presented in Figures 3-29 through 3-31. The data are compared in these figures with the corresponding data of the similitude suppressor with the convergent terminated inner nozzle (Model 10.1) to indicate no significant inner C-D effect.

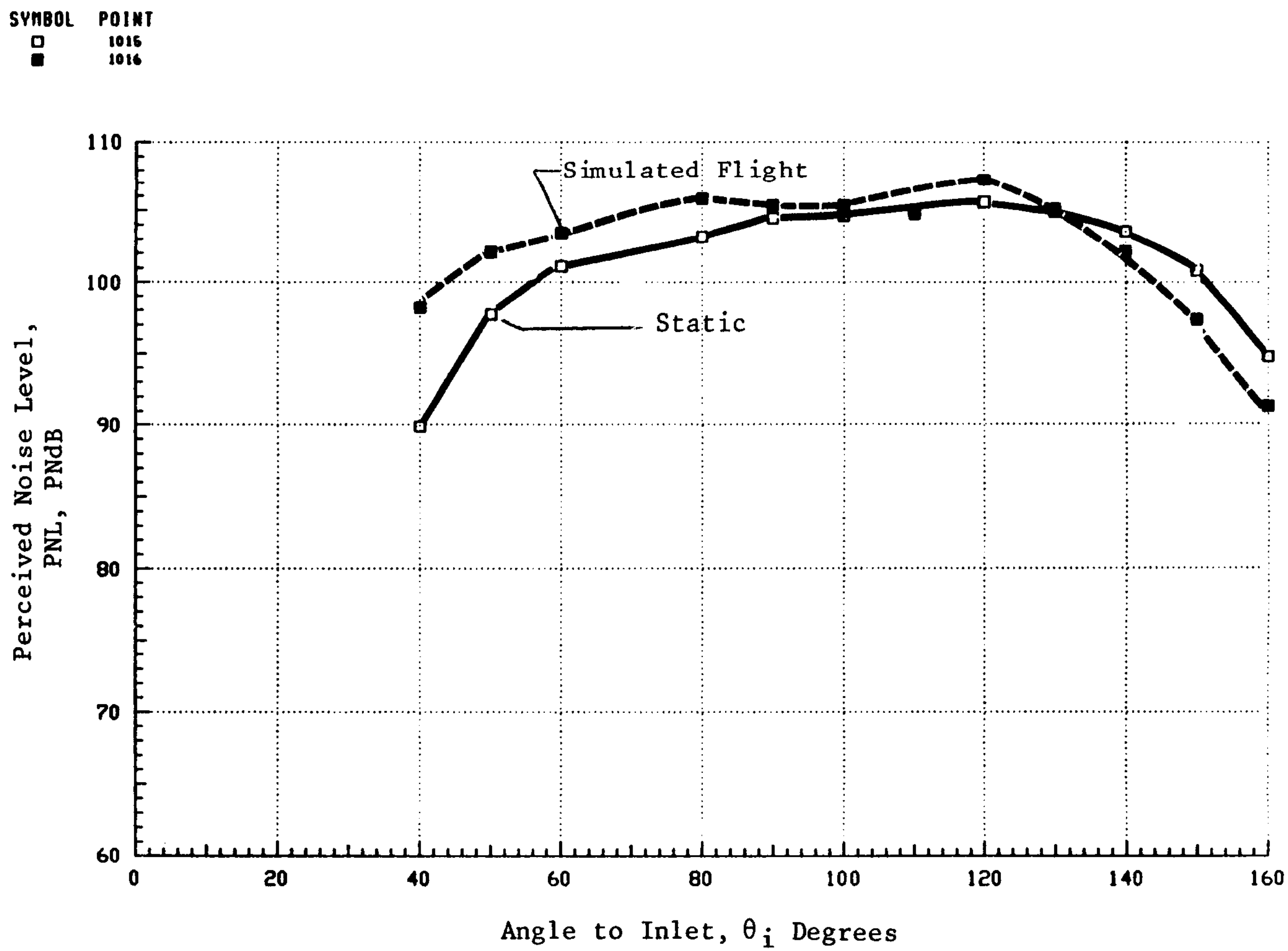

(a) PNL Directivity

Figure 3-27. Comparison of Static with Simulated Flight PNL- and OASPL Directivities of Similitude 20-Shallow-Chute Suppressor Nozzle (Model 10.1) at Typical AST Takeoff Conditions.

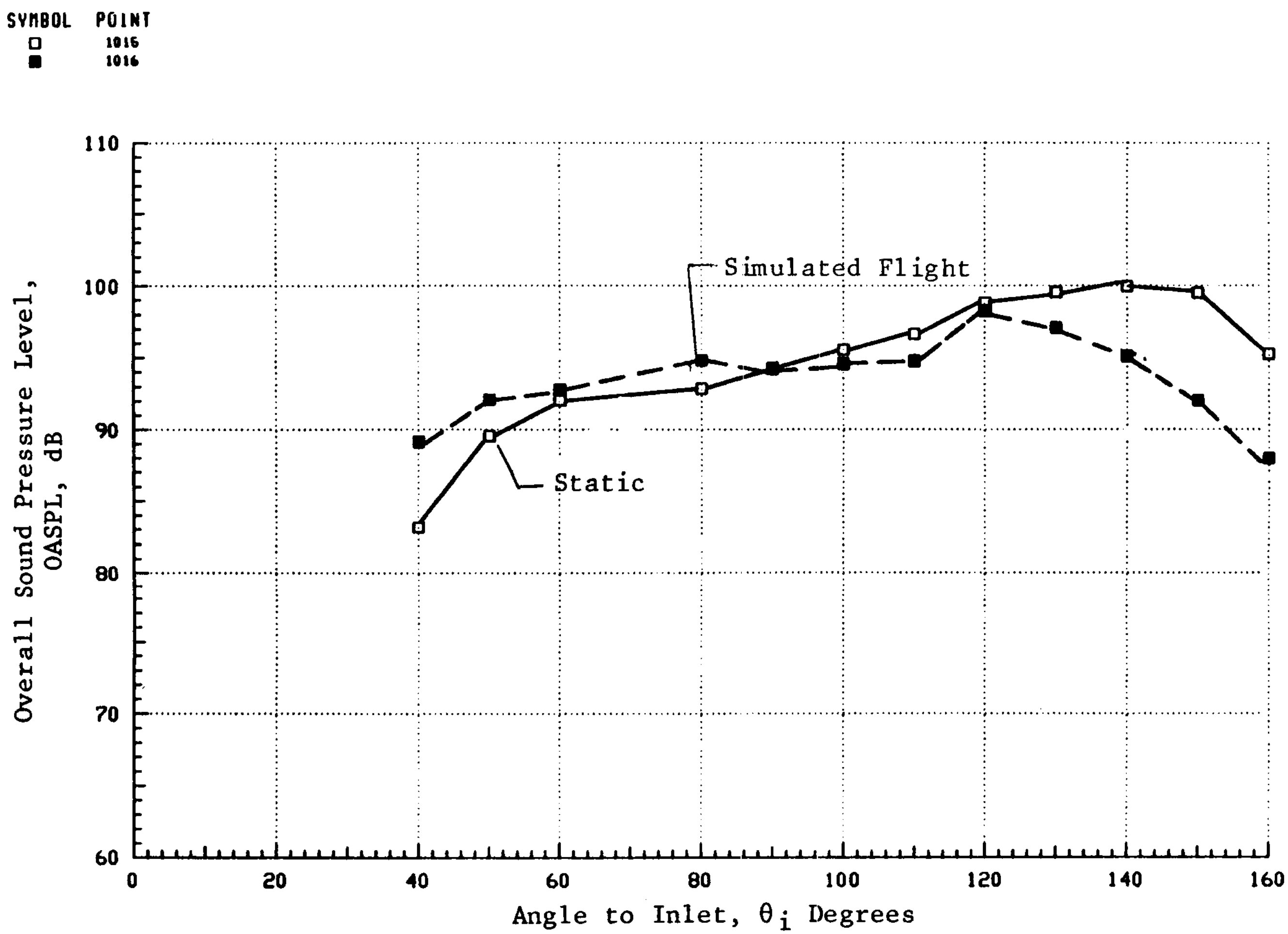

(b) OASPL Directivity

Figure 3-27. (Concluded)

Scaled to Product Size A^T 0.903m^2 (1,400 in^2) and extrapolated to 731.5m (2,400 ft) sideline.

Outer Stream Held Constant $P_r^o \sim 3.25$ and $T_T^o \sim 1740$ °R

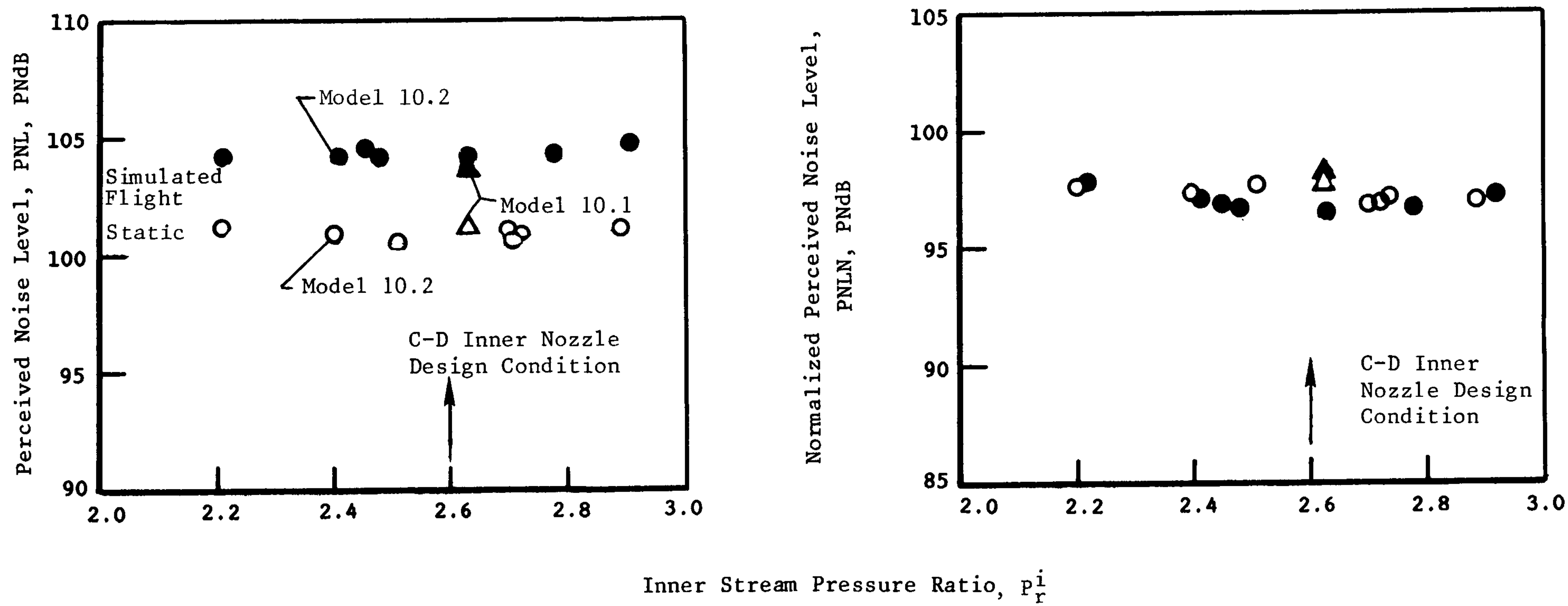

(a) Forward Quadrant, $\theta_i = 60^o$

(b) Aft Quadrant, $\theta_i = 130^o$

Figure 3-28. Typical Forward and Aft Quadrant PNL Data of the Similitude Suppressor Nozzle with a C-D Terminated Inner Nozzle (Model 10.2) Over an Inner-Stream Pressure Ratio Range.

SYMBOL	POINT	COMMENT	P_r^o	$T_T^o(^oR)$	V_j^o(fps)	P_r^i	T_T^i (°R)	V_j^i(fps)	P_r^{mix}	$T_T^{mix}(^oR)$	V_j^{mix}(fps)	NF
)	1015	10•1; Conv. Inner	3.25	1745	2464	2.63	876	1594	3.11	1601	2320	-7.3
	1027	10•2; C-D Inner	3.24	1734	2455	2.69	866	1603	3.10	1565	2290	-7.3

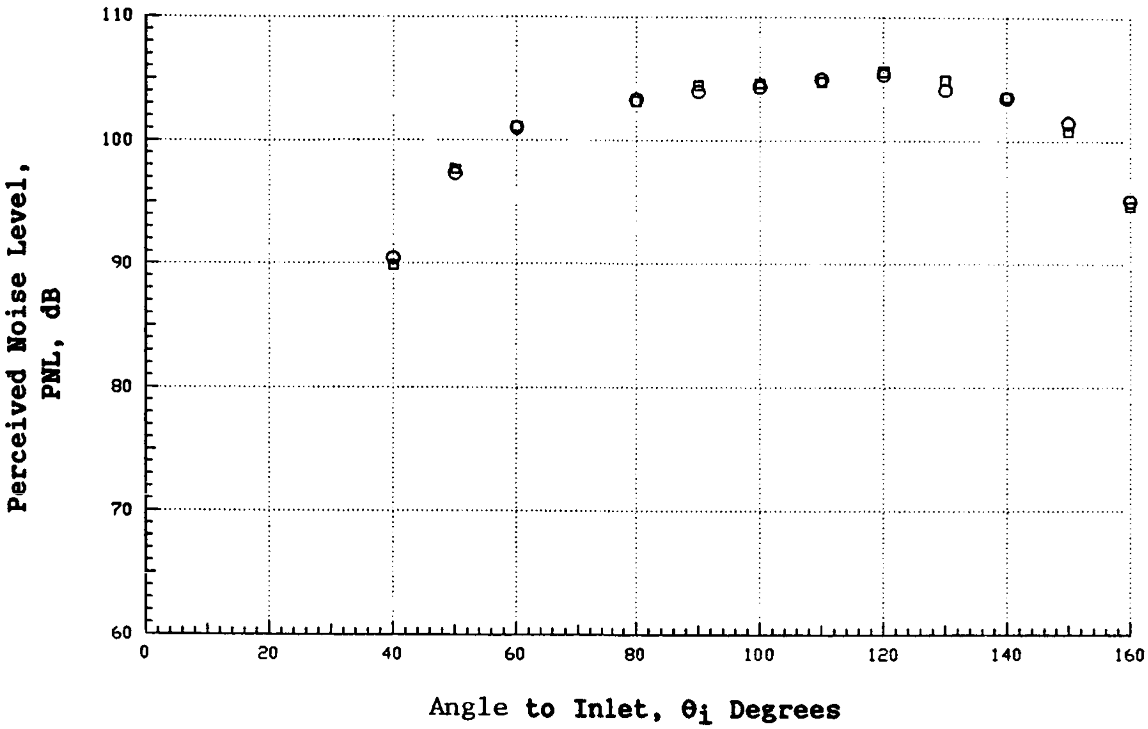

(a) PNL Directivity

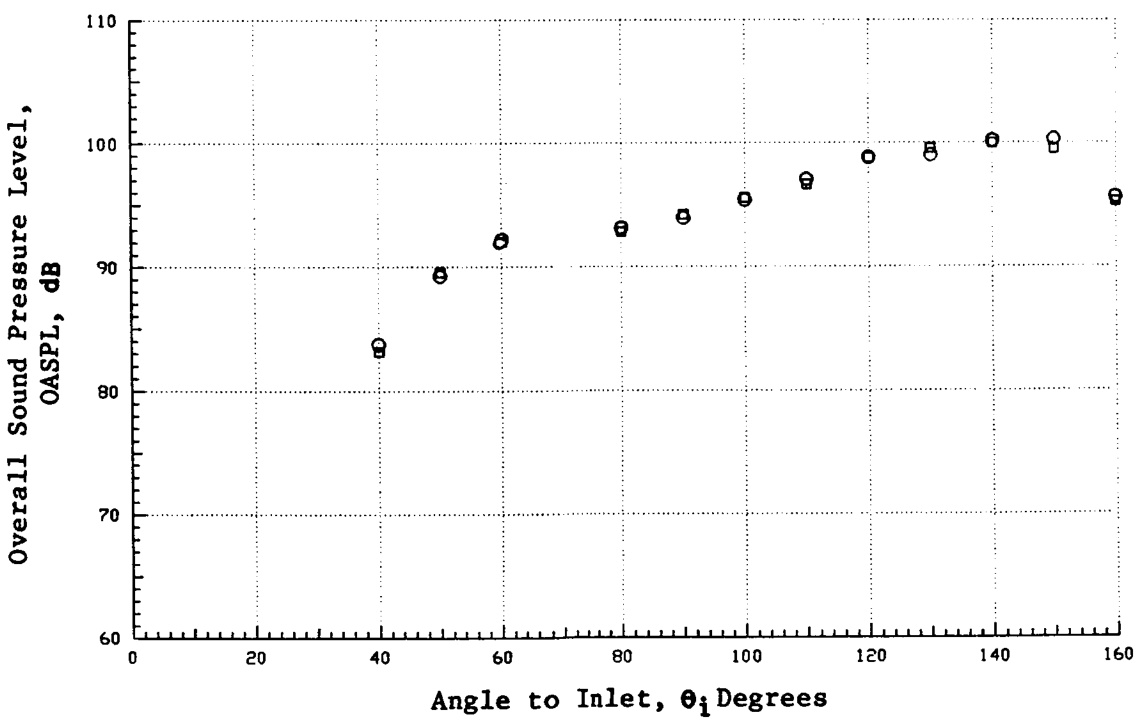

(b) OASPL Directivity

Figure 3-29. Static PNL- and OASPL Directivities of Similitude 20-Shallow-Chute Suppressor with Convergent Inner (Model 10.1) and C-D Inner (Model 10.2) at Typical AST Takeoff Condition.

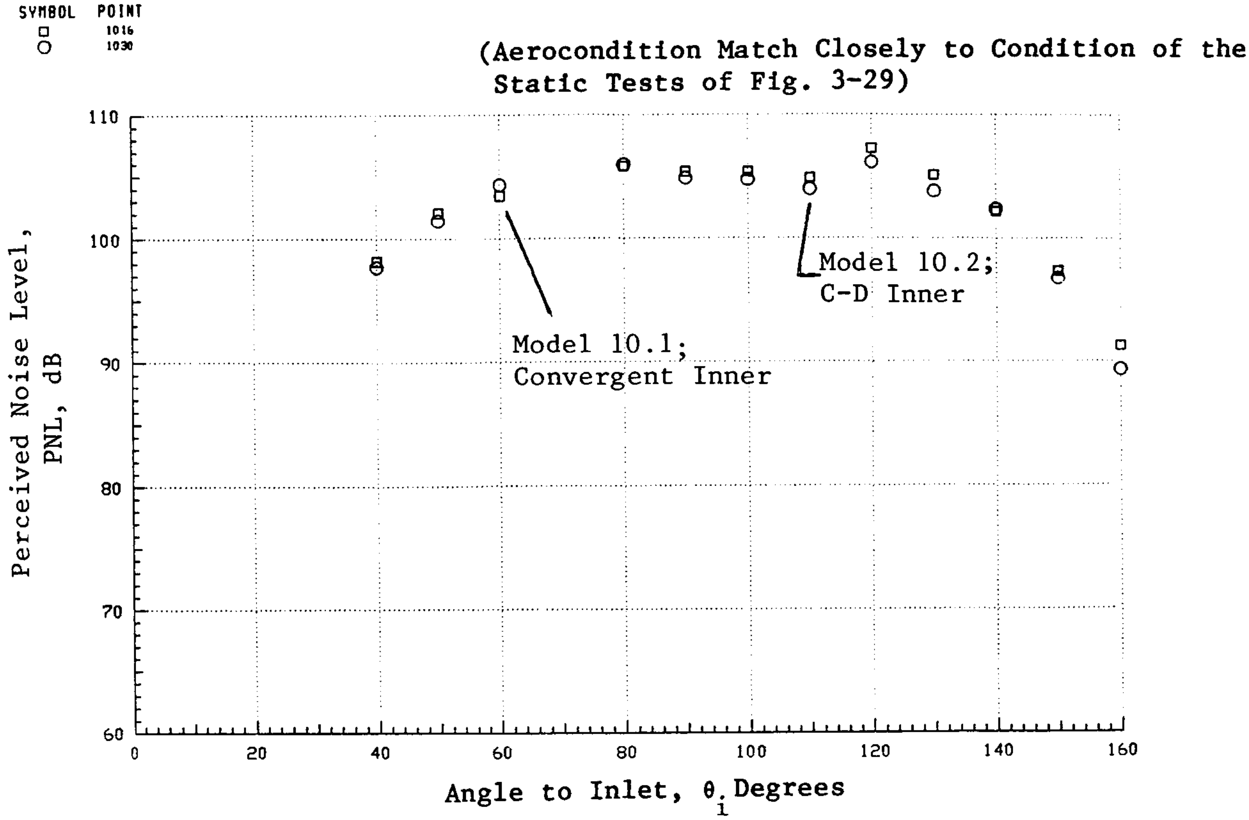

(a) PNL - Directivity

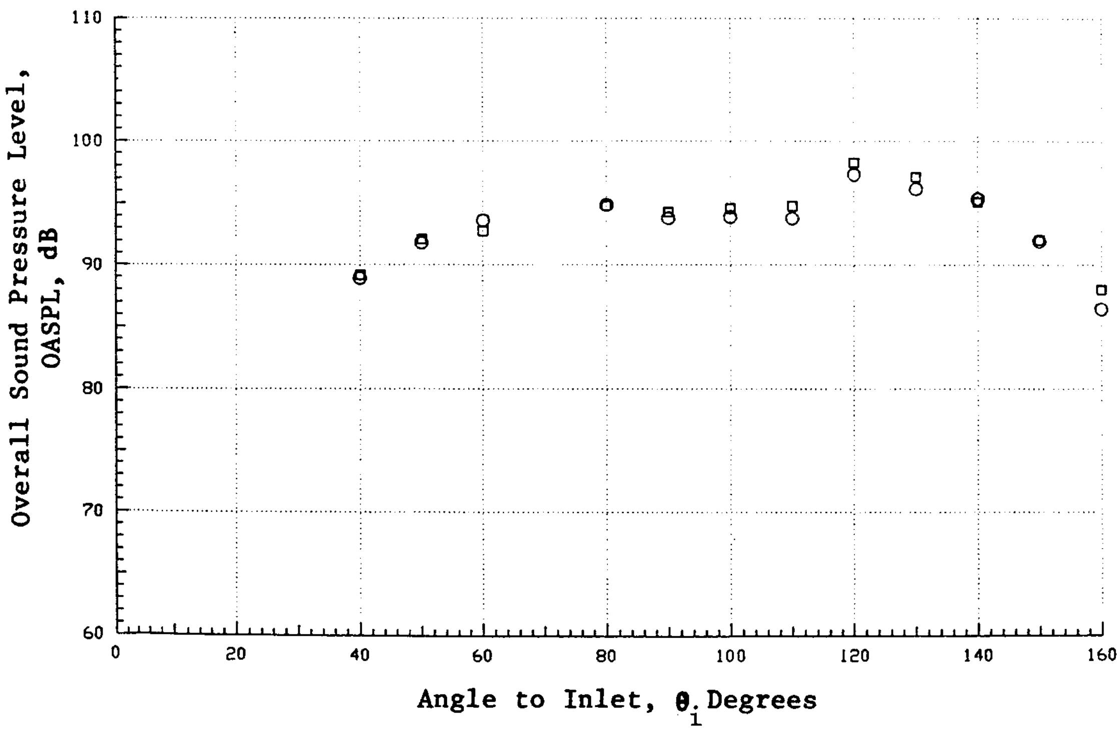

(b) OASPL - Directivity

Figure 3-30. Simulated Flight PNL- and OASPL Directivities of Similitude 20-Shallow-Chute Suppressor with Convergent Inner (Model 10.1) and C-D Inner (Model 10.2) at Typical AST Takeoff Condition.

(See Fig. 3-29 for the Aerodynamic Flow Condition)

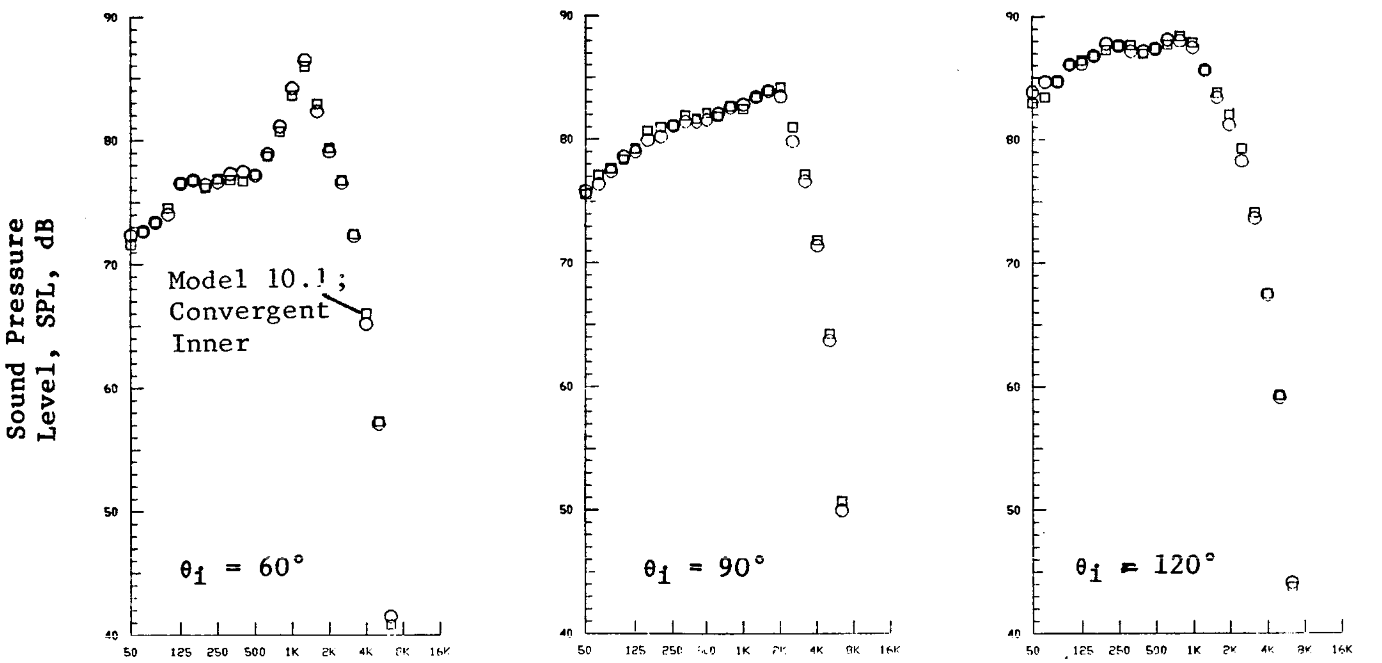

(a) Static

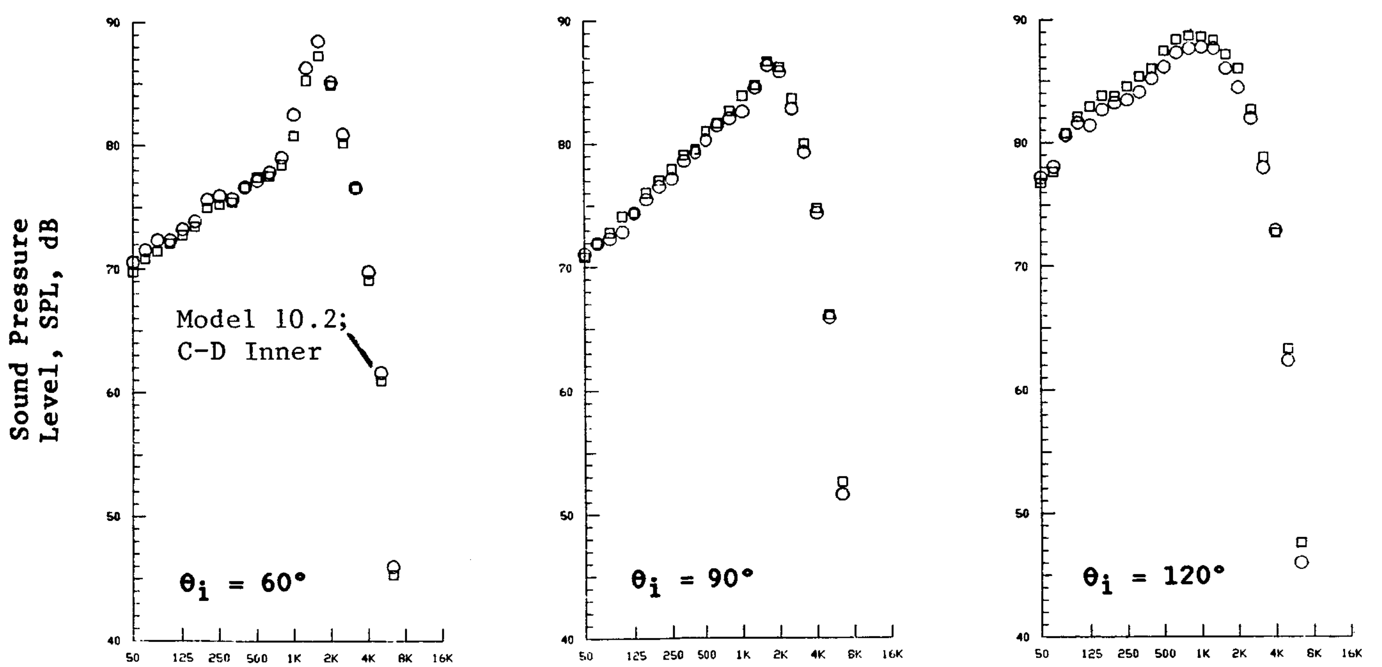

(b) Simulated Flight

Figure 3-31. Typical Static and Simulated Flight Spectra of Similitude 20-Shallow-Chute Suppressor with Convergent Inner (Model 10.1) and C-D Inner (Model 10.2) at Typical AST Takeoff Condition.

3.1.4.3 Acoustic Characteristics of the Modified DOT 20- and 40-Shallow-Chute-Suppressor Nozzles

The aft angle normalized PNL and OASPL levels of the two modified DOT suppressors measured at θ_i = 120° and 130° are presented in Figures 3-32 through 3-35. In these figures, the data are presented as a function of 10 log (V_j^{mix}/a_{amb}). Similiar to those of the similitude suppressor configuration (Model 10.1), the data were obtained over a range of flow variables that are typical of an AST/VCE operating cycle. The measured data are compared in each of these figures with the data of the conical baseline nozzle and the similitude 20-shallow-chute suppressor nozzle. An examination of these figures indicates that, on an overall basis, no significant differences in the aft angle acoustic data exist between the similitude and DOT 20-shallow-chute suppressor models. However, the 40-shallow-chute model is observed to yield a lower PNL value at θ_i = 130° relative to the 20-shallow-chute models to the extent of 1.5 and 2.5 dB under static and simulated flight conditions, respectively, at relatively low V_j^{mix}. This additional suppression with the 40-shallow-chute model is noted at all mixed velocities that are less than the typical AST takeoff velocity of V_j^{mix} ~ 2,300 fps. At velocities greater than the 2,300 ft/sec, the noise levels of the 20-shallow-chute models are lower than those of the 40-element suppressor.

Typical forward angle PNL_{60} and PNL_{90} data are presented in Figures 3-36 and 3-37 for the static and simulated flight cases, respectively. The data are presented as a function of the mixed stream parameter β^{eff}. While the data of the two 20-shallow-chute suppressors agree, the 40-shallow-chute nozzle is observed to yield a better shock noise suppression over the range of test conditions. For example, at a typical AST takeoff condition, the 40-shallow-chute suppressor is observed to yield an additional static shock noise suppression of 4.5 and 3 PNdB at θ_i = 60° and 90°, respectively, relative to the 20-shallow-chute models. The corresponding suppression during the simulated flight tests are observed to be 5 and 4 PNdB. However, it should be noted that the benefit of the 40-chute nozzle relative to the 20-chute diminishes at higher effective pressure ratios.

The static and simulated flight PNL- and OASPL-directivities of the suppressor nozzles at a takeoff V_j^{mix} ~ 2300 fps are provided in Figures 3-38 and 3-39, respectively. Again, no significant differences are observed between the 20-shallow-chute nozzles data. However, the DOT 40-shallow-chute nozzle is observed to yield a peak noise level at θ_i = 140° while the peak level in the 20-shallow-chute nozzles data is at θ_i = 120°. The significant observation is in the considerable static-to-flight suppression achieved in the aft quadrant PNL and OASPL data of the 40-shallow-chute nozzle in contrast to what was observed earlier with the data of the 20-shallow-chute nozzles.

Typical spectral data corresponding to the flow conditions of Figures 3-38 and 3-39 are presented in Figures 3-40 and 3-41. At first, the significant differences in the front quadrant shock noise levels of the 20- and 40-shallow-chute suppressor nozzles are highlighted. Then, the significant flight suppression in the aft quadrant SPL levels of the 40-shallow-chute suppressor nozzle at all frequencies except at the extreme high frequencies, in contrast to what was observed earlier with the 20-shallow-chute data, is noted by comparing Figure 3-40c with Figure 3-41c.

Scaled to Product Size $A^T = 0.903m^2$ (1,400 in.^{2}) and Extrapolated to 731.5m (2,400 ft) Sideline.

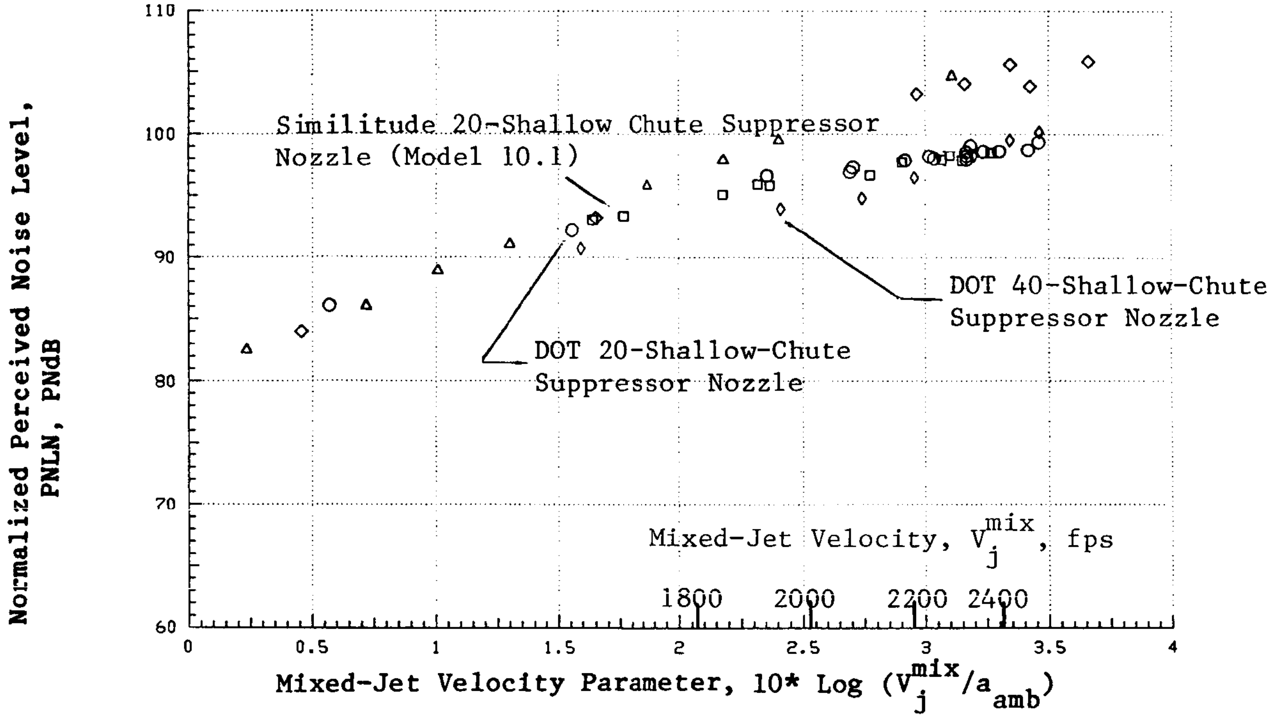

(a) Normalized PNL at θ_i = 120°

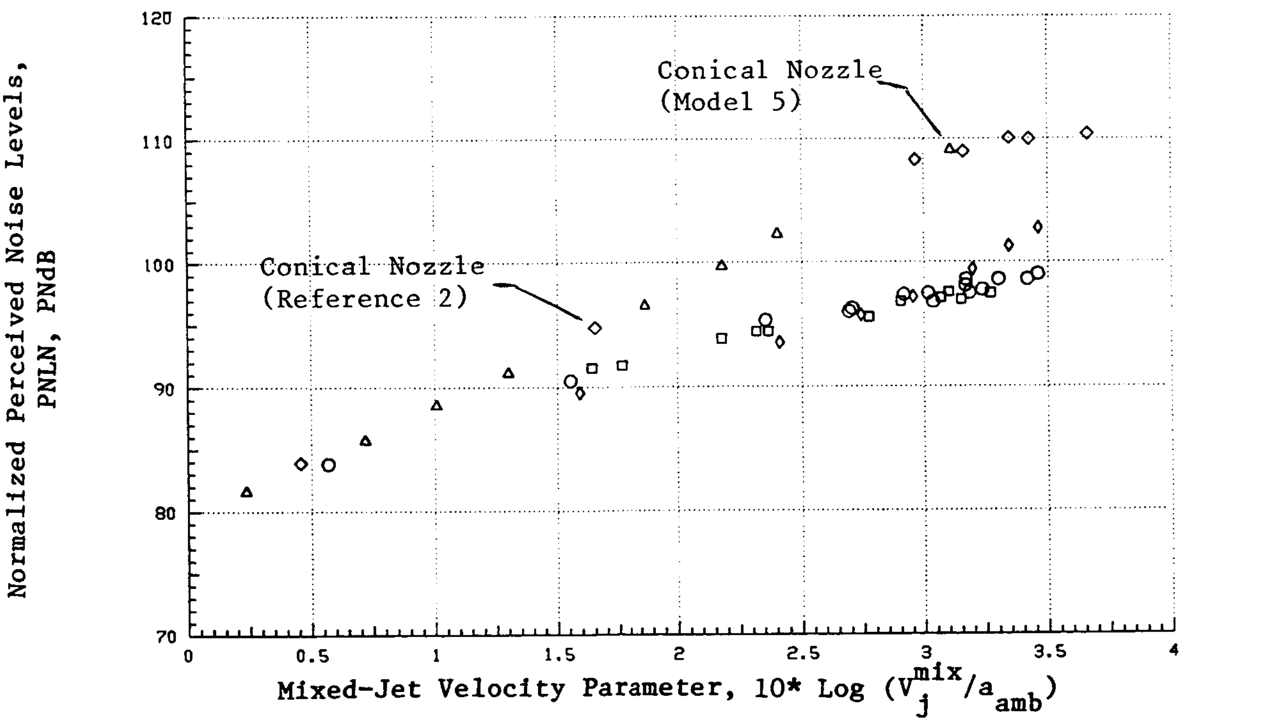

(b)Normalized PNL at θ_i = 130°

Figure 3-32. Static Aft Angle Normalized PNL Data of the Modified DOT 20- and 40-Shallow-Chute Suppressor Nozzles.

Scaled to Product Size $A^T = 0.903 m^2$ (1,400 in.^{2}) and Extrapolated to 731.5m (2,400 ft) Sideline.

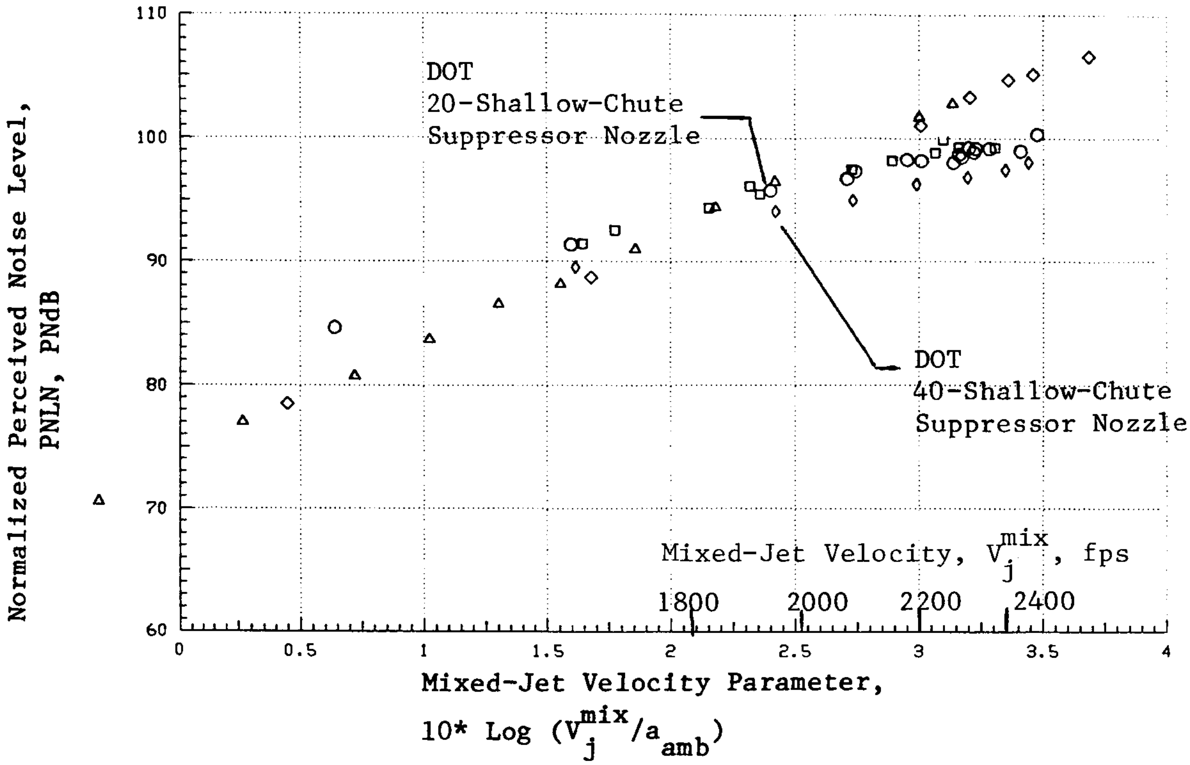

(a) Normalized PNL at θ_i = 120°

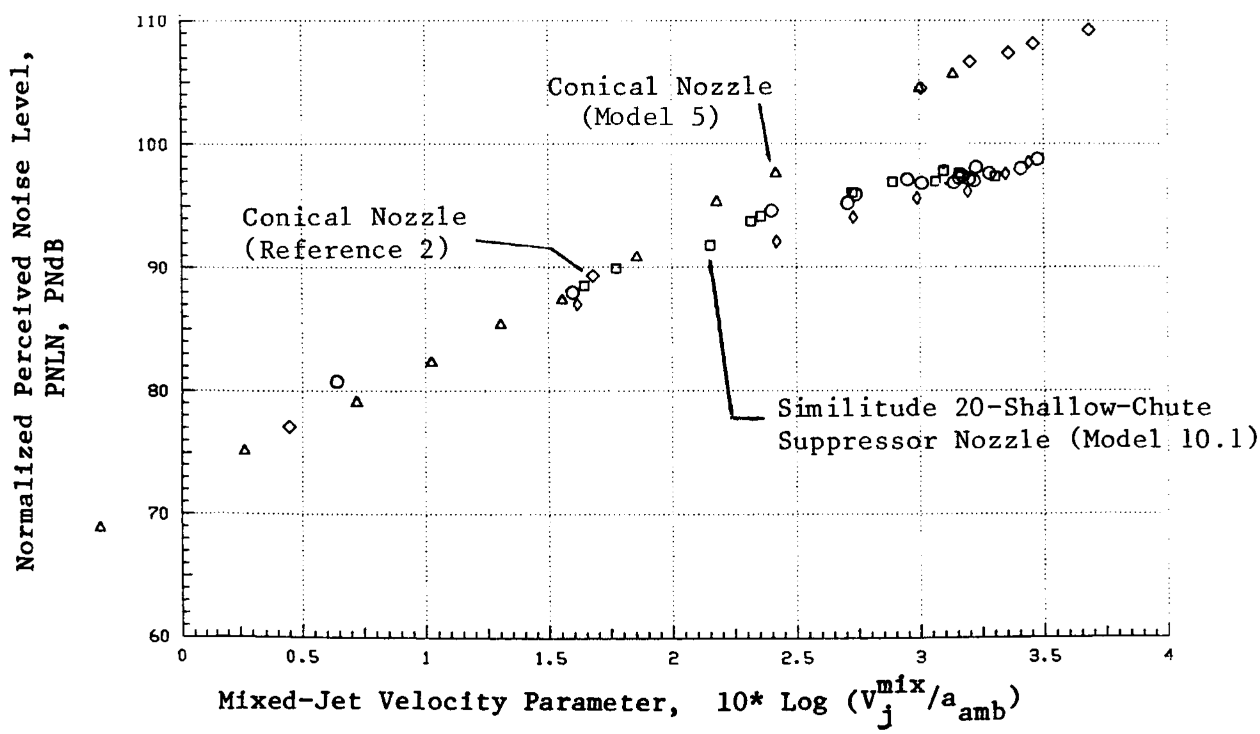

(b) Normalized PNL at θ_i = 130°

Figure 3-33. Simulated Flight Aft Angle Normalized PNL Data of the Modified DOT 20- and 40-Shallow-Chute Suppressor Nozzles.

Scaled to Product Size $A^T = 0.903m^2$ (1,400 in.^{2}) and Extrapolated to 731.5m (2,400 ft) Sideline.

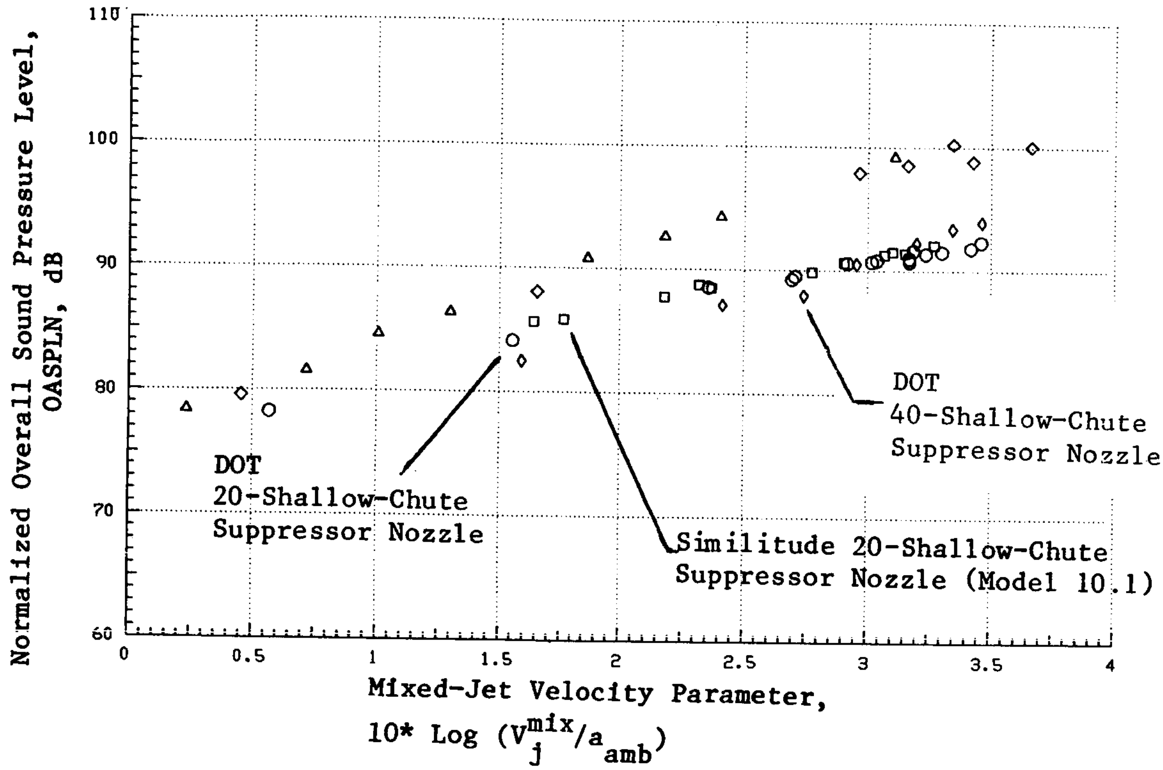

(a) Normalized OASPL at θ_i = 120°

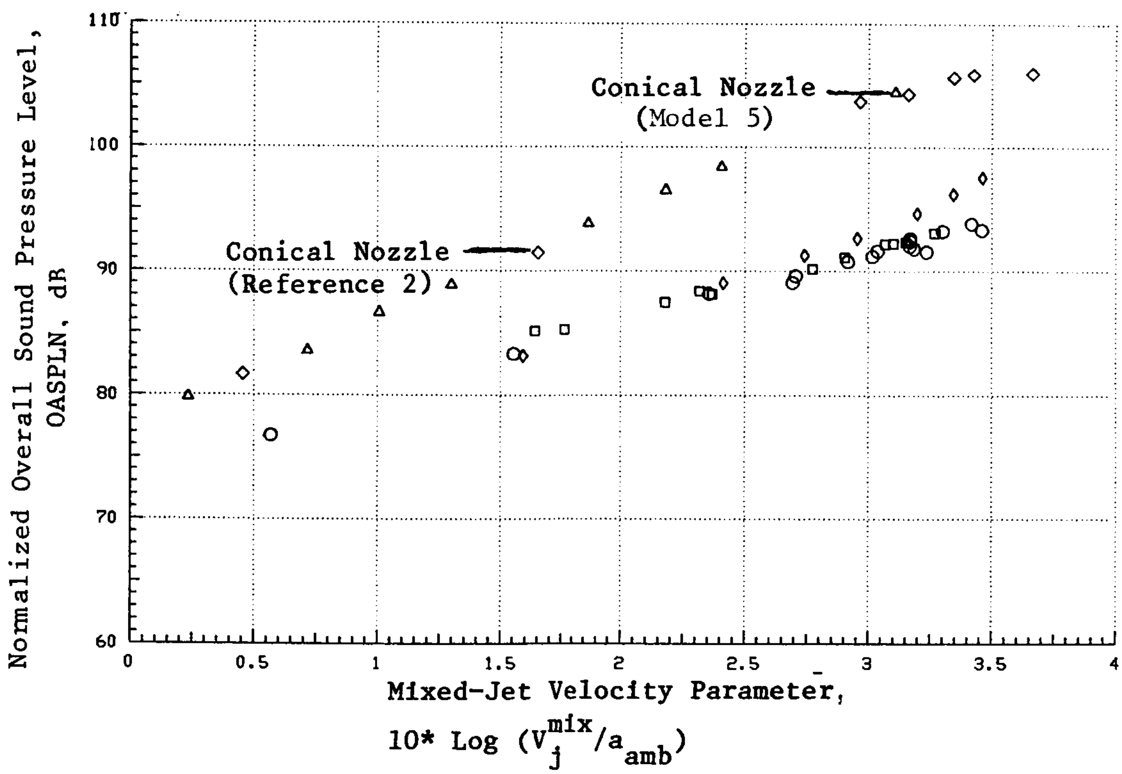

(b) Normalized OASPL at θ_i = 130°

Figure 3-34. Static Aft Angle Normalized OASPL Data of the Modified DOT 20- and 40-Shallow-Chute Suppressor Nozzles

Scaled to Product Size $A^T = 0.903 m^2$ (1,400 in.^{2}) and Extrapolated to 731.5m (2,400 ft) Sideline.

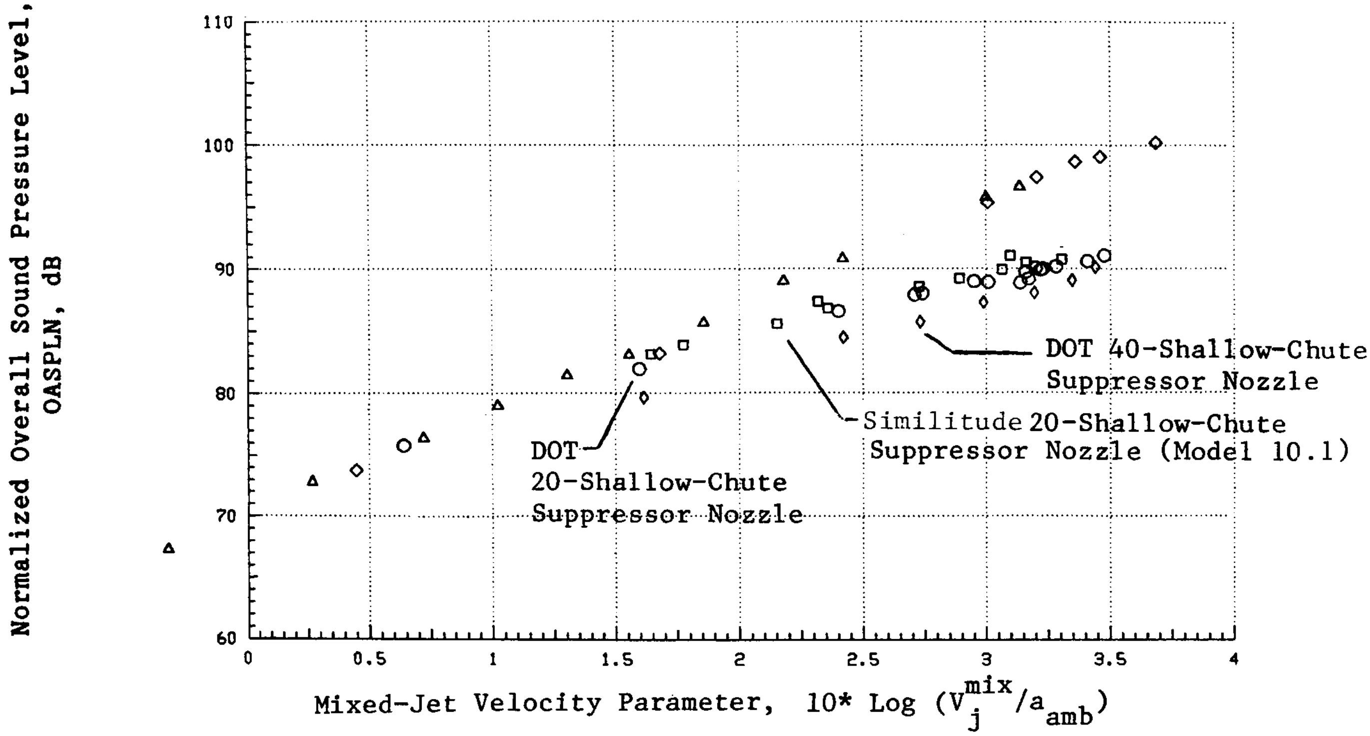

(a) Normalized OASPL at θ_i = 120°

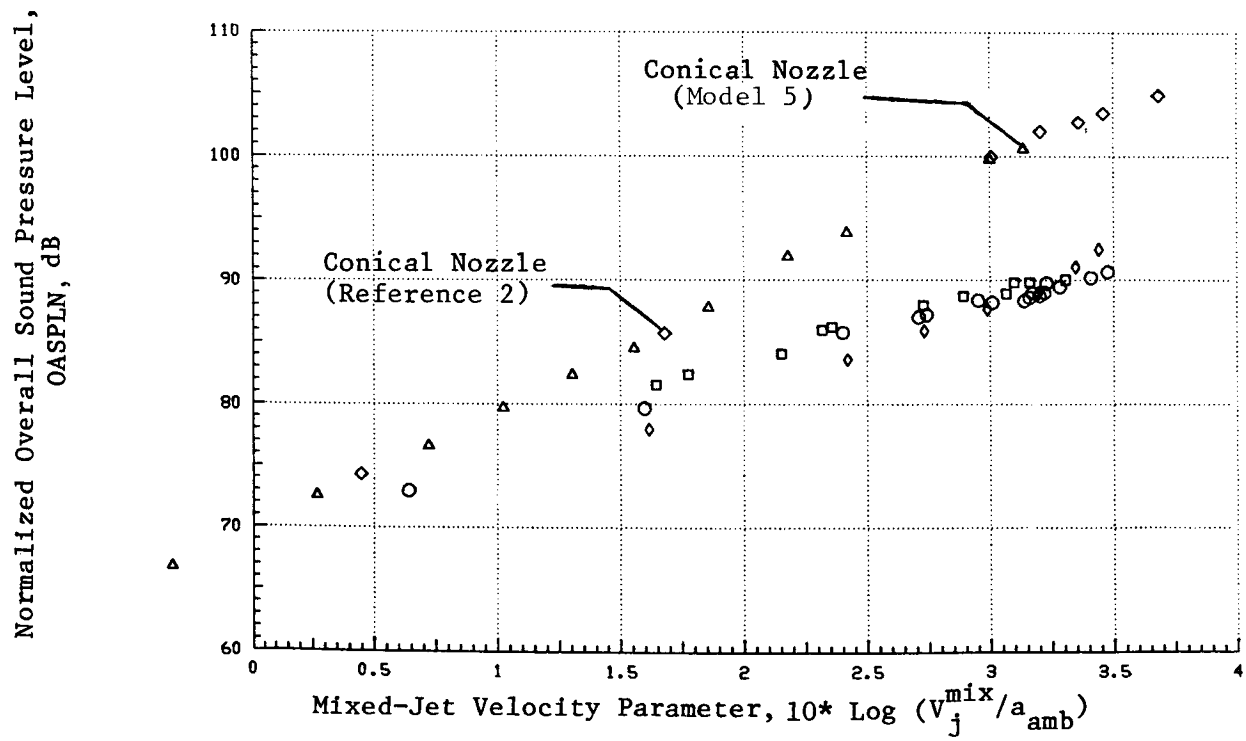

(b) Normalized OASPL at θ_i = 130°

Figure 3-35. Simulated Flight Aft Angle Normalized OASPL Data of the Modified DOT 20- and 40-Shallow-Chute Suppressor Nozzles.

Scaled to Product Size $A^T = 0.903m^2$ (1,400 in.^{2}) and Extrapolated to 731.5m (2,400 ft) Sideline.

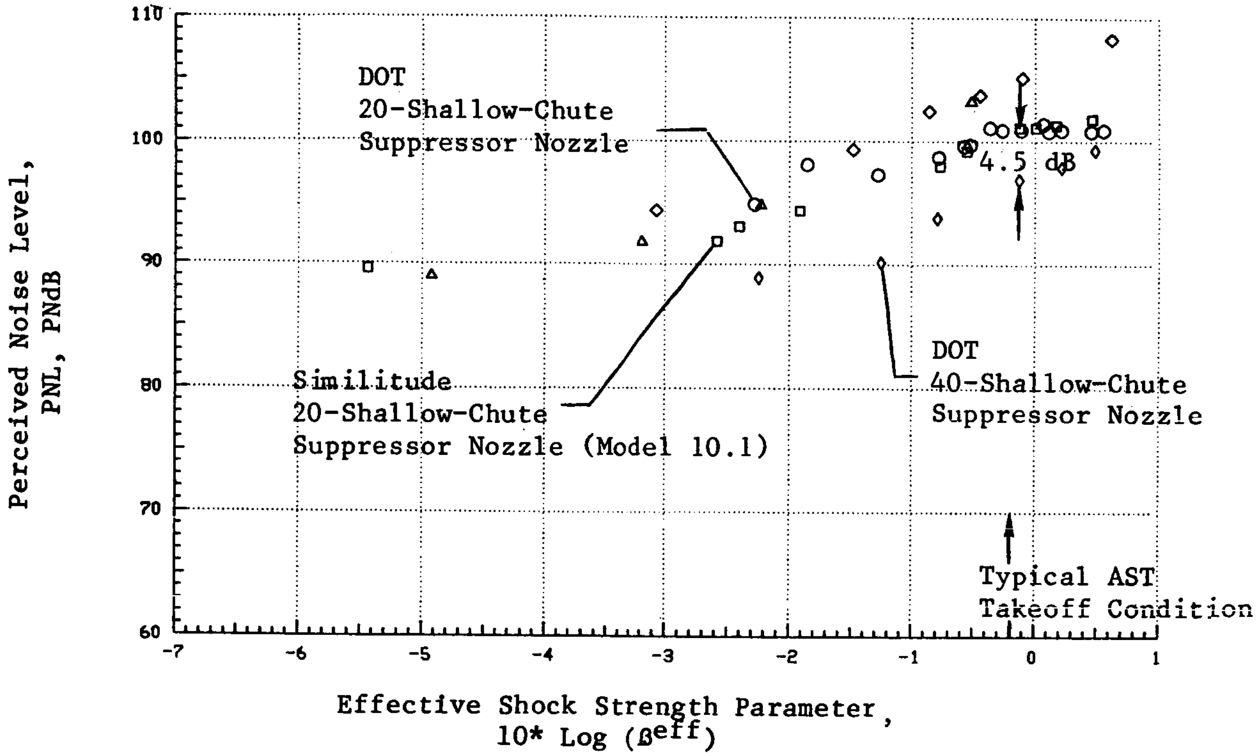

(a) Directivity Angle, θ_i = 60°

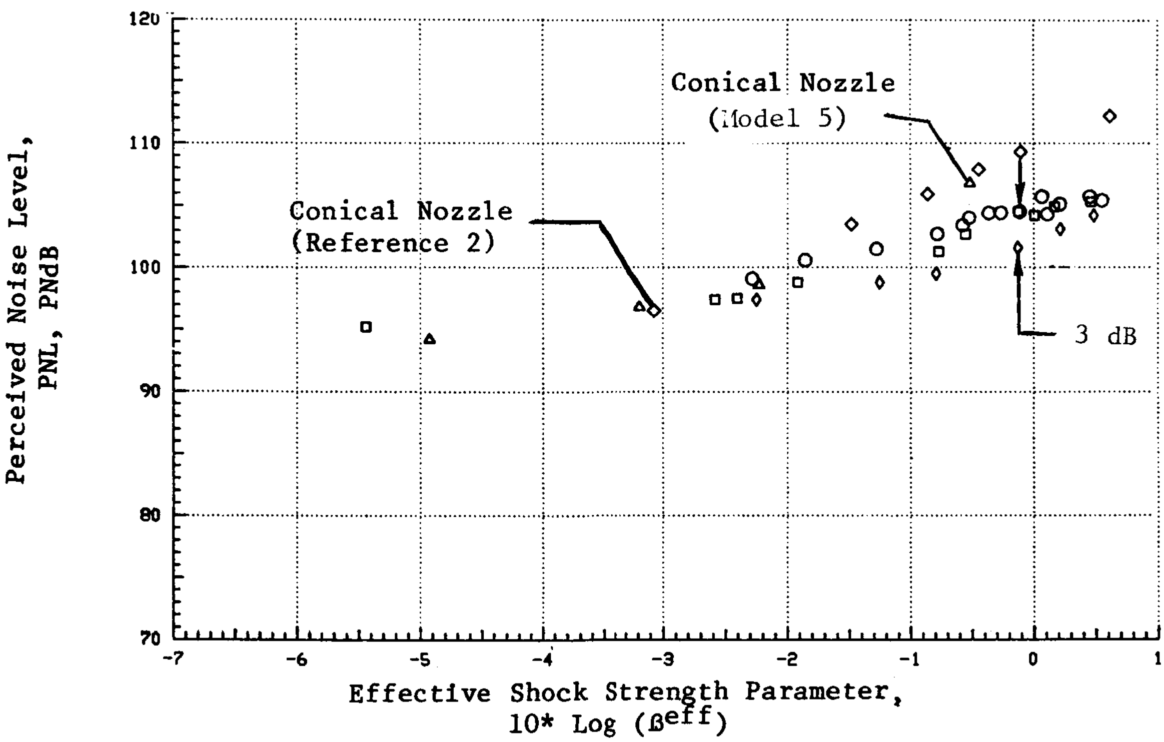

(b) Directivity Angle, θ_i = 90°

Figure 3-36. Static Front Quadrant PNL Data of the Modified DOT 20- and 40- Shallow-Chute Suppressor Nozzles

Scaled to Product Size $A^T = 0.903m^2$ (1,400 in.^{2}) and Extrapolated to 731.5m (2,400 ft) Sideline.

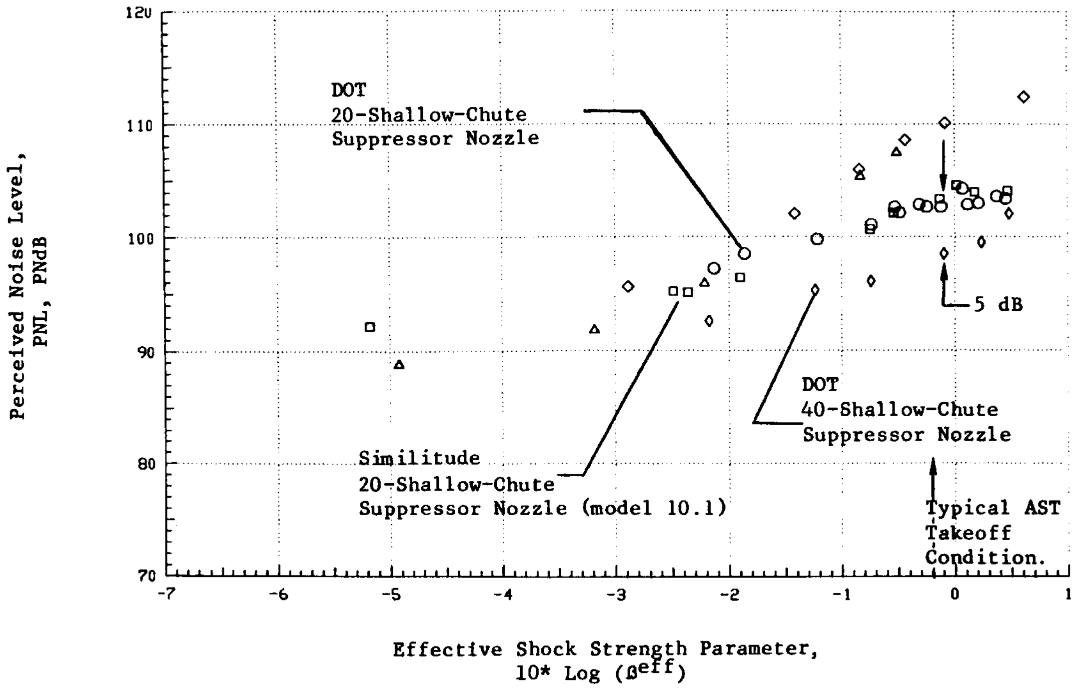

(a) Directivity Angle, θ_i = 60°

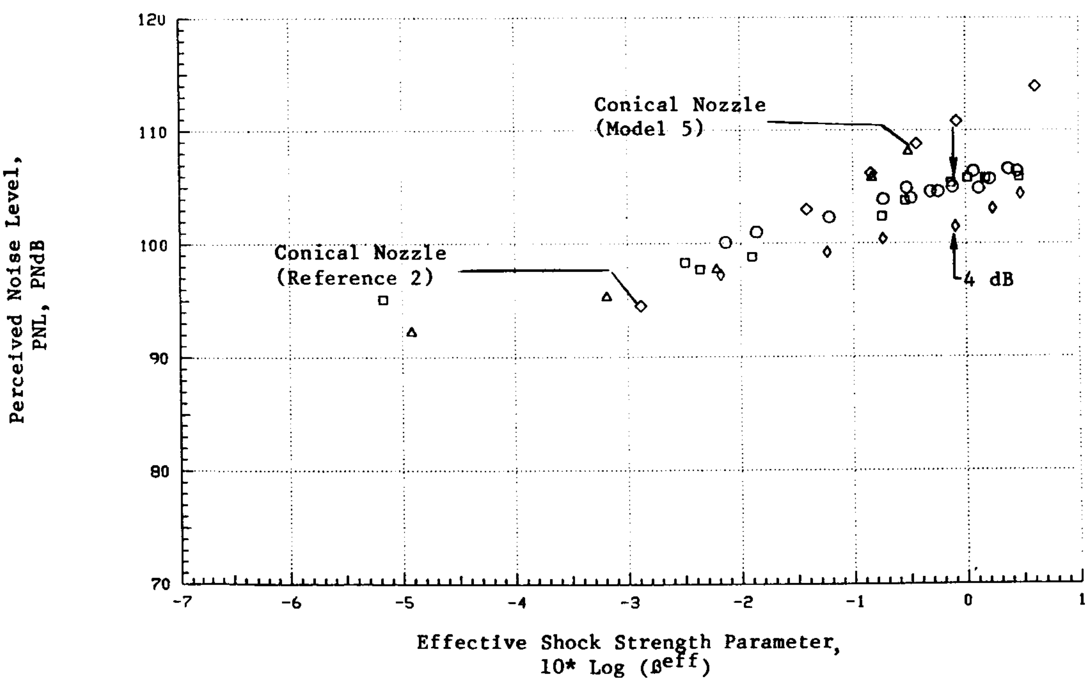

(b) Directivity Angle, θ_i = 90°

Figure 3-37. Simulated Flight Front Quadrant PNL Data of the Modified DOT 20- and 40-Shallow-Chute Suppressor Nozzles.

Scaled to Product Size A^T = 0.903m^2 (1,400 in.^{2}) and Extrapolated to 731.5m (2,400 ft) Sideline.

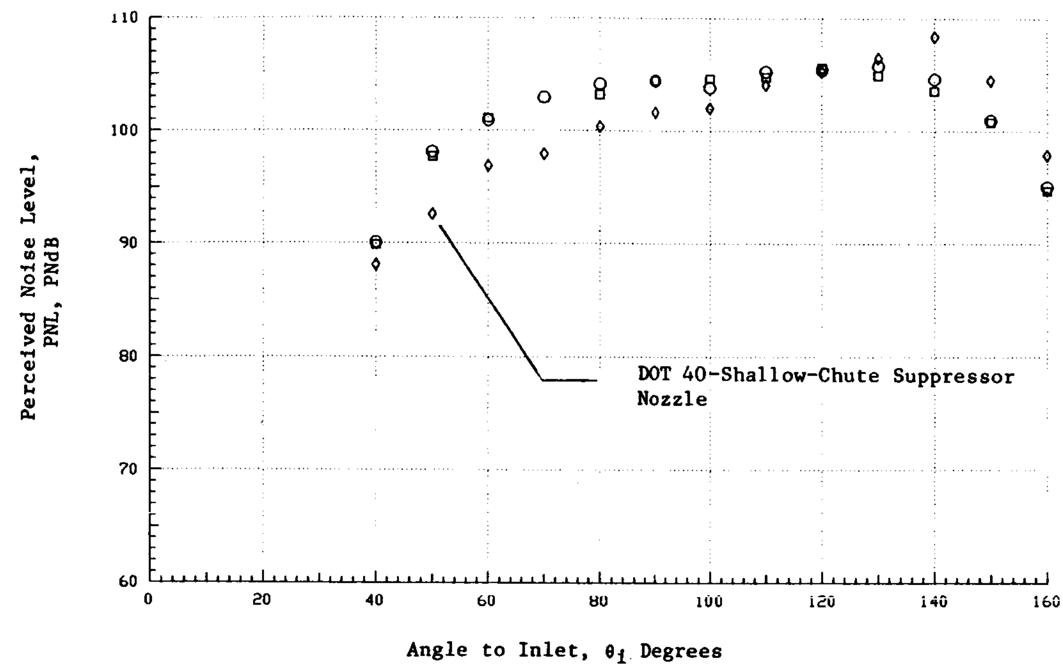

(a) Perceived Noise Level

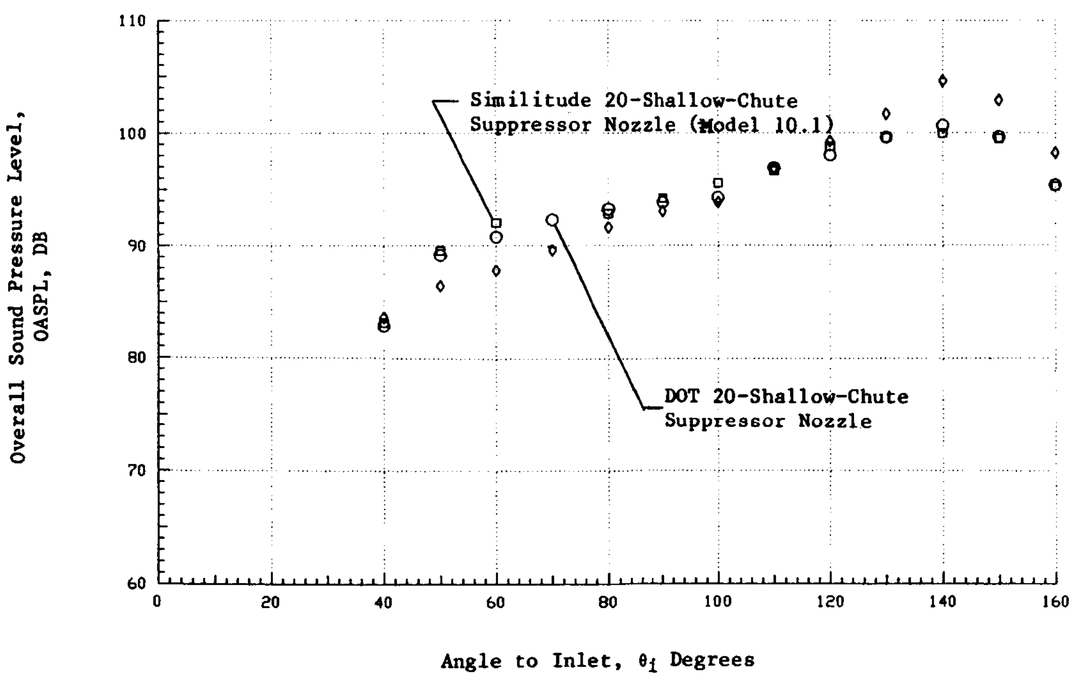

(b) Overall Sound Pressure Level

Figure 3-38. Static PNL- and OASPL-Directivities of the Modified DOT 20- and 40-Shallow Chute Suppressor Nozzles at Typical AST Takeoff Condition.

SYMBOL	POINT
□	1016
○	2020
◇	4020

Scaled to Product Size $A^T = 0.903 m^2$ (1,400 in.^{2}) and Extrapolated to 731.5m (2,400 ft) Sideline.

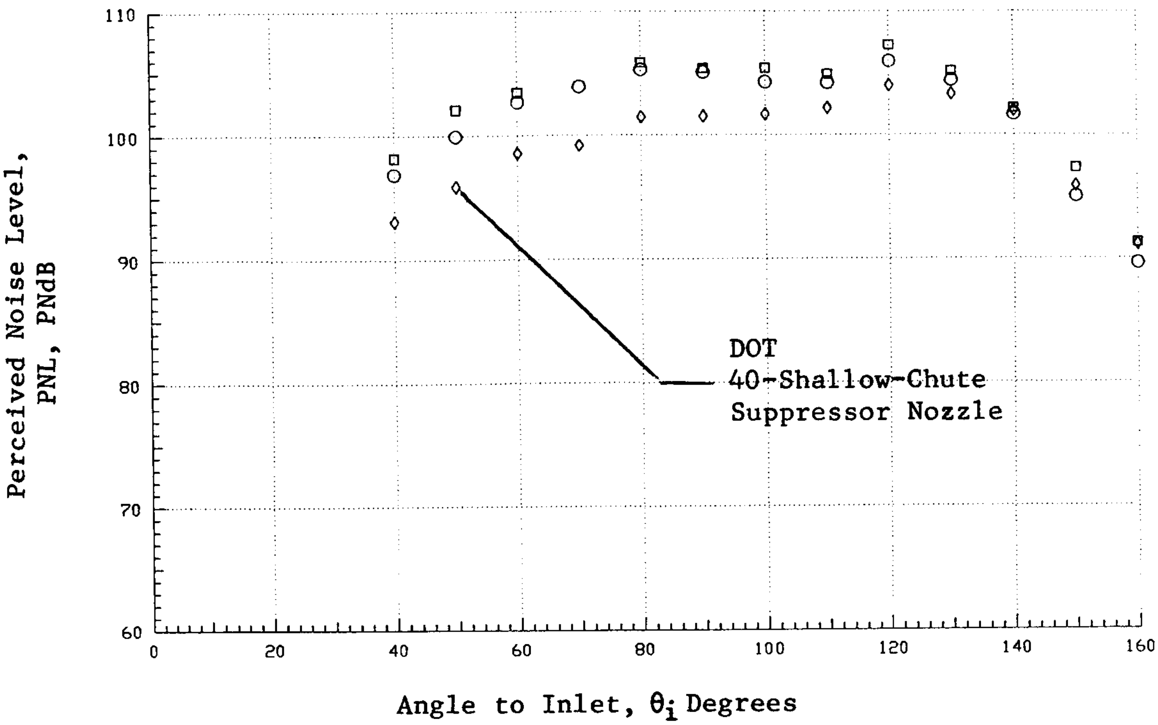

(a) Perceived Noise Level

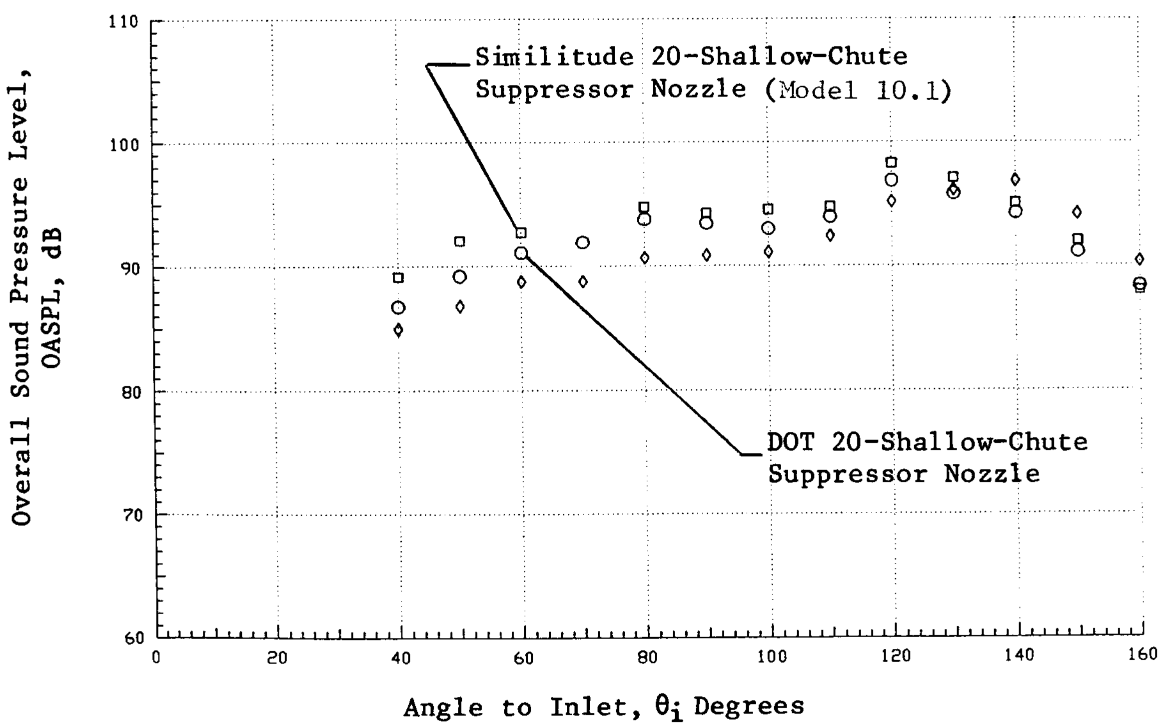

(b) Overall Sound Pressure Level

Figure 3-39. Simulated Flight PNL- and OASPL-Directivities of the Modified DOT 20- and 40-Shallow-Chute Suppressor Nozzles at Typical AST Takeoff Condition.

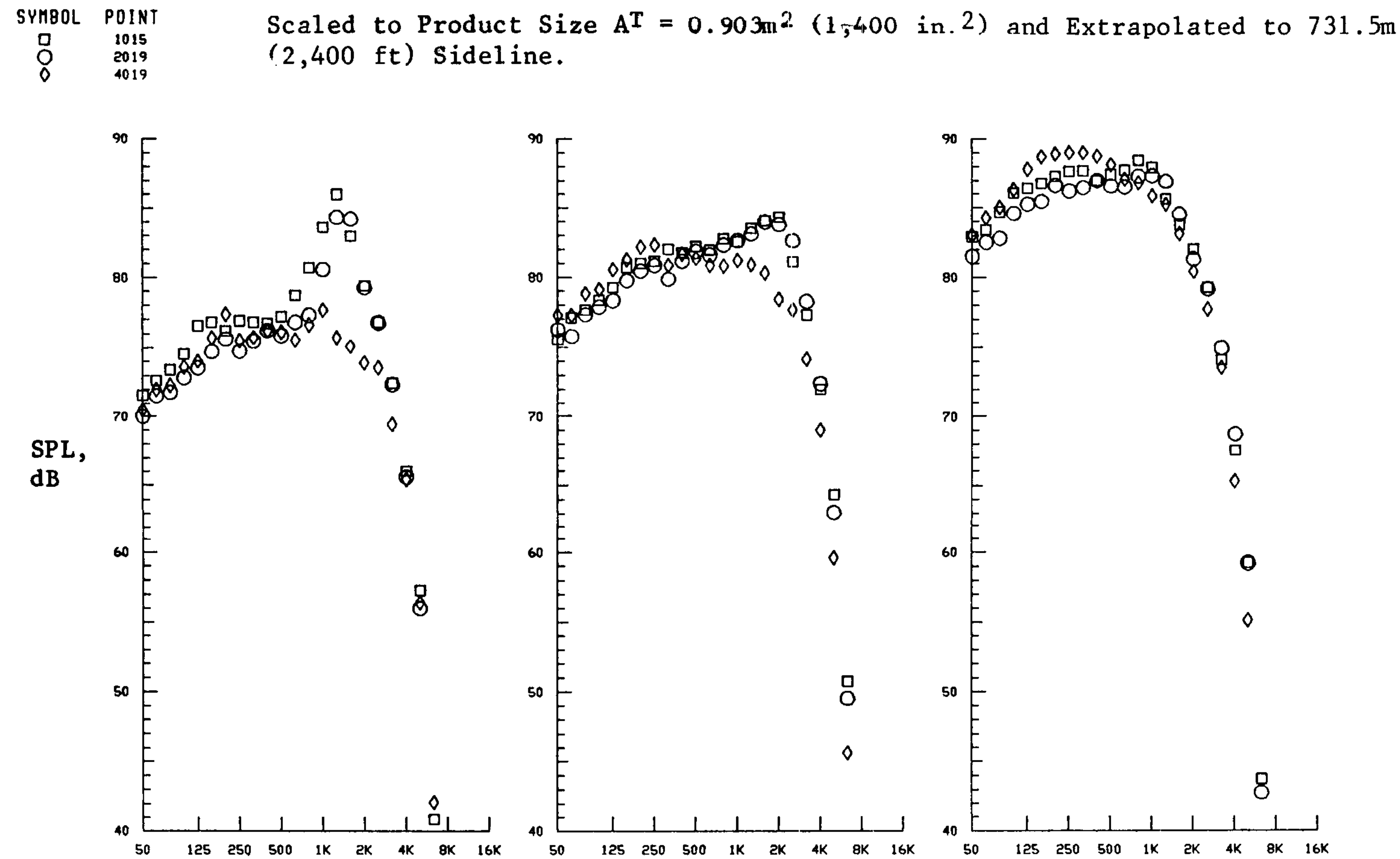

1/3 Octave Band Center Frequency, Hz

(a) Directivity Angle, $\theta_i = 60°$ (b) Directivity Angle, $\theta_i = 90°$ (c) Directivity Angle, $\theta_i = 120°$

Figure 3-40. Typical Static Spectral Data of The Modified DOT 20- and 40-Shallow-Chute Suppressor Nozzles at Typical AST Takeoff Condition.

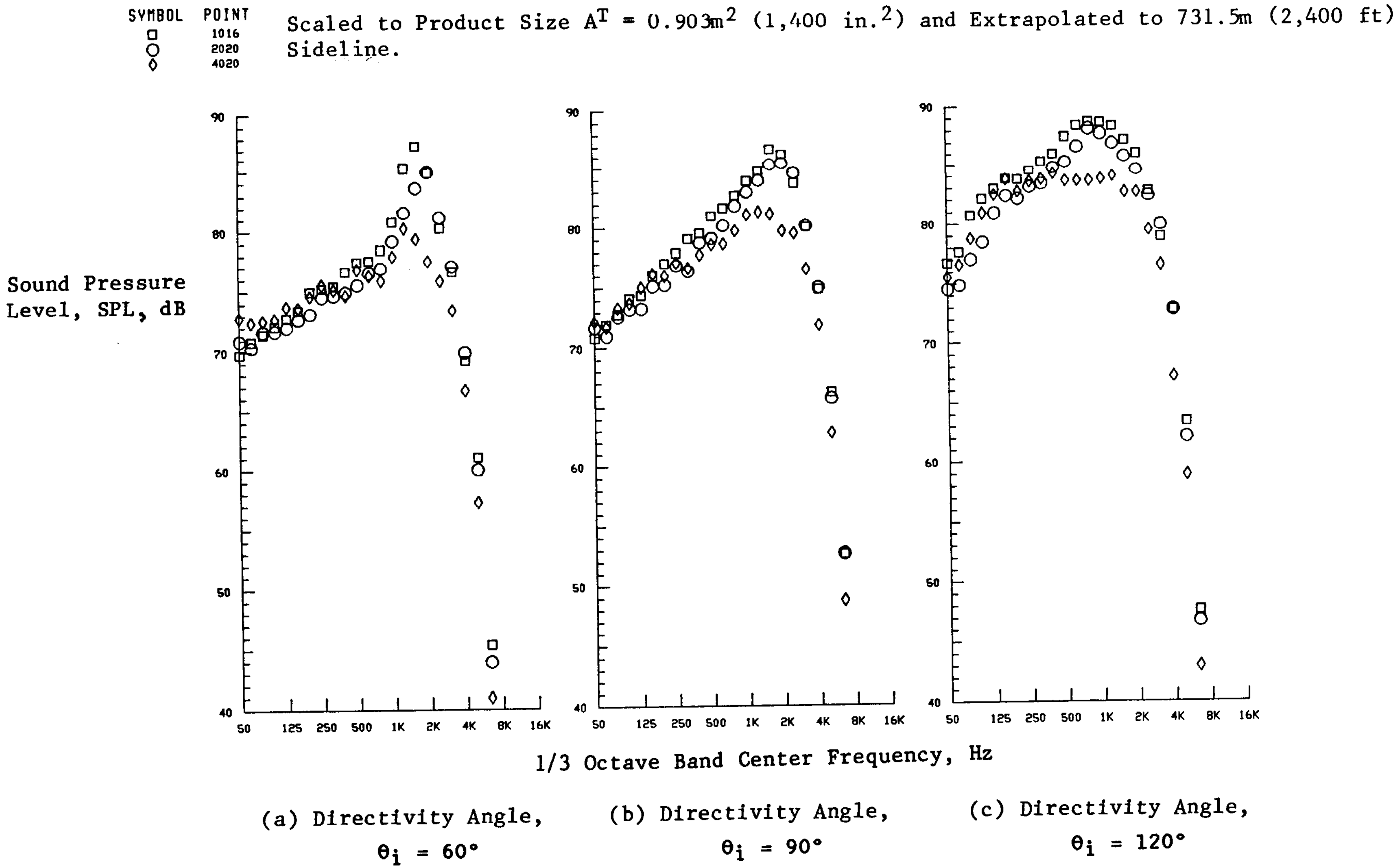

Figure 3-41. Typical Simulated Flight Spectral Data of the Modified DOT 20- and 40-Shallow-Chute Suppressor Nozzles at Typical AST Takeoff Condition.

In summary, the data indicate no significant differences between the acoustic characteristics of the similitude and DOT-modified 20-shallow-chute coannular plug nozzles. However, the modified DOT 40-shallow-chute nozzle is observed to result in better shock noise suppression in the front quadrant relative to the 20-shallow-chute nozzles. In the aft quadrant, the 40-shallow-chute configuration results in a lower PNL data for $V_j^{mix} <$ ~ 2,300 fps. For velocities greater than this range, the 20-shallow-chute nozzle is observed to yield lower PNL data.

3.1.4.4 Effect of Velocity Ratio

In order to evaluate the effect of the velocity ratio on the acoustic characteristics of the modified DOT 20-shallow-chute nozzle, tests have been conducted with different ratios of the inner to outer stream velocities. This was obtained by holding the outer stream velocity constant at V_j^o = 2,480 fps and varying the inner stream velocity V_j^i from 990 to 1,740 fps so as to achieve velocity ratios of 0.4 to 0.7. The measured static and simulated flight (V_{ac} = 400 fps) acoustic data are summarized in Figures 3-42 and 3-43, respectively. The data include normalized PNL at θ_i = 120° (which is also the PNL_{max}), and PWL and V_j^{mix} as a function of the velocity ratio. An examination of the figures indicates that a change in the velocity ratio in the range of 0.4 to 0.7 had no significant effect upon the peak noise levels.

In order to normalize the acoustic data to a constant V_j^{mix}, a regression analysis was performed using the acoustic data in the velocity range of V_j^{mix} = 1,900 to 2,400 ft/sec. The measured normalized peak PNL data have been normalized to a constant V_j^{mix} and are presented also in Figures 3-42 and 3-43. The data indicate a ±0.5 dB difference in the peak PNL data of the modified DOT 20-shallow-chute suppressor nozzle over the velocity ratio range of 0.4 to 0.7.

3.1.4.5 Additional Comments

The objective of the free-jet transformation process employed during the data reduction procedure is to modify the far-field SPL spectra that are measured at various angles to the jet axis during a simulated free-jet experiment so as to yield SPL spectra that would have been obtained during an actual flight.

A generalized description of the transformation procedure, along with the modifications and refinements that have been incorporated over the years, has been summarized in detail in References 3 and 17. In this procedure, an empirical formula to account for the free-jet turbulence absorption is employed that limits it to maximum of 3 dB cutoff. This absorption coefficient is also a function of the frequency.

Some typical results are presented in this section that compare the simulated flight data with and without the turbulence correction. The data obtained with the conical baseline, modified DOT 20- and 40-shallow-chute suppressor nozzles are presented in Figures 3-44 through 3-46. The data in these figures correspond to a mass-averaged exhaust velocity of V_j^{mix} ~ 2,300 fps. An examination of these figures indicates that at aft angles corresponding to the peak values in PNL the turbulence correction accounts for 2, 3, and 2.5 dB in the flight data of conical, modified DOT 20- and

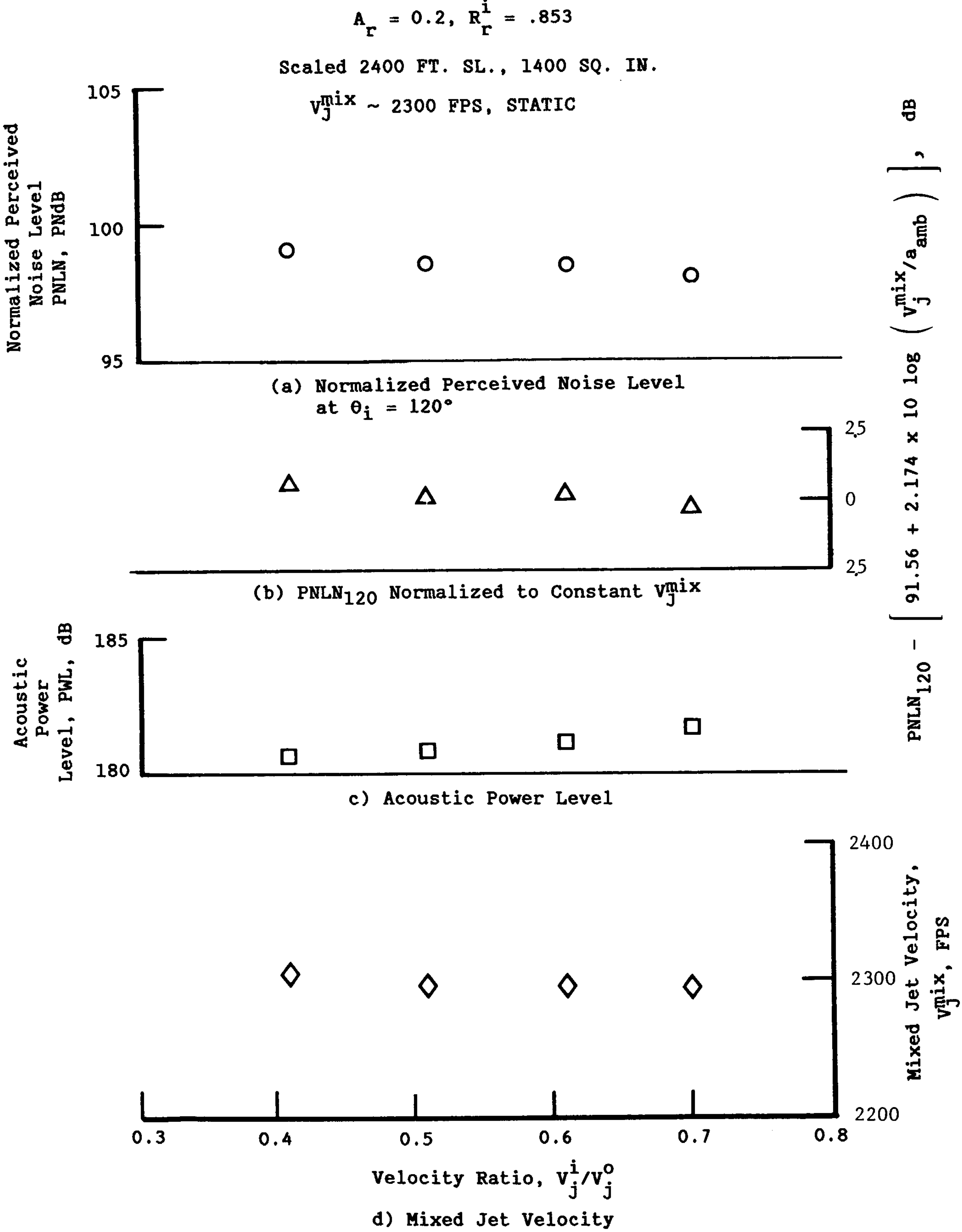

Figure 3-42. Effect of Velocity Ratio on the Acoustic Characteristics of the Modified DOT 20-Shallow-Chute Suppressor (Static).

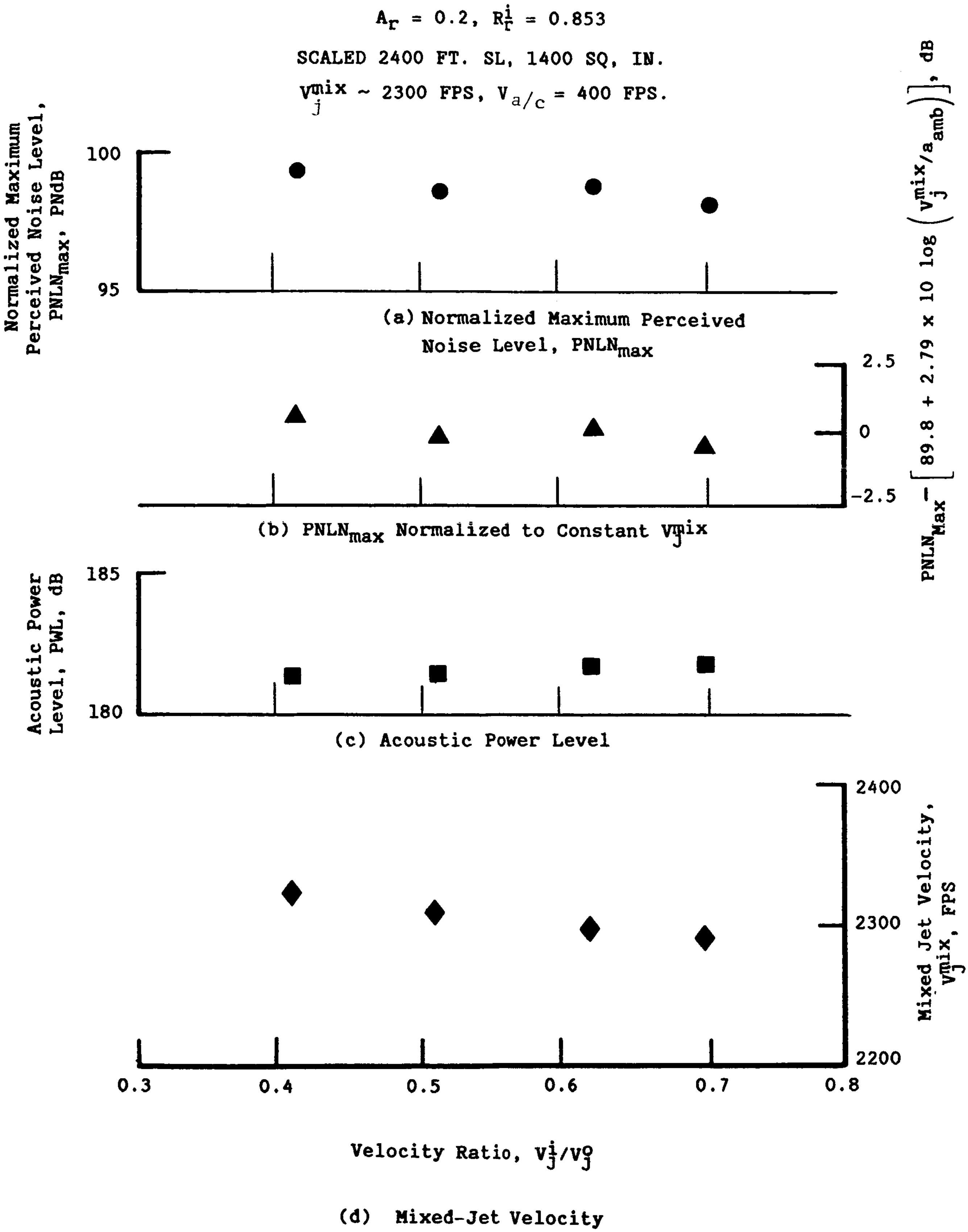

Figure 3-43. Effect of Velocity Ratio on the Acoustic Characteristics of the Modified DOT 20-Shallow-Chute Suppressor Nozzle (Simulated Flight)

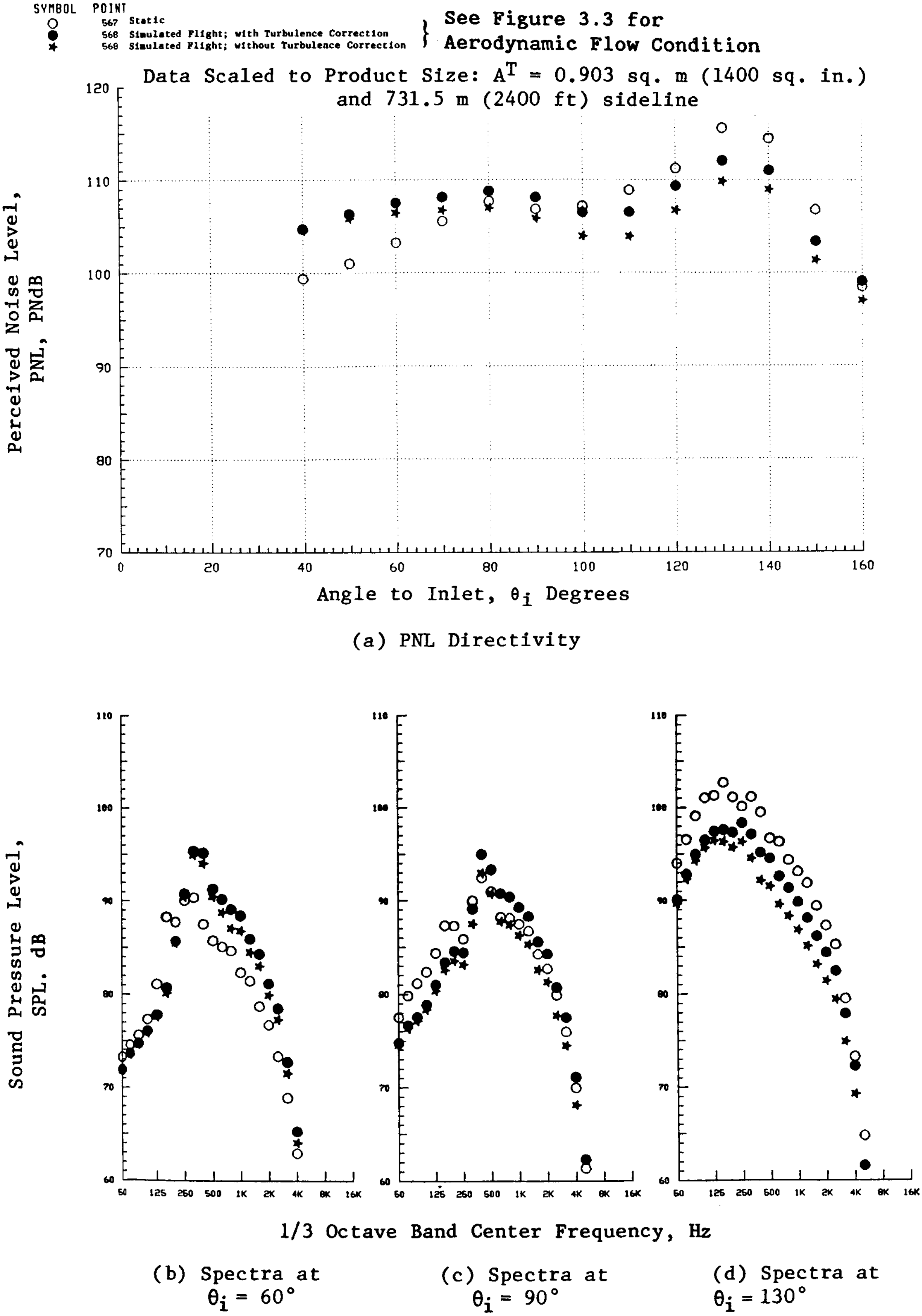

Figure 3-44. Simulated Flight Data of a Conical Baseline Nozzle, at V_j ~2300 fps, With and Without the Turbulence Correction.

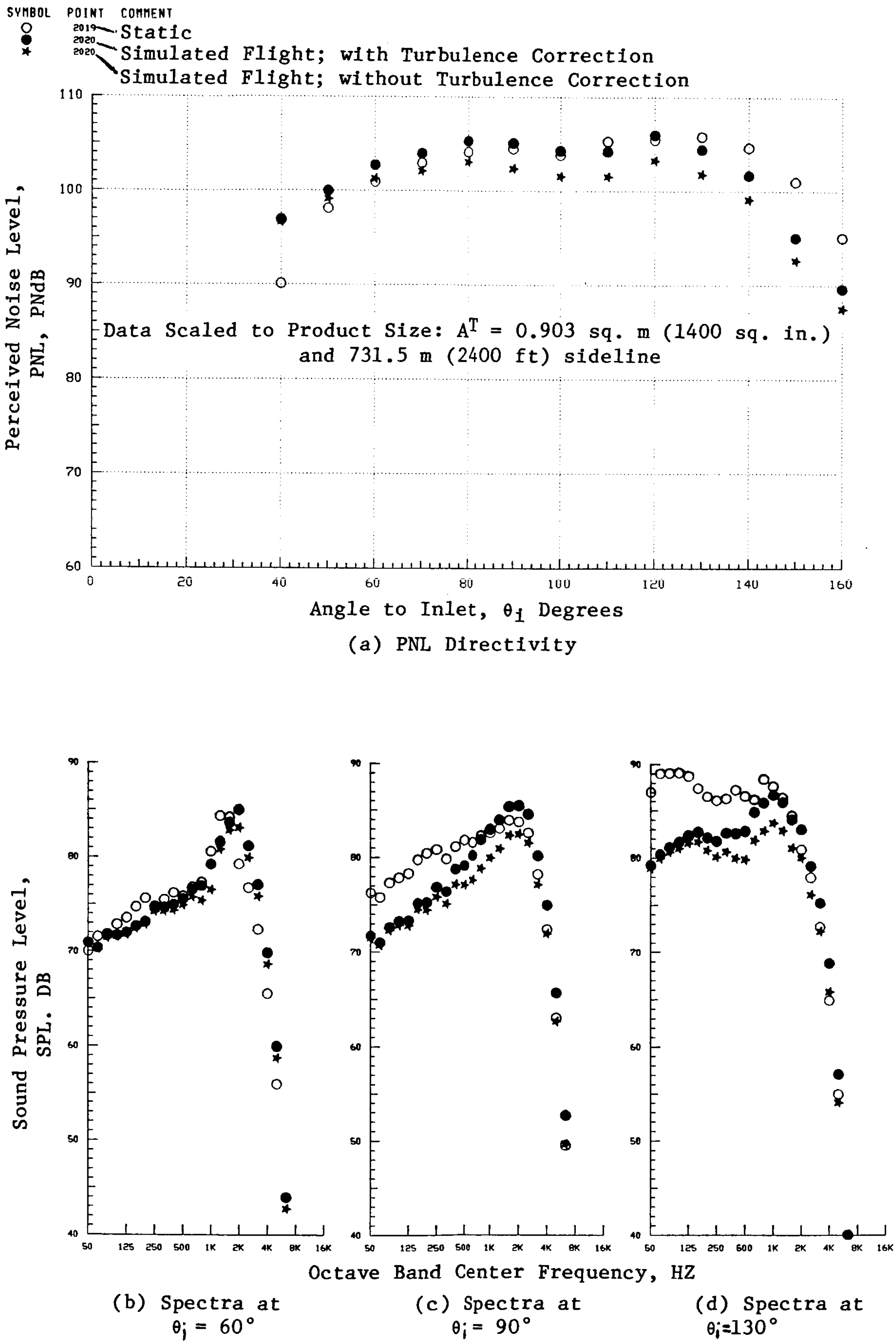

Figure 3-45. Simulated Flight Data of Modified 20-Shallow-Chute Mechanical Suppressor Nozzle, at V_j^{mix} ~2300 fps With and Without Turbulence Correction.

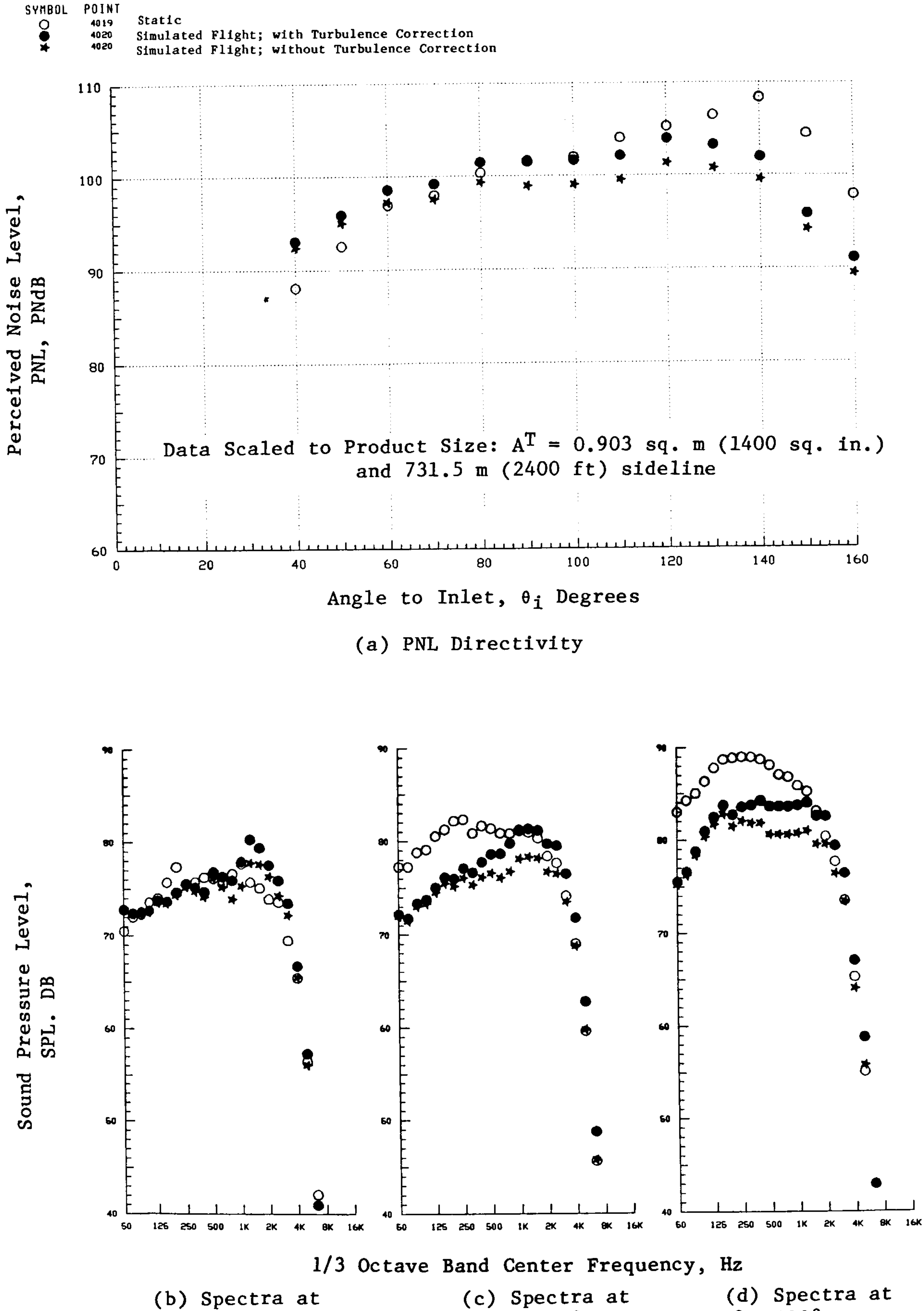

Figure 3-46. **Simulated Flight Data of Modified 40-Shallow-Chute Mechanical Suppressor Nozzle, at V_j^{mix} ~2300 fps with and without the Turbulence Correction.**

40-shallow-chute nozzles, respectively. The differences are mainly due to the relative relationships between the low and high frequency SPLS of these configurations. The higher the high frequency content, higher is the turbulence correction applied.

The empirical turbulence correction has been obtained using the data of conical nozzles. Because of the significant differences in high frequency content of the aft angle suppressor spectra, the data seem to suggest that the empirical expression as used needs to be further examined and possibly modified for use in the flight transformation of the suppressor data.

3.1.5 Effectiveness of Convergent-Divergent Flowpath for Reduction of Shock Cell Noise; Single Flow Unsuppressed C-D Annular Plug Nozzle (Model 9.1)

Shock cell broadband noise is a significant contributor to the total noise radiated from jets operating at supercritical pressure ratios. In fact, it has been identified in Reference 3 as a potential engine noise problem for an AST at takeoff. In an effort to reduce the shock cell noise, static tests have been conducted (Refs. 2 and 12 through 14) with C-D nozzles. From ambient temperature single flow static tests with circular nozzles having C-D termination that was designed for an ideal expansion at a Mach number of 1.5, the effectiveness of a C-D termination in the reduction of shock cell noise has been demonstrated in Reference 13. In addition, the data of Reference 13 indicate a reduction of 6 dB in the OAPWL of a circular C-D nozzle at its design condition relative to a convergent conical nozzle also operating at the same condition. It is the objective of this program to demonstrate with heated jets and under both static and simulated flight conditions, the effectiveness of a properly designed C-D flowpath in the control of the shock cell noise of both annular and coannular unsuppressed plug nozzles. The single flow C-D annular plug nozzle (Model 9.1) forward quadrant acoustic data are presented and the C-D effectiveness is discussed in this subsection. Acoustic results obtained with dual stream C-D coannular plug nozzles (Models 9.2 through 9.4) are presented separately in Subsection 3.1.6.

The convergent-divergent annular plug nozzle (Model 9.1), the details of which are presented in Figure 2-9, is designed for a shock-free flow at an exit jet Mach number M_j of 1.44 (P_r = 3.3 and T_T = 1,760° R). The radius ratio R_r at the throat and exit are 0.855 and 0.789, respectively. To demonstrate the effectiveness of the designed C-D contour in the control of shock cell noise at and in the vicinity of its shock-free condition, static and simulated flight (V_{ac} ~ 122 m/sec or 400 fps) tests were conducted over a pressure ratio range of 2.94 to 3.54 (i.e., M_j = 1.34 to 1.48). The PNL data measured in a typical forward quadrant angle of θ_i = 60° are plotted in Figure 3-47 as a function of shock strength parameter β. The data are compared in this figure with the results of the circular conical baseline nozzle (Model 5). An examination of the figure indicates a broad region of effectiveness of C-D design in reducing the foward quadrant shock noise under both static and simulated flight conditions. In addition, this figure indicates that, at θ_i = 60°, a maximum reduction of 6.5 and 9 dB is obtained with the use of the C-D annular plug nozzle (Model 9.1) relative to a conical nozzle under static and simulated flight conditions, respectively. The jet Mach number corresponding to this maximum effective condition is observed, under both static and simulated flight conditions, to be M_j = 1.43 (P_r = 3.24) which is close to the C-D design condition of M_j = 1.44 (P_r = 3.3). The overall effectiveness of the C-D contour in the reduction of

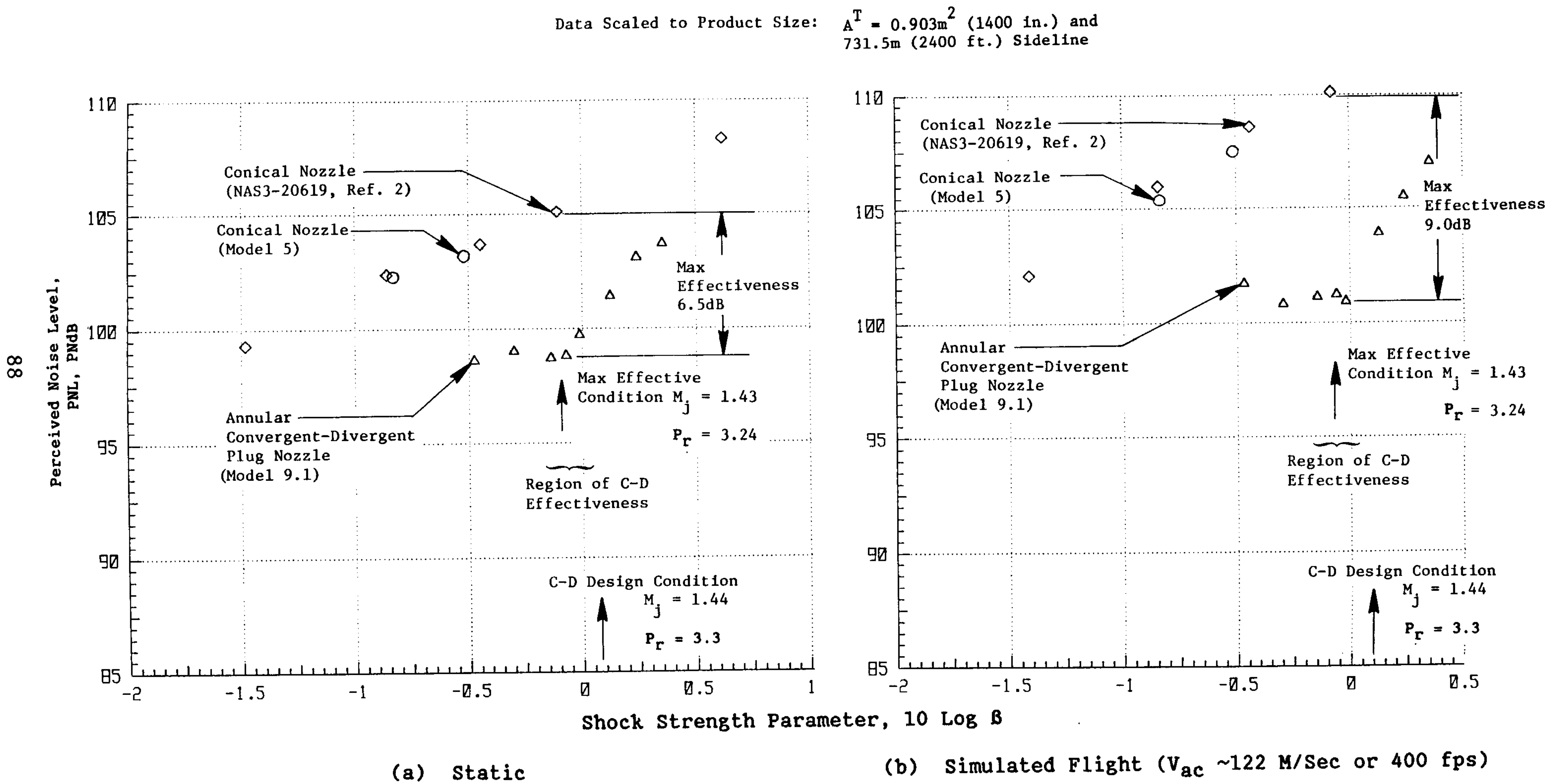

Figure 3-47. Shock Noise Reduction for a C-D Annular Plug Nozzle Relative to a Conical Nozzle; Static and Simulated Flight PNL Data at θ_i = 60°.

shock cell noise over the supersonic test range is demonstrated by the data presented in Figures 3-48 (a) and (b) which summarize, respectively, all of the measured forward quadrant (θ_i = 40° through 90°) static and simulated flight PNL data.

Since no diagnostic (e.g., Schlieren or LV) tests were scheduled with the Model 9 series of nozzles, it cannot be ascertained at this time whether all of the shock cell noise has been eliminated by the C-D annular nozzle at its maximum effective condition. However, an estimation can be made by comparing the forward quadrant static data measured at the maximum effective flow condition with the corresponding simulated flight data. If such a comparison indicates no or minimal forward quadrant noise amplification due to flight, then it can be inferred that the shock cell noise has been mitigated considerably by the C-D design. Such a comparison at $M_j \sim 1.43$ is presented in Figure 3-49 along with a similar set of results obtained with the circular conical baseline nozzle (Model 5). An examination of this figure indicates a comparatively small amount of flight amplification of the front quadrant C-D annular nozzle (Model 9.1) static data (for example, 1.2 dB amplification for Model 9.1 compared to 5.0 dB amplification for conical nozzle, both being measured at θ_i = 60°). Hence, it is concluded that, while the forward quadrant shock cell noise is not completely eliminated by the current C-D design, it is mitigated by a significant amount.

Static and simulated flight front quadrant spectral data of Model 9.1 at its maximum effective condition (M_j = 1.43) are, respectively, presented in Figures 3-50 and 3-51. Therein, the data are compared with the corresponding conical baseline nozzle data. While, for a quantitative comparison, the C-D annular plug nozzle data need to be compared with a convergent annular plug nozzle data (these are planned currently under a separate contract), the data presented in Figures 3-50 and 3-51 qualitatively confirm the significant C-D/plug benefit observed in the front quadrant over the entire frequency range of interest.

Typical front quadrant simulated flight spectral data of the C-D annular plug nozzle (Model 9.1) at $P_r \sim 2.9$, 3.05 and 3.24 are presented in Figure 3-52. These data indicate that over a broad range of frequencies the sound pressure levels measured at the off-design pressure ratio of 2.9 decrease as the pressure ratio is increased to the maximum effective condition of 3.24. This decrease in the SPL's with an increase in the pressure ratio indicates a weakening of the shock cell structure as the optimum operating condition of the C-D annular plug nozzle is reached.

The qualitative effectiveness of the C-D annular plug nozzle [Model 9.1: $(R_r)_{throat}$ = 0.855, $(R_r)_{exit}$ = 0.789] has been demonstrated so far by comparing the measured data with that of a conical baseline nozzle (Model 5). As earlier mentioned, the data need to be compared with those of an equivalent convergent annular plug nozzle having an exit radius ratio equal to that of the C-D annular plug nozzle at its exit plane. While no such configuration was tested specifically during this program, a review of scale-model nozzle tests over the years at GE revealed sets of data of two comparable convergent annular plug nozzles obtained during the DOT program (Ref. 11). These nozzles, referred to as Model 4 and Model 5 in Reference 11, were cylindrical shroud plug nozzles (exhaust area = 11.05 in.^{2}) with convergent flow geometry and having an exit plane radius ratio of 0.789 and 0.853, respectively. The farfield acoustic data were obtained in an outdoor

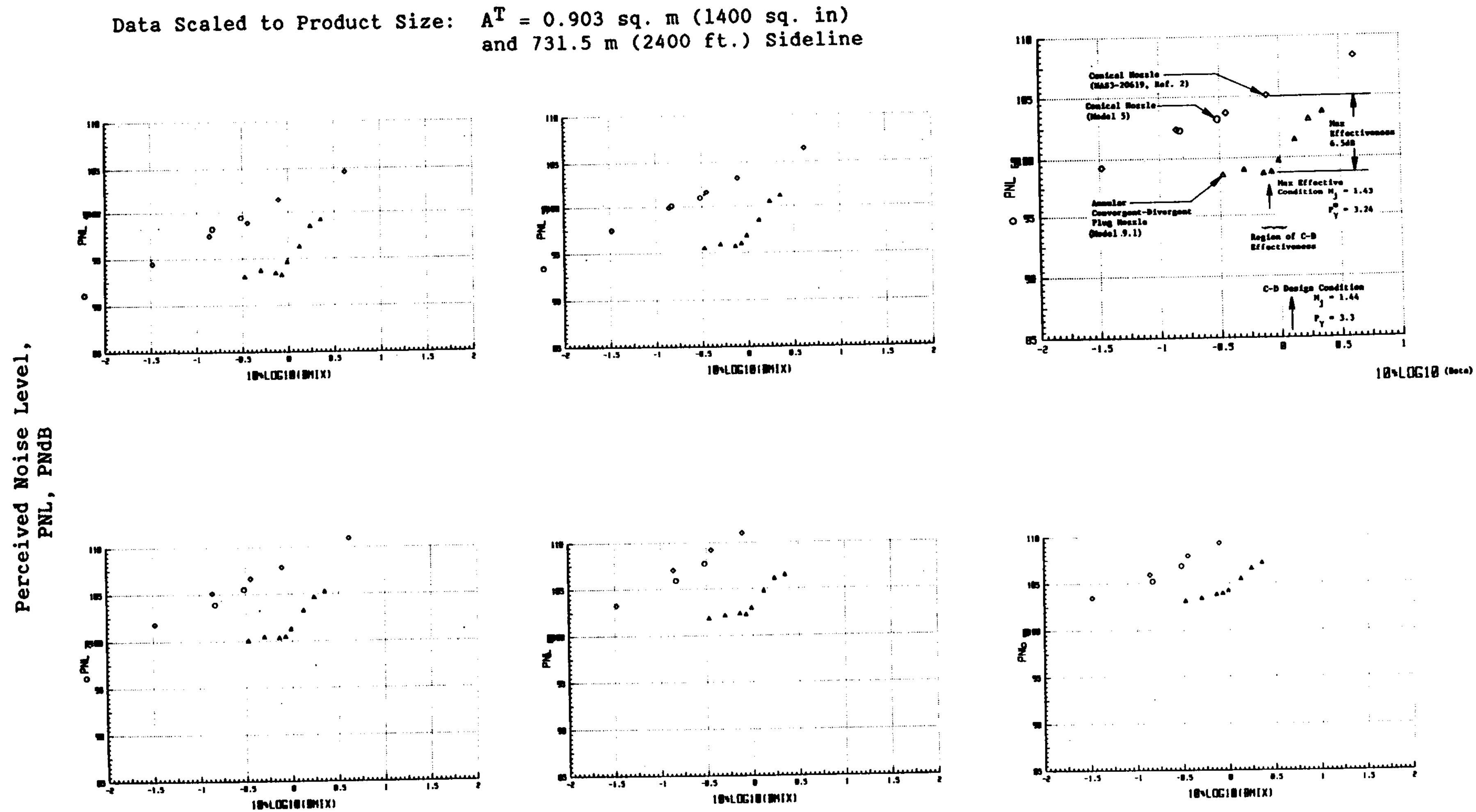

Shock Strength Parameter, 10 log β

a) Static (V_{ac} = 0 FPS) PNL Results

Figure 3-48. Effectiveness in Front Quadrant Noise Reduction for a C-D Annular Plug Nozzle.

Data Scaled to Product Size: A^T = 0.903 sq. in. (1400 sq. in.) and 731.5m (2400 ft.) Sideline.

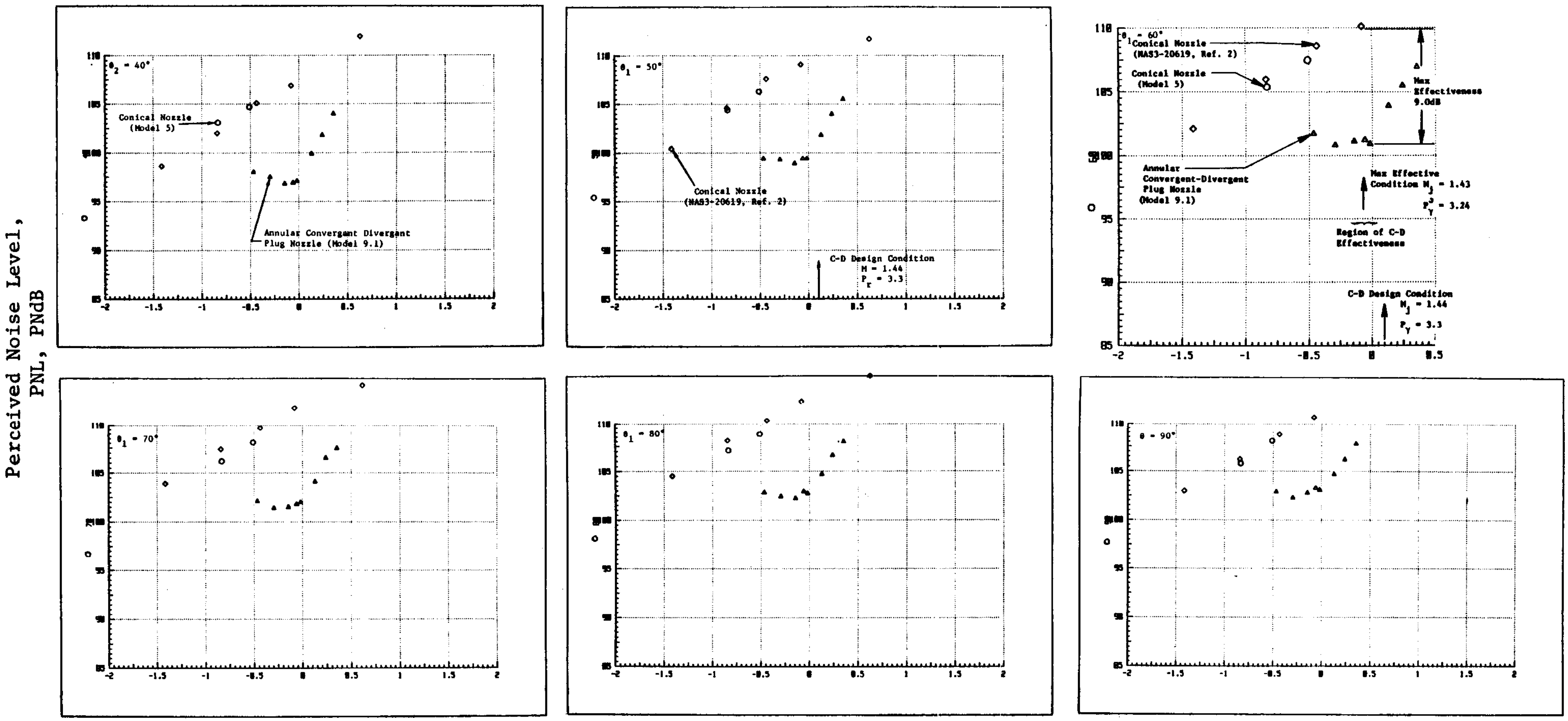

Shock Strength Parameter, 10 Log β

b) Simulated Flight (V_{ac} = 122 M/Sec or 400 FPS) PNL Results

Figure 3-48. Effectiveness in Front Quadrant Noise Reduction for a C-D Annular Plug Nozzle (Concluded).

Static	Flight	P_r	T_T (° R)	V_j (f/s)
◇	◆	3.17	1700	2410
△	▲	3.24	1750	2460

Data Scaled to Product Size: A^T = 0.903 m^2 (1400 in.^{2}) and 731.5 m (2400 ft) Sideline

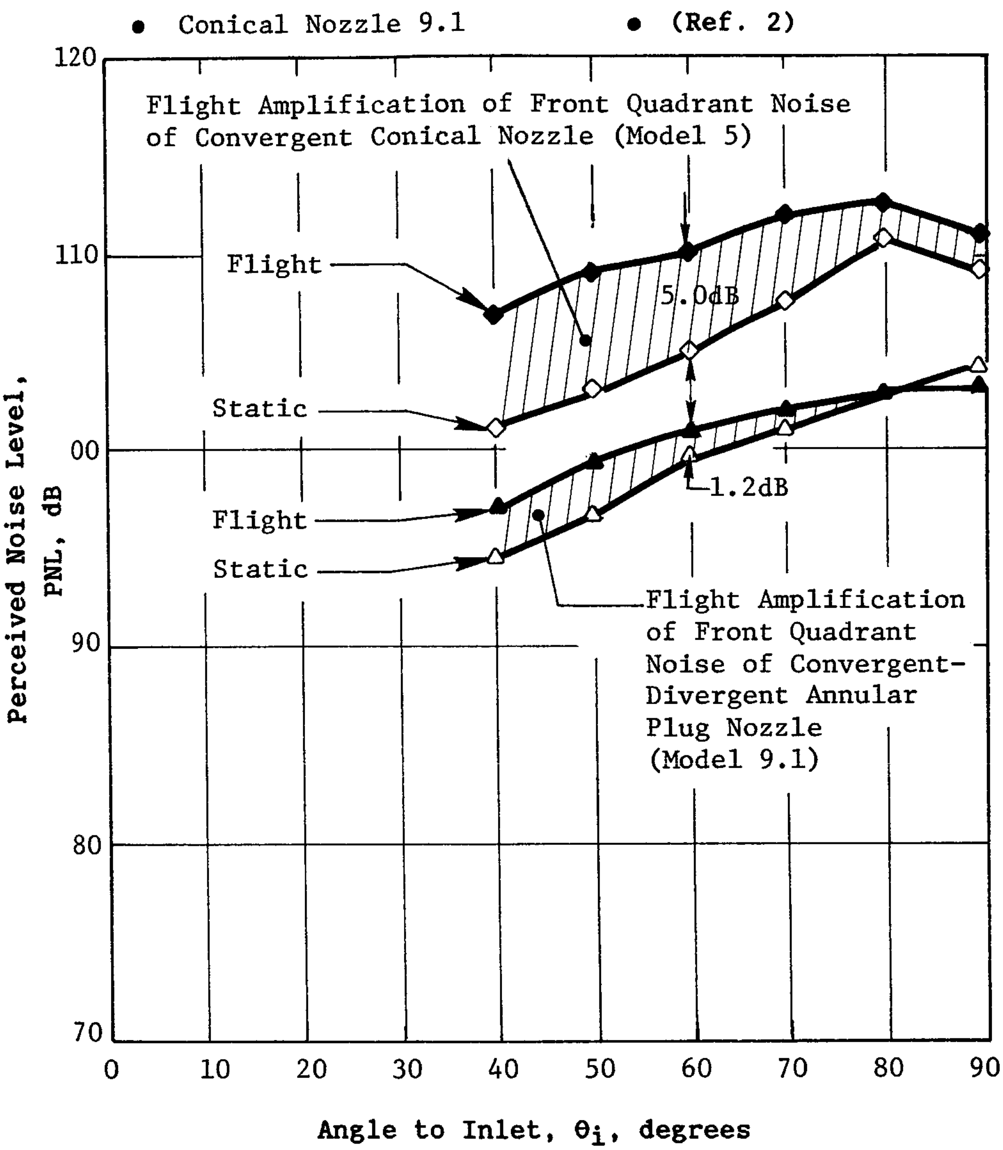

Figure 3-49. Front Quadrant Noise Amplification Due to Flight (V_{ac} = 400 fps) of a Conical and Convergent-Divergent Annular Plug Nozzle at AST/VCE Takeoff Condition.

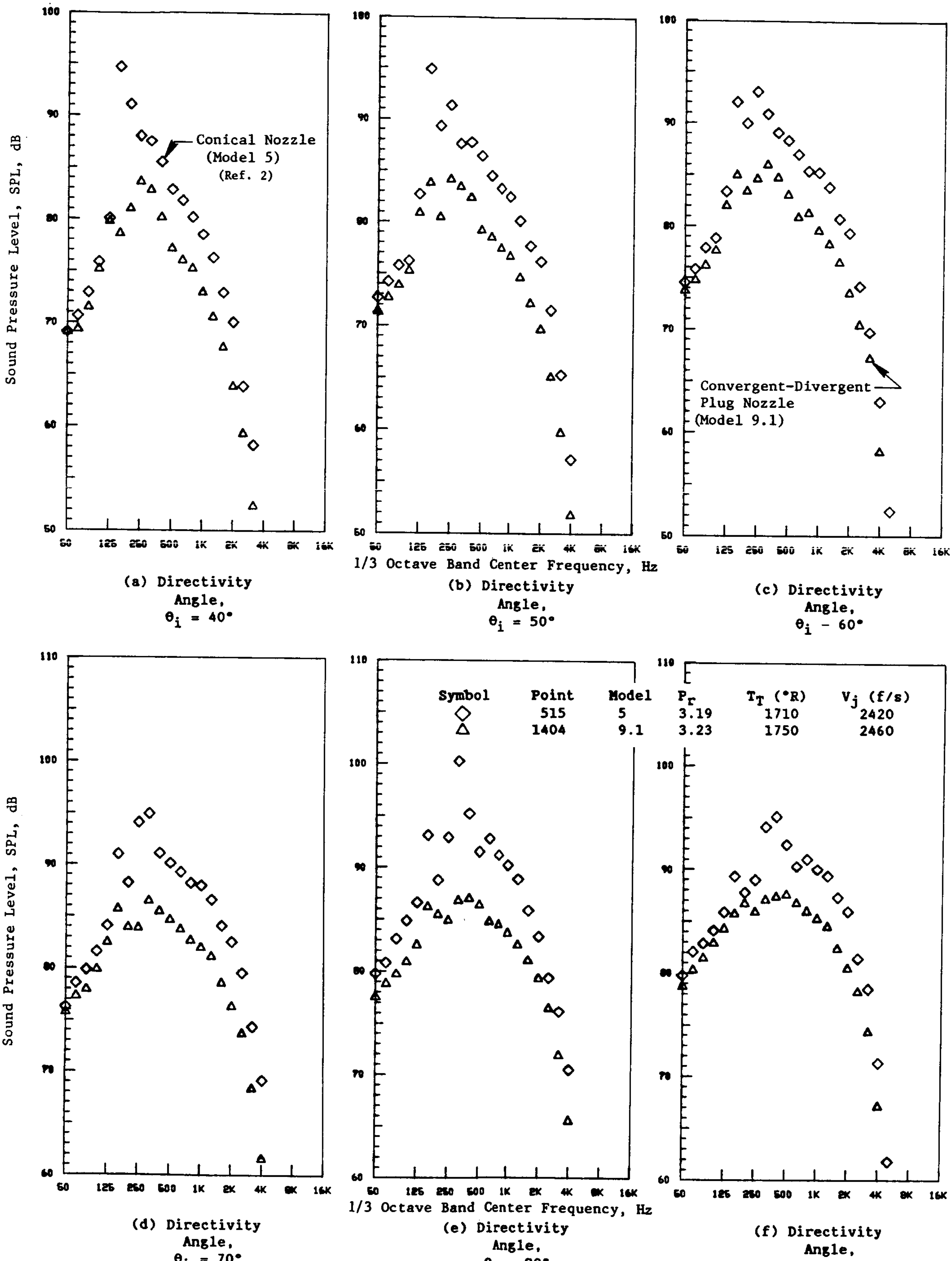

Figure 3-50. Spectral Comparison Between Conical (Model 5) and Convergent-Divergent Annular Plug Nozzle (Model 9.1) at Flow Conditions that Correspond to Maximum C-D Effectiveness; Static Data.

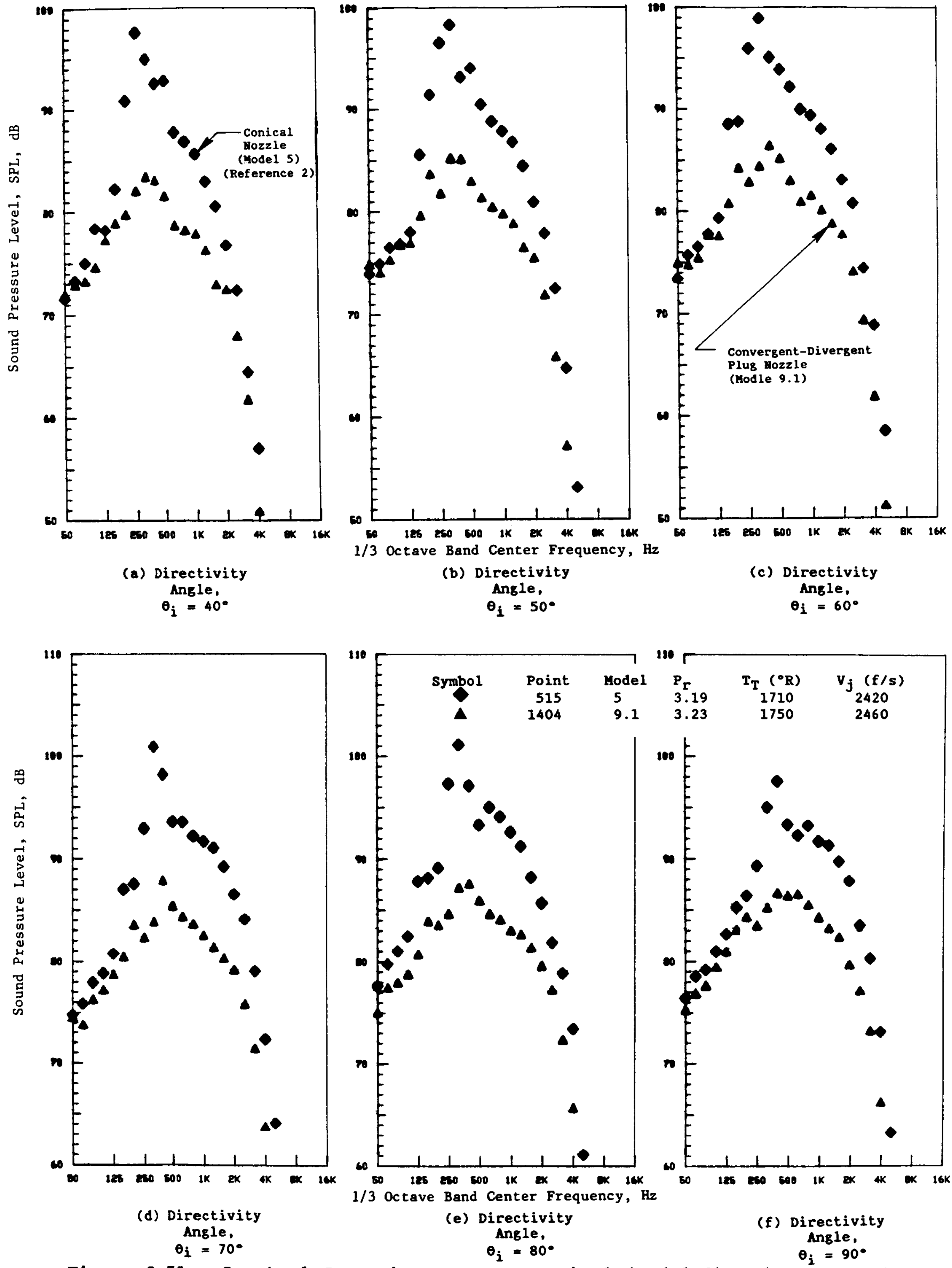

(a) Directivity Angle, θ_i = 40°

(b) Directivity Angle, θ_i = 50°

(c) Directivity Angle, θ_i = 60°

(d) Directivity Angle, θ_i = 70°

(e) Directivity Angle, θ_i = 80°

(f) Directivity Angle, θ_i = 90°

Figure 3-51. Spectral Comparison Between Conical (Model 5) and Convergent-Divergent Annular Plug Nozzle (Model 9.1) at Flow Conditions that Correspond to Maximum C-D Effectiveness; Simulated Flight (V_{ac} = 400 FPS) Data.

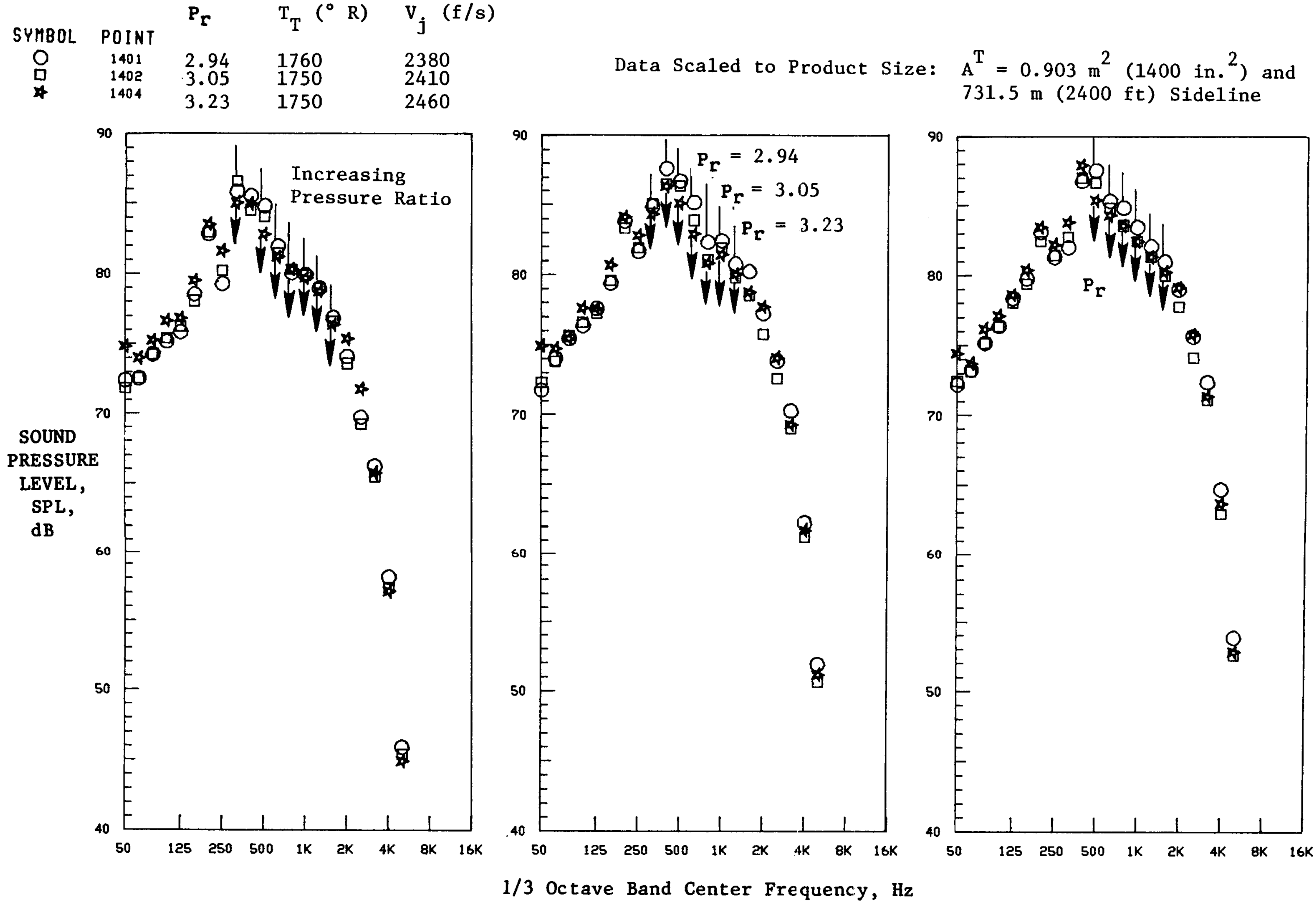

(a) Directivity Angle, $\theta_i = 50°$

(b) Directivity Angle, $\theta_i = 60°$

(c) Directivity Angle, $\theta_i = 70°$

Figure 3-52. Typical Front Quadrant Convergent- Divergent Annular Plug Nozzle Spectra at Flow Conditions in the Vicinity of the C-D Maximum Effective Conditions; Simulated Flight Test Results (V_{ac} = 400 FPS).

static facility and are reported in Reference 11 scaled to a nozzle exhaust area of 0.218 m^2 (338 $in.^2$) and extrapolated to a 731.5 m (2,400 ft) sideline. The current C-D annular plug nozzle static PNL data at θ_i = 60°, scaled to the above-mentioned size, are presented in Figure 3-53 as a function of shock strength parameter β and are compared with the corresponding data of the two convergent annular plug nozzles. This comparison indicates that the magnitude of the C-D benefit at θ_i = 60° relative to a convergent plug nozzle, with both operating at the maximum effective C-D nozzle condition, is (1) 3.6 dB when the exit radius ratio of the convergent and C-D annular plug nozzles are both equal to 0.789, and (2) 2.3 dB when the exit radius ratio of the convergent configuration is equal to that of the C-D nozzle at its throat. In addition, the data of Figure 3-53 confirm the existence of a C-D benefit over a range of off-design flow conditions.

Comparison of forward quadrant PNL- and OASPL-directivities and selected spectra of the C-D annular plug nozzle (Model 9.1) at its maximum effective condition with corresponding convergent annular plug nozzle data of Model 5 of Reference 11 is provided in Figure 3-54.

3.1.6 Effectiveness of Convergent-Divergent Flowpath for Reduction of Shock Cell Noise; Dual Flow Unsuppressed Coannular Plug Nozzles (Models 9.2, 9.3, and 9.4)

The effectiveness of a suitably designed C-D flowpath on an annular plug nozzle in mitigating the shock cell noise was established in the previous subsection. In this subsection, the effectiveness of the C-D flowpath on dual flow, unsuppressed coannular plug nozzles is demonstrated using the acoustic data of the following three dual flow configurations:

1. Model 9.2: Outer stream nozzle is the C-D contoured Model 9.1 (maximum effective at M_j^o = 1.43) and the inner nozzle is convergent with the inner flow subsonic (M_j^i ~ 0.91)

2. Model 9.3: Outer nozzle is convergent with an inner C-D nozzle designed for optimum expansion at M_j^i = 1.38 (P_r^i = 3.1)

3. Model 9.4: An all C-D coannular nozzle assembled using the outer C-D nozzle of Model 9.2 and the inner C-D nozzle of Model 9.3.

The acoustic data obtained with Models 9.2, 9.3, and 9.4 are presented and discussed next in Subsections 3.1.6.1 and 3.1.6.2.

3.1.6.1 Dual Flow Unsuppressed Coannular Plug Nozzle with a C-D Outer and a Convergent Inner

The C-D effectiveness of a coannular plug nozzle, having a C-D flowpath for a supersonic outer stream and a convergent flowpath for a subsonic inner stream, from the point of view of shock cell noise reduction, is deduced from the data presented in Figure 3-55. In this figure, the forward quadrant static PNL data of conical baseline nozzle (Model 5), similitude unsuppressed coannular plug nozzle with convergent exhausts on both the streams (Model 8), and the coannular plug nozzle having a C-D outer and a convergent inner (Model 9.2) are compared with their corresponding simulated flight (V_{ac} ~ 122 m/sec or 400 fps) measured PNL results. The flow conditions of the outer stream of both Models 8 and 9.2 correspond to the maximum effective operating

- Static Data
- Data Scaled to $A^T = 0.218\ m^2$ (328 in.^{2}) and 731.5 m (2400 ft) Sideline

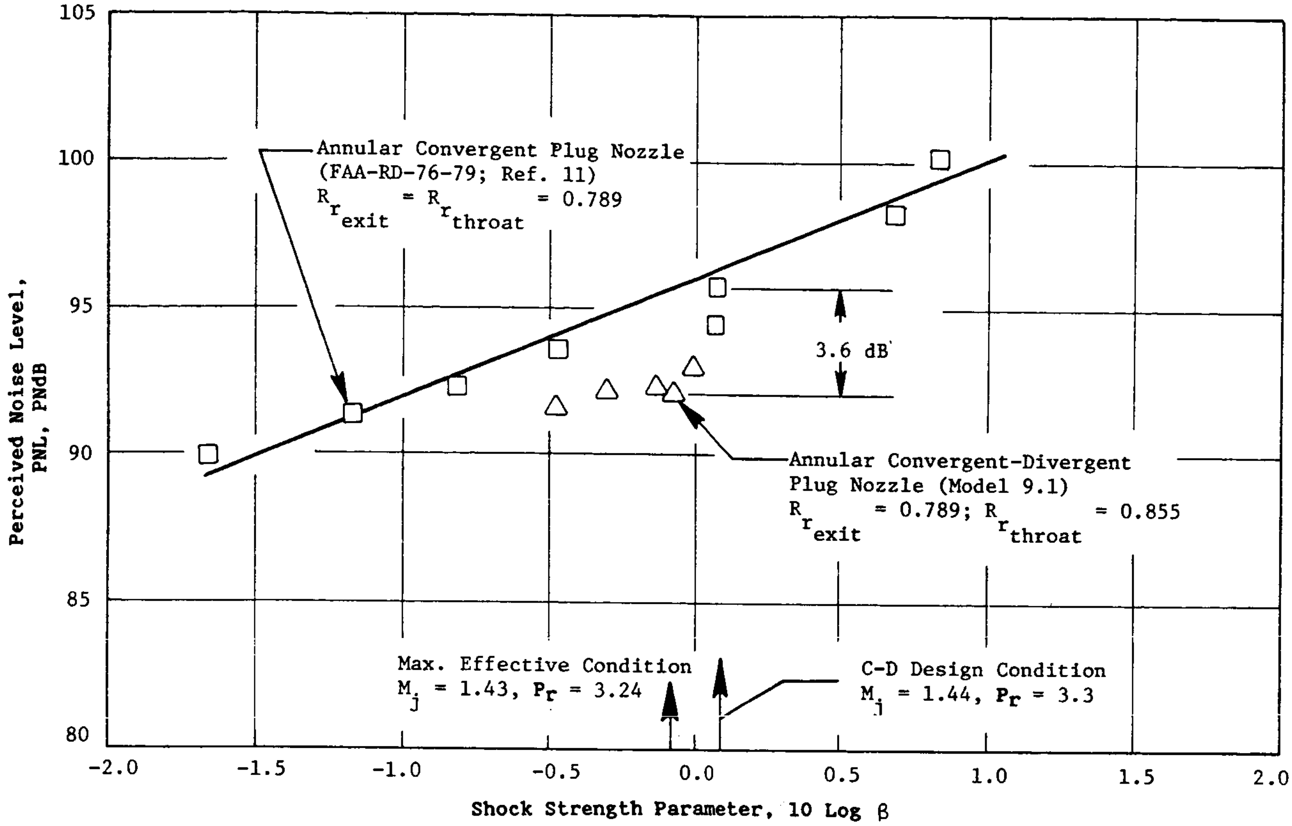

(a) Exit R_r of C-D and Convergent Annular Plug Nozzles = 0.789.

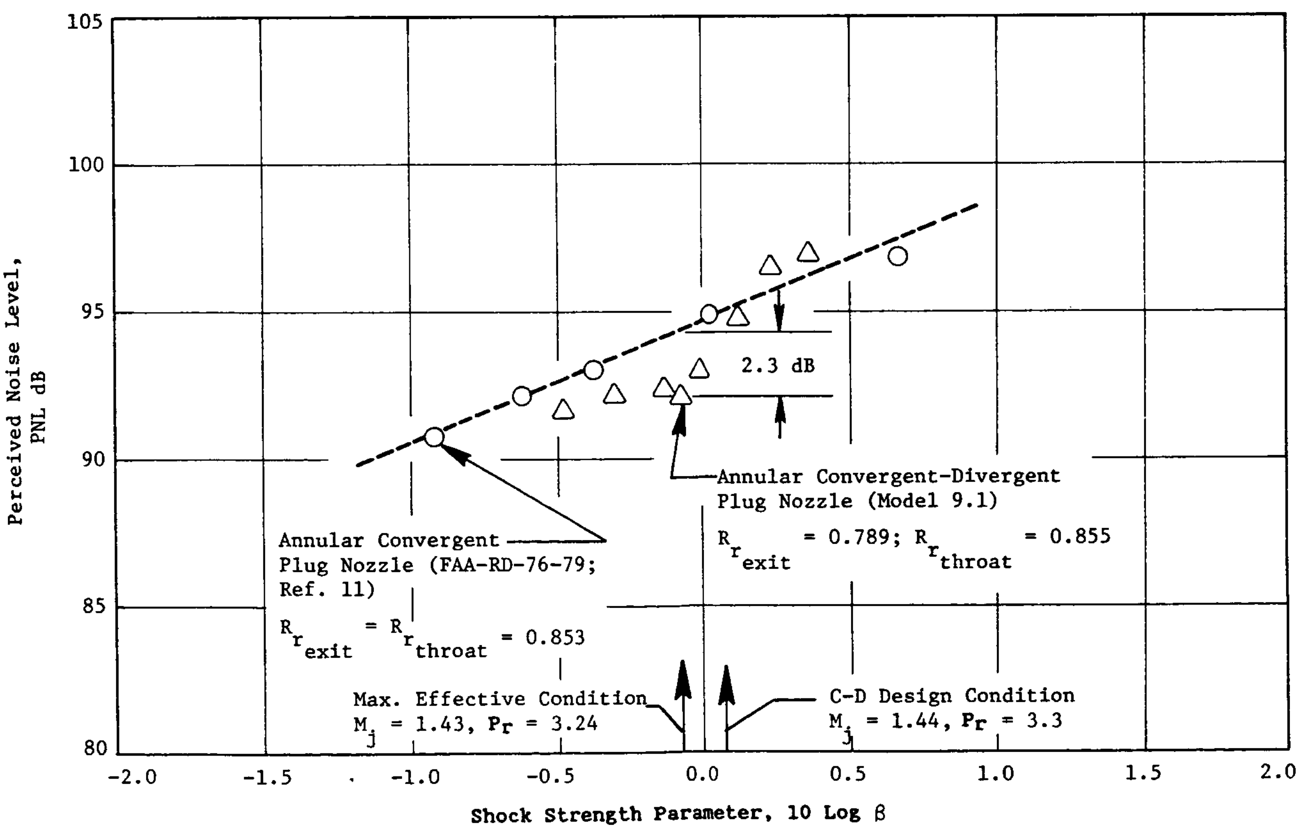

(b) Throat R_r of C-D Annular Plug Nozzle = Exit R_r of Convergent Annular Plug Nozzle = 0.853.

Figure 3-53. Comparison of Convergent-Divergent Annular Plug Nozzle PNL with Available Data of Convergent Annular Plug Nozzles at $\theta_i = 60°$.

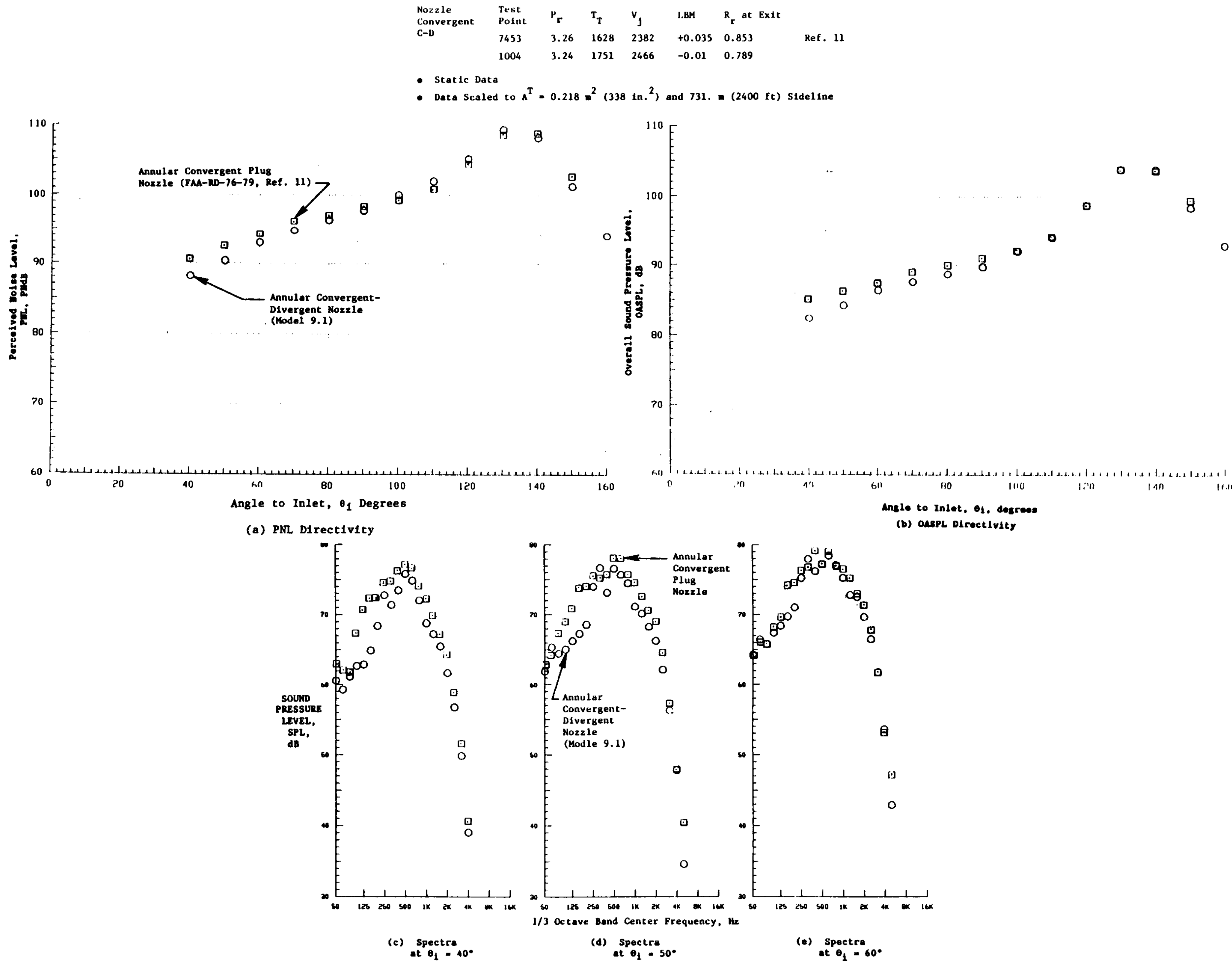

Figure 3-54. Comparison of Forward Quadrant PNL-, OASPL-Directivity, and Typical Spectra of Convergent-Divergent Annular Plug Nozzle at

Static	Flight	Model	Flowpath	P_r^o	T_T^o	V_j^o	P_r^i	T_T^i	V_j^i	P_r^{mix}	T_T^{mix}	V_j^{mix}
△	▲	5	Conv.	3.17	1700	2490	-	-	-	3.17	1700	2410
○	●	8	Outer Conv. & Inner Conv.	3.30	1750	2490	1.45	930	1060	3.01	1680	2340
□	■	9.2	Outer C-D & Inner Conv.	3.25	1760	2480	1.73	900	1250	2.96	1640	2305

• Data Scaled to Product Size: $A^T = 0.903\ m^2$ ($1400\ in.^2$) and 731.5 m (2400 ft) Sideline

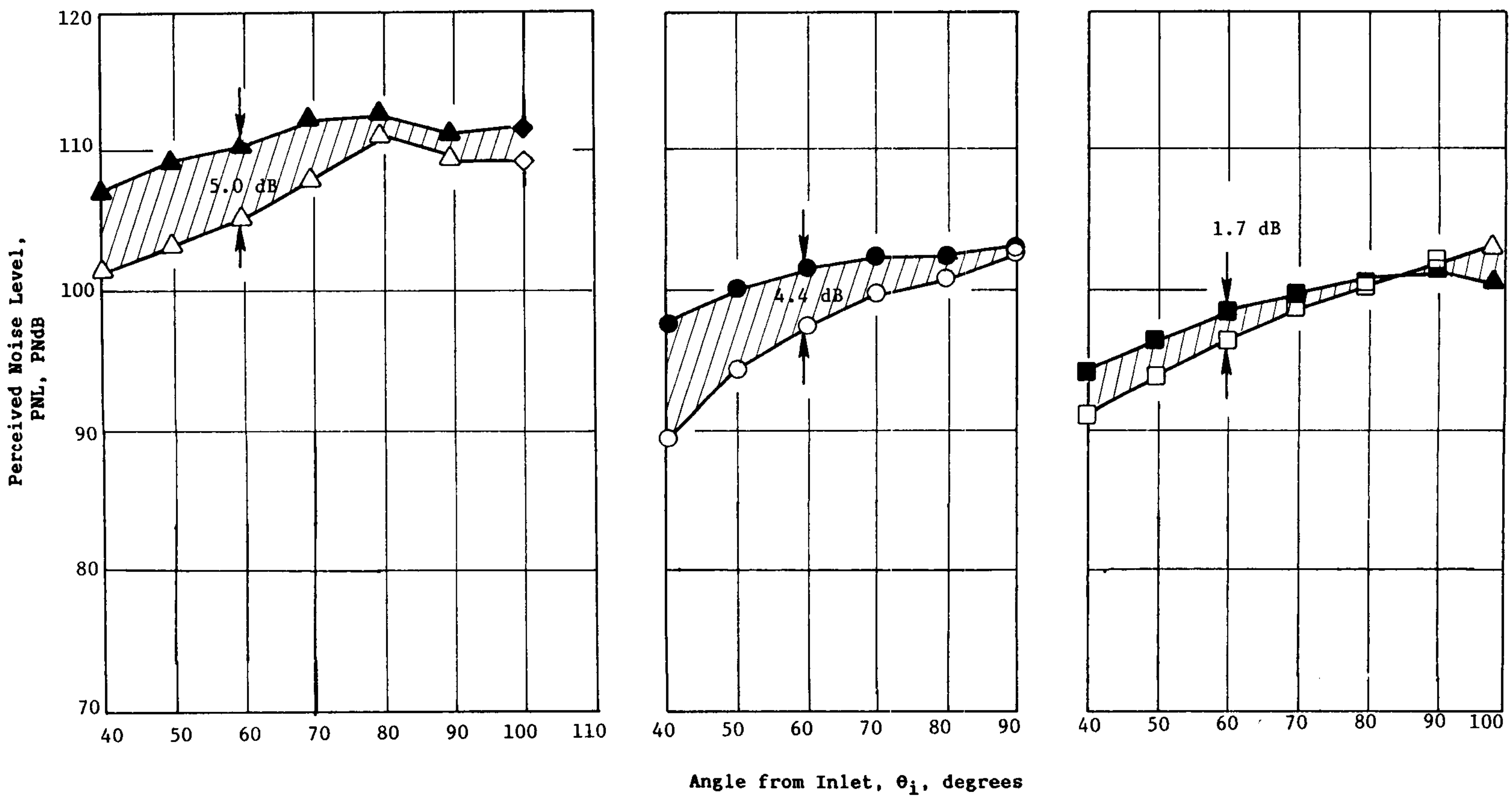

(a) Conical Baseline Nozzle (Model 5)

(b) Similitude Coannular Nozzle with Convergent Flowpaths on Both Outer & Inner Streams (Model 8)

(c) Coannular Nozzle with Convergent-Divergent Flowpath on Outer and Convergent Flowpath on Inner Stream (Model 9.2)

Figure 3-55. Comparison of the Forward Quadrant PNL Flight Amplifiction of Conical Baseline Nozzle, Coannular Plug Nozzle with Convergent Flowpaths, and Coannular Plug Nozzle with Outer C-D and Covergent Inner (Typical AST Takeoff Condition).

condition ($M_j^o \sim 1.43$) of the outer C-D nozzle that was individually determined during the Model 9.1 C-D annular plug nozzle tests. The flow conditions on the convergent inner stream of both the Model 8 and 9.2 nozzles are maintained subsonic. In addition, the aero conditions of the mixed streams of the three configurations correspond to a typical AST/VCE takeoff condition. An examination of this figure indicates that the flight amplification of the front quadrant static data is a minimum for the Model 9.2 data. For example, amplification by 1.7, 4.4 and 5.0 dB due to flight is observed in the static PNL data at $\theta = 60°$ of Model 9.2, Model 8, and conical baseline nozzle, respectively. From this observation, it is qualitatively concluded that, similar to the single flow C-D annular plug nozzle (Model 9.1), the forward quadrant shock noise of the coannular Model 9.2 though not completely eliminated is mitigated to a significant extent.

Spectral comparison between the conical baseline, Models 8 and 9.2 forward quadrant static data at the flow conditions of Figure 3-55 are presented in Figure 3-56. The corresponding data obtained during the simulated flight tests are presented in Figure 3-57. An examination of these figures indicates that the C-D benefit of the outer stream of Model 9.2 over the convergent Model 8 results is not observed strongly in the static spectral data. However, a significant reduction in the broadband shock noise during a simulated flight is indicated with the Model 9.2 data relative to the results of Model 8.

During the initial phase of the analyses of Model 9.2 shock cell noise data, efforts were made to substantiate the earlier determined maximum effective condition of the single stream C-D nozzle but currently having the subsonic inner stream. At first, this was achieved by comparing the Model 9.2 PNL data at $\theta = 60°$ with those of the C-D annular plug nozzle (Model 9.1) using the C-D stream condition (β^o) as the shock correlating parameter. This comparison for both the static and simulated flight tests is presented in Figure 3-58. An examination of this figure indicates that the range of outer stream pressure ratios during which the outer C-D nozzle is effective in mitigating the shock cell noise is more or less independent of the presence or absence of the subsonic inner stream. Hence, the maximum C-D effective condition (i.e., $M_j \sim 1.43$) determined from the Model 9.1 C-D annular nozzle tests can be considered also as the maximum C-D effective condition of the outer stream of the Model 9.2. In addition, the comparison that is presented in Figure 3-58 seems to suggest at the outset that with the C-D outer stream at its maximum effective condition the presence of the subsonic inner stream results in a 2.5 dB reduction in the PNL of the single flow C-D annular plug nozzle at $\theta = 60°$. However, a reexamination of the mixed stream flow variables for a given C-D stream condition indicates that they differ considerably and thereby produce different thrusts. This is made clear by the aerodynamic and performance data that are tabulated on the top of Figure 3-58. Therefore, this suggests that, similar to using a mixed stream velocity V_j^{mix} as the correlating parameter for aft angle coannular jet noise data (Ref. 15), a mixed stream parameter must be employed as the characteristic function to correlate the front quadrant coannular shock noise test results. In this report, the mixed stream parameter β^{eff} defined as

$$\beta^{eff} = \sqrt{\left(M_j^{eff}\right)^2 - 1}$$

Symbol	Model	Flowpath	P_r^o	T_T^o	V_j^o	P_r^i	T_T^o	V_j^i	P_r^{mix}	T_T^{mix}	V_j^{mix}
◇	5	Conv.	3.17	1700	2490	-	-	-	3.17	1700	2410
○	8	Outer Conv. Inner Conv.	3.30	1750	2490	1.45	930	1060	3.01	1680	2340
□	9.2	Outer C.D. & Inner Conv.	3.25	1760	2480	1.73	900	1250	296	1640	2305

- Data Scaled to Produce Size: $A^T = 0.903\ m^2$ (1400 in.^{2}) and 731.5 m (2400 ft) Sideline

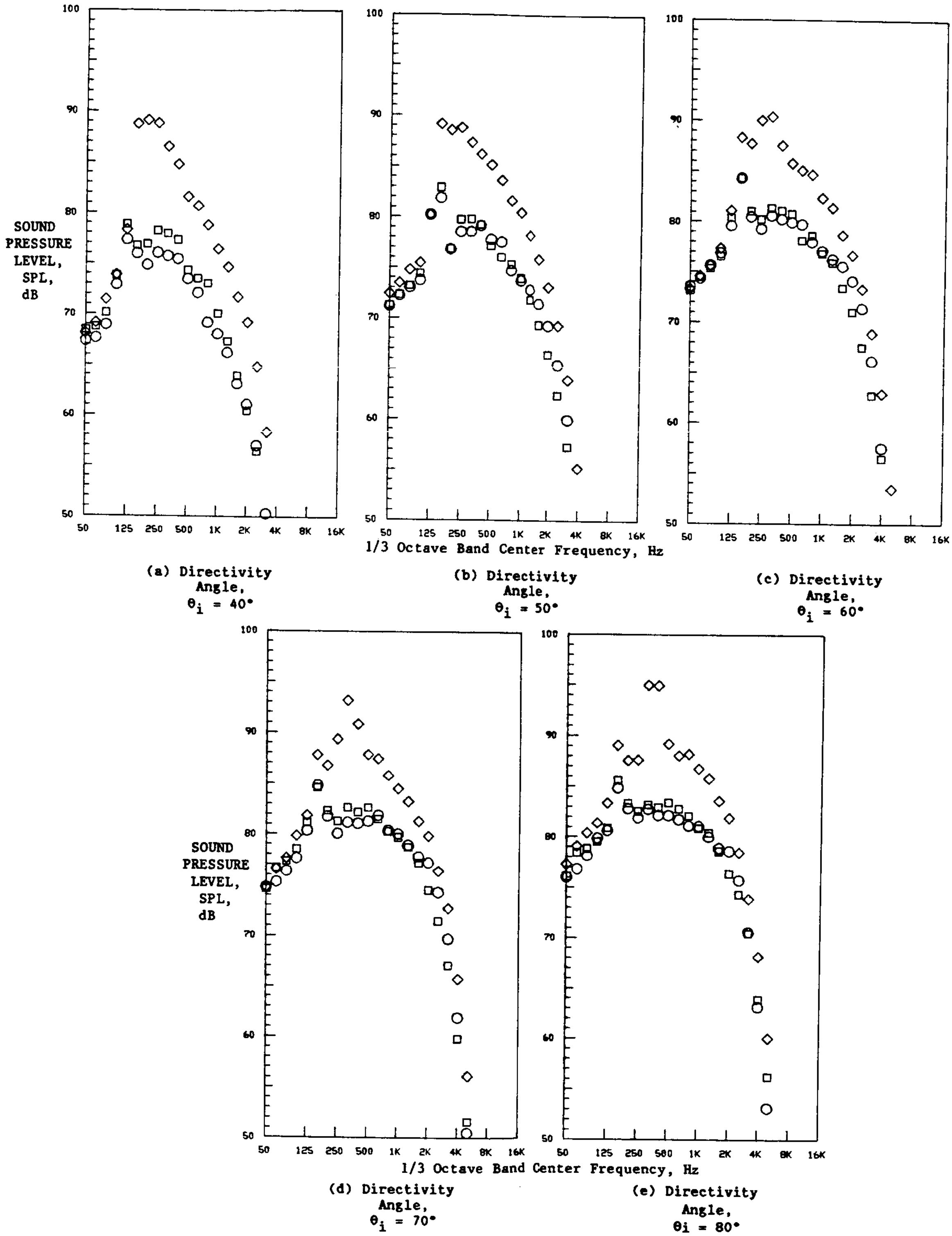

Figure 3-56. Front Quadrant Spectral Comparison Between Conical Baseline Nozzle (Model 5), Coannular Plug Nozzle with Convergent Flowpaths (Model 8), and Coannular Plug Nozzle with Outer Stream C-D and Stream Inner Convergent at Typical AST/VCE Takeoff Condition (Static).

Symbol	Model	Flowpath	P_T^o	T_T^o	V_j^o	P_T^i	T_T^i	V_j^i	P_T^{mix}	T_T^{mix}	V_j^{mix}
◇	5	Conv.	3.17	1700	2490	-	-	-	3.17	1700	2410
○	8	Outer Conv. Inner Conv.	3.30	1750	2490	1.45	930	1060	3.01	1680	2340
□	9.2	Outer C.D. & Inner Conv.	3.25	1760	2480	1.73	900	1250	296	1640	2305

• Data Scaled to Product Size: $A^T = 0.903\ m^2$ (1400 in.^{2}) and 731.5 m (2400 ft) Sideline

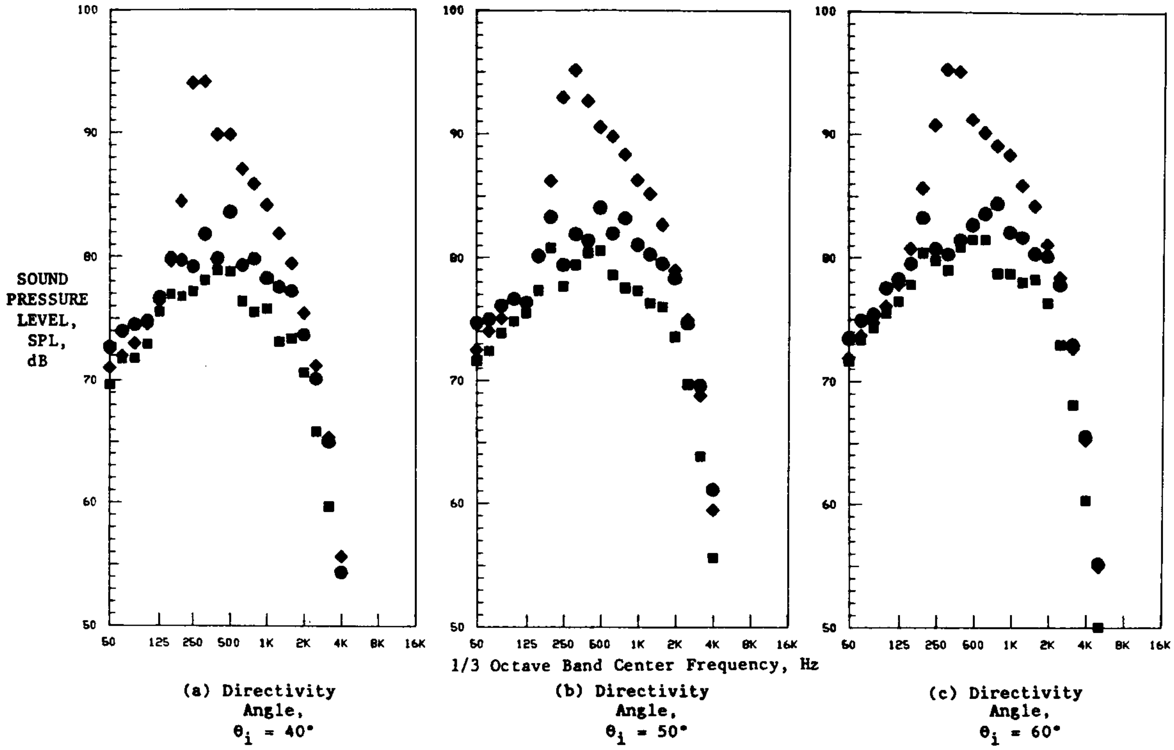

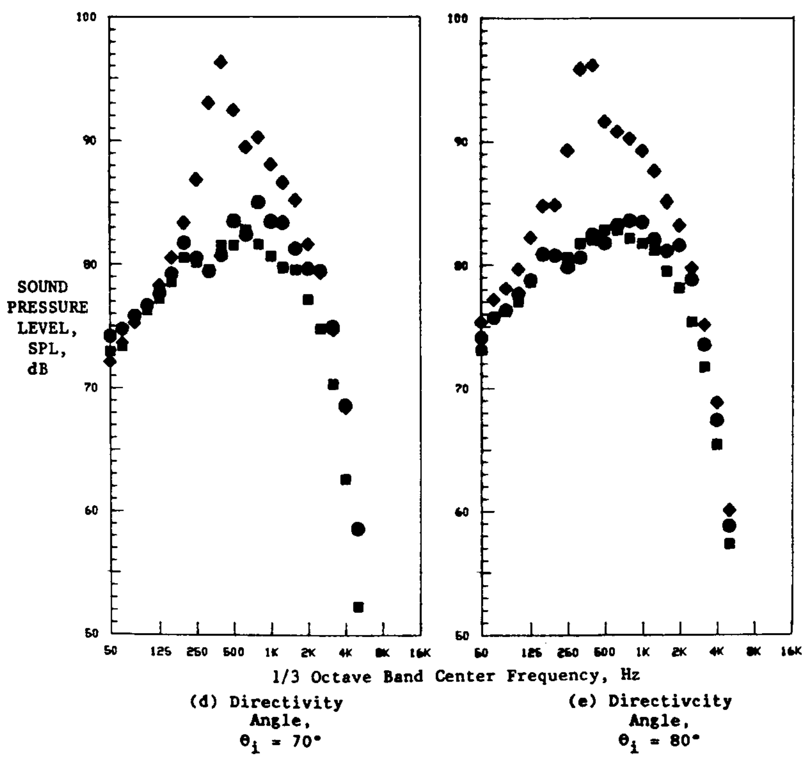

Figure 3-57. Front Quadrant Spectral Comparison Between Conical Baseline Nozzle (Model 5), Coannular Plug Nozzle with Convergent Flowpaths (Model 8), and Coannular Plug Nozzle with Outer Stream C-D and Inner Stream Convergent at Typical AST/VCE Takeoff Condition (Simulated Flight).

	Model	P_r^o	T_T^o	V_j^o	P_r^i	T_T^i	V_j^i	F
Max Effective Condition	9.1	3.24	1750	2470	-	-	-	63400
	9.2	3.25	1760	2480	1.73	900	1250	56400

Data Scaled to Produce Size: $A^T = .903\ m^2\ (2400\ in^2)$ and Extrapolated to 731.5 m (2400 ft.) Sideline.

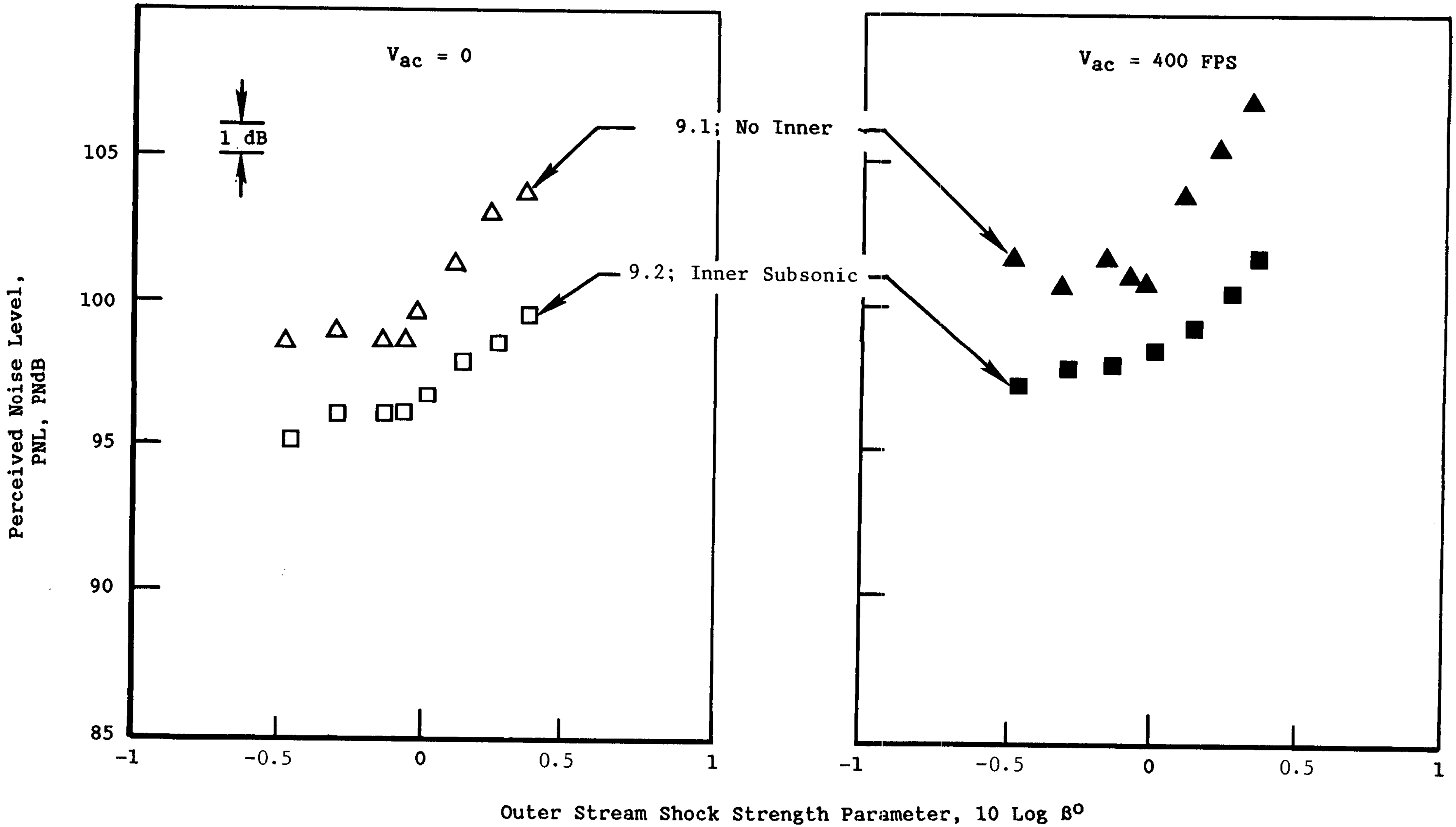

Figure 3-58. Comparison of Coannular Model 9.2 (Outer C-D and Inner Convergent and Subsonic) PNL Data with Those of C-D Annular Plug Nozzle Using an Outer Stream Correlating Parameter (ß°) at θi = 60°.

where

$$\left(M_j^{eff}\right)^2 = \left[\left(P_r^{eff}\right)^{\frac{\gamma-1}{\gamma}} -1\right]\frac{2}{\gamma-1} \quad : \gamma = 1.4$$

is used as the characteristic parameter for correlating coannular nozzle shock noise data. The effective pressure ratio, P_r^{eff}, in the above expression is obtained from the following equation that is derived from momentum considerations:

$$P_r^{eff} = \frac{P_r^o + P_r^i \quad A_r}{1 + A_r}$$

The earlier presented coannular plug nozzle PNL data of Model 9.2 at $\theta = 60°$ have been so correlated and are presented in Figure 3-59 along with the data of C-D annular plug nozzle. An examination of this figure indicates an acceptable correlation between the two sets of data under both static and simulated flight conditions. Henceforth, all the coannular nozzle shock cell noise data are correlated based on the above defined characteristic correlating parameter β^{eff}.

Additional confirmation of the effectiveness of the C-D outer nozzle of coannular nozzle Model 9.2 in mitigating the shock cell noise is provided in Figure 3-60. In this figure, the Model 9.2 PNL data at $\theta_i = 60°$ obtained with the inner stream operating at a subcritical condition ($P_r^i \sim 1.7$) and the C-D outer stream pressure ratio P_r^o varied from 2.9 to 3.5 is compared with similar data for coannular nozzle Model 1A ($A_r = 0.2$ and $R_r^o = 0.853$) of Reference 2. The outer nozzle of Model 1A has been designed for a perfect expansion at $P_r^o \sim 3.2$ by simply extending the outer shroud such that the required area ratio for the expansion of the supersonic stream is reached just downstream of the throat. The convergent inner nozzle similar to that of Model 9.2 was operated also at a subcritical condition ($P_r^i \sim 1.6$). This comparison demonstrates the necessity and the resultant acoustic benefit of a suitable contour on the C-D termination relative to no benefit obtained with the Model 1A nozzle that was designed with no specific contouring procedures.

Typical front quadrant PNL-directivity and spectral data of coannular plug nozzles with outer convergent (Model 8), outer C-D but with no contour (Model 1A), and outer C-D with effective contour (Model 9.2) are presented in Figures 3-61 through 3-62. The inner nozzles of these three configurations were convergent with a subsonic inner stream. The data, particularly the flight results, demonstrate the importance and the necessity of an effective contouring of the C-D termination.

3.1.6.2 Dual Flow Unsuppressed Coannular Plug Nozzle with C-D Flowpaths on Both Outer and Inner Streams

Results, obtained with and without a subsonic inner stream, were presented earlier in Subsections 3.1.5 and 3.1.6.1 to demonstrate the effectiveness of a convergent-divergent outer nozzle in mitigating the shock

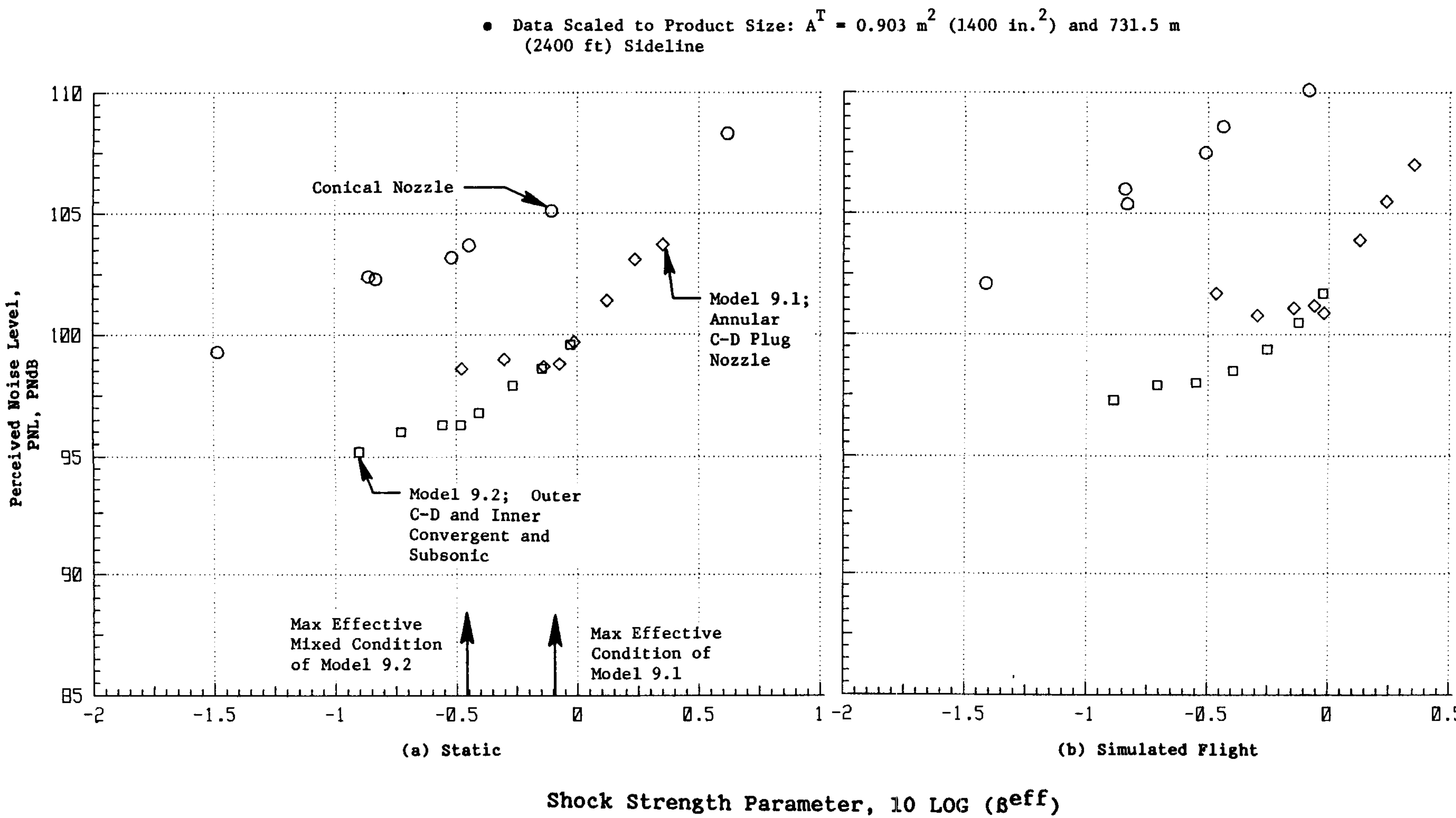

Figure 3-59. Comparison of Coannular Model 9.2 (Outer C-D and Inner Convergent and Subsonic) PNL Data with Those of C-D Annular Plug Nozzle Using a Mixed Stream Correlating Parameter β^{eff} at $\theta_i = 60°$.

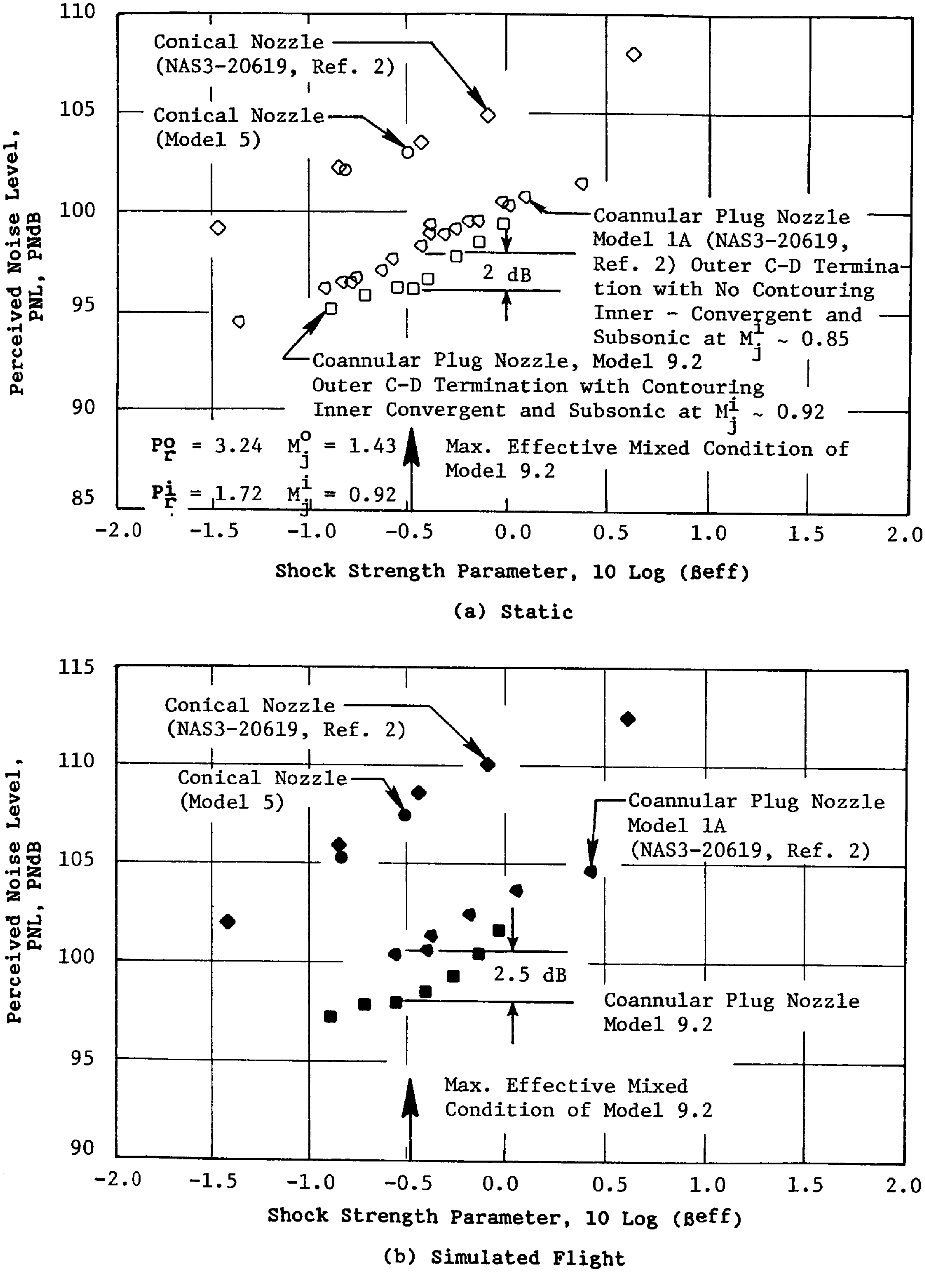

Figure 3-60. Effect of Proper Contouring Procedures on the C-D Termination.

(Aerodynamic Flow Conditions are Presented in Figures 3.62 and 3.63.)

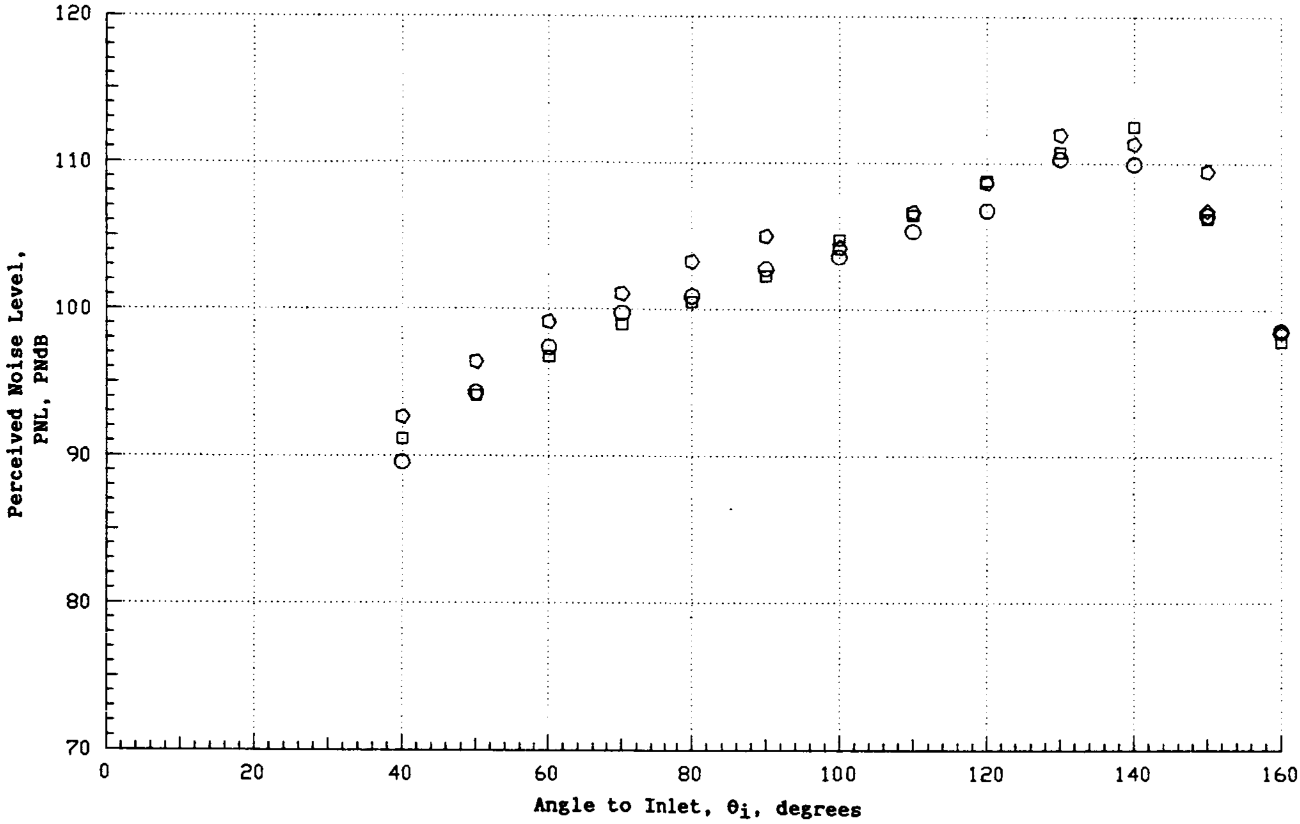

(a) Static

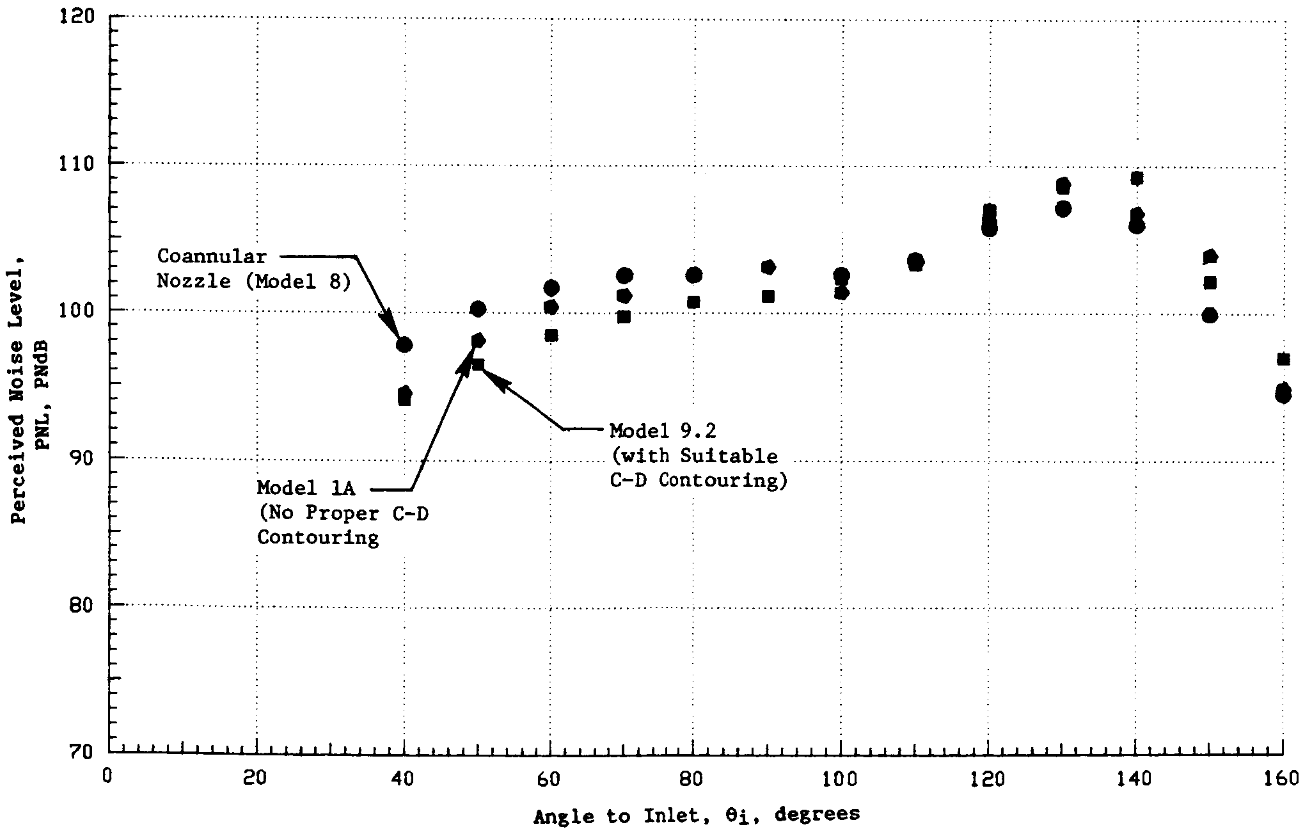

(b) Simulated Flight

Figure 3-61. Comparison of PNL Directivity of Coannular Plug Nozzles to Demonstrate the Acoustic Benefit of a Suitable C-D Contouring Procedure.

SYMBOL	POINT	Model	P_T^o	T_T^o	V_j^o	P_T^i	T_T^i	V_j^i	P_T^{mix}	T_T^{mix}	V^{mix}	NF
○	8211	8	3.3	1757	2487	1.45	931	1062	3.01	1673	2343	-6.7
□	2004	9.2	3.25	1761	1478	1.73	898	1349	2.96	1638	2303	-6.8
◇	121	1A	3.23	1700	2426	1.72	814	1184	2.96	1584	2263	-6.8

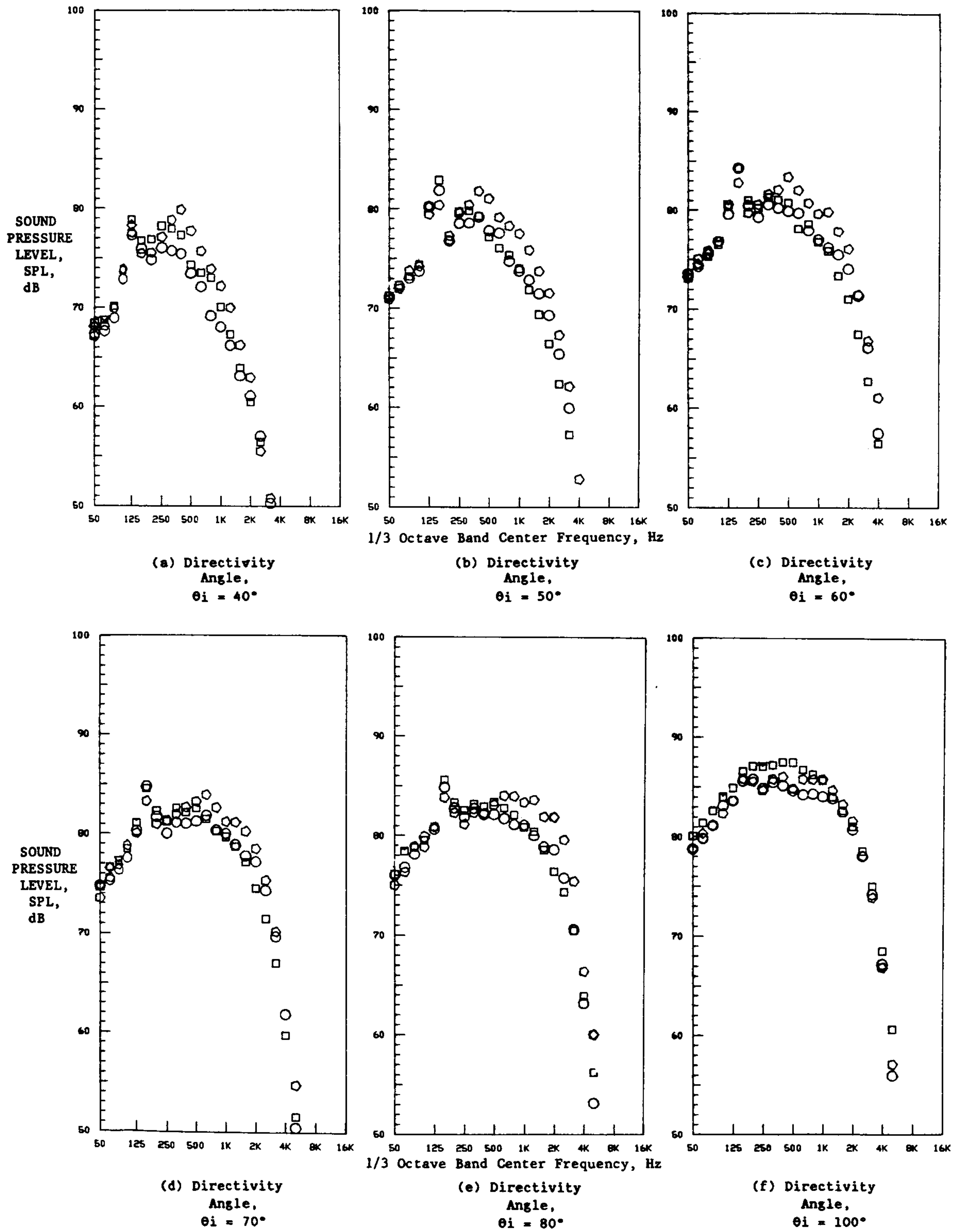

Figure 3-62. Spectral Comparison of Coannular Plug Nozzles to Demonstrate the Acoustic Benefit of a Suitable C-D Contouring Procedure (Static).

SYMBOL	POINT	Model	P_r^o	T_T^o	vo	P_r^i	T_T^i	Vi	P_r^{mix}	T_T^{mix}	Vmix	NF
●	8212	8	3.31	1774	2502	1.45	956	1079	3.02	1692	2360	-6.8
■	2404	9.2	3.26	1756	2476	1.73	906	1256	2.96	1636	2304	-6.9
⬢	122	1A	3.23	1716	2440	1.73	810	1186	2.46	1596	2274	-6.8

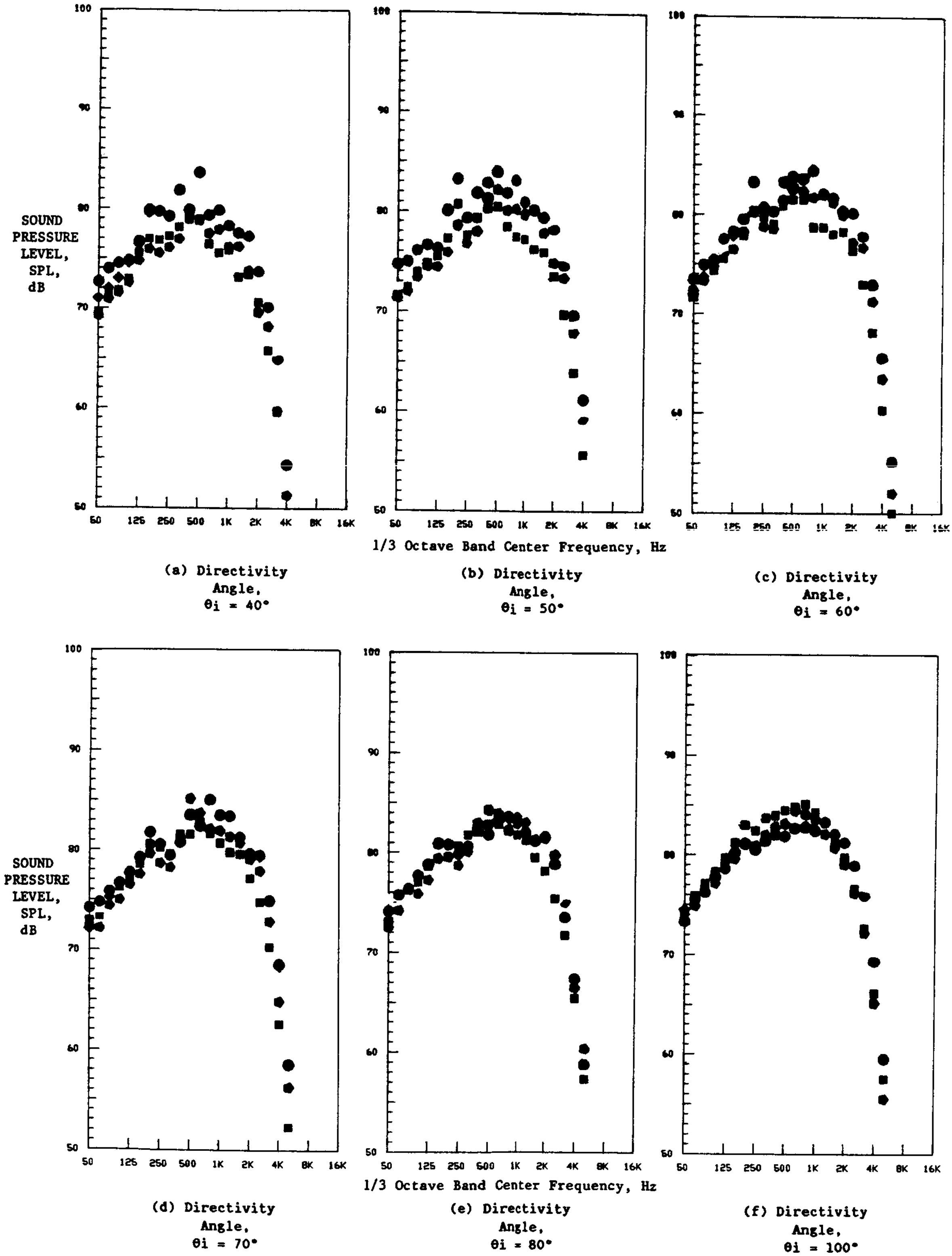

Figure 3-63. Spectral Comparison of Coannular Plug Nozzles to Demonstrate the Acoustic Benefit of a Suitable C-D contouring Procedure (Simulated Flight).

cell noise. The presented data also indicated the procedure employed in selecting the maximum effective condition of the C-D outer nozzle to be $M_J^o \sim 1.43$ ($P_r^o \sim 3.24$) which reasonably agrees with the isentropic shock-free design condition of $M_J^o = 1.44$ ($P_r^o = 3.3$). In this subsection, the acoustic data of an all C-D coannular configuration consisting of the above-mentioned C-D outer nozzle and a C-D inner nozzle designed for a shock-free condition at $M_J^i = 1.38$ ($P_r^i = 3.1$) are presented to demonstrate the total effectiveness of C-D flowpaths on unsuppressed coannular plug nozzles. The data used to determine the inner stream optimum conditions also are presented in this subsection.

Selection of the Optimum C-D Inner Nozzle Condition

In order to verify the shock-free design condition and to determine the region of C-D effectiveness of the convergent-divergent inner nozzle, acoustic data were measured over an inner stream pressure ratio range of 2.5 to 3.6 with an outer nozzle that is

1. Convergent and operated subsonic at $M_J^o \sim 0.91$ ($P_r^o \sim 1.71$) with $T_T^o = 1{,}200°$ R (Model 9.3)

2. C-D and operated at the optimum supersonic condition of $M_J^o \sim 1.43$ ($P_r^o \sim 3.24$) with $T_T^o = 1750°$ R (Model 9.4).

Typical forward quadrant PNL data, as a function of P_r^i, measured during these tests are summarized in Figure 3-64. An examination of this figure indicates that the tested C-D inner nozzle is most effective in mitigating the shock cell noise at (1) $P_r^i \sim 3.25$ when the outer stream is subsonic and (2) $P_r^i \sim 3.0$ where the outer stream is supersonic and fully expanded (at $M_J^o \sim 1.43$). In addition, the effectiveness of the C-D inner stream which is comparatively small in magnitude is observed over a wider range of its operating pressure ratios for the case of the full expanded outer stream when compared to the case of the subsonic outer stream.

C-D Coannular Nozzle Data

The C-D coannular nozzle (Model 9.4: $A_r = 0.212$, R_r^o at exit = 0.789, R_r^o at throat = 0.855, R_r^i at exit = 0.908) is described in detail in Section 2.4.3. To demonstrate the effectiveness of this C-D contour in the control of shock noise, static and limited free-jet acoustic tests were conducted over an operating pressure ratio range of 2.8 to 3.6 on both the inner and outer streams. This pressure ratio range includes the optimum conditions of the outer and inner C-D nozzles that were determined, as described in earlier sections, as equal to 3.24 ($M_J^o = 1.43$) and 3.0 ($M_J^i = 1.36$), respectively. The PNL data at 60° obtained from these tests are summarized in Figure 3-65 as a function of the mixed stream shock noise correlating parameters β^{eff}. The data are compared in these figures with the conical baseline nozzle data. This comparison indicates that, during static acoustic tests, the C-D coannular plug nozzle at its maximum effective operating condition resulted in 5.8 dB reduction in PNL from that of an equivalent conical baseline nozzle. The corresponding outer and inner nozzle operating pressure ratios are 3.24 and 3.0, respectively, which coincide with the optimum conditions determined from the earlier described tests. However, the region of C-D effectiveness is smaller compared to that of the C-D annular nozzle (Model 9.1).

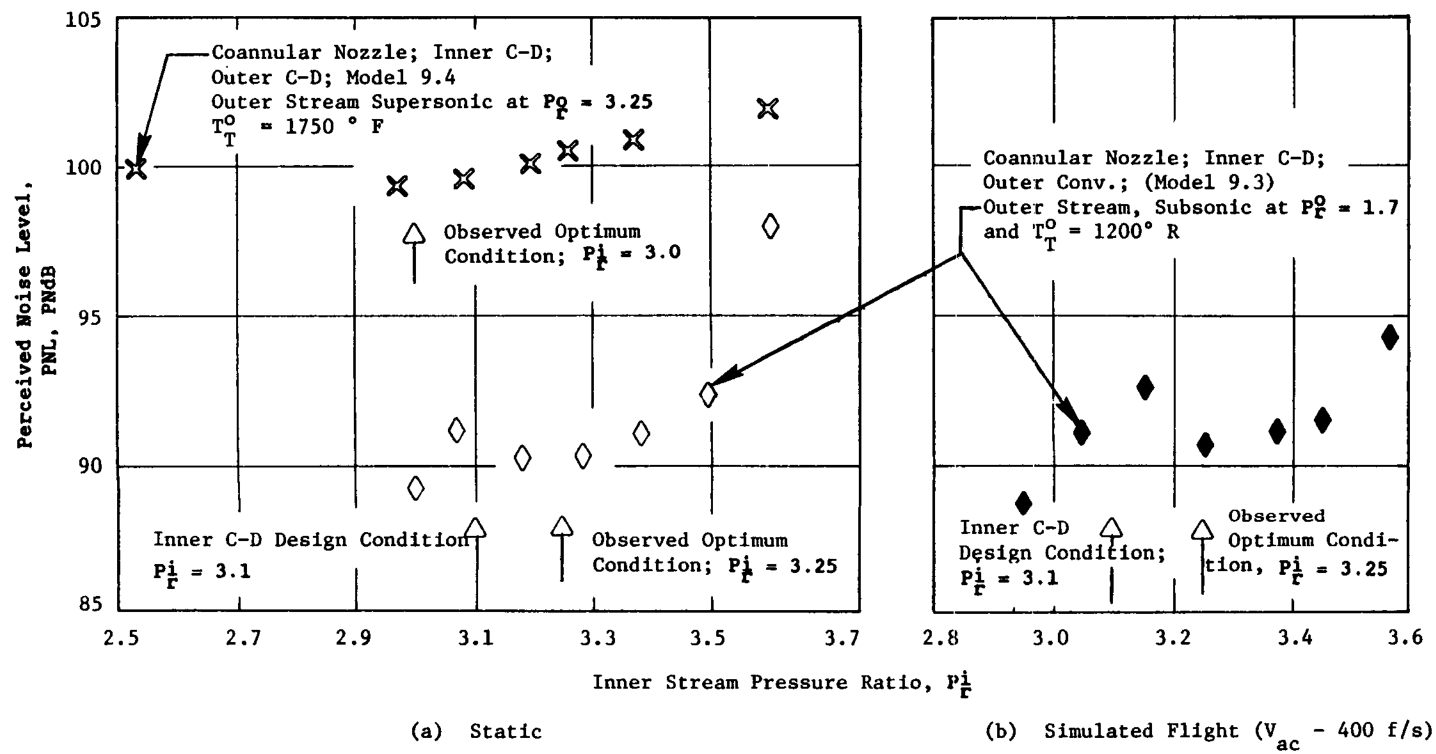

Figure 3-64. Variation of Observed C-D Inner Stream Optimum Condition with Subsonic and Supersonic Outer Streams at $\theta_i = 60°$.

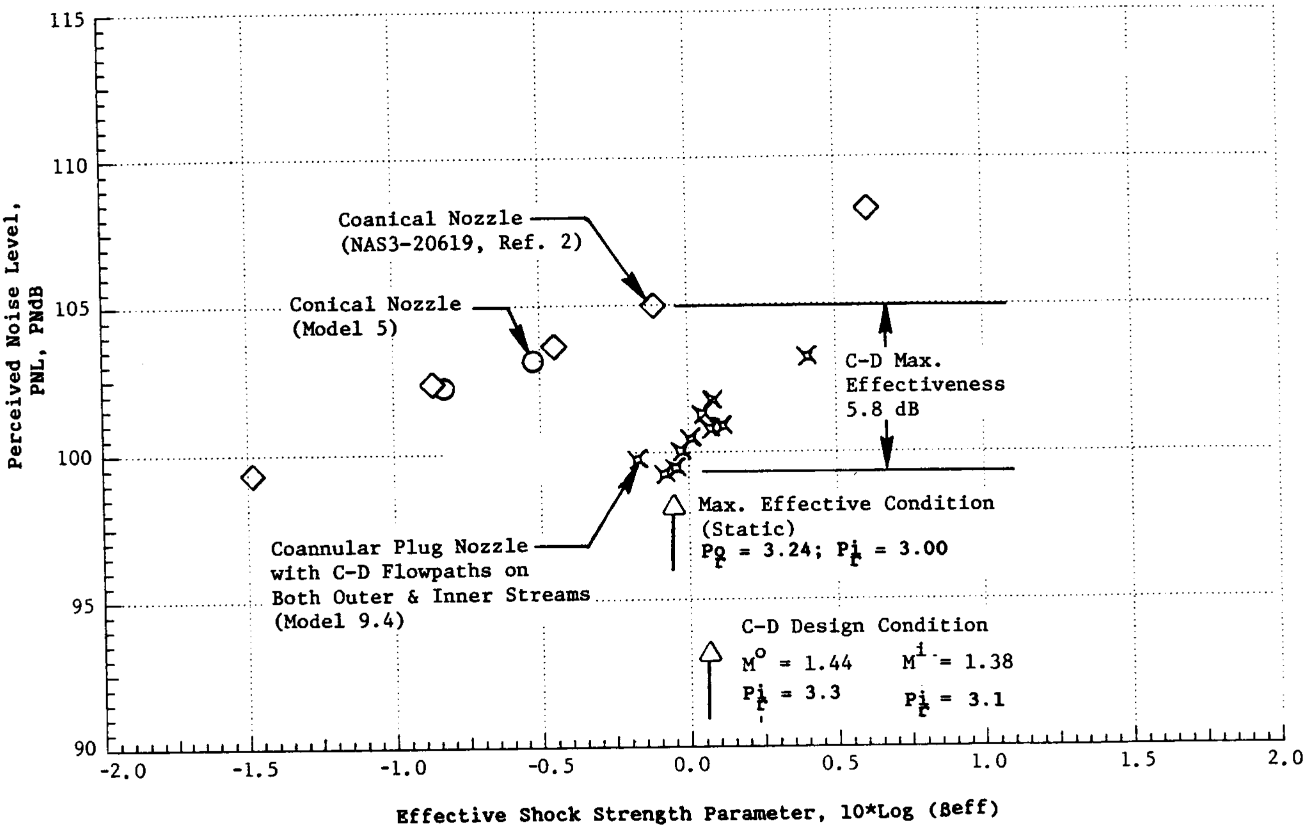

(a) Static

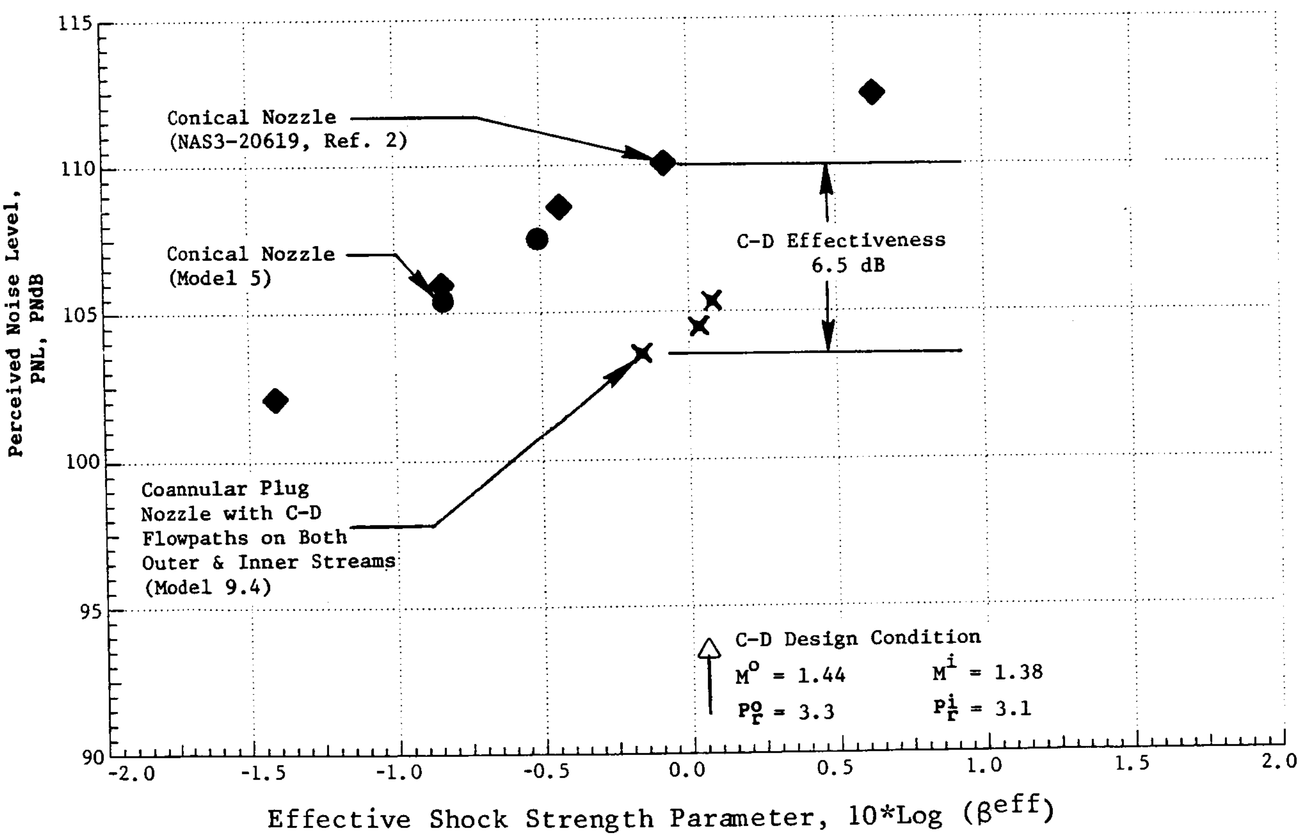

(b) Simulated Flight (V_{ac} = 122 m/sec or 400 f/s)

Figure 3-65. C-D Effectiveness in Shock Noise Reduction for a Coannular Plug Nozzle with C-D Terminations on Both Inner and Outer Nozzles.

Static front quadrant PNL-, OASPL-directivity, and spectral data of the C-D coannular nozzle at its maximum effective operating condition is presented in Figures 3-66 and 3-67. The data are compared in these figures with those of the conical baseline nozzle (Model 5) and the similitude coannular nozzle configuration (Model 8: $A_r = 0.194$, $R_r^o = 0.846$, $R_r^i = 0.933$) having convergent flowpaths at reasonably matched aerodynamic flow conditions. The comparison of the convergent coannular nozzle directivity data with those of the C-D coannular nozzle results indicate, in general, a C-D benefit at all angles in the front quadrant. At $\theta_i = 60°$, for example, the reduction in PNL relative to the convergent coannular nozzle is 2.3 dB. It is to be noted that this reduction is the same as what was observed, under similar flow conditions, between the convergent annular and C-D annular plug nozzles having exit radius ratios of 0.853 and 0.789, respectively. The outer stream exit radius ratios of the Model 8 and Model 9.4 nozzles are 0.846 and 0.789, respectively. The spectral comparison of Figure 3-67 indicates that in the front quadrant and at frequencies greater than 250 Hz the C-D nozzle SPL's are less than those of the similitude convergent coannular nozzle (Model 8). Simulated flight test data corresponding to the static conditions of Figure 3-66 and 3-67 are presented in Figure 3-68. While a benefit with the C-D nozzle relative to convergent coannular nozzle is indicated, the magnitude of the benefit is observed to be less in flight when compared to what was observed under static conditions. Typical SPL benefits observed at the 1/3-octave band center frequency of 1,000 Hz and in the front quadrant are indicated in Figures 3-67 and 3-68.

Additional comparisons of the static and simulated flight C-D coannular nozzle data (Model 9.4) at flow conditions that are in the region of C-D effectiveness with those of a second convergent coannular plug nozzle are provided in Figures 3-69 and 3-70. The data of the later nozzle correspond to those of Model 3 ($A_r = 0.194$, $R_r^o = 0.853$, $R_r^i = 0.933$) of Reference 2. The observations made based upon the data of Figures 3-67 and 3-68 correspond, in general, also to the data presented in Figures 3-69 and 3-70.

<u>Off-Design Comparison of the C-D Coannular Plug Nozzle Data</u>

Comparison of the static and simulated flight PNL data of the C-D coannular plug nozzle (Model 9.4) at $\theta_i = 60°$ with available convergent coannular plug nozzle (Model 8) test results over a range of operating conditions is provided in Figure 3-71. The Model 8 data shown in this figure correspond to supersonic operating conditions on both the inner and outer streams. A reduction in the forward quadrant noise data with the C-D nozzle is noted, under both static and flight conditions, over a region of off-design conditions. Because of the completeness of the static data, the off-design region is clearly indicated in Figure 3-71(a).

For comparative purposes, the PNL_{60} data of conical, C-D annular plug (Model 9.1), and coannular plug (Model 9.2: C-D outer nozzle, convergent and subsonic inner nozzle) nozzles are repeated in Figure 3-71.

3.1.6.3 Additional Significant Observations with C-D Annular and Coannular Plug Nozzles

Acoustic data measured in the front quadrant were presented in Subsections 3.1.6.1 and 3.1.6.2 to demonstrate the region of C-D effectiveness

Symbol	Point	P_r^o	T_T^o (° R)	V_j^o (f/s)	P_r^i	T_T^i (° R)	V_j^i (f/s)	P_r^{mix}	T_T^{mix} (° R)	V_j^{mix} (f/s)
◇	513	3.17	1701	2411	-	-	-	3.17	1701	2411
○	8001	3.18	1736	2438	3.12	833	1667	3.10	1539	2270
★	4001	3.24	1747	2464	3.00	876	1678	3.12	1552	2287

Data Scaled to Product Size: $A^T = 0.903\ m^2$ (1400 in.^{2}) and 731.5 m (2400 ft) Sideline

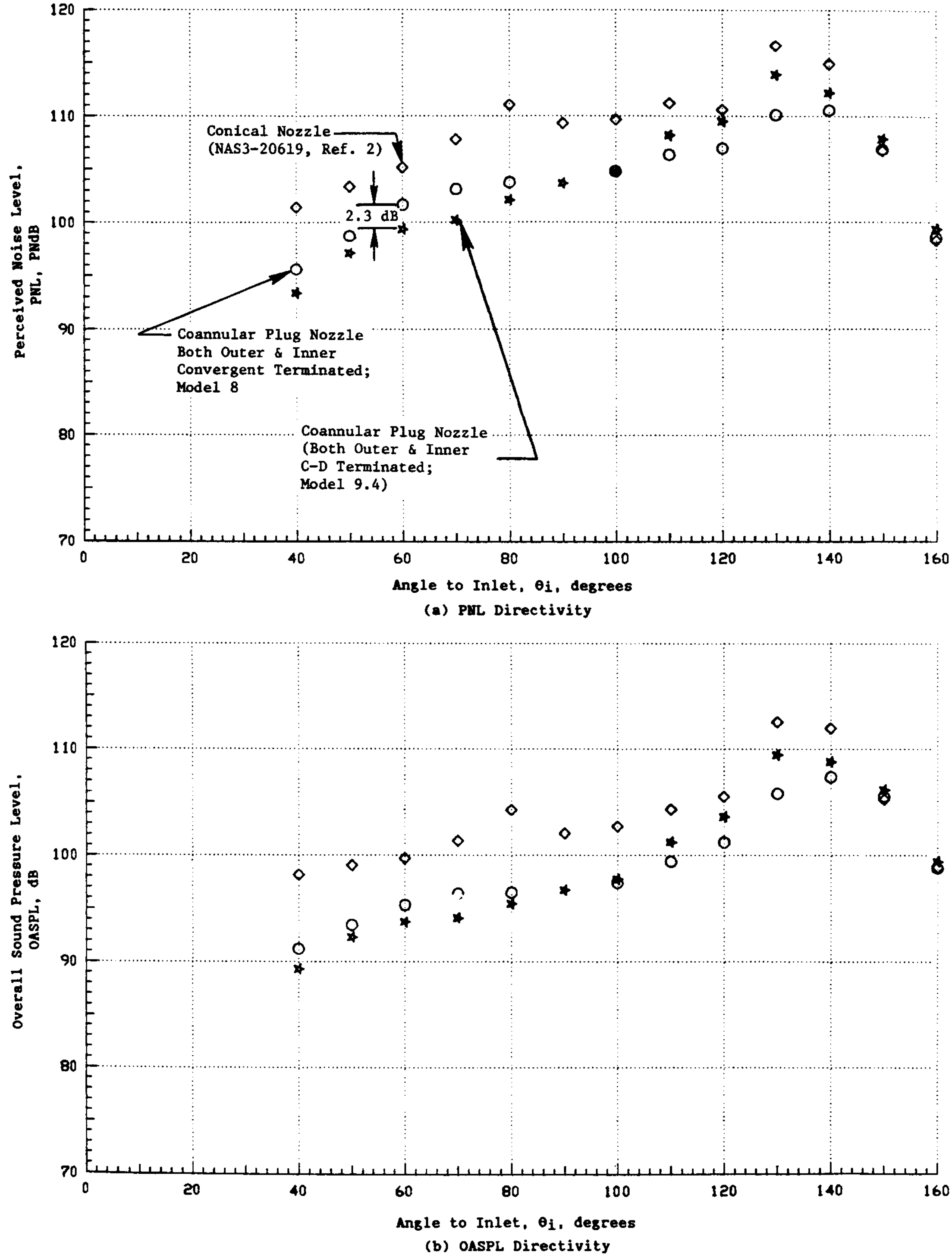

Figure 3-66. Comparison of Forward Quadrant Static PNL and OASPL Directivity Between Conical (Model 5), Convergent Terminated Coannular Plug Nozzle (Model 8), and C-D Terminated Coannular Plug Nozzle (Model 9.4).

(See Figure 3-66 for Aerodynamic Conditions)

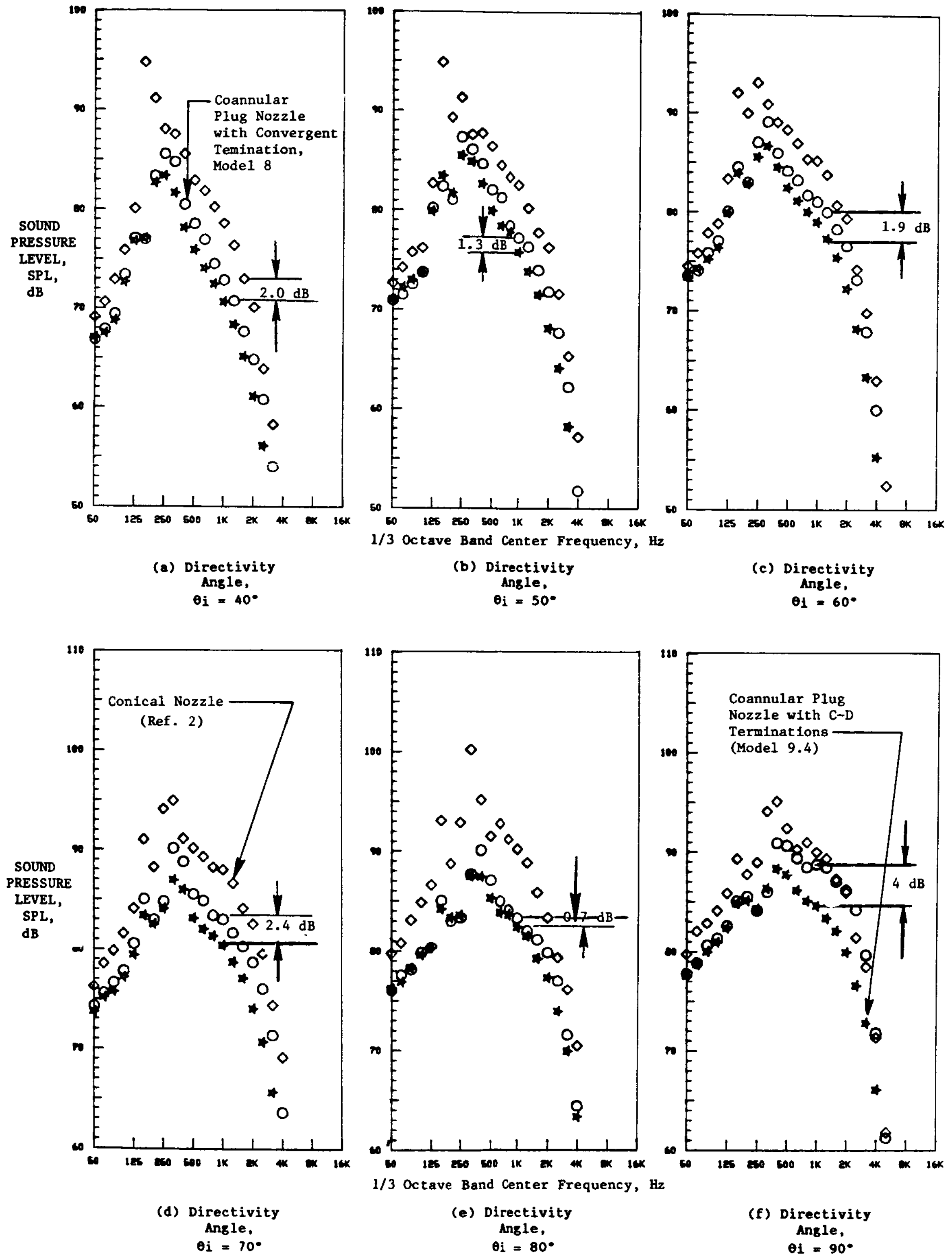

Figure 3-67. Comparison of Typical Forward Quadrant Static Spectra Between Conical (Model 5), Convergent Terminated Coannular Plug Nozzle (Model 8), and C-D Terminated Coannular Plug Nozzle (Model 9.4).

Symbol	Point	P_T^o	T_T^o (° R)	V_j^o (f/s)	P_T^i	T_T^i (° R)	V_j^i (f/s)	P_T^{mix}	T_T^{mix} (° R)	V_j^{mix} (f/s)
◆	515	3.19	1709	2422	-	-	-	349	1709	2422
●	8002	3.20	1734	2444	3.10	837	1666	3.11	1541	2276
★	4404	3.25	1750	2470	3.27	877	1740	3.18	1540	2294

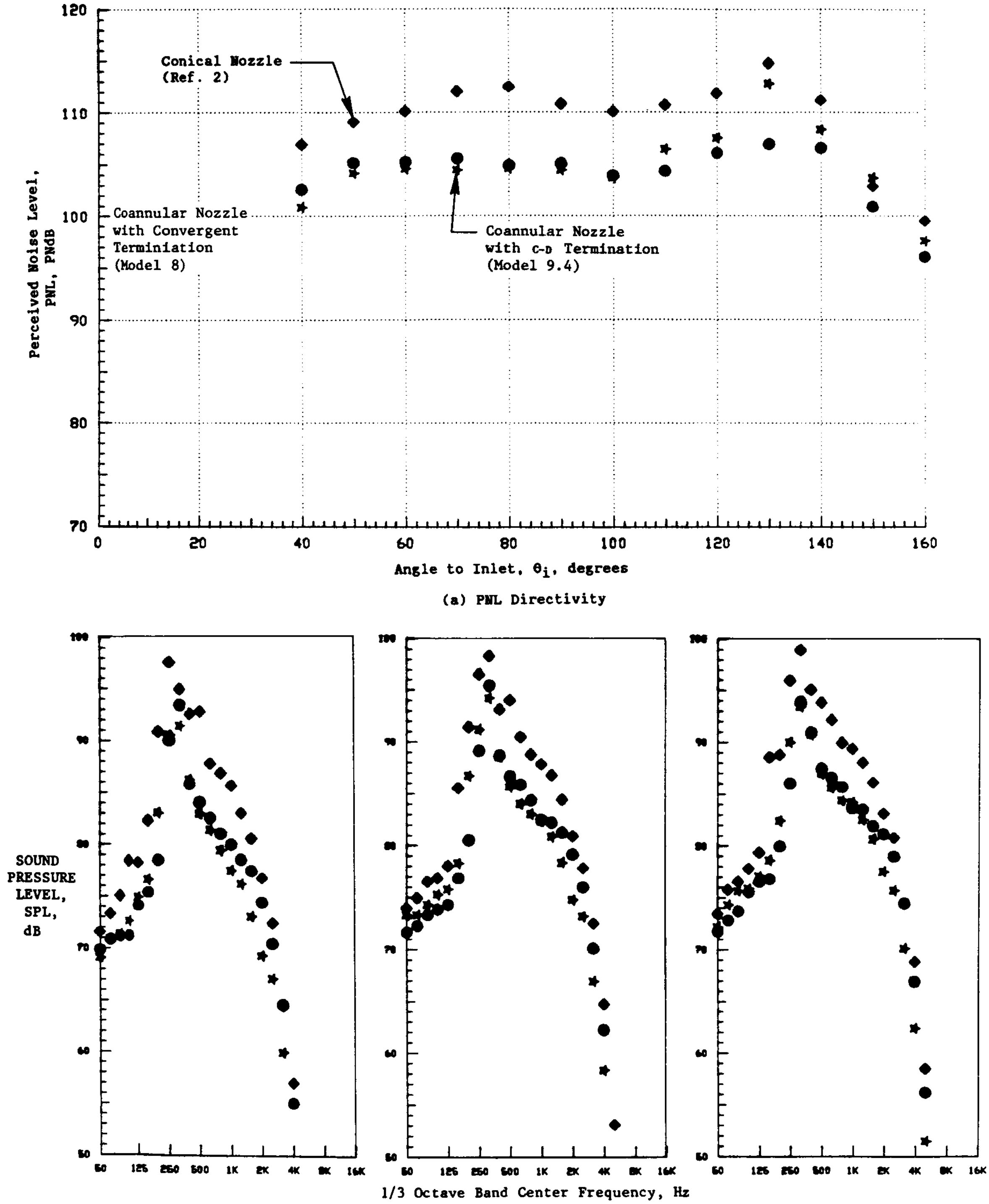

(a) PNL Directivity

(b) Spectra at $\theta i = 40°$

(c) Spectra at $\theta i = 50°$

(d) Spectra at $\theta i = 60°$

Figure 3-68. Comparison of Forward Quadrant Simulated Flight PNL-Directivity and Typical Spectra Between Conical (Model 5), Convergent Terminated Coannular Plug Nozzle (Model 8), and C-D Terminated Coannular Nozzle (Model 9.4).

SYMBOL	POINT	P_r^o	T_T^o(°R)	V_j^o(fps)	P_r^i	T_T^i(°R)	V_j^i(fps)	P_r^{mix}	T_T^{mix}(°R)	V_j^{mix}(fps)
◇	513	3.17	1736	2438	-	-	-	3.17	1736	2438
✱	4003	3.25	1755	2472	3.17	876	1718	3.16	1548	2294
△	301	3.18	1719	2427	3.21	784	1634	3.10	1507	2247

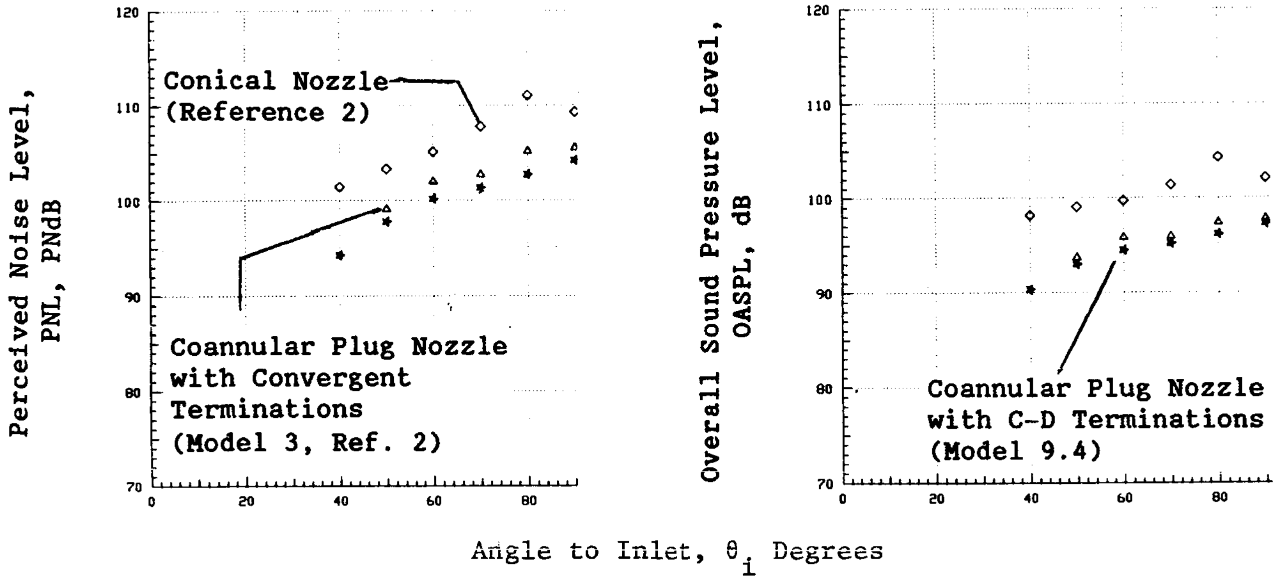

(a) PNL Directivity

(b) OASPL Directivity

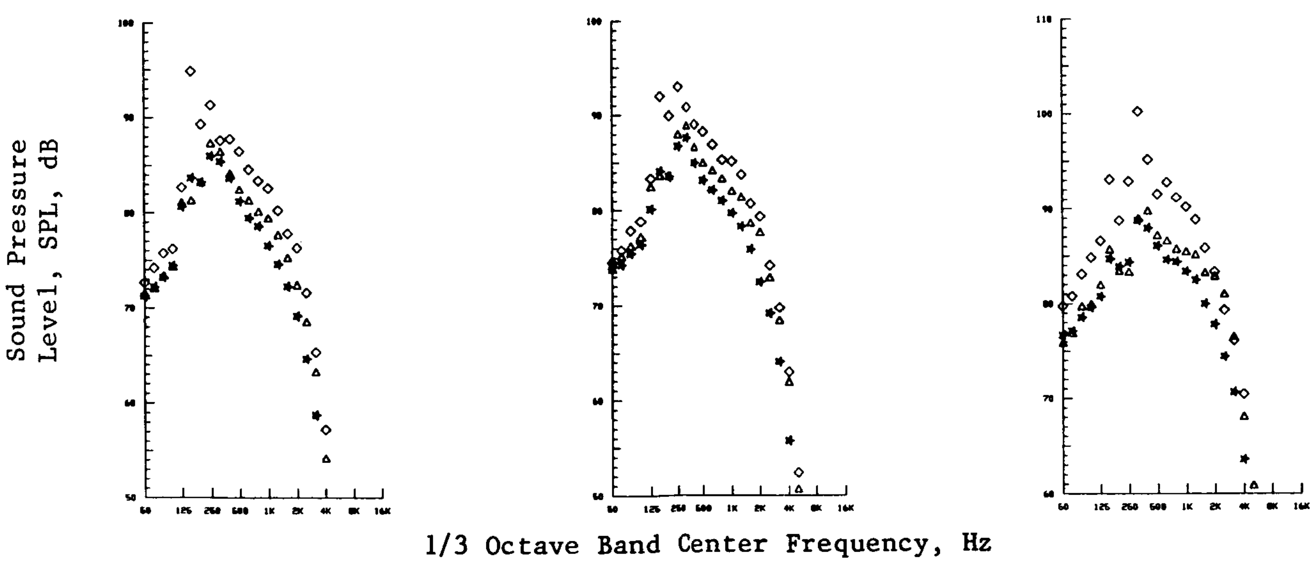

(c) Spectra at $\theta_i = 50°$

(d) Spectra at $\theta_i = 60°$

(e) Spectra at $\theta_i = 80°$

Figure 3-69. Additional Confirmation of the Effectiveness of C-D Terminated Coannular Plug Nozzle in Mitigating the Forward Quadrant Shock Noise (Static).

SYMBOL	POINT	P_r^o	T_T^o(°R)	V_j^o(fps)	P_r^i	T_T^i(°R)	V_j^i(fps)	P_r^{mix}	T_T^{mix}(°R)	V_j^{mix}(fps)
◆	515	3.19	1709	2422	-	-	-	3.19	1709	2422
▲	303	3.21	1724	2438	3.21	786	1636	3.12	1512	2257
✱	4044	3.25	1750	2470	3.27	877	1740	3.18	1540	2294

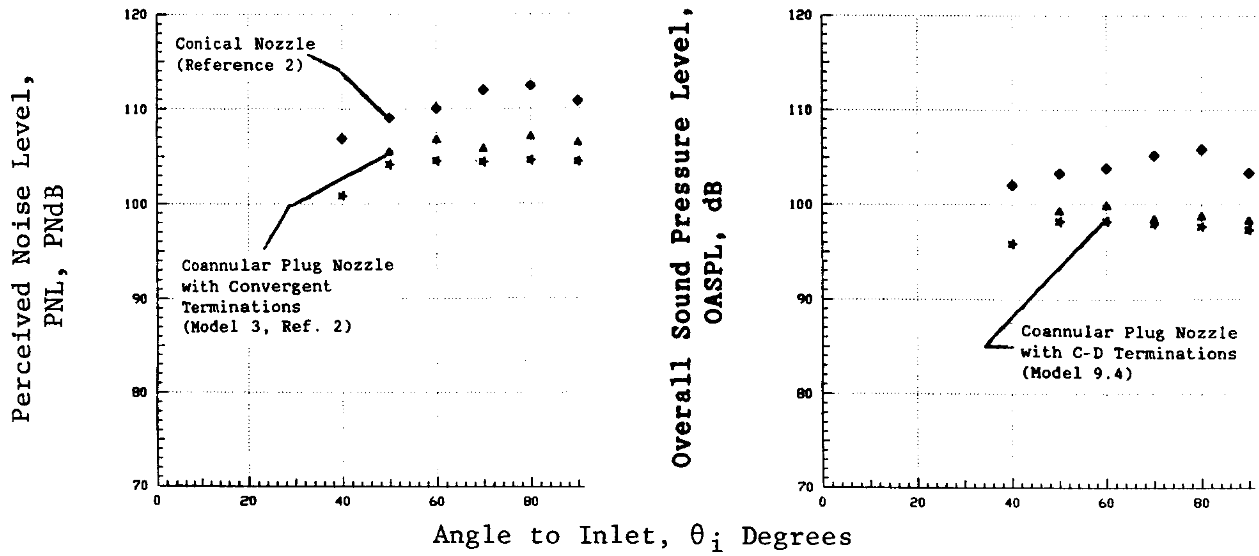

(a) PNL Directivity

(b) OASPL Directivity

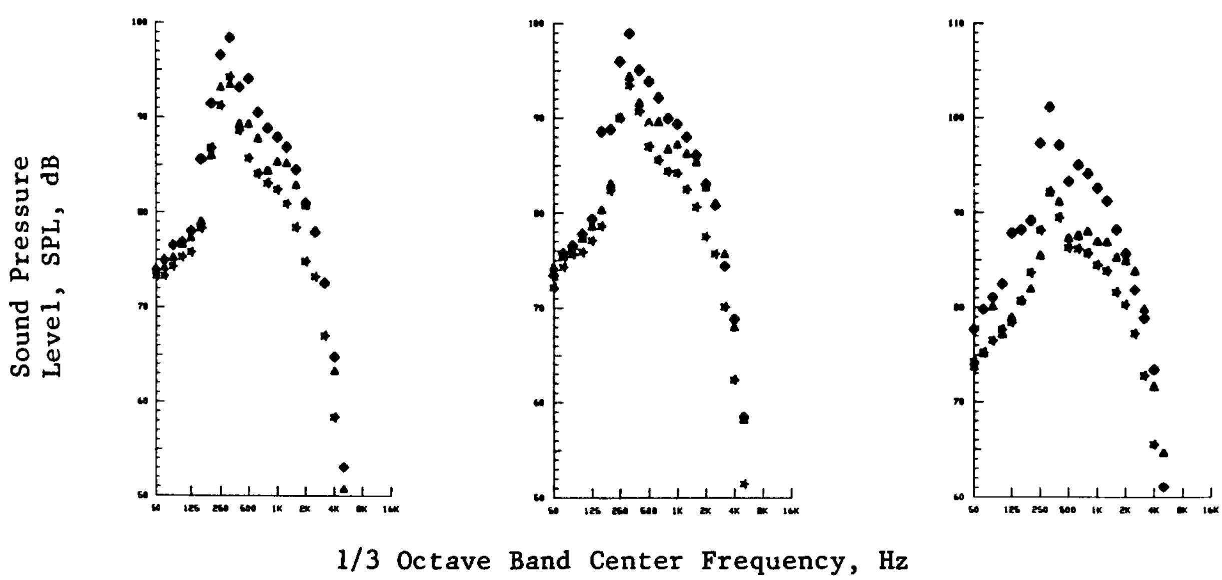

(c) Spectra at $\theta_i = 50°$

(d) Spectra at $\theta_i = 60°$

(e) Spectra at $\theta_i = 80°$

Figure 3-70. Additional Confirmation of the Effectiveness of C-D Terminated Coannular Plug Nozzle in Mitigating the Forward Quadrant Shock Noise (Simulated Flight).

Data Scaled to Produce Size: A^T = .903 sq. m (1400 sq. in.) and 731.5 m (2400 ft) sideline

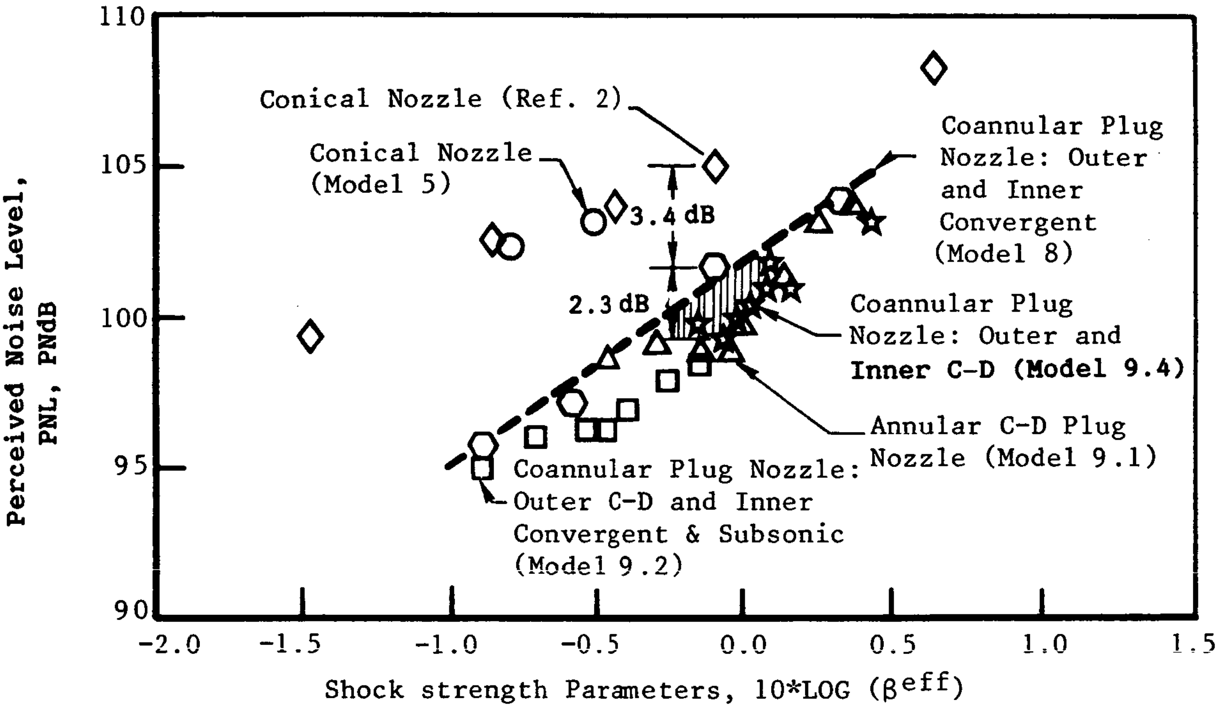

a) Static

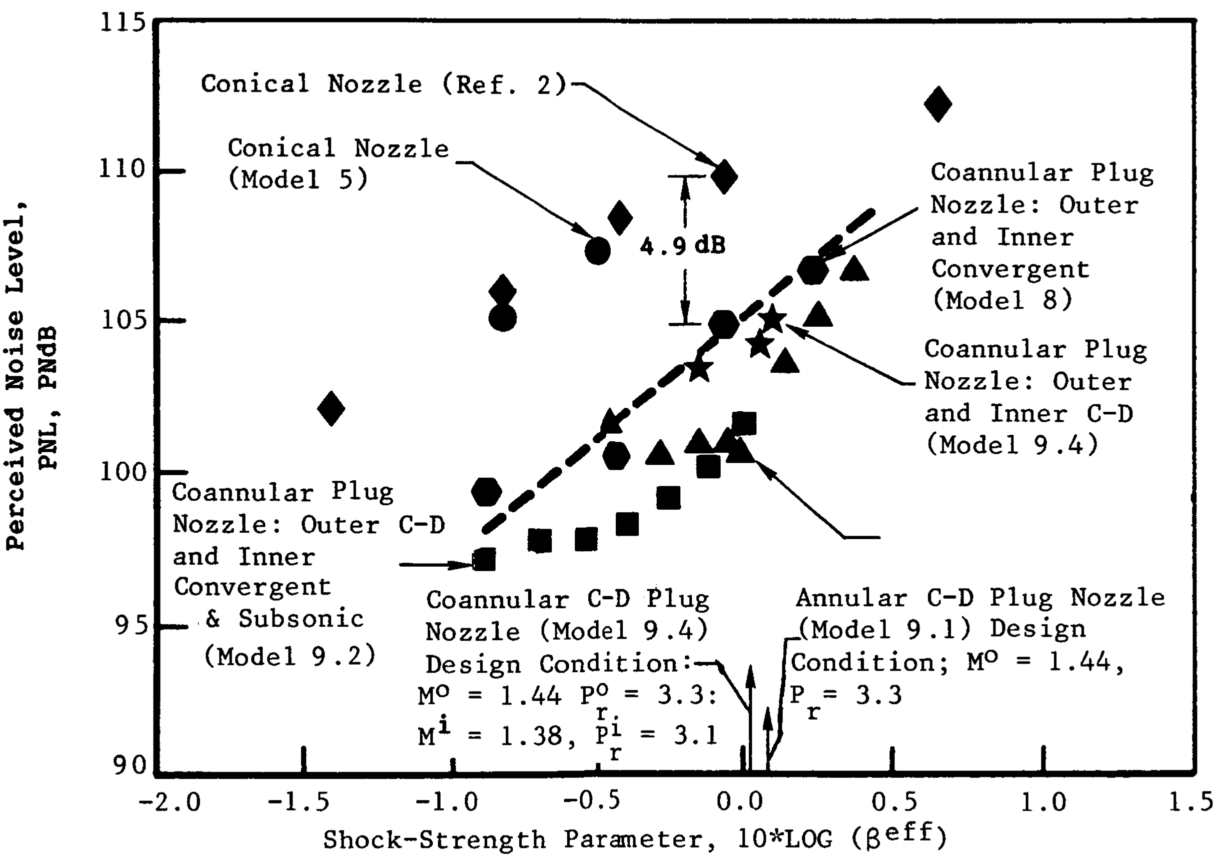

b) Simulated Flight (V_{ac} ~122 m/sec or 400 fps)

Figure 3-71. **Comparison of the C-D Coannular Plug Nozzle Data at θ_i = 60° with Those of Convergent Coannular Plug Nozzle Data Over a Range of Operating Conditions.**

and to indicate the magnitude of shock noise reduction observed with the tested C-D nozzles (Models 9.1 through 9.4). In this section, typical aft angle acoustic data measured during the course of those tests are presented and discussed.

The normalized PNL data at $\theta_i = 130°$ measured with the coannular plug nozzle having C-D flowpaths on both the outer and inner supersonic streams (Model 9.4) as a function of 10 log (V_j^{mix}/a_{amb}) are presented in Figure 3-72. The data are compared in this figure with data obtained with conical baseline nozzle (Model 5) and similitude coannular plug nozzle data with convergent flowpaths on both the outer and inner supersonic streams. An examination of this figure indicates that, for a given V_j^{mix}, the coannular plug nozzle with C-D flowpaths resulted in a higher noise level in the aft quadrant than the similitude convergent coannular plug nozzle. This trend in data is opposite to the observation made earlier using the front quadrant data of these two configurations wherein the C-D configuration resulted in a shock noise reduction (Figure 3-71). A probable explanation for this trend in the aft quadrant data is provided in the next paragraph.

It is to be recalled that the contoured design for the outer and inner nozzles of the C-D coannular plug configuration resulted in lower radius ratios ($R_r^o = 0.789$, $R_r^i = 0.908$) compared to those of the similitude coannular plug nozzle having convergent terminations ($R_r^o = 0.846$, $R_r^i = 0.933$). It has been shown in Reference 15 that a decrease in the outer stream radius ratio, for a given area ratio of coannular plug nozzles, results in an increase in the aft angle jet noise. This conclusion has been reached in Reference 15 after comparing the measured aft angle data of a series of coannular plug nozzles with convergent terminations and having outer stream radius ratios in the range of 0.853 to 0.902. A similar radius ratio effect has been reported in Reference 11 by comparing the aft angle acoustic data of convergent terminated annular plug nozzles with radius ratios in the range of 0.59 to 0.853. In addition, it is shown in Reference 2 that a decrement in the outer stream radius ratio from R_1 to R_2 results in an increment in the high frequency SPL's of the source spectrum by 50 log R_1/R_2. This empirical expression was derived from the measured SPL data of a large number of fixed area-ratio coannular plug nozzles with convergent terminations and having different outer stream radius ratios. Based on these experimental observations reported elsewhere in literature, some of the increment observed in the aft angle acoustic data of the C-D coannular plug nozzle (Model 9.4) relative to the convergent configuration can be attributed to the lower radius ratios of the model C-D nozzle.

Typical static PNL-directivity and aft quadrant spectral data of the C-D coannular plug nozzle (Model 9.4) are presented in Figures 3-73 and 3-74. The aerodynamic flow conditions correspond to the maximum effective condition that was determined earlier from the analyses of the front quadrant data (Figure 3-65). The measured data are compared in these figures with results obtained with coannular plug nozzles having (1) convergent outer and inner (Model 8) and (2) convergent outer and C-D inner (Model 9.3) and measured with flow conditions that reasonably match those of the effective condition of the all C-D nozzle. The acoustic data of Models 8 and 9.3 agree reasonably well in the aft quadrant indicating no significant effect of a convergent-divergent termination of the supersonic inner stream relative to a convergent exit. However, as noted before, significant differences in aft quadrant data are observed between the data of Models 9.4 and 8 which have C-D and convergent terminations on the outer stream, respectively.

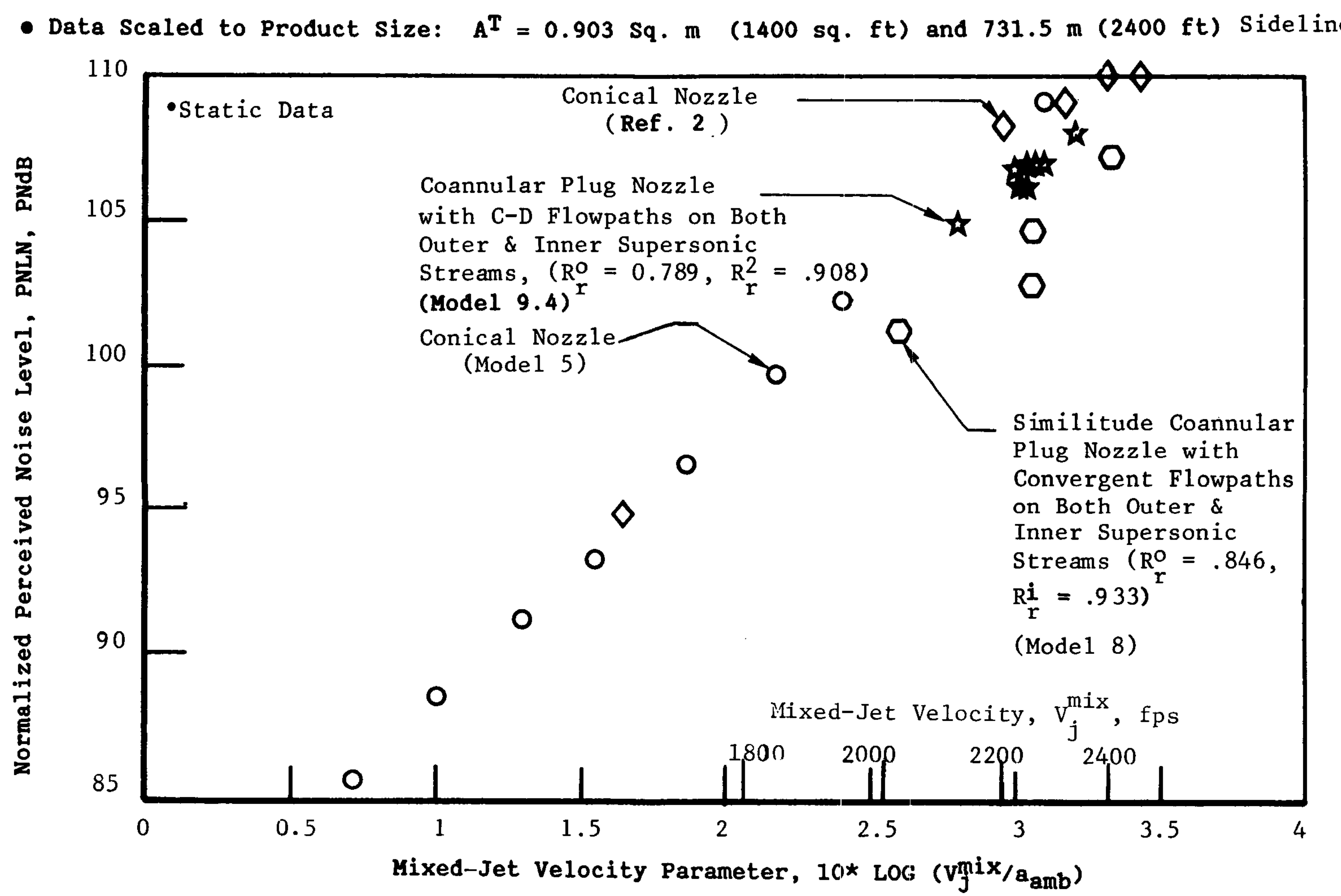

Figure 3-72. Normalized PNL Data of θ_i = 130° for Coannular Plug Nozzle with C-D Flowpaths on Both Inner and Outer Streams Compared with Data for Conical and Coannular Plug Nozzle with Convergent Flowpaths.

SYMBOL	POINT	P_r^o	$T_T^o(^oR)$	V_j^o(fps)	P_r^i	$T_T^i(^oR)$	V_j^i(fps)	P_r^{mix}	$T_T^{mix}(^oR)$	V_j^{mix}(fps)	NF	R_r^o
○	8001	3.18	1736	2438	3.12	833	1667	3.10	1539	2270	-7.4	.846
*	4001	3.24	1747	2464	3.00	876	1678	3.12	1532	2287	-7.6	.789
Δ	3012	3.26	1745	2467	3.12	938	1769	3.17	1562	2309	-7.7	.846

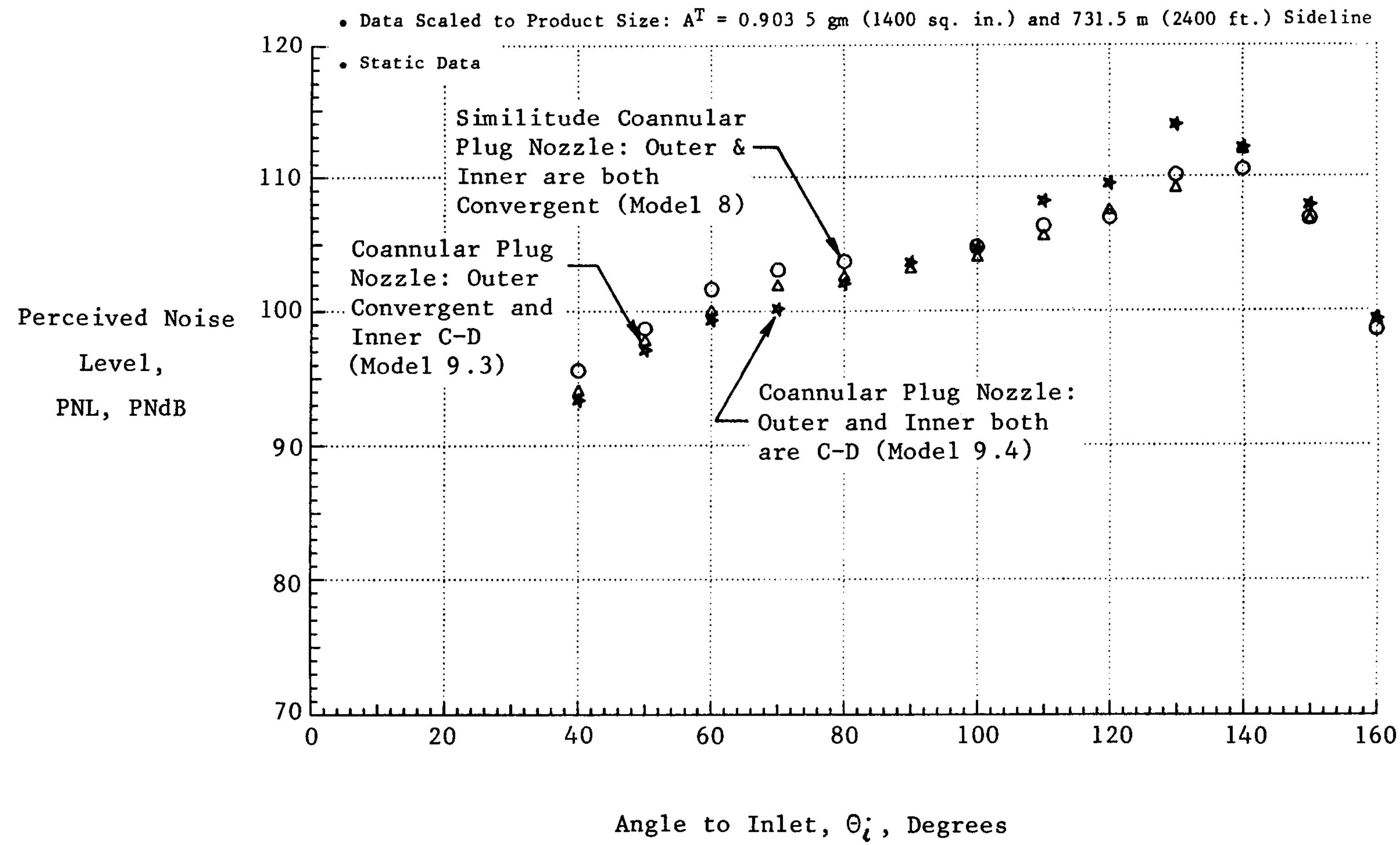

Figure 3-73. Comparison of Static PNL Directivity of Coannular Plug Nozzles with the Following Terminations: (a) C-D on Both Outer and Inner Streams; (b) Convergent on the Outer Stream and C-D on the Inner Stream; and (c) Convergent on Both Outer and Inner Streams.

See Figure 3.73 for Aerodynamics Flow Conditions

• Data Scaled to Product Size: A^T = 0.903 Sq.m (1400 sq. ft) and 731.5 m (2400 ft) Sideline

•Static Data

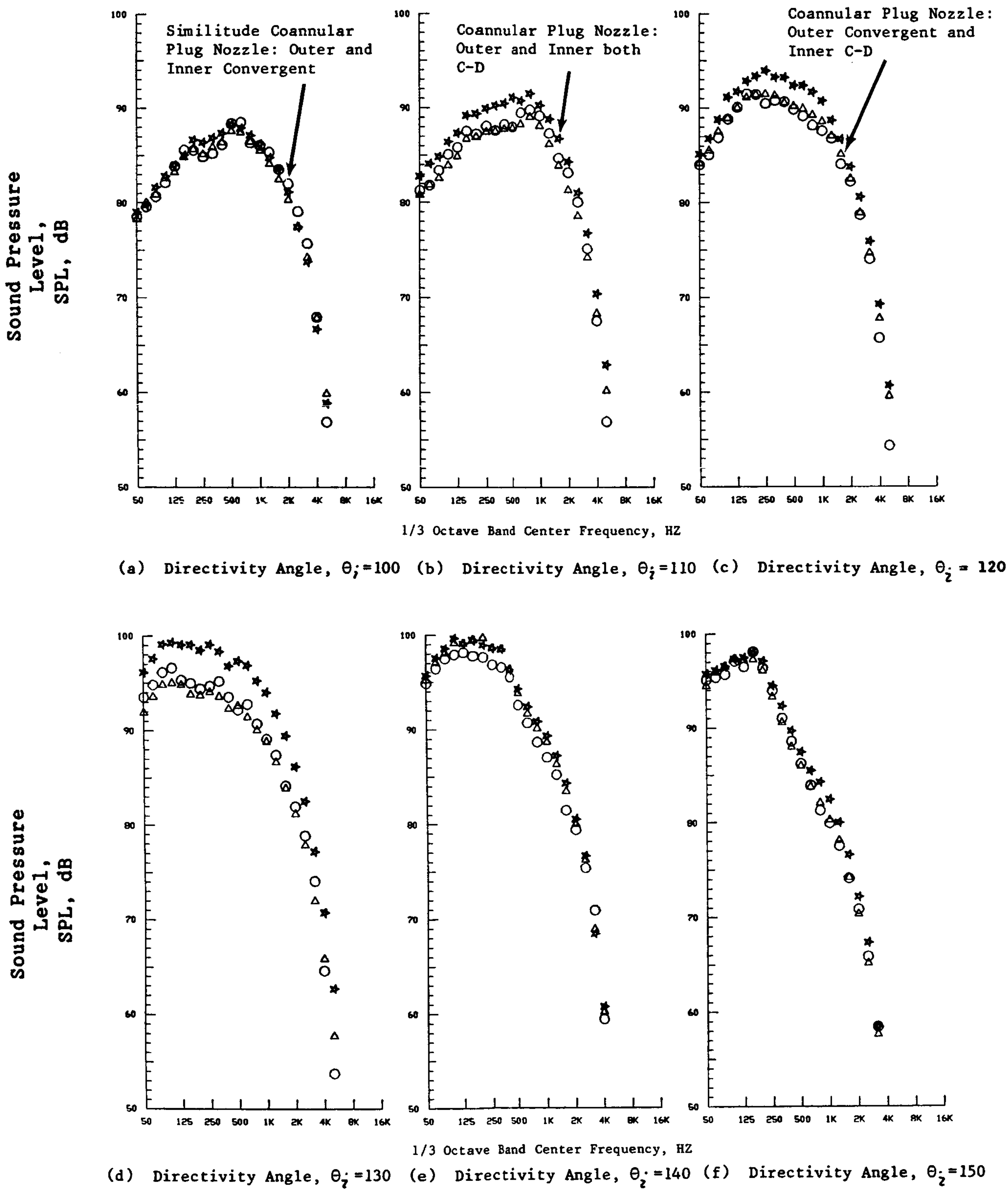

Figure 3-74. Complarison of Aft Quadrant Static Spectra of Coannular Plug Nozzles with the Following Terminations: (a) C-D on Both Outer and Inner Streams; (b) Convergent on the Outer Stream and C-D on the Inner Stream; and (c) Convergent on Both Outer and Inner Streams.

Additional comparison of static PNL-directivity and aft quadrant spectra of the coannular plug nozzle with C-D termination (Model 9.4) with that of a second convergent terminated coannular plug nozzle (Model 3, Ref. 2, $A_r = 0.194$, $R_r^o = 0.853$, $R_r^i = 0.933$) is presented in Figures 3-75 and 3-76. Observations similar to those noted with the earlier set of data are indicated again.

Further corroboration of the observations made above regarding the effect of the radius ratio is presented in Figures 3-77 and 3-78. In Figure 3-77 the normalized PNL at $\theta_i = 130°$ for the C-D annular nozzle (Model 9.1; $R_r = 0.789$) over a jet velocity range of 1,900 to 2,800 fps is compared with the available data of convergent annular plug nozzles ($R_r = 0.789$ and 0.853) of DOT program (Reference 11; typical front quadrant data of these two configurations have been presented earlier in Figure 3-53). An examination of this figure indicates a good agreement of the C-D annular plug nozzle aft quadrant data with those of the convergent annular plug nozzle having a radius ratio equal to that of the C-D configuration. A decrease in the magnitude of the jet noise of the convergent nozzle with an increase in its radius ratio is indicated by the DOT data. Typical PNL-directivity and selected aft quadrant spectral comparison between the C-D and convergent annular plug nozzles data, with both configurations having $R_r = 0.789$, is provided in Figure 3-78. The figure confirms the aft quadrant agreement between the data of convergent and C-D terminated annular plug nozzles, for a given set of flow conditions and a radius ratio.

Based on these observations, it is concluded that the increment observed in the aft angle acoustic data of C-D coannular plug nozzle (Model 9.4) relative to the convergent coannular plug nozzle (Model 8) is mainly because of the differences in their outer stream radius ratios.

3.2 DIAGNOSTIC LASER VELOCIMETER RESULTS

The General Electric Laser Velocimeter (LV) system has been used under earlier NASA contract efforts to measure the mean and turbulent velocities of scale-model nozzle plumes in the anechoic chamber (Reference 2) and engine demonstrator nozzle plumes in an outdoor facility (Reference 7). The LV has been found to be a useful diagnostic tool to explain some of the observed acoustic characteristics through these velocity measurements. During this investigation the LV system was employed to measure the plume characteristics of the similitude 20-shallow-chute mechanical suppressor nozzle. The specific objectives of this set of LV measurements were:

- Compare the plume characteristics of the similitude 20-shallow-chute and the coannular plug and conical baseline nozzles

- Evaluate the influence of free jet on the plume decay of the similitude 20-shallow-chute nozzle

- Compare the jet flow characteristics of the similitude 20-shallow-chute nozzle at typical takeoff and cutback cycle conditions

- Determine the influence of the inner stream termination (convergent or convergent-divergent) on the plume decay.

SYMBOL	POINT	P_r^o	$T_T^o(^oR)$	V_j^o(fps)	P_r^i	$T_T^i(^oR)$	V_j^i(fps)	P_r^{mix}	$T_T^{mix}(^oR)$	V_j^{mix}(fps)	N_F	R_r^o
☆	4003	3.25	1755	2472	3.17	876	1718	3.16	1548	2294	-7.7	.789
△	301	3.18	1719	2427	3.21	784	1634	3.10	1507	2247	-7.3	.853

•Data Scaled to Product Size: A^T = 0.903 Sq.in. (1400 sq.in) and 7315m (2400 ft) sideline

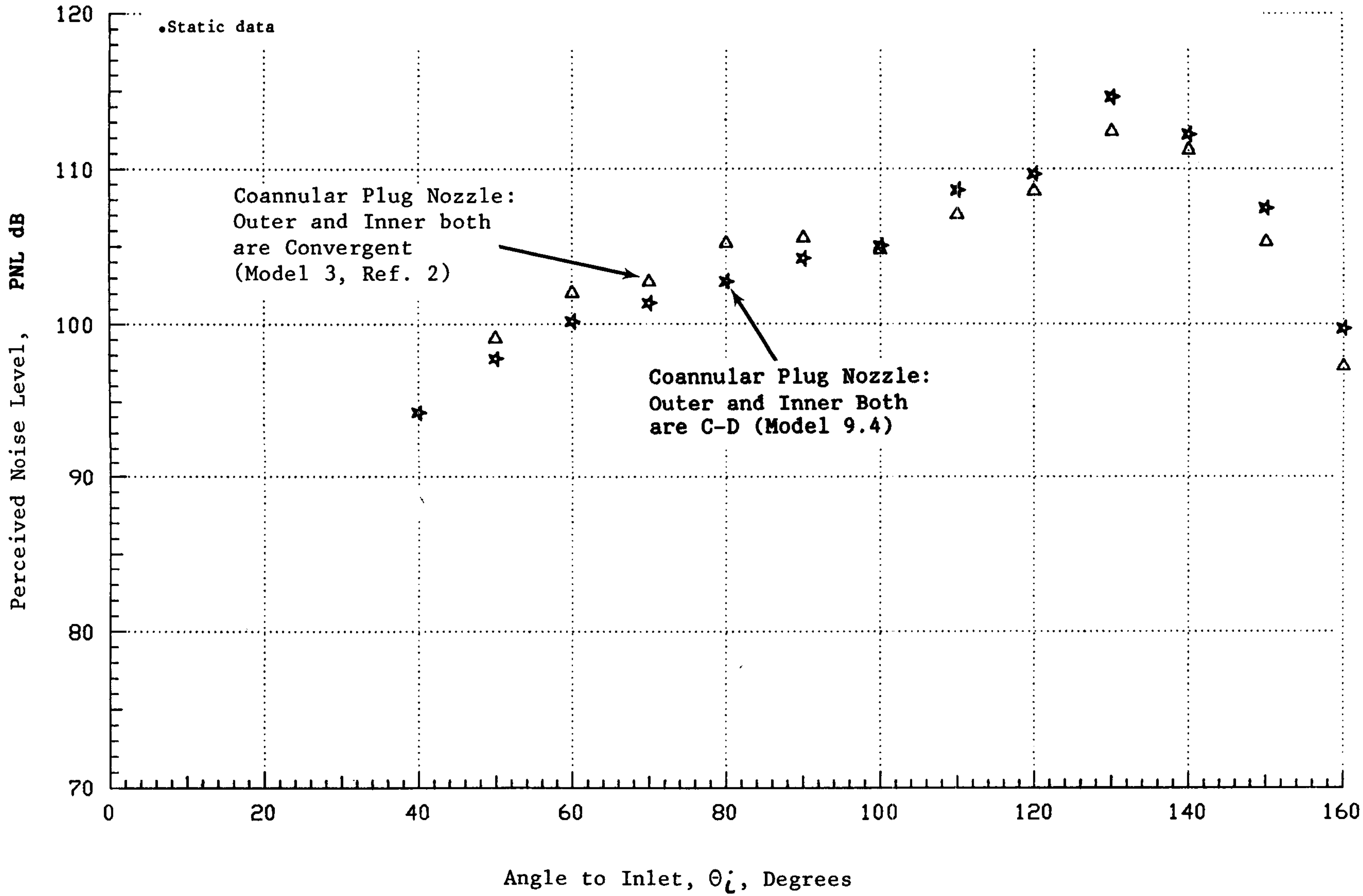

Figure 3-75. Additional Comparison of Static PNL Directivity of Coannular Plug Nozzles with Convergent and C-D Terminations.

(See Figure 3-75 for Aerodynamic Flow Conditions)

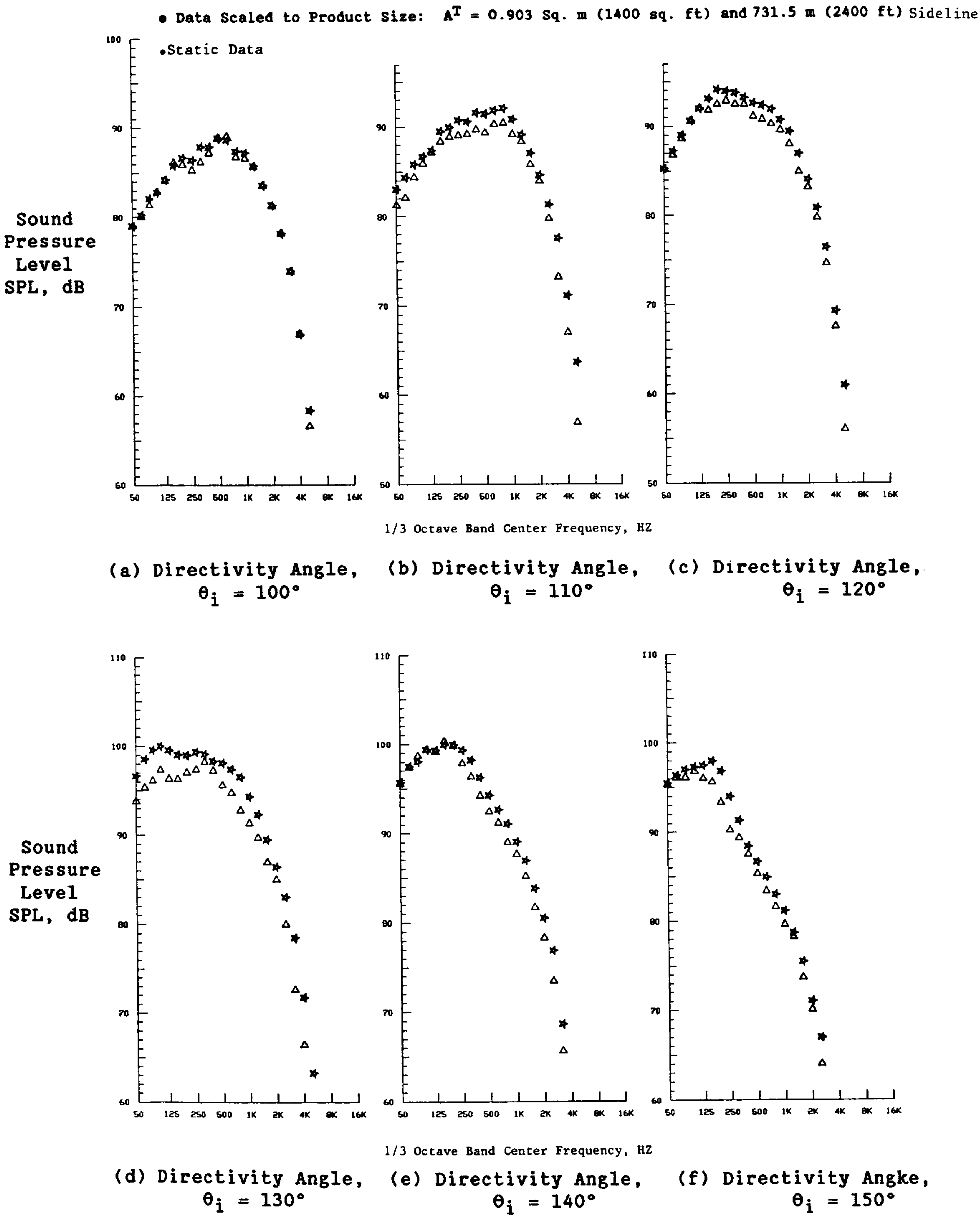

Figure 3-76. Additional Comparison of Aft-Angle Static Spectra of Coannular Plug Nozzles with Convergent and C-D Terminations.

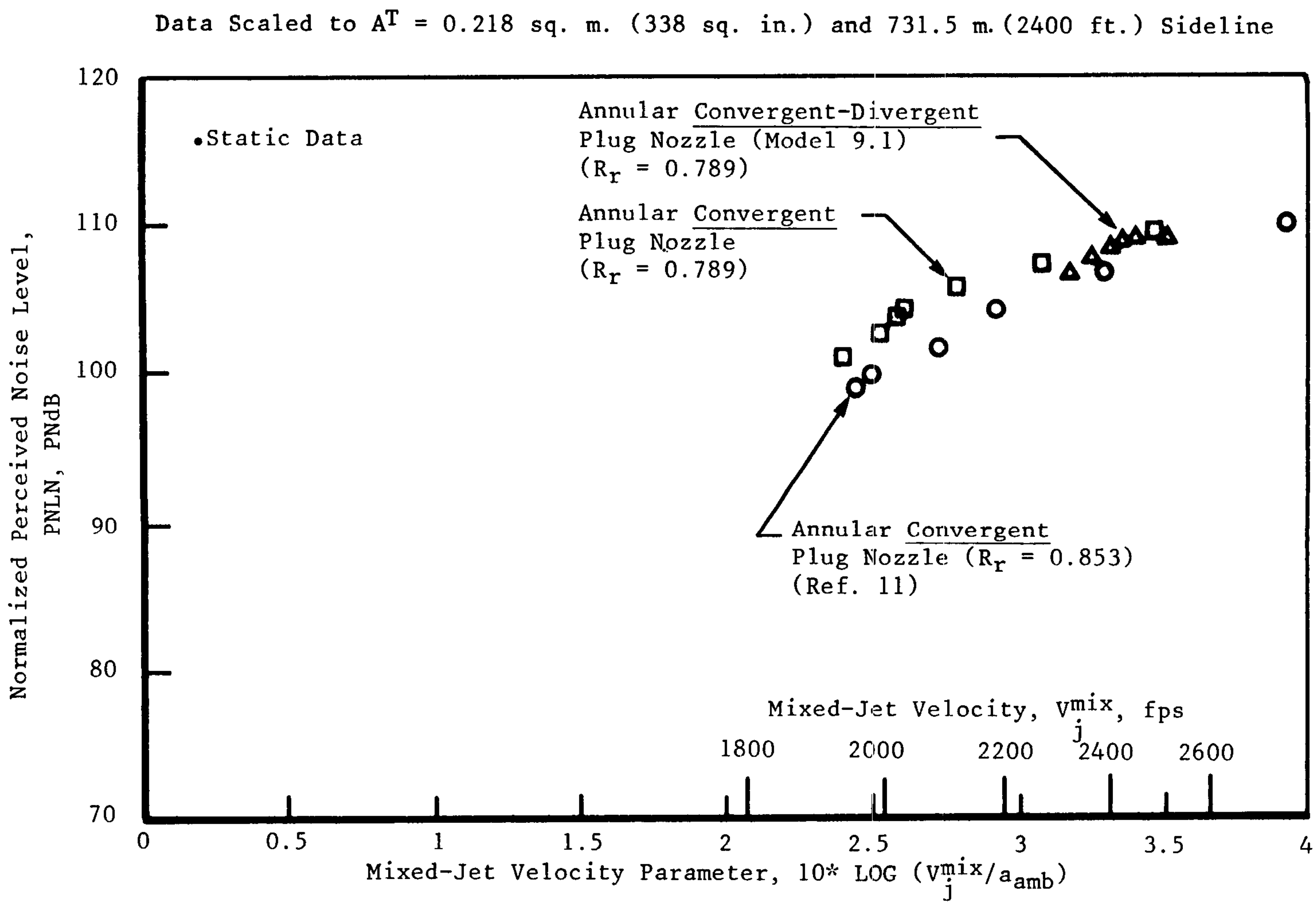

Figure 3-77. Comparison of Normalized PNL at θ_i = 130° for C-D Annular Plug Nozzle (R_r = 0.789) with Data of Convergent Annular Plug Nozzles (R_r = 0.789 and 0.853).

Symbol	Point	P_r	T_T	V_j	NF	R_r	LBM	LVM
△	1004	3.24	1751	2466	-0.93	0.789	-0.01	3.37
⊠	7653	3.30	1557	2337	-1.5	0.789	+0.06	3.09

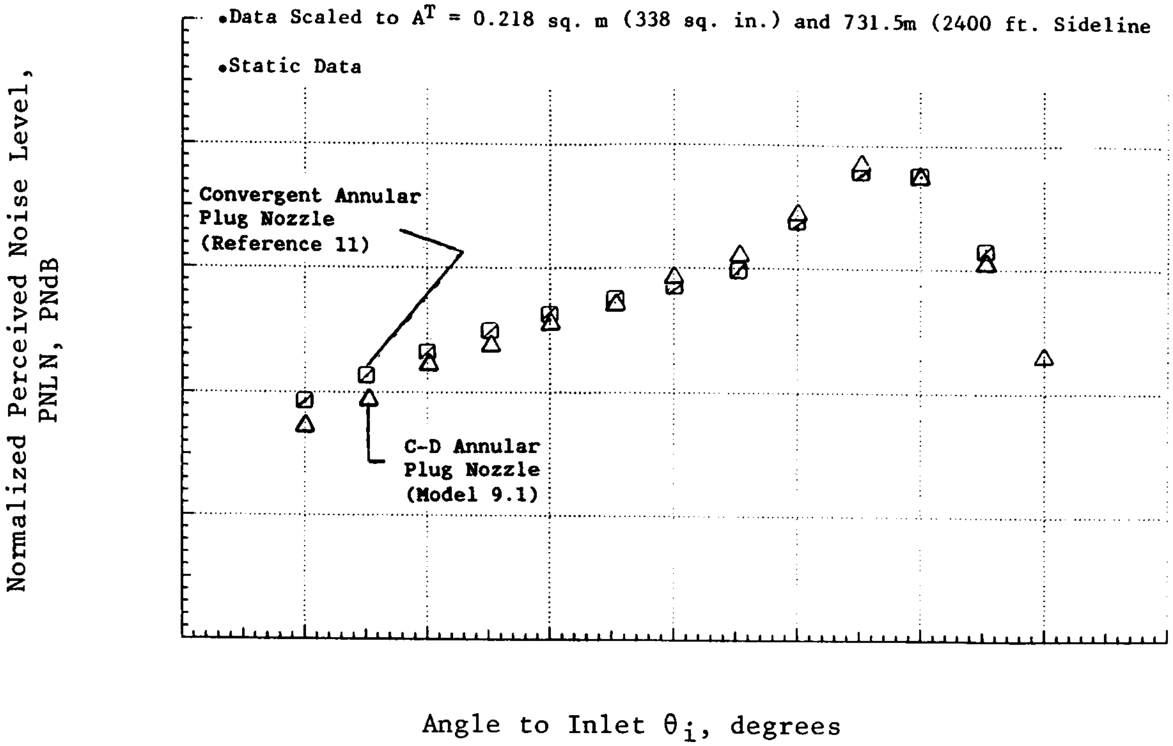

(a) Normalized PNL Directivity

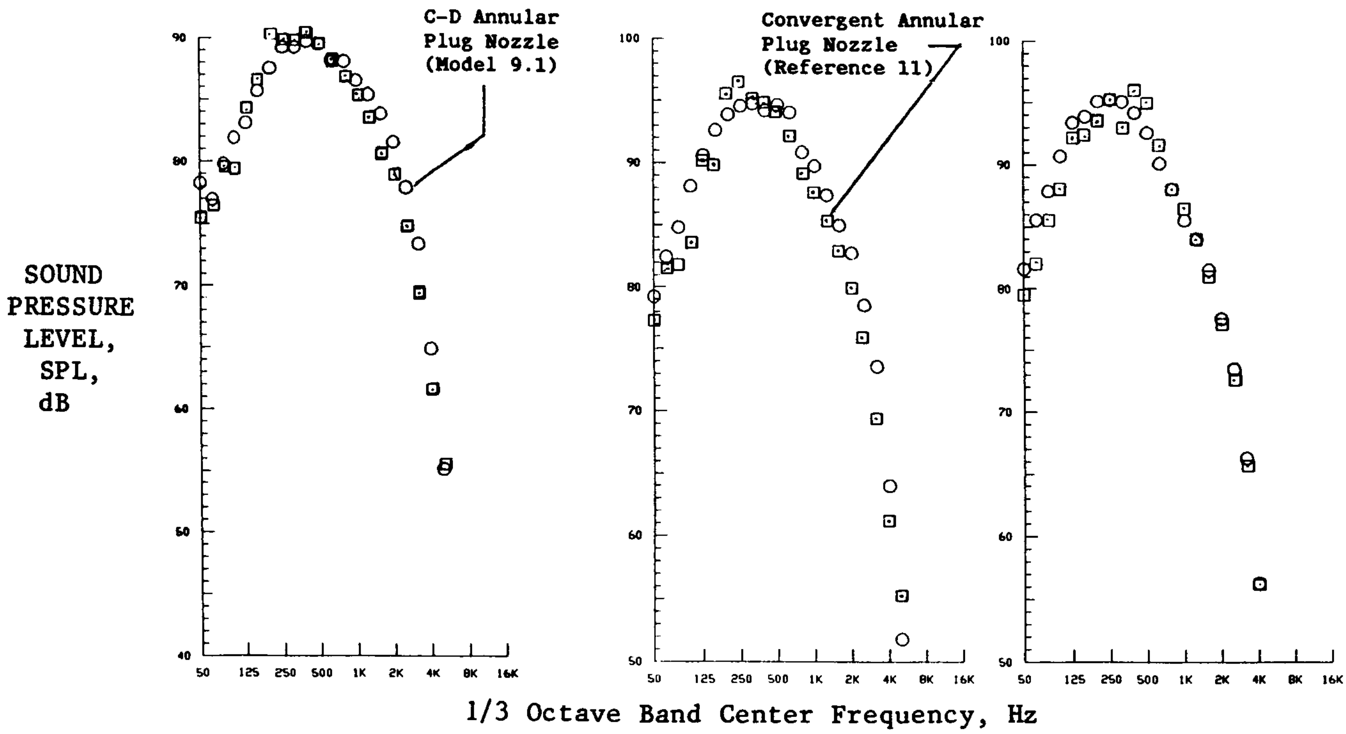

(b) Spectra at θ_i = 120°

(c) Spectra at θ_i = 130°

(d) Spectra at θ_i = 140°

Figure 3-78. Comparison of Normalized PNL-Directivity and Typical Aft-Quadrant Spectra of C-D Annular Plug Nozzle (R_r = 0.789) with Data for Convergent Annular Plug Nozzle (R_r = 0.789).

3.2.1 Plume Characteristics of the Similitude 20-Shallow-Chute, and Coannular and Conical Baseline Nozzles

Figures 3-79 compare the axial variation of the normalized mean and turbulent velocities of the similitude 20-shallow-chute nozzle, a coannular plug nozzle, and a conical nozzle for a static case. The LV data of coannular plug nozzle and conical nozzle are taken from Reference 2. The mass averaged aerodynamic conditions are listed in Figures 3-79 and are seen to be reasonably close. Whereas both the conical and the coannular nozzles exhibit strong shock cell patterns along the nozzle center line, there is no shock cell pattern along the nozzle centerline for the similitude 20-shallow-chute suppressor nozzle indicating the rapid decay of the supersonic stream (Figure 3-79(a). Also, the velocity decay rate for the conic nozzle is seen to be the lowest, followed by the coannular nozzle and then the 20-shallow-chute nozzle, indicating that the mechanical suppressor nozzle has an enhanced mixing rate compared to other nozzles. The enhanced mixing rate of the mechanical suppressor nozzle is directly attributable to the increased surface area of the jet that is available for shear by the ambient air. The turbulent velocity variation shown in Figure 3-79(b) confirms the above hypothesis. The turbulent velocity along the nozzle centerline for the 20-shallow-chute nozzle remains higher than others for $X/D_{eq} < 4$ due to the intense turbulent mixing that exists in the vicinity of the exit plane. For $X/D_{eq} > 5$, the jet stream of the 20-shallow-chute has itself decayed considerably and the turbulence level is lower compared to the coannular and conic nozzles.

Next, Figure 3-80 compares the typical radial profiles of the 20-shallow-chute and coannular and conic nozzles at $X/D_{eq}^{T} \simeq 4 - 5$. The jet plume of the 20-shallow-chute nozzle has decayed the most. Compared to the coannular nozzle, the jet plume of the 20-shallow-chute nozzle has lower peak velocities and has spread out more, reconfirming the high mixing rate of the suppressor nozzles. The radial profile of the conic nozzle shows a dip near the axis due to the presence of an oblique shock right at $X/D = 5.1$ [Figure 3-79(a)]. The radial profile of the coannular nozzle is asymmetric due to geometric asymmetry in the nozzle (see Ref. 2 for a detailed discussion on geometric asymmetry of coannular nozzles). The radial profile of the conic nozzle almost envelopes both the coannular and 20-shallow-chute nozzles indicating the poor mixing rate of conic nozzles.

The axial variation of the normalized mean and turbulent velocities of the 20-shallow-chute and coannular and conic nozzles are compared for a flight case (V_{ac} = 400 fps) in Figures 3-81. The mixing rates of the three nozzles in terms of the mean velocity decay [Figure 3-81(a)] and the turbulent velocity variation [Figure 3-81(b)] for the flight case bear a similar relationship to one another as in the static case. Figure 3-82 compares the radial profile of the three nozzles at $X/D_{eq}^{T} \simeq 4 - 5$. As in the static case, the radial profile of the conic nozzle envelopes those of the coannular and 20-shallow-chute nozzles.

3.2.2 Influence of Free Jet on Plume Decay of 20-Shallow-Chute Nozzle

The primary influence of a free jet is to reduce the velocity gradient between the jet and the ambient air thereby reducing the shear stress compared to the static case. A reduction in shear stress results in a slower decay rate of the mean velocity as well as lower turbulent velocities.

	A^T_2 (in^2)	TEST POINT	V_j^{mix} (fps)	T_T^{mix} (°R)	P_r^{mix}	
20-Shallow-Chute	24.36	1027	2289	1565	3.09	● Static
Coannular	21.06	301	2246	1506	3.10	
Conic	20.38	513	2411	1701	3.17	

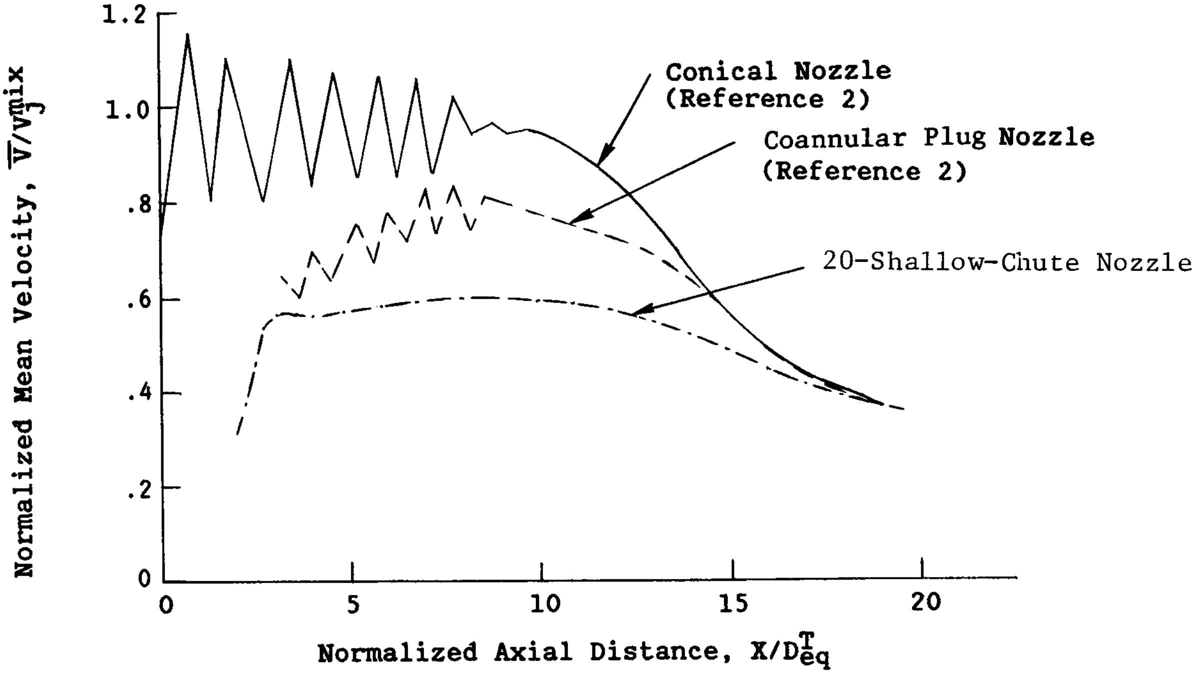

(a) Normalized Mean Velocity

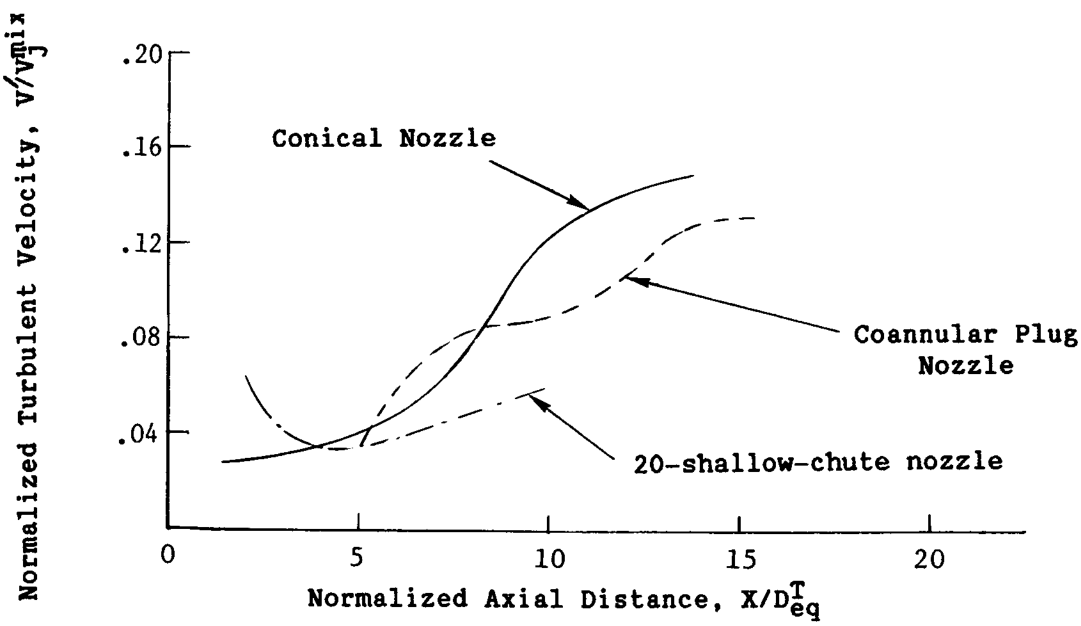

(b) Normalized Turbulent Velocity

Figure 3-79. Comparison of Axial Variation of the Normalized Mean and Turbulent Velocity of the 20-Shallow-Chute, Coannular, and Conical Nozzles for a Static Case.

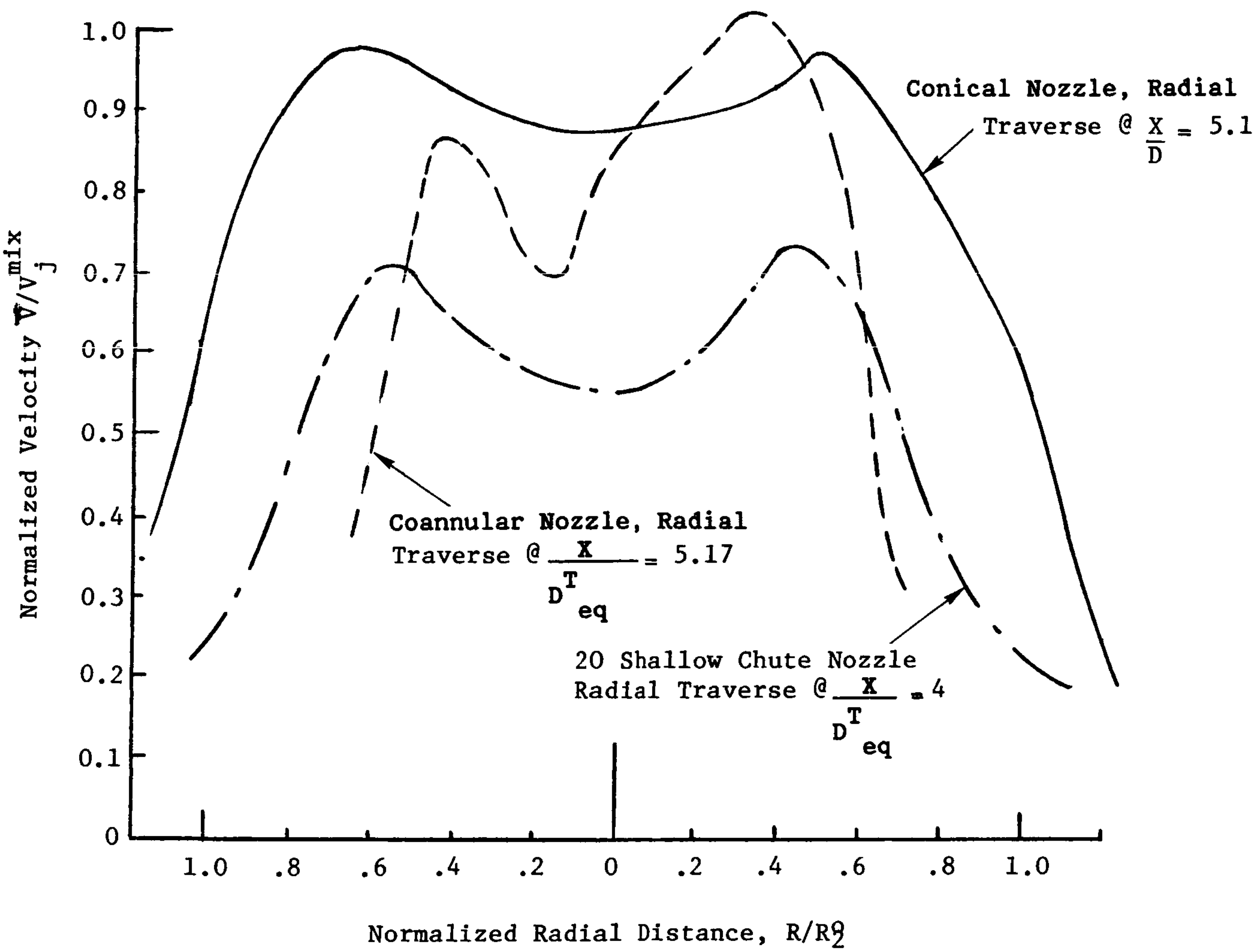

Figure 3-80. Comparison of Radial Profiles of Normalized Velocity of the 20-Shallow Chute, Coannular, and Conical Nozzles for a Static Case. (See Figure 3-79 for Aerodynamic Conditions.)

	A_2^T (in^2)	TEST POINT	V_j^{mix} (fps)	T_T^{mix} (°R)	P_r^{mix}
20-Shallow-Chute	24.36	1028	2303	1591	3.07
Coannular	21.06	303	2256	1512	3.12
Conic	20.38	515	2422	1709	3.19

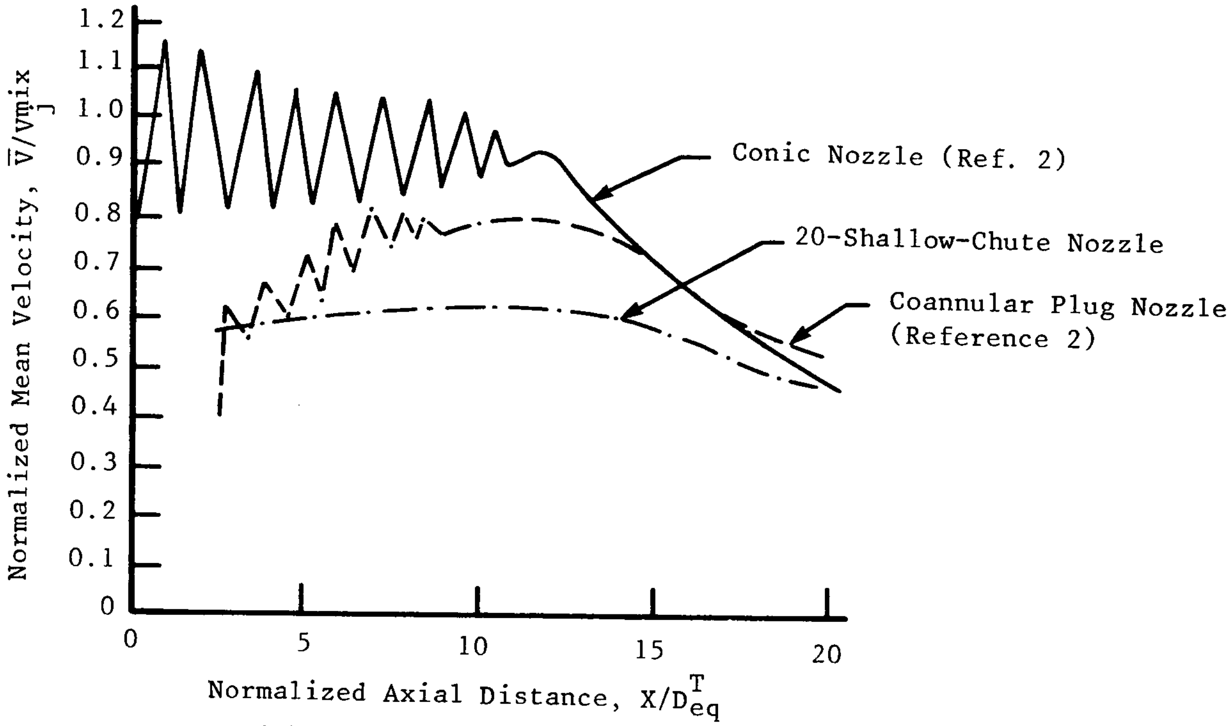

(a) Normalized Mean Velocity

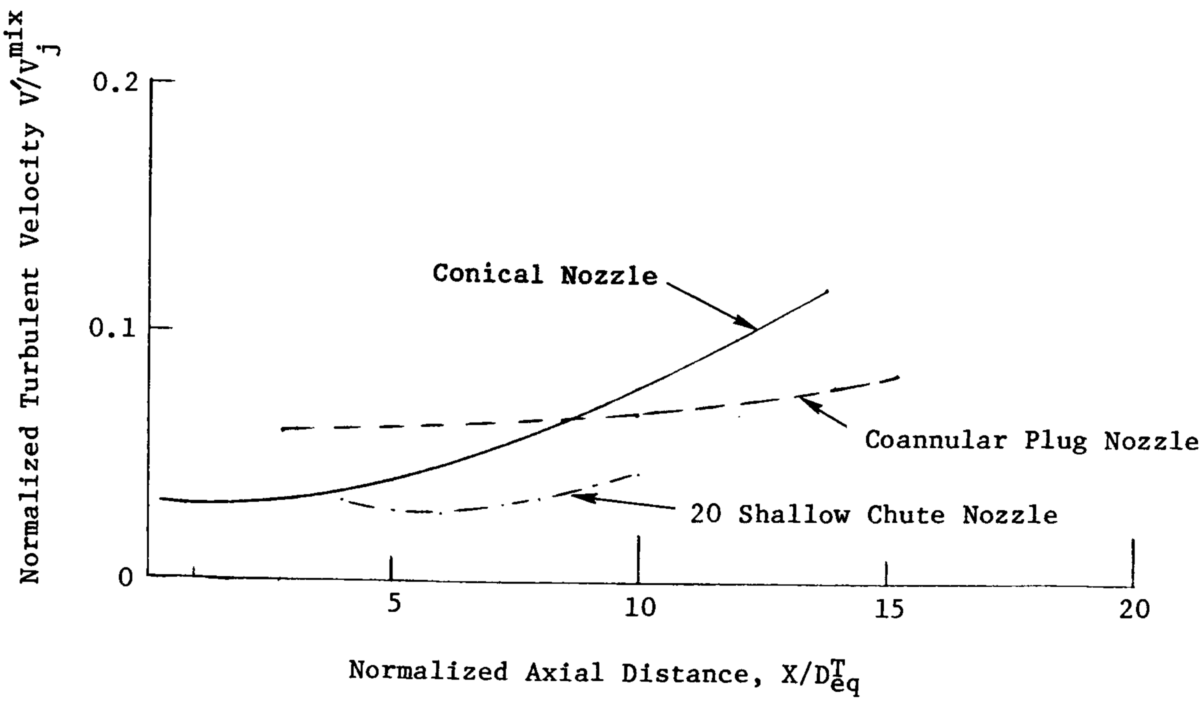

(b) Normalized Turbulent Velocity

Figure 3-81. Comparison of Axial Variation of the Normalized Mean and Turbulent Velocity of the 20-Shallow-Chute, Coannular, and Conical Nozzles for a Flight Case.

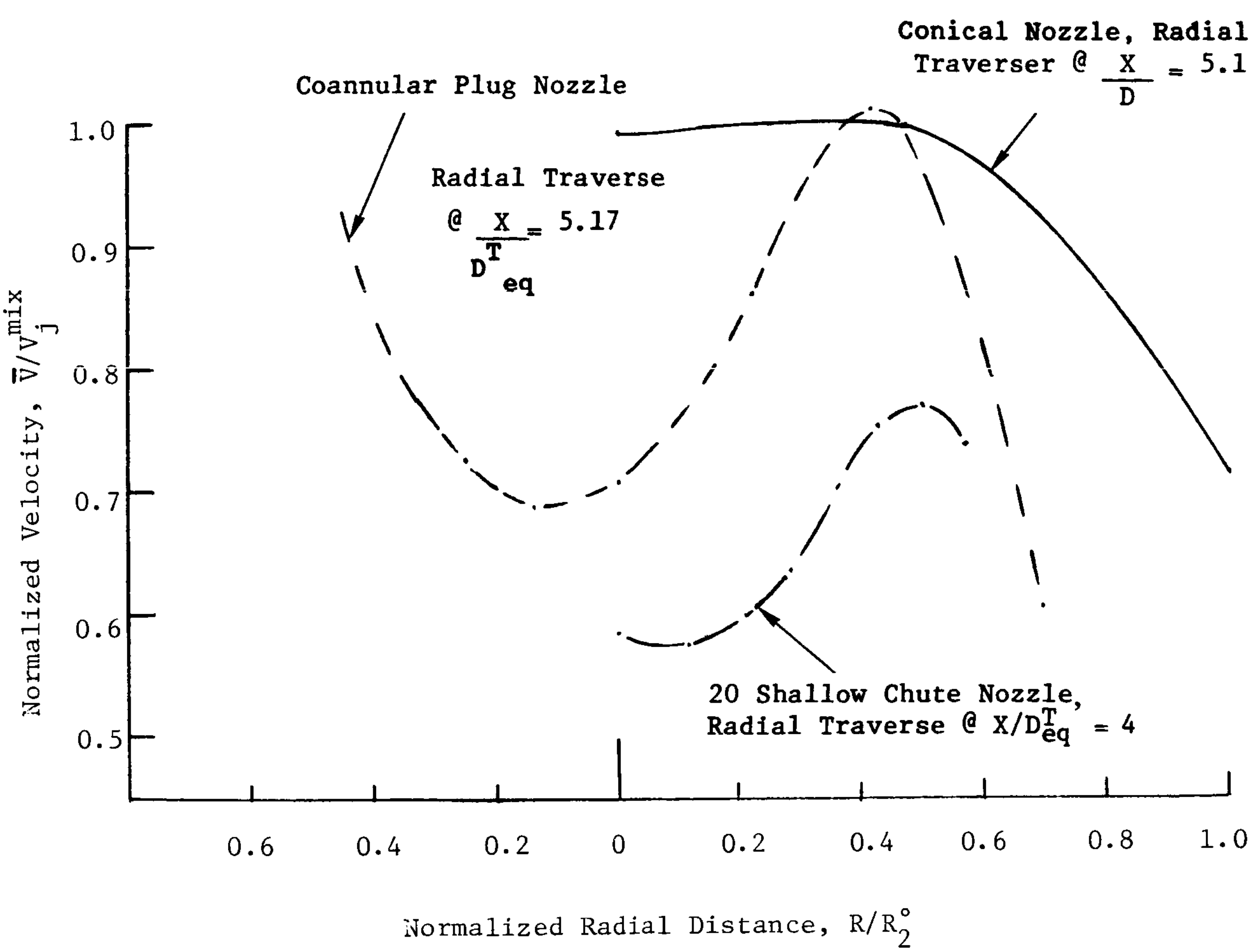

Figure 3-82. Comparison of Radial Profiles of Normalized Velocity of the 20-Shallow-Chute, Coannular, and Conical Nozzles for a Flight Case. (See Figure 3-81 for Aerodynamic Conditions).

Figure 3-83 compares the axial variation of the normalized mean velocity and turbulent velocity of the 20-shallow-chute nozzle for a static and a flight (V_{ac} = 400 fps) case. Due to reduced shear because of the free jet, the decay rate of the jet plume is seen to be lower for the flight case [Figure 3-83(a)]. Figure 3-83(b) shows that the turbulent velocities in the presence of a free jet are lower compared to the static case, again due to reduced turbulent shear stress. Recall that turbulent shear stress is directly proportional to the square of turbulent velocity.

Figure 3-84 compares the radial variation of the normalized mean and turbulent velocity of the 20-shallow-chute nozzle at $X/D^T_{eq} = 2$ to evaluate the influence of the free jet. Note in Figure 3-84(a) that the peak mean velocity for the flight case is higher than that of the static case due to reduced shearing. Also, the plume has shifted radially outwards in the presence of the free jet. The free jet is obtained by accelerating the ambient air through a fan blower. Hence, the static pressure within the free jet is lower compared to the static ambient air. The outward radial shift of the jet plume in simulated flight is a direct consequence of the reduced static pressure at the boundary between the jet and the free jet. Figure 3-84(b) compares the turbulent velocities with and without a free jet. As remarked above, it was observed that the turbulent velocities are lowered by the free jet due to reduced turbulent shear stress. Figure 3-85 shows the influence of the free jet on the radial profile at an axial location of $X/D^T_{eq} = 6$ where the jet plume is fully developed. It is evident that, due to the free jet, the plume has grown radially outward and has higher velocities. Unlike in the region close to the exit plane [Figure 3-84(a)], the jet velocities in the fully developed region of the jet are seen to be higher at all radial locations in the presence of the free jet. The solid boundaries, such as the plug surface, have significant influence on the jet plume structure close to the jet exit plane. Also, in reality, the static pressure within the jet is not equal to the ambient static pressure near the exit plane. Hence, the jet flow is not well established close to the exit plane; as soon as the jet plume senses a lower static pressure in the ambient due to the free jet, the jet plume seems to dart out radially. Whereas, in the fully developed region of the jet, a gradual jet static pressure equalization to ambient static pressure takes place; and the entire jet plume blows radially outward in simulated flight. The jet flow velocities remain higher at all radial locations for the flight case due to reduced shear.

3.2.3 Comparison of Jet Flow Characteristics of 20-Shallow-Chute Nozzle at Typical Takeoff and Cutback Cycle Conditions

Figure 3-86 compares the axial variation of the normalized mean velocity at the midpoint of the chute at typical takeoff (Test Pt. 1015) and cutback (Test Pt. 1019) conditions. Since the outer stream pressure ratio for the takeoff case is much higher than that for cutback case, one observes two shock cells for the takeoff case and none for the cutback case just downstream of the exit plane of the chutes (see Figure 3-86 for a listing of aerodynamic conditions). For $X/D^T_{eq} > 1.5$, the normalized velocity profiles look similar. Figure 3.88 compares the axial variation of the normalized mean velocity along the nozzle centerline at takeoff and cutback conditions. There are no shock cells along the nozzle centerline for the 20-shallow-chute nozzle. The normalized mean velocity profiles along the nozzle centerline are similar. Figure 3-88 compares the radial profiles of the normalized mean

Test Pt.	V_{ac} fps	V_j^o fps	T_T^o °R	P_r^o	V_j^i fps	T_T^i °R	P_r^i	$V_{j_{fps}}^{mix}$	$T_{T_{oR}}^{mix}$	P_r^{mix}
1027	0	2455	1734	3.24	1602	865	2.70	2289	1565	309
1025	400	2460	1738	3.25	1577	907	2.48	2303	1591	307

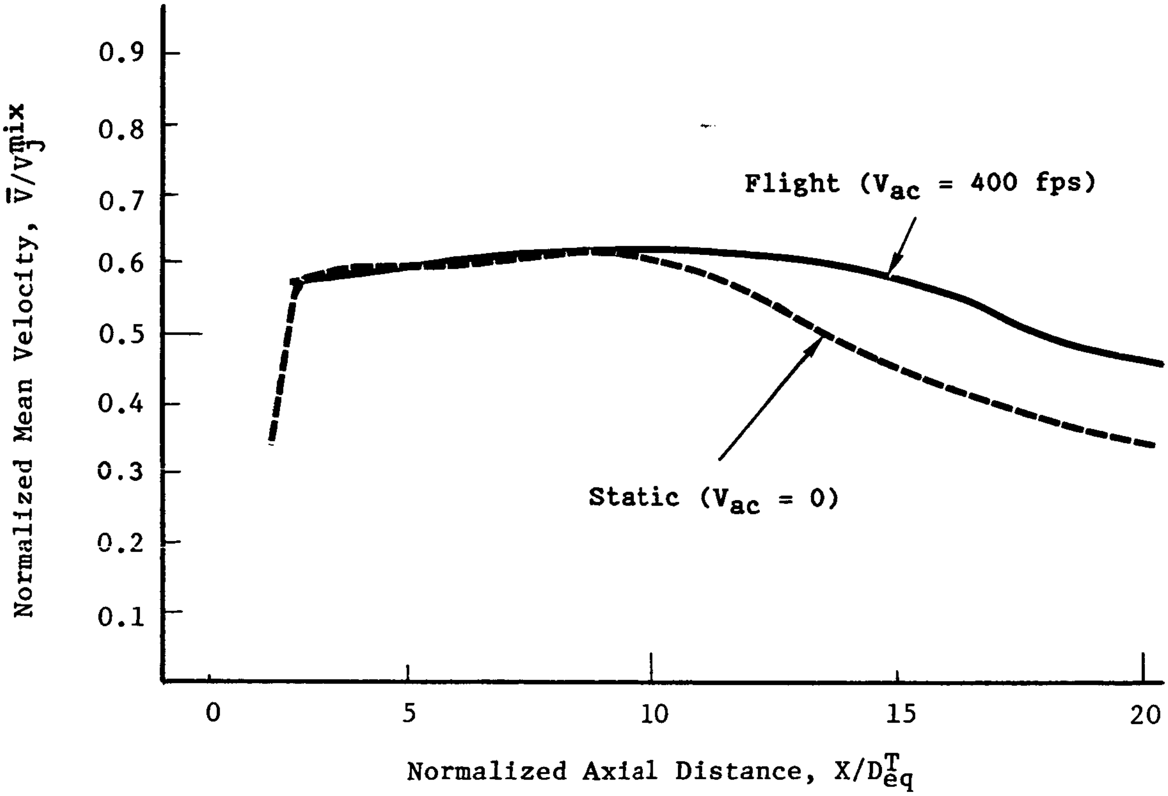

(a) Normalized Mean Velocity

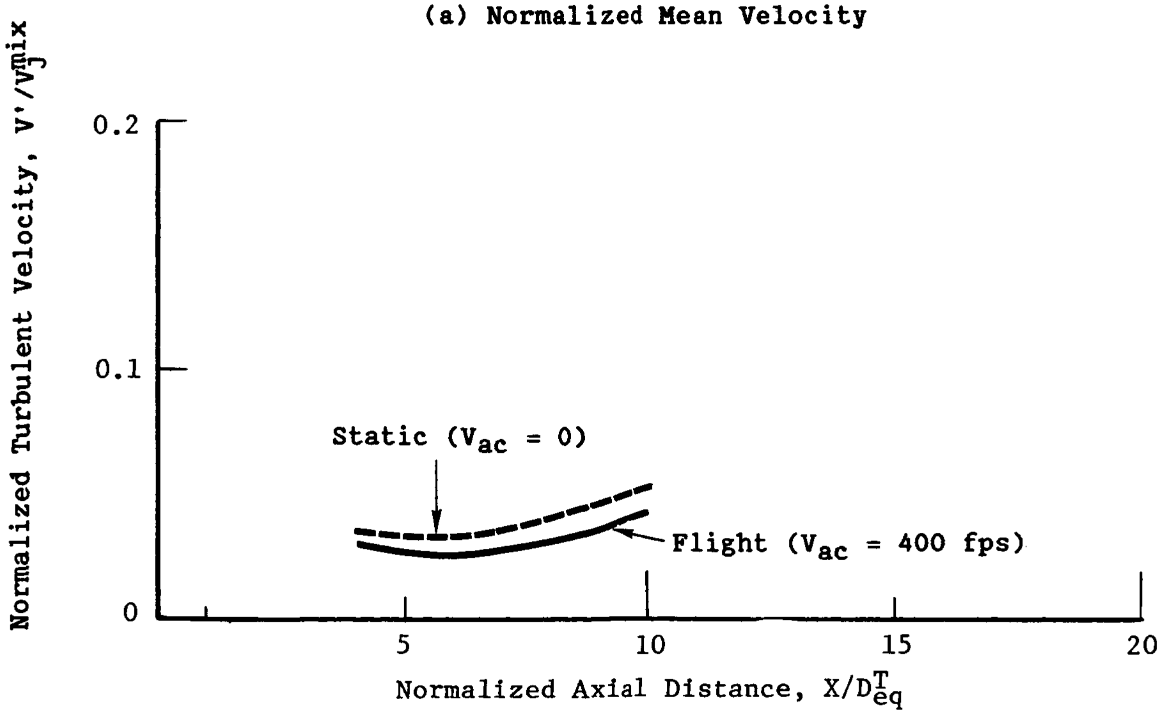

(b) Normalized Turbulent Velocity

Figure 3-83. Influence of the Freejet on the Axial Variation of the Normalized Mean and Turbulent Velocities of the 20-Shallow-Chute Nozzle.

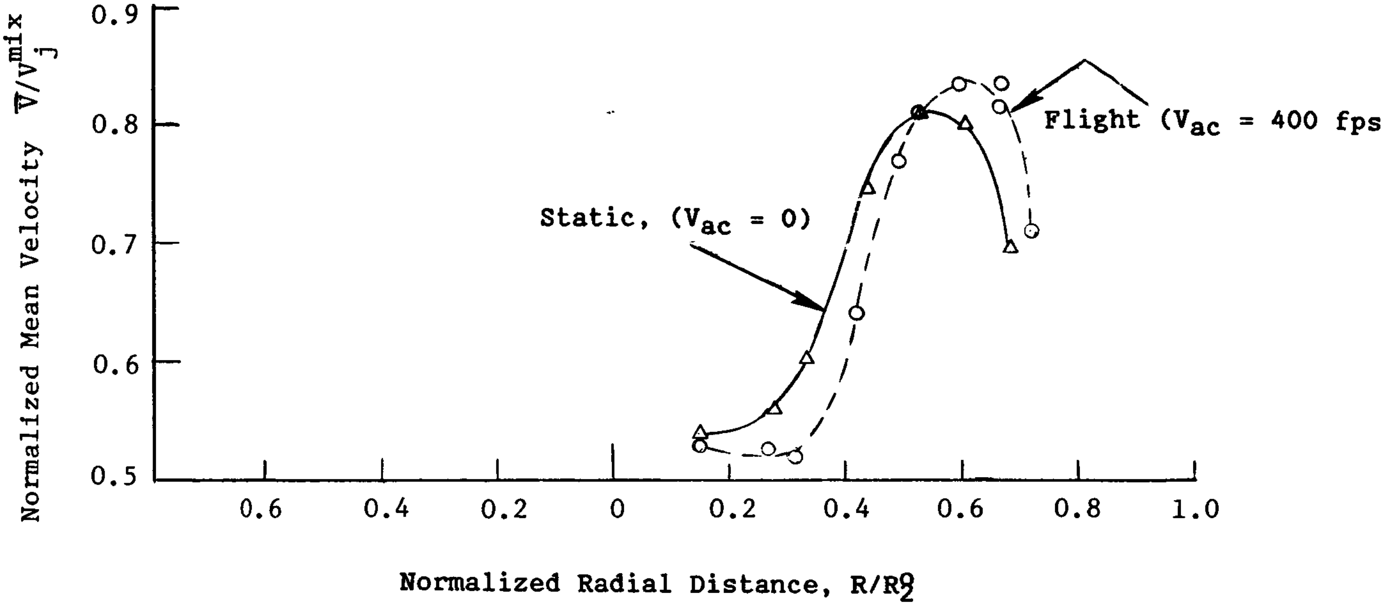

(a) Normalized Mean Velocity

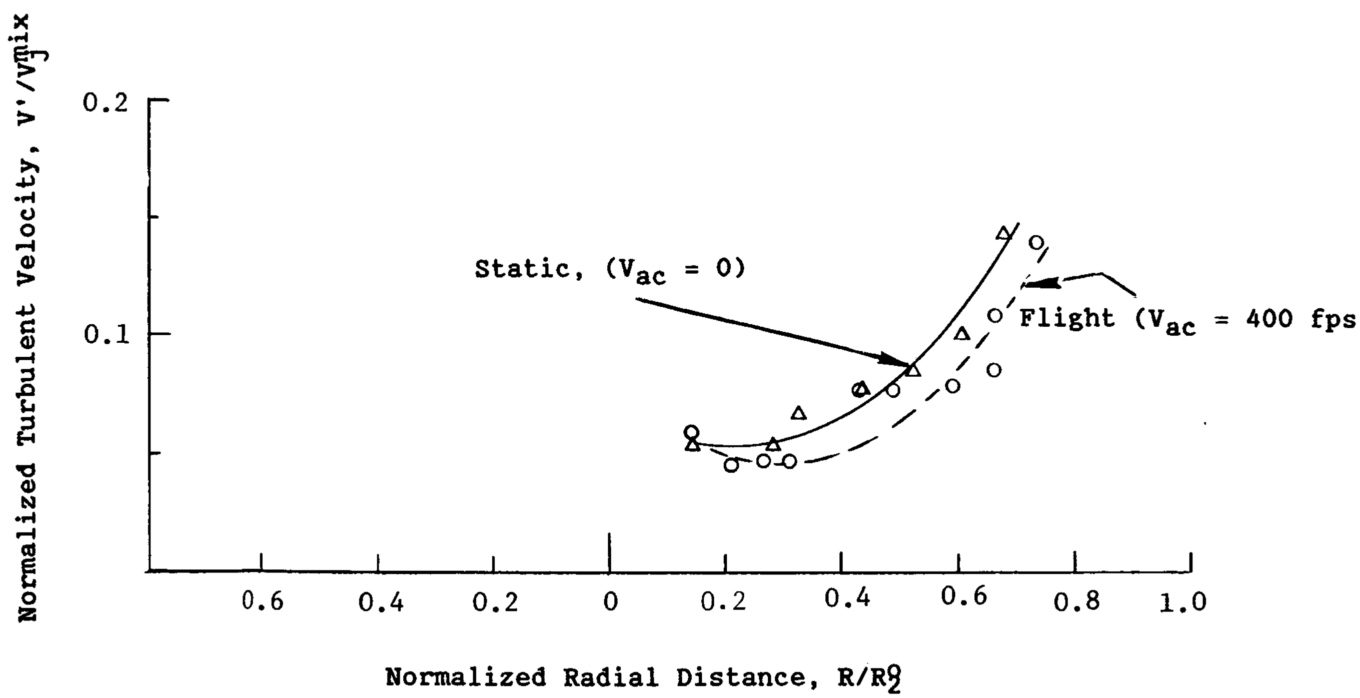

(b) Normalized Turbulence Velocity

Figure 3-84. Influence of the Free Jet on the Radial Variation of the Normalized Mean and Turbulent Velocities of the 20-Shallow-Chute Nozzle at X/D_{eg}^T = 2.0 (See Figure 3-83 for Aerodynamic Conditions)

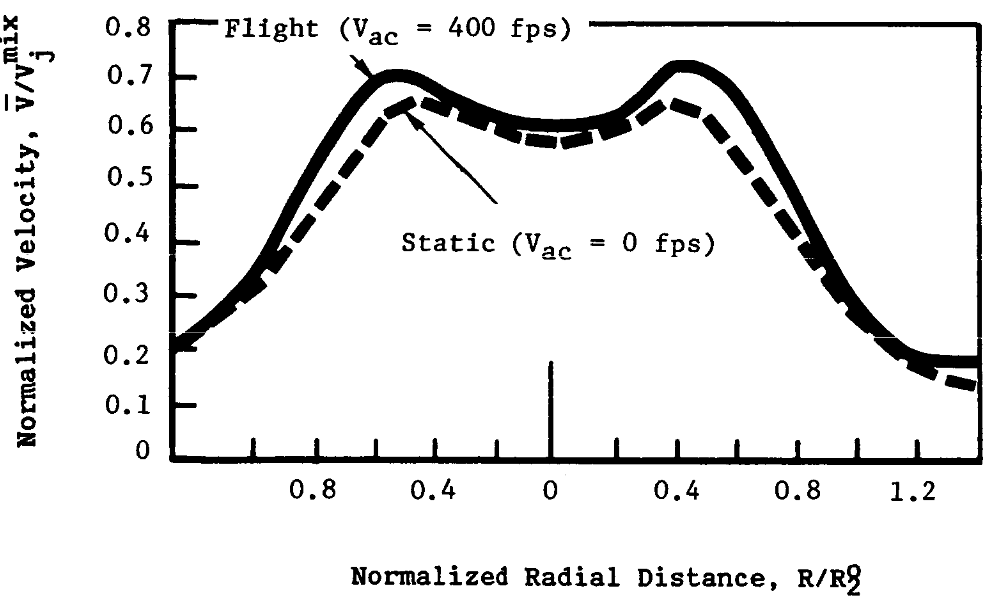

Figure 3-85. Influence of the Freejet on the Radial Profile of the 20-Shallow-Chute Nozzle in the Fully Developed Region ($X/D_{eq}^T = 6$). (See Figure 3-83 for Aerodynamic Conditions.)

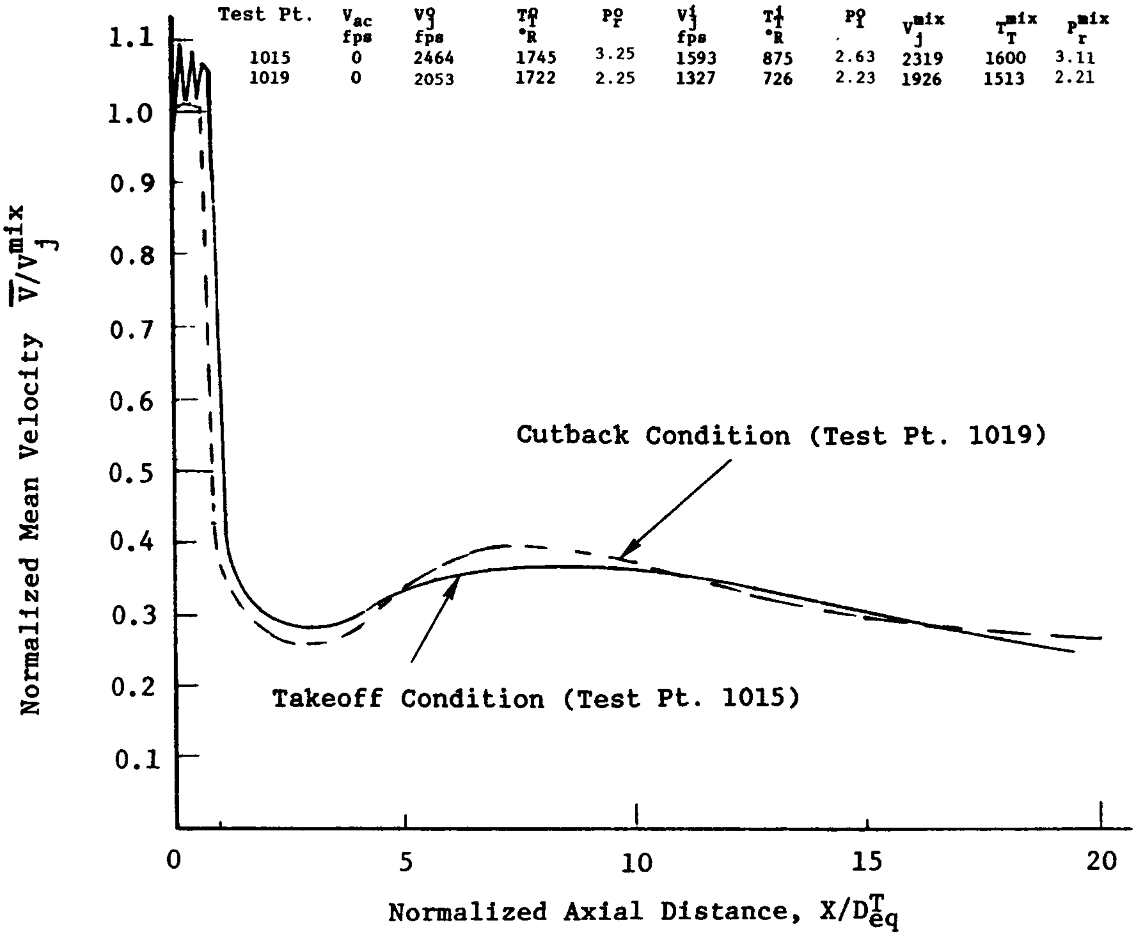

Test Pt.	V_{ac} fps	V_j^o fps	T_T^o °R	P_r^o	V_j^i fps	T_T^i °R	P_r^i	V_j^{mix}	T_T^{mix}	P_r^{mix}
1015	0	2464	1745	3.25	1593	875	2.63	2319	1600	3.11
1019	0	2053	1722	2.25	1327	726	2.23	1926	1513	2.21

Figure 3-86 Comparison of the Jet Flow Characteristics of the 20-Shallow-Chute Nozzle at Typical Takeoff and Cutback Conditions in Terms of the Axial Variation of Normalized Mean Velocity at the Midpoint of the Chute (Static).

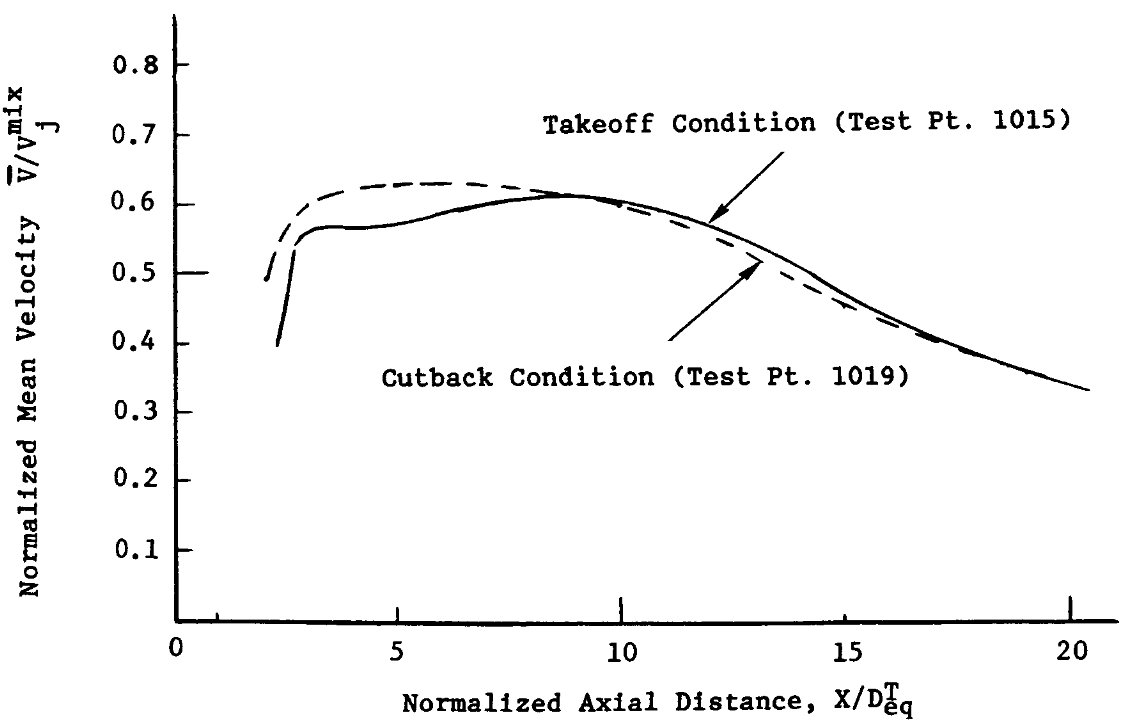

Figure 3-87. Comparison of the Jet Flow Characteristics of the 20-Shallow-Chute Nozzle at Typical Takeoff and Cutback Conditions in Terms of the Axial Variation of Normalized Mean Velocity Along the Nozzle Centerline (Static). (See Figure 3-86 for Aerodynamic Conditions.)

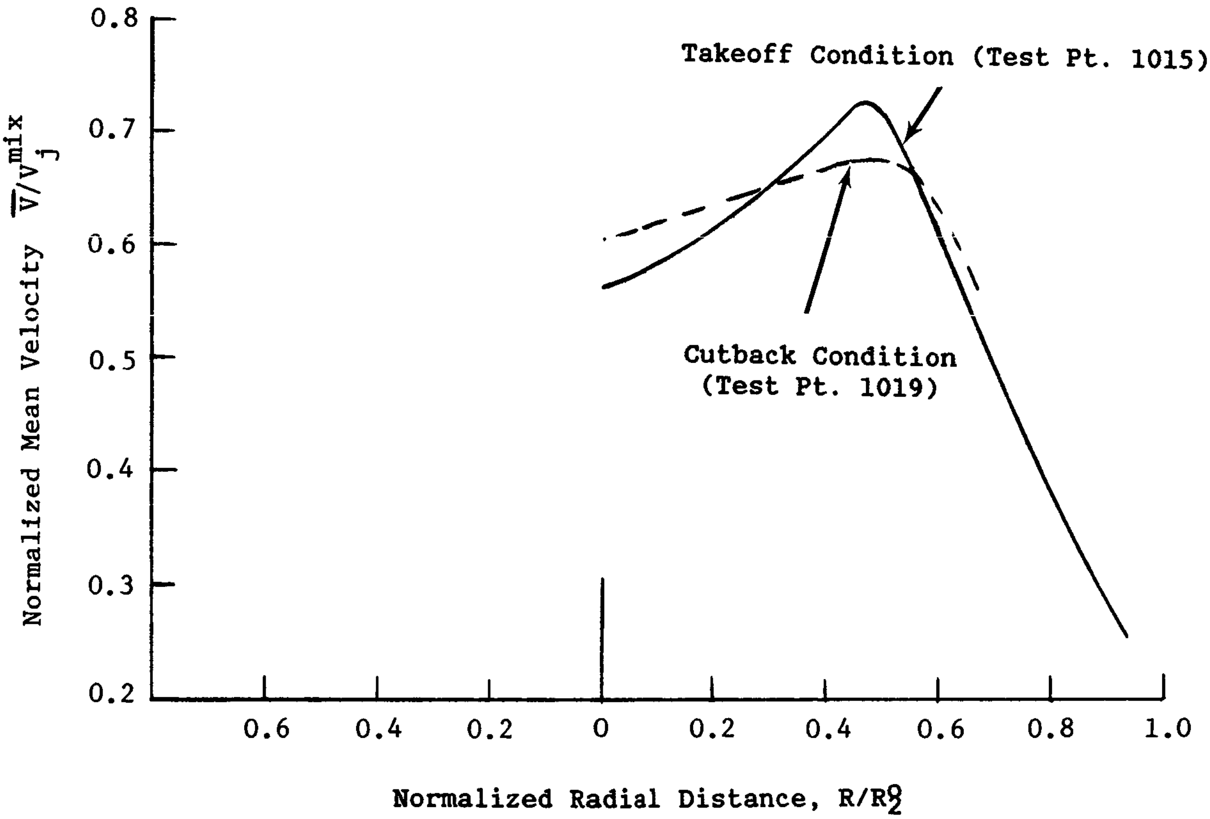

Figure 3-88. Comparison of the Jet Flow Characteristics of the 20-Shallow-Chute Nozzle at Typical Takeoff and Cutback Conditions in Terms of the Radial Variation of Normalized Mean Velocity at $X/D_{eq}^{T} = 4$ (Static). (See Figure 3-86 for Aerodynamic Conditions.)

velocity at X/D_{eq}^{T} = 4 for takeoff and cutback cases. The velocity profile for the cutback case is flatter compared to the takeoff case, indicating that the inverted velocity character for the cutback case is prematurely lost which is essentially at lower inner and outer jet velocities.

3.2.4 Influence of Inner Stream Termination on the Plume Decay

It was observed in Reference 2 that the presence of a "shockless" subsonic inner stream instead of a "shocked" supersonic inner stream considerably affected the entire shock cell structure of the coannular plug nozzle and resulted in substantial shock cell noise reduction of the nozzle. However, based on performance and other design considerations, a practicable AST cycle has to employ a supersonic inner stream. Hence, if the supersonic inner stream can be expanded in a shockless fashion, it could give substantial shock cell noise reduction for the entire nozzle, as did the shockless subsonic inner stream. The above rationale was utilized in choosing a convergent-divergent flowpath design for the inner stream of the 20-shallow-chute nozzle. The design Mach number for the inner stream was chosen to be 1.25 and the inner stream was expanded to the desired area ratio.

An LV study was conducted to observe the differences in the plume structures of the 20-shallow-suppressor nozzles employing a C-D flowpath (Model 10.2) and a convergent flowpath (Model 10.1) for the inner stream at the design Mach number. Figure 3-89 compares the influence of the inner stream termination on the radial distribution of normalized mean and turbulent velocities just downstream of the exit plane of the inner stream (@ X/D_{eq}^{T} = 0.8). Note the sudden jump in the mean velocity for both the models at $R/R_2^{o} \simeq 0.5 - 0.6$ indicating that the inner stream has not yet mixed with the outer stream. In the case of Model 10.1, the supersonic inner stream has not yet expanded to its design Mach number at X/D_{eq}^{T} = 0.8. Hence, the local static pressure is higher compared to that of Model 10.2 where the inner stream has been gradually expanded to the design Mach number. Hence, the inner stream for Model 10.1 is displaced radially outward compared to Model 10.2. The turbulent velocities for both the models as shown in Figure 3-89(b) indicate similar features indicating that the C-D termination has no noticeable effect on the turbulent velocities. The turbulent velocities reach peak values at $R/R_2^{o} \simeq 0.5 - 0.6$ for both nozzles, since it is the region of maximum velocity gradient between the inner and outer streams and hence maximum turbulent shear stress.

Next, the influence of the inner stream termination on the axial distribution of normalized mean velocity is studied (Figure 3-90). The axial traverse is taken at a radial location corresponding to the midpoint of the inner stream. For Model 10.1, there is a sudden dip in the mean velocity indicating the presence of a shock cell; whereas for Model 10.2, the mean velocity is uniformly varying indicating the absence of the same. However, it is to be noted that the flow for $X/D_{eq}^{T} \leq 2$ follows the plug which has a half cone angle of 15° whereas the traverse of the LV system is parallel to the jet nozzle centerline. Hence, the extent of shock effectiveness of the inner stream cannot be fully evaluated. The influence of the inner stream termination on the plume is seen to decrease for $X/D_{eq}^{T} > 1.5$.

Test Pt.	V_j^o fps	T_T^o °R	P_r^o	V_j^i fps	T_T^i °R	P_r^i	V_j^{mix}	$T_{T_O}^{mix}$ °R	P_r^{mix}
1027	2455	1734	3.24	1602	865	2.70	2289	1565	3.09
1015	2464	1745	3.25	1543	825	2.63	2319	1600	3.11

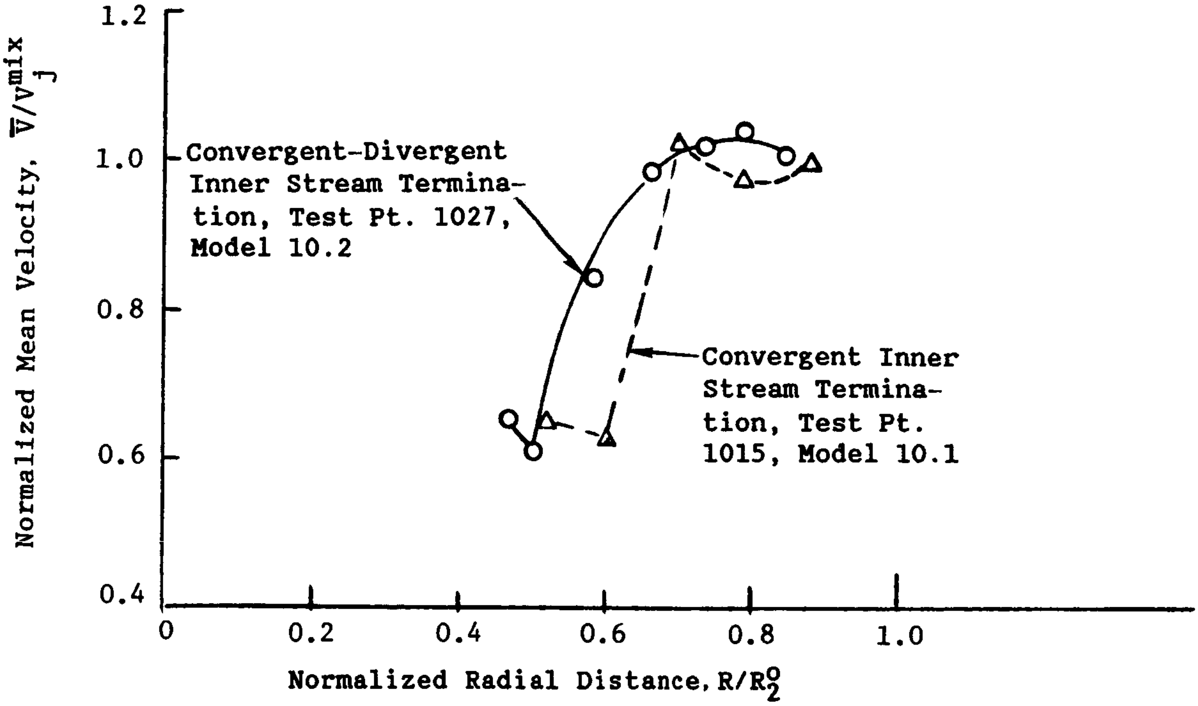

(a) Normalized Mean Velocity

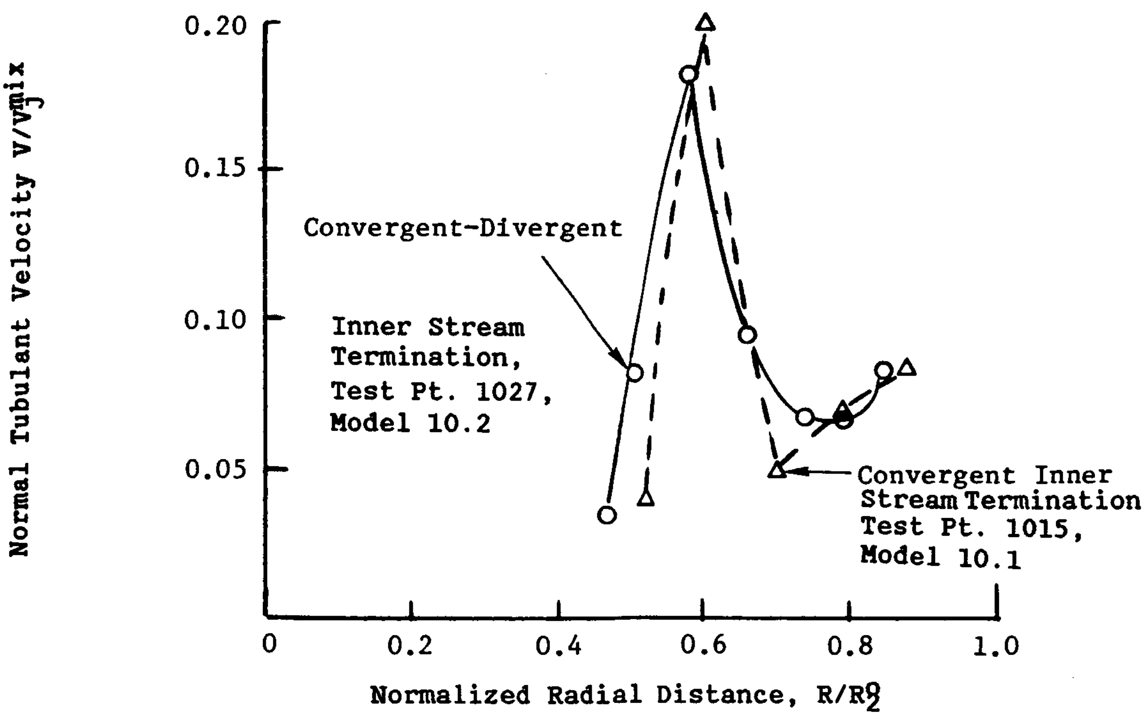

(b) Normalized Turbulent Velocity

Figure 3-89. Influence of Inner Stream Termination on the Radial Distribution of Normalized Mean and Turbulent Velocity for 20-Shallow-Chute Nozzle Just Downstream of Inner Stream Exit at X/D_{eq}^T = 0.8).

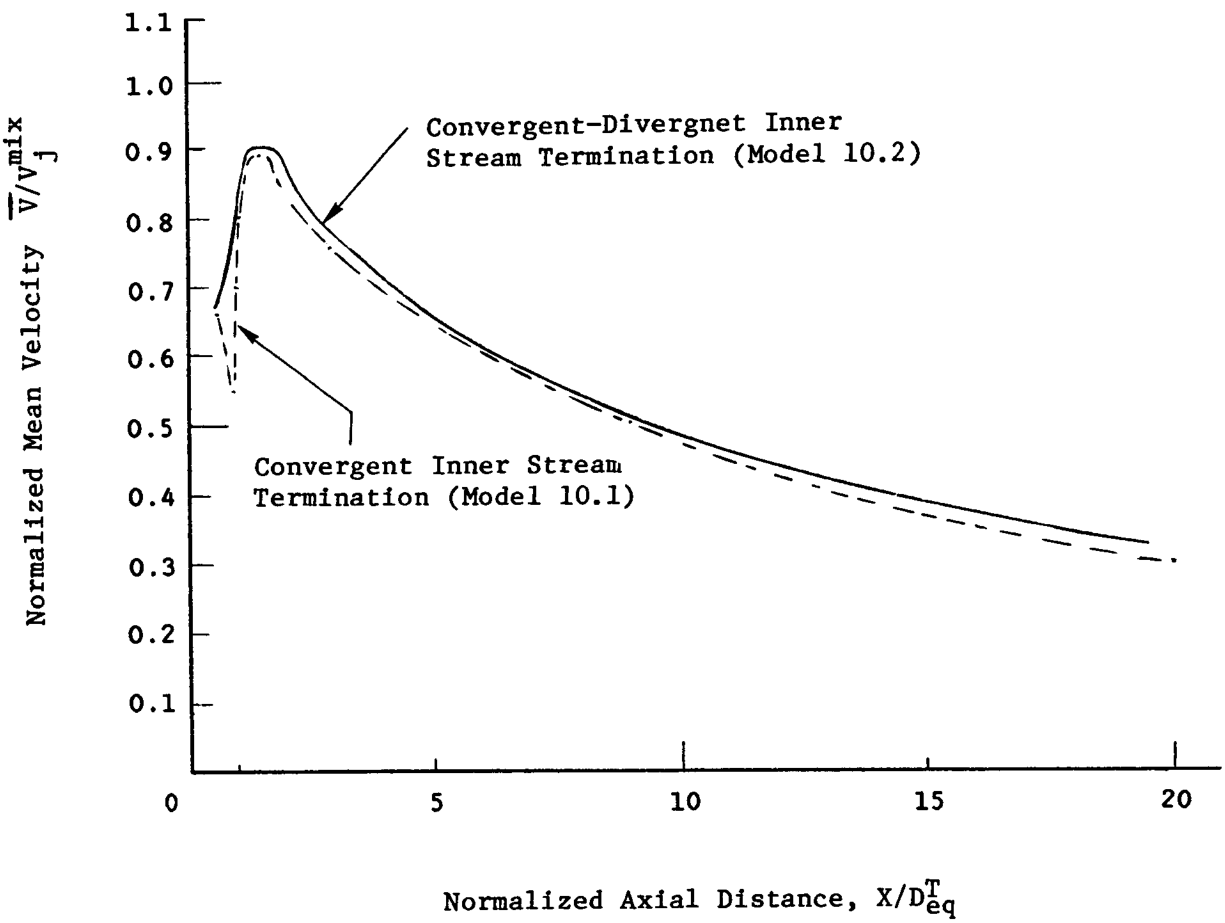

Figure 3.90. Influence of the Inner Stream Termination on the Axial Variation of the Normalized Mean Velocity at the Midpoint of the Inner Stream Exit Plane. (See Figure 3-89 for Aerodynamic Conditions.)

3.2.5 Concluding Remarks

The diagnostic LV measurements of the jet velocities of the 20-shallow-chute suppressor nozzle have given valuable insight into the mixing characteristics of the nozzle. The following are the significant concluding remarks of this study:

- The mixing rate of the 20-shallow-chute suppressor nozzle is considerably higher than that of conic and coannular nozzles both for static and free-jet conditions and thus has a faster mean velocity decay rate compared to the conic and coannular nozzles.

- The influence of free jet on the jet plume of the 20-shallow-chute nozzle is to reduce the turbulent shear stress and the decay rate and to make the jet plume grow radially outward.

- The jet flow characteristics of the 20-shallow-chute nozzle at takeoff and cutback conditions look similar except near the chute exit plane. A shock cell structure is observed in front of the chutes for the takeoff case and no such structure for the cutback case due to the higher pressure ratio of the takeoff case. The radial profiles for the cutback case appear flatter indicating that the inverted velocity character for low jet velocity conditions is prematurely lost.

- The full extent of the effectiveness of the C-D termination for the inner stream could not be evaluated. However, the influence of the C-D termination was exhibited in terms of static pressure variations at the inner stream exit plane.

3.3 DIAGNOSTIC BASE PRESSURE RESULTS WITH THE SIMILITUDE 20-SHALLOW-CHUTE SUPPRESSOR NOZZLE (Model 10.1)

In addition to the acoustic and LV tests with the similitude 20-shallow-chute suppressor nozzle (Model 10.1), experiments were performed to obtain static pressure measurements in the base pressure regions of the chutes of the similitude mechanical suppressor. The objective of these tests was to obtain an assessment of the influence of the suppressor total temperature (T_T^o), over a range of its operating pressure ratio (P_r^o), on the suppressor base pressure and hence on the nozzle thrust coefficient.

The suppressor instrumentation and the methodology adopted for estimating the base pressure drag in the chute are presented in Appendix III. The aerodynamic flow conditions of the tests along with the measured data are to be found in the Volume II of the CDR of this program. Significant results obtained from these measurements are summarized in this subsection.

Figures 3-91 through 3-97 summarize the significant parameters as described below:

Figure 3-91: Suppressor base to ambient pressure ratio versus outer nozzle pressure ratio at various simulated velocities

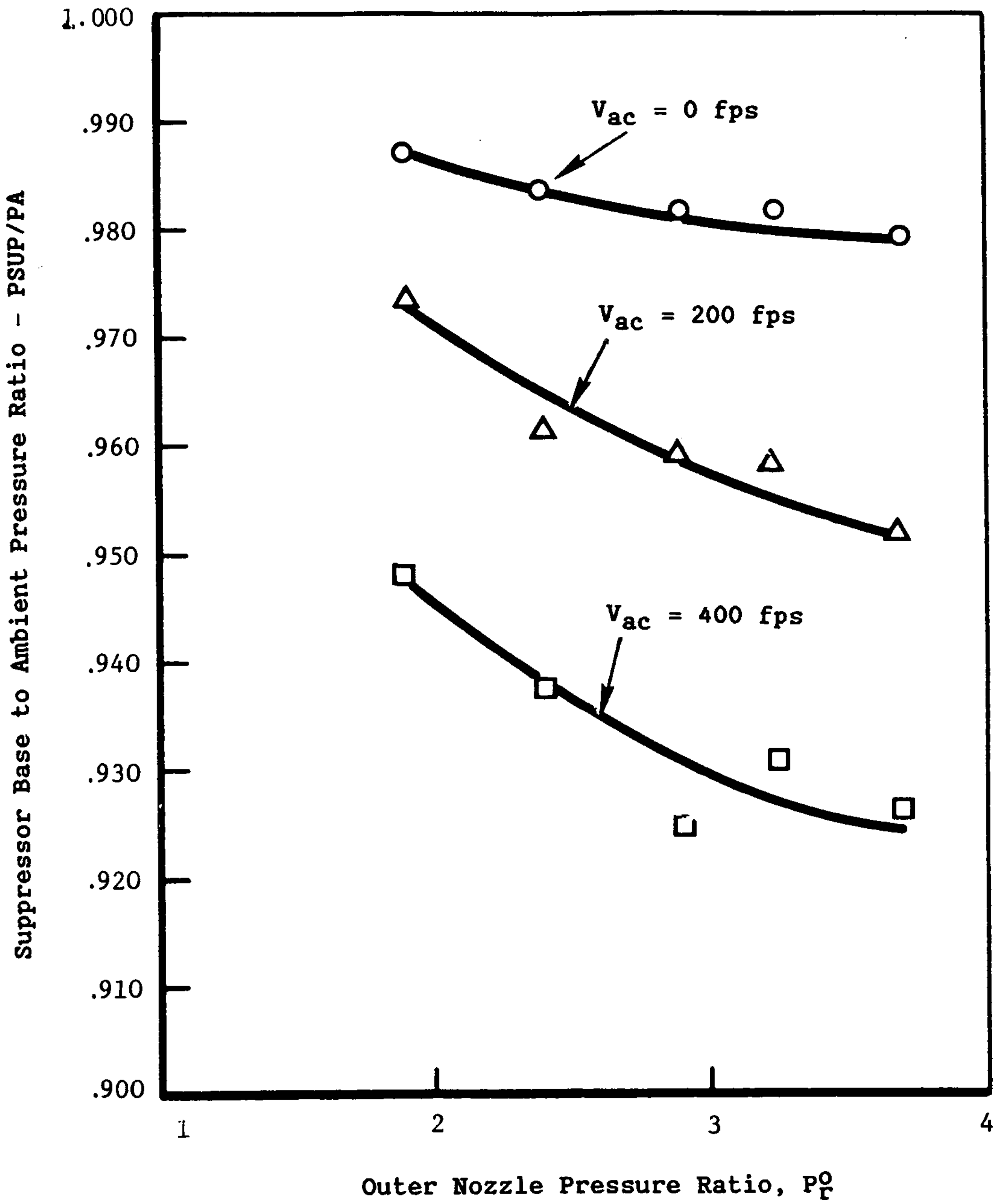

Figure 3-91. Suppressor Base to Ambient Pressure Ratio Versus Outer Nozzle Pressure Ratio at Various Simulated Flight Velocities.

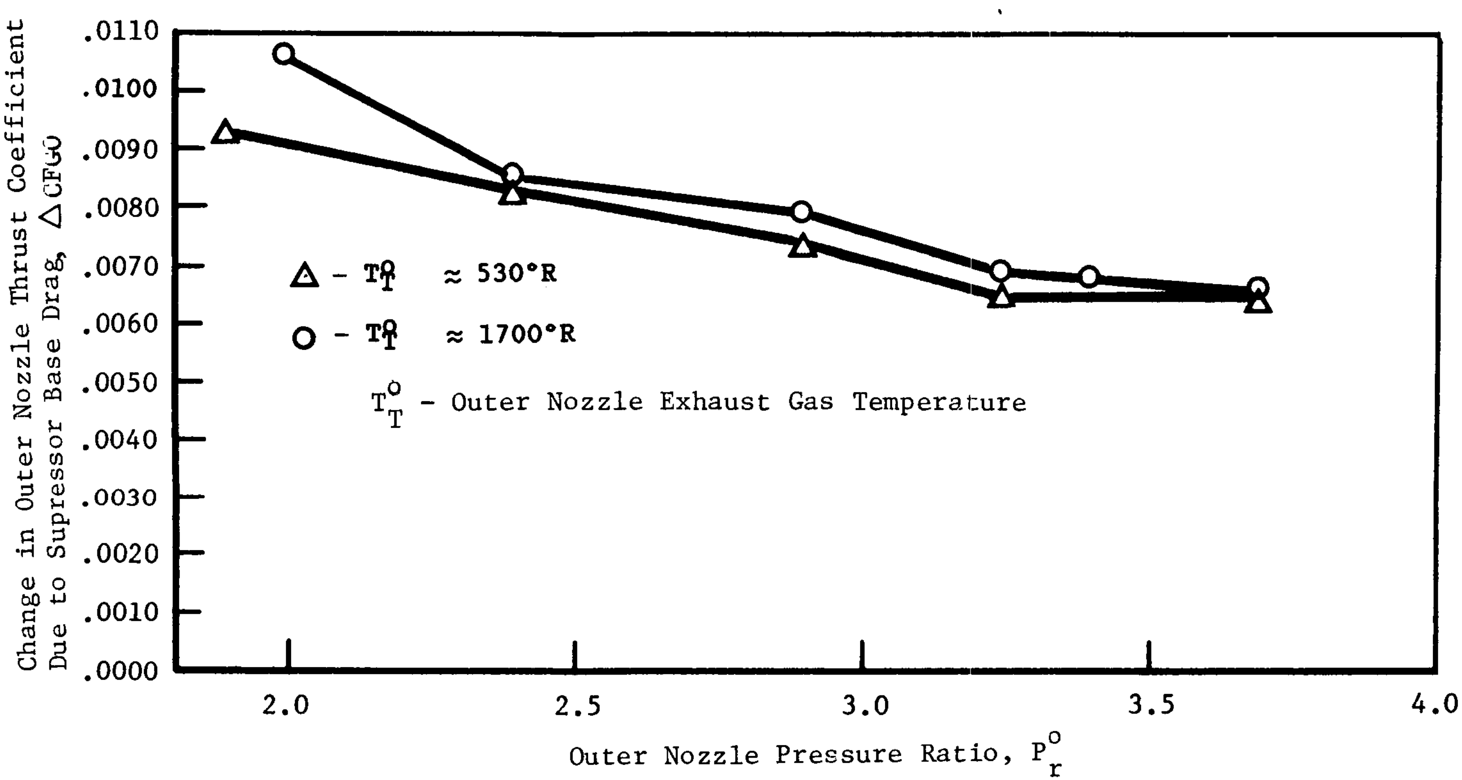

Figure 3-92. Change in Outer Nozzle Thrust Coefficient Versus Outer Nozzle Pressure Ratio at Different Gas Total Temperatures.

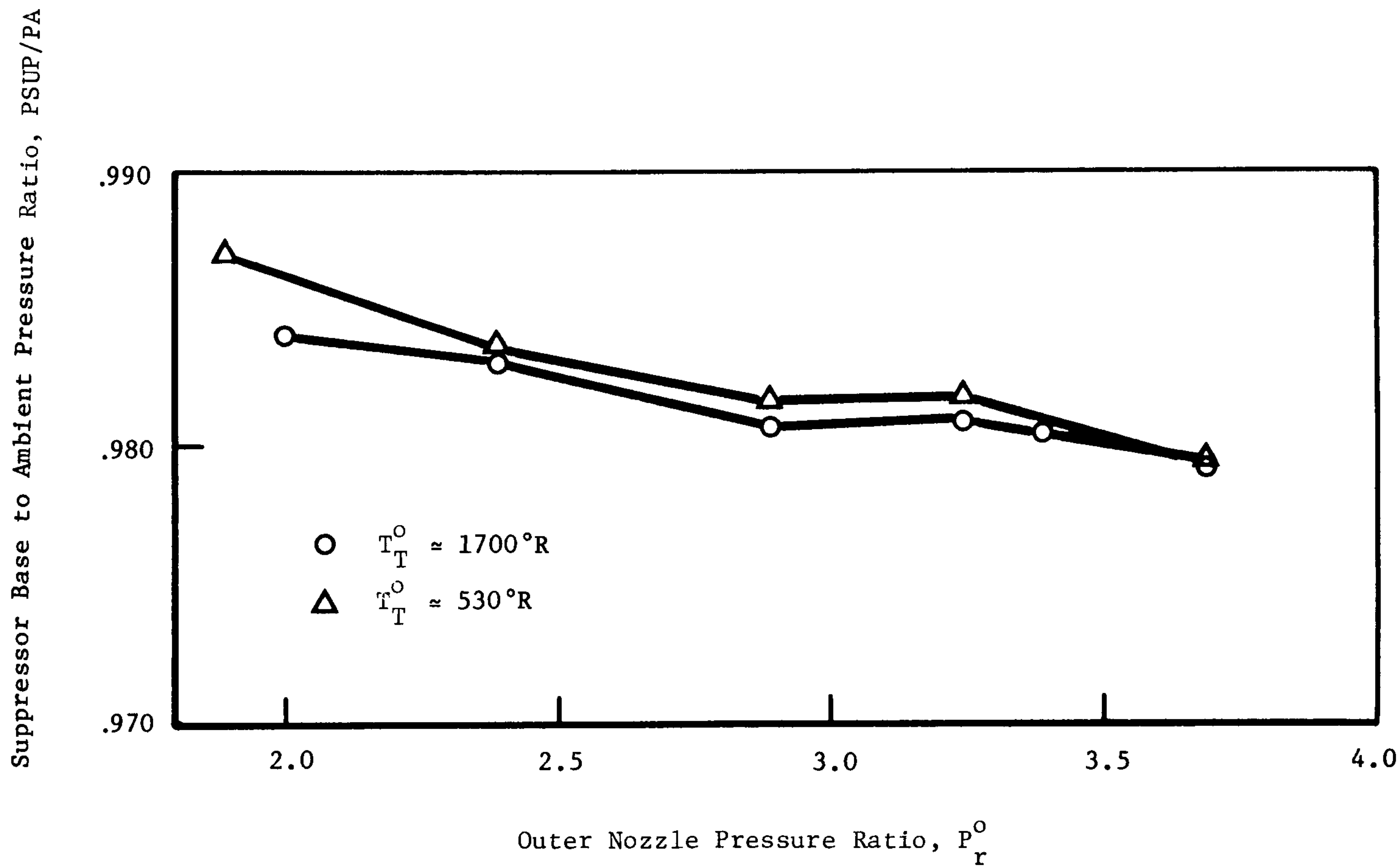

Figure 3-93. Suppressor Base to Ambient Pressure Ratio Versus Outer Nozzle Pressure Ratio at Different Gas Total Temperatures.

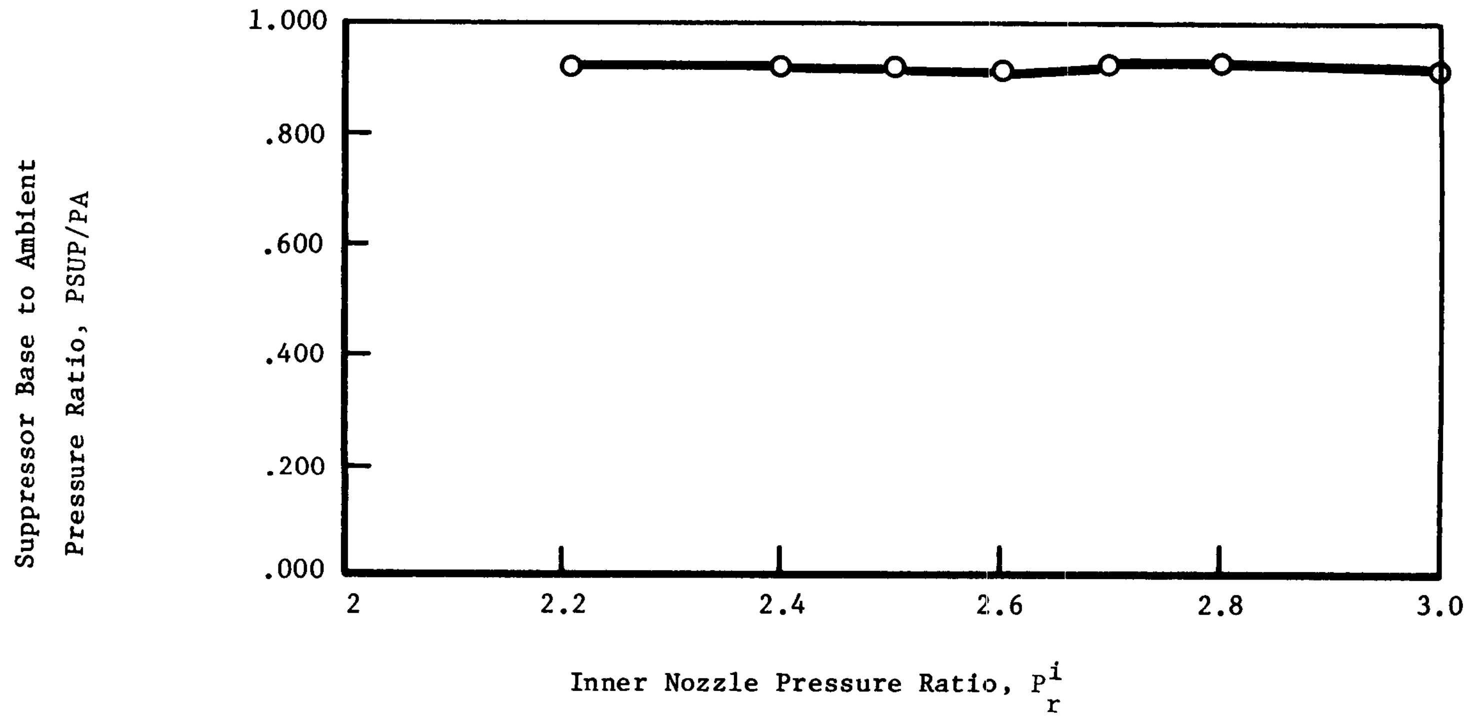

Figure 3-94. Suppressor Base to Ambient Pressure Ratio Versus Inner Nozzle Pressure Ratio, Holding the Outer Nozzle Pressure Ratio Constant at 3.24 (V_{ac} = 400 fps).

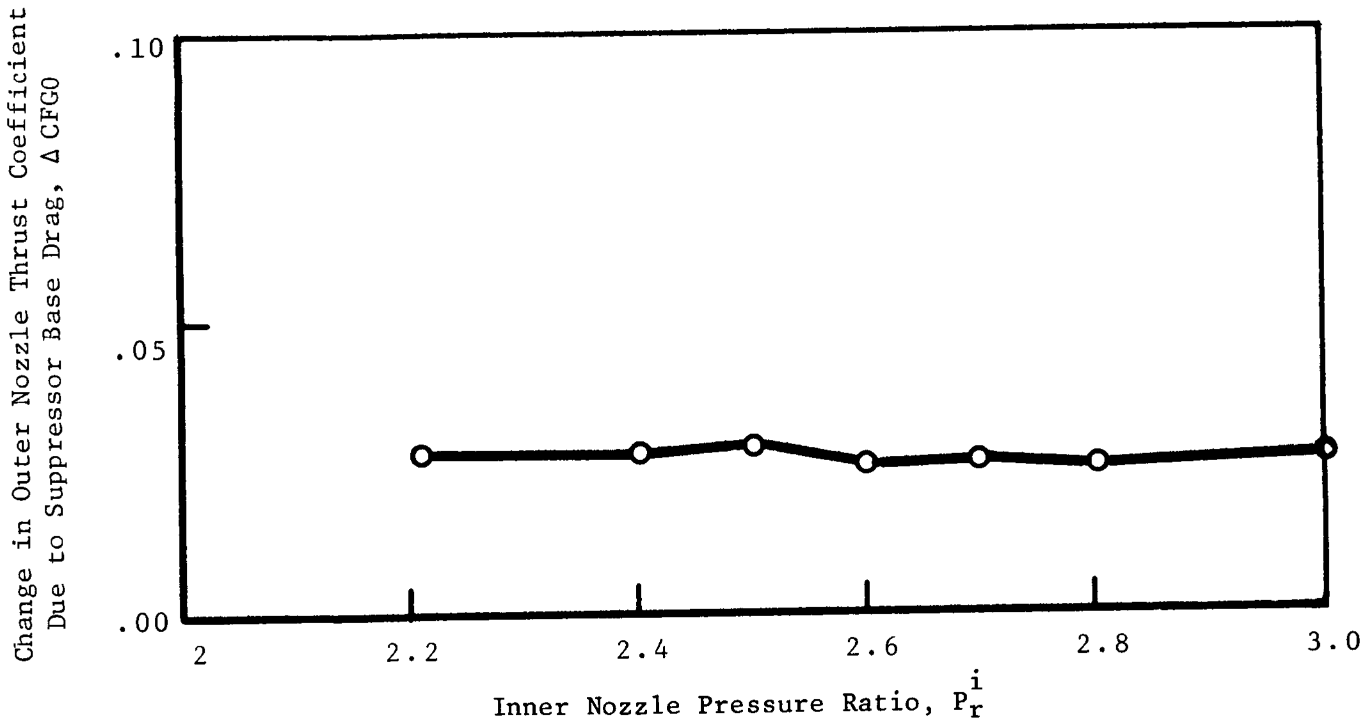

Figure 3-95. Change in Outer Nozzle Thrust Coefficient Versus Inner Nozzle Pressure Ratio, Holding the Outer Nozzle Pressure Ratio Constant at 3.24 (Velocity of Aircraft, V_{ac} = 400 fps).

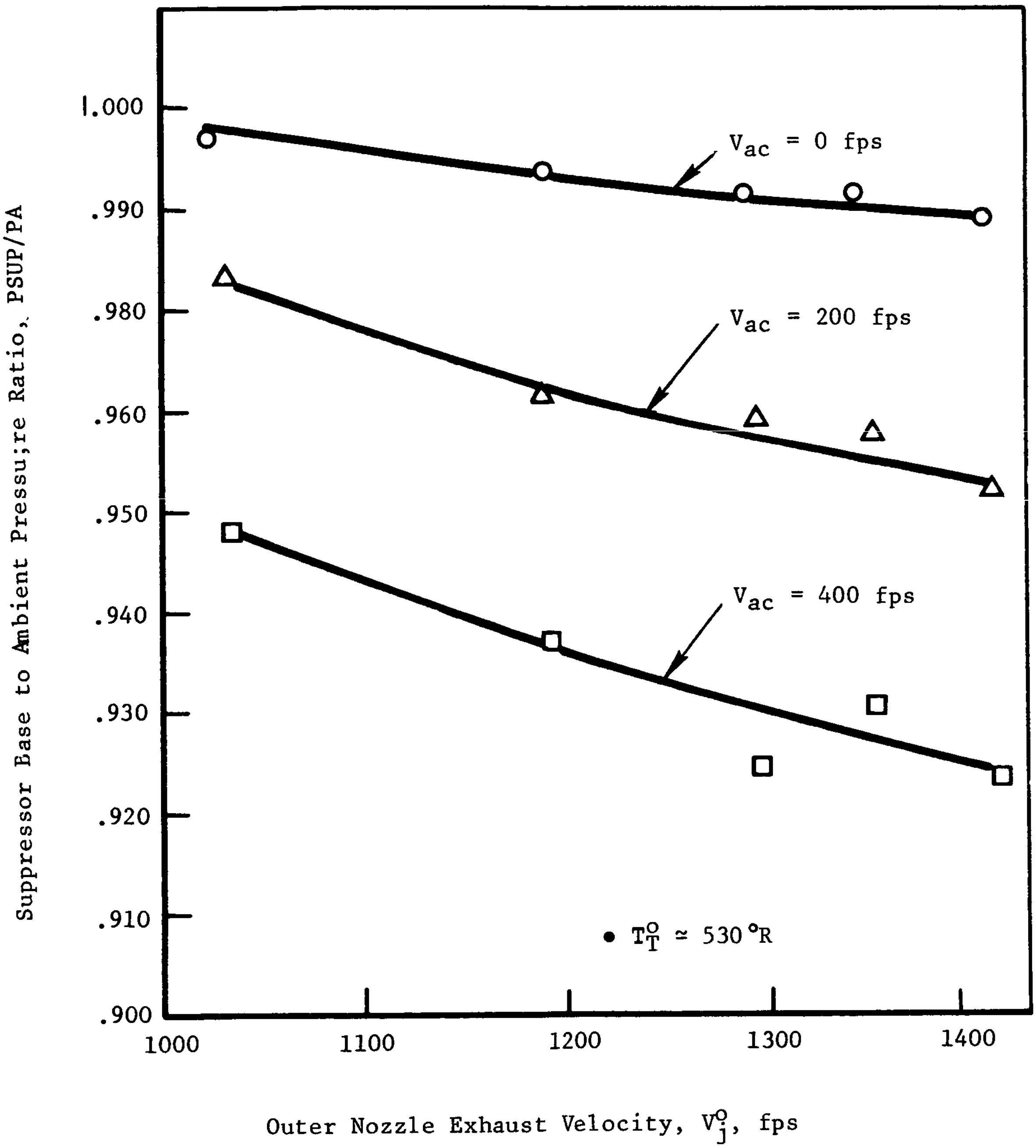

Figure 3-96. Suppressor Base to Ambient Pressure Ratio Versus Outer Nozzle Exhaust Velocity at Different Aircraft Velocities.

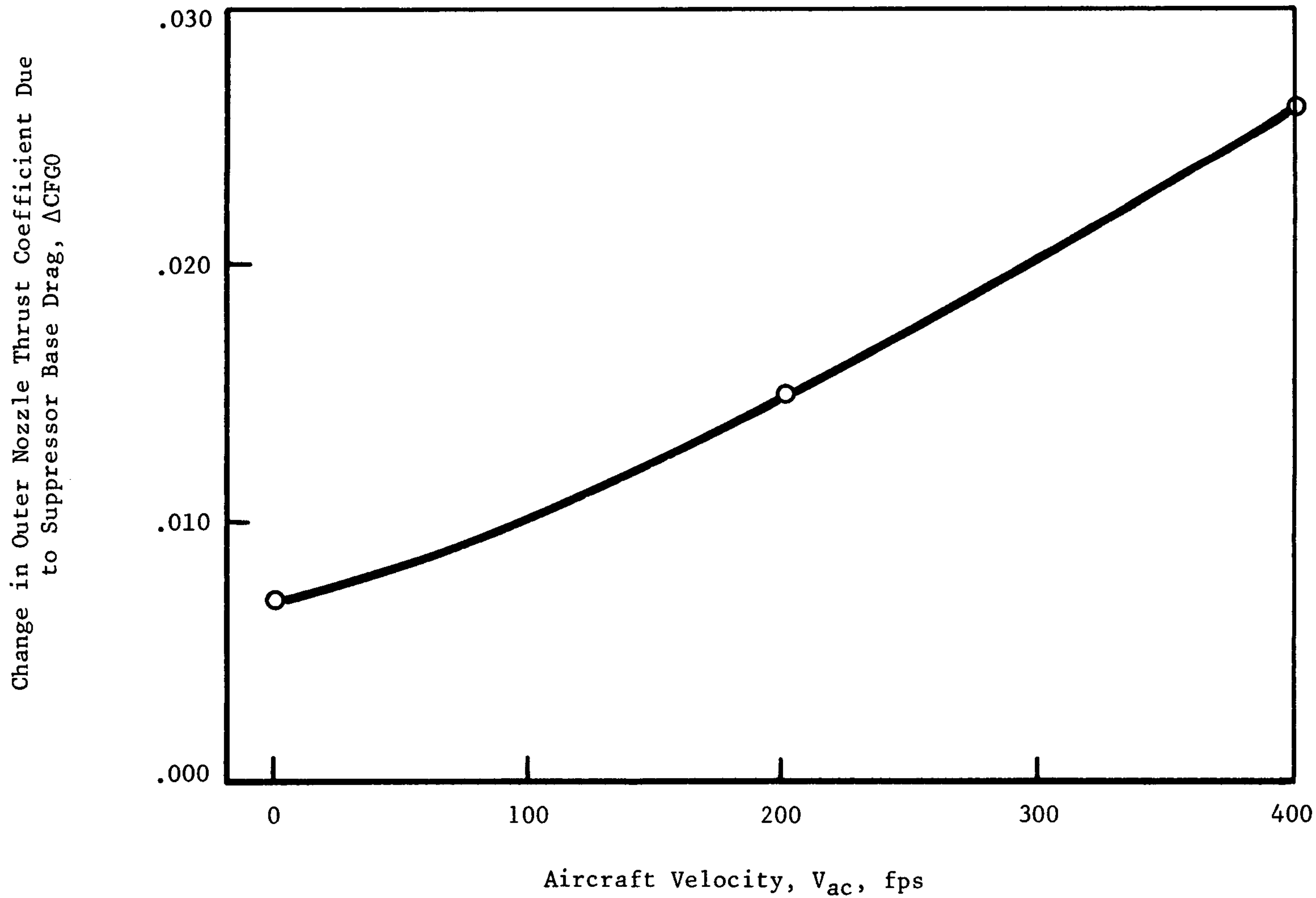

Figure 3-97. Change in Outer Nozzle Thrust Coefficient Versus Aircraft Velocities Holding Inner and Outer Nozzle Pressure Ratios Constant at 3.2 and 3.25, Respectively, (Outer Nozzle Exhaust Velocity $\simeq$ 2460 fps).

Figure 3-92:	Change in outer nozzle thrust coefficient versus outer nozzle pressure ratio at different gas total temperatures
Figure 3-93:	Suppressor base to ambient pressure ratio versus outer nozzle pressure ratio at different gas total temperatures
Figure 3-94:	Suppressor base to ambient pressure ratio versus inner nozzle pressure ratio, holding the outer nozzle pressure ratio constant at 3.24
Figure 3-95:	Change in outer nozzle thrust coefficient versus inner nozzle pressure ratio, holding the outer nozzle pressure ratio constant at 3.24
Figure 3-96:	Suppressor base to ambient pressure ratio versus outer nozzle exhaust velocity at different aircraft velocities
Figure 3-97:	Change in outer nozzle thrust coefficient versus aircraft velocities holding inner and outer nozzle pressure ratios constant at 3.2 and 3.25, respectively.

Based on these figures, the following observations can be made for the similitude 20-shallow-chute suppressor nozzle (Model 10.1):

- Over the pressure ratios between 1 and 4, the inner nozzle flow does not influence suppressor base drag.
- Outer nozzle exhaust gas total temperature influences suppressor base drag only slightly.
- Suppressor base drag increases with aircraft velocity as well as outer nozzle exhaust velocity.

Hence, it can be concluded that the suppressor base drag estimation can be made with tests using high pressure air at room temperature.

4.0 ENGINEERING SPECTRAL PREDICTION METHOD FOR MECHANICAL SUPPRESSORS

As part of a NASA Lewis/General Electric Contract NAS3-20619, a prediction method was developed to predict the spectral characteristics of jet mixing and shock cell noise from coannular plug nozzles operated in the inverted velocity mode (Ref. 18). The prediction method of Reference 18 is based on a modern theoretical development (M*G*B*) (Ref. 19) developed by the General Electric Company which has unified concepts of source spectrum, convective amplification, and fluid shrouding effects to predict the jet mixing noise from the turbulent eddies. In this method, the jet plume is subdivided into discrete volume elements each being the size of a turbulent eddy and associated with a source strength and frequency. The convection amplification and fluid shrouding effects on each turbulent eddy are evaluated based on the local aerodynamic conditions and its location. In order to keep the engineering spectral prediction procedure of Reference 18 simple enough, yet use these physical concepts, a semiempirical approach was adopted to model the source spectrum, convection amplification and fluid shrouding effects for a coannular plug nozzle operated in the inverted velocity profile mode. A natural extension is to see if the engineering sprectral prediction procedure can be generalized for other nozzle concepts such as mechanical suppressors or conventional high bypass, coannular jet nozzles. Reference 20 describes the extension to the prediction to predict the jet mixing noise of high bypass coannular jet nozzles. The object of the present study is to extend the prediction procedure developed in Reference 18 to predict the sprectral characteristics of mechanical suppressor nozzles in general and 20-shallow-chute suppressor nozzle in particular.

4.1 METHODOLOGY OF PREDICTION PROCEDURE

The methodology for predicting jet mixing and shock cell noise for mechanical suppressor nozzles closely follows that for coannular plug nozzles with inverted velocity profile and consists of the following steps:

- Identify the appropriate velocity and length scales for the premerged and merged portions of the jet noise spectrum
- Establish the source spectrum
- Model the convective amplification effects due to convecting turbulent eddies
- Evaluate the acoustic mean flow interaction in terms of refraction effects and mean flow convective amplification effects
- Evaluate the shock cell noise of under- or over-expanded supersonic flows
- Determine the influence of flight on jet and shock noise.

4.1.1 Source Spectrum and Assumed Characteristic Velocity and Length Scales

Source spectrum refers to the jet mixing noise spectrum without air attenuation at $\theta_i = 90°$. At $\theta_i = 90°$, there are no convective amplification effects due to eddies as the eddies are moving normal to the observer and there are no acoustic mean flow interactions as the mean flow cannot refract rays perpendicular to itself and there are no convective effects of mean flow at an observer normal to itself. The source spectrum for inverted flow nozzles consists of two portions, namely, the high frequency portion which is generated by the small scale eddies of the high velocity outer jet before it merges with the inner jet and the low frequency portion which is generated by the large scale eddies of the mixed stream. For mechanical suppressors, the characteristic velocity and length scales chosen to predict the source spectrum are:

	Premerged Spectrum (i.e., High Frequency Spectrum)	Merged Spectrum (i.e., Low Frequency Spectrum)
Velocity scale	Outer jet velocity, V_j^o	Mass averaged velocity, V_j^{mix}
Length scale	Suppressor element hydraulic diameter, D_{hyd}^o	Equivalent conic nozzle diameter based on total flow area, D_{eq}^T

where, $D_{eq}^T = \sqrt{\frac{4}{\pi}(A^i + A^o)}$ with A^i = Inner stream flow area and A^o = Outer (suppressor) stream flow area

and $D_{hyd}^o = \frac{4A^e}{p^e}$ with A^e = Outer (suppressor) stream element flow area, p^e = Noise generating perimeter of suppressor stream element (Figure 4-1)

Also, $A^e = \frac{\text{Outer (suppressor) stream flow area}}{\text{Number of elements}}$

and $p^e = w_{flow}^o + 2(R_2^o - R_1^o)$

The data base utilized to establish the locations of peak Strouhal numbers for the merged and premerged spectra consists of the 20-, 30-, and 40-shallow-chute suppressors tested by G.E. under FAA-DOT Contract No. DOT-OS-30034 (Ref. 11) and modified DOT 20-shallow-chute suppressor nozzle tested under the present program. With the choice of the length and velocity scales outlined as above, the acoustic data base for suppressor nozzles was used to determine the normalized spectrum. As in the case of coannular plug nozzles, the peak Strouhal number for the low frequency (i.e., merged) portion of the spectrum is observed to be correlated by:

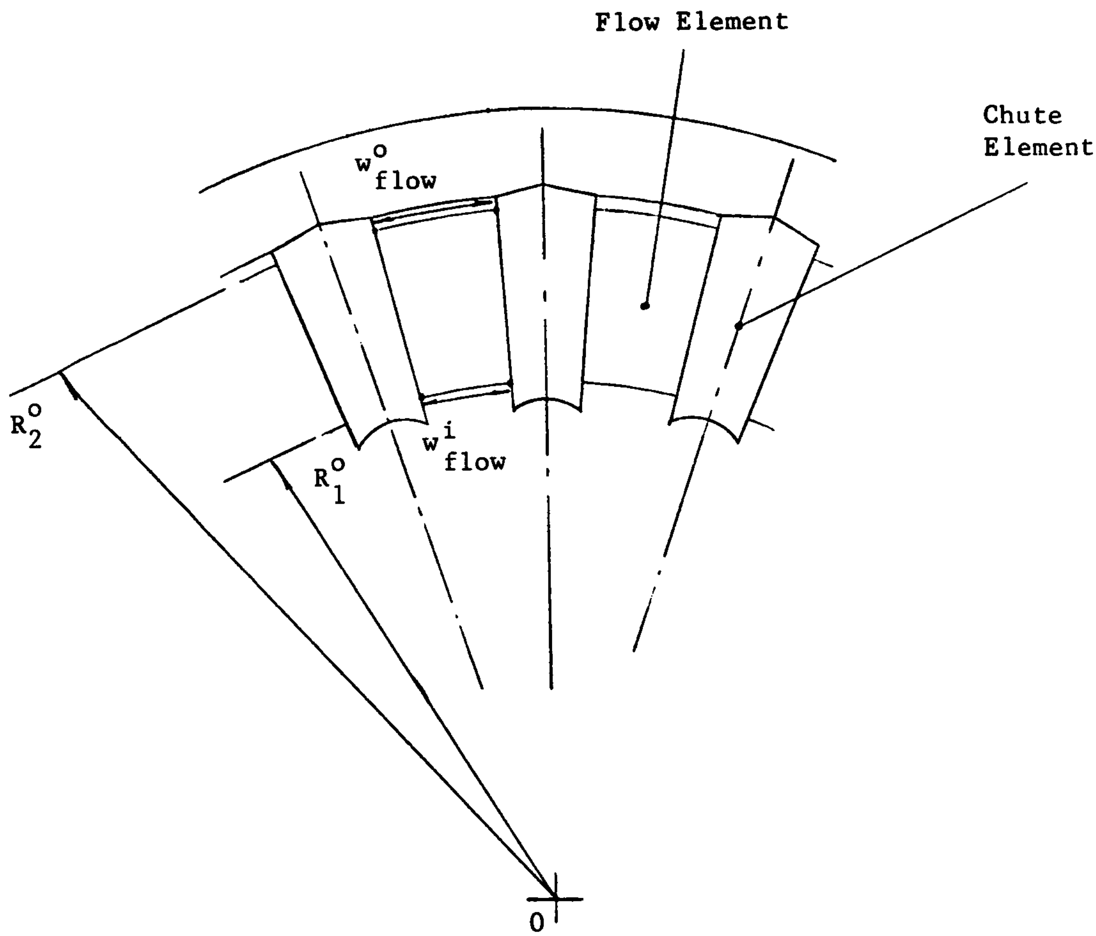

Figure 4-1. Typical Chute Suppressor Element Geometry.

$$\frac{f_p^{LF}\ D_{eq}^T}{V_j^{mix}} \left\{ \frac{T_T^{mix}}{T_{amb}} \right\}_{eff} = 0.9 \qquad (1)$$

where $\left\{ \frac{T_T^{mix}}{T_{amb}} \right\}_{eff} = 0.65 \left\{ \frac{T_T^{mix}}{T_{amb}} \right\} + 0.35$

with T_T^{mix} = Total temperature of the mass averaged flow

and T_{amb} = Ambient temperature.

The SAE method (Ref. 21) employs a similar equation to Equation 1 to predict the peak Strouhal number for conic nozzles. Again, the peak Strouhal number for the high frequency (i.e., premerged) portion of the spectrum for suppressors 'correlates by the same relationships as for coannular plug nozzles and is given by

$$\frac{fp^{HF}\ D_{hyd}^o}{V_j^o} \left\{ \frac{T_T^o}{T_{amb}} \right\}_{eff} = 1.18 \qquad (2)$$

where $\left\{ \frac{T_T^o}{T_{amb}} \right\}_{eff} = 0.65 \left\{ \frac{T_T^o}{T_{amb}} \right\} + 0.35$

with T_T^o = Total temperature of the suppressor (outer) stream.

The above choice of velocity and length scales for mechanical suppressors was observed to predict correctly the locations of peak frequencies. As an initial guess, the shape of the lossless source spectrum for the merged and premerged portions of the mechanical suppressors was assumed to be identical to those of coannular plug nozzles; and the results indicated that the shape of the spectra had to be changed. The acoustic power distribution into the various frequency bands depends on factors such as the jet plume decay rate and the geometric shape of the nozzle planform. Since there are large differences in the above factors for the coannular plug nozzles and mechanical suppressors, a "universal" source spectrum valid for all types of nozzles cannot be proposed. Hence, the source spectra for the merged and premerged portions for the mechanical suppressors had to be derived from the data base. The subsequent procedure was followed: the coannular plug nozzle source spectra were assumed as an initial guess. Subsequent reshaping was made by comparing it with the lossless data for mechanical suppressors. Simultaneous attention was given to include the shock cell noise component at $\theta_i = 90°$ (see Section 4.2.4 for details regarding modeling shock cell noise component).

A normalized low frequency source spectrum is extracted from the data base by incorporating the well-established Lighthill velocity (Ref. 22) and Hoch jet density dependence laws (Ref. 23) and spherical spreading law and is given by:

$$SPLN^{LF}(f) = SPL^{LF}(f) - C \log_{10} (V_j^{mix}/a_{amb})$$

$$- 10 \log_{10} (\rho_j^{mix}/\rho_{amb})^{\omega} - 10 \log \quad (A^T/R^2) \qquad (3)$$

where

$$C^* = \begin{cases} 75 \text{ for } (V_j^{mix}/a_{amb}) \leq 2.0 \\ \text{and} \\ 80 \text{ for } (V_j^{mix}/a_{amb}) > 2 \end{cases}$$

a_{amb} = Ambient speed of sound

ρ_j^{mix} = Jet density corresponding to the mass averaged jet conditions

ρ_{amb} = Ambient air density

ω = Jet density exponent of Hoch (Ref. 23)

A^T = Total flow area

R = Distance to the far field from jet nozzle exhaust plane

Figure 4-2 compares the normalized low frequency spectra from coannular plug nozzles and mechanical suppressors. Note that the peak level for suppressors is lower, which is due to the rapid decay of the jet in the case of suppressors. This fact is indicated by the measured mean and turbulent velocity variation along the nozzle centerline by a laser velocimeter for both coannular plug nozzle from NASA Contract NAS3-20619 (Ref. 2) and the similitude 20-shallow-chute suppressor at a typical takeoff condition (Figure 4-3). The mean velocity decay is faster and the turbulent velocity is lower for normalized axial distance, $(x/D_{eq}^T) > 5$ for the suppressor compared to the coannular plug nozzle. The large scale eddies which radiate the low frequency noise are predominantly located at regions far downstream of the jet exhaust plane, (typically $(x/D_{eq}^T) \geq$ 4-5). These large scale eddies are traveling slower in the case of suppressors. Also, the turbulence intensity $[(v')^2]$ of these eddies is lower for the suppressor. Hence, the peak noise

---

*Though the classical Lighthill's theory of jet noise predicts a V_j^{8th} power law, the data supports a $V_j^{7.5th}$ power law for a jet Mach number ≤ 2 and V^{8th} power law for a jet Mach number > 2.

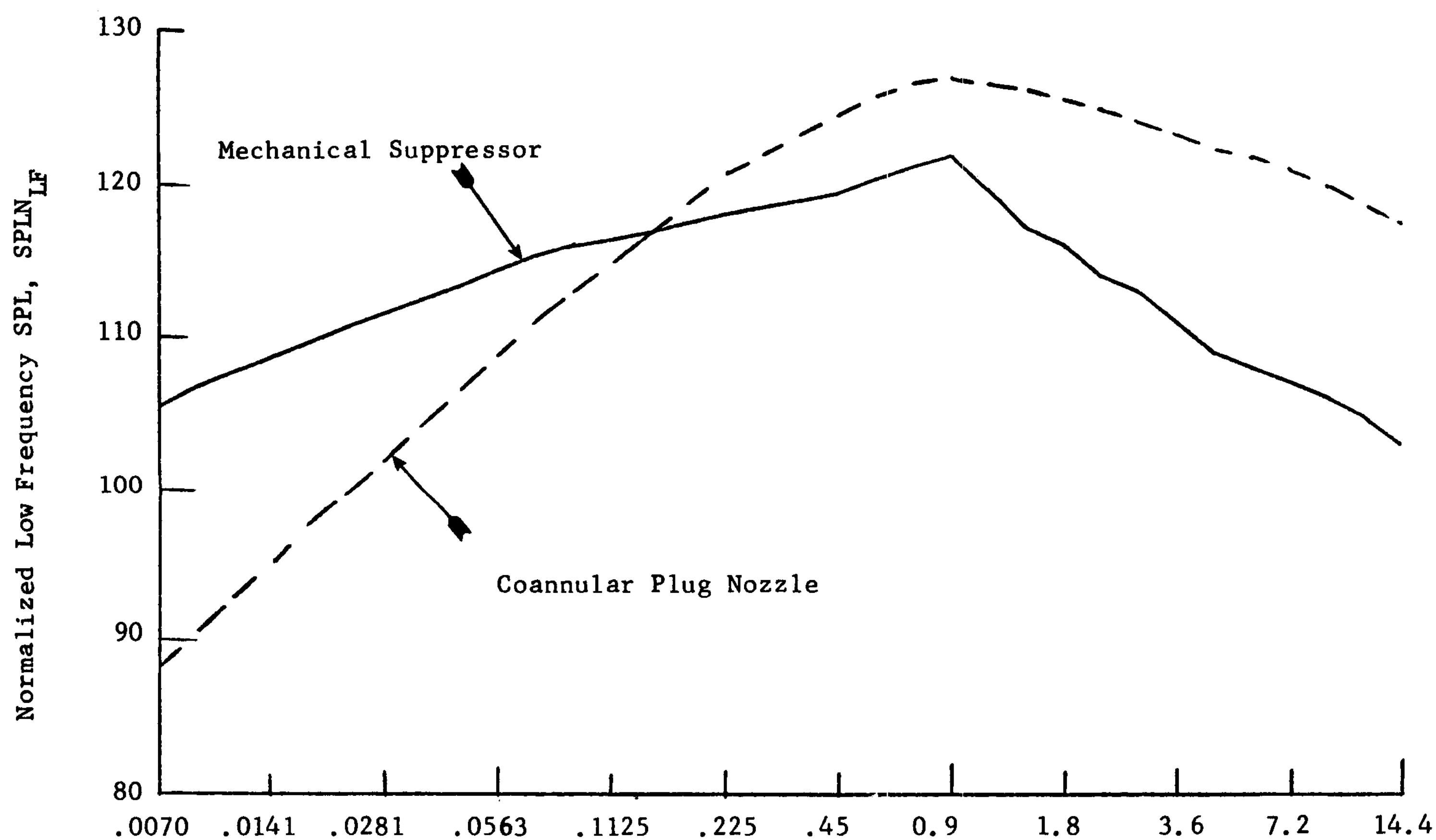

Mixed Stream Strouhal Number, $S_t^{mix} = \frac{f\, D_{eq}^{T}}{V_j^{mix} - V_{ac}} \times \left(\frac{T_T^{mix}}{T_{amb}}\right)_{eff}$

Figure 4-2. Normalized Low-Frequency Source Spectrum at $\theta_i = 90°$.

Model	Model No.	A_{Total} in^2	Test Point	V_j^{mix} fps	T_T^{mix} ^oR	P_r^{mix}
20 Shallow Chute	10.2	24.36	1015	2300	1585	3.09
Coannular Plus Nozzle	3	21.06	301	2246	1506	3.10

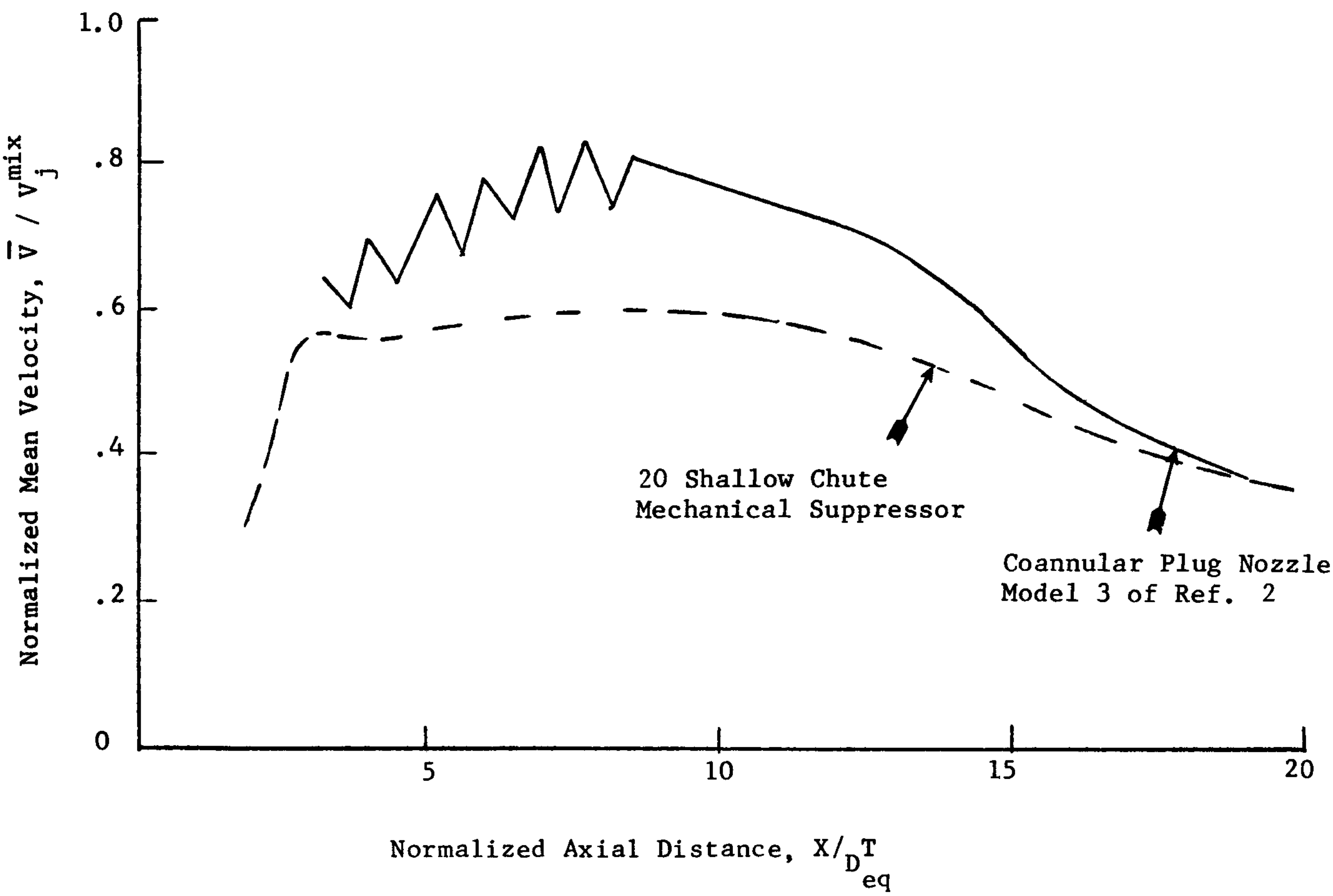

(a) Normalized Mean Veloicity

Figure 4-3. Comparison of Typical Nozzle Centerline Velocity Characteristics of a Mechanical Suppressor Nozzle and a Coannular Plug Nozzle, as Measured by Laser Velocimetry.

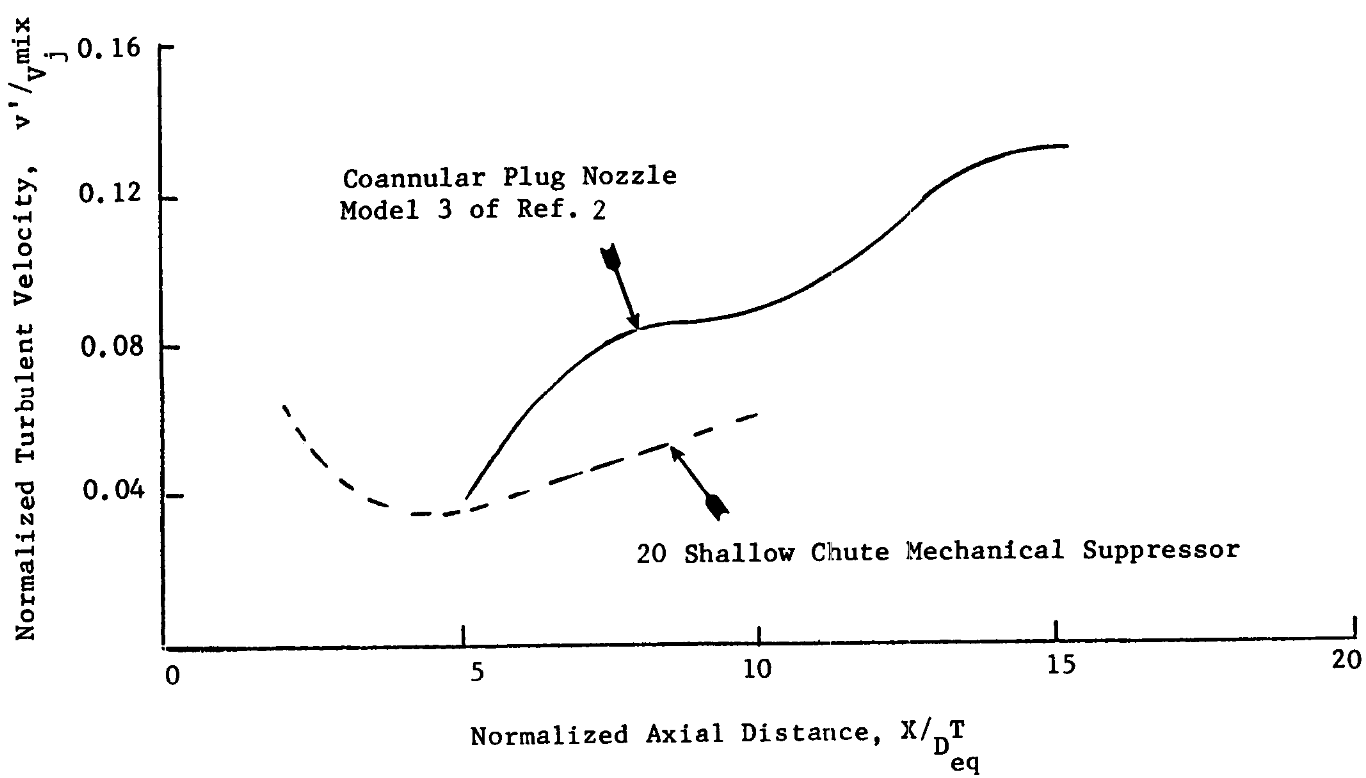

(b) Turbulent Velocity

Figure 4-3. Concluded.

level for the low frequency portion of the source spectrum of the mechanical suppressor is lower. The shape of the spectrum is also altered to reflect the inherent differences between the suppressor and coannular nozzles as indicated by the data base.

Figure 4-4 compares the normalized high frequency source spectrum of suppressor and coannular plug nozzles both extracted from appropriate data bases. Strouhal number based on the hydraulic diameter of the individual flow element of the suppressor and as defined by Equation 2 does seem to collapse the high frequency spectra together. However, there are differences to be noted at the high frequency end (i.e., $S_{\xi}^{o} \geq 1.18$). The suppressor generates more high frequency noise due to the increased turbulence at stations close to the nozzle exhaust plane compared to coannular plug nozzles as depicted in Figure 4-3b. The spectral normalization factors for the high frequency portion of the source spectrum for the suppressors are identical to those for the coannular nozzles. The normalized high frequency spectrum is given by:

$$\begin{aligned} SPLN^{HF}(f) = SPL^{HF}(f) &- 80 \log_{10} (V_j^o/a_{amb}) - 10 \log_{10} (\rho_j^o/\rho_{amb})^{\omega} \\ &- 10 \log_{10} (A^o/R^2) + 50 \log_{10} (R_r^o) - 10 \log_{10} (1 + A_r^i) \\ &- 15 \log_{10} [4.42 (V_r^i)^2 - 4.56 V_r^i + 2.15] \end{aligned} \tag{4}$$

where ρ_j^o = Jet density of the outer stream

R_r^o = Outer stream radius ratio

A_r^i = Ratio of inner flow area to outer (suppressor) flow area

V_r^i = Ratio of inner velocity to outer velocity

In order to verify the choice of the various spectral normalization factors utilized in arriving at normalized source spectra for the merged (Equation 3) and the premerged (Equation 4) portions of the jet mixing noise of mechanical suppressors and also to verify the modeling of shock cell noise of suppressors (Subsection 4.2.4), the predicted source spectrum (i.e., lossless spectrum at $\theta_i = 90°$) is compared in Figure 4-5 with the data for a typical takeoff condition on model scale size for the modified DOT 20-shallow-chute suppressor nozzle at a 40' arc distance. The agreement between the data and prediction of the lossless source spectrum is reasonably good except at very low frequencies (i.e., f $\leq$ 160 Hz) and at very high frequencies (i.e., f $\geq$ 50 kHz) on model scale. The data at the low frequency end are not reliable as the anechoic chamber cutoff frequency is 250 Hz. For frequencies less than 250 Hz, the measurements do not represent true far field measurements. The data at the high frequency end contain frequency dependent preamplification factor in order to improve the frequency response

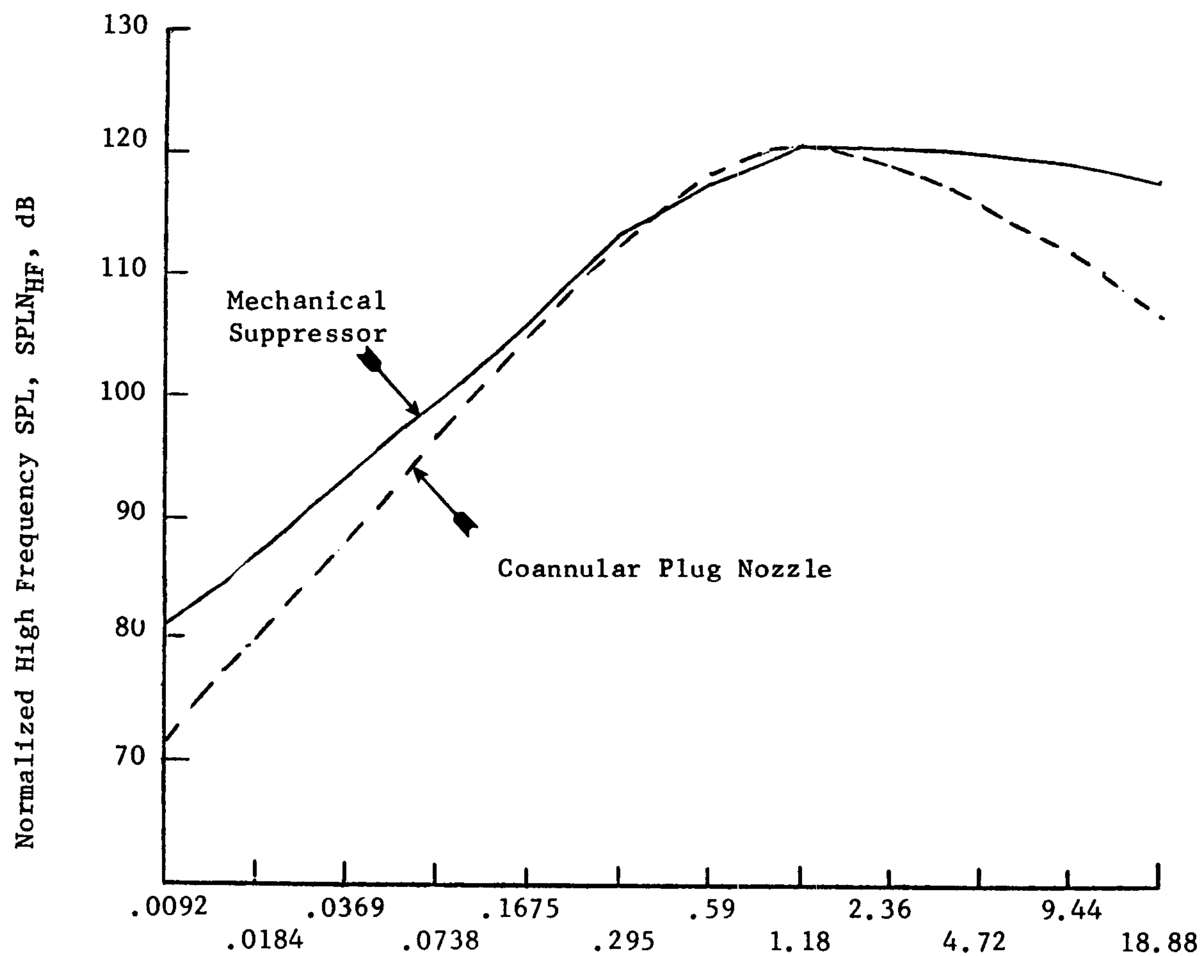

Outer-Stream Strouhal Number, $S_t^o = \dfrac{f\ D^o_{hyd}}{V^o_j - V_{ac}} \times \left(\dfrac{T^o_T}{T_{amb}}\right)_{eff}$

Figure 4-4. Normalized High Frequency Source Spectrum at $\theta_i = 90°$.

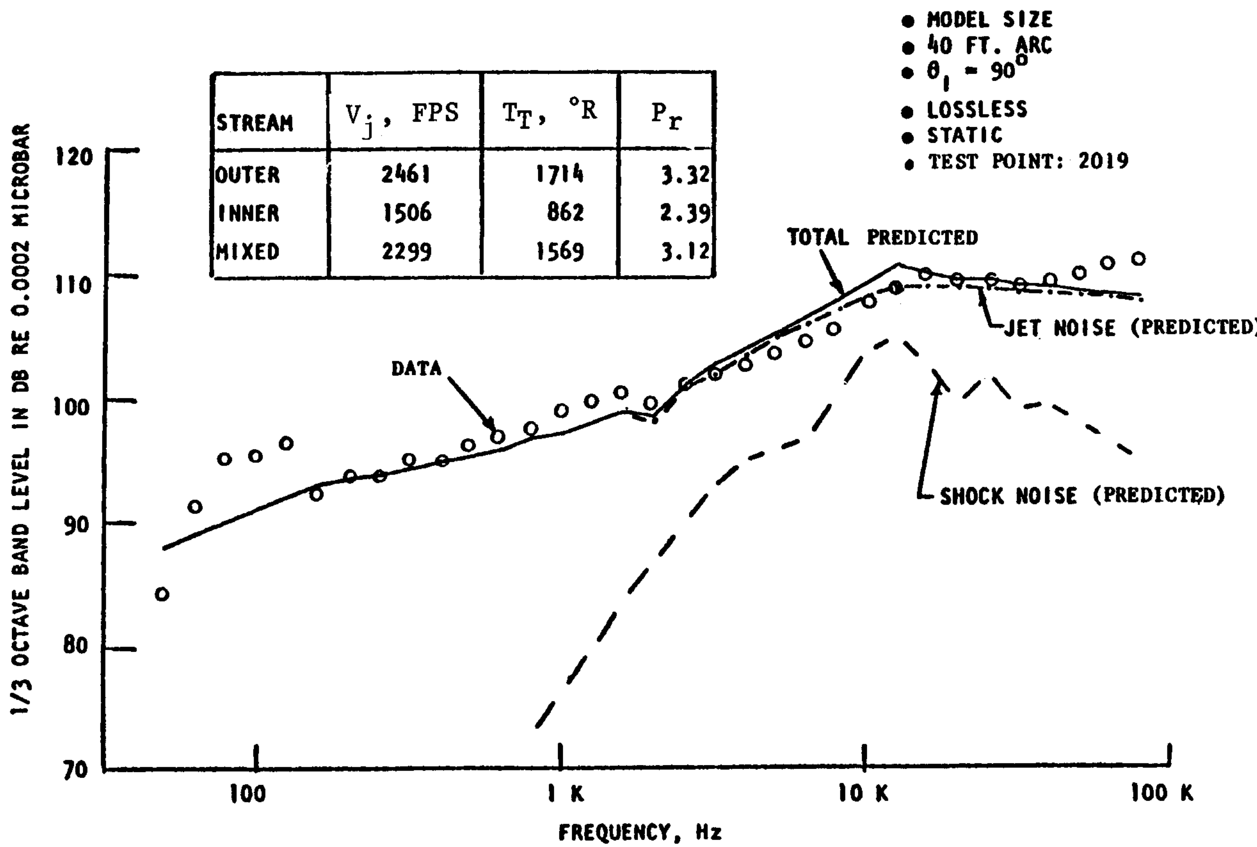

STREAM	V_j, FPS	T_T, °R	P_r
OUTER	2461	1714	3.32
INNER	1506	862	2.39
MIXED	2299	1569	3.12

Figure 4-5. Comparison of Data and Prediction for Lossless Jet and Shock Noise Spectrum at θ_i = 90° for Modified DOT 20-Shallow-Chute Coannular Plug Nozzle Mechanical Suppressor.

of the microphones at the high frequencies. In the case of mechanical suppressors which generate more high frequency noise compared to other nozzles, the preamplification factor might be amplifying the high frequency noise more than necessary. Thus, the jet mixing noise source spectra modeled according to Equations 3 and 4 and shock noise modeled as in Subsection 4.2.4 does indeed agree well with the data, except for very low and very high frequencies.

Once the source spectrum for jet mixing noise is determined, one has to evaluate the convective amplification effects due to moving turbulent eddies and the acoustic mean flow interactions.

4.1.2 Convective Amplification Effects

Convective amplification of the jet noise occurs due to the relative motion of the noise sources (i.e., turbulent eddies) with respect to the observer. The relative motion of the eddies amplifies the noise in the direction of motion and attenuates in the opposite direction.

The mixing rates of jets from other nozzles are different and result in modified jet decay rates. Correspondingly, the turbulent eddies, which are nothing but moving sources, are traveling at various speeds and exhibit different convective amplification effects. Also, the noise radiation is preferentially directed in the Mach cone of each eddy which results in considerable amplification in some regions of the aft quadrant and attenuation in the front quadrant which is in the shadow zone of each eddy. These two concepts have been utilized to empirically model the convective amplification effects of the jets and are respectively identified by:

- Eddy convection Mach number, M_c
- Convective amplification factor, $N(\theta_i)$.

M_c and $N(\theta_i)$ for each type of nozzle have to be derived from the appropriate data base to reflect the differences in the mixing rate. Compared to a coannular plug nozzle, the mixing rate of the jet with the ambient air for suppressors is higher (Figure 4-3); and hence, the eddies are convecting at a lower speed. For coannular plug nozzles, the eddy convection Mach number is given by (Ref. 18):

$$M_c = \frac{1}{2} \left(0.55 + \frac{0.39}{V_r^i}\right) V_j/a_{amb} \tag{5}$$

A relation similar in form to Equation 5 was sought to calculate the eddy convection Mach number for suppressors. Since the eddies travel slower in the case of mechanical suppressors, lower eddy convection Mach numbers were sought. The best possible agreement of the predictions with the acoustic data over a range of aerodynamic conditions was obtained for the following choice of M_c:

$$M_c = \frac{1}{2} \left(0.4 + \frac{0.2}{V_r^i}\right) V_j/a_{amb} \tag{6}$$

The convection Mach number for the premerged portion of the spectrum is evaluated using V_j^o, and for the merged portion is evaluated using V_j^{mix} in Equation 6. The convection amplification factor, $N(\theta_i)$, determines the angular dependence of convection effects. For conical nozzles, it has been shown previously (Refs. 24 through 26) that $N(\theta_i)$ remains at a constant value of 3 until the critical angle for total internal reflection of acoustic waves is reached [i.e., $N(\theta_i) = 3$ for $\theta_i \leq (\theta_i)_{cr}$]. The region of $\theta_i < (\theta_i)_{cr}$ is also referred to as the zone of silence. The propagation of acoustic waves for $\theta_i > (\theta_i)_{cr}$ is particularly enhanced by radiation in the Mach cone. This results in considerable amplification of noise in the aft quadrant. For conic nozzles the value of N approaches 7 for $\theta_i \rightarrow 180°$. Figure 4-6 compares the angular dependence of N for suppressor and coannular nozzles. The transition from a value of 3 to 7 for N has been determined by using the appropriate data base. One should note the slower rise in N for a suppressor nozzle indicating that, because of more rapid mixing with the ambient air, a sharp cutoff mechanism of total internal reflection does not exist for suppressor nozzles, as it did for conic or coannular nozzles. Utilizing Equation 6 and Figure 4-6, the convection amplification effect for suppressor nozzles is evaluated by:

$$\Delta SPL_{C.A.} = N(\theta_i) \quad 10 \log_{10} \left[(1 + M_c \cos \theta_i)^2 + \mu^2 M_c^{\,2} \right]^{1/2} \qquad (7)$$

where $\mu = 0.325$ (Ref. 27).

The Doppler shifted frequency heard by the observer located at angle θ_i due to moving eddies is given by:

$$f\bigg|_{\theta_i} = \frac{f_{90°}}{\left[(1 + M_c \cos \theta_i)^2 + \alpha^2 M_c^{\,2}\right]^{1/2}} \qquad (8)$$

The Doppler shifting of frequencies increases the frequency (i.e., pitch) if the noise source is moving towards the observer and reduces it if it is moving away from the observer. Hence, the peak noise frequency is reduced in the front quadrant and increased in the aft quadrant compared to the peak frequency of the source spectrum.

4.1.3 Acoustic Mean Flow Interaction

The noise generated by the turbulent eddies has to pass through a region of temperature and velocity gradients of the decaying mean flow field before reaching the observer. The effect of these mean flow gradients is to refract the sound towards the jet axis (i.e., $\theta_i = 180°$). Also, there is additional convective amplification not due to the source (i.e., turbulent eddy) convection, but due to the fluid motion. These two effects are termed as acoustic mean flow interaction, and they depend strongly on the noise source location; the closer the source is to the jet boundary, the less is the influence of acoustic mean flow interaction. Mani (Refs. 28 and 29) and Balsa (Refs. 24 and 26) quantitatively evaluated these effects by solving the Lilley's equation and thus predicted the radiation field of moving quadrupole sources immersed in parallel sheared flows. These theoretical developments arrived at a fluid shielding integral whose sign determines whether the

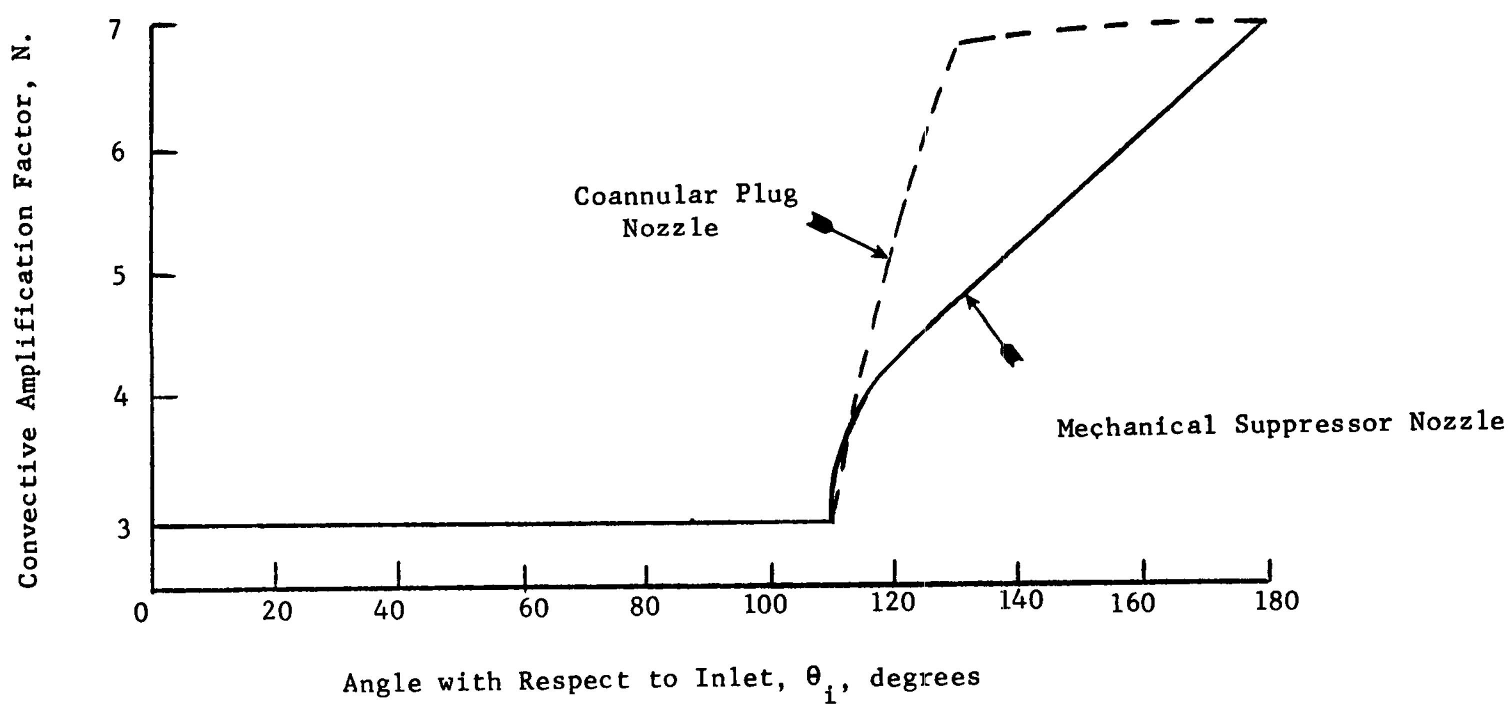

Figure 4-6. Directivity of Convective Amplification Factor of Coannular Plug Nozzle and Mechanical Suppressor Nozzle.

solution for the acoustic pressure is oscillatory or exponentially decaying with radial distance (Ref. 19). Following the development in Reference 19, the reduction in noise level radiated by a slice of jet is given by:

$$(\Delta SPL)_{slice} = 10 \log_{10} \left[\left| \exp \frac{-2i\, \Omega\delta}{a_{amb}} \right| \right] \tag{9}$$

where Ω = source radian frequency

$i = \sqrt{-1}$

δ = shielding integral = $\int_{r_1}^{r_2} g(r)\, dr$

r_1 and r_2 are the radial limits of the slice

$g(r)$ = shielding function defined by:

$$g^2(r) = \frac{\dfrac{(1 + M \cos \theta_i)^2}{(a/a_{amb})^2} - \cos^2 \theta_i}{(1 + M_c \cos \theta_i)^2} \tag{10}$$

where $M = \dfrac{V(r)}{a_{amb}}$ and a = local sonic speed

Thus, if $g^2(r)$ is negative, the acoustic mean flow interaction as modeled by Equation 9 results in an exponential decay of the noise radiated. If $g^2(r)$ is positive, Equation 9 yields

$$(\Delta SPL)_{slice} = 0$$

The radial locations at which $g^2(r)$ equals zero are called turning points. Equations 9 and 10 need aerodynamic information of the plume at different axial stations to evaluate the shielding effect. For the engineering prediction procedure being developed, instead of computing the shielding effect at each slice of jet, an average shielding function, $\bar{g}$, is defined below with M_c being based on the characteristic mean velocity of the flow rather than the local mean flow velocity and sonic speed based on exit conditions:

$$\left| \bar{g}^{\,2} \right|^{1/2} = \left[\left| \frac{(1 + M_c \cos \theta_i)^2}{(a/a_{amb})^2} - \cos^2 \theta_i \right| \right]^{1/2} \tag{11}$$

Equating Equation 11 to zero and solving for the critical angle $(\theta_i)_{cr}$ yields:

$$\cos(\theta_i)_{cr} = -\frac{1}{(a/a_{amb}) + M_c} \qquad (12)$$

It can be seen that for $\theta_i > (\theta_i)_{cr}$, g is imaginary and will yield exponential decay and the resulting fluid shielding. For $\theta_i < (\theta_i)_{cr}$, g is real and results in an oscillatory pressure distribution and no fluid shielding. An interesting point to be noted is that the application of Snell's law for a moving medium with a Mach number M_c (V/a_{amb}) shows that the critical angle for total internal reflection is given by Equation 12 and that for $\theta_i > (\theta_i)_{cr}$ the sound rays ought to be totally internally reflected.

The amount of SPL reduction due to fluid shielding for the case of suppressors is estimated in an identical way as for coannular nozzles and is given by:

$$\Delta SPL(f)_{shielding} = H\left(\frac{fD}{a_{amb}}\right) \times 2\pi a_{amb} \times \frac{|\bar{g}|}{\left[(1 + M_c \cos\theta_i)^2 + \alpha^2 M_c^2\right]^{1/2}} \qquad (13)$$

where $H\left(\frac{fD}{a_{amb}}\right)$ is a nondimensional shielding factor estimated as a function of the Strouhal number, $\left(\frac{fD}{a_{amb}}\right)$. The shielding factor $H\left(\frac{fD}{a_{amb}}\right)$ utilized for the merged and premerged portions of the suppressor nozzles is identical to the one utilized for the merged and premerged portions of the coannular nozzles indicating the versatility of this formulation (Figure 4-7). In estimating $\Delta SPL(f)_{shielding}$ for premerged and merged portions of the spectrum, the Strouhal number has to be evaluated utilizing the appropriate length scales.

4.1.4 Shock Cell Noise

When a convergent nozzle is operated at a supercritical pressure ratio or when a convergent-divergent nozzle is operated at an off-design pressure ratio, an oblique shock and expansion wave pattern is established in the jet stream by means of which the jet static pressure equalization to ambient pressure occurs. The strength of these shock waves reduces downstream due to the deceleration caused by the mixing process as well as due to the partial static pressure equalization obtained by the upstream shock and expansion wave structure. When the turbulent eddies which are the products of the unsteady mixing process are convected through the shock structure, acoustic waves are emitted by the shock fronts. These acoustic waves from the various shock fronts can either constructively or destructively interfere. Since turbulent eddies are being convected with a broad range of velocities through the shock fronts, the shock cell noise has a broadband character. However, since the shock cell spacing is fairly regular, the interference pattern between the acoustic waves emitted by the shock fronts results in fairly strong reinforcements or cancellations. Hence, the shock cell noise exhibits a "peak" broadband character.

The above concepts were developed by Harper-Bourne and Fisher (Ref. 30) in their semiempirical method (HBF) to predict the shock cell noise of round convergent nozzles. In Reference 18, the HBF method with some modifications was used to predict the shock cell noise of coannular plug

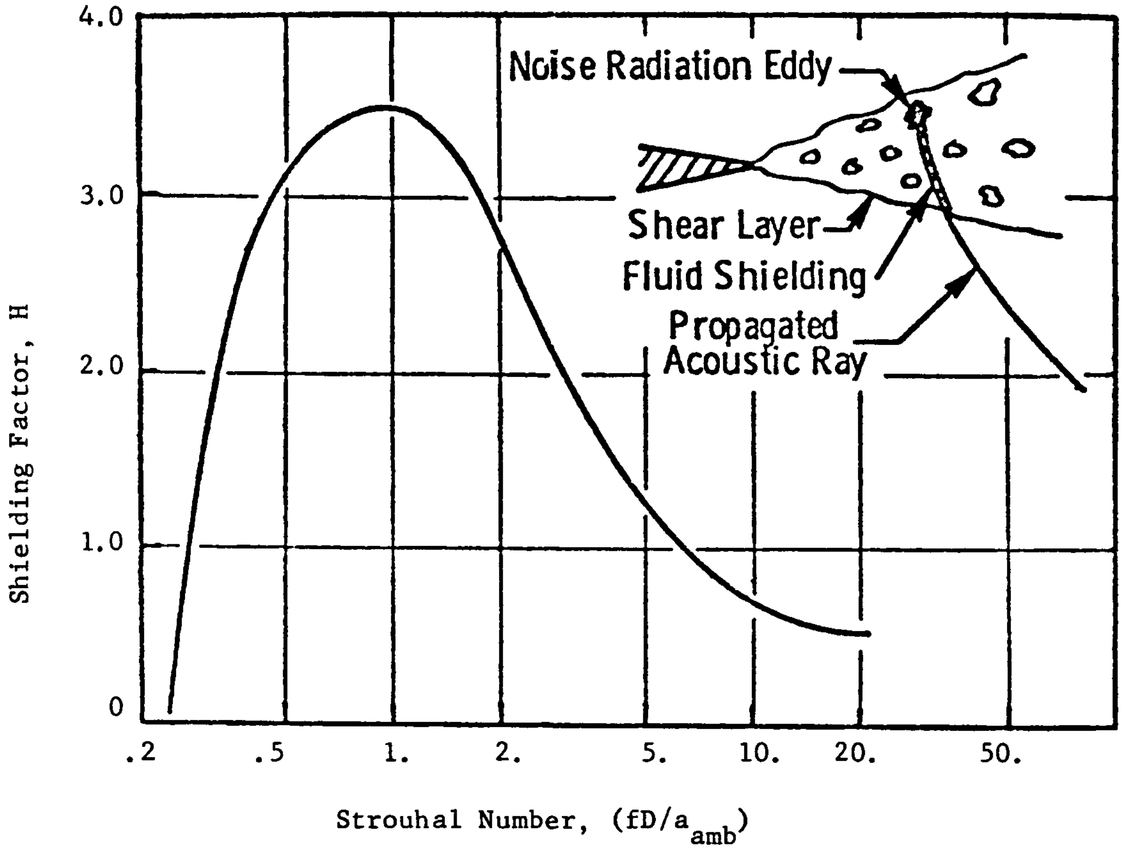

Figure 4-7. Dependence of the Shielding Factor on the Strouhal Number for Merged and Premerged Regions of the Mechanical Suppressor Nozzle.

nozzles. Owing to the success of the modified HBF method for the shock cell noise of coannular plug nozzles, it is used to predict the shock cell noise of suppressors also. For dual flow coannular plug nozzles, the characteristic shock cell dimension was chosen to be the equivalent diameter based on total flow area. The characteristic shock cell dimension for suppressor nozzles is, however, changed and chosen to be the suppressor element hydraulic diameter, D^o_{hyd}, since this choice of length scale is seen to predict correctly the location of peak shock noise frequency in the front quadrant. A physical explanation follows. Since the decay rate of flow elements of suppressors is quite rapid, the individual flow elements might be decelerated by the ambient air to sonic or subsonic conditions before they interact with one another. Thus, the shock cell structure of one flow element does not influence the shock cell structures of other flow elements. Now, since the multi-element shock cell structures would act as uncorrelated noise sources, the shock noise level has to be raised by 10 $\log_{10}$ (number of flow elements). The number of shock cells in each flow element shock cell structure is chosen to be two as in the case of coannular plug nozzles.

4.1.5 Flight Effect on Jet and Shock Cell Noise

The flight effect on the suppressor jet and shock cell noise is estimated as for the coannular plug nozzles and are reproduced here for reference purpose (Ref. 18). The location of peak frequencies for merged and premerged portions are respectively given by:

$$\frac{fp^{LF}\, D^T_{eq}}{V^{mix}_j} \left\{ \frac{T^{mix}_T}{T_{amb}} \right\}_{eff} \left\{ \frac{V^{mix}_j - V_{ac}}{V^{mix}_j} \right\} = 0.9 \qquad (14)$$

and

$$\frac{fp^{HF}\, D^o_{hyd}}{V^o_j} \left\{ \frac{T^o_T}{T_{amb}} \right\}_{eff} \left\{ \frac{V^o_j - V_{ac}}{V^o_j} \right\} = 1.18 \qquad (15)$$

where V_{ac} = aircraft velocity.

Also, the static source spectrum levels for merged and premerged portions are respectively reduced by:

$$SPL^{LF}_{flight} - SPL^{LF}_{static} = (\Delta SPL^{LF})_{flight\ effect}$$

$$= 20 \log_{10} \left[\frac{V^{mix}_j - V_{ac}}{V^{mix}_j} \right] \qquad (16)$$

and

$$SPL^{HF}_{flight} - SPL^{HF}_{static} = (\Delta SPL^{HF})_{flight\ effect}$$

$$= 20 \log_{10} \left[\frac{V^o_j - V_{ac}}{V^o_j} \right] \qquad (17)$$

Equations 14 through 17 summarize the changes made to predict the source spectrum for flight cases. Next, the effect of aircraft velocity on the eddy convection Mach number, M_c is given by:

$$M_c = \frac{1}{2} \left(0.4 + \frac{0.2}{V_r^i} \right) \frac{(V_j - V_{ac})}{a_{amb}} \quad \text{for } V_r^i < 1.0 \tag{18}$$

The appropriate jet velocities are used to calculate M_c for premerged and merged portions of the spectrum.

Next, the flight effect on the shock cell noise is to amplify the noise in the front quadrant and reduce it in the aft quadrant (namely, dynamic effect) and Doppler shifting of the shock frequency. The dynamic effect is given by:

$$SPL_{flight} - SPL_{static} = 40 \log_{10} (1 + M_{ac} \cos \theta_i) \tag{19}$$

where $M_{ac} = \dfrac{V_{ac}}{a_{amb}}$

The Doppler shifting of the frequency is given by:

$$f_{flight} = \frac{f_{static}}{(1 + M_{ac} \cos \theta_i)} \tag{20}$$

4.2 COMPARISON WITH EXPERIMENTAL DATA OF SIMILITUDE 20-SHALLOW-CHUTE SUPPRESSOR NOZZLE (MODEL 10.1)

The prediction methodology described in Subsection 4.2 has been translated into a computer code in the Fortran language (see Ref. 31 for a listing of the computer code, user's instructions, and sample input/output). This computer program requires approximately 35K bits of memory on a Honeywell 6000 series computer system. Typical central processor unit (cpu) time for 10 cases is 50 seconds, indicating that this program is quite suitable for extensive parametric variations, a necessary requirement of a design tool.

The prediction procedure has been utilized to forecast the spectral and overall characteristics of the similitude 20-shallow-chute suppressor nozzle (Figure 2-14) and compared with the data.

The selected static and flight cases correspond to typical AST takeoff and cutback conditions. The comparisons are made for a product size of $A^T = 1{,}400$ in.^{2} and extrapolated to a 2,400 ft. sideline. Detailed comparisons are provided in Reference 31. In this section, measured and predicted data of the similitude suppressor are provided to demonstrate the prediction procedure.

Comparisons of the predictions and data for the similitude 20-shallow-chute suppressor nozzle for a typical AST takeoff (test point 1013) cycle condition at a 2,400 ft. sideline measuring distance for a product size engine (viz., $A^T = 1{,}400$ in.^{2}) are shown in Figures 4-8 through 4-12. The

Stream	V_j fps	P_r	T_T ^oR
Suppressor	2561	3.68	1732
Inner	1797	3.43	906
Mixed	2421	3.58	1580

- Test Point 1013
- 1400 in^2 Flow Area
- 2400' Sideline
- V_{ac} = 0.0 fps

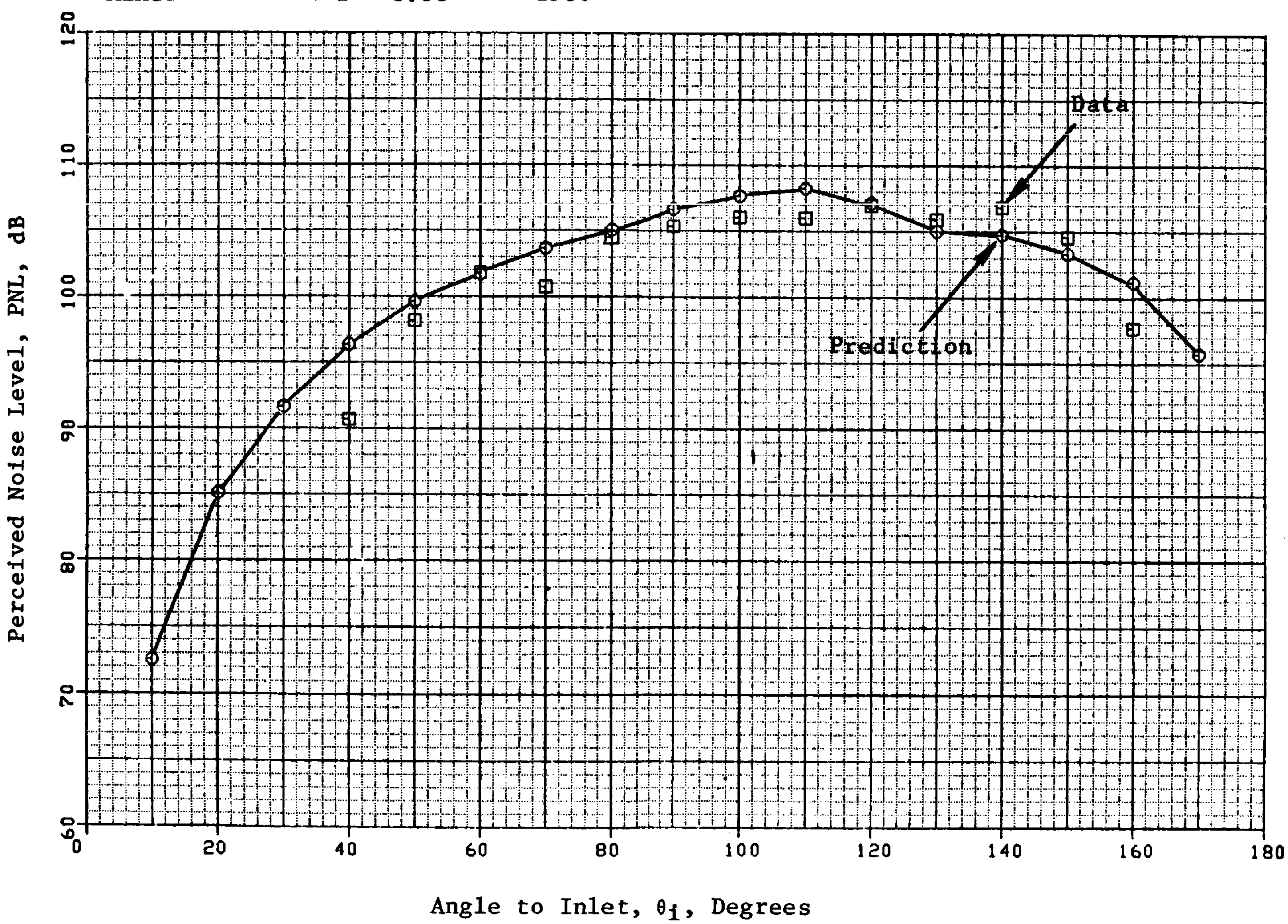

Figure 4-8. Comparison of Data and Prediction of PNL Directivity for Similitude 20-Shallow-Chute Suppressor Nozzle at Typical Takeoff Condition (Static).

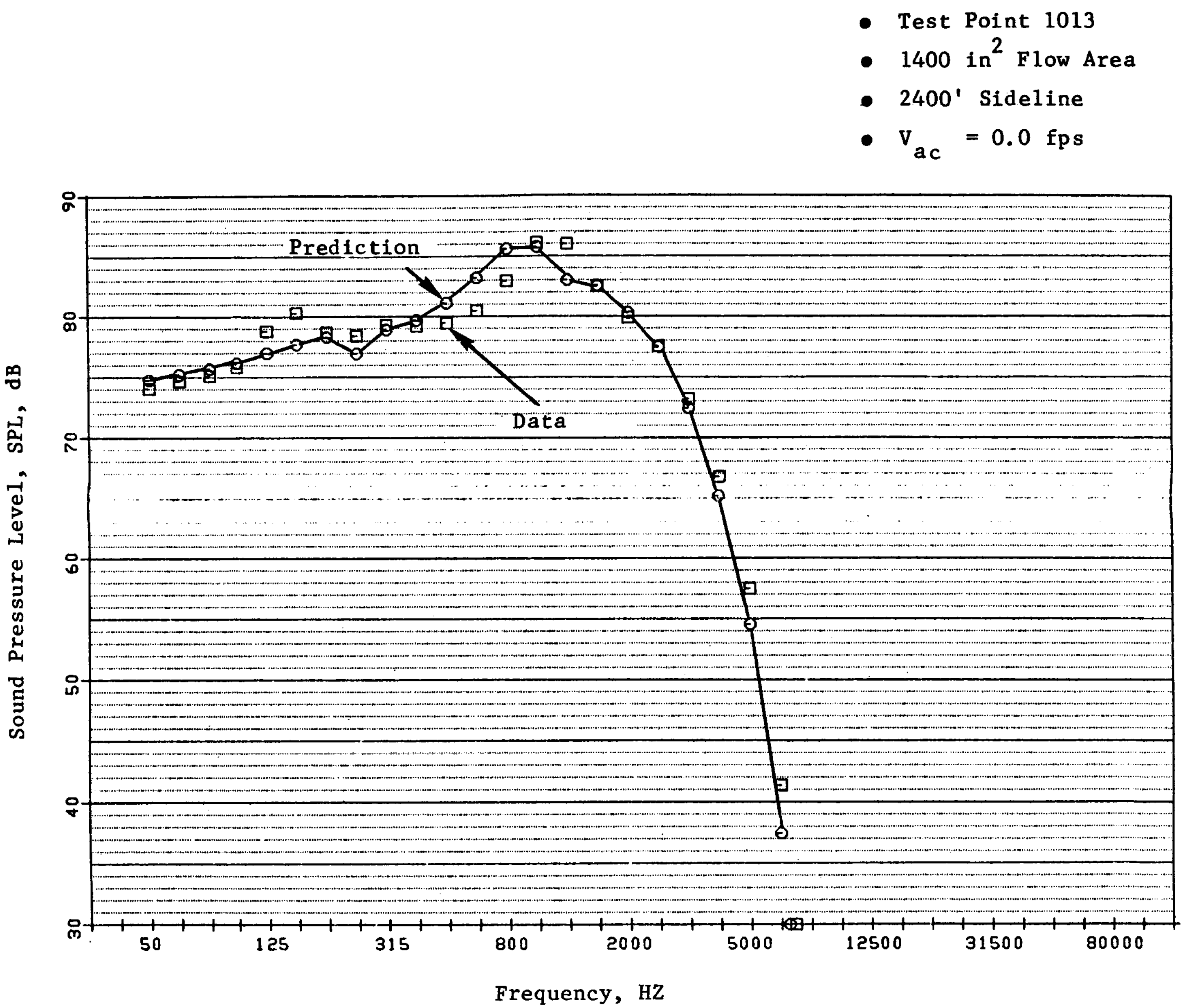

Figure 4-9. Comparison of Data and Prediction of Spectra at θ_i = 60° for Similitude 20-Shallow-Chute Suppressor Nozzle at Typical Takeoff Condition (Static).

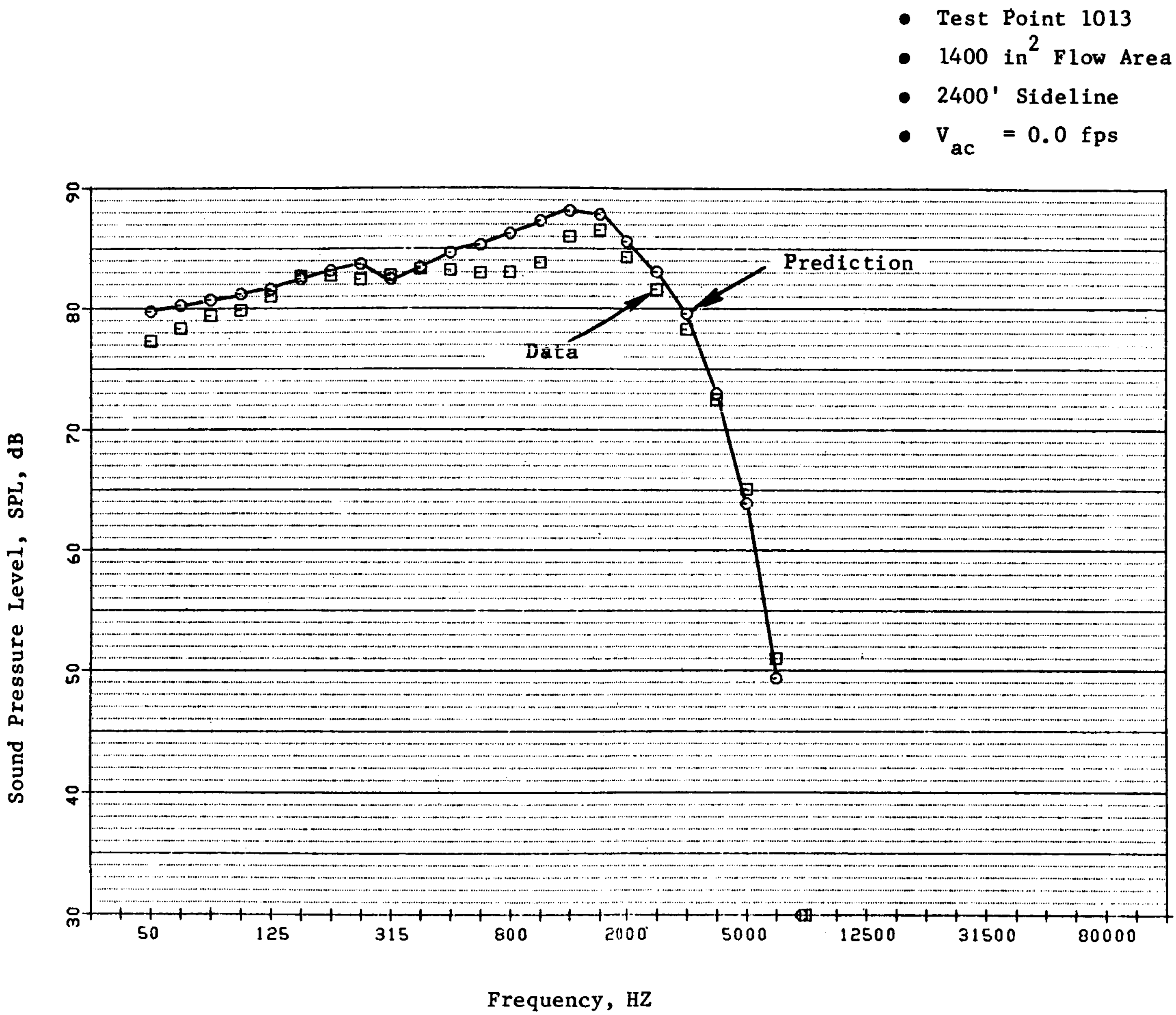

Figure 4-10. Comparison of Data and Prediction of Spectra at θ_i = 90° for Similitude 20-Shallow-Chute Suppressor Nozzle at Takeoff Condition (Static).

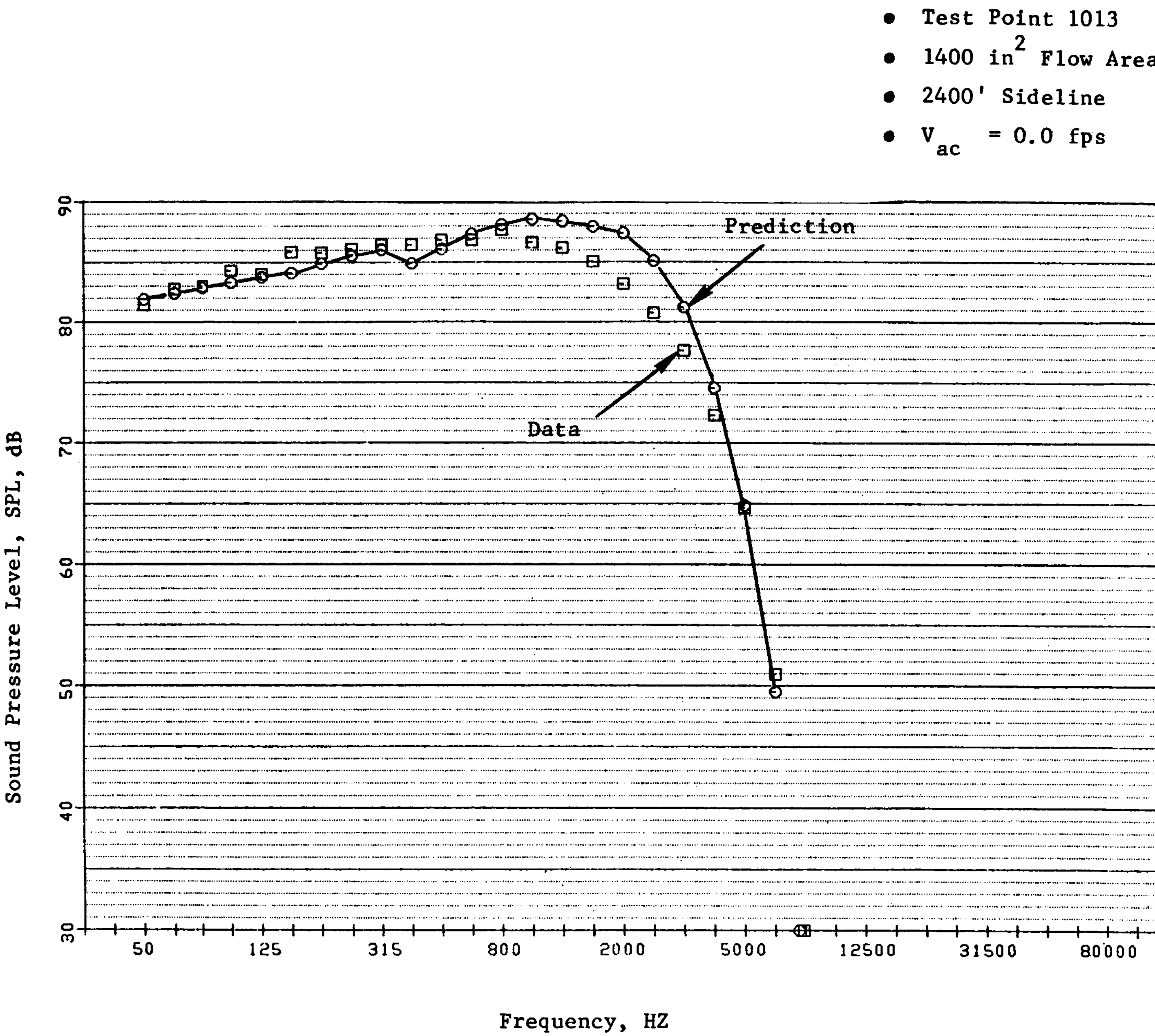

Figure 4-11. Comparison of Data and Prediction of Spectra at $\theta_i = 110°$ for Similitude 20-Shallow-Chute Suppressor Nozzle at Typical Takeoff Condition (Static).

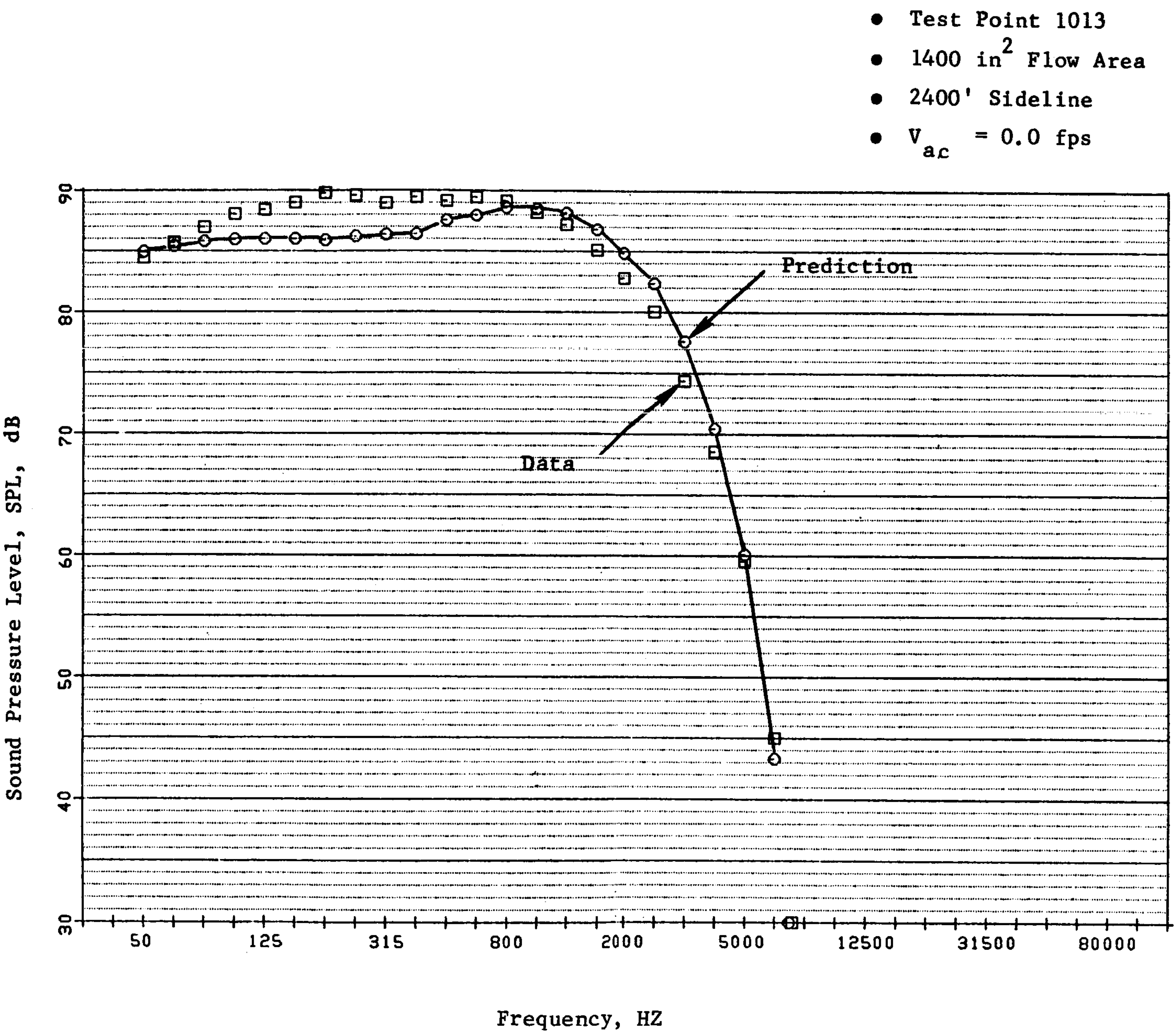

Figure 4-12. Comparison of Data and Prediction of Spectra at θ_i = 120° for Similitude 20-Shallow-Chute Nozzle at Typical Takeoff Condition (Static).

aerodynamic cycle conditions are shown in Figure 4-8. Figure 4-8 shows that the agreement between the data and predictions on a static PNL directivity basis is quite good except at $\theta_i = 160°$. At an extreme aft angle such as 160°, the convection amplification effect might be overpredicted. This would call for a lower value of convection amplification factor at the extreme aft angle. Figure 4-9 shows the spectral agreement between data and predictions in the front quadrant (namely, $\theta_i = 60°$) which is dominated by shock noise. The prediction method is seen to calculate both the location of peak shock noise frequency and the SPL quite accurately, thus validating the choice of characteristic shock cell noise parameters. Figure 4-10 shows the spectral agreement at $\theta_i = 90°$ where the convection amplification and fluid shielding effects are minimal. The agreement is good over the entire range of frequencies indicating that a proper choice of source spectra for merged and premerged portions has been made. Figures 4-11 and 4-12 show the spectral distribution at two aft angles (namely, $\theta_i = 110°$ and 120°, respectively). The shape and levels are in close agreement, thus validating the modeling of convection amplification effects and acoustic mean flow interactions.

Next, the prediction method is exercised to predict spectrally for a typical AST cutback (test point 1007) cycle condition. See Figure 4-13 for the aerodynamic cycle conditions. Figures 4-13 through 4-17 show the agreement between the data and predictions on a PNL and spectral bases. As noted before, the PNL directivity agreement fails at extreme aft angle ($\theta_i = 160°$), otherwise it is reasonable. The spectral distribution at $\theta_i = 60°$ (Figure 4-14) shows that peak shock noise frequency and corresponding noise levels are predicted correctly. Figure 4-15 shows excellent agreement at $\theta_i = 90°$ reinforcing the appropriate choice of the source spectra. Figures 4-15 and 4-17 show the spectral agreement at $\theta_i = 110°$ and 120°, respectively, to be reasonable.

Next, the corresponding takeoff and cutback conditions at an aircraft speed of 400 fps (i.e., $M_{ac} = 0.358$) are compared on a PNL directivity and spectral bases in Figures 4-18 through 4-27. See Figures 4-18 and 4-23, respectively, for the aerodynamic conditions for takeoff (test point 1014) and cutback (test point 1028) cases. Figure 4-18 shows that the agreement between predictions and data on a PNL basis for a takeoff case is excellent at all angles except at $\theta_i = 150°$ and 160°. Figure 4-19 shows that the spectral content at $\theta_i = 60°$ is predicted to agree well with the data. Figure 4-20 shows good agreement between data and predictions at $\theta_i = 90°$. Figures 4-21 and 4-22 also show good agreement in the aft angles. Similar observations on the data prediction comparison may be made for the flight cutback case by examining Figures 4-23 through 4-27. Thus, the good agreement for flight cases indicates that the flight effects modelled for coannular plug nozzles are also applicable for suppressor nozzles.

4.3 CONCLUSIONS AND RECOMMENDATIONS

An engineering spectral prediction procedure which incorporates the complex jet mixing noise generation and propagation mechanisms yet is mathematically simple has been developed to predict the spectral and overall characteristics of mechanical suppressor nozzles. This method has evolved out of a similar method for coannular plug nozzles operated in the inverted velocity mode and consists of the following modifications:

Stream	V_j fps	P_r	T_T ^oR
Suppressor	2266	2.79	1664
Inner	1605	2.80	843
Mixed	2135	2.74	1502

- Test Point 1007
- 1400 in^2 Flow Area
- 2400' Sideline
- V_{ac} = 0.0 fps

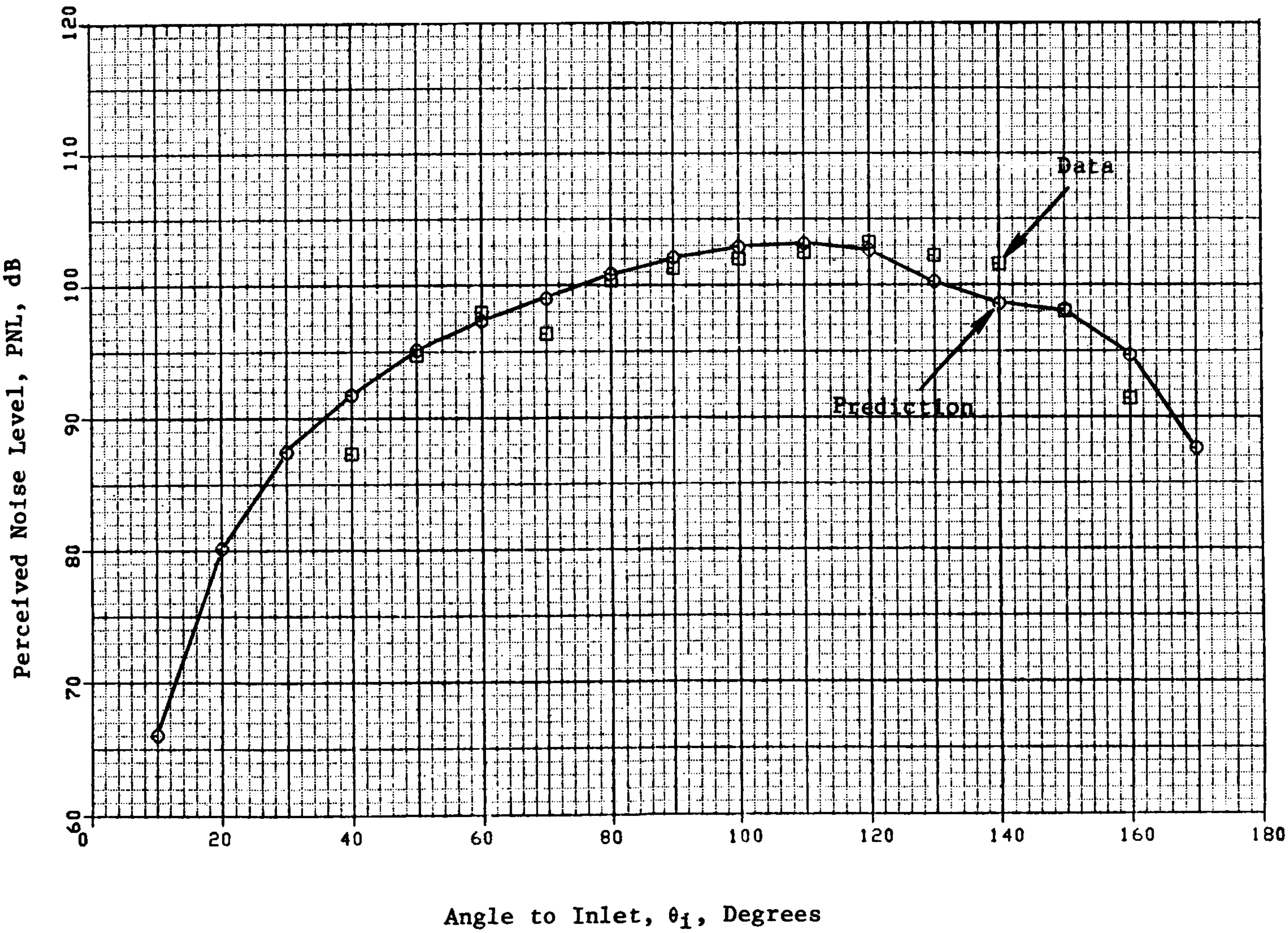

Figure 4-13. Comparison of Data and Prediction for PNL Directivity of Similitude 20-Shallow-Chute Suppressor Nozzle at Typical Cutback Condition (Static).

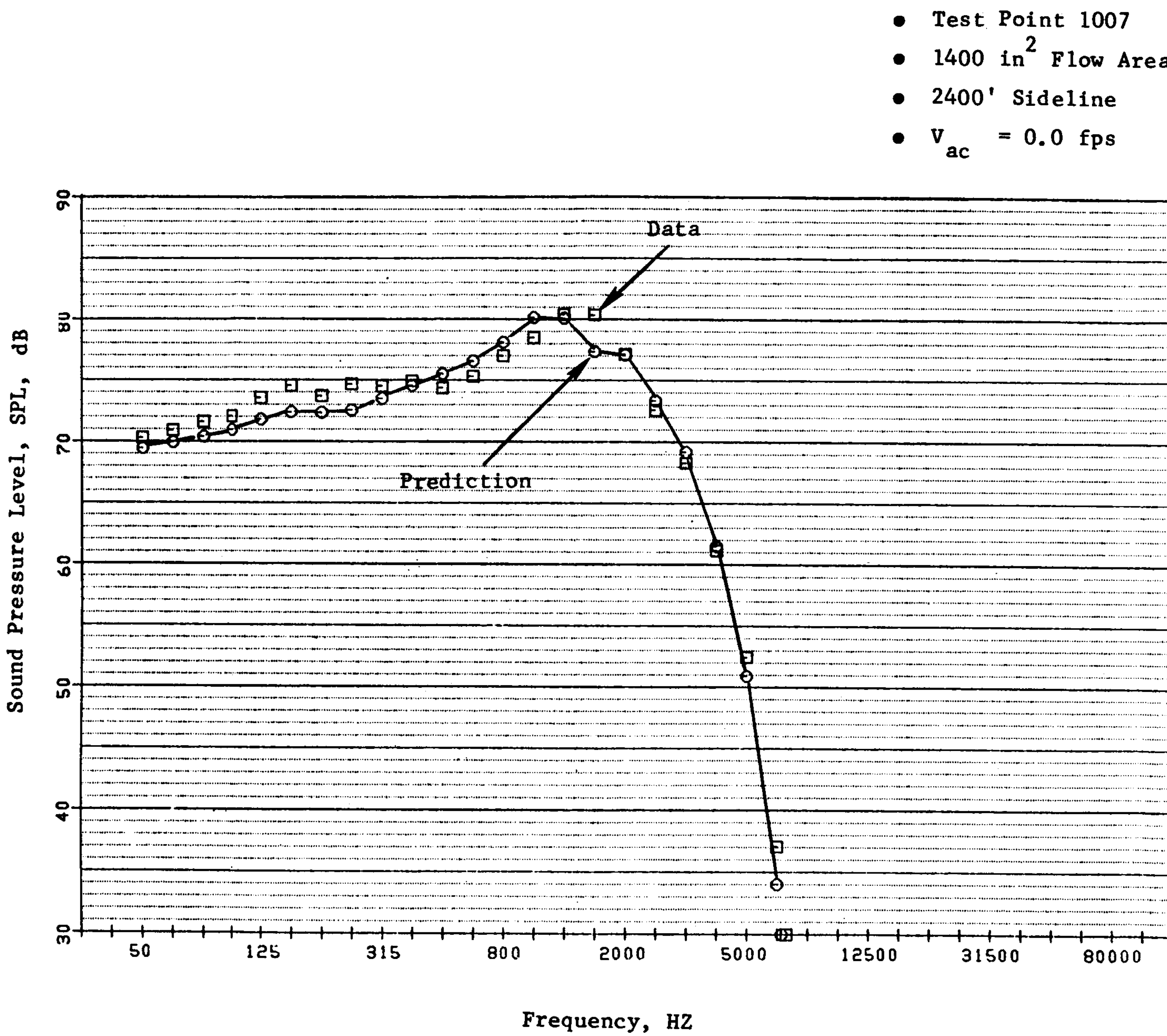

Figure 4-14. Comparison of Data and Prediction of Spectra at $\theta_i = 60°$ for Similitude 20-Shallow-Chute Suppressor Nozzle at Typical Cutback Condition (Static).

- Test Point 1007
- 1400 in^2 Flow Area
- 2400' Sideline
- V_{ac} = 0.0 fps

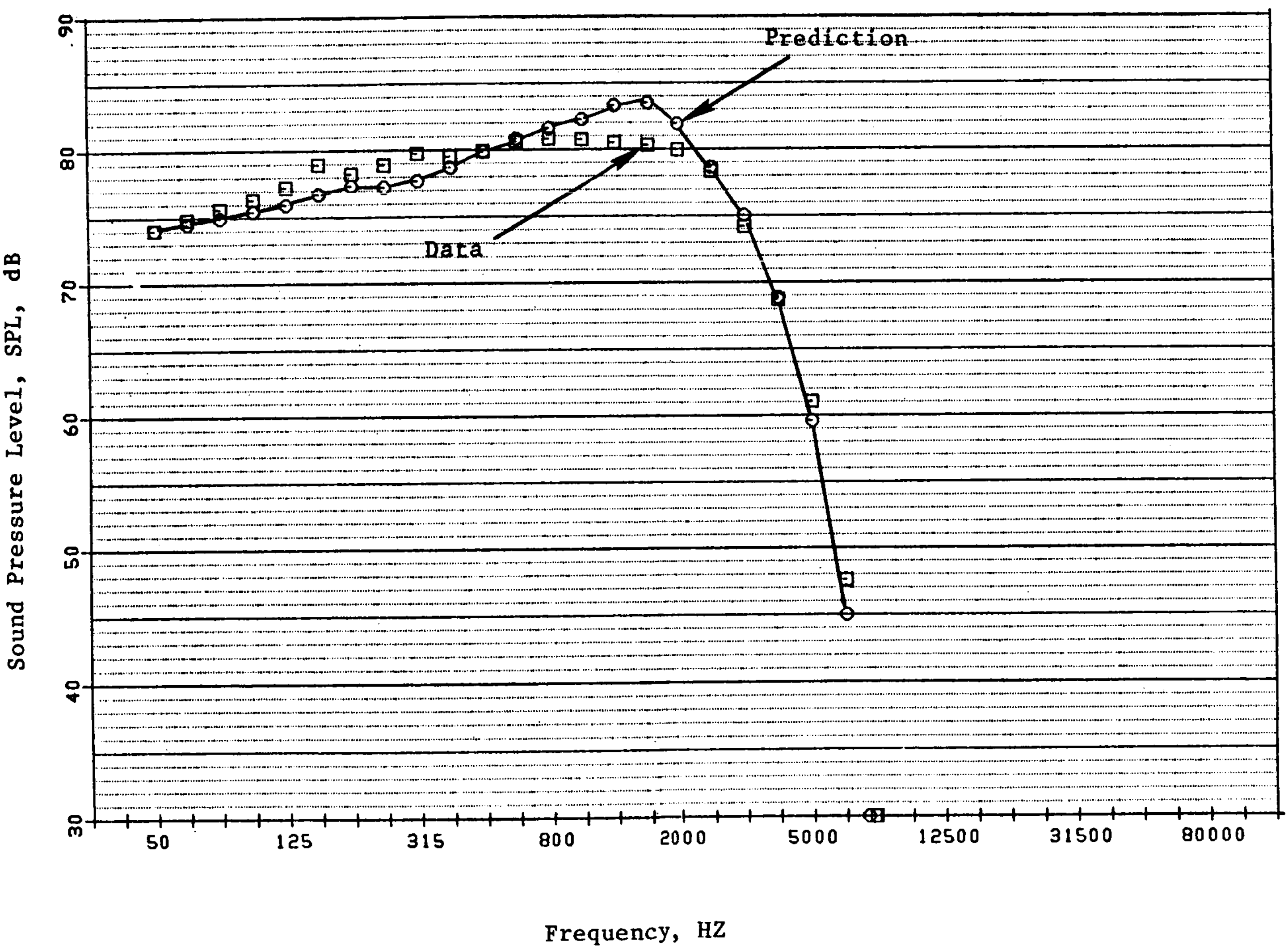

Figure 4-15. Comparison of Data and Prediction of Spectra at θ_i = 90° for Similitude 20-Shallow-Chute Suppressor Nozzle at Typical Cutback Condition (Static).

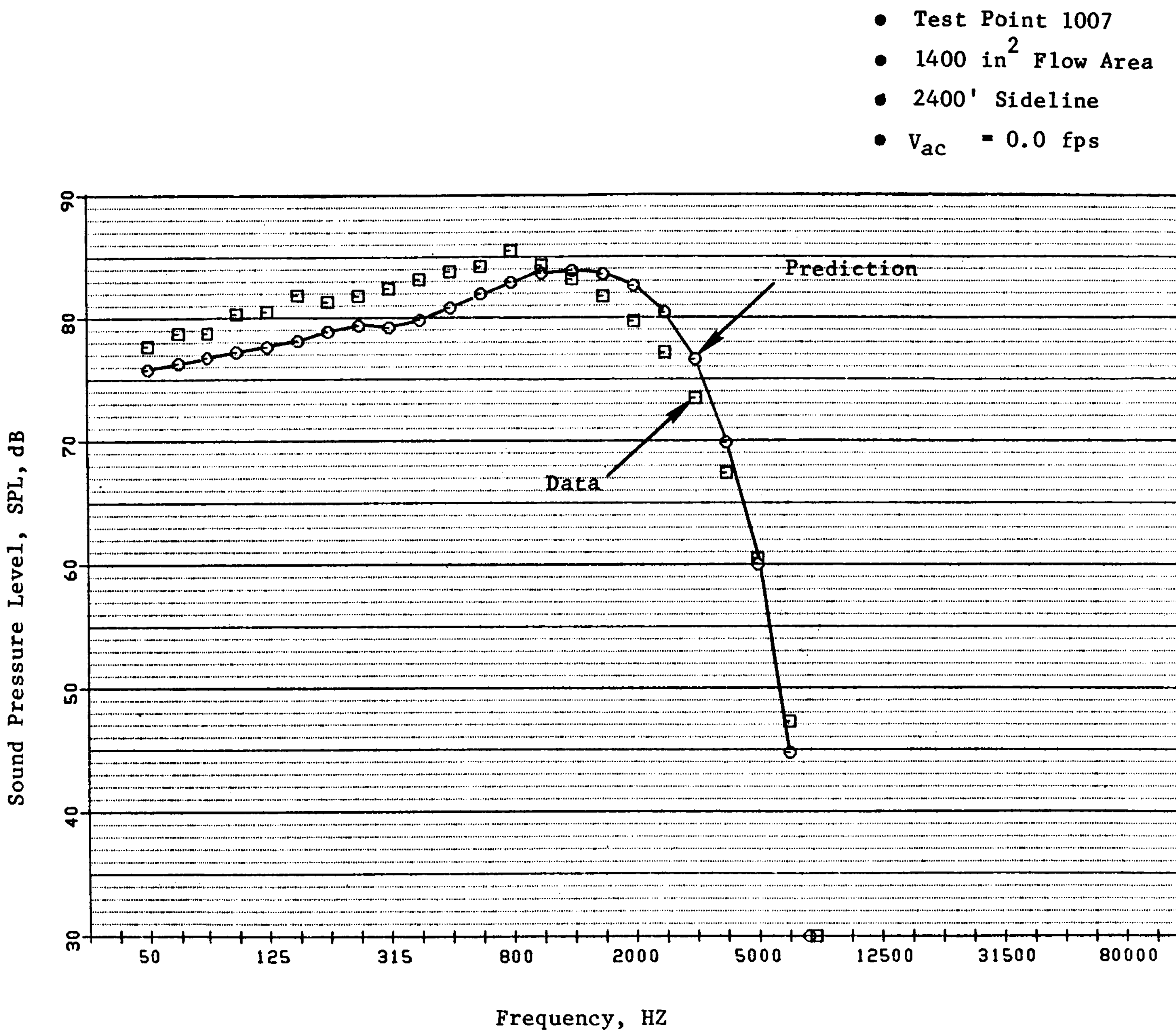

Figure 4-16. Comparison of Data and Prediction of Spectra at θ_i = 110° for Similitude 20-Shallow-Chute Suppressor Nozzle at Typical Cutback Condition (Static).

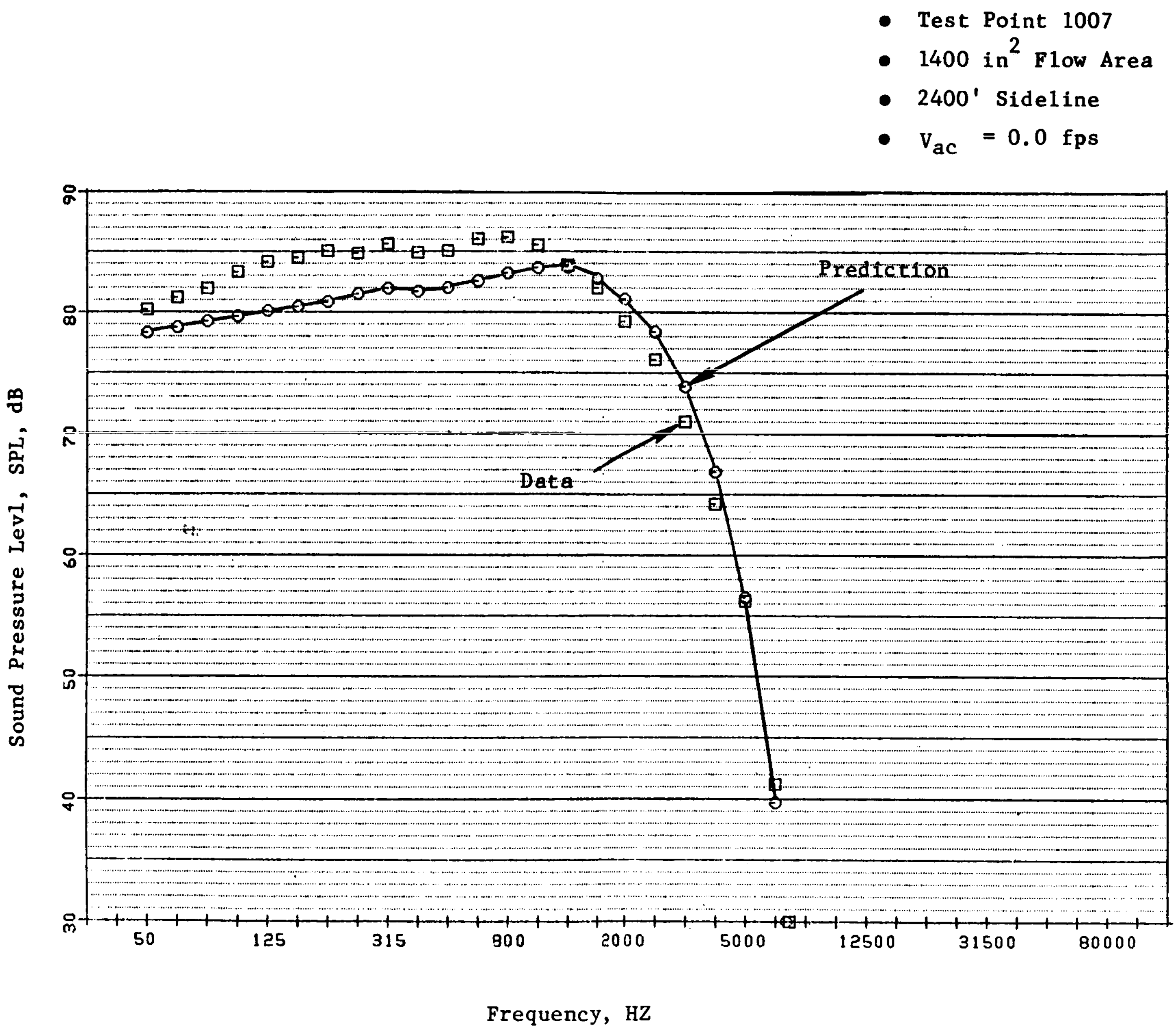

Figure 4-17. Comparison of Data and Prediction of Spectra at θ_i = 120° for Similitude 20-Shallow-Chute Suppressor Nozzle at Typical Cutback Condition (Static).

Stream	V_j fps	P_r	T_T °R
Suppressor	2584	3.70	1758
Inner	1825	3.43	934
Mixed	2446	3.60	1608

- Test Point 1014
- 1400 in^2 Flow Area
- 2400' Sideline
- V_{ac} = 400 fps

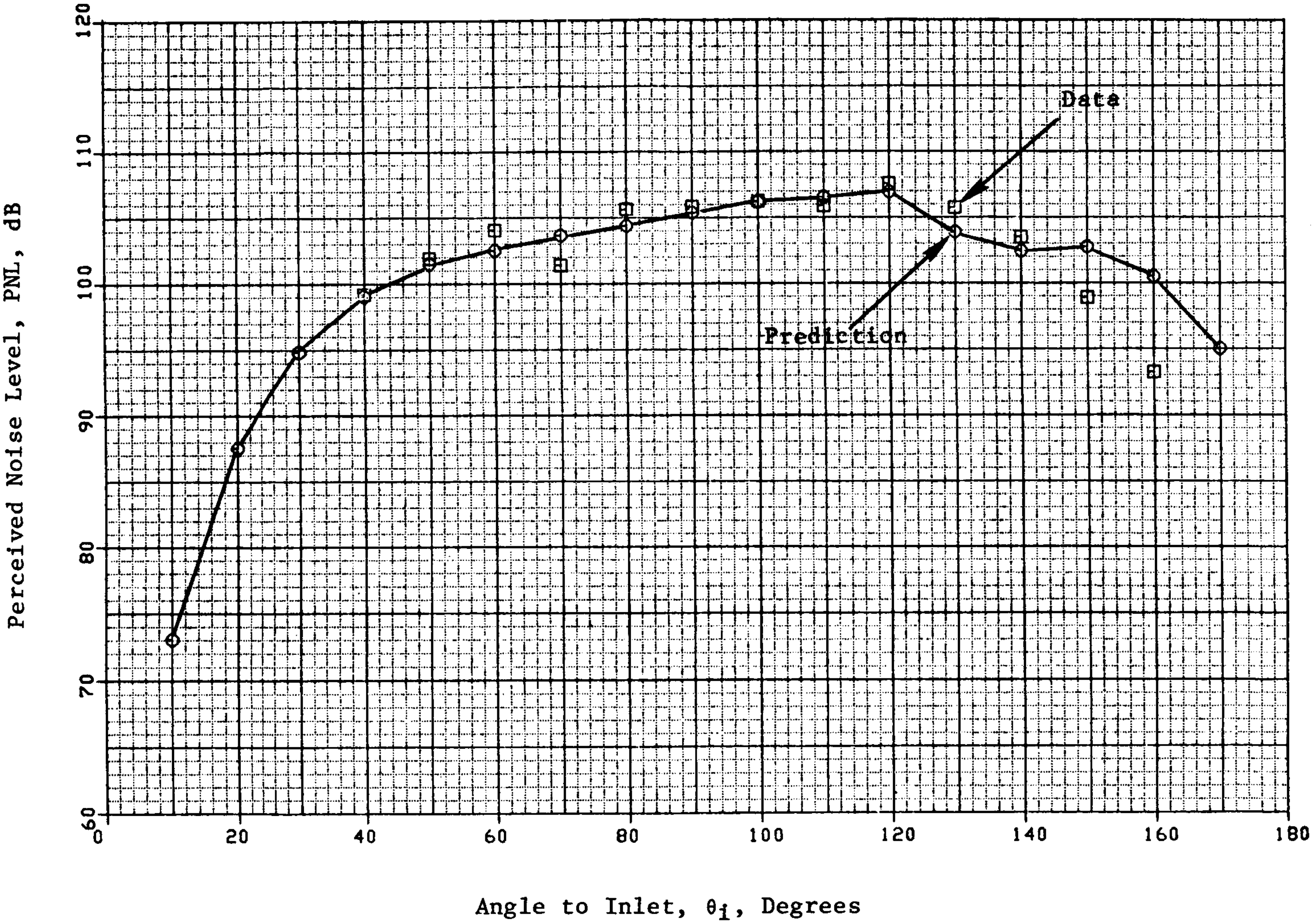

Figure 4-18. Comparison of Data and Prediction for PNL Directivcity of Similitude 20-Shallow-Chute Suppressor Nozzle at Typical Takeoff Condition (Flight).

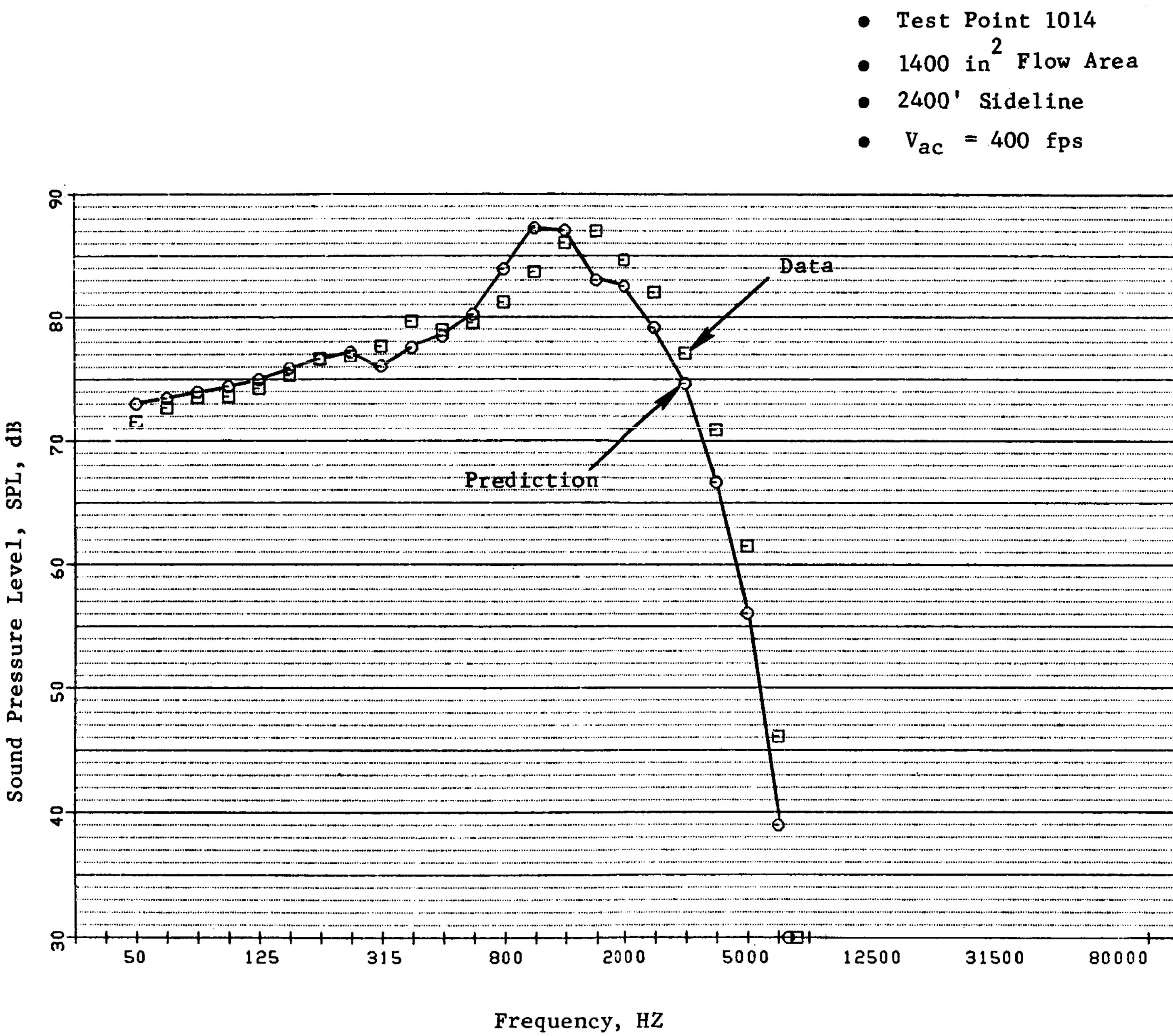

Figure 4-19. Comparison of Data and Prediction of Spectra at $\theta_i = 60°$ for Similitude 20-Shallow-Chute Suppressor Nozzle at Typical Takeoff Condition (Flight).

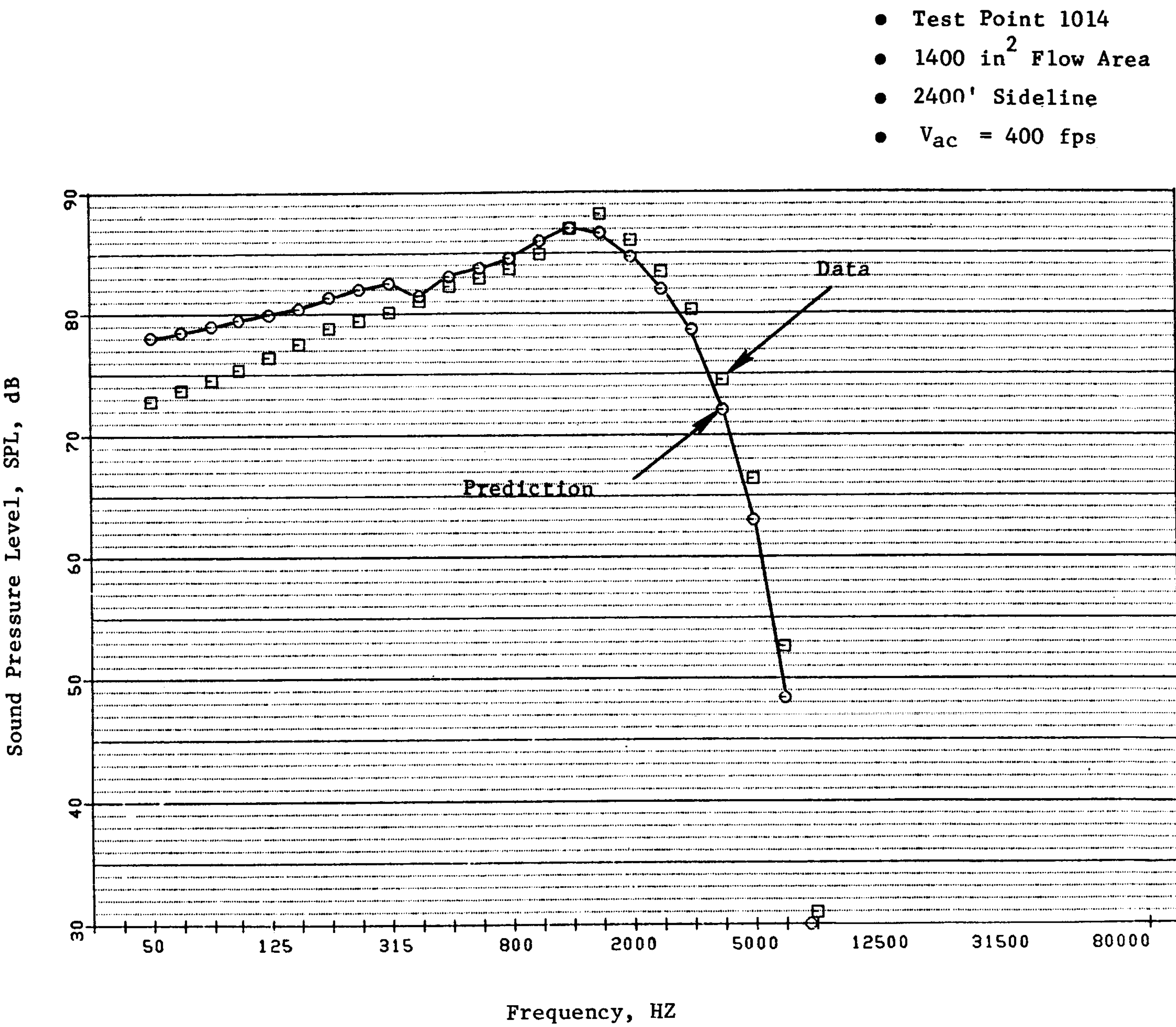

Figure 4-20. Comparison of Data and Prediction of Spectra at θ_i = 90° for Similitude 20-Shallow-Chute Suppressor Nozzle at Typical Takeoff Condition (Flight).

- Test Point 1014
- 1400 in^2 Flow Area
- 2400' Sideline
- V_{ac} = 400 fps

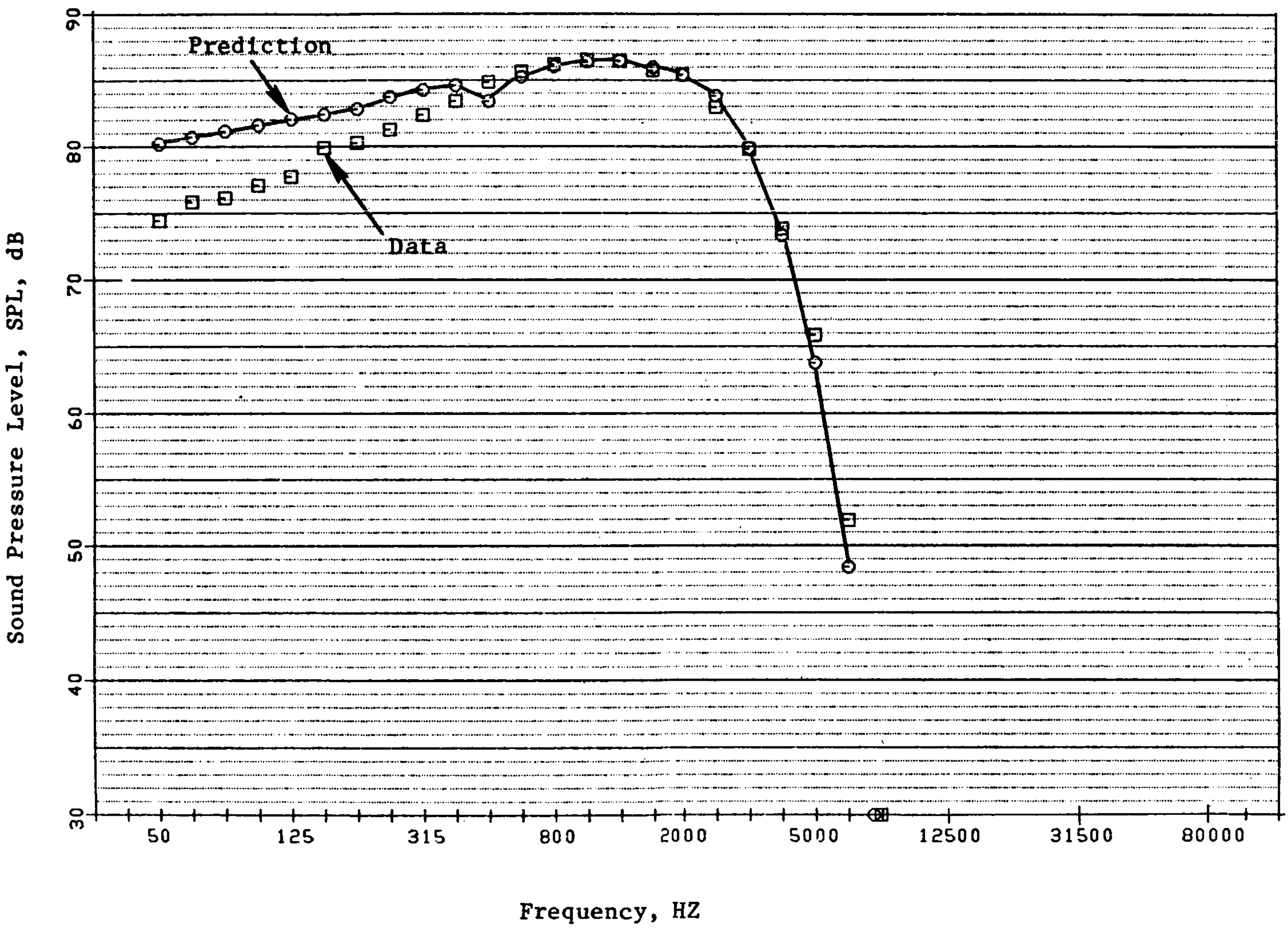

Figure 4-21. Comparison of Data and Prediction of Spectra at θ_i = 110° for Similitude 20-Shallow-Chute Suppressor Nozzle at Typical Takeoff Condition (Flight).

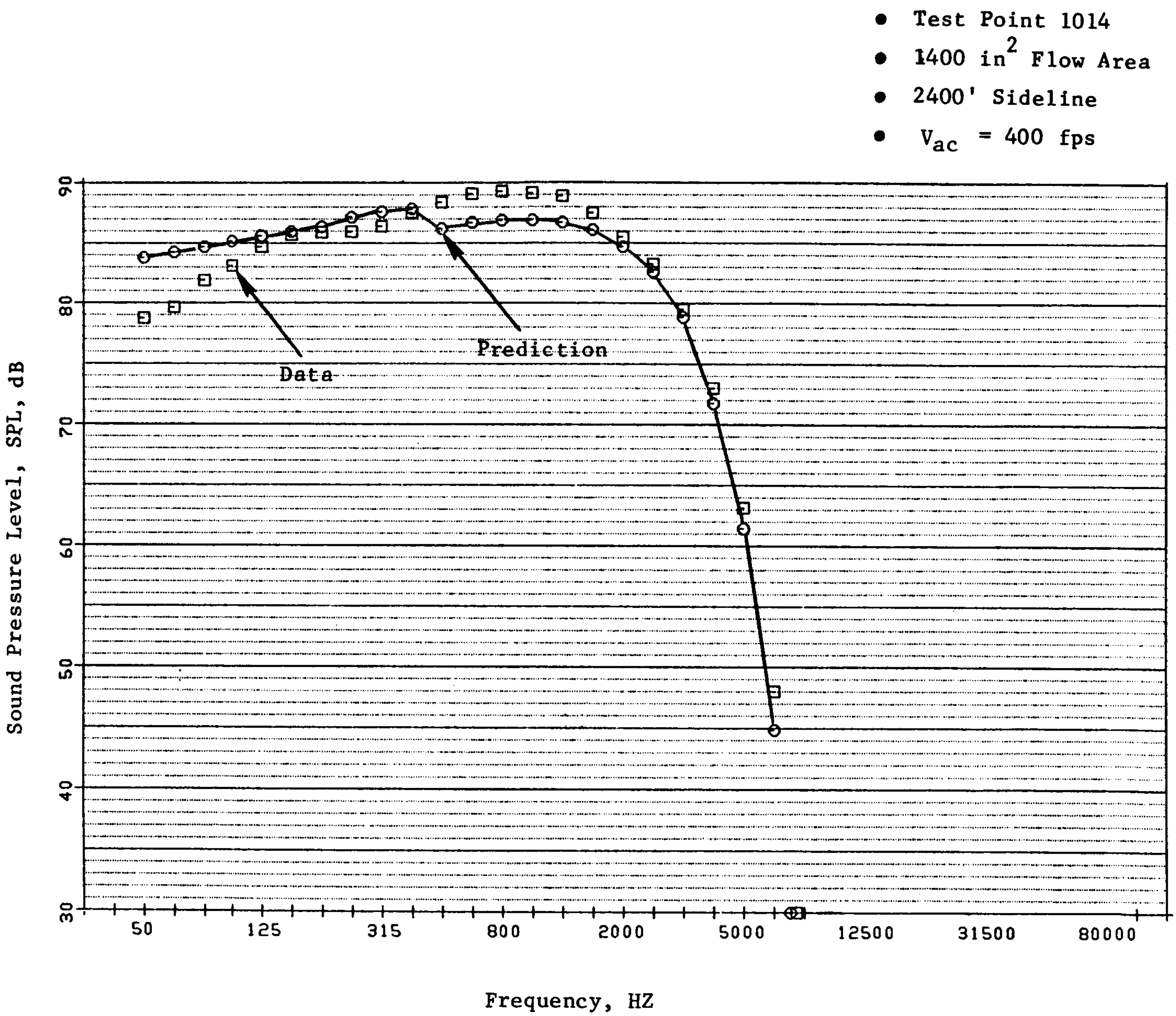

Figure 4-22. Comparison of Data and Prediction of Spectra at $\theta_i = 120°$ for Similitude 20-Shallow-Chute Suppressor Nozzle at Typical Takeoff Condition (Flight).

Stream	V_j fps	P_r	T_T °R
Suppressor	2269	2.80	1663
Inner	1626	2.80	863
Mixed	2143	2.76	1507

- Test Point 1008
- 1400 in^2 Flow Area
- 2400' Sideline
- V_{ac} = 400 fps

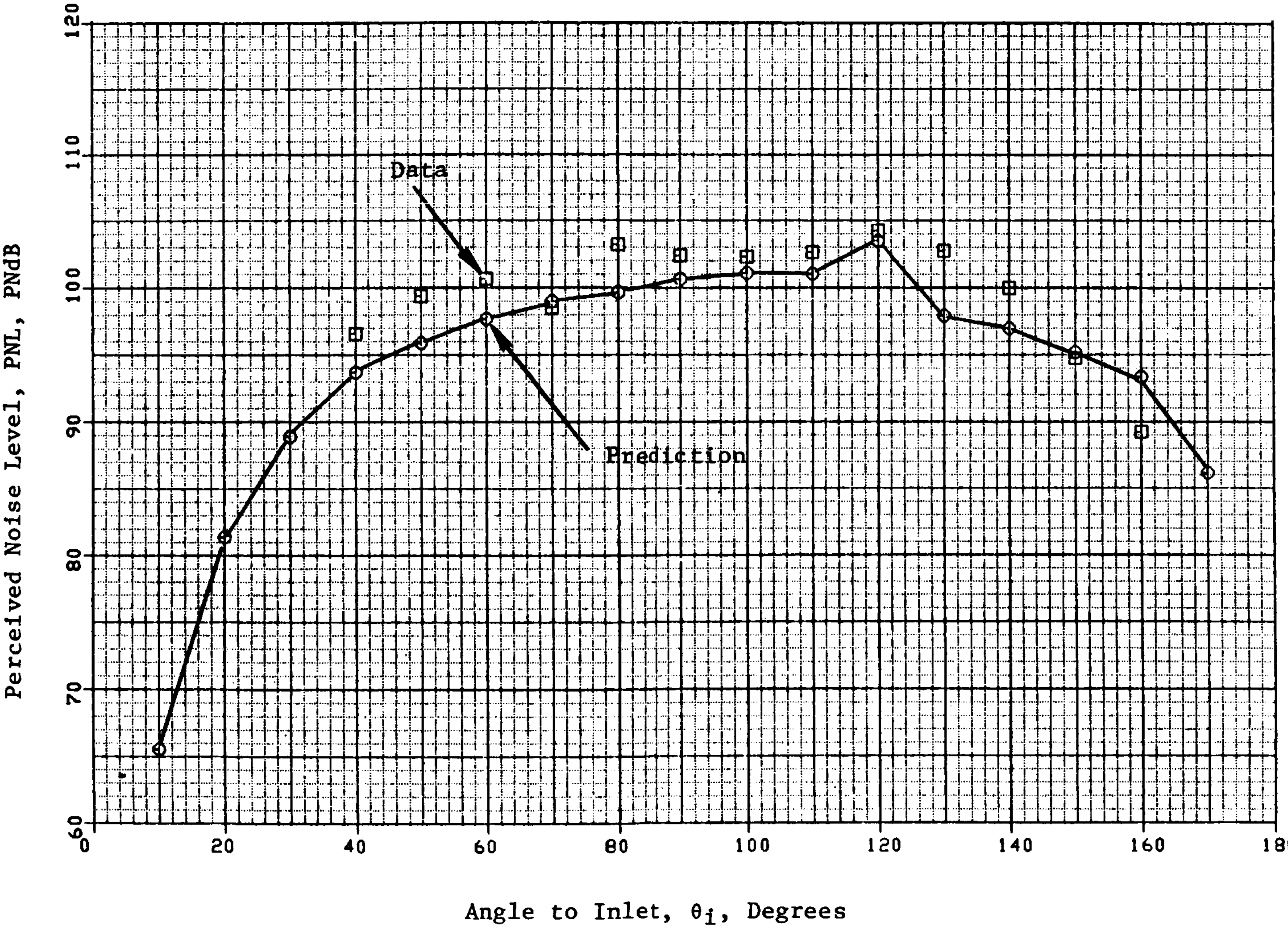

Figure 4-23. Comparison of Data and Prediction of PNL Directivity for Similitude 20-Shallow-Chute Suppressor Nozzle at Typical Cutback Condition (Flight).

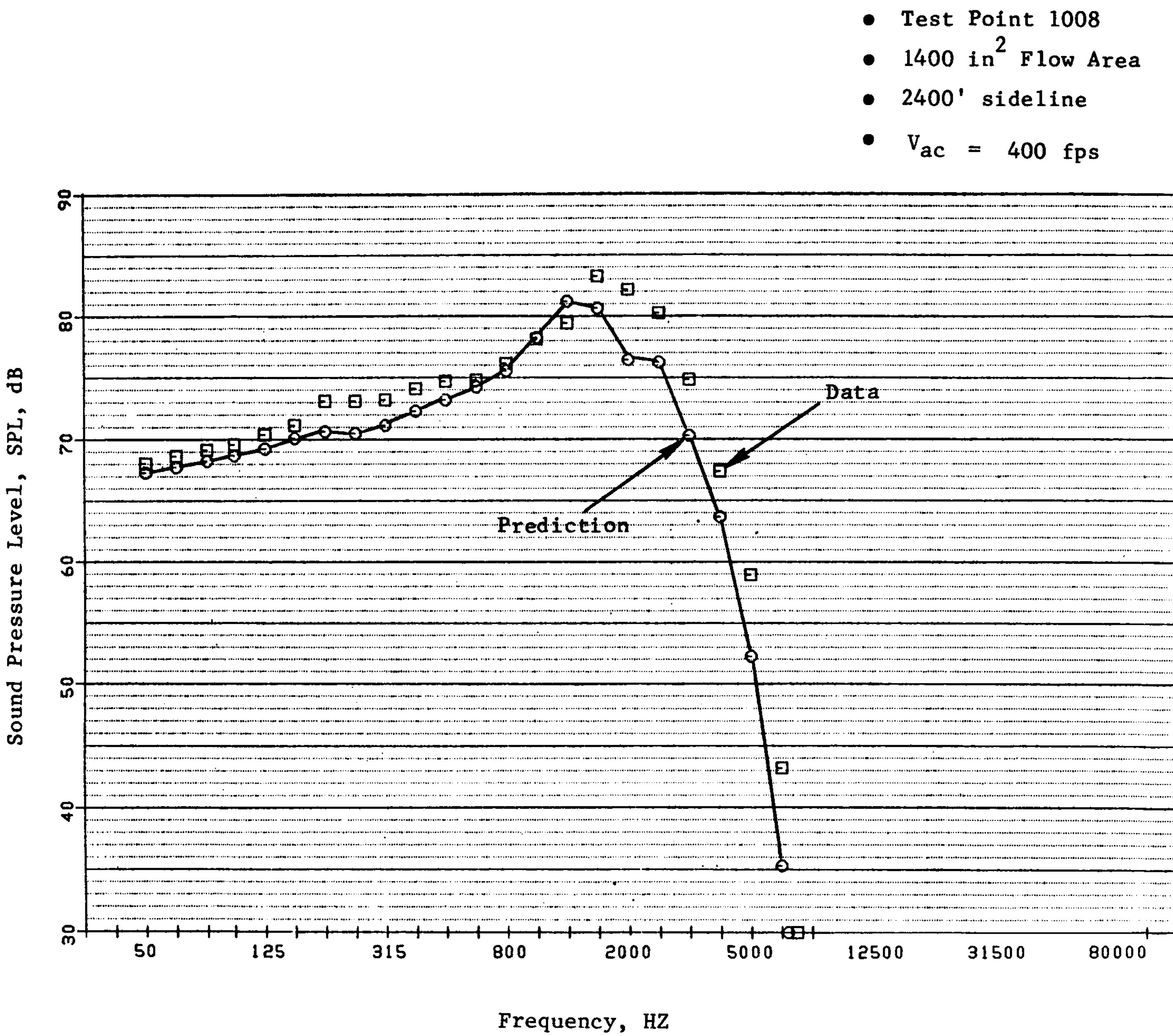

Figure 4-24. Comparison of Data and Prediction of Spectra at $\theta_i = 60°$ for Similitude 20-Shallow-Chute Suppressor Nozzle at Typical Cutback Condition (Flight).

- Test Point 1008
- 1400 in^2 Flow Area
- 2400' Sideline
- V_{ac} = 400 fps

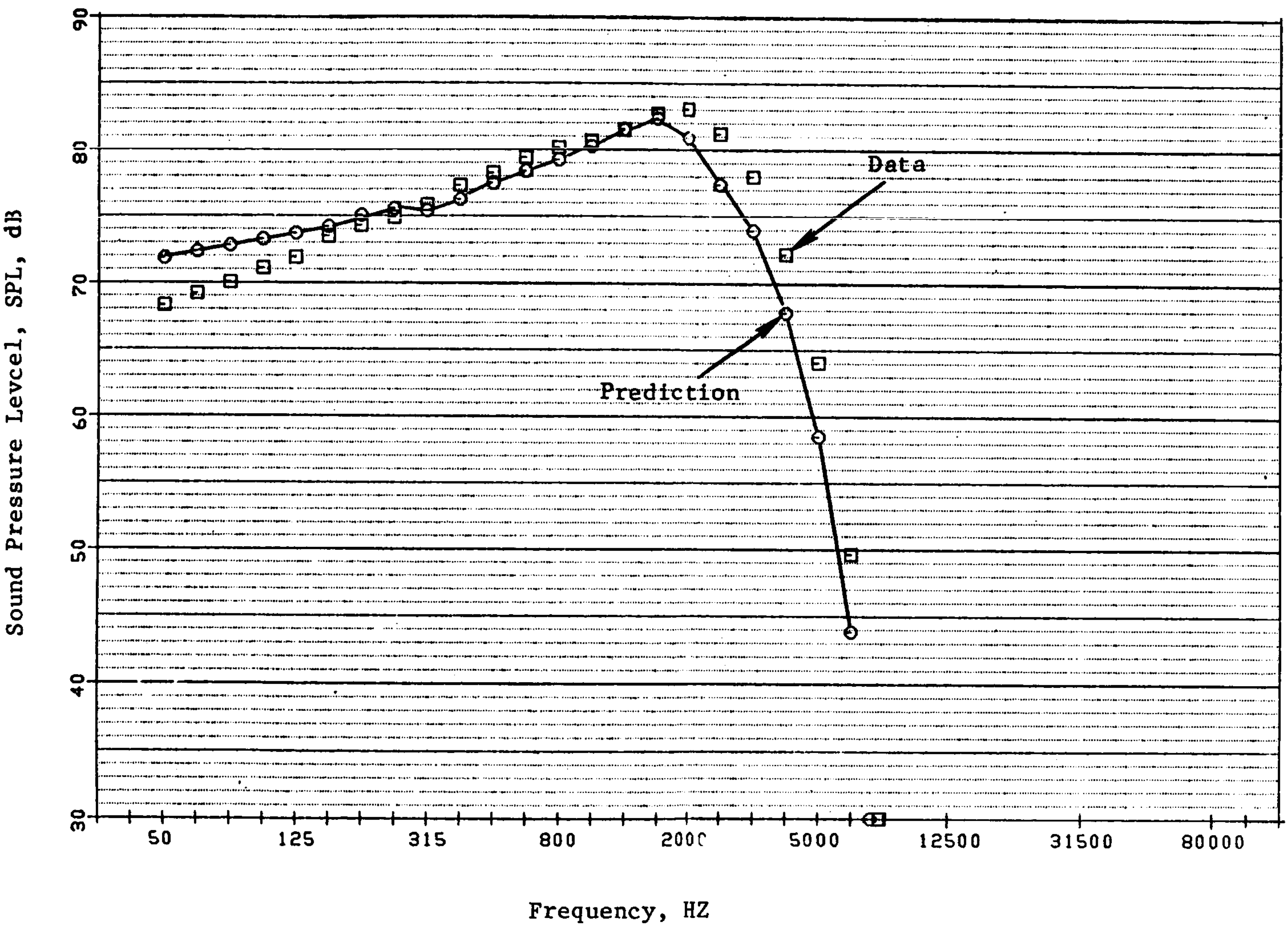

Figure 4-25. Comparison of Data and Prediction of Spectra at θ_i = 90° for Similitude 20-Shallow-Chute Suppressor Nozzle at Typical Cutback Condition (Flight).

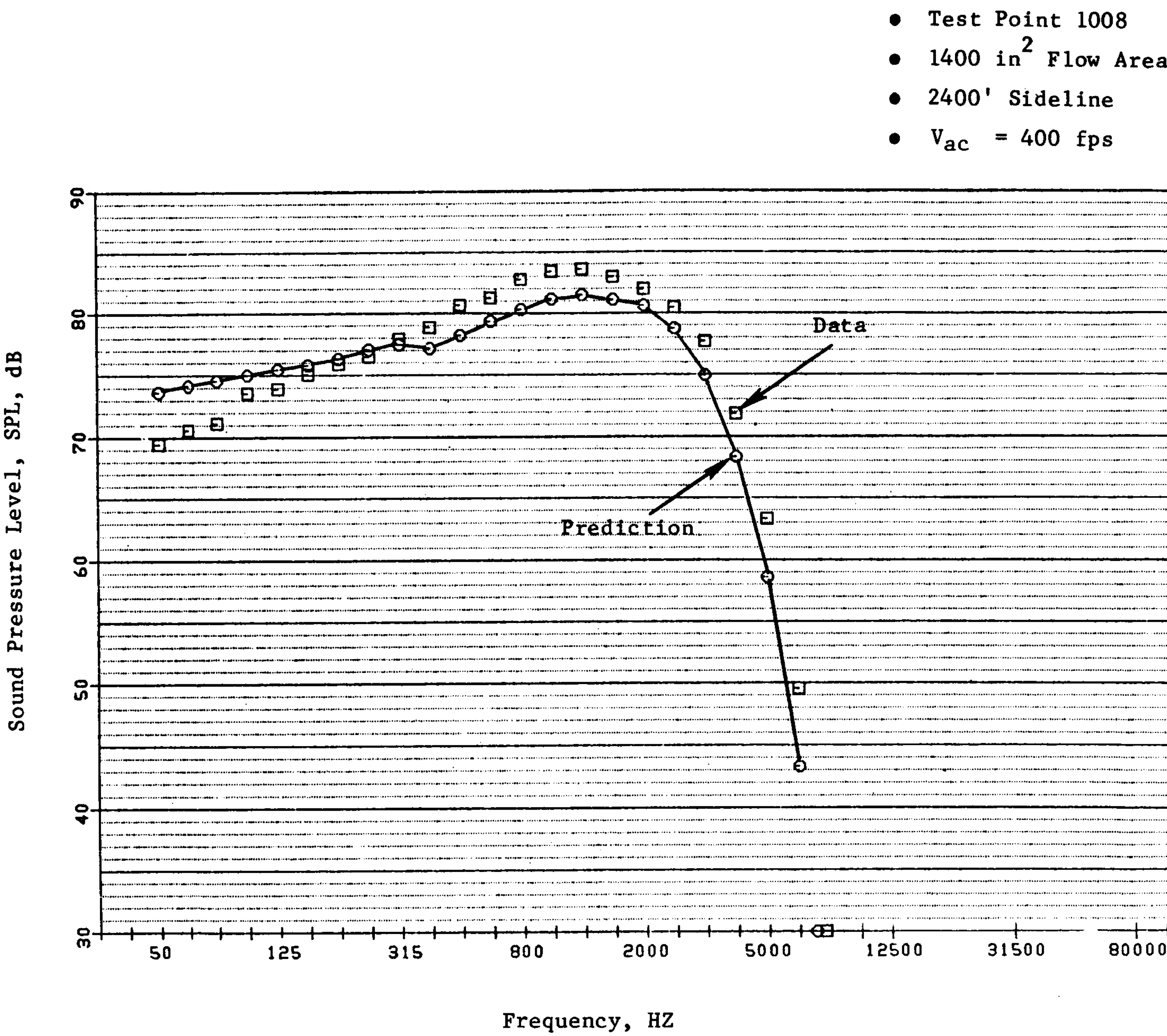

Figure 4-26. Comparison of Data and Prediction of Spectra at θ_i = 110° for Similitude 20-Shallow-Chute Suppressor Nozzle at Typical Cutback Condition (Flight).

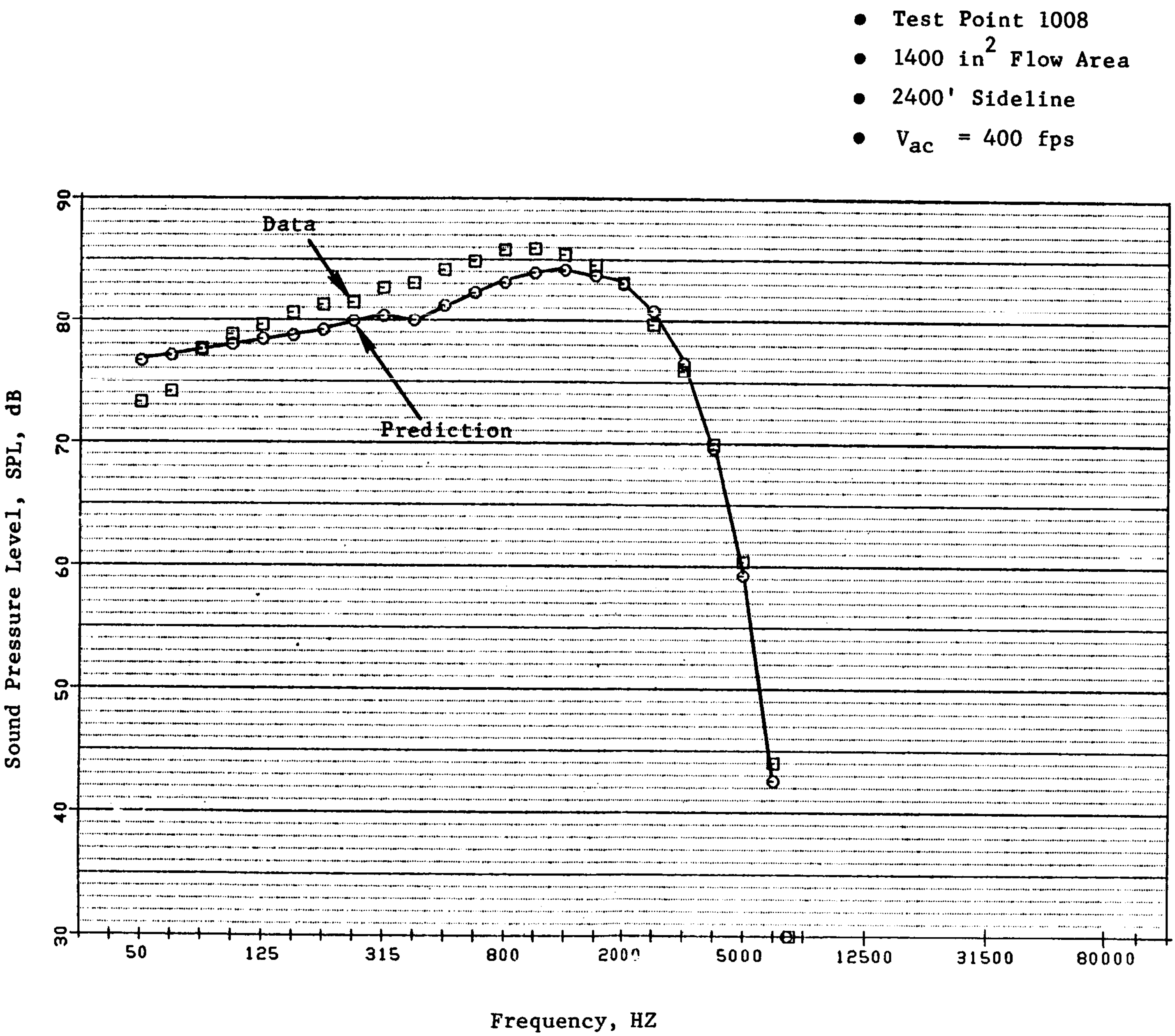

Figure 4-27. Comparison of Data and Prediction of Spectra at θ_i = 120° for Similitude 20-Shallow-Chute Suppressor Nozzle at Typical Cutback Condition (Flight).

- A set of appropriate length and velocity scales has been identified and the source spectra of the jet mixing noise of suppressors have been determined using the available data base on mechanical suppressors.

- A new convection amplification model characterizing the high mixing rates of mechanical suppressors is developed.

- Changes to reflect the multiple shock cell structures of the suppressor nozzles have been made to predict correctly the shock noise component.

The prediction procedure obtained has been shown to predict adequately the static and flight characteristics of the similitude suppressor nozzle. Some recommendations are suggested herein to improve the prediction procedure to represent better the acoustic data of mechanical suppressor nozzles.

It has been noted that the agreement between the data and prediction deteriorates in extreme aft angles. The agreement could be improved by reducing the effect of convective amplication at the extreme aft angles. Another aspect of improvement could be in the region of predicting the acoustic mean flow interactions. Although the nondimensional shielding function (i.e., H (fD/a_{amb}) has adequately represented the mean flow shrouding effect for mechanical suppressors as well as coannular plug nozzles, a better definition of the same for suppressors might improve the predictability of the procedure over the entire range of aft angles.

5.0 CONCLUSIONS

During this program, 10 scale-model nozzles were tested in the Anechoic Free-Jet Facility with the objectives of:

- Complementing the available conical baseline and coannular plug nozzle data.
- Validating the scaling criteria of both suppressed and unsuppressed coannular plug nozzles.
- Determining the effectiveness of incorporating C-D terminations on coannular plug nozzles.
- Estimating the acoustic characteristics of a scale-model coannular plug nozzle with a 20-shallow-chute suppressor in the outer stream that has been selected for tests on the test bed engine.
- Determining the effectiveness of incorporating a C-D termination on the inner stream of the above suppressor nozzle system.

To achieve these objectives, 113 static and 99 simulated free-jet ($V_{ac} \approx$ 122 mps or 400 fps) tests have been conducted. All dual flow tests had inverted velocity profiles. In addition, LV tests were conducted on three static and one simulated flight plumes of the scale-model suppressor nozzle.

The significant results from the analyses of the measured acoustic data are:

- Available baseline conical nozzle results and the measured data of this program agree to demonstrate repeatability.
- Conventional scaling criteria adopted in extrapolating acoustic data of model size unsuppressed coannular plug nozzles and conical baseline nozzle to engine nozzle characteristics are validated.
- At a mixed velocity of 700 mps (or 2,300 fps), the similitude suppressor nozzle yielded jet noise suppression to the extent of 11.5 and 9 PNdB at $\theta_i = 130°$ during static and simulated flight tests relative to baseline conical nozzle. The corresponding reductions in the OASPL data were 12 dB under both test conditions. The static-to-flight suppression loss of ~3 PNdB is due to the minimal alteration in flight of the high frequency premerged SPL levels. In the forward quadrant, the similitude suppressor nozzle was found to be ineffective in reducing the shock-cell noise relative to a coannular plug nozzle.
- No significant acoustic benefit was observed in both the front and the aft quadrants with a C-D inner termination on the similitude suppressor nozzle instead of the convergent inner termination.

- No significant differences were noted in the acoustic data of the similitude and modified DOT 20-shallow-chute suppressor nozzles. However, the modified DOT 40-shallow-chute suppressor nozzle was observed to result in better shock noise suppression in the front quadrant. In the aft quadrant, the 40-shallow-chute suppressor nozzle resulted in lower PNL data compared to the 20-shallow-chute configuration at V_j^{mix} < 700 mps (or 2,300 fps). For velocities greater than 700 mps (or 2,300 fps), the 20-shallow-chute nozzle was observed to yield lower aft angle PNL data.

- For a given outer stream velocity of the 20-shallow-chute suppressor nozzle, a change in the inner-to-outer stream velocity ratio over the range of 0.4 to 0.7 had no significant effect upon the peak PNL levels.

- The CD termination on annular and coannular plug nozzles has been shown to reduce front quadrant noise under both static and simulated flight conditions. At the measured maximum effective condition, the static and simulated flight PNL_{60} data, respectively, indicate (1) 6 and 9 dB reduction with the C-D annular plug nozzle relative to baseline conical nozzle and (2) 2 and 2.5 dB reduction with the coannular plug nozzle having a contoured C-D on the outer nozzle (and a convergent inner nozzle with a subsonic flow) relative to a similar coannular plug nozzle having no properly contoured outer C-D termination. Finally, relative to a coannular plug nozzle with both streams convergent terminated, the coannular plug nozzle with both streams C-D terminated resulted in a reduction of 2.3 dB in the static PNL_{60}.

- The C-D benefit on the annular plug nozzle data is observed over a range of off-design conditions.

- For a given V_j^{mix}, the coannular plug nozzle with both streams C-D terminated resulted in a higher noise level in the aft quadrant compared to the convergent coannular plug nozzle of this study. However, based on available data, this increase in the aft angle PNL data is attributed to the lower radius ratio of the model C-D nozzle relative to that of the convergent nozzle.

The significant results from the analyses of the similitude suppressor LV data are:

- The mixing rate and hence the mean velocity decay rate of the 20-shallow-chute suppressor nozzle is higher than those of baseline conical and coannular plug nozzles under both static and simulated flight conditions.

- A shock cell structure is observed distinctly in front of the suppressor chutes at flow conditions typical of an AST/VCE at takeoff.

- The effectiveness of the C-D termination on the inner stream of the suppressor nozzle could not be evaluated from the LV data.

Finally, an engineering spectral prediction procedure has been developed to predict the spectral and directivity characteristics of mechanical suppressors. In the process, appropriate length and velocity scales have been identified and a new convection amplification model has been developed. The predicted acoustic data of the similitude 20-shallow-chute suppressor nozzle have been compared with the measured results and a good agreement between the two sets of data is indicated.

6.0 NOMENCLATURE

A_r	Coannular nozzle inner-to-outer area ratio
A_R	Suppressor area ratio
A	Cross sectional exit area
a	Speed of sound
C-D	Convergent-Divergent
CDR	Comprehensive Data Report
dB	Decibel
D_{eq}	Equivalent conical nozzle diameter based on total flow area
D	Diameter
d_1^c, d_2^c	Chute depths (see Table 2-II for details)
F	Thrust
f	Frequency
FTFSDR	Flight Transformed Full Scale Data Reduction computer program
g	Shielding function
h	Annular step height dimension
H	Nondimensional shielding function
Hz	Hertz, cycles per second
L	Distance along outer shroud from outer nozzle throat to exit
LVM	Defined as 10 log (V_j/a_{amb})
M	Mach number
mps	Meter per second
N	Convection amplification factor
NF	Normalization Factor; defined as $-10 \log\left(\frac{F}{F_{ref}}\right)\left(\frac{\rho}{\rho_{amb}}\right)^{\omega-1}$
OAPWL	Overall sound power level

OASPLN	Normalized overall sound pressure level, OASPL+NF
1/3 OAPWL	1/3 octave band sound power level
P	Pressure
P_r	Pressure Ratio; defined as ratio of total to ambient
PNL	Perceived noise level
PNLN	Normalized perceived noise level; defined as = PNL+NF
PWL	Sound power level, dB re 10^{-12} W
R	Radial distance to the observer from the jet nozzle exhaust plane
RH	Relative humidity
R_r	Radius ratio, inner to outer S Outer nozzle throat height
SPL	Sound pressure level
SPLN	Normalized sound pressure level; defined in Equation 3, Section 4.0
St	Strouhal number
T	Temperature
V	Ideally expanded velocity
VCE	Variable cycle engine
W_1^c, W_2^c, W_1^F, W_2^F,	Flow element widths (see Table 2-II for details)
$\dot{W}$	Weight flow rate
x	Axial distance measured from the jet exhaust plane
α	Atmospheric attenuation
γ	Specific heat ratio
β	Shock strength parameter
ΔdB, Δ(f)	(From Figure 2-5)
δ	Shielding integral
θ_i	Microphone angle measured relative to inlet
θ_1, θ_2	Plug angles (Figure 2-12)

μ	Turbulence constant = 0.325 (Ref. 27)
ρ	Jet static density
ω	Density exponent
Ω	Source radian frequency

<u>Subscripts</u>

ac	Free-jet conditions
amb	Ambient conditions
Eff	Effective
c	Convection
cr	Critical condition for total internal reflection
e	Nozzle exit
eq	Equivalent
hyd	Hydraulic
j	Based on ideal jet conditions
p	Peak
r	Ratio
ref	Reference
T	Total flow condition
t	Throat

<u>Superscripts</u>

e	Suppressor element
eff	Effective condition of a coannular nozzle (see Subsection 3.1.6.1 for definition)
i	Inner stream
HF	High frequency (premerged)
LF	Low frequency (merged)

mix	Fully mixed conditions
o	Outer stream
T	Total
'	Turbulent quantity

<u>REFERENCES</u>

1. Janardan, B. A., Brausch, J. F., Hoerst, D. J., Selmeier, J. P. and Knott, P. R., "Free-Jet Investigation of Mechanically Suppressed High-Radius-Ratio Coannular Plug Model Nozzles," Comprehensive Data Reports, Volumes I and II, R81AEG484, 1981.

2. Knott, P. R., Janardan, B. A., Majjigi, R. K., Bhutiani, P. K. and Vogt, P. G., "Free-Jet Acoustic Investigation of High-Radius-Ratio Coannular Plug Nozzles, NASA CR- , 1981.

3. Clapper, W. S., et. al., "High Velocity Jet Noise Source Location and Reduction; Task IV - Development/Evaluation of Techniques for Inflight Investigation," R77AEG189, Report No. FAA-RD-76-79, IV, Final Report, U.S. Department of Transportation, February 1977.

4. Knott, P. R., et. al., "Supersonic Jet Exhaust Noise Investigation," AFAPL-TR-74-25, June 1974.

5. Knott, P. R., "Super onic Jet Exhaust Investigation - Volume I Summary Report," AFAPL-TR-76-73, July 1, 1976.

6. Shields, F. D. and Bass, H. E., "Atmospheric Absorption of High Frequency Noise and Application to Fractional - Octave Bands," University of Mississippi, NASA CR-2760, June 1977.

7. Vdoviak, J. W., Knott, P. R., and Ebacker, J. J., "Aerodynamic/Acoustic Performance of YJ101/Double Bypass VCE With Coannular Plug Nozzle," Final Report, General Electric Company, R80AEG369, NASA CR-159869, January 1981.

8. Knott, P. R. and Nash, D., "Design Report for the Variable Cycle Testbed Engine Exhaust System," General Electric Company, R80AEG030, May 1980 (also published as TM 80-216, General Electric, Evendale, May 1980).

9. Wolf, J. P., "Preliminary Design of an AST Jet Engine Exhaust System Incorporating a 20-Chute Suppressor in the Outer Stream of an Annular Two Steam Plug Nozzle," TM 79-535, September 1979.

10. Patton, M. E., "Diagnostic Evaluation of Lobed Mixer Exhaust Nozzle Aero-Acoustic Characteristics of Energy Efficient Engine," TM 80-528, General Electric Company, May 1981.

11. Brausch, J. F., et. al., "High Velocity Jet Noise Source Location and Reduction; Task III - Experimental Investigation of Suppression Principles," Volume II and III, R78AEG627, U.S. Department of Transportation, December 1978.

12. Benzakein, M. J. and Knott, P. R., "Supersonic Jet Exhaust Noise," AFAPL-TR-72-52, August 1972.

13. Seiner, J. M., Norum, T. D., and Maestrello, L., "Effects of Noise Design from Supersonic Jets," NASA CP-2100, pp. 479-492, November 1979.

14. Tanna, H. K., "An Experimental Study of Jet Noise - Part II: Shock Associated Noise," J. of Sound and Vibration (1977) 50 (3), pp. 429-444.

15. Knott, P. R., Blozy, J. T., and Staid, P. S., "Acoustic and Aerodynamic Performance Investigations of Inverted Velocity Profile Coannular Plug Nozzles," NASA CR-3149, June 1979.

16. Keith, J. S., Ferguson, D. R., Markle, C. L., Heck, P. H., and Lahti, D. J., "Analytical Method for Predicting the Pressure Distribution About a Nacelle at Transonic Speeds," NASA CR-2217, July 1973.

17. Clapper, W. S., et. al., "High Velocity Jet Noise Source Location and Reduction, Task V - Investigation of Inflight Aeroacoustic Effects on Suppressed Exhausts, Vol. V," R78AEG628, Report No. FAA-RD-76-79, Final Report, U.S. Department of Transportation, January 1979.

18. Bhutiani, P. K., "A Unique Coannular Plug Nozzle Jet Noise Prediction Procedure," AIAA Paper No. 80-1007, June 1980.

19. Mani, R., et. al., "High Velocity Jet Noise Source Location and Reduction," FAA-RD-76-79, Vol. II.

20. Yamamoto, K., "High Bypass Jet Noise," General Electric Technical Information Series, R81AEG197, 1981.

21. Anon., "Jet Exhaust Noise Prediction," AIR876, SAE A-21 Committee, New York, September 1975.

22. Lighthill, M. J., "On Sound Generated Aerodynamically: 1. General Theory," Proc. Roy. Soc. Lon., Vol. A211, 1952, pp. 564-587.

23. Hoch, R. E., Duponchel, J. P., Cocking, B. J., and Bryce, W. D., "Studies of the Influence of Density on Jet Noise," J. of Sound Vibration, Vol. 28, No. 4, 1973, pp. 649-668.

24. Balsa, T. F., "Fluid Shielding of Low Frequency Convected Sources by Arbitrary Jets," J. of Fluid Mechanics, Vol. 70, Part 1, 1975, pp. 17-36.

25. Balsa, T. F., "The Shielding of a Convected Source by an Annular Jet with an Application to the Performance of Multitube Suppressors," J. of Sound and Vibration, Vol. 44, No. 2, 1976, pp. 179-189.

26. Balsa, T. F., "The Far Field of High Frequency Convected Singularities in Sheared Flows, With Application to Jet-Noise Prediction," J. of Fluid Mechanics, Vol. 74, Part 2, 1976, pp. 193-208.

27. Ribner, H. S., "Aerodynamic Sound From Fluid Dilatations - A Theory of the Sound From Jets and Other Flows," UTIA Report No. 86, 1962.

28. Mani, R., "The Influence of Jet Flow on Jet Noise, Part 1, The Noise of Unheated Jets," J. of Fluid Mechanics, Vol. 73, Part 4, 1976, pp. 779-793.

29. Mani, R., "The Influence of Jet Flow on Jet Noise, Part 2, The Noise of Heated Jets," J. of Fluid Mechanics, Vol. 73, Part 4, 1976, pp. 779-793.

30. Harper-Bourne, M. and Fisher, M. J., "The Noise From Shock Waves in Supersonic Jets," AGARD Conference, Paper No. CPP-131, 1973.

31. Majjigi, R. K., "A Unique Spectral Acoustic Prediction Method for Jet and Shock Cell Noise of Mechanical Suppressor Nozzles," General Electric Company, R81AEG363, May 1981.

APPENDIX I - SUMMARY OF AERODYNAMIC FLOW CONDITIONS AND ACOUSTIC TEST DATA

The aerodynamic flow conditions corresponding to the acoustic test points taken on each of the test configurations are tabulated in this appendix. The data are tabulated in both the SI and English units.

The prescribed variables are defined in Table I-I. Sample sheets describing the variables listed in the aerodynamic data tables are presented in Table I-II. In addition to the inner and outer stream flow parameters, the tabulated data contain the mixed stream conditions that were calculated after assuming that the two streams were perfectly mixed. The mixed velocity (V_J^{mix}) and the mixed temperature (T_T^{mix}) are given by

$$V_J^{mix} = \frac{V_j^o \dot{W}^o + V_j^i \dot{W}^i}{\dot{W}^o + \dot{W}^i}$$

and

$$T_T^{mix} = \frac{T_T^o \dot{W}^o + T_T^i \dot{W}^i}{\dot{W}^o + \dot{W}^i}$$

From the known mixed velocity and total temperature, other mixed flow parameters are calculated using standard isentropic relations. The ambient pressure and temperature along with the relative humidity in the GE Anechoic Facility at the time of the test are presented also in these tables.

The normalization factor, NF, found in these tables are employed to normalize the measured PNL to a reference thrust as follows:

PNLN = normalized PNL = PNL + NF

where

$$NF = -10 \log \left(\frac{F}{F_{ref}}\right) \left(\frac{\rho}{\rho_{amb}}\right)^{\omega-1}$$

The normalized data are used to determine the dependence of aft angle jet noise on the acoustic Mach number by plotting PNLN against 10 log (V_j/a_{amb}).

The acoustic data that are summarized in the tables are far-field PNL results [scaled to an AST nozzle size of 9,032 cm^2 (1,400 in.^{2}) and extrapolated to a 731.5 m (2,400 ft) sideline] at selected angles of θ_i = 50°, 60°, 70°, 90°, 120°, 130°, 140° relative to an engine inlet.

The test results are summarized in Tables I-III through I-XII.

Table I-I. Definition of Symbols Used in Aerodynamic Data Tables

F	Total Thrust
LVM	Defined as 10 log (V_j/a_{amb})
LBM	Defined as 10 log $\sqrt{(M_j^2 - 1)}$
NF	PNL Normalization Factor; defined as $-10 \log \left(\frac{F}{F_{ref}}\right)\left(\frac{\rho}{\rho_{amb}}\right)^{\omega-1}$
P_{amb}	Ambient Pressure
P_r	Nozzle Pressure Ratio
T_{amb}	Dry Bulb Ambient Temperature
T_T	Nozzle Total Temperature
V_{ac}	Free-Jet Velocity
V_j	Nozzle Exhaust Velocity (Ideal)
$\hat{W}$	Ideal Calculated Weight Flow Rate

Table I-II. Description of Aerodynamic Data Sheet.

(English Units)

NOZZLE - MODEL 5 AREA [MODEL SIZE - INNER = 0.00 , OUTER = 20.38 ; FULL SIZE - TOTAL = 1400.00] SQ.IN.

TEST POINT	V_{ac}	P^o_r	T^o_T	V^o_j	W^o	P^i_r	T^i_T	V^i_j	W^i	P^{mix}_r	T^{mix}_T	V^{mix}_j	F	V^i_j/V^o_j
	FT/SEC		DEG R	FT/SEC	LB/SEC		DEG R	FT/SEC	LB/SEC		DEG R	FT/SEC	LB	

- Model Number
- Inner & Outer Nozzle Throat Areas (Model Size)
- Total Throat Area of Scaled Nozzle (AST Size)
- Test Point Number
- Free Jet Velocity (Simulated Aircraft Velocity)
- Outer Stream Flow Variables
- Inner Stream Flow Variables
- Mixed Stream Conditions
- Total Thrust
- Inner to Outer Stream Exhaust Velocity Ratio

TEST POINT	T_{amb}	P_{amb}	RH	NF	LVM	LBM	PNL (FULL SIZE, 2400 FT SIDE LINE), dB ANGLE RELATIVE TO INLET, DEGREES 50	70	90	110	120	130	140	OAPWL
	DEG R	PSIA	%	dB										dB

- Dry Bulb Temperature
- Barometric Pressure
- Relative Humidity
- PNL Normalization Factor Defined as $-10 \log \left(\frac{F}{F_{ref}}\right)\left(\frac{\rho}{\rho_{amb}}\right)^{\omega-1}$; Normalized PNL = PNL + NF
- LVM: $10 \log\left(V_j^{mix}/a_{amb}\right)$
- LBM: $10 \log \sqrt{M_j^2-1}$
- Perceived Noise Level at Selected Angles Relative to Inlet and @ 2400 ft. sideline; Nozzle Scaled to 1400 sq. in. AST Size
- Overall Power Level

Table I-II. Description of Aerodynamic Data Sheet (Concluded).

(International Units)

NOZZLE - MODEL 8 AREA [MODEL SIZE - INNER =0.0023 , OUTER = 0.0116 ; FULL SIZE - TOTAL = 0.9031] sq.m.

TEST POINT	V_{ac}	V_j^o	T_T^o	T_j^o	P_r^o	$\dot{W}^o$	F^o	V_j^i	T_T^i	T_j^i	P_r^i	$\dot{W}^i$	F^i	V_j^{mix}	T_T^{mix}	T_j^{mix}	P_r^{mix}	$\dot{W}^T$	F^T	V_j^i/V_j^o
	m/s	m/s	°K	°K		kg/s	N	m/s	°K	°K		kg/s	N	m/s	°K	°K		kg/s	N	

Model Number

Inner & Outer Nozzle Throat Areas (Model Size)

Total Throat Area of Scaled Nozzle (AST Size)

Test Point Number

Free Jet Velocity (Simulated Aircraft Velocity)

Outer Stream Flow Variables

Inner Stream Flow Variables

Mixed Stream Conditions

Total Variables

Inner to Outer Stream Exhaust Velocity Ratio

Table I-III. Aerodynamic Data of Conical Baseline Nozzle (Model 5).

(English Units)

NOZZLE - MODEL 5 AREA [MODEL SIZE - INNER = 0.00 , OUTER = 20.38 ; FULL SIZE - TOTAL = 1400.00] SQ.IN.

TEST POINT	V_{ac} FT/SEC	P^o_r	T^o_T DEG R	V^o_j FT/SEC	$\dot{W}^o$ LB/SEC	P^i_r	T^i_T DEG R	V^i_j FT/SEC	$\dot{W}^i$ LB/SEC	P^{mix}_r	T^{mix}_T DEG R	V^{mix}_j FT/SEC	F LB	V^i_j/V^o_j
541	0	1.19	844	707	336.5	1.00	520	0	0.0	1.19	843	707	7399	0.00
542	400	1.19	848	705	333.3	1.00	520	0	0.0	1.19	848	705	7304	0.00
543	0	1.24	905	810	363.4	1.00	520	0	0.0	1.24	904	809	9147	0.00
544	400	1.24	891	803	365.3	1.00	520	0	0.0	1.24	891	802	9114	0.00
545	0	1.27	1146	954	338.9	1.00	520	0	0.0	1.27	1146	954	10051	0.00
546	400	1.26	1132	938	336.7	1.00	520	0	0.0	1.26	1131	937	9816	0.00
547	0	1.35	1138	1056	384.0	1.00	520	0	0.0	1.35	1138	1056	12606	0.00
548	400	1.34	1119	1045	386.2	1.00	520	0	0.0	1.34	1118	1045	12547	0.00
549	0	1.47	1143	1201	445.4	1.00	520	0	0.0	1.47	1143	1200	16626	0.00
550	400	1.47	1139	1200	446.7	1.00	520	0	0.0	1.47	1139	1200	16663	0.00
551	0	1.58	1215	1342	476.8	1.00	520	0	0.0	1.58	1215	1341	19884	0.00
552	400	1.58	1202	1333	478.6	1.00	520	0	0.0	1.58	1202	1332	19824	0.00
553	0	1.63	1304	1432	477.4	1.00	520	0	0.0	1.63	1304	1432	21246	0.00
554	400	1.63	1302	1429	477.0	1.00	520	0	0.0	1.63	1301	1429	21190	0.00
555	0	1.76	1302	1534	523.6	1.00	520	0	0.0	1.76	1301	1534	24969	0.00
556	400	1.77	1286	1526	527.4	1.00	520	0	0.0	1.77	1285	1525	25014	0.00
557	0	1.87	1331	1625	551.0	1.00	520	0	0.0	1.87	1330	1624	27826	0.00
558	400	1.87	1327	1622	551.4	1.00	520	0	0.0	1.87	1327	1621	27794	0.00
559	0	2.01	1395	1746	576.7	1.00	520	0	0.0	2.01	1394	1746	31303	0.00
560	400	2.01	1381	1738	579.6	1.00	520	0	0.0	2.01	1381	1738	31307	0.00

TEST POINT	T_{amb} DEG R	P_{amb} PSIA	RH %	NF dB	LVM	LBM	PNL (FULL SIZE, 2400 FT SIDE LINE), dB ANGLE RELATIVE TO INLET, DEGREES 50	60	70	90	120	130	140	OAPWL dB
541	539.5	14.54	39	-3.7	-2.07	-10.00	60.1	61.8	63.8	67.3	68.9	66.5	65.1	146.4
542	526.9	14.53	45	-3.8	-2.03	-10.00								
543	539.2	14.54	39	-4.4	-1.48	-10.00	64.2	65.9	68.0	71.4	73.9	71.4	70.1	149.8
544	528.3	14.53	45	-4.4	-1.47	-10.00								
545	535.4	14.54	41	-4.9	-0.75	-10.00	69.0	71.0	73.2	77.2	79.5	78.4	75.6	155.0
546	528.9	14.53	41	-4.8	-0.80	-10.00	69.5	70.8	72.2	73.1	72.1	69.5	66.0	151.7
547	536.5	14.54	41	-5.1	-0.31	-10.00	72.0	73.9	76.1	79.9	83.1	82.3	79.6	158.3
548	529.5	14.53	41	-5.1	-0.33	-10.00	72.3	73.4	74.7	75.8	75.6	73.8	70.6	152.1
549	539.0	14.54	39	-5.3	0.23	-10.00	75.9	77.6	80.0	83.4	87.8	86.9	85.9	163.0
550	530.0	14.53	41	-5.3	0.27	-10.00	76.0	77.3	78.6	79.9	82.3	80.4	77.9	156.8
551	538.5	14.54	39	-5.2	0.72	-10.00	78.9	81.0	72.5	86.5	91.2	90.9	90.4	166.9
552	530.4	14.53	46	-5.1	0.72	-10.00	79.5	80.9	82.0	83.8	85.9	84.2	82.9	160.4
553	536.8	14.54	40	-4.8	1.01	-10.00	80.7	82.7	84.8	88.9	93.7	93.3	93.2	169.7
554	530.7	14.53	46	-4.7	1.02	-10.00	81.5	83.0	84.0	85.8	88.4	87.0	85.8	162.6
555	538.3	14.54	39	-4.9	1.30	-10.00	82.7	84.7	86.6	90.5	96.0	96.1	97.2	172.3
556	531.6	14.53	46	-4.9	1.30	-10.00	83.6	85.2	86.1	88.0	91.5	90.3	89.4	165.3
557	538.0	14.54	40	-4.9	1.55	-10.00	85.0	86.7	88.6	92.2	97.8	98.1	99.5	174.2
558	535.1	14.53	41	-4.9	1.55	-10.00	85.2	86.4	87.6	89.7	93.1	92.3	92.5	167.5
559	537.1	14.54	40	-4.9	1.87	-4.92	87.4	89.0	91.1	94.2	100.7	101.4	104.6	177.5
560	534.7	14.53	41	-4.9	1.86	-4.92	87.7	88.8	89.7	92.2	95.9	95.7	96.1	170.4

Table I-III. Aerodynamic Data of Conical Baseline Nozzle (Model 5) (Continued).

(English Units)

NOZZLE - MODEL 5

TEST POINT	V_{ac} FT/SEC	P_r^o	T_T^o DEG R	V_j^o FT/SEC	$\dot{W}^o$ LB/SEC	P_r^i	T_T^i DEG R	V_j^i FT/SEC	$\dot{W}^i$ LB/SEC	P_r^{mix}	T_T^{mix} DEG R	V_j^{mix} FT/SEC	F LB	V_j^i/V_j^o
561	0	2.16	1472	1876	602.4	1.00	520	0	0.0	2.16	1471	1876	35125	0.00
562	400	2.16	1464	1871	604.1	1.00	520	0	0.0	2.16	1464	1871	35135	0.00
563	0	2.32	1508	1976	638.8	1.00	520	0	0.0	2.32	1507	1975	39232	0.00
564	400	2.32	1507	1977	639.5	1.00	520	0	0.0	2.32	1507	1976	39285	0.00
565	0	2.76	1678	2267	718.1	1.00	520	0	0.0	2.76	1678	2266	50592	0.00
566	400	2.76	1666	2257	720.7	1.00	520	0	0.0	2.76	1665	2257	50561	0.00
567	0	2.91	1685	2324	756.9	1.00	520	0	0.0	2.91	1685	2323	54662	0.00
568	400	2.92	1689	2327	757.4	1.00	520	0	0.0	2.92	1688	2327	54785	0.00

TEST POINT	T_{amb} DEG R	P_{amb} PSIA	RH %	NF dB	LVM	LBM	PNL (FULL SIZE, 2400 FT SIDE LINE), dB ANGLE RELATIVE TO INLET, DEGREES 50	60	70	90	120	130	140	OAPWL dB
561	537.1	14.54	40	-4.9	2.18	-3.19	90.4	91.8	93.4	96.8	102.8	104.6	108.7	179.9
562	534.2	14.53	41	-4.9	2.18	-3.19	90.8	91.8	93.2	95.3	99.3	100.2	101.5	174.4
563	536.8	14.54	40	-5.3	2.41	-2.23	93.5	94.8	96.2	98.6	104.8	107.6	109.2	181.1
564	533.7	14.53	41	-5.3	2.42	-2.22	95.4	95.9	96.7	97.7	101.8	102.9	104.8	177.1
565	538.6	14.53	40	-6.1	2.99	-0.83	100.1	102.3	103.9	105.2	109.9	113.5	112.3	186.0
566	532.6	14.53	41	-6.1	3.00	-0.83	104.4	105.4	106.2	105.8	107.9	110.6	110.6	184.1
567	537.3	14.53	40	-6.5	3.11	-0.52	101.0	103.2	105.5	106.8	111.2	115.6	114.4	188.0
568	532.2	14.53	41	-6.5	3.13	-0.51	106.3	107.5	108.1	108.1	109.3	112.1	111.0	185.5

Table I-III. Aerodynamic Data of Conical Baseline Nozzle (Model 5) (Concluded).

(International Units)

NOZZLE - MODEL 5 AREA [MODEL SIZE - INNER =0.0000 , OUTER = 0.0131 ; FULL SIZE - TOTAL = 0.9031] sq.m.

TEST POINT	V_{ac}	V_j^o	T_T^o	T_j^o	P_r^o	$\dot{W}^o$	F^o	V_j^i	T_T^i	T_j^i	P_r^i	$\dot{W}^i$	F^i	V_j^{mix}	T_T^{mix}	T_j^{mix}	P_r^{mix}	$\dot{W}^T$	F^T	V_j^i/V_j^o
	m/s	m/s	°K	°K		kg/s	N	m/s	°K	°K		kg/s	N	m/s	°K	°K		kg/s	N	
541	0.	215.5	468.9	445.7	1.1938	152.6	2057	0.	288.9	288.9	1.0000	0.0	0	215.6	257.2	445.7	1.1938	153.	2057	0.00
542	122.	214.9	471.1	448.2	1.1914	151.2	2030	0.	288.9	288.9	1.0000	0.0	0	214.9	258.5	448.2	1.1914	151.	2030	0.00
543	0.	246.9	502.8	472.6	1.2433	164.8	2542	0.	288.9	288.9	1.0000	0.0	0	246.9	275.7	472.6	1.2433	165.	2542	0.00
544	122.	244.8	495.0	465.6	1.2426	165.7	2533	0.	288.9	288.9	1.0000	0.0	0	244.7	271.6	465.6	1.2426	166.	2533	0.00
545	0.	290.8	636.7	597.1	1.2699	153.7	2794	0.	288.9	288.9	1.0000	0.0	0	290.8	349.4	597.1	1.2699	154.	2794	0.00
546	122.	285.9	628.9	590.2	1.2632	152.7	2728	0.	288.9	288.9	1.0000	0.0	0	285.9	344.9	590.2	1.2632	153.	2728	0.00
547	0.	321.9	632.2	583.3	1.3462	174.2	3504	0.	288.9	288.9	1.0000	0.0	0	322.0	346.9	583.3	1.3462	174.	3504	0.00
548	122.	318.5	621.7	573.4	1.3446	175.2	3488	0.	288.9	288.9	1.0000	0.0	0	318.6	341.0	573.4	1.3446	175.	3488	0.00
549	0.	366.1	635.0	571.6	1.4729	202.0	4622	0.	288.9	288.9	1.0000	0.0	0	366.0	348.4	571.6	1.4729	202.	4622	0.00
550	122.	365.8	632.8	569.4	1.4743	202.6	4632	0.	288.9	288.9	1.0000	0.0	0	365.8	347.2	569.4	1.4743	203.	4632	0.00
551	0.	409.0	675.0	596.6	1.5822	216.3	5528	0.	288.9	288.9	1.0000	0.0	0	409.0	370.5	596.6	1.5822	216.	5528	0.00
552	122.	406.3	667.8	590.2	1.5803	217.1	5511	0.	288.9	288.9	1.0000	0.0	0	406.2	366.5	590.2	1.5803	217.	5511	0.00
553	0.	436.5	724.4	635.9	1.6301	216.5	5906	0.	288.9	288.9	1.0000	0.0	0	436.5	397.5	635.9	1.6301	217.	5906	0.00
554	122.	435.6	723.3	635.1	1.6284	216.4	5891	0.	288.9	288.9	1.0000	0.0	0	435.7	396.8	635.1	1.6284	216.	5891	0.00
555	0.	467.6	723.3	621.1	1.7646	237.5	6941	0.	288.9	288.9	1.0000	0.0	0	467.6	396.8	621.1	1.7646	238.	6941	0.00
556	122.	465.1	714.4	613.1	1.7663	239.2	6954	0.	288.9	288.9	1.0000	0.0	0	465.1	391.9	613.1	1.7663	239.	6954	0.00
557	0.	495.3	739.4	625.0	1.8736	249.9	7736	0.	288.9	288.9	1.0000	0.0	0	495.2	405.6	625.0	1.8736	250.	7736	0.00
558	122.	494.4	737.2	623.2	1.8726	250.1	7727	0.	288.9	288.9	1.0000	0.0	0	494.3	404.5	623.2	1.8726	250.	7727	0.00
559	0.	532.2	775.0	643.4	2.0099	261.6	8702	0.	288.9	288.9	1.0000	0.0	0	532.3	425.1	643.4	2.0099	262.	8702	0.00
560	122.	529.7	767.2	637.1	2.0101	262.9	8703	0.	288.9	288.9	1.0000	0.0	0	529.7	421.1	637.1	2.0101	263.	8703	0.00
561	0.	571.8	817.8	667.2	2.1597	273.2	9765	0.	288.9	288.9	1.0000	0.0	0	571.8	448.6	667.2	2.1597	273.	9765	0.00
562	122.	570.3	813.3	663.4	2.1601	274.0	9768	0.	288.9	288.9	1.0000	0.0	0	570.3	446.2	663.4	2.1601	274.	9768	0.00
563	0.	602.3	837.8	670.7	2.3195	289.8	10907	0.	288.9	288.9	1.0000	0.0	0	602.3	459.5	670.7	2.3195	290.	10907	0.00
564	122.	602.6	837.2	670.3	2.3217	290.1	10921	0.	288.9	288.9	1.0000	0.0	0	602.4	459.3	670.3	2.3217	290.	10921	0.00
565	0.	691.0	932.2	715.7	2.7594	325.7	14065	0.	288.9	288.9	1.0000	0.0	0	690.9	511.6	715.7	2.7594	326.	14065	0.00
566	122.	687.9	925.6	710.0	2.7578	326.9	14056	0.	288.9	288.9	1.0000	0.0	0	688.0	507.6	710.0	2.7578	327.	14056	0.00
567	0.	708.4	936.1	708.0	2.9150	343.3	15196	0.	288.9	288.9	1.0000	0.0	0	708.2	513.6	708.0	2.9150	343.	15196	0.00
568	122.	709.3	938.3	709.3	2.9192	343.6	15230	0.	288.9	288.9	1.0000	0.0	0	709.4	514.7	709.3	2.9192	344.	15230	0.00

Table I-IV. Aerodynamic Data of Similitude Unsuppressed Coannular Plug Nozzle (Model 8).

(English Units)

NOZZLE - MODEL 8   AREA (MODEL SIZE - INNER = 3.50; OUTER = 18.05; FULL SIZE = 1400.00) SQ. IN.

TEST POINT	V_{ac} FT/SEC	P^o_r	T^o_T DEG R	V^o_j FT/SEC	$\dot{W}^o$ LB/SEC	P^i_r	T^i_T DEG R	V^i_j FT/SEC	$\dot{W}^i$ LB/SEC	P^{mix}_r	T^{mix}_T DEG R	V^{mix}_j FT/SEC	F LB	V^i_j/V^o_j
8301	0	3.09	1735	2414	665.5	1.94	1250	1611	96.0	2.91	1674	2312	54731	0.67
8302	400	3.25	1754	2471	694.8	1.93	1282	1628	94.3	3.04	1697	2369	58126	0.66
8303	0	2.93	1758	2379	626.2	1.86	1296	1592	90.1	2.76	1700	2280	50770	0.67
8304	400	2.93	1760	2380	625.7	1.86	1307	1600	89.9	2.75	1702	2282	50751	0.67
8305	0	2.29	1730	2107	494.6	2.16	830	1402	131.9	2.24	1540	1958	38137	0.67
8306	400	2.30	1740	2117	494.4	2.14	828	1392	131.0	2.24	1549	1965	38199	0.66
8307	0	2.02	1567	1860	459.5	1.99	833	1336	121.7	2.00	1413	1750	31620	0.72
8308	400	2.04	1578	1876	461.0	1.99	832	1337	121.9	2.01	1422	1763	31943	0.71
8309	0	1.95	1543	1804	447.3	2.15	625	1213	151.5	1.94	1311	1654	30794	0.67
8310	400	1.93	1587	1813	435.1	1.90	778	1253	120.3	1.90	1411	1692	29205	0.69
8311	0	1.70	1396	1540	403.7	1.83	615	1082	128.8	1.70	1207	1429	23663	0.70
8312	400	1.69	1412	1540	397.3	1.79	612	1062	126.2	1.68	1219	1424	23180	0.69
8313	0	1.56	1365	1403	371.3	1.72	569	989	126.1	1.57	1163	1298	20069	0.71
8314	400	1.57	1326	1387	374.0	1.67	603	991	117.0	1.57	1154	1292	19726	0.72
8315	0	1.51	1320	1333	362.0	1.59	597	943	112.2	1.51	1148	1240	18286	0.71
8316	400	1.51	1327	1334	356.3	1.59	595	943	111.4	1.51	1152	1241	18041	0.71
8317	0	1.47	1305	1277	347.7	1.56	588	917	110.1	1.47	1132	1190	16939	0.72
8318	400	1.47	1285	1271	347.9	1.56	599	926	107.9	1.47	1123	1189	16847	0.73
8319	0	1.34	1253	1104	305.9	1.42	587	816	95.5	1.35	1095	1035	12917	0.74
8320	400	1.35	1229	1103	308.7	1.41	599	821	93.0	1.35	1083	1037	12956	0.75

TEST POINT	T_{amb} DEG R	P_{amb} PSIA	RH %	NF dB	LVM	LBM	PNL (FULL SIZE, 2400 FT SIDE LINE), dB ANGLE RELATIVE TO INLET, DEGREES 50	60	70	90	120	130	140	OAPWL dB
8301	518.4	14.60	62	-6.4	3.16	-0.54	94.2	96.9	99.2	106.4	107.0	110.0	110.7	184.2
8302	528.2	14.60	43	-6.7	3.23	-0.32	97.9	99.3	100.8	103.9	105.0	107.3	106.8	180.7
8303	519.1	14.60	62	-5.9	3.10	-0.84	94.0	96.2	98.4	105.8	106.4	109.2	110.7	183.3
8304	542.8	14.60	43	-6.1	3.01	-0.84	96.2	98.2	99.4	100.9	103.6	105.6	105.5	179.2
8305	520.1	14.60	62	-4.9	2.44	-2.47	89.6	91.4	93.4	101.0	102.0	103.1	104.1	178.3
8306	535.1	14.60	43	-5.0	2.39	-2.46	94.1	94.9	95.8	100.1	98.9	99.5	97.3	173.9
8307	521.1	14.61	49	-4.6	1.94	-4.80	85.9	87.8	89.9	98.0	98.2	100.1	99.0	174.1
8308	537.9	14.60	41	-4.8	1.91	-4.59	89.9	91.9	91.6	96.5	95.8	95.0	92.8	172.1
8309	521.8	14.61	49	-5.1	1.70	-5.44	85.4	87.4	89.4	97.2	97.1	98.2	97.2	172.5
8310	535.8	14.60	41	-4.6	1.73	-7.78	86.8	87.4	88.8	94.3	93.1	92.7	89.9	168.6
8311	536.4	14.47	72	-5.4	1.00	-10.00	79.5	81.4	83.5	91.3	91.3	90.4	90.3	166.4
8312	551.4	14.45	39	-5.5	0.93	-10.00	81.0	82.3	83.3	88.2	87.0	82.7	83.3	161.5
8313	526.4	14.61	41	-5.4	0.62	-10.00	77.9	79.4	81.6	85.1	88.7	89.7	86.6	163.3
8314	551.7	14.45	39	-5.6	0.50	-10.00	78.0	79.1	79.7	84.8	83.0	79.4	78.8	158.0
8315	522.5	14.61	49	-5.4	0.44	-10.00	76.2	77.8	80.0	87.1	86.8	87.8	84.1	161.7
8316	548.5	14.45	41	-5.5	0.34	-10.00	76.8	77.8	78.9	83.4	80.6	77.3	76.2	156.7
8317	522.5	14.61	45	-5.4	0.26	-10.00	75.3	77.0	79.0	82.5	85.6	85.9	82.6	160.2
8318	550.7	14.45	41	-5.5	0.14	-10.00	76.0	76.8	77.8	82.8	78.7	75.1	74.5	155.4
8319	523.2	14.61	45	-5.2	-0.35	-10.00	71.3	73.4	75.2	78.5	80.9	80.9	78.3	156.3
8320	549.9	14.45	41	-5.3	-0.45	-10.00	71.2	72.4	72.6	78.0	73.0	70.4	67.2	151.7

Table I-IV. Aerodynamic Data of Similitude Unsuppressed Coannular Plug Nozzle (Model 8) (Continued).

(English Units)

NOZZLE - MODEL 8

TEST POINT	V_{ac} FT/SEC	P^o_r	T^o_T DEG R	V^o_j FT/SEC	$\dot{W}^o$ LB/SEC	P^i_r	T^i_T DEG R	V^i_j FT/SEC	$\dot{W}^i$ LB/SEC	P^{mix}_r	T^{mix}_T DEG R	V^{mix}_j FT/SEC	F LB	V^i_j/V^o_j
8321	0	1.27	1239	986	272.2	1.33	586	742	85.5	1.27	1083	927	10314	0.75
8322	400	1.27	1215	980	273.0	1.33	600	751	83.5	1.27	1070	926	10264	0.77
8323	0	1.31	959	930	336.4	1.31	584	717	82.5	1.31	884	888	11566	0.77
8323	0	1.31	959	930	336.4	1.31	584	717	82.5	1.31	884	888	11566	0.77
8325	0	1.22	933	791	288.3	1.23	578	627	71.6	1.22	862	758	8485	0.79
8326	400	1.23	931	796	290.3	1.22	601	634	69.4	1.22	867	764	8547	0.80
8327	0	1.20	858	726	286.5	1.13	580	484	53.7	1.19	814	688	7275	0.67
8328	400	1.20	895	734	276.9	1.14	599	509	54.9	1.19	845	696	7184	0.70
8330	400	1.95	1541	1801	447.1	2.16	619	1213	153.5	1.94	1305	1651	30821	0.67
8001	0	3.17	1736	2438	677.8	3.12	832	1666	189.4	3.09	1539	2269	61180	0.68
8002	400	3.20	1734	2444	681.9	3.10	836	1665	186.9	3.11	1541	2276	61468	0.68
8211	0	3.30	1757	2487	700.0	1.45	931	1062	78.2	3.01	1673	2343	56694	0.43
8212	400	3.31	1774	2502	696.6	1.45	956	1079	77.1	3.02	1692	2360	56769	0.43

TEST POINT	T_{amb} DEG R	P_{amb} PSIA	RH %	NF dB	LVM	LBM	PNL (FULL SIZE, 2400 FT SIDE LINE), dB ANGLE RELATIVE TO INLET, DEGREES 50	60	70	90	120	130	140	OAPWL dB
8321	523.3	14.61	45	-5.0	-0.82	-10.00	68.5	70.2	72.6	80.3	77.5	77.0	73.9	153.0
8322	547.7	14.45	43	-4.9	-0.93	-10.00	0.	0.	0.	0.	0.	0.	0.	0.
8323	524.1	14.61	43	-5.0	-1.02	-10.00	65.6	67.5	69.5	77.0	72.2	70.8	70.9	150.9
8323	524.1	14.61	45	-5.0	-1.02	-10.00	67.0	68.9	71.0	74.1	75.6	75.4	72.8	151.4
8325	524.2	14.61	45	-4.2	-1.70	-10.00	62.8	64.6	66.9	69.6	70.7	71.1	67.4	147.3
8326	536.4	14.60	41	-4.2	-1.72	-10.00	66.8	70.0	70.7	75.7	68.1	67.0	62.5	151.9
8327	525.2	14.61	45	-3.6	-2.13	-10.00	61.7	63.7	66.0	68.9	70.7	67.7	64.2	145.2
8328	536.8	14.60	41	-3.7	-2.12	-10.00	66.7	69.9	70.3	76.2	70.3	67.4	62.0	154.6
8330	537.5	14.60	41	-5.4	1.62	-5.41	90.6	92.0	92.0	96.4	94.0	94.3	91.2	170.9
8001	526.9	14.49	66	-7.4	3.05	-0.11	98.7	101.7	103.1	107.8	107.0	110.1	110.6	183.7
8002	545.3	14.45	48	-7.6	2.99	-0.09	105.2	105.2	105.5	105.1	106.1	106.9	106.6	182.3
8211	529.4	14.49	66	-6.7	3.18	-0.37	94.3	97.4	99.8	102.8	106.8	110.3	110.0	183.1
8212	542.7	14.45	55	-6.8	3.15	-0.36	100.3	101.7	102.6	107.3	105.8	107.2	106.0	181.7

Table I-IV. Aerodynamic Data of Similitude Unsuppressed Coannular Plug Nozzle (Model 8) (Concluded).

(International Units)

NOZZLE - MODEL 8 AREA [MODEL SIZE - INNER =0.0023 , OUTER = 0.0116 ; FULL SIZE - TOTAL = 0.9031] sq.m.

TEST POINT	V_{ac}	V_j^o	T_T^o	T_j^o	P_r^o	$\dot{W}^o$	F^o	V_j^i	T_T^i	T_j^i	P_r^i	$\dot{W}^i$	F^i	V_j^{mix}	T_T^{mix}	T_j^{mix}	P_r^{mix}	$\dot{W}^T$	F^T	V_j^i/V_j^o
	m/s	m/s	°K	°K		kg/s	N	m/s	°K	°K		kg/s	N	m/s	°K	°K		kg/s	N	
8301	0.	735.8	963.9	718.6	3.0921	301.9	13879	491.3	694.6	580.4	1.9374	43.5	1336	704.9	510.3	703.8	2.9051	345.	15215	0.67
8302	122.	753.2	974.4	716.9	3.2456	315.2	14832	496.3	712.5	596.6	1.9298	42.8	1327	722.3	517.4	705.4	3.0361	358.	16159	0.66
8303	0.	725.1	976.7	739.4	2.9292	284.0	12874	485.3	720.5	610.2	1.8556	40.9	1240	695.0	518.2	725.7	2.7556	325.	14114	0.67
8304	122.	725.4	977.8	740.3	2.9277	283.8	12867	487.7	726.3	615.1	1.8575	40.8	1242	695.6	519.0	727.1	2.7549	325.	14109	0.67
8305	0.	642.2	961.1	776.8	2.2936	224.3	9004	427.4	461.5	370.6	2.1551	59.8	1598	597.0	469.6	693.0	2.2361	284.	10602	0.67
8306	122.	645.3	966.7	781.1	2.3000	224.3	9043	424.6	460.1	370.4	2.1365	59.4	1576	599.0	472.2	696.9	2.2379	284.	10619	0.66
8307	0.	566.9	870.6	724.7	2.0222	208.4	7385	407.4	462.9	380.3	1.9901	55.2	1405	533.6	430.7	653.4	1.9968	264.	8790	0.72
8308	122.	571.8	876.7	728.8	2.0372	209.1	7472	407.5	462.3	379.7	1.9928	55.3	1407	537.5	433.5	656.7	2.0090	264.	8880	0.71
8309	0.	549.9	857.2	720.3	1.9532	202.9	6973	369.8	347.3	279.2	2.1461	68.7	1588	504.4	399.6	609.2	1.9432	272.	8561	0.67
8310	122.	552.6	881.7	743.8	1.9279	197.4	6816	382.0	432.7	360.0	1.9029	54.6	1302	515.7	430.3	661.6	1.9012	252.	8119	0.69
8311	0.	469.4	775.6	674.2	1.7000	183.1	5373	330.1	341.9	287.7	1.8301	58.4	1205	435.7	367.9	580.8	1.6982	242.	6578	0.70
8312	122.	469.4	784.4	683.8	1.6876	180.2	5285	324.0	340.1	287.9	1.7927	57.2	1159	434.2	371.7	588.6	1.6816	237.	6444	0.69
8313	0.	427.6	758.3	674.2	1.5610	168.4	4501	301.5	316.5	271.2	1.7162	57.2	1077	395.7	354.6	572.1	1.5657	226.	5579	0.71
8314	122.	422.8	736.7	654.3	1.5651	169.6	4481	302.3	335.2	289.7	1.6663	53.1	1003	394.0	351.7	567.4	1.5653	223.	5484	0.72
8315	0.	406.3	733.3	656.9	1.5128	164.2	4169	287.6	331.9	290.8	1.5897	50.9	914	378.2	350.2	570.4	1.5109	215.	5083	0.71
8316	122.	406.6	737.2	660.7	1.5108	161.6	4107	287.6	330.6	289.4	1.5927	50.5	908	378.3	351.2	572.3	1.5093	212.	5015	0.71
8317	0.	389.2	725.0	655.2	1.4660	157.7	3836	279.6	326.8	287.9	1.5586	49.9	873	362.8	345.3	566.8	1.4677	208.	4709	0.72
8318	122.	387.4	713.9	644.6	1.4698	157.8	3820	282.3	333.2	293.5	1.5587	48.9	863	362.5	342.3	561.4	1.4720	207.	4683	0.73
8319	0.	336.5	696.1	643.9	1.3423	138.8	2917	248.8	326.4	295.6	1.4150	43.3	673	315.6	333.8	560.9	1.3457	182.	3591	0.74
8320	122.	336.2	682.8	630.3	1.3497	140.0	2941	250.5	333.1	301.9	1.4112	42.2	660	316.3	330.2	554.2	1.3521	182.	3601	0.75
8321	0.	300.5	688.3	646.6	1.2660	123.5	2319	226.3	325.8	300.3	1.3298	38.8	548	282.8	330.1	563.7	1.2702	162.	2867	0.75
8322	122.	298.7	675.0	633.5	1.2683	123.8	2311	228.9	333.3	307.3	1.3300	37.9	542	282.3	326.4	556.9	1.2728	162.	2853	0.77
8323	0.	283.5	532.8	493.3	1.3140	152.6	2703	218.8	324.6	300.8	1.3059	37.4	511	270.7	269.7	455.3	1.3098	190.	3215	0.77
8323	0.	283.5	532.8	493.3	1.3140	152.6	2703	218.8	324.6	300.8	1.3059	37.4	511	270.7	269.7	455.3	1.3098	190.	3215	0.77
8325	0.	241.1	518.3	489.8	1.2227	130.8	1971	191.2	321.2	303.0	1.2264	32.5	387	231.2	262.8	452.6	1.2214	163.	2358	0.79
8326	122.	242.6	517.2	488.7	1.2259	131.7	1995	193.4	334.4	315.8	1.2221	31.5	380	233.0	264.5	455.3	1.2237	163.	2376	0.80
8327	0.	221.3	476.7	452.5	1.2018	130.0	1797	147.5	322.5	311.7	1.1270	24.4	224	209.7	248.2	430.6	1.1896	154.	2022	0.67
8328	122.	223.7	497.2	472.4	1.1969	125.6	1755	155.4	332.9	320.9	1.1374	24.9	241	212.3	257.8	447.4	1.1868	151.	1997	0.70
8330	122.	548.9	856.1	719.3	1.9512	202.8	6959	370.0	344.1	275.9	2.1649	69.6	1609	503.3	397.9	606.4	1.9436	272.	8568	0.67
8001	0.	743.1	964.4	713.7	3.1749	307.4	14280	508.1	462.6	334.1	3.1232	85.9	2728	691.8	469.1	632.3	3.0950	393.	17008	0.68
8002	122.	744.9	963.3	711.2	3.2004	309.3	14399	507.7	464.8	336.6	3.0967	84.8	2689	693.8	469.8	632.2	3.1132	394.	17088	0.68
8211	0.	758.0	976.1	715.0	3.2990	317.5	15043	323.8	517.4	465.8	1.4506	35.5	717	714.4	510.2	696.9	3.0065	353.	15761	0.43
8212	122.	762.6	985.6	721.9	3.3091	316.0	15063	329.1	531.6	478.5	1.4535	35.0	719	719.5	515.9	704.5	3.0168	351.	15782	0.43

Table I-V. Aerodynamic Data of Annular Plug Nozzle.

(English Units)

NOZZLE - MODEL 9.1 AREA [MODEL SIZE - INNER = 0. , OUTER = 18.05 ; FULL SIZE - TOTAL = 1400.00] SQ.IN.

TEST POINT	V_{ac} FT/SEC	P^o_r	T^o_T DEG R	V^o_j FT/SEC	$\dot{W}^o$ LB/SEC	P^i_r	T^i_T DEG R	V^i_j FT/SEC	$\dot{W}^i$ LB/SEC	P^{mix}_r	T^{mix}_T DEG R	V^{mix}_j FT/SEC	F LB	V^i_j/V^o_j
1001	0	2.94	1746	2374	752.0	1.00	518	0	0.0	2.94	1746	2374	55486	0.00
1002	0	3.04	1743	2404	778.9	1.00	518	0	0.0	3.04	1743	2404	58201	0.00
1003	0	3.15	1754	2443	803.2	1.00	518	0	0.0	3.15	1754	2443	60988	0.00
1004	0	3.24	1751	2466	826.9	1.00	518	0	0.0	3.24	1751	2466	63375	0.00
1005	0	3.34	1755	2497	852.6	1.00	518	0	0.0	3.34	1755	2497	66173	0.00
1006	0	3.44	1754	2521	877.7	1.00	518	0	0.0	3.44	1754	2521	68773	0.00
1007	0	3.54	1769	2557	899.7	1.00	518	0	0.0	3.54	1769	2557	71505	0.00
1008	0	3.19	1748	2452	816.7	1.00	518	0	0.0	3.19	1748	2452	62242	0.00
1401	400	2.94	1758	2384	750.6	1.00	518	0	0.0	2.94	1758	2384	55618	0.00
1402	400	3.04	1750	2410	778.2	1.00	518	0	0.0	3.04	1750	2410	58293	0.00
1403	400	3.14	1757	2444	801.6	1.00	518	0	0.0	3.14	1757	2444	60893	0.00
1404	400	3.23	1749	2463	826.0	1.00	518	0	0.0	3.23	1749	2463	63235	0.00
1405	400	3.35	1751	2495	854.7	1.00	518	0	0.0	3.35	1751	2495	66278	0.00
1406	400	3.44	1765	2529	874.9	1.00	518	0	0.0	3.44	1765	2529	68767	0.00
1407	400	3.54	1746	2540	906.4	1.00	518	0	0.0	3.54	1746	2540	71558	0.00
1408	400	3.20	1752	2457	817.8	1.00	518	0	0.0	3.20	1752	2457	62449	0.00

TEST POINT	T_{amb} DEG R	P_{amb} PSIA	RH %	NF dB	LVM	LBM	PNL (FULL SIZE, 2400 FT SIDE LINE), dB ANGLE RELATIVE TO INLET, DEGREES 50	60	70	90	120	130	140	OAPWL dB
1001	538.3	14.59	63	-6.4	3.20	-0.48	95.5	98.6	100.0	103.1	109.5	113.0	112.1	186.0
1002	536.2	14.59	63	-6.7	3.26	-0.30	95.9	99.0	100.4	103.4	110.2	114.1	112.2	186.6
1003	535.7	14.58	63	-6.9	3.33	-0.14	95.7	98.7	100.3	103.8	111.0	115.2	112.8	187.5
1004	535.7	14.59	63	-7.1	3.37	-0.01	96.8	99.7	101.2	104.2	111.7	115.6	113.5	188.1
1005	535.4	14.58	63	-7.3	3.43	0.12	98.4	101.4	103.2	105.4	111.8	116.2	112.9	189.1
1006	536.1	14.58	63	-7.5	3.47	0.24	100.5	103.1	104.6	106.5	112.1	116.3	113.6	189.8
1007	536.6	14.58	63	-7.7	3.53	0.35	101.2	103.7	105.2	107.1	112.3	116.5	114.2	190.5
1008	536.4	14.59	63	-7.0	3.34	-0.07	96.0	98.8	100.4	103.9	111.2	115.5	113.1	188.7
1401	541.4	14.59	65	-6.4	3.20	-0.47	99.4	101.7	102.1	102.9	108.1	111.4	110.9	184.1
1402	540.7	14.59	65	-6.7	3.25	-0.30	99.3	100.8	101.4	102.3	108.3	112.0	110.9	184.6
1403	533.3	14.59	65	-6.9	3.34	-0.15	98.9	101.1	101.5	102.8	109.2	112.2	111.9	185.1
1404	540.0	14.59	65	-7.1	3.35	-0.02	99.4	100.9	102.0	103.1	109.4	113.0	112.0	187.0
1405	541.4	14.59	65	-7.4	3.40	0.13	101.8	103.9	104.1	104.7	110.9	113.6	112.1	187.7
1406	540.2	14.59	65	-7.5	3.46	0.24	104.0	105.5	106.5	106.2	110.9	114.2	112.4	188.5
1407	538.2	14.59	64	-7.8	3.49	0.35	105.5	107.0	107.5	107.8	111.5	114.7	112.9	188.4
1408	541.1	14.59	65	-7.1	3.33	-0.06	99.4	101.2	101.8	103.3	109.4	112.9	112.1	186.7

Table I-V. Aerodynamic Data of Annular Plug Nozzle (Concluded).

(International Units)

NOZZLE - MODEL 9.1 AREA [MODEL SIZE - INNER =0. , OUTER = 0.0116 ; FULL SIZE - TOTAL = 0.9031] sq.m.

TEST POINT	V_{ac}	V_j^o	T_T^o	T_j^o	P_r^o	$\dot{W}^o$	F^o	V_j^i	T_T^i	T_j^i	P_r^i	$\dot{W}^i$	F^i	V_j^{mix}	T_T^{mix}	T_j^{mix}	P_r^{mix}	$\dot{W}^T$	F^T	V_j^i/V_j^o
	m/s	m/s	°K	°K		kg/s	N	m/s	°K	°K		kg/s	N	m/s	°K	°K		kg/s	N	
1001	0.	723.6	970.0	733.4	2.9387	341.1	15425	0.	288.2	288.2	1.0000	0.0	0	723.6	532.2	733.4	2.9387	341.	15425	0.00
1002	0.	732.7	968.3	725.2	3.0415	353.3	16180	0.	288.2	288.2	1.0000	0.0	0	732.7	531.3	725.2	3.0415	353.	16180	0.00
1003	0.	744.6	974.4	723.2	3.1470	364.3	16955	0.	288.2	288.2	1.0000	0.0	0	744.6	534.6	723.2	3.1470	364.	16955	0.00
1004	0.	751.6	972.8	716.3	3.2366	375.1	17619	0.	288.2	288.2	1.0000	0.0	0	751.6	533.7	716.3	3.2366	375.	17619	0.00
1005	0.	761.1	975.0	711.7	3.3417	386.7	18397	0.	288.2	288.2	1.0000	0.0	0	761.1	534.9	711.7	3.3417	387.	18397	0.00
1006	0.	768.4	974.4	705.6	3.4390	398.1	19119	0.	288.2	288.2	1.0000	0.0	0	768.4	534.6	705.6	3.4390	398.	19119	0.00
1007	0.	779.4	982.8	706.2	3.5412	408.1	19879	0.	288.2	288.2	1.0000	0.0	0	779.4	539.2	706.2	3.5412	408.	19879	0.00
1008	0.	747.4	971.1	717.6	3.1939	370.4	17304	0.	288.2	288.2	1.0000	0.0	0	747.4	532.8	717.6	3.1939	370.	17304	0.00
1401	122.	726.6	976.7	738.4	2.9438	340.5	15462	0.	288.2	288.2	1.0000	0.0	0	726.6	535.8	738.4	2.9438	340.	15462	0.00
1402	122.	734.6	972.2	728.1	3.0449	353.0	16206	0.	288.2	288.2	1.0000	0.0	0	734.6	533.4	728.1	3.0449	353.	16206	0.00
1403	122.	744.9	976.1	724.8	3.1430	363.6	16929	0.	288.2	288.2	1.0000	0.0	0	744.9	535.5	724.8	3.1430	364.	16929	0.00
1404	122.	750.7	971.7	715.8	3.2310	374.7	17580	0.	288.2	288.2	1.0000	0.0	0	750.7	533.1	715.8	3.2310	375.	17580	0.00
1405	122.	760.5	972.8	709.7	3.3453	387.7	18426	0.	288.2	288.2	1.0000	0.0	0	760.5	533.7	709.7	3.3453	388.	18426	0.00
1406	122.	770.8	980.6	710.3	3.4384	396.8	19118	0.	288.2	288.2	1.0000	0.0	0	770.8	538.0	710.3	3.4384	397.	19118	0.00
1407	122.	774.2	970.0	696.3	3.5422	411.1	19894	0.	288.2	288.2	1.0000	0.0	0	774.2	532.2	696.3	3.5422	411.	19894	0.00
1408	122.	748.9	973.3	718.9	3.2015	370.9	17361	0.	288.2	288.2	1.0000	0.0	0	748.9	534.0	718.9	3.2015	371.	17361	0.00

Table I-VI. Aerodynamic Data of Coannular Plug Configuration with C-D Outer Nozzle and Convergent Inner Nozzle (Model 9.2).

(English Units)

NOZZLE - MODEL 9.2 AREA [MODEL SIZE - INNER = 3.97 , OUTER = 18.05 ; FULL SIZE - TOTAL = 1400.00] SQ.IN.

TEST POINT	V_{ac} FT/SEC	P_r^o	T_T^o DEG R	V_j^o FT/SEC	$\dot{W}^o$ LB/SEC	P_r^i	T_T^i DEG R	V_j^i FT/SEC	$\dot{W}^i$ LB/SEC	P_r^{mix}	T_T^{mix} DEG R	V_j^{mix} FT/SEC	F LB	V_j^i/V_j^o
2001	0	2.95	1760	2387	613.3	1.73	903	1254	111.7	2.71	1628	2212	49856	0.53
2002	0	3.04	1750	2410	634.8	1.73	904	1254	111.4	2.79	1623	2237	51891	0.52
2003	0	3.15	1747	2439	657.3	1.73	898	1250	111.8	2.87	1623	2266	54172	0.51
2004	0	3.25	1761	2478	676.1	1.73	898	1249	111.7	2.96	1638	2303	56407	0.50
2005	0	3.36	1758	2503	698.0	1.73	896	1249	111.9	3.04	1639	2329	58643	0.50
2006	0	3.45	1771	2537	715.2	1.73	902	1252	111.6	3.12	1653	2363	60740	0.49
2007	0	3.55	1754	2549	740.0	1.73	900	1250	111.5	3.21	1642	2378	62963	0.49
2008	0	3.20	1752	2457	667.0	1.73	900	1250	111.6	2.91	1629	2284	55271	0.51
2401	400	2.95	1763	2390	611.8	1.74	913	1269	111.7	2.71	1631	2216	49853	0.53
2402	400	3.06	1778	2433	630.4	1.73	904	1255	111.3	2.79	1646	2256	52018	0.52
2403	400	3.16	1752	2444	656.2	1.73	907	1257	111.1	2.88	1629	2272	54186	0.51
2404	400	3.26	1756	2476	677.6	1.73	906	1257	111.3	2.96	1636	2304	56500	0.51
2405	400	3.36	1785	2525	692.9	1.73	902	1254	111.6	3.05	1662	2348	58733	0.50
2406	400	3.47	1767	2538	718.2	1.73	906	1257	111.4	3.14	1651	2366	61003	0.50
2407	400	3.56	1765	2558	738.6	1.73	899	1251	111.8	3.21	1651	2386	63069	0.49

TEST POINT	T_{amb} DEG R	P_{amb} PSIA	RH %	NF dB	LVM	LBM	PNL (FULL SIZE, 2400 FT SIDE LINE), dB ANGLE RELATIVE TO INLET, DEGREES 50	60	70	90	120	130	140	OAPWL dB
2001	530.6	14.53	59	-6.1	2.92	-0.90	92.6	95.2	97.9	101.3	107.8	108.7	110.0	183.1
2002	532.0	14.52	59	-6.4	2.96	-0.73	93.4	96.0	98.3	101.7	108.1	109.3	111.0	184.1
2003	532.5	14.51	61	-6.6	3.02	-0.56	93.6	96.3	98.4	101.9	108.8	110.5	111.7	184.7
2004	532.9	14.52	61	-6.8	3.09	-0.41	94.1	96.8	99.0	102.3	108.8	110.8	112.5	185.2
2005	534.8	14.52	60	-7.0	3.13	-0.27	95.1	97.9	100.1	103.1	109.8	111.3	112.9	185.4
2006	538.0	14.51	60	-7.2	3.18	-0.15	95.7	98.6	100.8	103.7	109.7	111.4	112.9	185.4
2007	539.2	14.51	60	-7.4	3.20	-0.03	96.9	99.6	101.6	104.3	110.4	112.1	112.4	185.7
2008	533.2	14.52	61	-6.7	3.05	-0.48	93.5	96.3	98.6	102.1	108.9	110.4	111.4	184.7
2401	554.2	14.49	60	-6.3	2.84	-0.89	95.5	97.3	99.0	100.1	105.8	106.4	105.7	179.3
2402	553.0	14.49	60	-6.5	2.92	-0.71	95.3	97.9	99.5	100.6	106.6	107.2	107.0	180.2
2403	552.1	14.49	60	-6.7	2.95	-0.55	96.4	98.0	99.4	100.9	107.0	107.6	107.6	180.7
2404	551.2	14.50	60	-6.9	3.01	-0.40	96.5	98.5	99.8	101.2	107.1	108.6	109.3	181.8
2405	548.9	14.49	59	-7.1	3.11	-0.25	96.9	99.4	100.8	101.9	108.2	109.0	110.1	182.8
2406	548.7	14.49	59	-7.3	3.14	-0.13	98.2	100.5	101.8	102.5	108.2	109.3	110.1	183.0
2407	546.7	14.52	59	-7.4	3.18	-0.02	99.5	101.7	102.9	103.8	108.9	109.9	110.3	183.7

Table I-VI. Aerodynamic Data of Coannular Plug Configuration with C-D Outer Nozzle and Convergent Inner Nozzle (Model 9.2) (Concluded).

(International Units)

NOZZLE - MODEL 9.2 AREA [MODEL SIZE - INNER =0.0026 , OUTER = 0.0116 ; FULL SIZE - TOTAL = 0.9031] sq.m.

TEST POINT	V_{ac}	V_j^o	T_T^o	T_j^o	P_r^o	$\dot{W}^o$	F^o	V_j^i	T_T^i	T_j^i	P_r^i	$\dot{W}^i$	F^i	V_j^{mix}	T_T^{mix}	T_j^{mix}	P_r^{mix}	$\dot{W}^T$	F^T	V_j^i/V_j^o
	m/s	m/s	^oK	^oK		kg/s	N	m/s	^oK	^oK		kg/s	N	m/s	^oK	^oK		kg/s	N	
2001	0.	727.6	977.8	738.9	2.9488	278.2	12650	382.3	501.8	429.1	1.7303	50.7	1210	674.4	496.2	696.8	2.7052	329.	13860	0.53
2002	0.	734.6	972.2	728.1	3.0449	287.9	13218	382.4	502.7	429.9	1.7290	50.5	1207	682.0	494.9	689.3	2.7856	338.	14426	0.52
2003	0.	743.4	970.6	719.9	3.1506	298.1	13852	381.0	498.9	426.7	1.7291	50.7	1207	690.7	494.9	683.4	2.8729	349.	15060	0.51
2004	0.	755.3	978.3	719.6	3.2540	306.7	14475	380.9	499.4	427.2	1.7277	50.7	1206	702.2	499.5	684.6	2.9581	357.	15681	0.50
2005	0.	762.9	976.7	712.1	3.3563	316.6	15095	380.8	498.3	426.1	1.7291	50.8	1207	710.1	499.6	679.2	3.0438	367.	16303	0.50
2006	0.	773.3	983.9	712.1	3.4527	324.4	15678	381.9	501.1	428.5	1.7293	50.6	1207	720.5	504.0	680.7	3.1243	375.	16886	0.49
2007	0.	776.9	974.4	699.1	3.5549	335.7	16299	381.0	500.1	427.8	1.7267	50.6	1204	725.1	500.5	670.5	3.2107	386.	17504	0.49
2008	0.	748.9	973.3	718.9	3.2015	302.5	14160	381.2	500.1	427.8	1.7277	50.6	1206	696.2	496.8	683.4	2.9150	353.	15366	0.51
2401	122.	728.5	979.4	740.1	2.9516	277.5	12634	386.8	507.3	432.8	1.7434	50.7	1225	675.7	497.3	698.2	2.7102	328.	13859	0.53
2402	122.	741.6	987.8	739.7	3.0555	285.9	13253	382.7	502.7	429.7	1.7308	50.5	1207	687.7	502.0	699.2	2.7929	336.	14461	0.52
2403	122.	744.9	973.3	721.8	3.1555	297.6	13857	383.2	504.3	431.2	1.7299	50.4	1206	692.6	496.8	685.8	2.8778	348.	15064	0.51
2404	122.	754.7	975.6	717.1	3.2600	307.4	14497	383.3	503.8	430.7	1.7315	50.5	1209	702.3	498.7	682.9	2.9648	358.	15707	0.51
2405	122.	769.6	991.7	723.3	3.3649	314.3	15118	382.5	501.2	428.3	1.7324	50.6	1210	715.9	506.7	689.2	3.0502	365.	16328	0.50
2406	122.	773.6	981.7	709.4	3.4688	325.8	15749	383.3	503.3	430.2	1.7321	50.5	1209	721.2	503.3	678.8	3.1389	376.	16959	0.50
2407	122.	779.7	980.6	703.6	3.5581	335.0	16324	381.5	499.9	427.4	1.7299	50.7	1209	727.3	503.3	674.3	3.2130	386.	17534	0.49

Table I-VII. Aerodynamic Data of Coannular Plug Configuration with Convergent Outer Nozzle and C-D Inner Nozzle (Model 9.3).

(English Units)

NOZZLE - MODEL 9.3 AREA [MODEL SIZE - INNER = 3.97 , OUTER = 18.05 ; FULL SIZE - TOTAL = 1400.00] SQ.IN.

TEST POINT	V_{ac} FT/SEC	P_r^o	T_T^o DEG R	V_j^o FT/SEC	$\dot{W}^o$ LB/SEC	P_r^i	T_T^i DEG R	V_j^i FT/SEC	$\dot{W}^i$ LB/SEC	P_r^{mix}	T_T^{mix} DEG R	V_j^{mix} FT/SEC	F LB	V_j^i/V_j^o
3001	0	1.69	1181	1409	427.4	2.94	812	1608	199.6	1.92	1063	1472	28699	1.14
3002	0	1.69	1181	1410	427.2	3.03	836	1651	202.7	1.93	1070	1487	29116	1.17
3003	0	1.70	1180	1412	428.4	3.16	857	1698	208.6	1.96	1074	1505	29804	1.20
3004	0	1.70	1180	1412	428.8	3.27	866	1728	214.7	1.98	1075	1517	30349	1.22
3005	0	1.70	1181	1412	428.3	3.37	839	1720	225.4	2.00	1063	1517	30836	1.22
3006	0	1.69	1177	1408	428.4	3.44	870	1764	225.8	2.02	1071	1531	31132	1.25
3007	0	1.70	1177	1410	429.3	3.56	846	1759	237.0	2.04	1059	1534	31775	1.25
3008	0	1.00	520	1	0.	3.06	852	1673	510.2	3.06	852	1673	58501	0.00
3009	0	1.00	520	1	0.	3.11	840	1672	523.3	3.11	840	1672	59990	0.00
3010	0	1.00	520	1	0.	3.26	844	1705	546.9	3.26	844	1705	63917	0.00
3011	0	3.26	1773	2488	673.1	3.30	903	1771	213.7	3.19	1563	2315	63818	0.71
3012	0	3.26	1745	2467	678.5	3.12	938	1769	198.2	3.17	1562	2309	62922	0.72
3401	400	1.70	1200	1428	428.8	2.95	832	1631	199.1	1.93	1083	1492	29132	1.14
3402	400	1.70	1201	1429	428.6	3.05	850	1669	203.5	1.95	1088	1506	29586	1.17
3403	400	1.70	1211	1434	426.8	3.16	888	1730	206.4	1.97	1105	1530	30125	1.21
3404	400	1.70	1213	1438	426.9	3.26	883	1745	213.6	1.99	1103	1540	30655	1.21
3405	400	1.70	1214	1438	426.8	3.38	871	1753	222.5	2.01	1096	1546	31204	1.22
3406	400	1.70	1217	1439	426.1	3.46	891	1787	225.2	2.03	1104	1559	31573	1.24
3407	400	1.70	1210	1434	426.9	3.57	877	1793	234.7	2.05	1092	1561	32105	1.25
3412	400	3.26	1761	2478	675.7	3.12	934	1765	198.7	3.17	1572	2316	62954	0.71

TEST POINT	T_{amb} DEG R	P_{amb} PSIA	RH %	NF dB	LVM	LBM	PNL (FULL SIZE, 2400 FT SIDE LINE), dB ANGLE RELATIVE TO INLET, DEGREES 50	60	70	90	120	130	140	OAPWL dB
3001	526.3	14.42	65	-6.3	1.17	-8.33	87.4	89.4	86.6	91.6	93.1	93.9	94.4	170.9
3002	526.2	14.42	65	-6.3	1.22	-7.22	90.1	91.9	88.7	93.0	94.1	95.4	96.2	172.0
3003	524.5	14.42	63	-6.3	1.27	-6.15	88.0	90.3	87.3	92.5	94.2	96.2	96.7	172.2
3004	524.5	14.42	63	-6.3	1.31	-5.57	87.7	90.4	87.7	92.7	94.7	96.3	97.8	172.9
3005	523.9	14.42	62	-6.4	1.31	-5.16	88.6	91.2	88.4	93.8	94.6	95.9	97.0	172.6
3006	524.3	14.42	62	-6.4	1.35	-4.94	90.2	92.5	89.9	94.7	95.5	96.9	98.6	173.4
3007	523.9	14.42	62	-6.5	1.36	-4.54	96.0	98.1	94.6	98.5	97.9	98.1	100.5	175.3
3008	526.5	14.43	65	-10.0	1.72	-0.27	96.9	99.4	96.6	101.5	99.8	98.6	98.9	175.9
3009	525.7	14.43	65	-10.1	1.73	-0.19	97.5	99.8	97.1	101.7	100.1	98.6	98.7	176.1
3010	525.4	14.43	65	-10.4	1.81	0.02	98.9	101.1	98.5	103.0	101.2	99.9	99.7	177.3
3011	555.4	14.48	79	-7.8	3.02	0.03	97.7	100.2	101.7	103.5	108.0	109.7	111.7	186.8
3012	556.8	14.49	79	-7.7	3.00	-0.02	97.8	100.0	101.9	103.1	107.4	109.1	112.0	186.6
3401	551.2	14.49	79	-6.5	1.13	-7.52	87.9	88.7	89.7	88.9	89.5	87.8	87.4	165.7
3402	554.6	14.49	78	-6.5	1.16	-6.65	91.0	91.2	91.6	90.9	91.2	89.0	88.6	167.6
3403	554.2	14.49	78	-6.5	1.23	-5.95	92.3	92.7	92.8	92.0	92.3	90.3	90.2	168.7
3404	556.1	14.49	78	-6.5	1.25	-5.43	90.2	90.7	91.4	91.0	91.4	90.5	90.5	168.1
3405	556.7	14.49	78	-6.6	1.26	-5.00	90.2	91.3	91.7	91.3	90.4	90.2	90.8	168.4
3406	557.5	14.49	78	-6.6	1.30	-4.75	91.1	91.5	92.8	92.2	90.2	90.6	91.0	168.6
3407	557.1	14.49	79	-6.7	1.30	-4.45	93.6	94.4	95.1	94.2	92.2	91.2	91.7	170.2
3412	549.7	14.49	79	-7.7	3.04	-0.02	104.7	104.7	105.1	104.5	106.3	107.4	107.8	183.3

Table I-VII. Aerodynamic Data of Coannular Plug Configuration with Convergent Outer Nozzle and C-D Inner Nozzle (Model 9.3) (Concluded).

(International Units)

NOZZLE - MODEL 9.3 AREA [MODEL SIZE - INNER =0.0026 , OUTER = 0.0116 ; FULL SIZE - TOTAL = 0.9031] sq.m.

TEST POINT	V_{ac}	V_j^o	T_T^o	T_j^o	P_r^o	$\dot{W}^o$	F^o	V_j^i	T_T^i	T_j^i	P_r^i	$\dot{W}^i$	F^i	V_j^{mix}	T_T^{mix}	T_j^{mix}	P_r^{mix}	$\dot{W}^T$	F^T	V_j^i/V_j^o
	m/s	m/s	°K	°K		kg/s	N	m/s	°K	°K		kg/s	N	m/s	°K	°K		kg/s	N	
3001	0.	429.5	656.1	568.3	1.6920	193.9	5203	490.4	451.5	331.8	2.9394	90.5	2775	448.8	324.1	492.6	1.9151	284.	7978	1.14
3002	0.	429.8	656.1	568.7	1.6919	193.8	5202	503.3	464.7	338.6	3.0285	91.9	2892	453.3	326.3	494.6	1.9334	286.	8094	1.17
3003	0.	430.4	655.6	567.9	1.6955	194.3	5225	517.6	476.4	343.1	3.1551	94.6	3060	458.8	327.6	494.5	1.9620	289.	8285	1.20
3004	0.	430.4	655.6	567.4	1.6965	194.5	5231	526.8	481.6	343.4	3.2653	97.4	3206	462.5	327.8	493.2	1.9849	292.	8437	1.22
3005	0.	430.4	656.1	568.1	1.6952	194.3	5223	524.3	466.2	329.4	3.3727	102.2	3349	462.7	324.0	485.9	2.0037	297.	8572	1.22
3006	0.	429.2	653.9	566.6	1.6934	194.3	5212	537.8	483.8	339.9	3.4422	102.4	3442	466.7	326.6	489.1	2.0180	297.	8655	1.25
3007	0.	429.8	653.9	566.1	1.6962	194.7	5229	536.3	470.3	327.1	3.5628	107.5	3603	467.7	322.9	481.5	2.0433	302.	8833	1.25
3008	0.	0.	288.9	288.9	1.0000	0.	0	510.0	473.6	344.1	3.0580	1124.9	16264	510.0	259.8	344.1	3.0580	0.	16264	0.00
3009	0.	0.	288.9	288.9	1.0000	0.	0	509.9	466.9	337.5	3.1142	1153.8	16678	509.9	256.2	337.5	3.1142	0.	16678	0.00
3010	0.	0.	288.9	288.9	1.0000	0.	0	519.8	469.2	334.7	3.2625	1205.8	17769	519.8	257.4	334.7	3.2625	0.	17769	0.00
3011	0.	758.3	985.0	724.6	3.2582	305.3	14471	540.1	502.0	356.8	3.3031	96.9	3271	705.8	476.6	637.3	3.1949	402.	17742	0.71
3012	0.	751.9	969.4	712.3	3.2564	307.8	14463	539.3	521.4	376.7	3.1221	89.9	3029	703.8	476.3	638.0	3.1746	398.	17493	0.72
3401	122.	435.3	666.7	576.9	1.7021	194.5	5291	497.4	462.7	339.6	2.9532	90.3	2807	455.0	330.3	501.4	1.9262	285.	8099	1.14
3402	122.	435.6	667.2	577.3	1.7019	194.4	5290	508.9	472.5	343.6	3.0502	92.3	2935	459.1	331.6	502.1	1.9456	287.	8225	1.17
3403	122.	437.1	672.8	582.2	1.7019	193.6	5289	527.3	493.7	355.3	3.1629	93.6	3085	466.6	337.0	508.7	1.9689	287.	8375	1.21
3404	122.	438.3	673.9	583.3	1.7039	193.6	5302	531.9	491.1	350.2	3.2639	96.9	3220	469.4	336.3	506.2	1.9900	291.	8522	1.21
3405	122.	438.3	674.4	583.6	1.7042	193.6	5304	534.5	484.2	342.1	3.3761	100.9	3370	471.3	334.2	501.3	2.0118	295.	8675	1.22
3406	122.	438.6	676.1	585.1	1.7035	193.3	5299	545.0	495.4	347.6	3.4563	102.1	3478	475.4	336.6	503.8	2.0281	295.	8777	1.24
3407	122.	437.1	672.2	581.9	1.7020	193.6	5290	546.5	487.4	338.8	3.5730	106.5	3635	475.9	332.9	496.4	2.0500	300.	8925	1.25
3412	122.	755.3	978.3	719.2	3.2568	306.5	14470	538.0	518.9	374.8	3.1223	90.1	3031	706.0	479.4	642.5	3.1723	397.	17502	0.71

Table I-VIII. Aerodynamic Data of Coannular Plug Configuration with C-D Outer and Inner Nozzles (Model 9.4).

(English Units)

NOZZLE - MODEL 9.4 AREA [MODEL SIZE - INNER = 3.97 , OUTER = 18.05 ; FULL SIZE - TOTAL = 1400.00] SQ.IN.

TEST POINT	V_{ac} FT/SEC	P_r^o	T_T^o DEG R	V_j^o FT/SEC	$\dot{W}^o$ LB/SEC	P_r^i	T_T^i DEG R	V_j^i FT/SEC	$\dot{W}^i$ LB/SEC	P_r^{mix}	T_T^{mix} DEG R	V_j^{mix} FT/SEC	F LB	V_j^i/V_j^o
4001	0	3.24	1747	2464	674.6	2.97	876	1676	195.0	3.12	1551	2287	61812	0.68
4002	0	3.25	1752	2470	675.5	3.06	872	1693	201.4	3.14	1549	2291	62445	0.69
4003	0	3.25	1755	2472	675.1	3.17	875	1718	208.2	3.16	1547	2294	62996	0.70
4004	0	3.25	1754	2472	675.6	3.26	860	1721	216.2	3.18	1537	2290	63480	0.70
4005	0	3.25	1758	2475	674.5	3.37	858	1739	223.8	3.19	1533	2291	63979	0.70
4006	0	3.25	1733	2456	677.9	2.53	878	1567	165.5	3.07	1565	2281	59804	0.64
4007	0	3.25	1734	2458	678.4	3.59	871	1789	235.7	3.23	1511	2285	64932	0.73
4008	0	2.80	1736	2319	583.3	3.26	869	1730	214.9	2.82	1502	2160	53608	0.75
4009	0	3.60	1741	2551	750.3	3.25	882	1741	212.5	3.46	1551	2372	70988	0.68
4010	0	3.60	1742	2550	748.7	1.62	970	1227	99.2	3.24	1651	2395	63123	0.48
4011	0	3.60	1741	2550	750.0	3.62	865	1788	238.9	3.52	1529	2365	72720	0.70
4012	0	3.21	1752	2459	665.7	3.28	887	1751	213.5	3.15	1542	2287	62499	0.71
4013	0	3.31	1752	2488	687.8	3.28	885	1748	213.7	3.23	1546	2312	64792	0.70
4014	0	3.15	1746	2439	655.6	3.28	877	1740	214.6	3.10	1531	2266	61313	0.71
4015	0	3.36	1758	2505	696.3	3.28	881	1744	214.2	3.27	1551	2325	65821	0.70
4016	0	3.25	1751	2470	676.5	3.47	861	1759	230.1	3.21	1524	2289	64510	0.71
4404	400	3.25	1751	2470	675.5	3.28	877	1740	214.7	3.18	1539	2294	63479	0.70
4406	400	3.25	1746	2468	676.9	2.53	880	1569	165.5	3.07	1576	2291	59988	0.64
4407	400	3.25	1741	2463	677.5	3.59	878	1796	235.0	3.23	1518	2291	64975	0.73
4408	400	2.81	1750	2332	582.7	3.27	884	1747	213.8	2.83	1517	2175	53850	0.75

TEST POINT	T_{amb} DEG R	P_{amb} PSIA	RH %	NF dB	LVM	LPM	PNL (FULL SIZE, 2400 FT SIDE LINE), dB ANGLE RELATIVE TO INLET, DEGREES 50	60	70	90	120	130	140	OAPWL dB
4001	541.1	14.49	76	-7.6	3.02	-0.08	97.1	99.4	100.2	103.7	109.5	113.9	112.2	188.4
4002	544.3	14.49	76	-7.6	3.02	-0.04	97.1	99.6	100.9	103.8	109.3	113.9	112.0	188.8
4003	543.1	14.49	76	-7.7	3.03	-0.02	97.8	100.2	101.4	104.2	109.7	114.6	112.2	189.9
4004	544.6	14.49	76	-7.8	3.01	0.01	98.2	100.6	102.1	104.7	109.8	114.2	111.6	189.2
4005	545.9	14.49	76	-7.8	3.01	0.03	98.6	100.9	103.3	105.0	109.9	114.7	112.0	189.9
4006	535.9	14.46	72	-7.3	3.03	-0.18	97.5	99.9	100.9	103.6	108.6	113.8	110.5	187.5
4007	534.1	14.46	72	-7.9	3.05	0.08	100.3	102.0	103.9	106.2	109.2	115.1	112.8	189.2
4008	535.1	14.46	72	-6.9	2.80	-0.58	99.1	101.4	102.3	104.4	107.0	111.8	110.0	186.0
4009	533.6	14.46	72	-8.2	3.21	0.35	100.0	101.7	103.1	106.0	110.5	116.3	113.4	191.5
4010	534.2	14.46	72	-7.4	3.25	-0.01	97.7	99.7	101.3	104.3	109.7	115.1	112.5	190.1
4011	536.5	14.46	72	-8.4	3.19	0.42	101.5	103.3	104.7	107.3	110.6	116.7	113.7	192.3
4012	549.2	14.46	74	-7.7	2.99	-0.04	98.9	101.2	102.6	105.1	109.1	114.5	111.9	188.5
4013	548.7	14.46	74	-7.9	3.04	0.08	98.4	100.8	102.0	104.8	109.3	115.2	112.3	189.3
4014	548.6	14.46	74	-7.6	2.95	-0.10	99.7	101.6	103.2	105.2	108.5	114.0	111.6	188.0
4015	547.8	14.46	74	-7.9	3.07	0.13	98.7	100.9	102.1	105.0	109.2	114.9	111.9	188.7
4016	546.4	14.49	76	-7.9	3.01	0.06	99.4	101.4	103.7	105.5	109.7	114.3	112.3	189.4
4404	542.9	14.46	74	-7.7	3.03	0.01	104.2	104.6	104.5	104.4	107.5	112.8	108.3	186.2
4406	546.4	14.47	74	-7.4	3.01	-0.17	103.7	104.4	104.3	103.2	112.3	107.4	102.7	185.4
4407	544.7	14.46	74	-7.9	3.02	0.09	105.4	106.0	106.0	104.7	113.1	108.7	104.1	186.5
4408	548.5	14.47	74	-7.0	2.78	-0.57	104.3	104.4	103.9	103.7	105.4	110.0	105.8	182.6

Table I-VIII. Aerodynamic Data of Coannular Plug Configuration with C-D Outer and Inner Nozzles (Model 9.4) (Continued).

(English Units)

NOZZLE - MODEL 9.4

TEST POINT	V_{ac} FT/SEC	P_r^o	T_T^o DEG R	V_j^o FT/SEC	$\dot{W}^o$ LB/SEC	P_r^i	T_T^i DEG R	V_j^i FT/SEC	$\dot{W}^i$ LB/SEC	P_r^{mix}	T_T^{mix} DEG R	V_j^{mix} FT/SEC	F LB	V_j^i/V_j^o
4409	400	3.60	1741	2550	750.3	3.28	883	1747	214.1	3.47	1550	2372	71100	0.69
4410	400	3.61	1751	2561	750.7	1.63	963	1228	100.2	3.26	1658	2404	63576	0.48
4411	400	3.60	1739	2549	750.7	3.62	867	790	238.9	3.52	1528	2365	72765	0.70

TEST POINT	T_{amb} DEG R	P_{amb} PSIA	RH %	NF dB	LVM	LBM	PNL (FULL SIZE, 2400 FT SIDE LINE), dB ANGLE RELATIVE TO INLET, DEGREES 50	60	70	90	120	130	140	OAPWL dB
4409	541.8	14.46	74	-8.3	3.18	0.35	103.6	104.1	104.7	105.5	108.9	114.4	110.4	189.4
4410	549.4	14.46	74	-7.5	3.21	0.01	100.2	101.8	102.9	103.6	108.0	114.0	109.6	187.2
4411	542.1	14.46	74	-8.5	3.17	0.42	105.6	106.2	106.8	107.1	109.5	114.9	110.7	190.1

Table I-VIII. Aerodynamic Data of Coannular Plug Configuration with C-D Outer and Inner Nozzles (Model 9.4) (Concluded).

(International Units)

NOZZLE - MODEL 9.4 AREA [MODEL SIZE - INNER =0.0026 , OUTER = 0.0116 ; FULL SIZE - TOTAL = 0.9031] sq.m.

TEST POINT	V_{ac}	V_j^o	T_T^o	T_j^o	P_r^o	$\dot{W}^o$	F^o	V_j^i	T_T^i	T_j^i	P_r^i	$\dot{W}^i$	F^i	V_j^{mix}	T_T^{mix}	T_j^{mix}	P_r^{mix}	$\dot{W}^T$	F^T	V_j^i/V_j^o
	m/s	m/s	°K	°K		kg/s	N	m/s	°K	°K		kg/s	N	m/s	°K	°K		kg/s	N	
4001	0.	751.0	970.6	714.4	3.2385	306.0	14359	511.1	486.8	356.8	2.9668	88.5	2824	697.1	473.0	636.3	3.1231	394.	17184	0.68
4002	0.	752.9	973.3	715.9	3.2476	306.4	14413	516.2	484.9	352.3	3.0594	91.4	2947	698.4	472.4	634.3	3.1436	398.	17360	0.69
4003	0.	753.5	975.0	717.1	3.2491	306.2	14421	523.8	486.5	349.9	3.1680	94.4	3091	699.3	471.7	632.2	3.1621	401.	17513	0.70
4004	0.	753.5	974.4	716.7	3.2513	306.4	14433	524.6	477.9	340.9	3.2610	98.1	3215	698.0	468.6	627.1	3.1751	405.	17648	0.70
4005	0.	754.4	976.7	718.6	3.2495	305.9	14423	530.1	476.8	336.9	3.3718	101.5	3363	698.4	467.5	624.7	3.1903	407.	17787	0.70
4006	0.	748.6	962.8	707.8	3.2476	307.5	14385	477.7	488.1	374.6	2.5267	75.1	2240	695.4	477.1	645.6	3.0657	383.	16626	0.64
4007	0.	749.2	963.3	708.2	3.2516	307.7	14408	545.3	484.2	336.2	3.5850	106.9	3643	696.6	460.8	612.8	3.2333	415.	18051	0.73
4008	0.	706.8	964.4	738.9	2.7967	264.6	11690	527.4	482.8	344.4	3.2638	97.5	3213	658.6	458.0	632.9	2.8189	362.	14903	0.75
4009	0.	777.5	967.2	690.9	3.6042	340.3	16537	530.7	490.1	349.8	3.2528	96.4	3197	723.0	472.9	617.7	3.4638	437.	19735	0.68
4010	0.	777.2	967.8	691.8	3.5971	339.6	16496	374.1	538.9	470.2	1.6225	45.0	1052	730.1	503.5	672.7	3.2447	385.	17549	0.48
4011	0.	777.2	967.2	690.7	3.6021	340.2	16524	545.2	480.8	332.8	3.6223	108.4	3692	721.1	466.1	605.6	3.5154	449.	20217	0.70
4012	0.	749.5	973.3	718.4	3.2078	302.0	14143	533.9	493.3	351.4	3.2784	96.8	3232	697.1	470.0	630.5	3.1499	399.	17375	0.71
4013	0.	758.3	973.3	712.0	3.3141	312.0	14783	533.0	491.8	350.4	3.2762	96.9	3229	704.8	471.4	627.7	3.2339	409.	18013	0.70
4014	0.	743.4	970.0	719.3	3.1534	297.4	13817	530.6	487.4	347.3	3.2757	97.3	3228	691.0	466.9	628.6	3.1045	395.	17045	0.71
4015	0.	763.5	976.7	711.9	3.3616	315.8	15069	531.8	489.4	348.7	3.2764	97.2	3229	708.9	473.0	628.1	3.2700	413.	18299	0.70
4016	0.	752.9	972.8	715.2	3.2516	306.9	14436	536.3	478.4	335.3	3.4718	104.4	3498	697.9	464.8	619.7	3.2099	411.	17934	0.71
4404	122.	752.9	972.8	715.1	3.2526	306.4	14418	530.5	487.3	347.2	3.2757	97.4	3229	699.2	469.3	627.7	3.1829	404.	17648	0.70
4406	122.	752.2	970.0	713.2	3.2546	307.0	14432	478.4	489.3	375.3	2.5292	75.1	2244	698.3	480.5	650.0	3.0708	382.	16677	0.64
4407	122.	750.7	967.2	710.9	3.2520	307.3	14416	547.5	488.1	338.8	3.5870	106.6	3647	698.3	462.9	615.7	3.2348	414.	18063	0.73
4408	122.	710.8	972.2	744.7	2.8050	264.3	11742	532.6	491.2	350.0	3.2745	97.0	3228	663.0	462.6	639.1	2.8287	361.	14971	0.75
4409	122.	777.2	967.2	691.0	3.6023	340.3	16534	532.5	490.8	349.6	3.2771	97.1	3231	723.0	472.7	617.2	3.4663	437.	19766	0.69
4410	122.	780.6	972.8	694.7	3.6149	340.5	16611	374.4	535.2	466.2	1.6300	45.4	1063	732.7	505.5	674.7	3.2593	386.	17675	0.48
4411	122.	776.9	966.1	690.1	3.6023	340.5	16533	545.8	481.8	333.6	3.6232	108.4	3695	721.1	465.9	605.3	3.5165	449.	20229	0.70

Table I-IX. Aerodynamic Data of Similitude 20-Shallow-Chute Mechanical Suppressor with Convergent Inner Nozzle (Model 10.1).

(English Units)

NOZZLE - MODEL 10.1 AREA [MODEL SIZE - INNER = 4.11 , OUTER = 23.99 ; FULL SIZE - TOTAL = 1400.00] SQ.IN.

TEST POINT	V_{ac} FT/SEC	P^o_r	T^o_T DEG R	V^o_j FT/SEC	W^o LB/SEC	P^i_r	T^i_T DEG R	V^i_j FT/SEC	W^i LB/SEC	P^{mix}_r	T^{mix}_T DEG R	V^{mix}_j FT/SEC	F LB	V^i_j/V^o_j
1001	0	1.99	1442	1766	475.8	1.94	805	1292	107.5	1.97	1324	1678	30437	0.73
1002	400	2.00	1478	1795	471.6	1.96	858	1342	104.9	1.98	1365	1712	30692	0.75
1003	0	2.28	1507	1959	532.4	2.29	779	1406	129.0	2.26	1365	1850	38048	0.72
1004	400	2.29	1528	1975	529.7	2.31	804	1433	127.8	2.27	1387	1870	38217	0.73
1005	0	2.39	1582	2056	543.1	2.41	800	1462	133.9	2.36	1427	1938	40793	0.71
1006	400	2.39	1618	2081	536.9	2.42	823	1485	132.1	2.36	1461	1963	40829	0.71
1007	0	2.79	1664	2266	617.1	2.80	843	1605	151.2	2.74	1502	2135	51003	0.71
1008	400	2.80	1663	2269	619.1	2.80	863	1626	149.8	2.76	1507	2143	51229	0.72
1009	0	2.89	1744	2358	624.9	2.91	849	1637	156.6	2.84	1564	2213	53768	0.69
1010	400	2.90	1747	2363	625.5	2.92	882	1671	153.9	2.85	1576	2226	53926	0.71
1011	0	3.40	1734	2496	737.0	3.26	876	1737	173.0	3.32	1570	2352	66523	0.70
1012	400	3.41	1745	2506	735.2	3.26	927	1786	167.9	3.33	1592	2372	66584	0.71
1013	0	3.68	1732	2561	798.5	3.43	906	1797	178.6	3.58	1580	2421	73545	0.70
1014	400	3.70	1758	2584	794.2	3.43	934	1825	176.0	3.60	1608	2446	73776	0.71
1015	0	3.25	1745	2464	701.1	2.63	875	1593	139.5	3.11	1600	2319	60601	0.65
1016	400	3.24	1759	2473	696.3	2.63	908	1624	137.0	3.11	1619	2333	60445	0.66
1017	0	1.88	1576	1772	427.2	1.86	778	1233	104.7	1.85	1418	1665	27538	0.70
1018	400	1.88	1570	1771	428.5	1.86	801	1252	103.3	1.86	1421	1670	27603	0.71
1019	0	2.25	1722	2083	490.3	2.23	726	1337	130.1	2.21	1513	1926	37141	0.64
1020	400	2.27	1732	2098	492.5	2.24	764	1373	126.9	2.23	1533	1949	37535	0.65

TEST POINT	T_{amb} DEG R	P_{amb} PSIA	RH %	NF dB	LVM	LBM	PNL (FULL SIZE, 2400 FT SIDE LINE), dB ANGLE RELATIVE TO INLET, DEGREES 50	60	70	90	120	130	140	OAPWL dB
1001	520.9	14.43	74	-4.9	1.76	-5.44	87.0	89.6	87.8	95.2	98.3	96.7	96.0	172.4
1002	539.4	14.40	50	-5.0	1.77	-5.17	91.3	92.2	89.7	95.1	97.5	94.9	90.9	171.2
1003	523.2	14.42	74	-5.5	2.18	-2.40	90.3	93.1	91.3	97.5	100.6	99.4	98.2	175.3
1004	540.3	14.40	50	-5.6	2.15	-2.36	93.6	95.1	92.3	97.7	100.0	97.4	94.6	174.6
1005	525.4	14.42	74	-5.7	2.37	-1.91	91.6	94.4	92.8	98.8	101.5	100.1	99.3	176.3
1006	541.9	14.40	50	-5.7	2.36	-1.90	95.4	96.4	94.0	98.8	101.2	99.8	96.1	176.3
1007	529.4	14.42	73	-6.6	2.77	-0.77	94.7	98.0	96.4	101.3	103.3	102.2	101.6	180.1
1008	544.6	14.40	50	-6.8	2.73	-0.75	99.4	100.7	98.6	102.4	104.2	102.8	100.0	179.8
1009	535.5	14.41	36	-6.8	2.90	-0.55	95.4	99.2	97.8	102.7	104.5	103.6	102.6	180.3
1010	544.6	14.40	48	-6.8	2.89	-0.54	100.4	102.2	99.3	103.8	105.0	103.7	100.9	180.6
1011	540.1	14.42	36	-7.9	3.15	0.17	98.3	101.3	100.4	104.9	105.8	104.9	104.6	182.4
1012	546.3	14.41	48	-7.9	3.16	0.17	102.0	104.0	101.7	105.8	107.2	105.5	102.5	182.7
1013	541.9	14.41	36	-8.4	3.27	0.46	98.2	101.8	100.7	105.3	106.9	105.9	106.8	183.3
1014	543.7	14.40	48	-8.4	3.31	0.47	101.9	104.1	101.4	105.9	107.6	105.7	103.5	183.0
1015	537.7	14.41	36	-7.3	3.10	-0.13	97.7	101.1	99.8	104.5	105.6	104.9	103.6	181.6
1016	544.6	14.40	48	-7.3	3.10	-0.13	102.1	103.4	101.7	105.4	107.2	105.1	102.2	182.5
1017	543.1	14.41	48	-4.6	1.64	-10.00	85.9	88.3	87.1	94.1	97.6	96.1	94.5	171.6
1018	544.6	14.41	48	-4.6	1.64	-10.00	90.2	92.1	89.3	94.0	96.0	93.1	88.7	169.9
1019	531.0	14.42	73	-4.9	2.32	-2.59	88.5	91.9	90.5	97.4	100.9	99.4	97.7	176.1
1020	544.1	14.41	48	-5.1	2.32	-2.49	93.9	95.2	92.8	98.3	101.2	98.8	95.8	175.3

Table I-IX. Aerodynamic Data of Similitude 20-Shallow-Chute Mechanical Suppressor with Convergent Inner Nozzle (Model 10.1) (Continued).

(English Units)

NOZZLE - MODEL 10.1

TEST POINT	V_{ac} FT/SEC	P_r^o	T_T^o DEG R	V_j^o FT/SEC	W^o LB/SEC	P_r^i	T_T^i DEG R	V_j^i FT/SEC	W^i LB/SEC	P_r^{mix}	T_T^{mix} DEG R	V_j^{mix} FT/SEC	F LB	V_j^i/V_j^o
1041	0	3.26	1732	2458	706.4	3.20	869	1719	170.5	3.19	1564	2314	63081	0.70
1042	400	3.26	1741	2465	704.5	3.24	873	1731	172.3	3.19	1570	2320	63245	0.70

TEST POINT	T_{amb} DEG R	P_{amb} PSIA	RH %	NF dB	LVM	LBM	PNL (FULL SIZE, 2400 FT SIDE LINE), dB ANGLE RELATIVE TO INLET, DEGREES 50	60	70	90	120	130	140	OAPWL dB
1041	542.9	14.41	36	-7.6	3.07	0.01	97.5	101.1	100.0	104.2	105.6	104.8	104.3	182.3
1042	546.7	14.42	36	-7.7	3.06	0.01	101.6	104.6	103.3	105.8	106.5	104.6	102.7	182.5

Table I-IX. Aerodynamic Data of Similitude 20-Shallow-Chute Mechanical Suppressor with Convergent Inner Nozzle (Model 10.1) (Concluded).

(International Units)

NOZZLE - MODEL 10.1   AREA [MODEL SIZE - INNER =0.0027 , OUTER = 0.0155 ; FULL SIZE - TOTAL = 0.9031] sq.m.

TEST POINT	V_{ac}	V_j^o	T_T^o	T_j^o	P_r^o	$\dot{W}^o$	F^o	V_j^i	T_T^i	T_j^i	P_r^i	$\dot{W}^i$	F^i	V_j^{mix}	T_T^{mix}	T_j^{mix}	P_r^{mix}	$\dot{W}^T$	F^T	V_j^i/V_j^o
	m/s	m/s	°K	°K		kg/s	N	m/s	°K	°K		kg/s	N	m/s	°K	°K		kg/s	N	
1001	0.	538.3	801.1	667.9	1.9921	215.8	7261	394.0	447.3	370.1	1.9419	48.8	1200	511.7	403.8	613.6	1.9698	265.	8461	0.73
1002	122.	547.1	821.1	684.2	2.0034	213.9	7316	409.3	477.1	393.7	1.9587	47.6	1216	522.1	416.3	631.9	1.9836	261.	8532	0.75
1003	0.	597.1	837.2	673.6	2.2818	241.5	9009	428.7	433.2	341.7	2.2937	58.5	1567	564.1	416.2	609.4	2.2565	300.	10577	0.72
1004	122.	602.0	848.9	682.6	2.2891	240.3	9041	437.0	446.7	351.7	2.3103	58.0	1583	570.0	422.8	618.8	2.2662	298.	10624	0.73
1005	0.	626.7	878.9	699.8	2.3878	246.3	9648	445.7	444.6	345.7	2.4123	60.7	1692	590.9	435.1	630.5	2.3590	307.	11341	0.71
1006	122.	634.3	898.9	716.3	2.3915	243.5	9655	452.7	457.7	355.7	2.4171	59.9	1695	598.5	445.4	645.9	2.3632	303.	11351	0.71
1007	0.	690.7	924.4	707.2	2.7860	279.9	12081	489.5	468.5	349.2	2.7961	68.6	2098	651.0	457.9	637.7	2.7429	348.	14179	0.71
1008	122.	691.6	923.9	705.9	2.7974	280.8	12137	495.8	479.5	357.1	2.8045	67.9	2104	653.4	459.3	638.9	2.7565	349.	14242	0.72
1009	0.	718.7	968.9	735.8	2.8936	283.4	12733	499.0	471.7	347.8	2.9066	71.0	2215	674.7	477.0	659.3	2.8412	354.	14948	0.69
1010	122.	720.2	970.6	736.7	2.9010	283.7	12769	509.5	490.5	361.3	2.9154	69.8	2222	678.5	480.6	663.7	2.8538	354.	14992	0.71
1011	0.	760.8	963.3	699.0	3.4012	334.3	15897	529.5	486.9	347.4	3.2614	78.5	2596	716.9	478.7	633.6	3.3173	413.	18494	0.70
1012	122.	763.8	969.4	703.4	3.4062	333.5	15918	544.5	515.1	367.6	3.2591	76.2	2592	723.0	485.5	642.3	3.3297	410.	18511	0.71
1013	0.	780.6	962.2	682.6	3.6838	362.2	17673	547.8	503.6	354.2	3.4258	81.0	2773	738.1	481.8	624.1	3.5820	443.	20446	0.70
1014	122.	787.6	976.7	693.3	3.6958	360.2	17734	556.5	519.3	365.1	3.4300	79.8	2776	745.8	490.4	635.3	3.5952	440.	20510	0.71
1015	0.	751.0	969.4	713.0	3.2465	318.0	14927	485.7	486.6	369.2	2.6289	63.3	1920	707.0	487.9	658.5	3.1078	381.	16847	0.65
1016	122.	753.8	977.2	719.6	3.2416	315.8	14881	495.0	504.8	382.8	2.6330	62.1	1922	711.3	493.6	666.7	3.1080	378.	16804	0.66
1017	0.	540.1	875.6	743.9	1.8754	193.8	6539	376.1	432.6	362.2	1.8621	47.5	1116	507.7	432.4	669.6	1.8544	241.	7655	0.70
1018	122.	539.8	872.2	741.1	1.8787	194.4	6556	381.6	445.1	372.6	1.8631	46.9	1117	509.0	433.1	670.3	1.8588	241.	7674	0.71
1019	0.	634.9	956.7	776.9	2.2538	222.4	8822	407.5	403.4	320.8	2.2314	59.0	1502	587.1	461.3	682.9	2.2058	281.	10325	0.64
1020	122.	639.5	962.2	779.8	2.2730	223.4	8929	418.6	424.6	337.3	2.2360	57.6	1506	594.3	467.5	690.7	2.2268	281.	10435	0.65
1041	0.	749.2	962.2	706.7	3.2590	320.4	15004	524.0	483.1	346.4	3.2032	77.3	2532	705.5	476.8	637.9	3.1896	398.	17537	0.70
1042	122.	751.3	967.2	710.7	3.2584	319.6	15004	527.7	485.4	346.8	3.2444	78.2	2578	707.3	478.7	640.4	3.1942	398.	17582	0.70

Table I-X. Aerodynamic Data of Similitude 20-Shallow-Chute Mechanical Suppressor with C-D Inner Nozzle (Model 10.2).

(English Units)

NOZZLE - MODEL 10.2 AREA [MODEL SIZE - INNER = 4.00 , OUTER = 19.88 ; FULL SIZE - TOTAL = 1400.00] SQ.IN.

TEST POINT	V_{ac} FT/SEC	P_r^o	T_T^o DEG R	V_j^o FT/SEC	$\dot{W}^o$ LB/SEC	P_r^i	T_T^i DEG R	V_j^i FT/SEC	$\dot{W}^i$ LB/SEC	P_r^{mix}	T_T^{mix} DEG R	V_j^{mix} FT/SEC	F LB	V_j^i/V_j^o
1021	0	3.24	1739	2459	683.7	2.20	911	1484	130.8	3.03	1606	2302	58284	0.60
1022	400	3.25	1734	2456	685.9	2.21	941	1515	129.6	3.04	1607	2306	58456	0.62
1023	0	3.24	1744	2463	682.8	2.40	899	1545	143.8	3.06	1597	2303	59169	0.63
1024	400	3.24	1717	2443	689.1	2.41	937	1582	141.6	3.07	1584	2296	59286	0.65
1025	0	3.24	1738	2458	684.3	2.51	902	1582	149.9	3.07	1587	2300	59649	0.64
1026	400	3.25	1732	2455	686.8	2.45	924	1582	144.6	3.07	1591	2303	59526	0.64
1027	0	3.24	1734	2455	685.4	2.70	865	1602	164.9	3.09	1565	2289	60512	0.65
1028	400	3.25	1738	2460	685.3	2.48	907	1577	147.6	3.07	1591	2303	59627	0.64
1029	0	3.24	1734	2455	685.4	2.72	874	1616	165.6	3.10	1566	2292	60629	0.66
1030	400	3.24	1726	2450	687.2	2.63	899	1614	157.6	3.09	1572	2294	60238	0.66
1031	0	3.24	1746	2464	682.4	2.73	894	1636	163.7	3.10	1581	2304	60595	0.66
1032	400	3.25	1761	2476	680.4	2.78	900	1656	166.8	3.11	1591	2314	60936	0.67
1033	0	3.24	1753	2469	681.3	2.89	880	1663	175.3	3.12	1574	2304	61349	0.67
1034	400	3.25	1745	2465	684.2	2.92	898	1686	174.9	3.14	1572	2306	61588	0.68

TEST POINT	T_{amb} DEG R	P_{amb} PSIA	RH %	NF dB	LVM	LBM	PNL (FULL SIZE, 2400 FT SIDE LINE), dB ANGLE RELATIVE TO INLET, DEGREES 50	60	70	90	120	130	140	OAPWL dB
1021	522.2	14.41	58	-6.9	3.13	-0.26	97.4	101.1	98.9	104.0	106.0	104.5	103.7	181.5
1022	538.4	14.42	35	-7.1	3.07	-0.25	101.6	104.3	101.4	105.4	106.5	104.8	102.5	181.5
1023	523.4	14.42	58	-7.1	3.13	-0.21	97.5	101.0	98.7	104.2	105.7	104.5	104.1	181.6
1024	535.5	14.42	44	-7.2	3.06	-0.20	101.2	104.1	101.6	105.3	106.2	104.4	102.2	181.8
1025	525.1	14.42	58	-7.1	3.11	-0.18	97.5	100.6	98.6	103.8	105.5	104.8	104,3	181.7
1026	534.8	14.42	44	-7.2	3.08	-0.19	101.7	104.5	101.2	105.3	106.2	104.2	102.1	181.8
1027	526.8	14.42	58	-7.3	3.09	-0.13	97.3	101.0	98.8	104.0	105.3	104.1	103.5	181.6
1028	536.2	14.42	44	-7.2	3.07	-0.18	101.7	104.2	101.7	105.5	106.5	104.0	102.4	181.8
1029	527.1	14.42	58	-7.3	3.09	-0.13	97.1	100.8	98.9	103.8	105.5	104.2	103.8	182.0
1030	536.5	14.42	44	-7.3	3.06	-0.15	101.5	104.3	101.8	104.9	106.1	103.8	102.3	181.6
1031	528.5	14.41	58	-7.3	3.11	-0.13	96.8	100.7	98.8	104.0	105.7	104.5	104.0	181.9
1032	533.2	14.42	44	-7.3	3.11	-0.11	101.3	104.4	101.6	105.4	106.0	104.1	102.0	181.3
1033	529.1	14.41	53	-7.4	3.10	-0.09	97.1	101.1	98.8	104.1	105.7	104.4	104.4	181.9
1034	531.6	14.42	44	-7.4	3.10	-0.07	102.5	104.8	102.2	105.7	106.4	104.6	102.0	181.8

Table I-X. Aerodynamic Data of Similitude 20-Shallow-Chute Mechanical Suppressor with C-D Inner Nozzle (Model 10.2) (Concluded).

(International Units)

NOZZLE - MODEL 10.2 AREA [MODEL SIZE - INNER =0.0026 , OUTER = 0.0128 ; FULL SIZE - TOTAL = 0.9031] sq.m.

TEST POINT	V_{ac}	V_j^o	T_T^o	T_j^o	P_r^o	$\dot{W}^o$	F^o	V_j^i	T_T^i	T_j^i	P_r^i	$\dot{W}^i$	F^i	V_j^{mix}	T_T^{mix}	T_j^{mix}	P_r^{mix}	$\dot{W}^T$	F^T	V_j^i/V_j^o
	m/s	m/s	°K	°K		kg/s	N	m/s	°K	°K		kg/s	N	m/s	°K	°K		kg/s	N	
1021	0.	749.5	966.1	710.9	3.2414	310.1	14526	452.4	506.2	404.3	2.1962	59.3	1677	701.8	489.6	665.6	3.0321	369.	16203	0.60
1022	122.	748.6	963.3	708.2	3.2453	311.1	14554	461.9	523.2	417.0	2.2122	58.8	1696	703.0	490.1	665.6	3.0419	370.	16251	0.62
1023	0.	750.7	968.9	713.1	3.2417	309.7	14529	471.1	499.4	389.0	2.3984	65.2	1920	702.0	486.9	660.1	3.0576	375.	16449	0.63
1024	122.	744.6	953.9	701.1	3.2436	312.6	14547	482.2	520.7	404.9	2.4106	64.2	1935	699.9	482.8	653.6	3.0686	377.	16482	0.65
1025	0.	749.2	965.6	710.3	3.2423	310.4	14534	482.2	501.4	385.7	2.5054	68.0	2048	701.3	484.0	654.9	3.0739	378.	16583	0.64
1026	122.	748.3	962.2	707.2	3.2483	311.5	14571	482.4	513.6	397.8	2.4462	65.6	1977	702.1	485.1	656.4	3.0744	377.	16549	0.64
1027	0.	748.3	963.3	708.4	3.2424	310.9	14539	488.5	480.9	362.2	2.6989	74.8	2283	697.9	477.1	643.8	3.0949	386.	16823	0.65
1028	122.	749.8	965.6	710.1	3.2473	310.8	14564	480.8	504.4	389.3	2.4751	67.0	2012	702.0	484.9	656.3	3.0746	378.	16577	0.64
1029	0.	748.3	963.3	708.5	3.2431	310.9	14542	492.8	485.6	364.7	2.7235	75.1	2313	698.7	477.5	644.1	3.1004	386.	16855	0.66
1030	122.	746.8	958.9	705.1	3.2440	311.7	14549	492.0	499.4	378.9	2.6279	71.5	2197	699.3	479.2	646.9	3.0928	383.	16747	0.66
1031	0.	751.0	970.0	713.9	3.2422	309.5	14531	498.7	497.1	373.3	2.7253	74.3	2315	702.3	482.1	650.5	3.1024	384.	16846	0.66
1032	122.	754.7	978.3	720.1	3.2452	308.6	14553	504.9	500.4	373.5	2.7838	75.7	2387	705.4	485.1	654.3	3.1127	384.	16941	0.67
1033	0.	752.6	973.9	716.6	3.2431	309.0	14536	507.1	488.9	360.9	2.8931	79.5	2519	702.3	479.8	646.0	3.1235	389.	17055	0.67
1034	122.	751.3	969.4	713.0	3.2487	310.3	14573	514.1	499.2	367.7	2.9168	79.3	2549	703.0	479.4	644.7	3.1358	390.	17122	0.68

Table I-XI. Aerodynamic Data of Modified DOT 20-Shallow-Chute Mechanical Suppressor Nozzle.

(English Units)

NOZZLE - MODEL DOT 20 AREA [MODEL SIZE - INNER = 4.75 , OUTER = 23.76 ; FULL SIZE - TOTAL = 1400.00] SQ.IN.

TEST POINT	V_{ac} FT/SEC	P_r^o	T_T^o DEG R	V_j^o FT/SEC	$\dot{W}^o$ LB/SEC	P_r^i	T_T^i DEG R	V_j^i FT/SEC	$\dot{W}^i$ LB/SEC	P_r^{mix}	T_T^{mix} DEG R	V_j^{mix} FT/SEC	F LB	V_j^i/V_j^o
2001	0	1.56	1244	1334	380.0	1.26	874	822	63.3	1.51	1191	1260	17372	0.62
2002	400	1.59	1247	1364	389.0	1.30	822	839	68.9	1.54	1183	1285	18293	0.62
2003	0	1.89	1425	1695	443.2	1.48	826	1023	87.1	1.82	1326	1584	26112	0.60
2004	400	1.92	1434	1718	447.1	1.52	802	1039	91.6	1.84	1326	1602	26839	0.61
2005	0	2.40	1577	2057	532.2	1.86	783	1234	118.2	2.28	1432	1907	38561	0.60
2006	400	2.44	1583	2078	538.9	1.85	805	1249	116.1	2.31	1445	1931	39308	0.60
2009	0	2.70	1644	2221	585.8	1.99	835	1336	122.6	2.55	1503	2068	45533	0.60
2010	400	2.73	1659	2242	587.8	1.98	841	1340	121.9	2.57	1518	2087	46037	0.60
2011	0	2.91	1703	2333	619.2	2.15	851	1417	131.4	2.74	1553	2173	50696	0.61
2012	400	2.94	1716	2352	622.1	2.14	874	1431	128.8	2.77	1571	2194	51210	0.61
2013	0	3.02	1717	2379	640.2	2.20	874	1456	132.9	2.85	1572	2220	53351	0.61
2014	400	3.08	1708	2390	654.1	2.19	855	1436	133.4	2.89	1563	2228	54548	0.60
2015	0	3.32	1708	2455	705.2	1.43	870	1007	80.6	3.01	1621	2306	56341	0.41
2016	400	3.36	1714	2471	711.4	1.42	890	1007	78.4	3.05	1632	2325	57087	0.41
2017	0	3.32	1708	2457	704.6	1.77	859	1246	107.0	3.04	1596	2297	57945	0.51
2018	400	3.34	1718	2469	706.8	1.76	873	1252	105.8	3.06	1607	2310	58355	0.51
2019	0	3.32	1714	2461	703.1	2.38	861	1508	144.6	3.12	1568	2298	60562	0.61
2020	400	3.31	1714	2459	702.0	2.40	874	1525	144.5	3.12	1570	2299	60500	0.62
2021	0	3.32	1717	2464	703.0	3.38	851	1733	205.9	3.26	1520	2298	64918	0.70
2022	400	3.32	1707	2456	704.9	3.41	842	1730	209.6	3.26	1509	2289	65080	0.70

TEST POINT	T_{amb} DEG R	P_{amb} PSIA	RH %	NF dB	LVM	LBM	PNL (FULL SIZE, 2400 FT SIDE LINE), dB ANGLE RELATIVE TO INLET, DEGREES 50	60	70	90	120	130	140	OAPWL dB
2001	509.3	14.39	81	-4.9	0.57	-10.00	79.8	82.3	84.2	88.4	90.9	88.7	86.4	164.1
2002	511.8	14.36	52	-4.9	0.64	-10.00	83.8	86.3	87.4	89.2	89.6	85.7	82.0	164.8
2003	510.7	14.39	81	-4.5	1.55	-10.00	84.5	87.6	89.6	93.8	96.7	95.0	94.6	171.0
2004	512.7	14.36	52	-4.6	1.60	-10.00	89.7	91.4	92.8	94.1	95.9	92.5	89.2	170.7
2005	511.7	14.38	62	-5.2	2.36	-2.28	91.6	94.9	96.6	99.1	101.9	100.6	100.1	176.5
2006	513.7	14.36	52	-5.3	2.40	-2.13	94.7	97.2	97.9	100.1	101.1	99.9	96.5	176.9
2009	511.8	14.38	62	-5.9	2.71	-1.28	94.5	97.3	98.9	101.5	103.2	102.2	101.2	178.1
2010	512.7	14.36	52	-5.9	2.74	-1.21	97.8	99.8	100.5	102.3	103.2	101.8	99.5	179.1
2011	513.0	14.38	62	-6.3	2.92	-0.78	96.1	98.7	100.4	102.7	104.2	103.7	102.8	179.5
2012	514.7	14.36	52	-6.3	2.95	-0.74	99.1	101.1	101.8	103.9	104.6	103.4	100.4	180.4
2013	511.8	14.38	62	-6.5	3.01	-0.58	96.9	99.6	101.0	103.4	104.7	104.0	102.7	179.9
2014	517.2	14.36	52	-6.7	3.01	-0.49	99.8	102.2	102.7	104.0	104.9	103.5	101.1	180.9
2015	511.3	14.38	62	-6.7	3.18	-0.37	97.6	101.1	102.4	104.4	105.7	104.2	103.4	180.7
2016	515.9	14.36	52	-6.7	3.20	-0.31	100.1	102.9	104.0	104.6	106.0	103.9	101.6	181.3
2017	511.0	14.35	62	-6.9	3.17	-0.27	98.0	100.9	102.5	104.4	105.4	105.0	104.0	180.9
2018	515.8	14.36	52	-6.9	3.17	-0.25	100.9	102.7	103.8	104.6	105.4	104.3	101.7	181.4
2019	511.3	14.35	60	-7.2	3.17	-0.11	98.1	100.9	102.9	104.5	105.4	105.8	104.6	181.3
2020	513.7	14.36	52	-7.2	3.16	-0.12	99.9	102.7	103.9	105.0	105.9	104.4	101.6	181.7
2021	511.3	14.35	60	-7.7	3.17	0.11	98.2	100.8	103.0	104.3	105.6	105.8	105.5	181.8
2022	514.6	14.36	52	-7.7	3.14	0.11	100.5	102.9	103.6	104.9	105.8	104.6	102.0	181.8

Table I-XI. Aerodynamic Data of Modified DOT 20-Shallow-Chute Mechanical Suppressor Nozzle (Continued).

(English Units)

NOZZLE - MODEL DOT 20

TEST POINT	V_{ac} FT/SEC	P_r^o	T_T^o DEG R	V_j^o FT/SEC	$\dot{W}^o$ LB/SEC	P_r^i	T_T^i DEG R	V_j^i FT/SEC	$\dot{W}^i$ LB/SEC	P_r^{mix}	T_T^{mix} DEG R	V_j^{mix} FT/SEC	F LB	V_j^i/V_j^o
2023	0	3.60	1720	2533	760.7	2.50	870	1553	151.0	3.37	1579	2370	67184	0.61
2024	400	3.60	1713	2528	763.0	2.49	866	1546	151.0	3.37	1572	2365	67206	0.61
2025	0	3.86	1731	2598	812.8	2.55	879	1575	153.0	3.59	1595	2435	73109	0.61
2026	400	3.86	1733	2600	812.2	2.54	893	1584	151.3	3.59	1601	2440	73081	0.61
2027	0	3.77	1712	2564	798.5	3.61	477	1327	294.5	3.46	1379	2230	75777	0.52
2028	400	3.76	1712	2564	797.8	2.56	622	1325	182.5	3.44	1509	2333	71091	0.52
2041	0	2.41	1578	2061	10.9	1.00	518	0	0.0	2.41	1577	2061	696	0.00
2042	400	2.41	1588	2067	10.8	1.00	518	0	0.0	2.41	1587	2067	696	0.00
2043	0	2.91	1704	2336	12.6	1.00	518	0	0.0	2.91	1704	2335	917	0.00
2044	400	2.91	1704	2335	12.6	1.00	518	0	0.0	2.91	1703	2334	916	0.00
2045	0	3.30	1719	2459	14.2	1.00	518	0	0.0	3.30	1719	2458	1087	0.00
2046	400	3.30	1737	2472	14.2	1.00	518	0	0.0	3.30	1736	2472	1089	0.00

TEST POINT	T_{amb} DEG R	P_{amb} PSIA	RH %	NF dB	LVM	LBM	PNL (FULL SIZE, 40 FT SIDE LINE), dB ANGLE RELATIVE TO INLET, DEGREES 50	60	70	90	120	130	140	OAPWL dB
2023	511.7	14.35	60	-7.7	3.30	0.21	89.5	91.4	93.2	94.7	99.2	100.9	102.6	182.2
2024	514.2	14.36	56	-7.7	3.28	0.21	90.6	91.7	92.1	94.4	97.9	97.2	96.3	183.1
2025	511.9	14.34	60	-8.1	3.42	0.45	89.8	91.6	93.4	95.6	99.9	101.9	104.4	182.9
2026	516.0	14.34	56	-8.1	3.41	0.45	90.3	92.2	92.3	95.2	98.7	98.3	97.8	183.4
2027	511.5	14.35	56	-8.9	3.04	0.55	89.3	91.9	93.2	95.1	99.7	100.5	102.0	182.3
2028	514.5	14.35	56	-8.2	3.22	0.37	90.7	92.8	92.8	95.5	98.1	97.2	96.2	183.0
2041	511.3	14.39	79	12.6	2.69	-1.85	106.4	109.8	108.4	110.8	115.7	116.9	119.0	160.5
2042	510.8	14.39	79	12.6	2.71	-1.86	109.4	109.3	109.1	110.4	114.7	115.2	115.4	159.5
2043	511.8	14.38	79	11.5	3.24	-0.53	111.8	111.9	112.5	113.9	118.7	120.1	122.6	162.9
2044	513.4	14.39	79	11.5	3.23	-0.53	114.1	113.9	113.6	114.0	117.8	119.0	119.4	163.3
2045	511.5	14.38	79	10.6	3.46	0.07	114.6	114.5	114.7	115.5	120.5	122.6	124.9	164.6
2046	513.5	14.39	79	10.7	3.47	0.07	116.2	115.9	115.6	115.8	119.7	120.6	120.7	164.8

Table I-XI. Aerodynamic Data of Modified DOT 20-Shallow-Chute Mechanical Suppressor Nozzle (Concluded).

(International Units)

NOZZLE - MODEL DOT 20 AREA [MODEL SIZE - INNER =0.0031 , OUTER = 0.0153 ; FULL SIZE - TOTAL = 0.9031] sq.m.

TEST POINT	V_{ac}	V_j^o	T_T^o	T_j^o	P_r^o	$\dot{W}^o$	F^o	V_j^i	T_T^i	T_j^i	P_r^i	$\dot{W}^i$	F^i	V_j^{mix}	T_T^{mix}	T_j^{mix}	P_r^{mix}	$\dot{W}^T$	F^T	V_j^i/V_j^o
	m/s	m/s	°K	°K		kg/s	N	m/s	°K	°K		kg/s	N	m/s	°K	°K		kg/s	N	
2001	0.	406.6	691.1	613.8	1.5555	172.4	4379	250.8	485.9	454.8	1.2625	28.7	449	384.3	363.1	592.3	1.5079	201.	4829	0.62
2002	122.	415.7	692.8	611.8	1.5878	176.4	4585	255.8	457.2	424.6	1.2951	31.3	499	391.7	360.6	584.8	1.5386	208.	5085	0.62
2003	0.	516.6	791.7	668.6	1.8931	201.0	6489	311.9	459.4	410.9	1.4769	39.5	769	482.9	404.3	628.2	1.8158	241.	7259	0.60
2004	122.	523.6	796.7	670.7	1.9211	202.8	6638	316.9	445.8	395.8	1.5161	41.5	822	488.6	404.4	625.9	1.8433	244.	7461	0.61
2005	0.	627.0	876.1	696.4	2.3987	241.4	9459	376.3	435.4	364.9	1.8555	53.6	1261	581.4	436.6	638.8	2.2802	295.	10720	0.60
2006	122.	633.4	879.4	696.2	2.4381	244.4	9675	380.7	447.6	375.4	1.8502	52.7	1252	588.6	440.5	642.1	2.3139	297.	10928	0.60
2009	0.	677.0	913.3	704.4	2.6990	265.7	11242	407.4	464.0	381.4	1.9865	55.6	1416	630.4	458.3	651.6	2.5493	321.	12658	0.60
2010	122.	683.4	921.7	709.4	2.7266	266.6	11387	408.6	467.3	384.2	1.9845	55.3	1411	636.1	462.9	656.9	2.5717	322.	12798	0.60
2011	0.	711.1	946.1	716.3	2.9070	280.9	12485	432.1	473.2	380.2	2.1494	59.6	1609	662.3	473.6	660.8	2.7428	340.	14094	0.61
2012	122.	716.9	953.3	720.1	2.9365	282.2	12643	436.4	485.8	391.0	2.1381	58.4	1593	668.8	479.0	667.1	2.7678	341.	14237	0.61
2013	0.	725.1	953.9	715.3	3.0190	290.4	13158	444.0	485.7	387.5	2.2036	60.3	1673	676.7	479.2	662.3	2.8453	351.	14832	0.61
2014	122.	728.5	948.9	707.1	3.0800	296.7	13509	437.8	475.3	379.9	2.1908	60.5	1655	679.2	476.5	655.2	2.8924	357.	15165	0.60
2015	0.	748.3	948.9	692.7	3.3159	319.9	14961	307.1	483.4	436.5	1.4297	36.6	701	703.1	494.3	673.8	3.0088	356.	15663	0.41
2016	122.	753.2	952.2	693.2	3.3567	322.7	15188	306.9	494.7	447.9	1.4170	35.6	682	708.8	497.6	676.2	3.0454	358.	15870	0.41
2017	0.	748.9	948.9	692.6	3.3204	319.6	14957	379.8	477.6	405.8	1.7687	48.5	1152	700.2	486.5	660.6	3.0400	368.	16109	0.51
2018	122.	752.6	954.4	695.7	3.3391	320.6	15078	381.7	485.1	412.6	1.7623	48.0	1145	704.2	490.0	664.7	3.0562	369.	16223	0.51
2019	0.	750.1	952.2	695.2	3.3198	318.9	14952	459.9	478.7	373.4	2.3850	65.6	1884	700.6	478.1	643.8	3.1184	385.	16837	0.61
2020	122.	749.5	952.2	695.6	3.3124	318.4	14916	464.8	486.1	378.5	2.3996	65.5	1903	700.9	478.7	644.9	3.1164	384.	16819	0.62
2021	0.	751.0	953.9	696.2	3.3220	318.9	14963	528.4	473.2	334.2	3.3769	93.4	3084	700.5	463.5	615.3	3.2567	412.	18048	0.70
2022	122.	748.6	948.3	692.4	3.3194	319.7	14959	527.4	467.8	329.3	3.4149	95.1	3133	697.9	459.9	610.2	3.2590	415.	18093	0.70
2023	0.	772.1	955.6	682.1	3.5986	345.0	16652	473.4	483.6	372.1	2.5033	68.5	2025	722.7	481.3	634.5	3.3674	414.	18678	0.61
2024	122.	770.5	951.7	679.2	3.5989	346.1	16666	471.4	481.2	370.6	2.4949	68.5	2017	721.1	479.4	631.9	3.3665	415.	18684	0.61
2025	0.	791.9	961.7	673.3	3.8580	368.7	18242	480.1	488.8	374.1	2.5506	69.4	2082	742.3	486.4	629.9	3.5913	438.	20325	0.61
2026	122.	792.5	962.8	674.4	3.8586	368.4	18246	482.9	496.2	380.1	2.5411	68.6	2070	743.8	488.1	632.3	3.5929	437.	20317	0.61
2027	0.	781.5	951.1	670.1	3.7657	362.2	17689	404.5	265.1	183.7	3.6132	133.6	3377	679.9	420.3	545.0	3.4563	496.	21067	0.52
2028	122.	781.5	951.1	670.5	3.7630	361.9	17673	404.1	345.6	264.3	2.5564	82.8	2090	711.2	460.1	600.9	3.4402	445.	19764	0.52
2041	0.	628.2	876.7	696.4	2.4064	4.9	193	0.	287.8	287.8	1.0000	0.0	0	628.2	480.9	696.4	2.4064	5.	193	0.00
2042	122.	630.0	882.2	701.0	2.4051	4.9	193	0.	287.8	287.8	1.0000	0.0	0	630.1	483.9	701.0	2.4051	5.	193	0.00
2043	0.	712.0	946.7	716.7	2.9110	5.7	254	0.	287.8	287.8	1.0000	0.0	0	712.0	519.5	716.7	2.9110	6.	254	0.00
2044	122.	711.7	946.7	716.4	2.9100	5.7	254	0.	287.8	287.8	1.0000	0.0	0	711.7	519.2	716.4	2.9100	6.	254	0.00
2045	0.	749.5	955.0	698.9	3.2964	6.4	302	0.	287.8	287.8	1.0000	0.0	0	749.4	524.0	698.9	3.2964	6.	302	0.00
2046	122.	753.5	965.0	706.2	3.2997	6.4	302	0.	287.8	287.8	1.0000	0.0	0	753.6	529.3	706.2	3.2997	6.	302	0.00

Table I-XII. Aerodynamic Data of Modified DOT 40-Shallow-Chute Mechanical Suppressor Nozzle.

(English Units)

NOZZLE - MODEL DOT 40 AREA [MODEL SIZE - INNER = 4.75 , OUTER = 23.76 : FULL SIZE - TOTAL = 1400.00] SQ.IN.

TEST POINT	V_{ac} FT/SEC	P^o_r	T^o_T DEG R	V^o_j FT/SEC	$\dot{W}^o$ LB/SEC	P^i_r	T^i_T DEG R	V^i_j FT/SEC	$\dot{W}^i$ LB/SEC	P^{mix}_r	T^{mix}_T DEG R	V^{mix}_j FT/SEC	F LB	V^i_j/V^o_j
4003	0	1.91	1413	1697	446.9	1.50	816	1036	89.3	1.83	1313	1587	26451	0.61
4004	400	1.91	1431	1708	441.7	1.51	831	1053	88.9	1.83	1330	1597	26355	0.62
4005	0	2.41	1579	2062	531.6	1.86	814	1258	115.5	2.29	1442	1918	38594	0.61
4006	400	2.43	1577	2069	535.6	1.85	815	1255	114.9	2.31	1442	1925	38934	0.61
4009	0	2.71	1640	2222	585.8	2.00	834	1342	123.0	2.56	1500	2069	45582	0.60
4010	400	2.71	1644	2225	585.1	2.03	819	1341	125.7	2.56	1498	2068	45712	0.60
4011	0	2.90	1705	2333	615.0	2.16	859	1427	130.8	2.74	1556	2173	50389	0.61
4012	400	2.93	1716	2350	618.7	2.16	863	1430	130.3	2.76	1567	2190	50994	0.61
4019	0	3.30	1728	2467	695.5	2.40	845	1500	146.7	3.10	1574	2298	60157	0.61
4020	400	3.33	1711	2462	704.4	2.42	848	1508	147.5	3.13	1561	2296	60812	0.61
4023	0	3.60	1726	2539	759.3	2.48	872	1549	149.4	3.37	1585	2376	67119	0.61
4024	400	3.62	1727	2544	761.9	2.51	868	1553	151.1	3.39	1585	2380	67545	0.61
4025	0	3.89	1735	2607	815.5	2.58	878	1582	154.7	3.62	1598	2443	73695	0.61
4026	400	3.88	1725	2599	818.0	2.58	869	1574	155.4	3.62	1588	2435	73678	0.61

TEST POINT	T_{amb} DEG R	P_{amb} PSIA	RH %	NF dB	LVM	LBM	PNL (FULL SIZE, 2400 FT SIDE LINE), dB ANGLE RELATIVE TO INLET, DEGREES 50	60	70	90	120	130	140	OAPWL dB
4003	503.7	14.33	69	-4.5	1.59	-10.00	83.3	85.4	89.4	93.7	95.2	94.0	91.5	171.1
4004	505.0	14.27	86	-4.4	1.61	-10.00	86.3	92.0	90.3	93.7	93.9	91.4	87.9	170.9
4005	504.2	14.33	69	-5.2	2.41	-2.25	87.3	88.9	93.0	97.4	99.1	98.7	98.6	175.5
4006	506.0	14.31	76	-5.2	2.42	-2.18	90.6	92.6	93.4	97.2	99.3	97.3	95.0	174.6
4009	504.3	14.33	69	-5.8	2.74	-1.25	89.3	90.2	95.4	98.8	100.6	101.6	101.5	178.2
4010	506.1	14.31	76	-5.9	2.73	-1.23	92.7	95.3	95.7	99.2	100.8	99.9	97.8	176.5
4011	504.6	14.32	69	-6.2	2.95	-0.79	89.9	93.8	95.8	99.5	102.7	103.4	105.2	179.2
4012	504.3	14.31	76	-6.2	2.99	-0.74	93.8	96.1	97.2	100.4	102.5	101.8	99.8	177.6
4019	504.6	14.32	66	-7.1	3.20	-0.13	92.6	96.9	98.0	101.6	105.3	106.5	108.4	181.8
4020	504.5	14.32	76	-7.1	3.19	-0.09	95.9	98.5	99.2	101.5	104.0	103.3	102.0	178.9
4023	504.5	14.32	66	-7.6	3.34	0.21	95.2	97.9	99.9	103.1	107.1	108.9	111.4	184.1
4024	504.9	14.31	76	-7.6	3.35	0.23	98.0	99.5	100.2	103.1	105.1	105.2	104.4	180.6
4025	504.7	14.30	66	-8.1	3.46	0.48	96.1	99.3	101.2	104.2	108.2	110.8	113.0	185.1
4026	506.2	14.31	76	-8.1	3.44	0.48	100.2	102.1	102.4	104.4	106.2	106.6	106.7	182.0

Table I-XII. Aerodynamic Data of Modified DOT 40-Shallow-Chute Mechanical Suppressor Nozzle (Concluded).

(International Units)

NOZZLE - MODEL DOT 40 AREA [MODEL SIZE - INNER =0.0031 , OUTER = 0.0153 ; FULL SIZE - TOTAL = 0.9031] sq.m.

TEST POINT	V_{ac}	V_j^o	T_T^o	T_j^o	P_r^o	$\dot{W}^o$	F^o	V_j^i	T_T^i	T_j^i	P_r^i	$\dot{W}^i$	F^i	V_j^{mix}	T_T^{mix}	T_j^{mix}	P_r^{mix}	$\dot{W}^T$	F^T	V_j^i/V_j^o
	m/s	m/s	°K	°K		kg/s	N	m/s	°K	°K		kg/s	N	m/s	°K	°K		kg/s	N	
4003	0.	517.2	785.0	661.6	1.9085	202.7	6554	315.8	453.8	404.2	1.4999	40.5	799	483.8	400.4	620.6	1.8317	243.	7353	0.61
4004	122.	520.6	795.0	670.3	1.9073	200.4	6517	321.1	461.9	410.6	1.5102	40.3	809	487.0	405.5	628.6	1.8324	241.	7327	0.62
4005	0.	628.5	877.2	696.8	2.4073	241.1	9472	383.7	452.6	379.3	1.8559	52.4	1256	584.9	439.7	642.8	2.2903	294.	10729	0.61
4006	122.	630.6	876.1	694.5	2.4265	242.9	9577	382.7	453.0	380.1	1.8483	52.1	1246	586.9	439.7	641.7	2.3052	295.	10824	0.61
4009	0.	677.3	911.1	702.2	2.7069	265.7	11245	409.2	463.8	380.5	2.0000	55.8	1426	630.6	457.4	649.5	2.5580	322.	12672	0.60
4010	122.	678.2	913.3	703.9	2.7092	265.4	11250	408.9	455.2	372.0	2.0271	57.0	1457	630.6	456.7	648.3	2.5616	322.	12708	0.60
4011	0.	711.1	947.2	717.7	2.9000	279.0	12395	435.1	477.6	383.3	2.1586	59.3	1613	662.6	474.4	662.3	2.7392	338.	14008	0.61
4012	122.	716.3	953.3	720.7	2.9303	280.6	12566	435.9	479.6	385.1	2.1568	59.1	1610	667.6	477.9	665.7	2.7638	340.	14177	0.61
4019	0.	751.9	960.0	702.1	3.3032	315.5	14823	457.2	469.9	365.9	2.4011	66.5	1900	700.5	479.8	647.1	3.1027	382.	16724	0.61
4020	122.	750.4	950.6	693.3	3.3304	319.5	14983	459.7	471.3	366.2	2.4203	66.9	1922	700.0	476.0	640.2	3.1299	386.	16906	0.61
4023	0.	773.9	958.9	684.3	3.6050	344.4	16660	472.3	484.9	373.9	2.4844	67.8	1999	724.4	483.3	637.1	3.3702	412.	18660	0.61
4024	122.	775.4	959.4	684.2	3.6212	345.6	16750	473.4	482.6	371.0	2.5094	68.5	2028	725.5	483.2	636.1	3.3860	414.	18778	0.61
4025	0.	794.6	963.9	673.8	3.8877	369.9	18372	482.5	487.8	371.9	2.5837	70.2	2115	744.9	487.2	629.7	3.6194	440.	20488	0.61
4026	122.	792.2	958.3	669.8	3.8847	371.0	18369	479.8	482.9	368.3	2.5811	70.5	2114	742.2	484.2	625.7	3.6159	442.	20483	0.61

APPENDIX II - AERODYNAMIC FLOW CONDITIONS OF LV TEST POINTS

Mean and turbulent velocity measurements of four selected plumes of the similitude 20-shallow-chute suppressor model nozzle were conducted using the laser velocimeter. Aerodynamic conditions that define the LV test points are presented in Table II-I of this appendix. These points include two static tests (LV test points 1 and 2) with the similitude 20-shallow-chute suppressor having a convergent inner nozzle (Model 10.1) and one static and one simulated free-jet test (at $V_{ac} \simeq 122$ mps/400 fps) with the similitude suppressor having a convergent-divergent inner nozzle (test points 3 and 4). The aerodynamic condition of LV test point 1 was selected to match one of the possible operating conditions of YJ101 testbed engine. While test points 1 and 3 have identical aerodynamic flow conditions that are typical of AST/VCE takeoff condition, they are static tests, respectively, with Models 10.1 (convergent inner) and 10.2 (C-D inner). Moreover, the flow variables of the inner stream match those for which the C-D inner exit of Model 10.2 was designed. Finally, LV test point 4 is a repeat of test point 3 but with a free jet to simulate a flight condition.

Table II-I. Aerodynamic Conditions of LV Test Points.

LV Test Point	Corresponding Acoustic Test Point	V_{ac} mps	Outer Stream			Inner Stream			Mixed Stream			Configuration
			P_r^o	T_T* °K	V_j^o** mps	P_r^2	T_T* °K	V_j^i** mps	P_r^{mix}	T_T^{mix}* °K	V_j^{mix}** mps	
1	1019	0	2.25	955 (1719)	635 (2083)	2.21	408 (735)	408 (1337)	2.24	806 (1451)	573 (1880)	Model 10.1; Aero Condition Matches a YJ101 Operating Condition
2	1015	0	3.24	969 (1745)	750 (2463)	2.59	496 (893)	488 (1600)	3.13	879 (1582)	701 (2299)	Model 10.1; P_r^i Corresponds to Design Condition of C-D Inner Nozzle of Model 10.2
3	1027	0	3.24	965 (1738)	750 (2462)	2.59	500 (901)	489 (1605)	3.13	870 (1566)	697 (2285)	Model 10.2; C-D Inner Nozzle Design Condition
4	1028	122 (400)	3.24	964 (1736)	750 (2462)	2.63	500 (901)	493 (1618)	3.14	868 (1563)	697 (2286)	Same as LV Test Point 3 But V_{ac} = 122 mps (400 fps)

*The Total Temperature in ( ) are in ° R

**The Velocities in ( ) are in fps.

APPENDIX III - SUPPRESSOR BASE PRESSURE MEASUREMENTS

The aerodynamic test conditions during which the base pressure data were recorded with the similitude 20-shallow-chute suppressor nozzle are presented in Table III-I. In addition to measurements over an operating line of a typical AST/VCE cycle, base pressure data were obtained over a range of suppressor pressure ratios, but at ambient temperature. These data were recorded with free-jet velocities of 0, 61 mps (200 fps) and 122 mps (400 fps).

The location of the static pressure probes in the chutes of the similitude 20-shallow-chute suppressor is shown in Figure III-1. Out of the 14 pressure probes installed in the designated chutes, measurements made with Probes 1 through 9 were used for the estimation of a representative pressure reading within the projected area of one chute. The other five, namely, Probes 10 through 14, were included for general study purposes only.

A sketch of the chute projected area along with the calculated values of the elemental strip areas applicable to each of the probes numbered 1 through 9 is shown in Figure III-2.

The expressions used in the calculation of the representative base pressure of each chute and the change in the nozzle thrust coefficient due to the base drag are summarized in Figure III-3.

Table III-I. Summary of Aerodynamic Flow Conditions of Base Pressure Tests

Base Pressure Test Point	Acoustic Test Point	P_r^o	T_T^o (° R)	P_r^i	T_T^i (° R)	V_{ac} (fps)
1	1001	1.99	1442	1.94	805	0
2	1003	2.28	1507	2.29	780	0
3	1005	2.38	1582	2.41	800	0
4	1007	2.78	1664	2.79	843	0
5	1009	2.89	1744	2.90	849	0
6	1011	3.40	1734	3.26	877	0
7	1015	3.24	1745	2.63	876	0
8	1019	2.25	1722	2.23	726	0
9	1041	3.26	1732	3.20	870	0
10	1017	1.87	1575	1.86	779	0
11	1002	2.00	1478	1.96	859	400
12	1004	2.29	1528	2.31	804	400
13	1006	2.39	1618	2.42	824	400
14	1008	2.79	1663	2.80	863	400
15	1020	2.27	1732	2.23	764	400
16	1010	2.90	1747	2.91	883	400
17	1016	3.24	1759	2.63	909	400
18	1012	3.40	1745	3.26	927	400
19	1018	1.88	1570	1.86	801	400
20		1.89	530	1.94	530	0
21		2.39	530	2.40	530	0
22		2.89	530	2.90	530	0
23		3.24	530	3.25	530	0
24		3.69	530	3.69	530	0
25		1.90	530	1.95	530	200
26		2.39	530	2.40	530	200
27		2.89	530	2.90	530	200
28		3.23	530	3.24	530	200
29		3.69	530	3.71	530	200
30		1.89	530	1.95	530	400
31		2.40	530	2.41	530	400
32		2.90	530	2.90	530	400
33		3.24	530	3.25	530	400
34		3.69	530	3.70	530	400

PRESS TAP NO.	CHUTE NO.	A	B	C
1	1	.079	—	—
2	2	.199	—	—
3	3	.320	—	—
4	4	.440	—	—
5	5	.560	—	—
6	6	.681	—	—
7	7	.802	—	—
8	8	.922	—	—
9	9	.199	.190	—
10	2	.199	—	.401
11	5	.560	—	.580
12	8	.922	—	.547
13	5	.560	—	(.558)
14	5	.560	.190	—

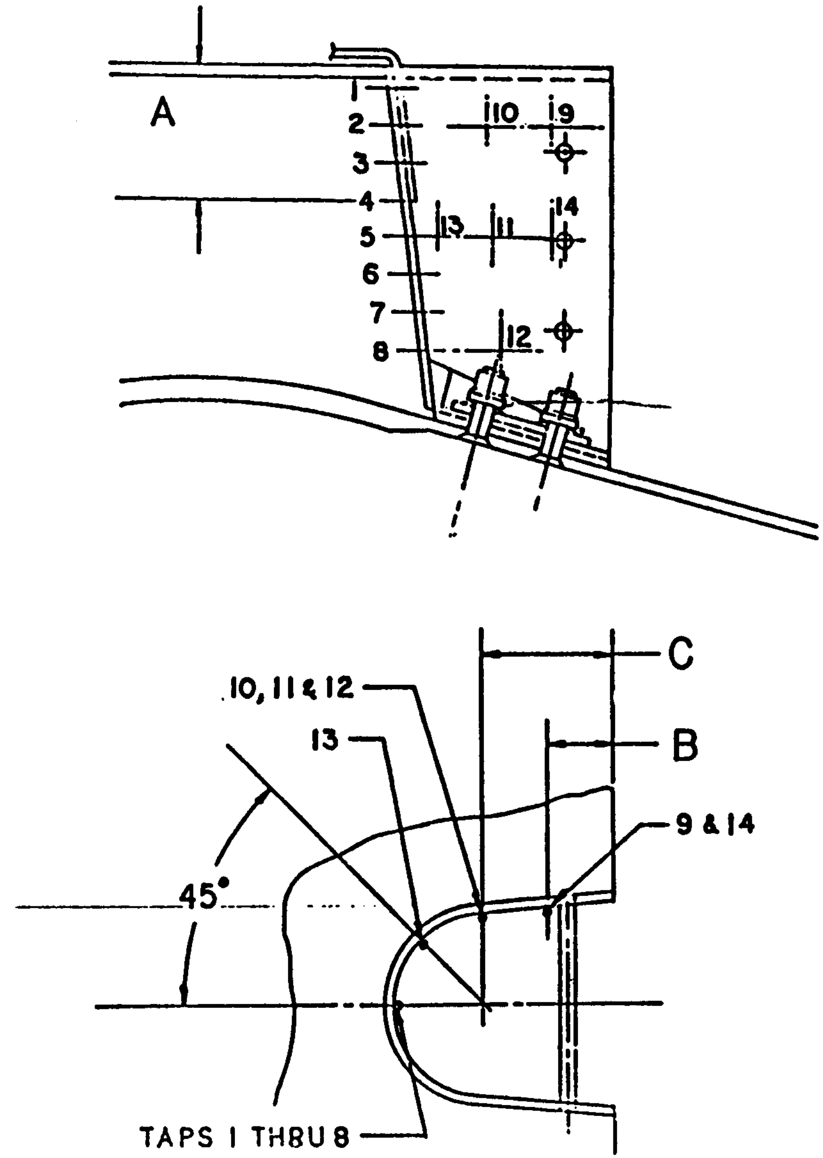

Figure III-1. Location of Fixed Static Pressure Probes in the Chutes of the Similitude 20-Shallow Chute Suppressor Nozzle.

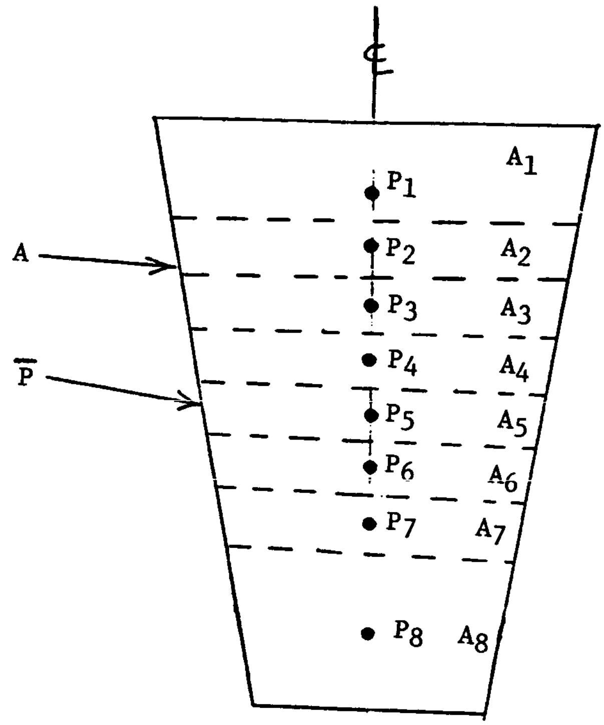

A_1 = 0.0952 in.^{2}

A_2 = 0.0806 in.^{2}

A_3 = 0.0799 in.^{2}

A_4 = 0.0778 in.^{2}

A_5 = 0.0763 in.^{2}

A_6 = 0.0755 in.^{2}

A_7 = 0.0741 in.^{2}

A_8 = 0.2162 in.^{2}

A = 0.7756 in.^{2}

Figure III-2. Projected Base Area of a Single Chute and Elemental Strip Areas.

SUPPRESSOR DRAG CALCULATION

$$PSUP/Pa = \bar{P}/Pa$$

$$\bar{P} = \frac{A_1P_1}{A} + \frac{A_2P_2}{A} + \frac{A_3P_3}{A} + \frac{A_4P_4}{A} + \frac{A_5P_5}{A} + \frac{A_6P_6}{A} + \frac{A_7P_7}{A} + \frac{A_8P_8}{A}$$

$$Fd = Pa\ (1 - PSUP/Pa)\ A$$

$$FD = 20\ Fd$$

$$\Delta C_{FGO} = \frac{FD}{FIDO}$$

NOMENCLATURE

A	Projected area of one chute in.^{2}
Ai	Elemental strip area within chute projected area
Fd	Suppressor drag contributed by a single chute base area
FIDO	Ideal outer nozzle thrust
FD	Total suppressor drag contributed by all chutes
Pa	Ambient pressure
Pi	Representative pressure reading within an elemental strip area of a chute
PSUP/Pa	Suppressor base to ambient pressure ratio
$\bar{P}$	Representative pressure reading within the projected area of one chute
ΔC_{FGO}	Change in outer nozzle thrust coefficient due to suppressor base drag

Figure III-3. Summary of the Expressions Used in the Calculation of the Base Drag

APPENDIX IV - C-D NOZZLE DESIGN CONSIDERATIONS

Previous attempts at reducing shock-associated noise through shock-free flow expansion have been made with annular jet systems. Figure IV-1 shows a coannular model with an outer C-D configuration from the NASA-Lewis/GE Contract NAS3-20619 (Ref. 2), and Figure IV-2 depicts a similar engine configuration tested on the YJ101 Test-Bed Engine under Contract NAS3-20582 (Ref. 7). In both instances, the convergent-divergent flowpath was configured within the basic constraint of utilizing a translating circular shroud. The translating circular shroud concept was selected as the closest approximation to product designs for AST/VCE exhaust systems. The translating shroud was required to accomplish proper flow expansion, allowing optimization of thrust coefficient at various flight conditions, in particular at supersonic cruise. Within this design constraint and in combination with the 15° plug, design of an exit plane to throat plane ratio (A_9/A_8), necessary to accomplish a C-D flowpath at takeoff, terminated the divergent flow section quite abruptly. This allowed only limited length for proper flow expansion before attaining the A_9/A_8 required to satisfy the expansion characteristics for shock-free flow at a selected takeoff type operating cycle. Additionally, ability to precondition the flow prior to the throat plane was limited by the cylindrical shroud design. Thus, gradual turning of the flow in a direction to assure that it would continue to follow the plug contour, once past the throat plane, was not accomplished. Flow turning, therefore, was felt to have continued past the throat plane and possibly interfered with the normal isentropic expansion process required to minimize or alleviate shock structure. Examination of the forward quadrant test data for the above model (typical data are shown in Figure IV-3) and engine configurations indicated minimal to negligible influence of the C-D design in the alleviation of the shock-cell associated noise.

A thorough reexamination of flowpath contouring procedures was conducted within the model design effort of this program and new criteria for the design of annular C-D flowpaths were identified. The new criteria precipitated principally from recent General Electric-funded design studies being conducted to optimize thrust performance of C-D flowpaths for other applications. General design elements are itemized in Figure IV-4 and are simplistically summarized as follows:

- Upstream flowpaths are to be designed to converge properly the flow into the throat plane such as to assure near complete flow turning prior to the throat plane. For annular plug nozzles, this corresponds to (1) moving the throat plane from a true radial position over the plug crown to an aft-of-the-plug crown position and (2) accomplishing a more gradual but vectored flow turning through contouring the outer shroud flowpath prior to throat plane.

- As changes in boundary layer conditions from throat plane to exit plane are normally assumed minimal, flow coefficients are assumed equal ($C_{D8} = C_{D9}$); and, based on the design pressure ratio, γ, fuel-to-air ratio and Mach number, the ideal A_9/A_8 is selected for isentropic flow expansion.

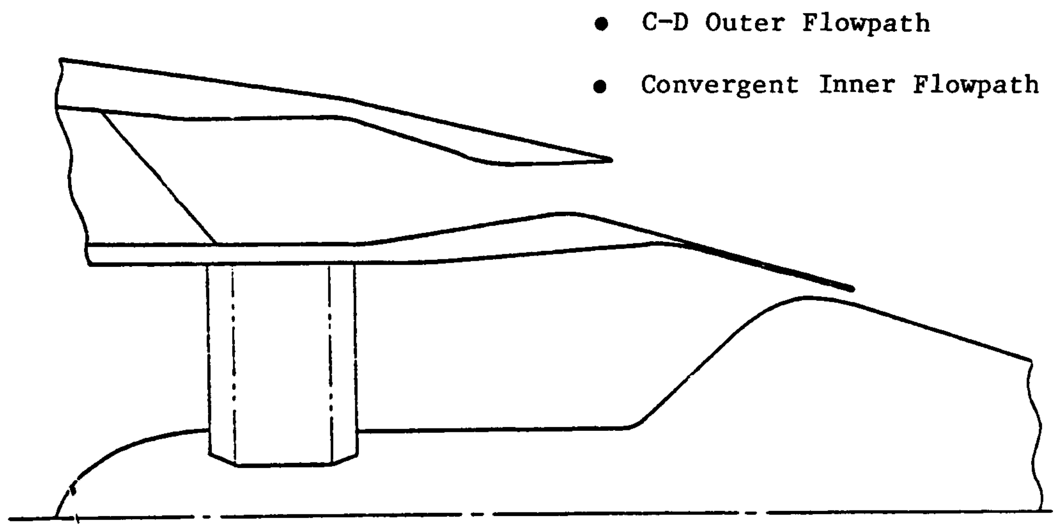

Figure IV-1. Outer Annular C-D Flowpath Design, Model Nozzle (NAS3-20619, Reference 2).

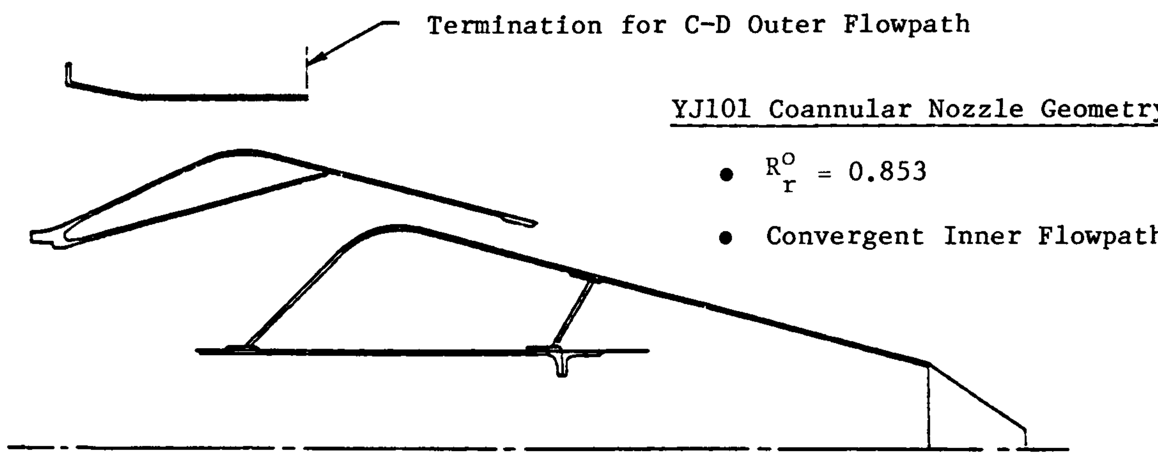

Figure IV-2. Outer Annular C-D Flowpath Design, YJ101 Engine (NAS3-20582, Reference 7).

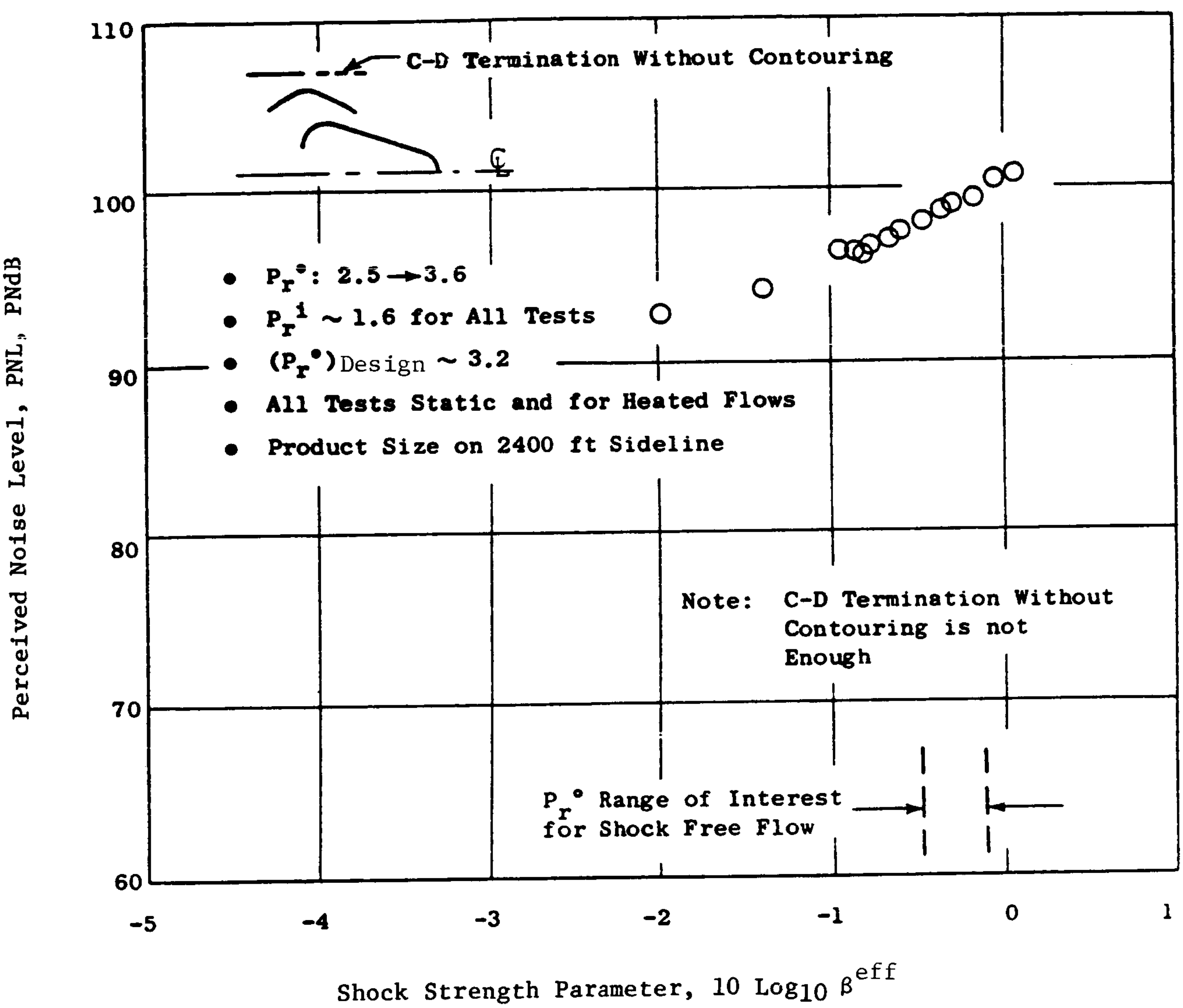

Figure IV-3. Coannular Plug Noxzle Acoustic Tests with Outer C-D Flow, But Without Proper Nozzle Contouring (Reference 2). PNL at $\theta_i = 60°$.

- Complete Flow Turning Prior to Throat Plane
- Select A_9/A_8 Ideal for Design Point (Pr, γ, F/A)
- Assume $C_{D8} = C_{D9}$
- Set $\theta_2 - \theta_1 \leq 5°$
- Allow Ample Divergent Length, ℓ, for Gradual Flow Expansion

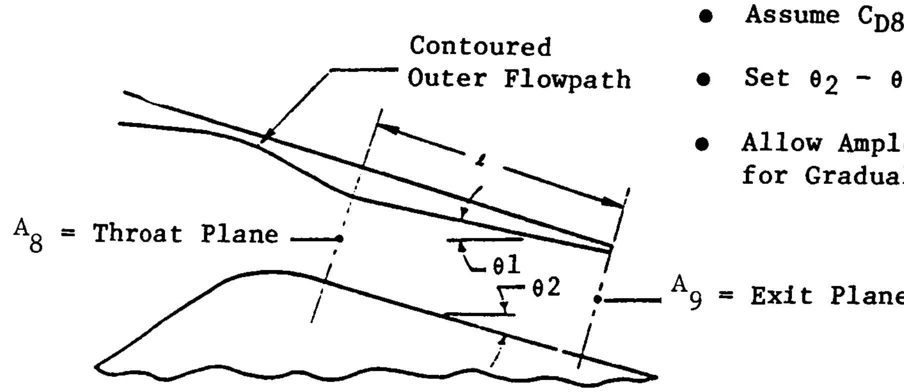

Figure IV-4. General Design Criteria for Annular C-D Flowpaths.

	NAS3-20019 Flowpath Using Early Design Criteria	NAS3-21608 Flowpath Using Current Design Criteria
Design PR	3.2	3.3
Flow Conditioning	Axial	Parallel to Plug
θ_2	15°	15°
θ_1	0°	10°
$\theta_2 - \theta_1$	15°	5°
l/h	0.85	3.4

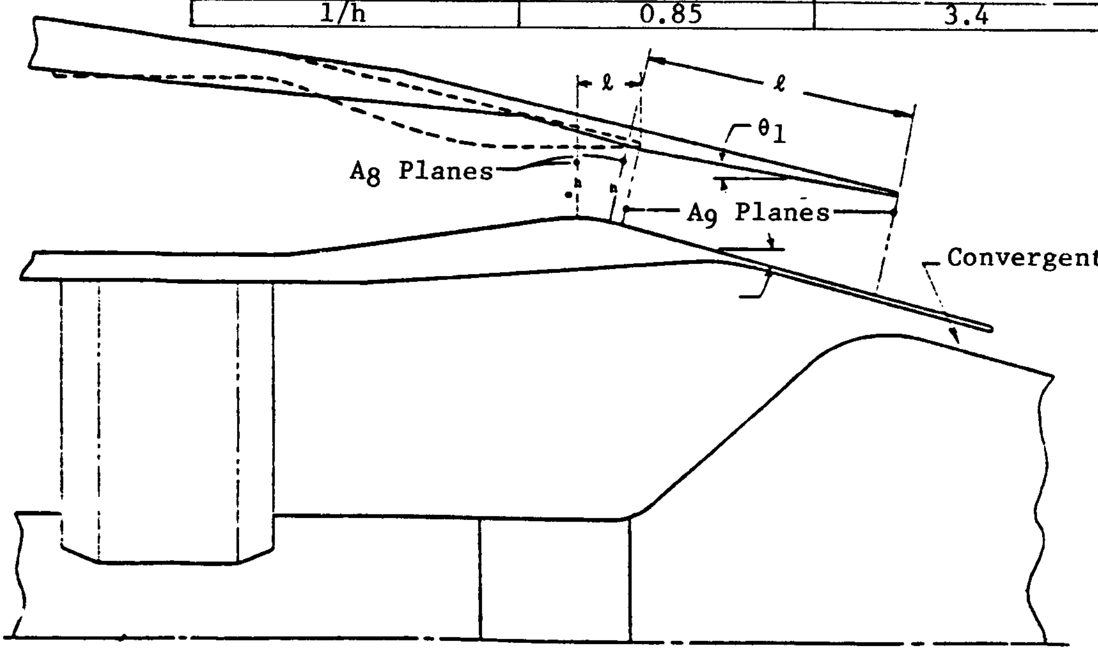

Figure IV-5. Comparison of Outer C-D Nozzle Flowpaths, Early and Current Design Criteria.

- For gradual flow divergence, plug angle minus shroud angle is set to $(\theta_2 - \theta_1) \leq 5°$. Previous designs had this value at 15°.

- The magnitude of θ_1 is to be iterated with length of divergent section, and design area ratio, A_9/A_8, until an adequate length of divergence is accomplished for gradual flow expansion.

A comparison of outer nozzle C-D flowpath designs using early and the more recent design criteria is shown in Figure IV-5. It is to be noted from this figure that the new design allows for preconditioning of the flow prior to the throat plane, by a $\theta_2 - \theta_1 = 5°$, and a length of divergent flowpath equal to 3.4 throat plane heights.

Based on the above considerations, detailed design of the annular C-D hardware was completed. Figure 2-10 summarizes the important dimensions. The design was later checked using the streamtube curvature (STC) computer program developed by the General Electric Company to analyze exhaust system internal flow fields (Ref. 16). Figure IV-6 illustrates the flow field solution generated by the STC program along with the calculated static pressure distribution along the center plug and the outer shroud. An examination of the nozzle exit matches the ambient pressure and hence denotes a complete expansion at the nozzle exit.

In addition to the above given design criteria, the following considerations pertaining to hardware design, manufacturing, and test setup were applied to ensure a complete expansion of the flow stream:

- For the annular plug convergent and C-D nozzle, use of support struts within two to three equivalent throat diameters upstream of the throat plane to maintain the outer flowpath hardware as an integral assembly to the inner flowpath hardware. This is to stabilize annular concentricity necessary to assure uniformity of flowpath and of A_9/A_8 ratios around the entire nozzle. The struts are aerodynamic in shape to minimize strut noise.

- A best estimate of the changes in the cold flow design dimensions is made to maintain the select design pressure ratio under hot flow operating conditions.

- Compatible materials were selected for various nozzle parts to accommodate thermal growth cycles relative to flowpath changes and thus ensure no leakage at flange connections. This is also necessary for general hardware safety at operating elevated temperatures.

- Flanges which connect various hardware pieces are normally designed to be drawn fit for axially bolted assemblies and interference fits for radially bolted assemblies and to hold flowpath concentricities and eliminate flow leakage from stream-to-stream or from stream-to-ambient.

- Contour tolerances and flowpath finishes are selected to assure accurately scalable models to AST/VCE product engine size.

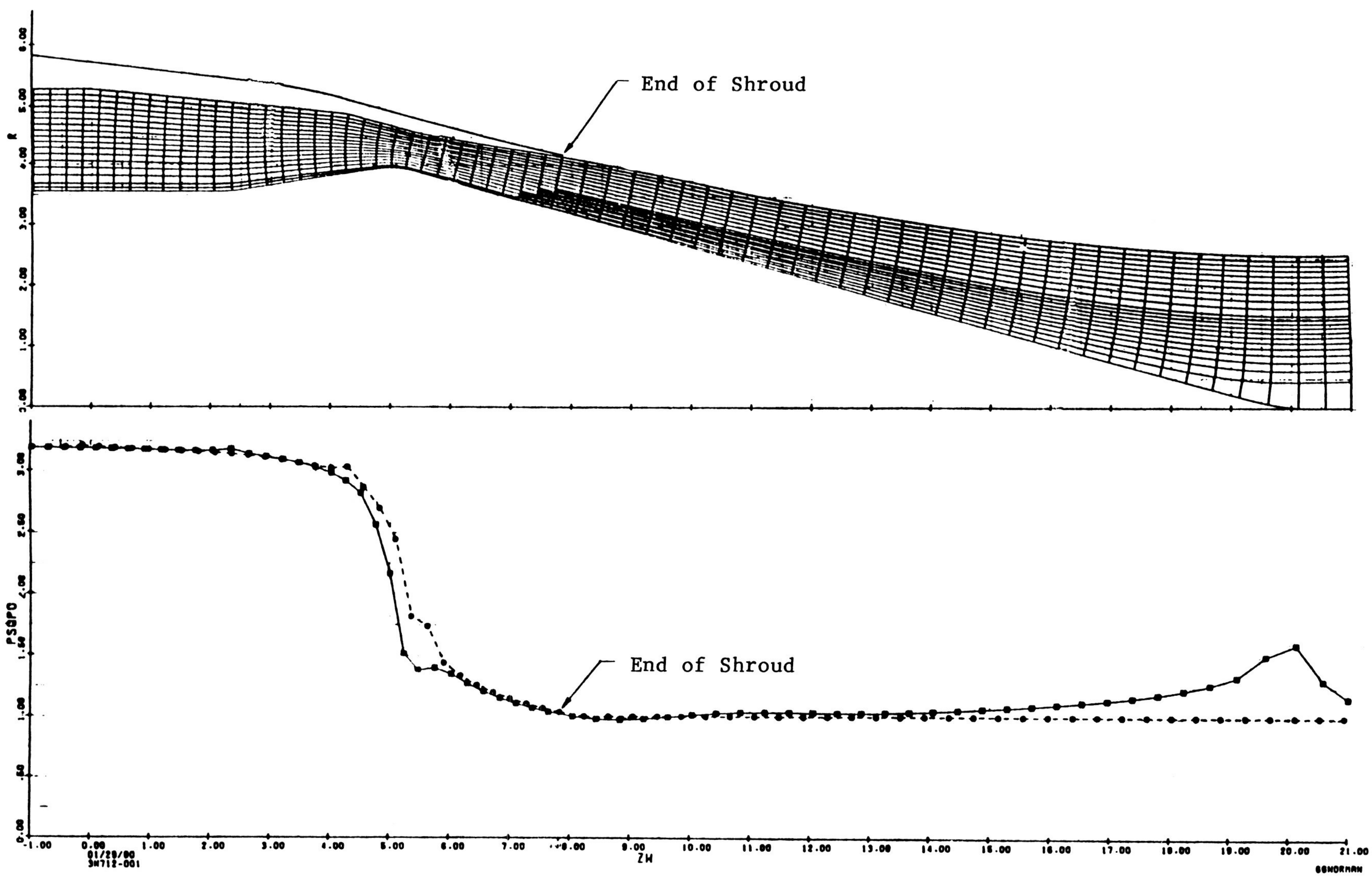

Figure IV-6. STC Results for Annular C-D Nozzle.

- Weldments and rough machined parts are stress relieved prior to final machining to assure dimensionally stable hardware. This is to assure that residual stresses are not present which, if relieved during high temperature testing, could distort aerodynamic flowpaths.

- Critical dimensions on all finished hardware are inspected in free-state prior to use and inspected dimensions recorded and checked for any discrepancy. Dimensional inspection of critical areas, such as annular throat and exit plant heights, is performed on the test configuration assembly to assure annular concentricity and proper buildup of flowpaths.

1. Report No.	2. Government Accession No.	3. Recipient's Catalog No.
NASA CR-3596		

4. Title and Subtitle

Free-Jet Investigation of Mechanically Suppressed, High-Radius-Ratio Coannular Plug Model Nozzles

5. Report Date

May 1985

6. Performing Organization Code

7. Author(s)

B. A. Janardan, R. K. Majjigi, J. F. Brausch, and P. R. Knott

8. Performing Organization Report No.

R81AEG484

10. Work Unit No.

9. Performing Organization Name and Address

General Electric Company
Aircraft Engine Business Group
Cincinnati, Ohio 45215

11. Contract or Grant No.

NAS3-21608

13. Type of Report and Period Covered

Contractor Report

12. Sponsoring Agency Name and Address

National Aeronautics and Space Administration
Washington, D.C. 20546

14. Sponsoring Agency Code

505-40-90 (E-2472)

15. Supplementary Notes

Final report. Project Manager, James R. Stone, Space Propulsion Technology Division, NASA Lewis Research Center, Cleveland, Ohio 44135.

16. Abstract

This report summarizes the experimental and analytical acoustic results of a scale-model investigation of unsuppressed and mechanically suppressed high-radius ratio coannular plug nozzles with inverted velocity and temperature profiles. Nine coannular nozzle configurations along with a reference conical nozzle were evaluated in General Electric's Anechoic Free-Jet Facility for a total of 212 acoustic test points. Most of the tests were conducted at Variable Cycle Engine conditions applicable to advanced high speed aircraft. The tested nozzles included coannular plug nozzles with a) both convergent and convergent-divergent (C-D) terminations in order to evaluate C-D effectiveness in the reduction of shock-cell noise and b) 20- and 40- shallow-chute mechanical suppressors in the outer stream in order to evaluate their effectiveness in the reduction of jet noise. In addition to the acoustic tests, mean and turbulent velocity measurements were made on selected plumes of the 20-shallow-chute configuration using a laser velocimeter. At a mixed jet velocity of 700 m/sec (~2300 ft/sec), the 20-shallow-chute suppressor configuration yielded peak aft quadrant suppression of 11.5 and 9 PNdB and forward quadrant suppression of 7 and 6 PNdB relative to a baseline conical nozzle during static and simulated flight, respectively. C-D terminations were observed to reduce shock-cell noise. In addition, acoustic scaling of model-scale data to engine size configurations was verified for conical and unsuppressed coannular nozzles. Finally, an engineering spectral prediction method was formulated for mechanically suppressed coannular plug nozzles.

17. Key Words (Suggested by Author(s))

Supersonic jet noise reduction; Mechanically suppressed coannular plug noise; Variable cycle engine; Flight noise simulation; Laser velocimeter measurements

18. Distribution Statement

[redacted]
Until May 1987

STAR Category 71

19. Security Classif. (of this report)	20. Security Classif. (of this page)	21. No. of pages	22. Price
Unclassified	Unclassified	248	

NASA-Langley, 1985